Search for leptonic CP violation
using measurements of neutrino oscillations
and neutrino-nucleus interactions

Kenji Yasutome

High Energy Physics Group
Division of Physics and Astronomy
Graduate School of Science
Kyoto University

Abstract

The universe consists of primarily matter. The origin of matter-antimatter asymmetry in the universe is unknown. Theories proposing that a lepton matter-antimatter asymmetry can be converted into a baryon asymmetry assume leptonic CP violation, which has not yet been observed. Discovering leptonic CP violation would support the theories and would be a key to understanding the origin of the matter-antimatter asymmetry in the universe. This thesis searches for leptonic CP violation by performing measurements of neutrino oscillation parameters and a measurement of neutrino cross sections using a new detector complex.

We need precise measurements of neutrino oscillation parameters to discover CP violation. The neutrino oscillation parameters are divided into a CP-violating phase (δ_{CP}), neutrino mixing angles ($\theta_{12}, \theta_{13}, \theta_{23}$), and neutrino mass squared differences (Δm_{21}^2, Δm_{32}^2). The angle θ_{23} is related to the octant problem; whether θ_{23} equals, less than or larger than $\pi/4$. The determination of Δm_{32}^2's sign determines the neutrino mass ordering; normal ordering ($m_{\nu_1} < m_{\nu_2} < m_{\nu_3}$) or inverted ordering ($m_{\nu_3} < m_{\nu_1} < m_{\nu_2}$). In this thesis, we tackle CP violation. The octant problem and the neutrino mass ordering are also considered.

The T2K experiment is a long-baseline accelerator neutrino experiment. Muon neutrinos or anti-muon neutrinos are generated at the proton accelerator (J-PARC), and the neutrino beam is directed towards a neutrino detector located 295 km away from J-PARC. T2K aims to discover leptonic CP violation and unravel the neutrino's properties. We perform an oscillation analysis using 19.663×10^{20} protons on target (POT) in the neutrino mode and 16.344×10^{20} POT in the anti-neutrino mode. We measure the ν_μ ($\overline{\nu}_\mu$) to ν_e ($\overline{\nu}_e$) oscillations and ν_μ ($\overline{\nu}_\mu$) to ν_μ ($\overline{\nu}_\mu$) oscillations to extract δ_{CP}, θ_{23} and Δm_{32}^2. CP conservation is rejected at the 90% confidence level. The 2σ confidence interval for δ_{CP} is [-π, -0.29] $\cup$ [3.04, π] in the normal ordering case. The 1σ confidence interval on $\sin^2 \theta_{23}$ is [0.460, 0.491] $\cup$ [0.526, 0.578] for the normal ordering. We see both cases ($\theta_{23} < \pi/4$ and $\theta_{23} > \pi/4$) within the 1σ intervals. The constraint on Δm_{32}^2 ($|\Delta m_{31}^2|$) is $2.506^{+0.047}_{-0.059} \times 10^{-3}$ eV^2/c^4 ($2.474^{+0.050}_{-0.056} \times 10^{-3}$ eV^2/c^4) for the normal (inverted) ordering. Regarding neutrino mass ordering, the normal ordering is weakly preferred with a Bayes factor of 2.8. The oscillation analysis is statistically limited, and the systematic uncertainty is not negligible. The systematic uncertainty from the uncertainty of neutrino interaction models has a large contribution.

For a further improvement in the precision of the oscillation parameters, we perform a neutrino cross section measurement using a new detector complex called WAGASCI-BabyMIND. The signal is defined as charged current muon neutrino interactions where no charged pions exist in the final state. We present cross section results on CH and H_2O targets with a peak neutrino energy of 0.86 GeV in limited phase space of the muon angle and momentum. Both measured integral and differential cross section as a function of muon momentum and angle are almost consistent with the neutrino interaction models used in our oscillation analysis. We compare the results with the predictions of other neutrino interaction models. No particular model is rejected or favored due to large statistical errors.

We demonstrate the impact of the conventional T2K near detector and WAGASCI-BabyMIND joint fit of the neutrino interaction samples on constraints of flux and cross section parameters. The improvement is around 30% at most to the fit without adding WAGASCI-BabyMIND samples. The constraints of the flux and cross section parameters are then used to extract δ_{CP}. The improvement is subtle in this analysis. Nevertheless, we pave the way for the application of the neutrino cross section measurements with the new detector complex to the oscillation analysis. This will offer a valuable approach to increase T2K's potential to discover leptonic CP violation.

Ms. Nao Izumi, and Ms. Hina Nakamura led by Prof. Masaki Ishitsuka, and Mr. Takashi Honjo, Prof. Yoshihiro Seiya from Osaka City University.

NINJA in WAGASCI

We invited the NINJA experiment, which specializes in neutrino interaction measurements with nuclear emulsions, to the same location where the WAGASCI measurements were performed. Massive thanks go to Prof. Tsutomu Fukuda, Dr. Ayami Hiramoto, and Dr. Takahiro Odagawa. We have meaningful discussions to mutually benefit from NINJA/WAGASCI measurements.

Oscillation analysis

I owe the neutrino oscillation analysis mainly to the four group leaders in T2K, Dr. Patrick Dunne, Dr. Clarence Wret, Dr. Ciro Riccio, and Dr. Benjamin Quilain. They always motivated us to obtain meaningful results in the analysis.

Brilliant teammates

Without the brilliant co-analyzers, we couldn't complete the oscillation analysis on a targeted schedule. I wish to thank Dr. Lukas Berns, Dr. Yohei Noguchi, Dr. Lucile Mellet, and Mr. Thomas Hovey for managing to finish all the analyses in time.

Cross section fitter, SuperxsllhFitter

Dr. Andrew Cudd developed his sophisticated fitting framework to extract cross sections, called Super-xsLLhFitter. He kindly provided any information we needed to apply his fitter to our analysis. Without him and the fitter, we wouldn't reach the final results on this time scale.

Contents

Part I

Introduction

1 Introduction to the thesis

1.1 Neutrino

Neutrinos are fundamental particles in the standard model (SM). They are neutral fermions that can interact with other particles only via weak force or gravity. A weak interaction of neutrinos occurs with an exchange of a $W^{\pm}$ boson (referred to as a charged current interaction) or a Z boson (referred to as a neutral current interaction). A charged current weak interaction can change a neutrino into its lepton partner (electron, muon, or tau). There are three neutrino flavors, corresponding to electron-neutrino, muon-neutrino, and tau-neutrino (ν_e, ν_μ, ν_τ).

Historically, W. Pauli first postulated the existence of an unknown neutral particle [1], which has later come to be known as the neutrino, to explain the electron's continuous spectrum in beta decay. Later, inspired by Pauli, E. Fermi established the theory of beta decay using this unknown neutral particle. The first observation of these neutrinos was achieved by F. Reines and C.L.Cowan et al. [2] in 1960. They made use of a nuclear reactor to observe anti-electron neutrinos. G.Danby et al. conducted an experiment generating a neutrino beam based on pion-decays ($\pi \to \mu\nu$) from a proton accelerator [3] in 1962. This experiment proved the existence of a distinct flavor of neutrino, muon neutrino other than the electron neutrino. In addition, utilizing a high-energy proton accelerator with 800 GeV protons enabled the DONUT experiment to observe the third flavor of neutrino, tau-neutrino [4] in 2001.

1.2 Neutrino oscillation

The neutrino flavors are not eigenstates of the Hamiltonian but are superpositions of three mass eigenstates, which are ν_1, ν_2, ν_3. A theory predicted that a neutrino could change its flavor in flight if there exists mixing between flavor and mass eigenstates of neutrinos and the masses of three mass eigenstates of neutrinos are different. This is referred to as "neutrino oscillation". The Super-Kamiokande (SK) experiment proved that the survival probability of neutrinos depends on their neutrino flavor, energy, and travel distance [5]. The experiment observed atmospheric neutrinos which were produced by pion decays initiated by the interaction between cosmic rays and the atmosphere. The experiment confirmed a deficit of muon-neutrinos in data with respect to the prediction "without oscillation" and the deficit was in line with the prediction taking into account oscillations. This was the case for muon-neutrino, while the experiment did not see a deficit of electron-neutrinos. On the other hand, the deficit of the electron neutrinos from the Sun was suggested by several experiments ([6–8]). The Sudbury Neutrino Observatory (SNO) found evidence that the neutrino oscillation caused the measured deficit of electron neutrinos in data compared to what was predicted from the Sun [9]. The unique feature of this experiment is that they utilized a heavy water target to discriminate the charged current neutrino interactions and neutral current interactions. Several experiments reported a deficit of electron neutrinos in data by measuring charged current interactions, compared to the solar models. They could not eliminate the possibility of the model prediction overestimating the actual electron neutrino flux. On the other hand, SNO was able to compare the neutrino flux measured by charged current interactions with the one measured by neutral current interactions. If the measured deficit by

other experiments was caused by the neutrino oscillation, the flux measured by charged current interactions was expected to be smaller. Therefore, the experiment was able to test the deficit independent of the solar models. In fact, SNO confirmed it was true. These experimental results also indicate that there exist at least three neutrinos in mass eigenstates at least two of which have non-zero masses.

As is already explained, we have known at least three flavors of neutrinos. The relationship between neutrinos in mass eigenstates and in flavor eigenstates is determined by a mixing matrix (PMNS matrix). The neutrino oscillation can be expressed by three mixing angles (θ_{12}, θ_{23}, θ_{13}), a CP-violating phase (δ_{CP}), and two mass squared differences ($\Delta m_{ij}^2 = m_{\nu_i}^2 - m_{\nu_j}^2$, where $\nu_{i(j)}$ is the $i(j)$th of neutrino mass eigenstates). It is necessary to experimentally determine these parameters. The parameters θ_{12} and Δm_{21}^2 have been precisely measured by solar neutrino experiments (for instance, Super-Kamikande [10]) and long-baseline reactor experiments (for instance, KamLAND [11]) so far. The value of θ_{13} has been constrained well by short-baseline reactor experiments (for instance, Daya Bay [12], RENO [13], and Double Chooz [14]). The parameters δ_{CP}, θ_{23}, and Δm_{32}^2 have been measured by atmospheric neutrino experiments and accelerator neutrino experiments (for instance, Super-Kamiokande [15] and T2K [16, 17]).

1.3 Unresolved issues in neutrino physics

The experiments have revealed important properties of neutrinos such as the neutrino oscillation. On the other hand, there are still unresolved issues. In particular, three important issues are tackled in this thesis; the CP violation in neutrinos, the neutrino mass ordering, and flavor symmetry of ν_μ and ν_τ.

1.3.1 CP violation in neutrinos

The CP violation in quarks was already discovered [18]. The CP violation can be a key to an important question in the universe where matters are dominant compared to anti-matters. The matter's abundant universe is among cosmological mysteries. The theory of Big-Bang nucleonsynthesis [19] and the observation of Cosmic Microwave Background (CMB) by Plank [20] independently extract the cosmological parameter of the baryon density ($\Omega_b h^2 = 0.0224 \pm 0.0001$ measured by Plank [20]), both of which are in agreement with each other. The value of $\Omega_b h^2$ is translated to the density of baryons (n_b) normalized by the relic blackbody photon density (n_γ). The equivalent value of $\eta_{10} = n_b/n_\gamma \times 10^{10}$ to $\Omega_b h^2 = 0.0224 \pm 0.0001$ is $5.8 \leq \eta_{10} \leq 6.6$ [19]. This implies the slight excess (by the order of 10^{-9}) in particles against anti-particles in the early universe have created the whole matter in the current universe after the annihilation, which is known as the matter-antimatter asymmetry or the Baryon Asymmetry of the Universe (BAU). The conditions to generate BAU are well known as the Sakharov conditions [21] that are the baryon number violation, the C violation, and the CP violation. Although the CP violation has been confirmed in quarks, it cannot explain the current baryon asymmetry by order of eight. Therefore, the CP violation in leptons or the mechanism for generating the baryon asymmetry is necessary to explain BAU. A promising solution was provided by M.Fukugita and T.Yanagida, who succeeded in explaining the BAU via a lepton asymmetry stemming from the CP violation in the leptonic sector assuming right-handed heavy neutrino [22]. In this scenario called leptogenesis, assuming the CP violation, the difference in the decay rate of right-handed neutrinos (N_1) between $N_1 \to l, H$ and $N_1 \to \bar{l}, \bar{H}$ results in the lepton number violation. This is converted into the baryon number violation via the sphaleron process preserving B-L [23].

Another theory [24] proposed that leptogenesis could be understood by the CP-violation of the active neutrino oscillation. In the early universe, inflationary universe, high-energy neutrinos are generated by the decay of inflatons (ϕ) as in

$$\phi \to \nu_{\text{ini}} + X, \bar{\phi} \to \bar{\nu_{\text{ini}}} + \bar{X}. \tag{1.1}$$

Until the neutrino scatters, generated neutrinos are subject to the flavor oscillation. Assuming the CP violation in this process, the flavor-dependent lepton asymmetry can occur, where no net lepton asymmetry is generated because the tau-neutrino asymmetry can be compensated by electron-neutrino and muon-neutrino asymmetry. When neutrinos are scattered off Higgs bosons, the lepton number violating interaction, $llHH$ interaction can occur, which washes out the lepton number asymmetry. However, this scattering happens in different manners between tau-neutrino and other flavors of neutrinos. The process can then make the lepton number violation. The lepton number asymmetry leads to the baryon number asymmetry through the sphaleron process.

The leptogenesis scenario via active neutrino oscillation assumes the CP-violation in the neutrino oscillation. The CP violation has not been observed. Long-baseline neutrino oscillation experiments are good probes for the CP-violation. Discovering or disproving it gives a hint to comprehending how the current universe was generated in the context of BAU.

1.3.2 Neutrino mass ordering

The observations of the neutrino oscillations indicate three neutrino masses are different. The mass scale of three mass eigenstates of neutrinos is found to be less than 1 eV/c^2. The current experiments have not reached the precision of measuring such tiny neutrino masses. On the other hand, the difference in neutrino masses can be measured by neutrino oscillations thanks to the fact that the probability of neutrino oscillations differs in matters compared to those in a vacuum, which is referred to as "matter effect". In neutral current interactions, all neutrino flavors are equally treated assuming matter consists of protons and neutrons, and electrons. Only electron neutrinos experience interactions with electrons present in the matter via charged current scattering. This effect is enhanced in the Sun, which affects the oscillation probability of electron neutrinos. Then solar neutrino experiments measuring the electron neutrino oscillations were able to determine the sign of Δm_{21}^2. On the other hand, the sign of Δm_{32}^2 is still unknown. Therefore, we have two cases of neutrino mass orderings, which are $m_{\nu_1} < m_{\nu_2} < m_{\nu_3}$ (Normal Ordering) and $m_{\nu_3} < m_{\nu_1} < m_{\nu_2}$ (Inverted Ordering). The neutrino mass ordering is another important issue in neutrino physics.

The neutrino mass ordering captures attention not only of fundamental particle physics but also of other fields such as nuclear physics, cosmology, and astrophysics. From the fundamental particle physics point of view, one of the approaches is neutrino oscillation experiments. In atmospheric neutrino experiments and long-baseline accelerator neutrino experiments, neutrinos travel in the earth interacting with matter where they are subject to the matter effects. The matter effects affect the neutrino oscillation probability in different ways depending on the neutrino mass ordering. Atmospheric neutrino experiments and long-baseline accelerator neutrino experiments have sensitivities to the mass ordering, both of which slightly prefer presently the normal ordering.

Another approach comes from nuclear physics in the context of the measurements of the neutrino absolute mass. The endpoint of the Kurie function for the β decay in the case of massive neutrinos deviates from the endpoint in the case of massless neutrinos. The precise

measurement of the shift of the endpoint is sensitive to the neutrino absolute mass. The behaviors of the deviation around the endpoint are different between the two mass orderings, which allows the experiment potentially to explore the right mass ordering. The energy resolution, however, limits the sensitivity.

The sum of all neutrinos' masses can be different depending on the neutrino mass ordering. [1] With the best-fit values for neutrino mass differences from neutrino oscillation experiments, the lower bound of the sum of neutrino masses is given, $\sum m_\nu > 0.06$ eV/c^2 (NO) and $\sum m_\nu > 0.1$ eV/c^2 (IO) [25]. The upper bound of the sum of neutrino masses is constrained by cosmological surveys. The total neutrino masses affect the shape and the size of the small-scale [2] matter power spectrum because of the growth rate of cold dark matters or baryons depleted due to the free-streaming of neutrinos [26]. The effect of the matter power spectrum is not large in galaxy clustering and gravitational lensing of galaxies, whereas the effect of the mass ordering on the CMB is inflated. CMB convergence angular power spectra are weighted by the matter spectrum, and the measurement of the power spectrum becomes sensitive to the sum of neutrino masses. These angular power spectra can be reconstructed from CMB temperature and polarization maps [27]. The stringent constraint on the sum of neutrino masses comes from the Plank satellite observation utilizing the gravitational lensing effect on CMB [28]. The constraint on the total neutrino mass leads to the higher sensitivity to the neutrino mass ordering combined with the results from oscillation experiments in particle physics. In addition to the gravitational lensing effect, precise measurements of the Hubble constant (H_0) play a role in increasing sensitivity because it has a strong anti-correlation with the total neutrino masses [25].

The preference for the normal ordering is currently around 3σ [25] by combining results from neutrino oscillation measurements, nuclear physics experiments, CMB observations, and Hubble constant measurements. It should be noted that the oscillation experiments have the fundamental role of examining the mass ordering.

1.3.3 Flavor symmetry

Recent experiments show the value of θ_{23} lies around $\pi/4$ ($\theta_{23} = \pi/4 + \epsilon$), but it is uncertain that ϵ is exactly 0 (maximal mixing) or less (more) than 0, known as the θ_{23} octant puzzle. The value of ϵ being 0 leads to $\mu - \tau$ flavor symmetry, which is reviewed concisely in [29]. Historically, this flavor symmetry was explored assuming $\theta_{23} = \pi/4$ and $\theta_{13} = 0$ which had been indicated by the earlier experiments. This assumption led to the permutation symmetry, which gave important insights into how the flavor structures are constructed in the mixing matrix. The recent experiments, however, prefer non-maximal mixing of θ_{23} and confirm the non-zero value of θ_{13}. An alternative approach, called "$\mu - \tau$ reflection symmetry" has been proposed [30], where the assumption of the theory is $\theta_{23} = \pi/4$ and $\delta_{\rm CP} = \pm\pi/2$, which are still allowed at 1σ to 2σ significance.

The consequences of the maximal mixing of θ_{23} leading to the $\mu - \tau$ flavor symmetry are also discussed in [29]. As for the connection to the Baryon Asymmetry of the Universe, the

---

[1]

$$\sum m_\nu = m_1 + \sqrt{m_1^2 + \Delta m_{21}^2} + \sqrt{m_1^2 + \Delta m_{31}^2} \quad \text{(Normal Ordering)},$$
$$\sum m_\nu = m_3 + \sqrt{m_3^2 + |\Delta m_{31}^2|} + \sqrt{m_3^2 + |\Delta m_{31}^2| + \Delta m_{21}^2} \quad \text{(Inverted Ordering)}. \tag{1.2}$$

[2]Here "small" refers to the neutrino's wavenumber being much larger than the minimum wavenumber after the thermal decoupling in the universe.

lepton and anti-lepton asymmetry is associated with the flavor symmetry. If the permutation symmetry is assumed, a certain strength of symmetry breaking is necessary for the current simple leptogenesis hypothesis to work well [31]. The strength of the symmetry breaking estimated from the currently expected θ_{13} is sufficient to make the simple leptogenesis hypothesis work.

More precise measurements of θ_{23} are going to reveal the existence of $\mu - \tau$ flavor symmetry, which also leads to giving an insight into the CP violation.

1.4 The T2K experiment

In order to unravel the three problems (the CP-violation, neutrino mass ordering, and the θ_{23} octant), the precise measurements of δ_{CP}, Δm_{32}^2 including its sign, and θ_{23} are imperative. For the δ_{CP} measurements, experiments must be sensitive to the difference in the oscillation probabilities of neutrino and anti-neutrino. To break the degeneracy of the two possible mass orderings, neutrinos should be subject to a sufficient matter effect in the earth. For the measurements of θ_{23}, a muon neutrino beam is preferable because the expected number of events in the dip of the survival probability for ν_μ beam varies depending on $\sin^2 2\theta_{23}$. Therefore, a long baseline neutrino experiment, accelerator or atmospheric neutrino experiments using both muon and anti-muon neutrinos generated is desirable. This thesis tackles these issues through one of the accelerator experiments, called "T2K experiment".

The T2K experiment has made use of the high-intensity proton beam accelerator (J-PARC) to produce neutrino beam and Super-Kamiokande (SK) as the far neutrino detector. The 30 GeV high-intensity proton beam provided by J-PARC accelerators is injected into a graphite target, producing charged pions. The T2K beamline is equipped with three electromagnetic horns to focus charged pions. The two-body decay of focused charged pions produces a high-intensity neutrino beam with a peak energy of 0.6 GeV directed toward SK. The polarity of the horns determines which charged pions are focused. This in turn provides a way to choose which neutrino beam (ν_μ or $\overline{\nu}_\mu$) is produced. The T2K experiment installed a suite of near neutrino detectors to characterize the neutrinos by measuring the interactions before oscillations set in. SK is a water Cherenkov detector, containing 50,000 tons of water viewed by about 11,000 PMTs.

As the initial neutrino flavor is mostly ν_μ (or $\overline{\nu}_\mu$) in the neutrino beam, the oscillation of $\nu_\mu\ (\overline{\nu}_\mu) \to \nu_e\ (\overline{\nu}_e)$ or $\nu_\mu\ (\overline{\nu}_\mu) \to \nu_\tau\ (\overline{\nu}_\tau)$ is measured. As the mean neutrino energy is around 1 GeV, most tau-neutrinos cannot undergo charged current interactions. Therefore, ν_e appearance ($\nu_\mu \to \nu_e$) and ν_μ disappearance ($\nu_\mu \to \nu_\mu$) are the objects measured in this experiment. While neutrinos travel to SK, they pass through the earth. The matter effect is not negligible. The size of the matter effect depends on the density of electrons along the propagation path of the neutrinos (n_e), the weak interaction coupling constant (G_F), and the travel length over neutrino energy (L/E). The oscillation probability of $\nu_\mu\ (\overline{\nu}_\mu) \to \nu_e\ (\overline{\nu}_e)$ can be expressed to first order in the matter effect by

$$P\left(\overset{\scriptscriptstyle(-)}{\nu}_\mu \to \overset{\scriptscriptstyle(-)}{\nu}_e\right) \simeq \sin^2\theta_{23}\frac{\sin^2 2\theta_{13}}{(A-1)^2}\sin^2[(A-1)\Delta_{31}]$$

$$\overset{(+)}{-}\,\alpha\frac{J_0\sin\delta_{\mathrm{CP}}}{A(1-A)}\sin\Delta_{31}\sin(A\Delta_{31})\sin[(1-A)\Delta_{31}]$$

$$+\,\alpha\frac{J_0\cos\delta_{\mathrm{CP}}}{A(1-A)}\cos\Delta_{31}\sin(A\Delta_{31})\sin[(1-A)\Delta_{31}]$$

$$+\,\alpha^2\cos^2\theta_{23}\frac{\sin^2 2\theta_{12}}{A^2}\sin^2(A\Delta_{31}),\tag{1.3}$$

where

$$\alpha = \Delta m_{21}^2/\Delta m_{31}^2$$
$$\Delta_{ij} = \Delta m_{ij}^2 L/4E$$
$$A = (-)2\sqrt{2}G_F n_e E/\Delta m_{31}^2$$
$$J_0 = \sin 2\theta_{12}\sin 2\theta_{13}\sin 2\theta_{23}\cos\theta_{13}.\tag{1.4}$$

Equations 1.3, 1.4 come from [32]. The sign of the second term in Equation 1.3 is negative for neutrinos and positive for anti-neutrinos. Since the neutrino mass ordering is related to the sign of Δm_{31}^2, Equation 1.3 is also sensitive to the mass ordering. The first term of Equation 1.3 is proportional to $\sin^2\theta_{23}$ which makes the ν_e ($\bar\nu_e$) appearance probability sensitive to the θ_{23} octant. As Equation 1.3 contains $\sin\delta_{\mathrm{CP}}$ term, whose signs are opposite between neutrino and anti-neutrino cases, it can change the appearance probability by at most $\pm$ 30% depending on δ_{CP} assuming the currently measured mixing angles. This makes the appearance probability sensitive to the CP violation.

1.5   Measurement of oscillation parameters

In this thesis, the oscillation analysis is performed with an improvement in the statistics compared to the previous release. In the T2K data taking, the measurement of neutrino beam profiles is essential to ensure the neutrinos are properly directed to the far detector. One of the neutrino beam monitors is called MUMON, which is the only monitor to measure the beam profiles on a bunch-by-bunch basis in T2K. We perform the calibration of electronics and sensors for the beam operation, and monitor the neutrino beam throughout the whole data taking. Only the neutrino beam that is satisfied with the criterion on the beam profiles is used in the oscillation analysis.

For the oscillation analysis, T2K has established a suite of methods. The analysis is divided into five steps; predicting neutrino flux precisely, establishing a robust neutrino interaction simulator, constraining flux and interaction parameters based on neutrino-nucleus cross section measurements from the near detectors, selecting analysis samples at SK, and finally extracting oscillation parameters by fitting to the data. The T2K oscillation analysis methods increase the sensitivity to CP violation and mass ordering to the highest level in the world. This thesis explains each step of the oscillation analysis and presents constraints on the neutrino oscillation parameters based on the latest oscillation analysis results from the T2K experiment.

Even though the T2K experiment has world-leading results on the CP violation, the mass ordering, and the θ_{23} octant, the precision has not been sufficient for the discoveries yet. The latest results are still statistically limited, but thanks to continuous efforts to increase the intensity

of the neutrino beam, the statistical uncertainty will be reduced to the level of the systematic uncertainty in the future. The reduction in the systematic uncertainty is expected to increase the discovery potential of T2K.

1.6 Difficulties in precise measurements of oscillation parameters for the T2K experiment

In extracting constraints on oscillation parameters by the T2K experiment, we compare the observed number of events to that of expected events by simulation. The expected number of events before oscillation is proportional to the product of neutrino flux, neutrino cross section, and detection efficiency at SK. Therefore, the measurement precisions are determined not only by statistical uncertainty but also by the systematic uncertainties coming from these factors.

The dominant systematic error comes from the uncertainty of interaction models. As the T2K neutrino energy is around 1 GeV, neutrino-nucleus interactions are complicated because of many-body interactions inside a nucleus, which is known as nuclear medium effects. This makes both precise theoretical calculations and precise measurements difficult, which leads to discrepancies between different models or between models and measurements. Poor understanding of neutrino interactions inflates the uncertainty on neutrino cross sections. A mis-modeling of neutrino interactions may have an effect on the energy reconstruction of neutrinos. As neutrino oscillation probability depends on neutrino energy, it is necessary to measure the number of expected events at the far detector as a function of neutrino energy in the oscillation analysis. In order to reconstruct neutrino energy, for most analysis samples, we assume simple charged current interactions where there is a charged lepton and no mesons or hadrons except outgoing nucleons in the final state, called CC0π events. We measure the lepton kinematics by the Cherenkov ring at SK to reconstruct the energy of the parent neutrino.

In reality, however, it is sometimes difficult to separate CC0π events from neutrino interactions where a single pion is produced (CC1π events) due to the nuclear medium effects that may cause pions to be absorbed inside the detector before being detected. When the reconstruction formula for the CC0π events is applied to the CC1π events contaminating into CC0π events, it introduces a bias into the reconstructed energy. The effect of this bias affecting the neutrino oscillation measurements can be mitigated with simulations, but the mis-modeling of nuclear medium effects can still cause the reconstruction bias in the analysis.

1.7 Measurement of neutrino interactions

The T2K experiment has performed various measurements on neutrino-nucleus interactions with its near detector. Disadvantages of the near detectors are its target material being mainly hydrocarbon (CH) and limited particle acceptance. As the far detector deploys a water target and has 4π acceptance for outgoing particles, there exist differences in target materials and acceptances between near and far detectors. These differences result in uncertainties in neutrino oscillation measurements.

In order to deal with these differences, we proposed a new detector complex called WAGASCI-BabyMIND detectors to measure neutrino interactions with similar conditions to the far detector. The main target detector, WAGASCI is comprised of plastic scintillators submerged in water with 4π coverage of outgoing charged particles thanks to the three-dimensional grid structure of the scintillators. This detector provides mainly a water target with hydrocarbon. The fraction of H_2O to CH is 4:1. As the interaction on the CH target can be the main background of this

measurement, we installed a fully CH target detector to constrain the cross section on the CH target in WAGASCI. Another characteristic of this detector complex is its location where the mean energy of the neutrino is different from that at the near detector location.

The detector installation was completed in 2019. We have taken physics data whose statistics correspond to 2.96×10^{20} protons on target. This thesis presents the primary cross section measurement with this detector complex. In addition to the cross section results, we also compare neutrino interaction models such as NEUT and GENIE with the data fit results. This thesis, moreover, shows the way of applying this measurement to the oscillation analysis to provide better constraints on neutrino interaction models.

1.8   Outline of the thesis

This thesis is comprised of four parts. The first part describes the current status of neutrino physics and focuses the subject on the T2K experiment. The second part explains the analysis methods from the T2K experiment and presents the latest oscillation analysis results. The third part switches the subject to a study of neutrino interactions aiming for improving the precision of constraints on the neutrino interaction and flux parameters used in the T2K oscillation analysis. The final part summarizes this thesis.

Chapter 2 covers the generic formalism of neutrino oscillations. Not only the derivation of mathematical formulae but the contemporary measurements of each oscillation parameter from various experiments are also shown. Chapter 3 describes the principle of the T2K experiment and overviews the experimental apparatus of T2K. Chapter 4 introduces the underlying neutrino interaction models and difficulties that accelerator neutrino experiments bear in common.

The next part starts with the measurement of the neutrino beam in Chapter 5. It is followed by the oscillation analysis methods of the T2K experiment in Chapter 6. The descriptions are based on the methods in the published results. The published results have been updated based on the analysis described in this chapter. The differences between the published results and the updated results are also mentioned. Chapter 7 presents the updated results of the oscillation analysis. The results are discussed in the contexts of the robustness, the impact on the neutrino community, and the future prospect to improve the T2K's sensitivity in Chapter 8. The current limitation of the oscillation analysis results is also considered in this section.

The third part discusses the measurement of neutrino interaction in the context of improving the sensitivity for the oscillation analysis with the T2K experiment. Chapter 9 describes detector complex to measure the neutrino interaction using the T2K neutrino beam line. Methodologies to analyze data in this analysis are described in Chapter 10. The definition of signal samples and event selections are discussed in Chapter 11 along with the analysis method of the cross section extraction. The results of the data fit are shown in Chapter 12 as well as consideration of these results. One way to apply cross section results to the oscillation analysis is presented in Chapter 13.

Chapter 14 in the final part concludes this thesis.

2 Neutrino oscillation

This chapter describes the neutrino oscillation starting from the general formalism to the three flavors case. In the end, the current measurement status of oscillation parameters of δ_{CP}, Δm_{21}^2, $\sin^2 \theta_{12}$, $\sin^2 \theta_{13}$, Δm_{32}^2, and $\sin^2 \theta_{23}$ are explained.

2.1 General formalism

This section introduces a formalism of the neutrino oscillation based on the reference [33]. We adopt the natural unit system where $c = 1, \hbar = 1$. We assume n flavor eigenstates denoted by ν_α are associated with n mass eigenstates denoted by ν_i via a unitary mixing matrix U. Each flavor/mass eigenstate is expressed by the following formulae

$$|\nu_\alpha\rangle = \sum_i U_{\alpha i} |\nu_i\rangle \qquad |\nu_i\rangle = \sum_\alpha (U^\dagger)_{i\alpha} |\nu_\alpha\rangle = \sum_\alpha U_{\alpha i}^* |\nu_\alpha\rangle, \tag{2.1}$$

where

$$U^\dagger U = 1 \qquad \sum_i U_{\alpha i} U_{\beta i}^* = \delta_{\alpha\beta} \qquad \sum_\alpha U_{\alpha i} U_{\alpha j}^* = \delta_{ij}. \tag{2.2}$$

Replacing the $U_{\alpha i}$ by $U_{\alpha i}^*$ gives the expressions for anti-neutrinos as in

$$|\bar{\nu}_\alpha\rangle = \sum_i U_{\alpha i}^* |\bar{\nu}_i\rangle. \tag{2.3}$$

The mass eigenstates $|\nu_i\rangle$ are stationary states and show a time dependence given by

$$|\nu_i(x,t)\rangle = \exp(-iE_i t) |\nu_i(x,0)\rangle. \tag{2.4}$$

The initial condition that neutrinos with the momentum p are emitted by a source positioned at $x = 0(t = 0)$ is represented by

$$|\nu_i(x,0)\rangle = \exp(ipx) |\nu_i\rangle. \tag{2.5}$$

In addition, we assume neutrinos are relativistic, which makes the following equation of

$$E_i = \sqrt{m_i^2 + p_i^2} \simeq p_i + \frac{m_i^2}{2p_i} \simeq E + \frac{m_i^2}{2E} \tag{2.6}$$

valid because of $p \gg m_i$, $E \simeq p$.

For further discussions, we assume the mass differences between two neutrino mass eigenstates are not identical to 0. Then a flavor neutrino is a coherent superposition of neutrino mass eigenstates. Neutrinos are detected as flavor states. The flavor states are expressed by

$$|\nu(x,t)\rangle = \sum_i U_{\alpha i} \exp(-iE_i t) |\nu_i\rangle = \sum_{i,\beta} U_{\alpha i} U_{\beta i}^* \exp(ipx - iE_i t) |\nu_\beta\rangle. \tag{2.7}$$

The assumption of neutrino being relativistic gives more specific expressions of E_i and it gives

$$|\nu(x,t)\rangle = \sum_{i,\beta} U_{\alpha i} U_{\beta i}^* \exp\left(ipx - iEt - i\frac{m_i^2}{2}\frac{1}{E}t \right) |\nu_\beta\rangle$$

$$\simeq \sum_{i,\beta} U_{\alpha i} U_{\beta i}^* \exp\left(-i\frac{m_i^2}{2}\frac{L}{E} \right) |\nu_\beta\rangle, \tag{2.8}$$

where $L = x = ct$. Equation 2.8 indicates non-zero mass differences change the phase whose effect is potentially significant at the macroscopic distance compensating for tiny mass differences. The time-dependent transition amplitude for a flavor conversion $\nu_\alpha \to \nu_\beta$ is given by

$$A(\alpha \to \beta)(t) = \langle \nu_\beta | \nu(x,t) \rangle = \sum_i U_{\alpha i} U_{\beta i}^* \exp\left(-i\frac{m_i^2}{2}\frac{L}{E} \right). \tag{2.9}$$

In an analogous way, the amplitude for an anti-neutrino transition is given in Equation 2.10, which is

$$A(\bar\alpha \to \bar\beta)(t) = \sum_{i,\beta} U_{\alpha i}^* U_{\beta i} \exp\left(-i\frac{m_i^2}{2}\frac{L}{E} \right). \tag{2.10}$$

The measurement of oscillation probability of $\nu_\alpha \to \nu_\beta (\alpha \neq \beta)$ and its conjugate process $\bar\nu_\alpha \to \bar\nu_\beta$ provides a way to test the hypothesis of the CP violation in neutrinos. One observable in this hypothesis testing is $\Delta P_{\alpha\beta}^{\mathrm{CP}}$ given by

$$\Delta P_{\alpha\beta}^{\mathrm{CP}} = P(\nu_\alpha \to \nu_\beta) - P(\bar\nu_\alpha \to \bar\nu_\beta) \qquad \alpha \neq \beta. \tag{2.11}$$

Each transition probability is obtained from the transition amplitude A using Equations 2.9, 2.10, which are

$$P(\nu_\alpha \to \nu_\beta) = |A(\nu_\alpha \to \nu_\beta)|^2 = \sum_i \sum_j U_{\alpha i} U_{\alpha j}^* U_{\beta i}^* U_{\beta j} \exp(-i(E_i - E_j)t)$$

$$= \sum_i |U_{\alpha i} U_{\beta i}^*|^2 + 2\mathrm{Re} \sum_{j>i} U_{\alpha i} U_{\alpha j}^* U_{\beta i}^* U_{\beta j} \exp\left(-i\frac{\Delta m_{ij}^2}{2} \right)\frac{L}{E}, \tag{2.12}$$

$$P(\bar\nu_\alpha \to \bar\nu_\beta) = |A(\bar\nu_\alpha \to \bar\nu_\beta)|^2 = \sum_i \sum_j U_{\alpha i} U_{\alpha j}^* U_{\beta i} U_{\beta j}^* \exp(-i(E_i - E_j)t)$$

$$= \sum_i |U_{\alpha i}^* U_{\beta i}|^2 + 2\mathrm{Re} \sum_{j>i} U_{\alpha i}^* U_{\alpha j} U_{\beta i} U_{\beta j}^* \exp\left(-i\frac{\Delta m_{ij}^2}{2} \right)\frac{L}{E}. \tag{2.13}$$

Here, Δm_{ij}^2 represents the mass differences of two neutrino mass eigenstates, ν_i and ν_j, defined by $\Delta m_{ij}^2 = m_{\nu_i}^2 - m_{\nu_j}^2$.

2.2 Three flavors case

The standard model assumes three-flavor neutrinos. In this section, we discuss the neutrino oscillation accordingly. Neutrino flavor eigenstates are the superpositions of neutrino mass eigenstates. Pontecorvo-Maki-Nakagawa-Sakata matrix (PMNS matrix) was proposed to describe the

mixing of three-flavor neutrinos. We use the following type of PMNS matrix to write down Equation 2.12.

$$U = \begin{pmatrix} c_{12}c_{13} & s_{12}c_{13} & s_{13}e^{-i\delta} \\ -s_{12}c_{23} - c_{12}s_{23}s_{13}e^{i\delta} & c_{12}c_{23} - s_{12}s_{23}s_{13}e^{i\delta} & s_{23}c_{13} \\ s_{12}s_{23} - c_{12}s_{23}s_{13}e^{i\delta} & -c_{12}s_{23} - s_{12}c_{23}s_{13}e^{i\delta} & c_{23}c_{13} \end{pmatrix}, \tag{2.14}$$

where $s_{ij} = \sin\theta_{ij}$ and $c_{ij} = \cos\theta_{ij}$. The parameter δ is the complex term. [3] In the standard model, the PMNS matrix is unitary. In this case, there are 4 degrees of freedom (three real numbers and one complex number) in a 3-by-3 complex matrix. Parameters θ_{ij} are the mixing angles in three-flavor neutrinos corresponding to the three real numbers. The parameter δ is the complex number as the rest of the degrees of freedom, which represents the strength of the CP-violation.

For the simplicity of the following discussions, the matter effect is not considered in the first place. In the absence of the matter effect, the probability of a flavor transition $\nu_\alpha \to \nu_\beta$ is calculated using Equation 2.12

$$
\begin{aligned}
P(\nu_\alpha \to \nu_\beta) &= \sum_i |U_{\alpha i}U_{\beta i}^*|^2 + 2\mathrm{Re}\sum_{j>i} U_{\alpha i}U_{\alpha j}^*U_{\beta i}^*U_{\beta j} \exp\left(-i\frac{\Delta m_{ij}^2}{2}\right)\frac{L}{E} \\
&= \sum_i |U_{\alpha i}U_{\beta i}^*|^2 + 2\mathrm{Re}\sum_{j>i} U_{\alpha i}U_{\alpha j}^*U_{\beta i}^*U_{\beta j}\left(\cos\left(\frac{\Delta m_{ij}^2 L}{2E}\right) + i\sin\left(\frac{\Delta m_{ij}^2 L}{2E}\right)\right) \\
&= \sum_i |U_{\alpha i}U_{\beta i}^*|^2 + 2\sum_{j>i} U_{\alpha i}U_{\alpha j}U_{\beta i}U_{\beta j} - 4\mathrm{Re}\sum_{j>i} U_{\alpha i}U_{\alpha j}^*U_{\beta i}^*U_{\beta j}\sin^2\left(\frac{\Delta m_{ij}^2 L}{4E}\right) \\
&\quad + 4\mathrm{Im}\sum_{j>i} U_{\alpha i}U_{\alpha j}^*U_{\beta i}^*U_{\beta j}\sin\left(\frac{\Delta m_{ij}^2 L}{4E}\right)\cos\left(\frac{\Delta m_{ij}^2 L}{4E}\right) \\
&= \delta_{\alpha\beta} - 4\mathrm{Re}(K_{\alpha\beta,ij})\sin^2\left(\frac{\Delta m_{ij}^2 L}{4E}\right) + 4\mathrm{Im}(K_{\alpha\beta,ij})\sin\left(\frac{\Delta m_{ij}^2 L}{4E}\right)\cos\left(\frac{\Delta m_{ij}^2 L}{4E}\right),
\end{aligned}
\tag{2.15}
$$

where

$$K_{\alpha\beta,ij} = U_{\alpha i}U_{\alpha j}^*U_{\beta i}^*U_{\beta j}. \tag{2.16}$$

Likewise, the transition probability of anti-neutrinos is calculated. The difference in oscillation probabilities between neutrinos and anti-neutrinos is given by

$$\Delta P_{\alpha\beta}^{\mathrm{CP}} = -16 J_{\alpha\beta} \sin\left(\frac{\Delta m_{12}^2}{4E}L\right)\sin\left(\frac{\Delta m_{23}^2}{4E}L\right)\sin\left(\frac{\Delta m_{13}^2}{4E}L\right), \tag{2.17}$$

where

$$J_{\alpha\beta} = \mathrm{Im}[U_{\alpha 1}U_{\alpha 2}^*U_{\beta 1}^*U_{\beta 2}] = \pm c_{12}s_{12}c_{23}s_{23}c_{13}^2 s_{13}\sin\delta. \tag{2.18}$$

The parameter $J_{\alpha\beta}$ is called the Jarlskog invariant, and the $\pm$ sign denotes cyclic permutation of $(\alpha, \beta) = (e, \mu), (\mu, \tau), (\tau, e)$. Assuming the mass differences and sine of the mixing angles are

---

[3]If we assume neutrinos are Majorana particles, three complex terms are necessary. The other two complex terms, however, do not show up in the calculation of oscillation probability. Thus, we introduce one complex term here.

non-zero, the measurement of the Jarlskog invariant provides a way to test the CP violation. When we consider the specific neutrino oscillation ($\nu_\mu \to \nu_e$), the oscillation probability is given by

$$
\begin{aligned}
P(\nu_\mu \to \nu_e) &= 4(s_{23}^2 s_{13}^2 c_{13}^2 + J_{\rm CP} \sin \Delta_{21}) \sin^2 \frac{\Delta_{31}}{2} \\
&+ 2(s_{21} s_{23} s_{13} c_{21} c_{23} c_{13}^2 \cos \delta - s_{21}^2 s_{23}^2 s_{13}^2 c_{13}^2) \sin \Delta_{31} \sin \Delta_{21} \\
&+ 4(s_{21}^2 c_{21}^2 c_{23}^2 c_{31}^2 + s_{21}^4 s_{23}^2 s_{13}^2 c_{13}^2 - 2 s_{21}^3 s_{23} s_{13} c_{21} c_{23} c_{13}^2 \cos \delta - J_{\rm CP} \sin \Delta_{31}) \sin^2 \frac{\Delta_{21}}{2} \\
&+ 8(s_{21} s_{23} s_{13} c_{21} c_{23} c_{13}^2 \cos \delta - s_{21}^2 s_{23}^2 s_{13}^2 c_{13}^2) \sin^2 \frac{\Delta_{31}}{2} \sin^2 \frac{\Delta_{21}}{2},
\end{aligned}
\tag{2.19}
$$

where $\Delta_{ij} = \frac{\Delta m_{ij}^2 L}{E}$, $J_{\rm CP} = c_{12} s_{12} c_{23} s_{23} c_{13}^2 s_{13} \sin \delta$. When the difference in the oscillation probability between $\nu_\mu \to \nu_e$ and $\bar{\nu}_\mu \to \bar{\nu}_e$ is expressed by

$$
A \equiv \frac{P(\nu_\mu \to \nu_e) - P(\bar{\nu}_\mu \to \bar{\nu}_e)}{P(\nu_\mu \to \nu_e) + P(\bar{\nu}_\mu \to \bar{\nu}_e)},
\tag{2.20}
$$

the leading order of A is written by

$$
A \approx \frac{J_{\rm CP} \sin \Delta m_{21}^2}{s_{23}^2 s_{13}^2 c_{13}^2}.
\tag{2.21}
$$

Thus, the measurement of both $\nu_\mu \to \nu_e$ and $\bar{\nu}_\mu \to \bar{\nu}_e$ oscillations is associated with the CP complex term ($\delta_{\rm CP}$). The parameters δ and $\delta_{\rm CP}$ are interchangeably used in this thesis.

Next, we assume the specific neutrino mass ordering expressed by

$$
\Delta m_{21}^2 \ll \Delta m_{31}^2 < \Delta m_{32}^2 \quad (\Delta m_{31}^2 \approx \Delta m_{32}^2).
\tag{2.22}
$$

This is called "Normal Ordering". The leading term of the transition probabilities, in particular $\nu_\mu \to \nu_e$ and $\nu_\mu \to \nu_\mu$ [4] are given by

$$
P(\nu_\mu \to \nu_e) \approx \sin^2 2\theta_{13} \sin^2 \theta_{23} \sin^2 \left(\frac{\Delta m_{32}^2 L}{4E} \right),
\tag{2.23}
$$

$$
P(\nu_\mu \to \nu_\mu) \approx 1 - \left(\cos^4 \theta_{13} \sin^2 2\theta_{23} + \sin^2 2\theta_{13} \sin^2 \theta_{23} \right) \sin^2 \left(\frac{\Delta m_{32}^2 L}{4E} \right),
\tag{2.24}
$$

around the neutrino energy region of $E \approx |\Delta m_{32}^2| L$.

Now we consider the matter effects to calculate the oscillation probability. The modified oscillation probability for $\nu_\mu (\bar{\nu}_\mu) \to \nu_e (\bar{\nu}_e)$ oscillations are written by

---

[4]This thesis calls $\nu_\mu \to \nu_e$ oscillation ν_e appearance and $\nu_\mu \to \nu_\mu$ oscillation ν_μ disappearance.

$$P\left(\overset{(-)}{\nu}_\mu \to \overset{(-)}{\nu}_e\right) = \sin^2\theta_{23} \frac{\sin^2 2\theta_{13}}{(A-1)^2} \sin^2[(A-1)\Delta_{31}]$$

$$\overset{(+)}{-} \alpha \frac{J_0 \sin\delta_{\mathrm{CP}}}{A(1-A)} \sin\Delta_{31} \sin(A\Delta_{31}) \sin[(1-A)\Delta_{31}]$$

$$+ \alpha \frac{J_0 \cos\delta_{\mathrm{CP}}}{\cos} \Delta_{31} \sin\Delta_{31} \sin(A\Delta_{31}) \sin[(1-A)\Delta_{31}]$$

$$+ \alpha^2 \cos^2\theta_{23} \frac{\sin^2 2\theta_{12}}{A^2} \sin^2(A\Delta_{31}), \tag{2.25}$$

where

$$\alpha = \Delta m_{21}^2 / \Delta m_{31}^2$$
$$\Delta_{ij} = \Delta m_{ij}^2 L / 4F$$
$$A = (-)2\sqrt{2}G_F n_e E / \Delta m_{31}^2$$
$$J_0 = \sin 2\theta_{12} \sin 2\theta_{13} \sin 2\theta_{23} \cos\theta_{13}. \tag{2.26}$$

As discussed in Chapter 1, the measurement of $\nu_\mu \to \nu_e$ in the energy region of $E \approx |\Delta m_{32}^2|L$ is sensitive to the θ_{23} octant, CP violation, and the neutrino mass ordering based on this formula.

2.3 Oscillation parameters

Based on the parametrization in the PMNS matrix, three mixing parameters (θ_{12}, θ_{13}, θ_{23}), one complex CP phase (δ_{CP}) are important for neutrino oscillation physics assuming three flavors of neutrinos. Only two mass differences have a degree of freedom because of the relationship, $\Delta m_{21}^2 + \Delta m_{32}^2 + \Delta m_{31}^2 = 0$. In addition, the neutrino oscillation probability depends on three mass differences (Δm_{21}^2, Δm_{32}^2, Δm_{31}^2), which must be determined experimentally. The experiments measuring solar neutrino (solar experiments) have explored the allowed regions of Δm_{21}^2 and $\sin^2\theta_{12}$. The experiments dedicated to measuring neutrinos from nuclear reactors (short-baseline reactor experiments) have dug into allowed regions of $\sin^2\theta_{13}$ and provide stringent constraints. The other parameters such as Δm_{32}^2 and $\sin^2\theta_{23}$ have been constrained by measurements with artificial muon neutrino beams produced by accelerators (accelerator experiments). The measurement of atmospheric neutrinos originating from interactions of cosmic rays in the atmosphere is sensitive to these parameters as well (atmospheric experiments). The following discussions give a summary of the experimental results of the parameter constraints.

2.3.1 Δm_{21}^2, $\sin^2\theta_{12}$

One of the long-standing disputes before the theory of neutrino oscillation was acknowledged was the deficit of the survival probability of the electron neutrinos from the sun in data compared to the contemporary theoretical prediction. The proposition of the Mikheyev-Smirnov-Wolfenstein effect (MSW effect) [34, 35] provided an insight into the interpretation of the deficit. The interpretation was useful for the experiments to find out a reasonable solution to the deficit in solar neutrino survival probability. The survival probability of solar neutrino considering the MSW effect is given by [36]

$$P_{ee} = \cos^4\theta_{13}\left(\frac{1}{2} + \frac{1}{2}\cos 2\theta_{12}^M \cos 2\theta_{12}\right), \tag{2.27}$$

where

$$\cos 2\theta_{12}^M = \frac{\cos 2\theta_{12} - \beta}{\sqrt{(\cos 2\theta_{12} - \beta)^2 + \sin^2 2\theta_{12}}} \qquad \beta = \frac{2\sqrt{2}G_F \cos^2\theta_{13} n_e E_\nu}{\Delta m^2}. \qquad (2.28)$$

Various kinds of experiments (Homestake [6], Kamiokande [7], SAGE [8,37,38], GALLEX [39–41]/GNO [42], Super-Kamiokande [10,43–47], SNO [48] and Borexino [49]) tackled the problem of solar neutrinos. In particular, the SNO experiment had a significant role in explaining the deficit in solar neutrino survival probability. As mentioned in Chapter 1, SNO utilized a heavy water target to discriminate the charged current neutrino interactions and neutral current interactions. This feature enabled SNO to compare the neutrino flux measured by charged current interactions with the one measured by neutral current interactions independent of solar neutrino models. The SNO experiment confirmed that the flux measured by charged current interactions was expected to be smaller than that by neutral current interactions. These results indicated the deficit in the solar neutrinos was attributed to the neutrino oscillation.

The solar neutrino experiments have then explored the allowed region of Δm_{21}^2-$\sin^2 2\theta_{12}$ space. Combining all the results from the solar neutrino experiments with the reactor experiment from KamLAND suggested the region of Δm_{21}^2 of 10^{-5} to 10^{-4} and a mixing angle of $\sin^2 2\theta_{12} = 0.5$ to 1 was the most probable. The global best-fit results are shown in [50];

$$\Delta m_{21}^2 = 7.53 \pm 0.18 \times 10^{-5}(\text{eV}^2) \qquad \sin^2\theta_{12} = 0.307^{+0.013}_{-0.012}. \qquad (2.29)$$

The errors represent the 1σ region to the best-fit values.

2.3.2 $\sin^2\theta_{13}$

The parameter $\sin^2\theta_{13}$ is associated with the survival probability of $\bar{\nu}_e$ given by

$$P(\bar{\nu}_e \to \bar{\nu}_e) \approx 1 - \sin^2\theta_{13}\sin^2\frac{\Delta m_{31}^2 L}{4E} - \sin^2\theta_{12}\cos^4\theta_{13}\sin^2\frac{\Delta m_{21}^2 L}{4E}. \qquad (2.30)$$

Reactor experiments utilize nuclear fusion emitting the anti-neutrino, which is detected by the inversed β-decay. One of the largest interests in this parameter is whether $\sin^2\theta_{13}$ is tiny (< 0.01) or not. As sine quantities for all the mixing angles appear in the Jarlskog invariant in Equation 2.18, the CP-violation is prohibited if any of the mixing angles is zero. Even if $\sin^2\theta_{13}$ is not zero but tiny (< 0.01), the sensitivity to the CP-phase drastically decreases. The relatively large (> 0.01) $\sin^2\theta_{13}$ is desired to explore the CP violation as well as determine the neutrino mass ordering. Several experiments [51,52] in the early 2000s showed the lower limit of $\sin^2\theta_{13}$ being around 0.10 at 90% confidence level considering the allowed regions of Δm_{32}^2. Three experiments, Daya Bay [12], RENO [13] and Double Chooz [14] have performed measurements, confirming $\sin^2\theta_{13}$ is large enough for an accelerator experiment to be able to explore the CP violation. Their results are world-leading for the constraints of $\sin^2\theta_{13}$. The latest result of the world average from reactor experiments [50] is

$$\sin^2\theta_{13} = 0.0220 \pm 0.0007. \qquad (2.31)$$

The error shows 1σ region to the best-fit value.

2.3.3 Δm_{32}^2 (Δm_{31}^2), $\sin^2\theta_{23}$ ($\sin^2 2\theta_{23}$)

The experimental results obtained so far give two kinds of scenarios regarding the neutrino mass (m_1, m_2, m_3) ordering.

- Normal ordering (NO): $m_1 < m_2 \ll m_3$

- Inverted ordering (IO): $m_2 > m_1 \gg m_3$

As for the mass differences, $\Delta m_{32}^2 \approx \Delta m_{31}^2$ is suggested in either case. The allowed regions of Δm_{32}^2-$\sin^2 \theta_{23}$ have been explored mainly by the long-baseline accelerator experiments and atmospheric experiments from the measurements of the $\nu_\mu \to \nu_\mu$ energy spectrum using

$$P(\nu_\mu \to \nu_\mu) = 1 - \sin^2 2\theta_{13} \sin^2 \theta_{23} + \sin^2 2\theta_{23} \cos^4 \theta_{13} \sin \frac{\Delta m_{32}^2 L}{4E}. \tag{2.32}$$

The uncertainty of $\sin^2 \theta_{23}$ is the largest compared to the precision of other mixing parameters. Therefore, in order to realize the precise measurement of $\delta_{\rm CP}$, a tighter constraint of $\sin^2 \theta_{23}$ is necessary. The leading term in Equation 2.25 is the first term which includes the contribution from $\sin^2 \theta_{23}$. If θ_{23} is non-maximal mixing ($\theta_{23} \neq \pi/4$), its octant symmetry is closely relevant to the $\delta_{\rm CP}$ sensitivity. It is worth noting that the second term in Equation 2.25 has parameter $\sin \delta_{\rm CP}$, which is sensitive to CP-violation and Δm_{31}^2 ($\approx \Delta m_{32}^2$) is associated with $\delta_{\rm CP}$ sensitivity as well. The global fit results are shown here.

$$|\Delta m_{32}^2| \, (\text{NO}) = 2.514^{+0.028}_{-0.027} \times 10^{-3} \, \text{eV}^2/\text{c}^4 \quad |\Delta m_{31}^2| \, (\text{IO}) = 2.497^{+0.028}_{-0.028} \times 10^{-3} \, \text{eV}^2/\text{c}^4, \tag{2.33}$$

$$\sin^2 \theta_{23}(\text{NO}) = 0.570^{+0.018}_{-0.024}. \tag{2.34}$$

The measurement errors in Equations 2.33, 2.34 represent 1σ errors to the best-fit values.

2.3.4 $\delta_{\rm CP}$

The measurement of $\delta_{\rm CP}$ is an important probe to determine if the CP violation exists in the lepton sector as in the quark sector. As all the sine and cosine quantities of mixing angles are expected to be non-zero and more importantly $\sin^2 \theta_{13}$ is a relatively large value, long-baseline accelerator experiments in principle have a high sensitivity to measure $\delta_{\rm CP}$ by a careful arrangement of experimental apparatus with high-intensity neutrino beam. In particular, L/E (the length of baseline / neutrino energy) is a characteristic of neutrino oscillation experiments. For the measurement of $\delta_{\rm CP}$, experiments choose the L/E quantity to maximize the effect of neutrino oscillations. The T2K and NOνA experiments are world-leading experiments both of which have the similar L/E. The T2K results in [53] are

$$\delta_{\rm CP} = -1.89^{+0.70}_{-0.58} \, (\text{NO}) \qquad \delta_{\rm CP} = -1.38^{+0.48}_{-0.54} \, (\text{IO}). \tag{2.35}$$

In addition, the CP conserving values $(0, \pi)$ were excluded at a 95% confidence level [53].

2.3.5 Summary of the oscillation parameter measurements

Table 1 shows the summary of measured oscillation parameters from the fit to global data [54].

Table 1: A summary of the measured mixing values for both mass ordering scenarios from the global fit analysis [54].

Mixing parameters	Normal Ordering (BestFit)		Inverted Ordering	
	best fit $\pm\ 1\sigma$	3σ range	best fit $\pm\ 1\sigma$	3σ range
$\sin^2\theta_{12}$	$0.304^{+0.013}_{-0.012}$	$0.269 \to 0.343$	$0.304^{+0.013}_{-0.012}$	$0.269 \to 0.343$
$\sin^2\theta_{23}$	$0.570^{+0.018}_{-0.024}$	$0.407 \to 0.618$	$0.575^{+0.017}_{-0.021}$	$0.411 \to 0.621$
$\sin^2\theta_{13}$	$0.02221^{+0.00068}_{-0.00062}$	$0.02034 \to 0.02430$	$0.02240^{+0.00062}_{-0.00062}$	$0.02053 \to 0.02436$
$\delta_{\mathrm{CP}}/\ ^\circ$	195^{+51}_{-25}	$107 \to 403$	286^{+27}_{-32}	$192 \to 360$
Δm^2_{21} $(10^{-5}\ \mathrm{eV}^2/\mathrm{c}^4)$	$7.42^{+0.21}_{-0.20}$	$6.82 \to 8.04$	$7.42^{+0.21}_{-0.20}$	$6.82 \to 8.04$
Δm^2_{31} (NO) / Δm^2_{32} (IO) $(10^{-5}\ \mathrm{eV}^2/\mathrm{c}^4)$	$2.514^{+0.028}_{-0.027}$	$2.431 \to 2.598$	$-2.497^{+0.028}_{-0.028}$	$-2.583 \to -2.412$

The oscillation parameters Δm^2_{21}, $\sin^2\theta_{12}$ and $\sin^2\theta_{13}$ are relatively well constrained based on the solar and reactor experiments whereas there are problems to be resolved in measurements of Δm^2_{32}, $\sin^2\theta_{23}$ and δ_{CP}. Accelerator experiments and atmospheric experiments have measured the latter three oscillation parameters. The early measurements are mostly limited by statistical errors in accelerator experiments. But the situation has been improved thanks to higher intensity beams and long-term operations, which in turn makes the systematic uncertainties non-negligible.

One of the pre-dominant systematic errors originates from the lack of understanding of neutrino interactions. Its tiny cross section requires a small segmented detector with a high positional resolution in a large volume in addition to long-run and successive data-taking to reduce the statistical uncertainty of the cross section measurements. Moreover, complex mechanisms in multi-body interactions between a neutrino and a nucleus make it difficult to establish a solid neutrino interaction model, which inflates the uncertainties on neutrino cross sections. In short, achieving a more precise understanding of neutrino interactions will help the accelerator experiments to solve the degeneracies of mass ordering and θ_{23} octant, and discover the CP violation. More details on neutrino interactions are discussed in Chapter 4.

3 The T2K experiment

This chapter overviews a long-baseline accelerator experiment called T2K experiment. The former part of this chapter introduces the motivations of T2K and experimental setups. The latter of this chapter describes the experimental apparatus and the status of T2K data taking.

3.1 Motivation

After the discovery of the neutrino oscillation with atmospheric neutrinos, a long-baseline neutrino experiment with accelerator neutrinos, T2K, was proposed to precisely measure the parameters of the PMNS matrix. The accelerator provides a high-energy proton beam and produces charged pions when those protons collide with a target material. The charged pions decay into muons and muon neutrinos. The main oscillation channels in the T2K experiment are ν_e ($\overline{\nu}_e$) appearance ($\nu_\mu \to \nu_e$) and ν_μ ($\overline{\nu}_\mu$) disappearance ($\nu_\mu \to \nu_\mu$). In the absence of the matter effect, the oscillation probability of the ν_e ($\overline{\nu}_e$) appearance including a partial sub-leading order is expressed by

$$P(\overset{(-)}{\nu_\mu} \to \overset{(-)}{\nu_e}) \approx \sin^2 2\theta_{13} \sin^2 \theta_{23} \sin^2 \left(\frac{\Delta m_{32}^2 L}{4E} \right) \overset{(-)}{+} J_{\mathrm{CP}} \sin \frac{\Delta m_{21}^2 L}{4E} \sin^2 \frac{\Delta m_{31}^2 L}{4E} + \mathcal{O}(\Delta m_{21}^2) \quad (E \approx |\Delta m_{32}^2| L),$$
(3.1)

where $J_{\mathrm{CP}} = \cos\theta_{12} \sin\theta_{12} \cos\theta_{23} \sin\theta_{23} \cos^2\theta_{13} \sin\theta_{13} \sin\delta_{\mathrm{CP}}$. Equation 3.1 indicates the measurement of $\nu_\mu \to \nu_e$ oscillation is sensitive to δ_{CP}, $\sin^2 2\theta_{13}$, and $\sin^2 2\theta_{23}$. The measurement of the difference in the probabilities between $\nu_\mu \to \nu_e$ and $\overline{\nu}_\mu \to \overline{\nu}_e$ oscillations contributes to digging into δ_{CP} through the Jarlskog invariant (J_{CP}). On the other hand, the measurement of $\nu_\mu \to \nu_\mu$, ν_μ disappearance is sensitive to $\sin^2 2\theta_{23}$ and $|\Delta m_{32}^2|$ according to

$$P(\nu_\mu \to \nu_\mu) \approx 1 - \left(\cos^4\theta_{13} \sin^2 2\theta_{23} + \sin^2 2\theta_{13} \sin^2 \theta_{23} \right) \sin^2 \left(\frac{\Delta m_{32}^2 L}{4E} \right) + \mathcal{O}(\Delta m_{21}^2) \quad (E \approx |\Delta m_{32}^2| L).$$
(3.2)

As well as measuring each parameter value, it is in principle possible to determine the neutrino mass ordering by utilizing the matter effects as in Equation 2.25 while neutrino travels through the matter in the earth. The T2K experiment was designed to achieve as high sensitivity as it could to, especially δ_{CP}.

3.2 Experimental setup

One of the key components in the long-baseline experiment is the proton accelerator providing the high-intensity beam. The T2K experiment [5] makes use of Japan Proton Accelerator Research Complex (J-PARC), which is located in Tokai, Ibaraki. The neutrino beamline was constructed inside the J-PARC facility to incident the neutrino beam to the far neutrino detector located 295 km away from the accelerator, Super-Kamiokande. The near detectors, constructed inside the J-PARC site, play important roles in monitoring neutrino beam flux and measuring neutrino interactions, whose results are used in the oscillation analysis. The far detector contains 50 kton water surrounded by photon detectors to detect neutrinos via Cherenkov radiation produced by charged particles from their interactions in the water. The overall setup for the T2K experiment is illustrated in Figure 1.

---

[5]T2K stands for "(T)okai" "to (2)" "(K)amioka"
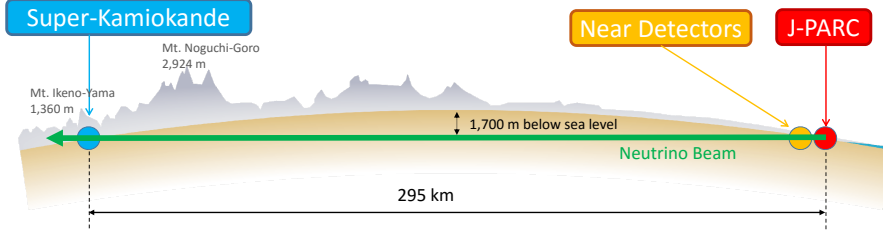
Figure 1: The overview of the T2K experiment; the proton beam accelerator (J-PARC), neutrino beamline and neutrino Near Detectors, and the far neutrino detector (Super-Kamiokande).

The neutrino oscillation probability depends on the distance divided by the neutrino energy (L/E). The distance in the experiment is fixed at 295 km. At this condition, the neutrino oscillation probability is illustrated as a function of neutrino energy in Figure 2.
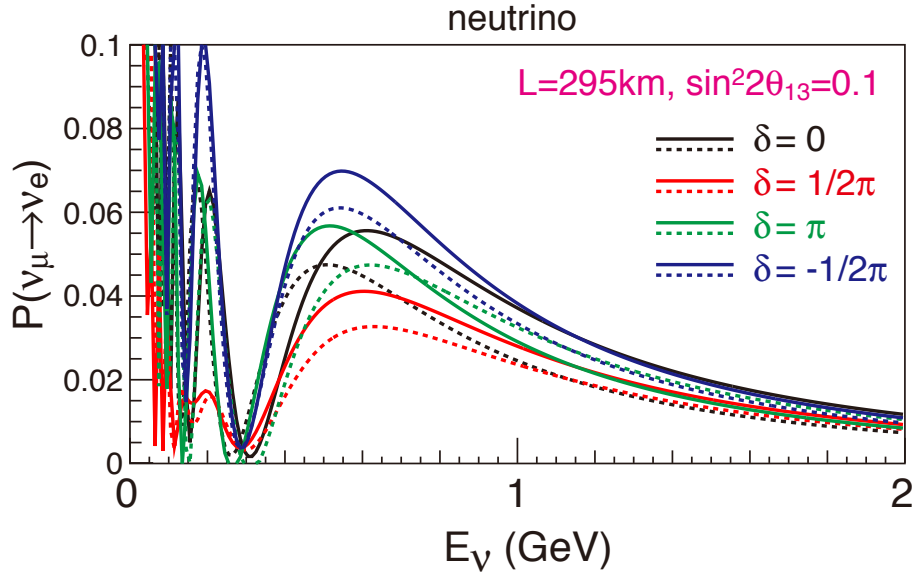
Figure 2: The neutrino oscillation probability for $\nu_\mu \rightarrow \nu_e$ as a function of neutrino energy (E_ν) assuming several scenarios of δ_{CP} values. The solid (dashed) lines correspond to normal (inverted) mass ordering.

The oscillation probability differs depending on the value of δ_{CP}. In the T2K setup, the maximum oscillation probability falls around 0.6 GeV. In order to measure as many neutrino oscillation events as possible, T2K tuned the peak position of the energy distribution to be around that energy. While the initial energy of the proton beam roughly determines the resulting neutrino beam, finer adjustment is achievable by changing the angle relative to the proton beam at which one observes the neutrinos. As pion decay is a two-body interaction involving μ and

ν_μ, the neutrino energy is expressed as a function of the pion energy and the direction of the neutrino by

$$E_\nu = \frac{m_\pi^2 - m_\mu^2}{2(\sqrt{p_\pi^2 + m_\pi^2} - p_\pi \cos\theta_\nu)}, \tag{3.3}$$

where $p_\pi(m_\pi), E_\mu(m_\mu)$ are the momentum (mass) of pion and energy (mass) of muon and θ_ν is the angle of the neutrino with respect to the angle of the produced pions. Equation 3.3 implies the relationship between neutrino energy and pion energy depends on the direction of the neutrino. Once the angle is fixed, the neutrino energy is expressed as a function of pion energy. This relationship contributes to the corresponding neutrino energy distribution as in the right plot in Figure 3. For instance, if we take 2.5 degrees, the red line in the left plot in Figure 3 shows the plateau around 0.6 GeV for E_ν, which in turn makes the peak around 0.6 GeV in the neutrino energy distribution (see the red line in the right plot in Figure 3).

(a) E_ν as a function of E_π (b) Neutrino flux at different angle of neutrino
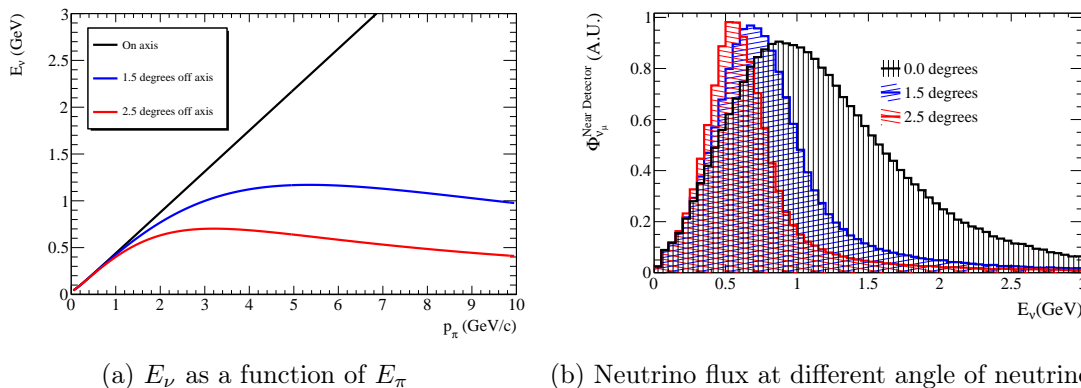
Figure 3: Relationships between neutrino energy and pion energy (left) and the neutrino fluxes corresponding to different neutrino angles (right). The black line shows the case of the neutrino angle being aligned with the proton beam axis. Both blue and red lines show the neutrino angle deviates from the proton beam axis.

The deviation from the proton beam axis is referred to as off-axis angle. The T2K experiment adopts this off-axis method and sets it to 2.5 degrees to tune the expected peak position to be 0.6 GeV. Another advantage of this method is to make the energy distribution narrower. A narrower band energy can help to reduce the impact of the errors in the reconstructed energy on the oscillation analysis.

3.3 Experimental apparatus

3.3.1 Beamline

The J-PARC accelerators consist of three types of accelerators [55]; Linear Accelerator, Rapid Cycling Synchrotron, and Main Ring. The Linear Accelerator (LINAC) injects H$^-$ ion from the source and accelerates it to 400 MeV by a high field gradient provided by normal conducting magnets. The accelerated H$^-$ ion is led to the injection area in the Rapid Cycling Synchrotron (RCS), where the electrons are stripped off by charge-exchange foils under the presence of an external electromagnetic field. The ions are then converted to protons. The RCS accelerates

protons up to 3 GeV, 5% of which are injected into the Main Ring Synchrotron (MR). At the present, MR is capable of boosting the proton's energy to about 30 GeV. During the beam operation, the accelerated protons are extracted by a set of five kicker magnets, when eight bunches of protons are kicked out from the orbit by one turn in a 2.48-second sequence. Each bunch width is 80 ns at 3σ, which in turn corresponds to the time structure of neutrino productions. The repetition cycle has been already upgraded to 1.36 seconds in 2022. This sequence is referred to as "spill". The beam power is determined by the proton per spill, proton energy, and the repetition cycle. Presently, 520 kW operation has been achieved.

The neutrino beamline [56] was constructed to generate a high-intensity neutrino beam and to monitor the beam profiles after the proton spill is extracted from the MR. The beamline consists of two sub-sections; the primary beamline and the secondary beamline. The primary beamline focuses the 30 GeV protons in the targeted direction for the T2K experiment, being equipped with both normal conducting and superconducting magnets. In order to ensure protons are focused, T2K developed several kinds of detectors to monitor the proton's intensity, position, and profiles. In addition, monitoring the loss of the proton beam is essential to achieve high-power beam operation as well as to secure stable operation. T2K installed the following monitors.

CT (Current Transformer)

Each CT is a 50-turn toroidal coil around a cylindrical ferromagnetic core [56]. It monitors the beam intensity with a 2% accuracy and 0.5% precision. The conventional measurement unit for CT in the T2K experiment is protons-on-target (POT).

ESM (Electrostatic Monitor)

ESM has four segmented cylindrical electrodes surrounding the proton beam orbit [56]. This structure helps to monitor the proton beam center position non-destructively.

SSEM (Segmented Secondary Emission Monitor)

SSEM has two thin titanium foils stripped horizontally and vertically, and an anode HV foil between them [56]. The proton beam hitting the foil produces secondary electrons that drift through the strip. Measurement of the charge distribution converted from the signal of secondary electrons provides information on the beam profile. SSEMs are only inserted into the orbit during the beam tuning.

BLM (Beam Loss Monitors)

Each BLM consists of a wire proportional counter filled with an $Ar - CO_2$ mixture [56]. To avoid serious radiation or damage to the equipment, it triggers an abort alert once the beam loss exceeds the threshold.

The well-tuned protons strike a 91.4 cm long monolithic graphite target. The secondary beamline has a role in maximizing the performance of neutrino production. The beamline consists of target stations, decay volume, and beam dump, which are illustrated in Figure 4. The target station is composed of the target, three magnetic horns, and a baffle. The target was installed inside the inner conductor of the first horn.

The electromagnetic forces from horns focus the direction of charged pions produced from the proton-target collision. Physics operation until 2021 ran all of the horns with an absolute current of 250 kA. The polarity of the horn current changes the charge of pions to be focused. Positive pion decays into μ^+ and ν_μ, whereas negative pion decays into μ^- and $\overline{\nu}_\mu$. Therefore, operating the experiment with opposite horn currents enables us to exchange the neutrinos between ν_μ and

$\overline{\nu}_\mu$. When ν_μ is made dominantly in the neutrino flux, the operation is referred to as "Forward Horn Current (FHC)" or neutrino mode, and in the inverted case, "Reversed Horn Current (RHC)" or anti-neutrino mode. Focused pions go into the decay volume, which is about 96 m long steel tunnel. This length of the tunnel was determined such that the most of relativistic pions decay inside it. At the end of the decay volume, a 3.174 m long graphite-core beam dump was installed to absorb most of the muons from pion decays.
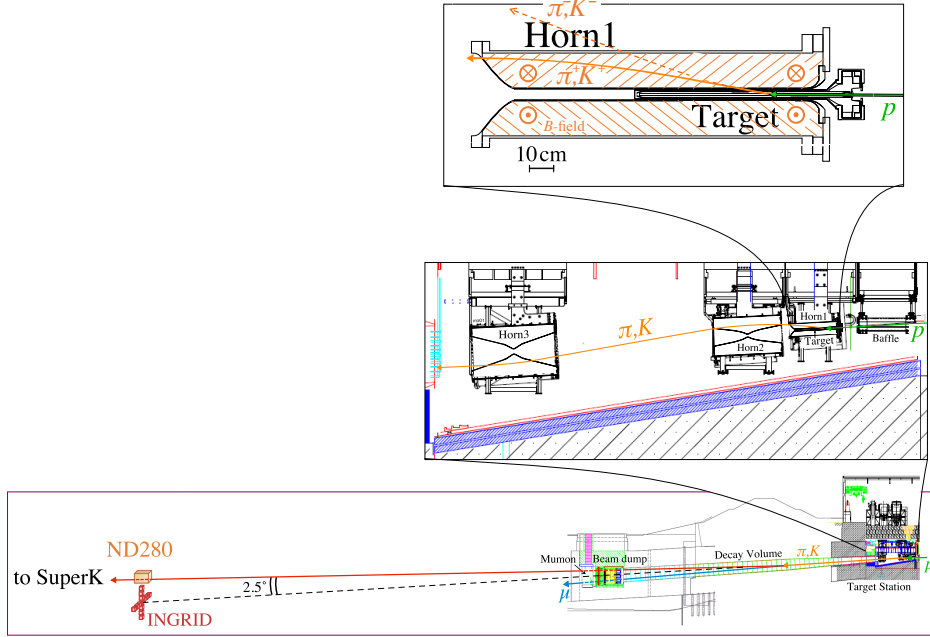
Figure 4: The illustration of the secondary beamline (target station, decay volume and beam dump). The equipment inside the target station is zoomed in so as to emphasize the role of electromagnetic horns.

3.3.2 Muon monitor (MUMON)

The muons with a momentum above 5.0 GeV/c can pass through the beam dump. The muons are produced by the two-body decay from pions together with neutrinos. Therefore, the neutrino profiles can be reconstructed by measuring the muon profiles. T2K developed the muon monitor (MUMON) to monitor the neutrino beam indirectly.

Performance requirements of MUMON are to measure the intensity of the muon beam with a precision better than 3% and beam direction with a precision better than 0.25 mrad, which corresponds to a 3 cm precision of the muon profile [57]. In addition, these measurements have to be achieved on a bunch-by-bunch basis in real-time even in low-intensity beam tuning. A certain bunch of T2K neutrino beam timing sometimes shifts with respect to the expected timing, which must be checked by MUMON. The location for MUMON is subject to the intense muon beam $(10^5 - 10^7 \ /cm^2/bunch)$ from intensely focused charged pions. It adds an imperative requirement of high radiation tolerance to the sensors employed for the muon monitor. MUMON was designed to meet all of the requirements. It comprises two different sets of detectors, both of which are

aligned in seven-by-seven arrays with a 25 cm gap between the neighboring sensors. One set of the arrays consists of the 49 sensors of Si PIN photodiode (HAMAMATSU® S3590-08). The other set of sensors is installed inside ionization chambers (IC). Both Si and IC arrays are installed on a movable stage to calibrate the response of each sensor using the actual muon beam. Figure 5 illustrates the schematic view of MUMON along with the array configuration.
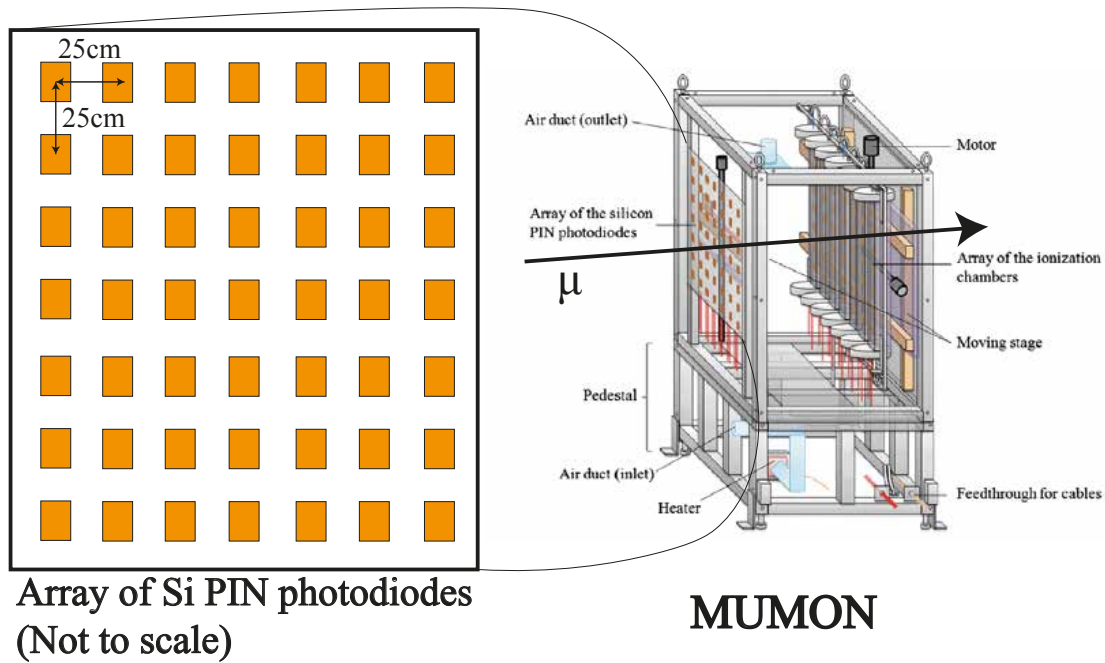
Figure 5: A schematic view of MUMON (right) [57] and zoom-in figure (left) for the seven-by-seven configuration of sensor arrays for Si PIN photosensors. The configuration for IC sensor arrays is the same as the one in the left figure except for each set of seven sensors being contained in a long aluminum tray inserted into the chambers. The "heater" inside the "pedestal" space controls the temperature inside the pit. And both Si and IC arrays are set on the movable stage, which is used for the purpose of calibration of each sensor.

Each Si PIN photodiode has a 10×10 mm^2 active area with a depletion layer thickness of 300 μm. The Si sensors have sufficiently high signal yields in each bunch. The high signal yields make it possible to tune the beam direction in the low-intensity beam operation. On the other hand, they are largely subject to the severe radiation environment. At the recent T2K beam intensity, half a year of operation yields 5.0×10^{20} protons on target (POT). In the beam intensity, a 1% signal decrease has been observed due to the radiation damage causing the depletion voltage to decrease. Nevertheless, the performance of Si is still reliable in the physics data taking as long as the decreasing rate can be understood well. In order to mitigate the effect of radiation damage on the profiling performance, half Si sensors are replaced with new ones on a one-year operation basis. Towards higher intensity beam operation, a new type of sensor replacing the Si sensor has been developed for the last several years.

The IC array consists of seven ionization chambers including seven sensors on an aluminum tray at an interval of 25 cm. As a medium of each chamber, the T2K experiment makes use of two types of gases. One option is the compound of Ar with 2% N$_2$, and the other is He with 1% N$_2$. As the signal yields to MIPs are proportional to the atomic number in the first-order

approximation, Ar gas is suitable in low-intensity beam operation. He gas, on the other hand, is desirable in high-intensity beam operation because of its high radiation tolerance. When either gas is filled in a chamber, a large number of ion pairs induced by a charged particle move to the electrodes of the opposite polarity, generating the ionizing current measured by an electrometer circuit. Mixing N_2 gas provides a quenching effect to make response faster. [6] Contrary to Si sensors, the responses from IC gases are stable even in continuous high-intensity beam operation as long as a constant gas temperature, pressure, and purity are maintained. One concern when Ar gas is used is the space charge effect, which causes a non-linear response in a high intensity beam operation. We have not seen such behavior when He gas is used. Equipped with both Si and IC sensors, MUMON can meet the requirements to guarantee stable beam operation for T2K.

A signal from each sensor travels through about a 30 m long cable running from the underground pit to the electronics container on the ground. A 65-MHz Flash Analog to Digital Converters (FADCs) is employed as the readout electronics. Each ADC has an input impedance of 50 Ω and an amplifier of gain-5 or gain-1 with a shaping time of 50 nsec [57]. The gain-5 amplifier is used for the IC sensors while the gain-1 amplifier is used for the Si sensors. In order to avoid signal saturation in FADCs, the readout system is instrumented with external attenuators capable of producing 0, 6, 15 or 30 dB. During the high-intensity beam operation, they attenuate Si (IC) signals with 30 (6) dB while in the low-intensity beam tuning, the electronics apply no attenuation.

3.3.3 Near Detectors

The T2K experiment installed a suite of detectors. Those detectors are located inside the underground pit, whose diameter and depth are 17.5 m and 37 m, respectively. The vital roles of near detectors are to monitor the neutrino beam and measure neutrino interactions. The T2K experiment employed many monitors to ensure the proton beam is aligned in the expected direction. In addition, it is also important to measure the neutrino direction and intensity directly. One of the detectors, INGRID, monitors the neutrino beam by measuring neutrinos traveling on axis. On the other hand, the expected neutrino flux at the far detector side has large uncertainties without constraints on the flux prediction by the measurements of neutrino interactions. The uncertainties from neutrino interaction models are also significant in the oscillation analysis. The measurements of neutrino interactions at another near detector complex, ND280 has contributed to the substantial reduction in the uncertainties coming from neutrino flux and interactions.

INGRID [56] (Interactive Neutrino GRID), is located on-axis to monitor the direction and intensity of neutrinos on a day-by-day basis. It consists of 14 modules (half modules in a horizontal row and the other half modules in a vertical row) to form a cross symbol. Each sub-module has a sandwich structure of 11 scintillator tracking layers and 9 iron planes [7]. The total mass of iron is 7.1 tons per module, which guarantees sufficient statistics to measure the neutrino direction with an accuracy higher than 0.4 mrad within the required precision for the T2K oscillation analysis with one-day neutrino beam operation. Figure 6 is one of the examples of reconstructed neutrino profiles in data.

---

[6]Another reason why N_2 is mixed is to mitigate the Jesse effect [58]. Due to this effect, the signal is insensitive to the number of impurities in the gas.

[7]Due to the weight restrictions in the assembly building, the iron plane was not installed between the 10th and 11th scintillator plane, which was confirmed not to have an impact on the tracking performance.
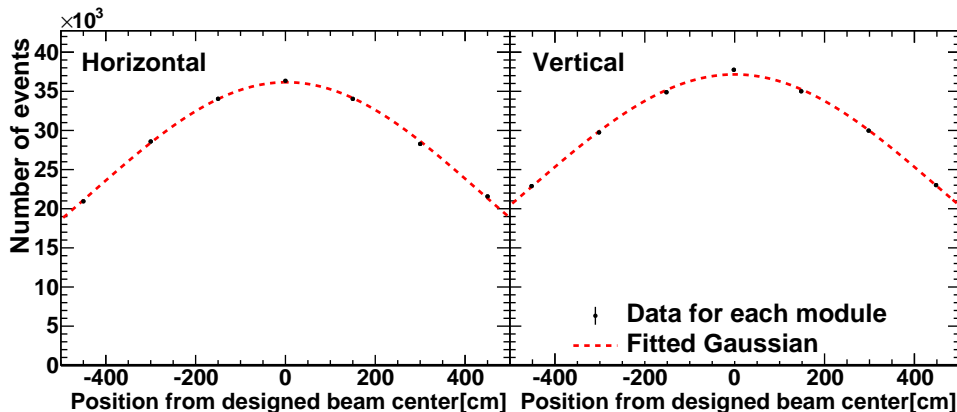
Figure 6: A neutrino profile at INGRID in the neutrino mode for the horizontal direction (left) and the vertical direction (right) with 1-day data during a physics operation. The dotted data point is fitted with the gaussian function. The mean X and Y centers from the fit results are used to check the neutrino direction.

The detector complex located 2.5 degrees off-axis at the 280 m site is called ND280 [56]. Detector specifications and arrangements were designed to satisfy several requirements for the oscillation analysis. Providing information on the neutrino flux at the far detector is one of the requirements to reduce systematic errors in the analysis. The ν_μ ($\overline{\nu}_\mu$) measurements are necessary to give constraints on the parameters in underlying neutrino interaction models. About 1% contamination from ν_e ($\overline{\nu}_e$) in the ν_μ ($\overline{\nu}_\mu$) beam ends up with the irreducible background in measurements of ν_e ($\overline{\nu}_e$) appearance. Therefore, it is an important task for ND280 to measure the ν_e ($\overline{\nu}_e$) component of the neutrino flux as a function of neutrino energy to predict the irreducible background.

UA1 Magnet and SMRD

The magnet surrounding the whole detector provides a dipole magnetic field of 0.2 T. This magnet consists of water-cooled aluminum coils and eight C-shaped flux return yokes. Each of these individual yokes is made of 16 iron planes, 48 mm thick, and spaced with 17 mm air gaps. Both coils and yokes are refurbished from the UA1 experiment at CERN [59]. In order to fill the air gaps between iron planes inside each yoke, additional active layers made of plastic scintillators, SMRD [60] were installed. SMRD acts to measure muon momentum escaping from the inner detectors. In addition, it triggers cosmic rays entering the ND280 detectors and detects beam-related background coming from interactions inside magnet yokes.

FGD and PØD

We developed two kinds of detectors to determine the neutrino interaction vertex. They are two fine-grained trackers, FGDs [61] and one pi-zero detector, PØD [62]. One FGD tracker called FGD1 fully consists of scintillator tracking planes, while the other FGD tracker called FGD2 consists of the sandwich structure of water layers and scintillator tracking planes. FGD1 acts as CH target detector and FGD2 acts as both CH and H_2O target detector. In addition, they detect charged particles emerging from the neutrino interaction vertex. PØD has a water-scintillator sandwich structure for charged particle detection but

also electromagnetic calorimeters for photon detection. One of the motivations of PØD is to detect neutral pions with the electromagnetic calorimeters.

TPC

Charged particles produced from the neutrino interaction in FGDs and PØD are further tracked down by other detectors. Three Time Projection Chambers, TPCs [63] were installed in the way of sandwiching two FGDs. Each TPC consists of the inner container for Ar-based drift gas. When the charged particles pass through the inner box, ionization electrons induced in the gas drift away from the central cathode and toward one of the readout planes. Bulk micromegas detectors amplify these electrons and sample the signal. TPCs are capable of creating a track of a charged particle. As all of the detectors are under the magnetic field provided by the UA1 magnet, the trajectory of each charged particle is bent depending on its charge and momentum. The curvature provides information on the charge and momentum of the particle by the TPCs. In addition, the measurement of the energy deposit left in the TPC delivers a powerful tool to distinguish the type of charged particles, especially proton-pion-muon separation when used with the measured momentum.

ECAL

Sampling electromagnetic calorimeters, ECALs [64] surround the vertex detectors and TPCs to cover the charged particles and photons exiting from those detectors. ECALs have an alternating structure of scintillator layers and lead absorber sheets. The key role of ECALs is photon detection, in particular from π^0 particles produced in the neutrino interactions inside the vertex detectors. The reconstruction of the energy and direction of photons fills up a full event reconstruction using all the information from inner detectors. It also plays a role in electron-muon-pion separation.

The near detector complex is illustrated in Figure 7. Most of the detectors rely on plastic scintillators and wavelength-shifting fiber (WLS) readouts, with photons from the fibers aggregating in the photosensors, called MPPC (Multi-pixel photon counter) [65]. MPPC is available even in the 0.2 T magnetic field provided by the UA1 magnet.
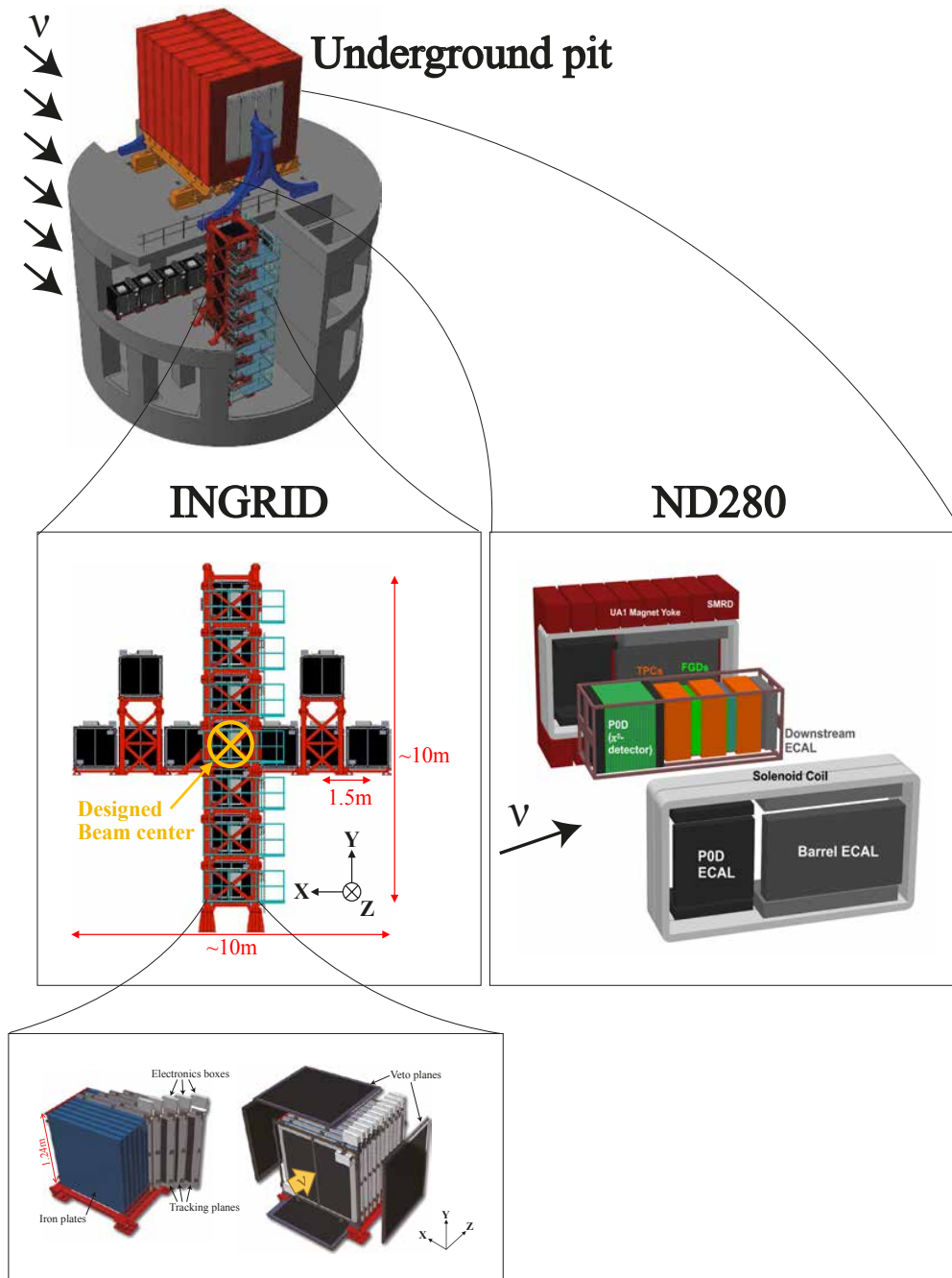
Figure 7: Illustrations of the underground pit housing Near Detector; INGRID and ND280 [56]. INGRID comprises seven sub-modules in a vertical row, seven sub-modules in a horizontal row, and two sub-modules. Each module has a sandwich structure of scintillator planes and iron planes. PØD and FGD detectors are tracking detectors while acting as neutrino targets. Three TPCs detect a particle trajectory. The surrounding electromagnetic calorimeters play a role in the detection of photons as well as charged particles. All detectors are encompassed by the UA1 magnet yoke providing a dipole magnetic field.

3.3.4 Far Detector (FD)

The primary destination of neutrino produced inside J-PARC is the T2K far detector, Super-Kamiokande (FD) [56, 66]. FD is located 295 km west of the beam source, but 2.5 degrees off-axis. The detector is the world's largest land-based water Cherenkov detector and contains 50,000 tons of ultra-pure water inside its cylindrical volume as a target material. The whole structure is divided into an inner detector (ID) and an outer detector (OD). An about 55 cm wide cylindrical structure forms the boundary between ID and OD. Both ID and OD surfaces are instrumented with photomultiplier tubes (PMTs). The number of ID PMTs is about 11,000 in total, which provides 40% PMT cathode coverage in the ID. The collective signals from the Cherenkov light from a charged particle form a ring image on the surface of the ID. Compared to the ID, the OD is only sparsely instrumented with 1,855 PMTs in total. Nevertheless, it plays an important role in rejecting cosmic ray muons and other backgrounds.

In the context of neutrino oscillation measurements, the separation of ν_e and ν_μ is the most prominent requirement for the FD. The basic strategy to distinguish these flavors is to analyze the pattern of a ring's edge. Electrons induce electromagnetic cascades while traveling inside water. Those cascades make a fuzzy ring image, which is a hallmark of an electron event. On the other hand, muons travel inside water as Minimum Ionizing Particles (MIPs), which makes a ring image clearer. This is the qualitative approach to tell ν_e from ν_μ. In fact, the event reconstruction adopts a likelihood approach to quantify the fuzziness of a ring image. As a result, the contamination of other flavors in a reconstructed ν_e sample is less than 1% level [53]. The event displays from Monte-Carlo simulations for both ν_e and ν_μ are shown in Figure 8.

The FD has several limitations in terms of oscillation analysis for the T2K experiment. One is related to a potential bias in the reconstruction of neutrino energy. The principle of neutrino detection at the FD relies on the Cherenkov light from a charged particle. The FD can identify a charged pion if it is above the Cherenkov threshold, in principle, but can also infer its presence by detecting the electron from its decay chain. The main interaction type is the charged current quasi-elastic scattering (CCQE), where the charged lepton and the outgoing nucleon exist in the final state. The energy reconstruction is applied assuming the interaction is CCQE for the main signal of the T2K oscillation analysis. Sometimes, produced pions in the neutrino interactions are trapped inside the nucleus. The event mimics the CCQE. When the calculation formula is applied to this kind of events, it introduces a natural bias into the energy reconstruction.

With respect to the bias, the two-particle two-hole (2p2h) interaction, where two protons get involved, is another concern. The 2p2h interaction may produce two protons in the final state which is distinct from CCQE, where only one proton is produced in a neutrino-nucleus interaction. The typical energy of excited protons in the interaction is not sufficient to create a Cherenkov light forming a ring image. Therefore, the 2p2h interaction mimics the CCQE interaction in the final state. Consequently, it causes another bias in energy reconstruction. Another limitation is that the FD is not capable of distinguishing the neutrino interaction from the anti-neutrino interaction because the FD is not magnetized. [8]

These limitations are covered by interaction model studies and flux predictions. For the nuclear medium effects, the dedicated model is introduced to evaluate the effect inside the nucleus. The analysis applies the external data to tune the parameters in the model. For the 2p2h inter-

---

[8]The current Super-Kamiokande contains 0.03% Gd dissolved into the water by mass fraction. This provides a way to discriminate the ν event from $\bar{\nu}$ event for CCQE interaction because $\bar{\nu}$ interaction is more likely to have a neutron exiting outside the nucleus. However, all analyses in this thesis were done without introducing the effect of Gd.

action, the T2K neutrino interaction generator incorporates an underlying model to parametrize a cross section for this interaction. The parameters for medium effects and the 2p2h interaction are constrained by the T2K Near Detector (ND280) measurements. The result is then propagated into the FD event predictions. The detailed descriptions are covered in Section 6.4. For the inability to separate neutrinos and anti-neutrinos, each analysis sample at the far detector is determined based on the type of beam operation that is neutrino-mode/FHC or anti-neutrino-mode/RHC (see Section 6.6 for details). In addition, neutrino and anti-neutrino components are examined by the neutrino flux predictions established by the T2K experiment. The detailed descriptions are found in Section 6.2.
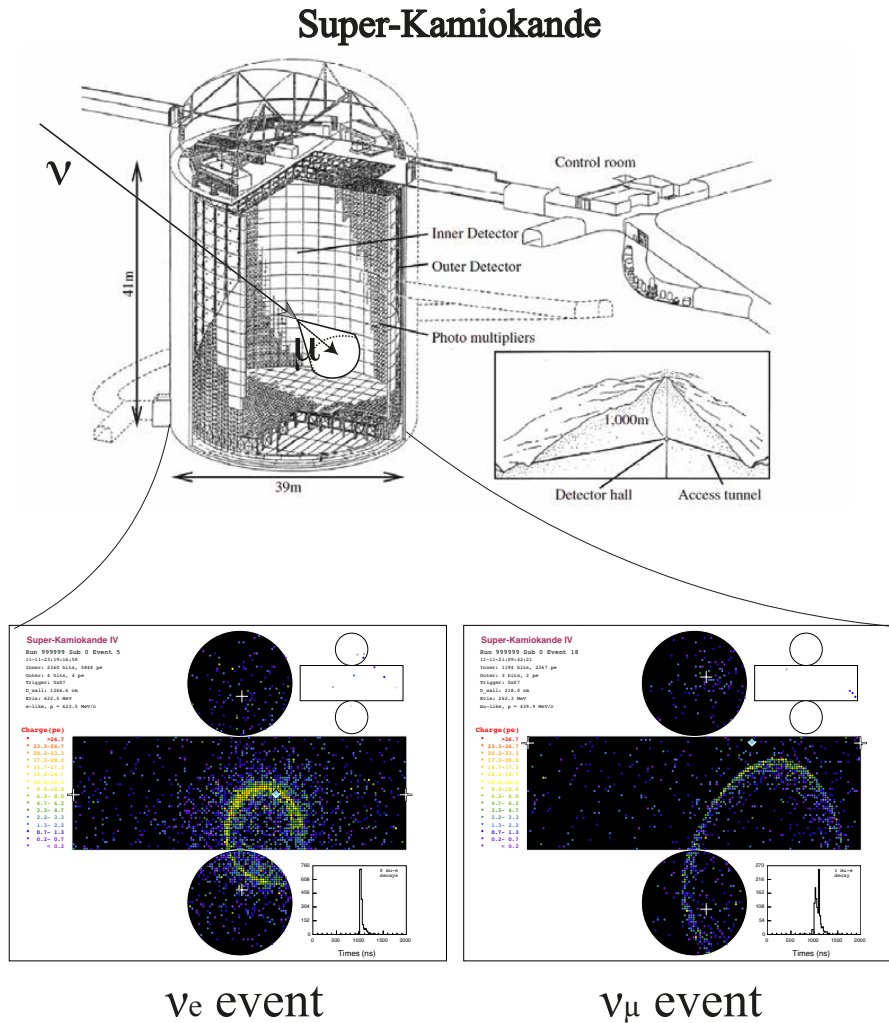
Figure 8: The upper figure shows a schematic view of the FD [56]. The cone produced by a muon from the neutrino interaction represents Cherenkov light. Also, the lower figures show event displays from Monte-Carlo simulations for ν_e event (lower left) and ν_μ event (lower right). The electron ring is subject to the electromagnetic shower, which makes the ring image relatively diffuse. On the other hand, the ring image for ν_μ event is clearer due to less interaction probability of muon inside water.

3.4 Data taking status

The T2K experiment has taken data since 2010. Table 2 shows the history of the T2K beam operation until 2021. The published oscillation analysis result and the updated result described in this thesis use data up to Run10 while Run11 data was not introduced because of the FD condition being changed. [9] Run10 data was newly added for the published result in [67, 68]. The stable beam operation is the outcome of the continuous operation of neutrino monitors, MUMON and INGRID. Figure 9 illustrates the history of accumulated POT and beam power in the T2K experiment. The current maximum beam power reaches 520 kW.

Table 2: History of the T2K beam operation. The last column refers to the amount of taken data in the Near Detector (ND) and in the Far Detector (FD).

Run number	Run start	Run end	Beam mode	POT($\times 10^{19}$) ND	FD
1	Jan. 2010	Jun. 2010	ν	–	3.26
2	Nov. 2010	Mar. 2011	ν	7.93	11.22
3	Mar. 2012	Jun. 2012	ν	15.81	15.99
4	Oct. 2012	May. 2013	ν	34.26	35.97
5	May. 2014	Jun. 2014	$\bar{\nu}$	4.35	5.12
			ν	–	2.44
6	Oct. 2014	Jun. 2015	$\bar{\nu}$	34.09	35.46
7	Feb. 2016	May. 2016	$\bar{\nu}$	24.38	34.98
			ν	–	4.84
8	Oct. 2016	Apr. 2017	ν	57.31	71.69
9	Oct. 2017	May. 2018	$\bar{\nu}$	20.54	87.88
			ν	–	2.04
10	Oct. 2019	Feb. 2020	ν	–	47.26
11	Mar. 2021	Apr. 2021	ν	–	17.81

---

[9]The SK collaboration has decided to dope a small fraction of Gadolinium (Gd) inside the water tank to make the neutron detection efficiency higher. The Gd doping has started in 2020 after Run10, and Run11 is the first data taking with Gd-water.
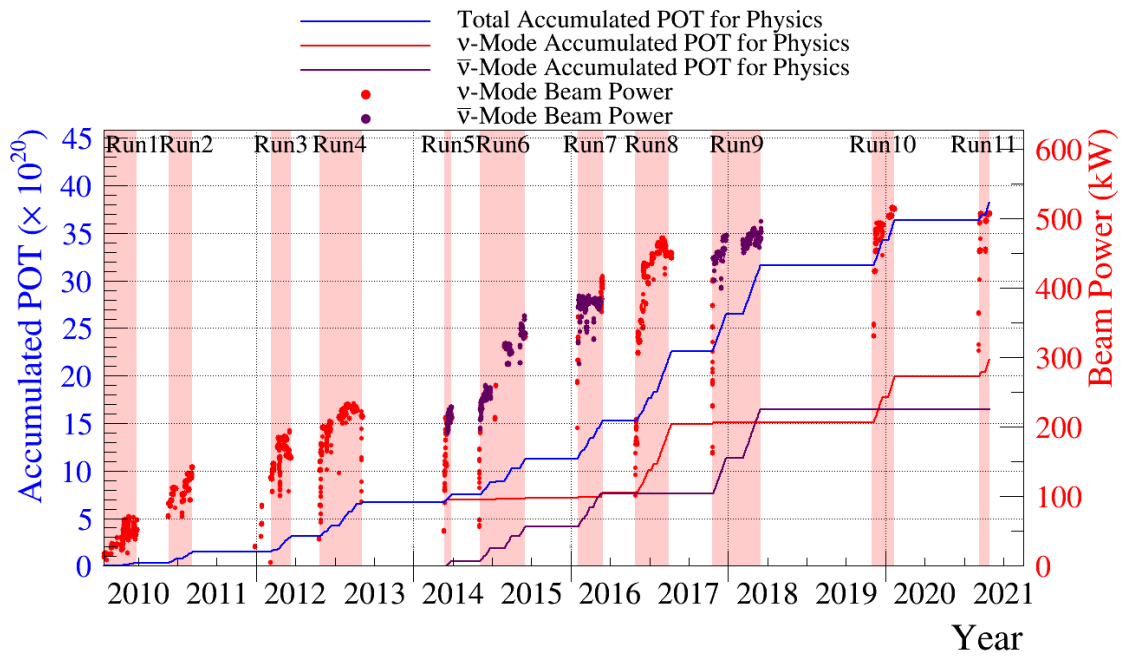
Figure 9: The history of accumulated POT and beam power in the T2K experiment [69]. The solid lines represent accumulated POT while dotted points represent the beam power. The Run number corresponds to the first column in Table 2.

4 Neutrino interaction in sub-GeV energy region

The uncertainty of neutrino interaction models is one of the dominant error sources in the oscillation analysis of T2K. This chapter describes neutrino-nucleus interaction theories and the experimental status of the measurements.

4.1 Overview

Neutrino electron scattering with point particles like electrons is a well-understood weak neutrino interaction. Neutrinos have interactions with hadrons, whose electric charges are distributed in space. For these interactions, the "Form factor", which represents the structure of the target, is introduced to take into account the electric charge distribution.

For measurements of accelerator neutrinos in particular for T2K, the energy scale of the neutrino beam is 1 GeV, where the interaction length is 1 fm. This is comparable to the size of a nucleus. Therefore, it is important to understand neutrino interactions with nucleons that are bound inside a nucleus. As the T2K near detector complex has mainly a CH target and the far detector has a water target, nuclear medium effects inside oxygen and carbon are necessary to be understood. Many models dealing with the nuclear effects have been extended from a model assuming a free nucleon as an interaction target. This chapter explains neutrino interactions with free nucleons and then elaborates on how the nuclear medium effects are considered in the extended models, citing a concise review of neutrino interactions [70].

Neutrino interactions via the weak force take place by exchanging either W^+/W^- boson or Z boson which corresponds to the charged current process or the neutral current process, respectively. The charged current neutrino interactions with a mean energy of 1 GeV are classified mainly into three interactions; quasielastic scattering, resonant interaction, and deep inelastic scattering. They are roughly differentiated by the energy of neutrino, which is shown in Figure 10. Figure 10 also shows the data points from experimental results. The measurements of total cross section and those in higher energy regions for the CCQE interaction are mostly consistent with theoretical predictions. On the other hand, the data results for the CCQE interaction in the sub-GeV region, resonant interaction (RES), and deep inelastic scattering (DIS) are not shown in this figure because of the lack of precise measurements for these neutrino interactions. This chapter focuses on these three interaction modes in sub-GeV energy regions corresponding to the T2K neutrino beam energy.
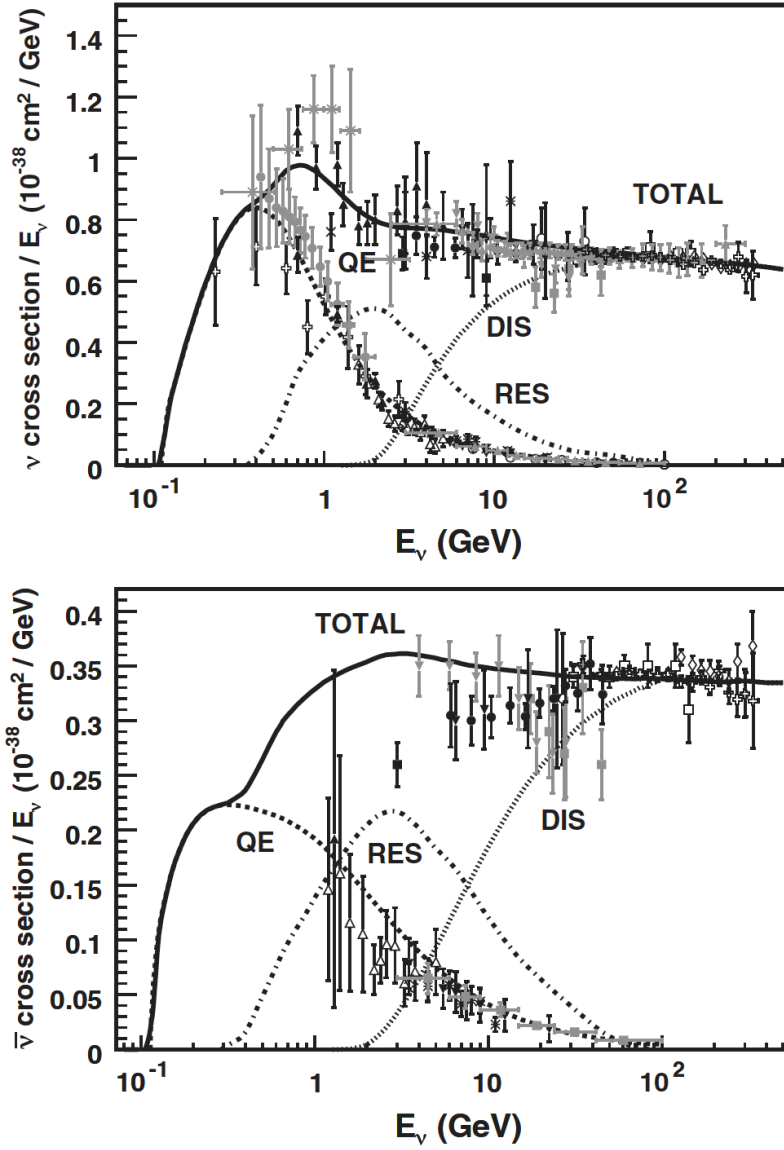
Figure 10: Total neutrino and antineutrino per nucleon charged current cross sections (for an isoscalar target) divided by neutrino energy and plotted as a function of energy [71]. These contributions include quasielastic scattering – QE (dashed), resonance production – RES (dot-dashed), and deep inelastic scattering – DIS (dotted). Example predictions for each are provided by the NUANCE generator ([72]). Note that the quasielastic scattering data and predictions have been averaged over neutron and proton targets and hence have been divided by a factor of 2 for the purposes of this plot. Dotted plots show data from various kinds of experiments: Black triangle dots ([73]), Asterisk dots points ([74]), Black rectangular dots ([75]), Star dots ([76]).

4.2   Interaction with free nucleon

4.2.1   Charged current quasi-elastic scattering

The quasi-elastic scattering is an interaction with a "small" momentum transfer, Q^2. In this thesis, quasi-elastic scattering is defined as the interaction where no other hadrons are produced. If the nucleon is free, charged current quasi-elastic scattering (CCQE) refers to the interactions of

$$\nu_l(k) + n(p) \rightarrow l^-(k') + p(p')$$
$$\bar{\nu}_l(k) + p(p) \rightarrow l^+(k') + n(p'),$$
(4.1)

where k, k' are four momenta of the neutrino (anti-neutrino) denoted by $\nu_l(\bar{\nu}_l)$ and lepton ($l^\pm$), p, p' are the four momenta of the incoming and outgoing nucleon (n, p). Figure 11 shows the Feynman diagram for the quasi-elastic scattering interactions.
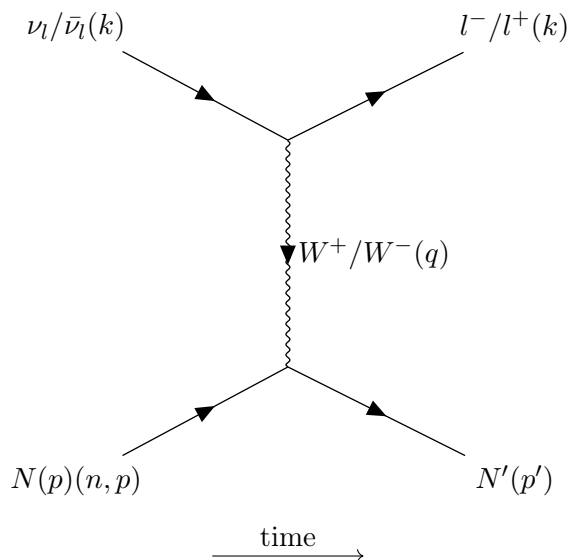

Figure 11: Feynman diagram for the neutrino-nucleus charged current quasi-elastic scattering. The time elapses from left to right.

One of the theoretical descriptions is seen in Llewellyn Smith's formalism [77]. The following discussions highlight how the differential cross section is extracted, showing the parametrizations and assumptions used in this formalism. The invariant matrix element M representing the Equation 4.1 is given by

$$M = \frac{G_F}{\sqrt{2}} \cos \theta_C I_\mu J^\nu,$$
(4.2)

where G_F is the Fermi coupling constant, θ_C is the Cabibbo angle, I_μ, J^ν are the leptonic weak current and the hadronic current, respectively. The leptonic weak current is expressed by

$$I_\mu = \bar{u}(\vec{k}')\gamma_\mu(1 \mp \gamma_5)u(\vec{k}),$$
(4.3)

where $\mp$ corresponds to neutrino $(-)$ or anti-neutrino $(+)$ induced interactions. The hadronic current is given by

$$J_\mu = \bar{u}(\overrightarrow{p}')\Gamma_\mu u(\overrightarrow{p}). \tag{4.4}$$

In the Llewellyn Smith's formalism, the contribution of the matrix (Γ_μ) is divided into the conserved vector current V_μ and the partially conserved axial current A_μ;

$$\Gamma_\mu = V_\mu - A_\mu. \tag{4.5}$$

The matrix elements for both vector and axial vector currents are given by

$$\langle N'|V_\mu|N(\overrightarrow{p})\rangle = \bar{u}(\overrightarrow{p}')\left[\gamma_\mu f_1(q^2) + i\sigma_{\mu\nu}\frac{q^\nu}{M+M'}f_2(q^2) + \frac{2q_\mu}{M+M'}f_3(q^2)\right]u(\overrightarrow{p})$$

$$\langle N'|A_\mu|N(\overrightarrow{p})\rangle = \bar{u}(\overrightarrow{p}')\left[\gamma_\mu\gamma_5 g_1(q^2) + i\sigma_{\mu\nu}\frac{q^\nu}{M+M'}\gamma_5 g_2(q^2) + \frac{2q_\mu}{M+M'}\gamma_5 g_3(q^2)\right]u(\overrightarrow{p}), \tag{4.6}$$

where $N, N' = n, p$, and $q^2 = (k-k')^2$ is the four-momentum transfer squared. The parameters M, M' are the masses of the initial and the final nucleon, respectively. The functions $f_i(q^2)$ and $g_i(q^2)$ represent the form factors.

The differential scattering cross section can be calculated using Mandelstam variables s, t, u [10]. The result is

$$\frac{d\sigma}{dq^2} = \frac{G_F^2 M^2 \cos^2\theta_C}{8\pi E_\nu^2}\left[A(q^2) \mp B(q^2)\frac{(s-u)}{M^2} + C(q^2)\frac{(s-u)^2}{M^4}\right], \tag{4.7}$$

where

$$A(q^2) = \frac{m^2-q^2}{4M^2}\left[\left(4-\frac{q^2}{M^2}\right)g_1^2(q^2) - \left(4+\frac{q^2}{M^2}\right)f_1^2(q^2) - \frac{q^2}{M^2}\left(1+\frac{q^2}{4M^2}\right)f_2^2(q^2)\right.$$

$$- \frac{4q^2}{M^2}f_1(q^2)f_2(q^2) - \frac{m_1^2}{M^2}\left(\left(f_1(q^2)+f_2(q^2)\right)^2 + \left(g_1(q^2)+2g_3(q^2)\right)^2\right)^2$$

$$\left.+ \left(\frac{q^2}{M^2}-4\right)g_3^2(q^2)\right],$$

$$B(q^2) = \frac{q^2}{M^2}g_1^2(q^2)\left[f_1(q^2)+f_2(q^2)\right],$$

$$C(q^2) = \frac{1}{4}\left[g_1^2(q^2) + (f_1(q^2))^2 - \frac{q^2}{4M^2}(f_2(q^2))^2\right]. \tag{4.8}$$

For the simplicity of the calculation, a set of assumptions $M' = M$, $s - u = 4ME_\nu + q^2$, $f_3(q^2) = g_2(q^2)$ is applied, where there are no second-class currents. The plus (minus) sign of the $B(q^2)$ term in Equation 4.7 is used for neutrino (anti-neutrino) interaction. The leading terms of the Equation 4.7 come from the contributions of $f_1^2(q^2)$ and $g_1^2(q^2)$, which correspond to a vector form factor and an axial vector form factor, respectively. The vector form factors are well understood with the relationship with the Dirac-Pauli form factors of the proton and the neutron ($F_{1,2}^p, F_{1,2}^n$ [78, 79]) by

$$f_{1,2}(q^2) = F_{1,2}^p(q^2) - F_{1,2}^n(q^2). \tag{4.9}$$

---

[10]Each variable in this context is $s = (k+p)^2 c^2$, $t = (k-k')^2 c^2$, $u = (k-p')^2 c^2$

The axial vector form factor is parametrized as

$$g_1(q^2) = g_A(0) \left[1 - \frac{q^2}{M_A^2}\right]^{-2}, \qquad (4.10)$$

assuming dipole type of form factor. The constant value $g_A(0)$ is determined experimentally from the β-decay of neutrons $(-1.2723 \pm 0.0023$ [19]). The parameter M_A represents the axial vector mass in a dipole type, characterizing the dipole behavior of the nucleon. The numerical value of M_A has been measured in various kinds of experiments from neutrino-nucleus scattering as well as the pion electroproduction. The electroproduction experiments suggested it was 1.069 ± 0.016 GeV/c^2 and the early neutrino interaction experiments using hydrogen and deuterium targets had similar results [80]. The results from some neutrino experiments such as NOMAD [81] and MINERνA [82] were consistent with them. On the other hand, some neutrino experiments preferred a higher value of M_A most of which lies in the range of 1.2-1.35 GeV/c^2. The recent T2K result showed $1.26^{+0.21}_{-0.18}$ GeV/c^2 [83]. Notably, the MiniBooNE experiment showed the results with the high statistics sample of ν_μ interactions on ^{12}C. The results were explained with $M_A = 1.35 \pm 0.17$ GeV/c^2. Varying M_A from 1.069 GeV/c^2 to 1.35 GeV/c^2 can change the cross section of the quasi-elastic scattering by approximately 30%. There are target differences between the earlier experiments and the MiniBooNE or the T2K experiment. The T2K experiments use carbon and oxygen targets, where the neutrino interactions are subject to nuclear medium effects due to the nucleon bound inside a nucleus although the Fermilab experiments used hydrogen and deuterium targets. We then need to take into account the nuclear medium effects to calculate neutrino-nucleus cross sections on the carbon or oxygen targets precisely. This issue is revisited in the latter section.

4.2.2 Charged current meson production

As the minimum threshold of neutrino energy for the meson production is determined by a pion mass, the threshold is 277.4 MeV/c^2 for the charged current charged-pion production. Neutrinos with higher energy above 1 GeV do not only get involved in the single-pion production but also promote multi-pion production or the production of strange mesons such as Kaon up to a few GeV energy. These meson productions are divided into two ways; resonant and non-resonant productions. The resonant production is dominant in the entire energy region except for the low energy corresponding to around the energy threshold of the meson production process. The resonant meson productions are characterized by the mass, parity, spin, and isospin of the excited states of the nucleon. They are represented by $R_{IJ}(M_R)$ where R is the name of the resonance at the nucleon's orbital angular momentum [11], I and J stand for their isospin and total angular momentum quantum numbers, and M_R is their mass. The first resonance is Δ^{++} one called $P_{33}(1232)$, which is dominant in the T2K experiment. In addition to this classification, the change in strangeness, ΔS is also important to differentiate the meson production process. The main processes can be represented by the following reactions.

- $\Delta S = 0$

  - $\nu_\mu(\bar{\nu}_\mu) + N \rightarrow \mu^-(\mu^+) + N' + \pi$
  - $\nu_\mu(\bar{\nu}_\mu) + N \rightarrow \mu^-(\mu^+) + N' + n\pi$

---

[11]Each angular momentum L=0, 1, 2 corresponds to S, P, D in terms of R

- $\Delta S = 1$

  - $\nu_\mu(\bar{\nu}_\mu) + N \rightarrow \mu^-(\mu^+) + N' + \eta$
  - $\nu_\mu(\bar{\nu}_\mu) + N \rightarrow \mu^-(\mu^+) + N' + K$

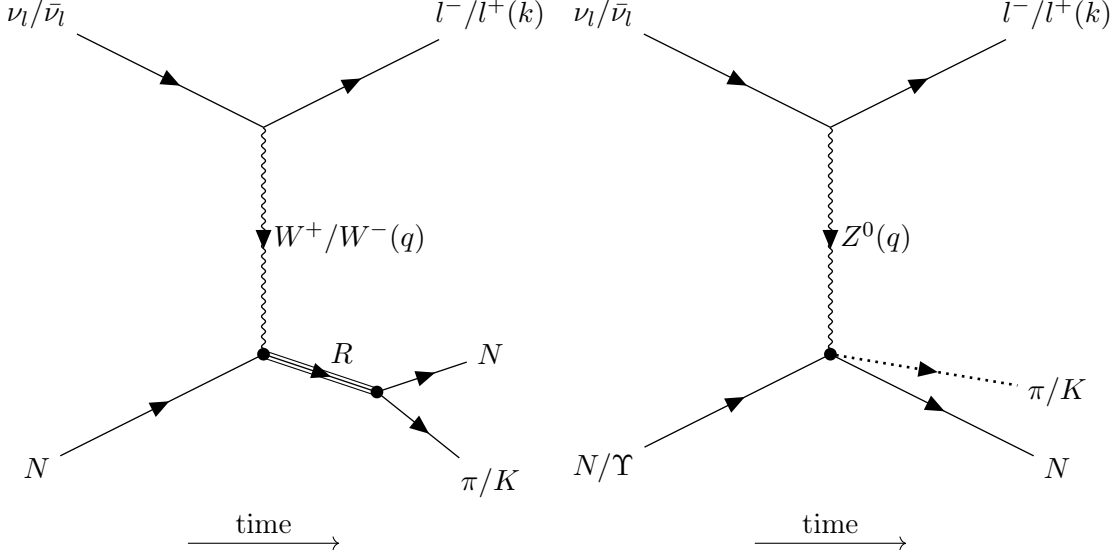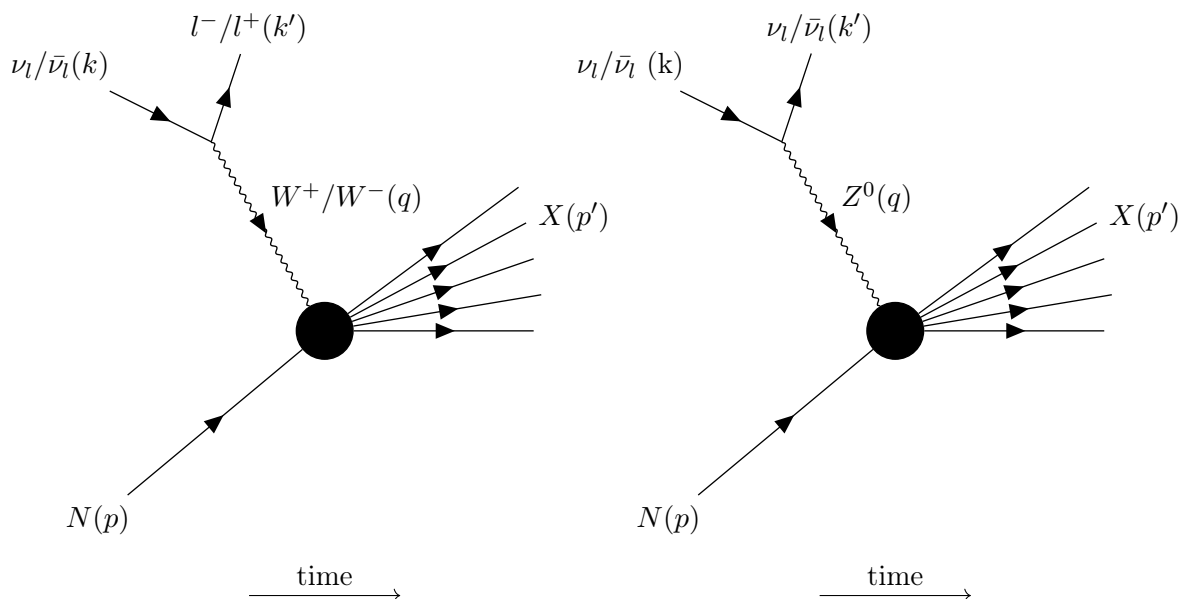Corresponding Feynman diagrams are shown in Figure 12.

Figure 12: Feynman diagrams for neutrino-nucleus charged current inelastic scattering (left) and neutral current inelastic scattering (right). In the left diagram, "R" refers to the nucleon resonance. The dominant resonance in the T2K experiment is $\Delta^{++}(1232)$ one. The time elapses from left to right.

The following discussions focus on the case of $\Delta S = 0$, especially via the Δ^{++} resonance, $P_{33}(1232)$. The cross section calculation flow is similar to that for quasi-elastic calculation except for the Γ matrix involving the hadronic current. The Γ matrix is divided into the vector and the axial vector currents. Corresponding form factors can be predicted by theories and measured by experiments. The vector form factors including vector mass, M_V were determined from the electromagnetic data [84] which was compared with theoretical calculations of helicity amplitude of Δ^{++} [85]. The axial vector part can be parametrized by a form factor C_5^A [86]. The shape of C_5^A is traditionally assumed to be the dipole form, which is expressed by

$$C_5^A(q^2) = \frac{C_5^A(0)}{(1 + q^2/M_{A,\Delta^{++}\mathrm{RES}}^2)}. \tag{4.11}$$

Experiments from Brookhaven National Laboratory (BNL) provided data [87, 88] to estimate those parameters, whose best fits suggested $C_5^A = 1.2, M_{A,\mathrm{RES}} = 0.73$ GeV/c^2. For the cross section of the single pion production process from almost free nucleons, the only bubble chamber experiments from ANL [89] and BNL [88] provided available data, which were conducted almost 40 years ago. These results are inconsistent with one another on the cross section of the single pion production ($\nu_\mu p \rightarrow \mu^- p \pi^+$) by about 30 - 40%. This in turn inflates the uncertainty on the cross section of the interaction.

The Kaon production process is not dominant in the sub-GeV energy region, whereas it becomes important to measure the interaction in a few GeV energy regions. Recently, the charged current induced single kaon production as a function of kaon's kinetic energy produced in the final state was measured by the MINERνA experiment [90].

4.2.3 Charged current deep inelastic scattering

Deep inelastic scattering (DIS) is characterized by high momentum transfer, q^2, and energy transfer, ν compared to inelastic scattering, both of which are typically over 1 GeV. The nucleon receiving the high energy ends up with a jet of hadrons. The typical interaction is described by

$$\nu_l/\bar{\nu}_l(k) + N(p) \rightarrow l^-/l^+(k') + X(p'); \quad l = e, \mu \tag{4.12}$$

where X stands for a jet of hadron. Feynman diagrams are also shown in Figure 13.

Figure 13: Feynman diagrams for neutrino-nucleus charged current deep inelastic scattering (left) and neutral current deep inelastic scattering (right). The time elapses from left to right.

Unlike the quasi-elastic and the meson production processes, the proton form factors in the case of the DIS process are independent of q^2 which is asymptotically a fixed value of x in the limit of $q^2 \rightarrow \infty, \nu \rightarrow \infty$, where x is known as the Bjorken scaling. Thus, the cross section scaling and the form factors depend only on x. The double differential cross section in this weak interaction process is calculated assuming V-A interactions in the limit of $q^2 \rightarrow \infty, \nu \rightarrow \infty$. The expression is

$$\frac{d^2\sigma}{dxdy} = \frac{G_F^2 s}{4\pi} \left[\left(1 + (1-y)^2\right) F_2(x, Q^2) \pm \left(1 - (1-y)^2\right) xF_3(x, Q^2) \right], \tag{4.13}$$

where $s = (p + k)^2 \simeq 2p \cdot k, y = p \cdot q/p \cdot k$ (y is the inelasticity parameter), both F_2 and F_3 are form factors for DIS. Equation 4.13 can be written by replacing form factors with quark (anti-quark) cross sections ($\overset{(-)}{u}(x), \overset{(-)}{d}(x), \overset{(-)}{c}(x), \overset{(-)}{s}(x)$);

$$\frac{d^2\sigma^{\nu p}}{dxdy} = \frac{G_F^2 s}{\pi}(d(x) + s(x) + (1 - y^2)(\bar{u}(x) + \bar{c}(x))),$$

$$\frac{d^2\sigma^{\bar{\nu} p}}{dxdy} = \frac{G_F^2 s}{\pi}(\bar{d}(x) + \bar{s}(x) + (1 - y^2)(u(x) + c(x))),$$

$$\frac{d^2\sigma^{\nu n}}{dxdy} = \frac{G_F^2 s}{\pi}(u(x) + s(x) + (1 - y^2)(\bar{d}(x) + \bar{c}(x))),$$

$$\frac{d^2\sigma^{\bar{\nu} n}}{dxdy} = \frac{G_F^2 s}{\pi}(\bar{u}(x) + \bar{s}(x) + (1 - y^2)(d(x) + c(x))). \tag{4.14}$$

Integrating all equations in Equation 4.14 over x, y between the limits 0 and 1 gives the expressions of total cross sections for an isoscalar nucleon target for neutrino and anti-neutrino induced processes;

$$\sigma^{\nu N} = \frac{G_F^2 s}{2\pi} \int x \left(q(x) + \frac{\bar{q}(x)}{3} \right) dx, \quad \sigma^{\bar{\nu} N} = \frac{G_F^2 s}{2\pi} \int x \left(\frac{q(x)}{3} + \bar{q}(x) \right) dx, \tag{4.15}$$

where $q(x), \bar{q}(x)$ are the probability density functions for quarks and anti-quarks. The CHARM experiment presented the experimental results of the total cross section for DIS using the neutrino beam ranging from 10 GeV to 160 GeV [91]. The results are

$$\sigma^{\nu N}/E_\nu = 0.677 \pm 0.002(\text{stat}) \pm 0.020(\text{syst}) \times 10^{-38}\text{cm}^2/\text{GeV}, \tag{4.16}$$

$$\sigma^{\bar{\nu} N}/E_{\bar{\nu}} = 0.335 \pm 0.004(\text{stat}) \pm 0.010(\text{syst}) \times 10^{-38}\text{cm}^2/\text{GeV}.$$

DIS is not dominant in the T2K experiment whereas this interaction has a non-negligible contribution in the background coming from neutrinos with high energy.

4.3 Interaction with nucleon bound inside nucleus

Most accelerator neutrino oscillation programs need to take into account the fact that the nucleon is bound inside the nucleus because the interaction length for the energy transfer in the T2K neutrino energy scale, the typical Q^2 for the 1 GeV neutrino interactions corresponds to the nucleon size of 1 fm.

Neutrino interactions are subject to nuclear medium effects which originate from, for instance, the nucleon not being at rest or having interactions with other nucleons. Many models have been proposed to describe neutrino interactions and tested by experiments. This section introduces several interaction models along with the nuclear medium effects, in particular for quasi-elastic scattering and resonant pion production processes, both of which are major concerns for the T2K experiment.

4.3.1 Interaction models for quasi-elastic scattering

The simplest nuclear model to study neutrino interactions is the non-relativistic global Fermi gas model [12] assuming the motion of nucleon is non-relativistic, which was first applied to neutrino interactions by Berman [92]. This model describes a system of non-interacting fermions relying on several assumptions.

---

[12]This model has been extended to "relativistic" Fermi gas model and "local" Fermi gas model

- Each energy state for nucleons, protons and neutrons is filled by two identical particles with opposite spins.

- All of the lowest states are filled up to a maximum Fermi momentum p_F at $T = 0$ K.

- Two different potential wells are allocated to neutrons and protons. The neutron's potential well is deeper than that of the proton's well because of the absence of the Coulomb repulsion.

- The average potential that every nucleon feels is a superposition of the potentials from other nucleons.

This model is able to account for several nuclear medium effects. We then discuss what the medium effects are and how they have an impact on the neutrino interactions.

Nucleon motion in a nucleus

The nucleon motion in a nucleus can affect neutrino interactions. In the picture of the shell model, the potential energy that nucleon feels in the nucleus acts as a mean-field, $V(r)$ in the Hamiltonian given by

$$H = -\frac{\overrightarrow{\nabla}^2}{2M} + V(r), \tag{4.17}$$

where M is the mass of the nucleon. This Hamiltonian can describe the motion of the nucleon. The solution of the Schrodinger equation with the Hamiltonian, Equation 4.17 gives the wave function of the nucleon in the momentum space. The momentum distribution of the nucleon follows the wave function. To calculate neutrino cross sections, the momentum of nucleon needs to be convoluted by this momentum distribution called Spectral Function (SF). The simplest case of the Fermi gas model gives the SF of

$$S(\overrightarrow{p}, E) \propto \theta(p_F - p)\delta(E - \sqrt{|\overrightarrow{p}|^2 + M^2} + \epsilon). \tag{4.18}$$

where $E, \overrightarrow{p}$ are the energy and momentum of the nucleon. This effect is visible in the shift of the elastic or quasi-elastic peak and the smearing of the peak depending on the SF.

Pauli Blocking

In the Fermi gas model, the ground state is defined as the state where all the nuclear states in the Fermi sea are filled up to the momentum p_F. Whatever reactions can excite a nucleon at a certain state creates a hole in the previously occupied state. This is called the creation of particle-hole (1p-1h). As both nucleons, proton and neutron are fermions, Pauli's exclusion principle is valid in this model. Consequently, if the states up to a certain momentum are already occupied by other nucleons, another nucleon's excitation is blocked. If the nucleon momentum is not high enough to excite to a higher state, the nucleon cannot get outside of the nucleus. This effect is called the Pauli Blocking, which ends up with the reduction in the cross section, especially in the region of the low momentum transfer.

Binding Energy

There exists binding energy among nucleons. As a result, the nucleons are off-mass shells,

and the energy-momentum relation ($p^2 = M$) is not guaranteed anymore. In fact, many theories indicate that the effective mass of nucleons is reduced, which is related to the strength of the potential energy responsible for nuclear binding. Assuming the neutrino interaction with a free nucleon, the energy-momentum conservation gives the relationship of the energy transfer expressed by

$$q_0 = \Delta E \simeq \frac{-q^2}{2M}. \tag{4.19}$$

The change in the effective mass of nucleons can violate this relationship, which may shift the peak of the energy distribution for free particles.

Coulomb correction

An outgoing lepton is subject to the Coulomb distortion in the Coulomb field of a nucleus. This effect can be considered by replacing the energy transfer q^0 with $q^0 - V_c(r)$ where $V_c(r)$ is the Coulomb potential expressed by

$$V_c(r) = Z_f \alpha 4\pi \left(\frac{1}{r} \int_0^r \frac{\rho_p(r')}{Z} r'^2 dr' + \int_\infty^r \frac{\rho_p(r')}{Z} r'^2 dr' \right), \tag{4.20}$$

where α is the fine structure constant, Z_f is +e (-e) for positively (negatively) charged leptons.

Considering all of the nuclear effects stated above, in the Fermi gas model, the free nucleon cross section is multiplied by a factor of $(1 - D(q^2, N, Z, k_F)/N)$, where N is the number of nucleon targets and D is a factor depending upon the four-momentum transfer squared, q^2, N, Z and the Fermi momentum k_F of the target nucleus. This non-relativistic Fermi gas model has been extended to the relativistic Fermi gas model by Smith and Moniz [93, 94]. In this model, the reduction factor $1 - D(q^2, N, Z, k_F)/N$ was replaced with the response function $R(\overrightarrow{q}, q_0)$. The expression for the double differential cross section is given by

$$\left(\frac{d^2\sigma}{d\Omega_l dE_l} \right) = C \left(\frac{d\sigma_{\text{free}}}{d\Omega_l} \right) R(\overrightarrow{q}, q_0),$$

$$R(\overrightarrow{q}, q_0) = \frac{1}{(4/3)\pi p_{F_N}^3} \int \frac{d^3 p_N M^2}{E_N E_{N'}} \delta(E_N + q_0 - E_B - E_{N'}) \theta(p_{F_N} - |\overrightarrow{p}_N|) \theta(|\overrightarrow{p}_N + \overrightarrow{q}| - p_{F_{N'}}),$$
$$\tag{4.21}$$

where $\frac{d\sigma_{\text{free}}}{d\Omega_l}$ is the free nucleon cross section for the neutrino or anti-neutrino scattering, $N, N' = n$ or p. In the charged current scattering, neutrinos interact with neutrons and anti-neutrinos interact with protons. Then the factor C is chosen to be $C = A - Z$ for a neutrino induced process and $C = Z$ for an anti-neutrino induced process. The global Fermi gas model assumes that Fermi momenta for both proton and neutron ($p_{F_N}, p_{F_{N'}}$) do not depend on their interaction points. They are expressed by

$$p_{F_N} = (3\pi^2 \rho_n)^{1/3}, \quad p_{F_{N'}} = (3\pi^2 \rho_p)^{1/3}, \tag{4.22}$$

where ρ_n and ρ_p are densities for neutron and proton. On the other hand, in the local Fermi gas model, these densities are assumed to depend on interaction points. The density functions are given by

$$\rho_p(r) = \frac{Z}{A}\rho(r), \quad \rho_n(r) = \frac{A-Z}{A}\rho(r), \tag{4.23}$$

where $\rho(r)$ is the nuclear density, which was determined experimentally by the electron-nucleus scattering experiments [95, 96]. In order to calculate the scattering cross section, the Fermi momenta need to be integrated over the whole nucleus.

Nucleon-Nucleon correlation

The nucleon-nucleon correlations have an important role to understand the neutrino interaction with nucleons in a nucleus, in particular for accelerator neutrino experiments such as T2K. Those correlations appear as either a short-range effect or a long-range effect, which corresponds to the exchange of pion or heavier mesons. The short-range effect is associated with the Meson Exchange Current effect (MEC), which happens when two nucleons exchange the mesons in flight in a nuclear medium shown in Figure 14. These nucleon-nucleon correlations are treated in the microscopic model by Martini [97] in the relativistic Fermi gas model by Nieves et al. [98] by taking into account the MEC diagrams such as the ones in Figure 14.
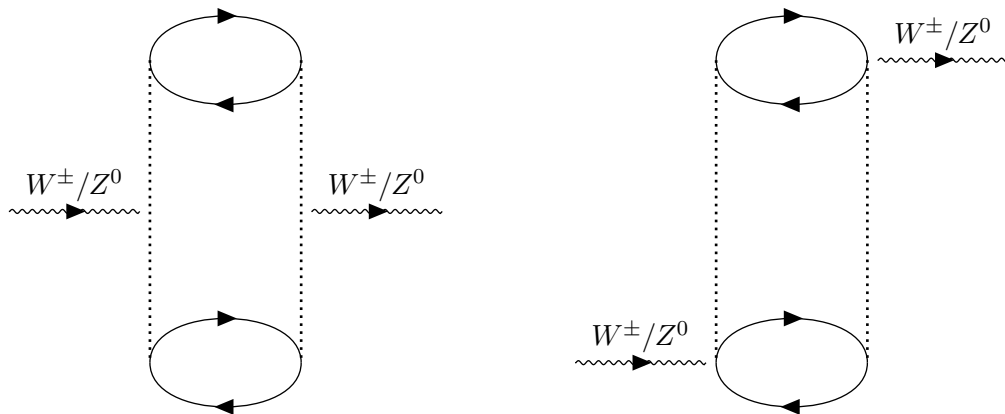
Figure 14: Feynman diagrams for some typical 2p-2h contributions from the meson exchange. Solid (dashed) lines denote nucleon (pion) propagators. Arrows pointing to the right (left) denote particle (hole) states. Both diagrams show the ph-ph interaction driven by pion exchange where the outgoing gauge boson is coupled to the pion (second nucleon) in the left (right) figure.

One of the hottest topics on the nuclear medium effects is the interpretation of discrepancies in the results of M_A. The MiniBooNE collaboration reported the differential cross section for the charged current quasi-elastic scattering process using a high statistic sample of ν_μ interactions in ^{12}C with the averaged energy of 750 MeV [99]. The results show the best-fit value of M_A was 1.35 ± 0.17 GeV/c^2 with the relativistic Fermi gas model while the world average at that moment was 1.026 GeV/c^2. This discrepancy indicated there were some missing contributions in the quasi-elastic interactions in the MiniBooNE measurements assuming the other experimental results were true or the value of M_A was wrong in the other experiments or there were invalid assumptions in underlying theoretical models. One of the early attempts to account for this discrepancy is to consider the Final State Interactions mimicking the quasi-elastic events. Even

if neutrino interactions produce hadrons or mesons along with a lepton, some of them may be re-absorbed by the nucleus. As a result, only the lepton can be detected in the final state, which ends up increasing the quasi-elastic like events in cross section measurements. Many theoretical models were proposed including these FSI effects. However, they could not explain the MiniBooNE M_A value in a consistent manner. On the other hand, Martini et al. and Nieves et al. emphasized there were additional contributions from MEC and nucleon-nucleon correlation effects. The enhancement in the cross section from the MiniBooNE experiments can be explained by taking into account the two-particle two-hole (2p-2h) excitations in addition to the interference with 1p-1h excitations. The theoretical calculation including these contributions has a better agreement with the MiniBooNE cross section results using the value of $M_A = 1.049$ GeV/c^2 [100]. On the other hand, there has been no clear evidence of 2p-2h excitations with neutrino probes while they are confirmed by electron scattering experiments. This is due in large part to the difficulty to separate the contributions from quasi-elastic events and the nucleon-nucleon correlations. This lack of understanding of 2p-2h contributions leads to the large systematic uncertainty on the neutrino oscillation measurements in T2K.

4.3.2   Interaction models for meson productions

The final state interactions (FSI) are important effects in neutrino meson productions with nucleon in a nucleus. When a pion is produced inside the nucleus, it is sometimes subject to scattering or absorption in the presence of strong interactions of final state pions in the nuclear medium. Consequently, there are several effects to be considered; the pion cannot get outside of the nucleus, the pion can change its direction, energy, and charge or even produce more pions. Considering the pion absorption, while it can enhance the yield of quasi-elastic scattering events, on the contrary, it should reduce the number of CC single pion production event candidates, CC1π in comparison with the theoretical predictions. The CC1π events mainly come from resonant and non-resonant pion productions. The earlier calculations of those processes were described in Rein and Sehgal model [101]. Then the model was modified for the inclusion of the nuclear medium effects, which was seen from the works [93] by Smith and Moniz in the non-relativistic global Fermi gas model explained in the previous section. The first implementation of the FSI effect in a theoretical model was done by Adler et al. [102]. This model uses a multipole scattering theory of pions. Another approach is to prepare a distorted wave function for pions replacing the plane wave function by solving the Klein-Gordon equation for pions in an optical potential. The approach of the distorted wave function was utilized in the model of distorted wave Born approximation (DWBA) [103] and Glauber model [104–106]. For high energy and forward angles corresponding to a low q^2 region, the Glauber model is a more accurate prescription for FSI. In addition, the model proposed by Vicente Vacas [107] should be noted because it is prevalent in neutrino interaction generators for neutrino programs.

Vicente's model disentangles the effects from pion absorption dominant in lower energy regions around a few hundred MeV and the pion production prevalent in the higher energy regions. In the initial iteration of the simulation, pions are generated given momentum and charge, which travel in z-direction, with a random impact parameter $\overrightarrow{b}$, obeying $|\overrightarrow{b}| < R$, where R is the upper bound for the nucleus radius. The pions are placed at $(\overrightarrow{b}, z_{\text{in}})$, where $z_{\text{in}} = -\sqrt{R^2 - |b^2|}$. The next iteration moves them along with the z-direction in small steps (equivalent to the length δl) until they get out of the nucleus or interact. The interaction probability of pion is assumed to be represented by $P(q, r, \lambda)$, where $\overrightarrow{q}, r$ are the pion momentum and charge, and r is its position. The value of $P(q, r, \lambda)\delta l$ is taken as a reference value to judge if the pion has an interaction

inside the nucleus. Inside the iteration loop, once that randomly generated number from 0 to 1 exceeds the reference value, the pion is assumed to have an interaction. Then it determines the interaction type according to the pre-calculated weights.

The modifications taking into account the FSI have non-negligible effects on the theoretical prediction compared to the free-nucleon cases [108]. The theoretical calculation was also compared to several kinds of neutrino interaction modes implemented in neutrino interaction generators (GiBUU [109], NuWro [110], GENIE [111], NEUT [112]) along with the experimental data, which is shown in Figure 15. There has not been a solid neutrino model to describe major experimental data for this interaction process.
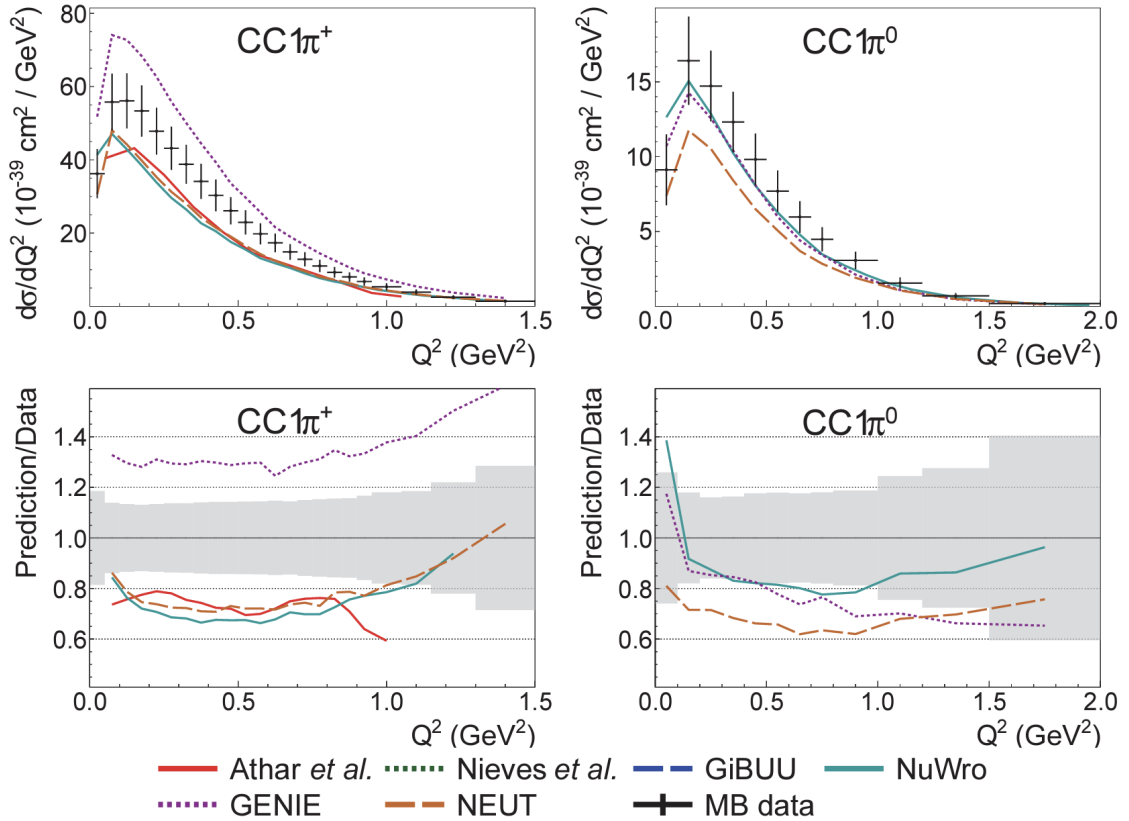
Figure 15: Comparisons of the differential cross section as a function of momentum transfer (Q^2) for CC1π^+ sample (left) and CC1π^0 sample (right) [113]. CC1π^+ (CC1π^0) refers to the interaction topology where there exists only one charged (neutral) pion in the final state. The MiniBooNE data [114] were compared with various neutrino generators (GiBUU, NuWro, GENIE, NEUT) and theoretical models (Athar et al. [115], Nieves et al. [116]).

4.4 Importance of interaction models in neutrino oscillation measurements

In T2K, the mean energy of neutrinos is around 1 GeV. In the oscillation analysis, we compare the event rate in data with the prediction obtained from the established model by theories and experiments. The event rate before the oscillation is mainly defined as a function of the neutrino flux, the neutrino cross section, and the signal detection efficiency. Knowledge about neutrino

interactions is important to reduce one of the systematic uncertainties on the neutrino oscillation measurements.

The nuclear medium effects are the major cause to impede the construction of a solid neutrino interaction model. Due to the T2K far detector's limitations to deal with the nuclear medium effects, the nuclear effects can affect the energy reconstruction of neutrinos. As the neutrino oscillation probability depends on the neutrino energy (see Equation 2.23 [13]), the energy reconstruction for signal samples is essential for the sensitivity to neutrino oscillation parameters. The simplest interaction to calculate neutrino energy among three major scattering processes is the quasi-elastic scattering where there are no additional hadrons in the final states. Assuming the quasi-elastic interaction, where muon is produced as a lepton, reconstructed neutrino energy without the nuclear medium effects is given by

$$E_\nu^{\mathrm{rec}} = \frac{M_p^2 + 2E_\mu M_n - M_n^2 - m_\mu^2}{2(M_n - E_\mu + P_\mu \cos\theta_\mu)}. \tag{4.24}$$

Considering the nuclear effects, the assumptions to derive this formula ($p^2 = M_n^2, p'^2 = M_p^2$) are not valid anymore because of the binding energy between nucleons and of the nucleons not being at rest. The modification is done by changing $p_n^2 \to (M_n - E_B)^2 - \overrightarrow{p}_n^2$ where E_B is the binding energy and $\overrightarrow{p_n}$ is the spectral function of the nucleon in a nucleus. It means the reconstructed energy has to depend on the effective binding energy and model-dependent spectral functions. Thus, in addition to the precise measurements of cross section, the understandings of the binding energy and spectral functions are also important for the precise measurements of neutrino oscillations.

The effect of the nucleon-nucleon correlations (2p2h interactions) on the reconstructed energy is not negligible. Misidentification of the 2p2h events as the CCQE events leads to an energy bias because nucleons take a part of the energy, which cannot be considered in Equation 4.24. In order to mitigate the effect of this energy bias by simulation, a deeper understanding of the ratio of interaction type in each signal sample is important.

The T2K near detector, ND280 has measured neutrino-nucleus cross sections to deepen the understanding of the effect of the neutrino interactions on the oscillation measurements. In addition, we have developed our own neutrino interaction simulator called NEUT to model the neutrino interactions including the nuclear medium effects such as Pauli blocking and 2p2h interactions. The ND280 measurements are utilized to constrain the interaction parameters in the models. The constraints can reduce the model uncertainties in a data-driven way, and increase the sensitivity of the neutrino oscillation measurements in T2K. On the other hand, the main target of the ND280 is hydrocarbons and the phase space coverage to the large angle scattering particles is limited due to the scintillator structure of the vertex detectors, FGDs and P∅D. These issues are discussed in part 3 in detail.

---

[13]

$$P(\nu_\mu \to \nu_e) \approx \sin^2 2\theta_{13} \sin^2 \theta_{23} \sin^2 \left(\frac{\Delta m_{32}^2 L}{4E} \right)$$

Part II
Measurement of neutrino oscillation parameters from the T2K experiment

5   Measurement of neutrino beam

Section 3.3 introduces the design of the T2K muon monitor, MUMON. The prominent role of MUMON is to confirm the neutrino beam is directed to Super-Kamiokande at 2.5 degrees off-axis by providing a sufficiently precise muon beam profile. It is necessary to monitor the neutrino beam direction on the accelerator bunch-by-bunch basis for the T2K beam operation to ensure the off-axis neutrino beam. This is because the timing of neutrino beams might change on a bunch-by-bunch basis, which must be monitored in order to collect good-quality data. The oscillation analysis described in this thesis has experienced an increase in statistics taken in Run10 as in Figure 9. One of the author's contributions to the analysis is to work on MUMON in order to monitor the neutrino profiles precisely throughout the data taking. The following descriptions cover the calibration methods and performance of the neutrino beam profile measurements.

5.1   Calibration

MUMON has 49 sensors in Si and IC detectors. The responses from the sensors should ideally be the same for the same signal. However, each channel may have a different response due to the radiation damage of the sensor or a small change in the circuit property. In order to correct the channel responses, we perform two kinds of calibrations for each beam operation in T2K.

The calibration on the first stage, electronics calibration is done to correct the response of each readout electronics. In the measurement of each channel's response, we input a set of signals of known charges to each channel. From the measured charges, we know the relationship between input charges and responses. Using the relationships, the differences in responses between channels can be corrected. This calibration is performed prior to the beam operation.

The calibration on the second stage, detector calibration is performed during the beam operation. The procedures are different between Si and IC detectors. During the detector calibration for Si sensors, the reference Si sensor is moved to the center of the seven-by-seven array. Then each of the sensors is moved to the center behind the reference sensor. The ratio of the signal yield from each sensor to the one from the reference sensor is measured. On the other hand, the reference sensor is not available for the IC detector. The whole array is moved in the way how the center position is moved to nine points in three by three with an interval of 25 cm between two neighboring points. These array movements end up producing nine data sets, corresponding to profiles at different beam positions. For each profile, χ^2 is calculated by taking into account the difference between yields calculated by the relative gain of each channel and the averaged yield of the channel. The summation of all χ^2 values is the function of the relative gain of 48 channels [14]. The minimum χ^2 method extracts the best-fit values of each relative gain.

Both detector calibrations correct the relative difference with respect to a certain yield of the reference sensor. These calibrations contribute to suppressing the individual difference at less than 0.1 % level.

---

[14]One relative gain is defined as 1.0, and then one degree of freedom is lost.

5.2 Waveform analysis

The proton beam pulse has an eight-bunch structure in a spill, which is also reflected in the muon beam structure. Figure 16 exemplifies typical waveforms of a channel observed in MUMON. A bunch-by-bunch yield is defined as the integral of ADC counts subtracted by the common pedestal in a spill. The average ADC outside the expected 1st and 8th bunch timings gives the pedestal for each spill. In order to reflect known factors from horn power supplies and proton beam width to affect muon flux, corresponding corrections are applied in the calculation. [15] The integral of yields in eight bunches defines a signal response of the channel. In the case of IC-He detector, the waveform is distorted due to the pileup effect. Since a He ion is much lighter than an Ar ion, the drift speed of He ion gas is faster. The time constant of capacitor discharge is slower than the shorter time of the charge collection in the circuit. Nevertheless, the yield is calculated in the same way as above. It may have a negative effect on the profile measurement. We have not so far seen the major effects of the pile-up on the neutrino beam profile measurement.

| (a) Si | (b) IC-He | (c) IC-Ar |
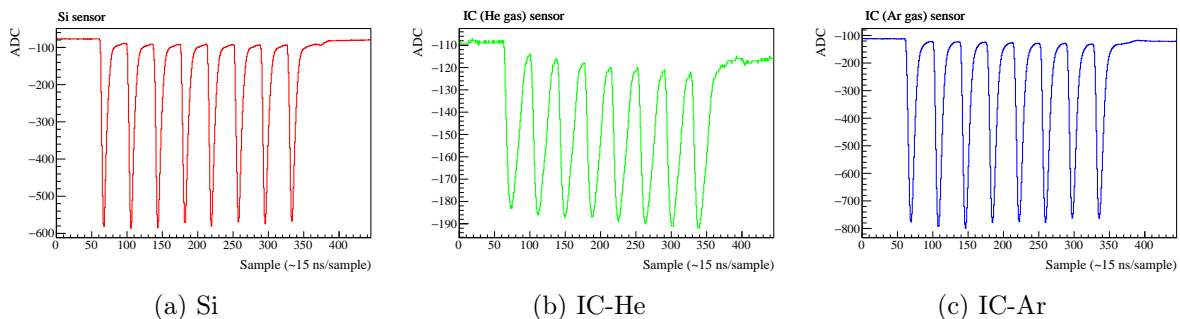
Figure 16: Examples of a waveform from each sensor (Left: Si, Middle: IC-He, Right: IC-Ar) at around 400 kW beam power operation in a spill. All of them clearly show an eight-bunch structure. The waveform in the case of IC-He has a distinct feature due to the pile-up effects.

5.3 Linearity and stability measurements

The linear relationship between the muon flux and the signal response from a sensor is the prominent requirement to profile the muon beam properly. As the muon flux is proportional to the initial proton beam intensity, we use Current Transformers (CT) installed in the primary beamline to estimate the muon flux. The response from Si or IC detectors is measured in the sense of the integral of all the forty-nine sensors. Then, the relationship between CT values and signal responses is tested. Figure 17 shows the result of linearity measurements for Si, IC (Ar) and IC (He) using the proton beam provided by J-PARC. The integral of the signal responses divided by the CT value is drawn against the corresponding proton beam power. The deviation from the perfect linearity stays within almost 1% fluctuation, which satisfies the requirement, 3% for all of the sensors. This is the case for IC-He as well. It also confirms pile-up effects seen in the waveform do not affect the linearity of the sensors significantly.

---

[15]The charged pions decay into muon, which forms muon flux into MUMON. The muon flux depends on how well the horns focus the pions, which is potentially affected by the horn current. The test measurement reveals the relationship between the power of the horn power supply and muon profiles. That turns into one of the correction factors. In addition, increased beam powers result in a high-intensity proton beam. This affects the proton beam width because of the repellent force between protons, which in turn has an impact on the muon flux. The Monte-Carlo simulation confirms the effect. The correction factor was determined by the simulation result.

(a) Si

(b) IC-He

(c) IC-Ar
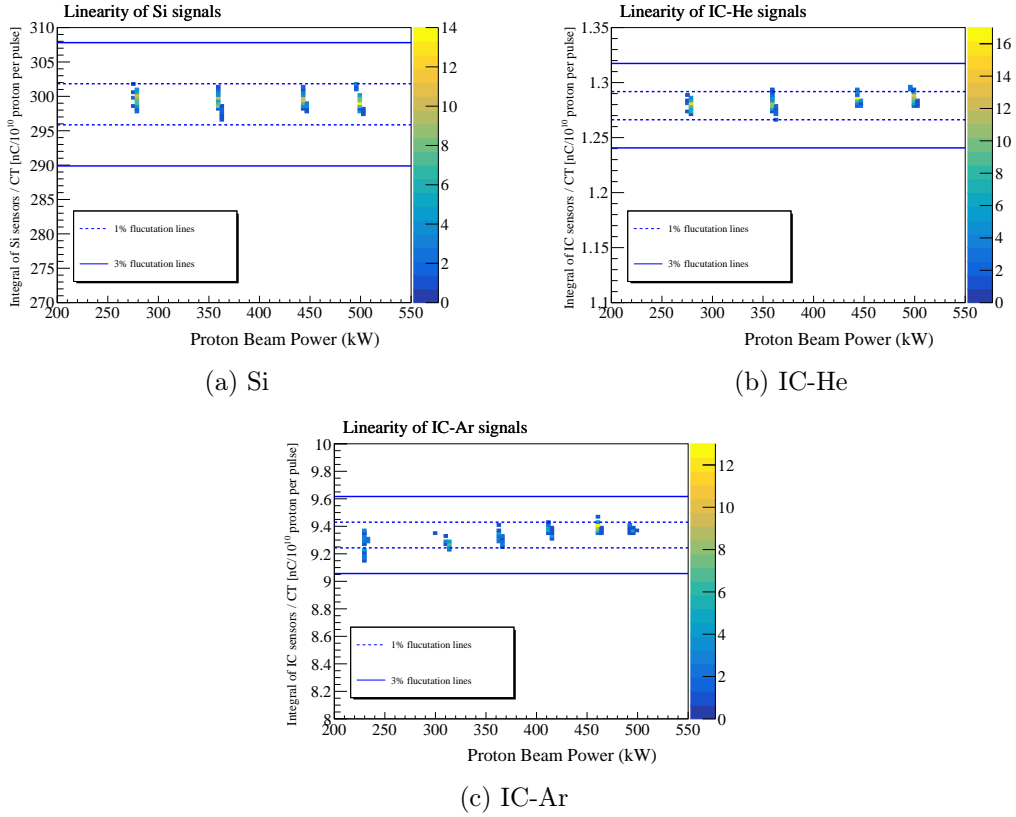
Figure 17: Results of linearity measurement with the beam power. Each point includes 50 spills for this measurement. These plots show the signal response defined as the integral of all the channels divided by the CT value at each beam power. The color refers to the population of the number of shots. If we were to achieve perfect linearity, the data points would be aligned with a constant straight line. Two lines indicate 1% (by a broken line) and 3% (by a solid line) fluctuations.

The stable response from both detectors during one period of physics operation is mandatory as an intensity monitor. [16] As discussed in the detector design, Si sensors are subject to signal degradation during high-intensity beam operation while IC sensors have a superior performance in terms of stability. At the beginning of the T2K experiment, as the beam intensity is lower due to the limitation of the beam power being up to 50 to 100 kW, the signal degradation did not matter. The current maximum beam power is over 500 kW. The impact of the signal degradation on the stability is necessary to check. Figure 18 shows the history of signal responses from each detector. The data set for the IC-Ar detector was physics data taken in 2019 while that for the IC-He and Si detector was data taken in 2021. Both IC sensors achieved stable operation within just 1% fluctuation of signal yields. In addition, they did not have any obvious tendency to degrade during the period. On the other hand, the tendency of the degradation in Si sensors is clearly seen in two weeks of the beam operation. The signal depletion rate is around 1% per

---

[16]We can conduct the T2K measurement in accordance with the availability of the Main Ring. The unit of operation time is a cycle. Each cycle corresponds to a one-month operation. The T2K experiment conducts one or two cycles in each period.

three months of operations under the 500 kW beam power. This degradation is not significant to determine the muon profile during the one-year operation for the T2K experiment at that moment as long as the replacement of Si sensors is done.

(a) Si

(b) IC-He

(c) IC-Ar
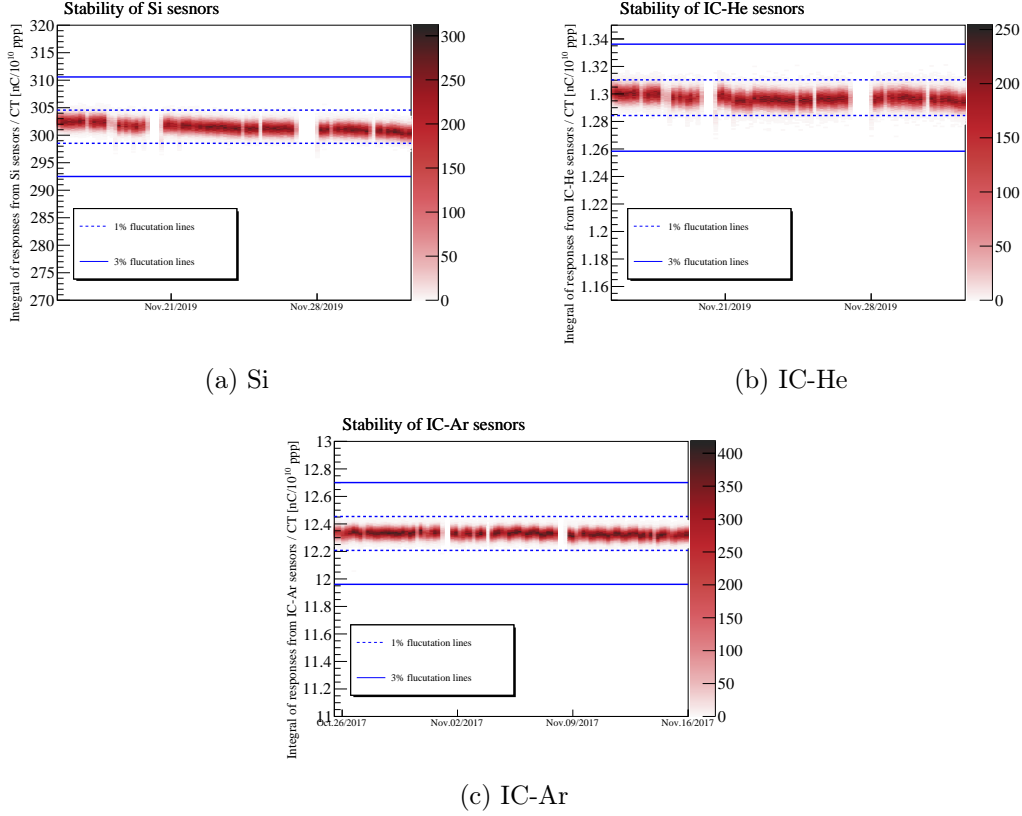
Figure 18: Results of stability measurement during around two weeks of the beam operation under 480 kW beam power. The integral of signal yields of all the sensors is normalized by the corresponding CT values. The normalized integral value is plotted as time elapses.

5.4   Measurement of muon beam profile

The aforementioned waveform analysis gives a bunch-by-bunch image of signal yields exemplified in Figure 19. This shows that MUMON satisfies one of the requirements; to measure the profile on a bunch-by-bunch basis. In the context of the oscillation analysis, the MUMON profile measurement is used as one of the criteria to select a good spill that can be used for the T2K oscillation analysis. The cut condition on the muon profile is described below.

- Beam angle is within 1 mrad, which corresponds to the fit center from Si and IC being less than 10 cm. The 1 mrad uncertainty on the beam angle results in the 2% and 3% uncertainties on the energy scale and the neutrino flux, respectively. These systematic uncertainties are not dominant compared to other uncertainties.

- The fluctuation on total signal yield in a spill from Si and IC is within $\pm$ 5% with respect to the average yield throughout the beam operation to be able to function as a backup detector of T2K on-axis near detector, INGRID, measuring the neutrino flux fluctuation.
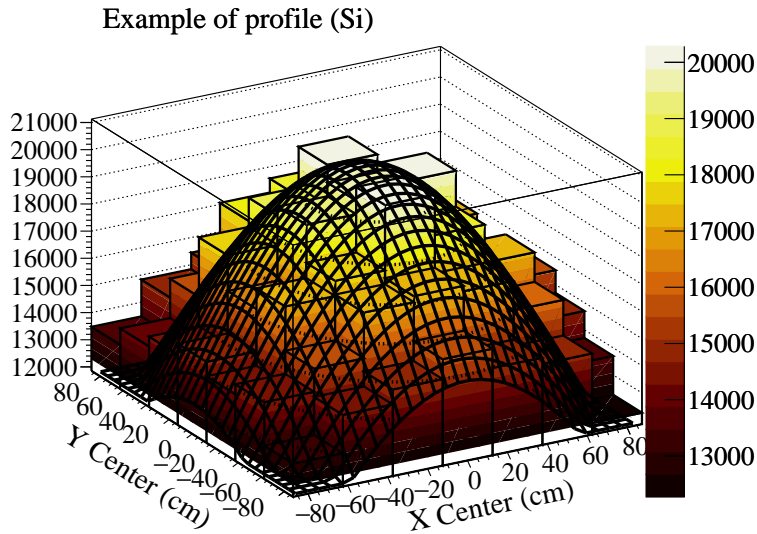
Figure 19: An example of muon beam profile measured by Si sensors in the first bunch under 480 kW proton beam operation. The profile width is typically 100 cm for both X and Y positions. The surface overlaid on the histogram represents the two-dimensional gaussian fitting.

The recent physics data taking was conducted in 2019 for two months and 2020 for two months. The selection results from MUMON in 2020 beam operation are shown in Figure 20. The figure includes only results from Si sensors. The profile measurement from IC sensors provided the same selection results. The center positions measured by MUMON satisfy the criteria throughout the period. However, the measurement of the integral of signal yields finds three spills that are deviated outside the criteria. All three spills are scrutinized by checking waveforms observed in several monitors. The overlaid waveform of these problematic spills on one of the waveforms from the good spills revealed a timing shift in MUMON. As the cause of the timing shift is unknown, those three spills are rejected from the good spill selections, which amounts to only 0.0004%. [17] Otherwise, MUMON confirmed that the T2K neutrino beam was properly focused in the aimed direction.

5.5 Summary

MUMON has fulfilled its role in monitoring neutrino beams. The author's contributions to the published paper are to maintain and operate MUMON during the T2K Run10, which corresponds to the updating statistics for the oscillation analysis described in this thesis.

---

[17]During the beam operation in 2019, two problematic spills were found in MUMON due to the same reason.
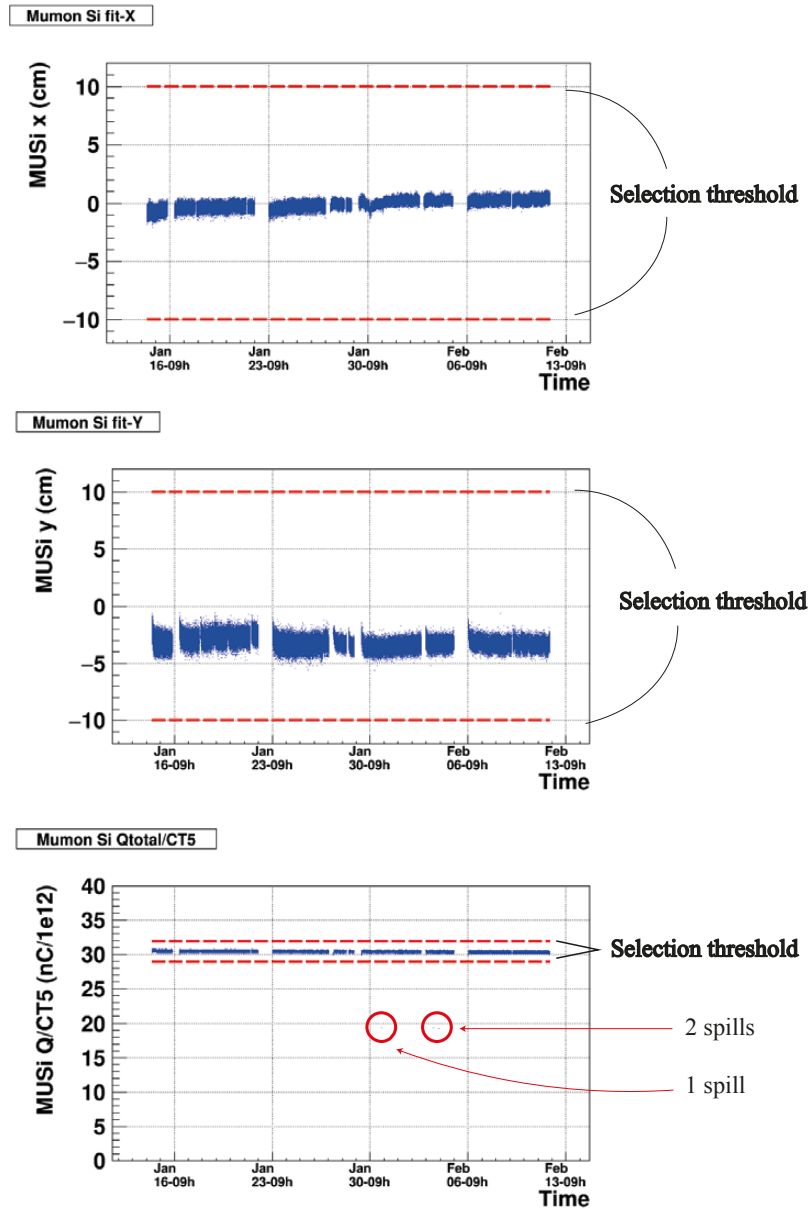
Figure 20: Results of the profile and intensity measurements from MUMON (only Si sensors). The top and middle figures show the profile center in the X and Y direction, respectively. All the spills pass the selection. The bottom one is the history plot for the intensity measurement. Based on the criteria, three spills are rejected.

6 Oscillation analysis methods

This chapter describes the analysis methods of the T2K experiment to measure the neutrino oscillation parameters.

6.1 Overview

The methods are divided into five steps; neutrino flux prediction, neutrino interaction modeling, near detector fitting, event reconstruction at the far detector, and far detector fitting. The precise prediction of the unoscillated neutrino flux at the far detector is essential. The error sources on the flux prediction come from beamline components and hadronic interactions. They are estimated in a Monte Carlo simulation framework with a hadronic interaction simulation tool. Furthermore, the T2K has made use of the external experimental results of the pion and kaon cross sections to constrain the uncertainties on hadronic interactions inside the target. Section 6.2 focuses on the method and the results of the flux prediction. We have developed a software package to simulate neutrino interactions including the nuclear medium effects. Section 6.3 introduces our framework to simulate neutrino interactions as well as the interaction models on which it is based. These flux prediction and neutrino interaction models include more than 100 parameters in total. Without any additional data-based constraints on these parameters, they inflate the systematic uncertainties. ND280 has collected neutrino data to measure the neutrino-nucleus cross sections. Near detector fitting frameworks utilize the data to give constraints on all the parameters simultaneously taking into account all the correlations among them. The method and the results are described in Section 6.4. At the far detector, the main measurement objects are ν_e appearance and ν_μ disappearance. Section 6.5 describes analysis samples including their selection criteria. The final step to get results on the neutrino oscillation parameters is the far detector fit with reconstructed events from data and all nuisance parameters. Section 6.6 overviews the core of the fitting algorithm.

The descriptions are based on the analysis in the published results [67]. In this thesis, several updates have been added to the published results. The differences between them are also described in this chapter.

6.2 Neutrino flux model

A precise estimation of unoscillated neutrino flux at the far detector is a key ingredient in the oscillation analysis. The T2K experiment has developed its own framework to provide the nominal flux prediction and its uncertainties. The simulation consists of three processes to produce the flux prediction.

1. Simulate proton-nucleus interactions inside the graphite target.

2. Geant3-based Monte-Carlo simulation reproduces the experimental apparatus of the secondary beamline. The simulation tracks down all of the particles exiting from the graphite target which are produced by proton interactions.

3. Tune the flux prediction from the Monte-Carlo simulation based on external experiments.

The T2K neutrino flux model relies on external software to handle hadronic interactions, FLUKA 2011.v2 [117] inside the target. The Geant3-based Monte-Carlo simulation, JNUBEAM [118] tracks down all particles exiting the target. In the Geant3 simulation, the initial proton beam

generator reflects every detail of the proton beam properties such as energy and beam direction. The geometry reflects the measurements of alignment and dimension for each piece of equipment. The output of JNUBEAM software provides the prior neutrino flux prediction based on the proton beam profiles that are measured in the beam operation. The hadronic interactions simulated by FLUKA are furthermore studied by external experiments such as NA61/SHINE. The NA61/SHINE experiments ([119–121]) dedicated to studying the hadronic interactions with proton beam has contributed to improving the precision of the flux prediction. They used a 2 cm long graphite target called thin target [119] and a 90 cm long graphite target called replica target [120, 121]. As the replica target has the same dimension as the T2K's graphite target and has larger phase space coverage for exiting pions, it has superior performance in understanding hadronic interactions for the T2K experiment.

In addition to the nominal neutrino flux prediction, we can estimate the uncertainties using the JNUBEAM software. The potential sources responsible for uncertainties on the neutrino flux are categorized into "beam-related" and "hadronic interactions". Beam-related mainly refers to the uncertainties coming from the misalignment of the target and horn, and magnetic field distortion. The uncertainties on hadronic interactions include the ones on primary proton interactions, meson multiplicities and kinematics, and secondary interactions. The NA61/SHINE results on the pion and kaon cross section are applied to constrain the uncertainties on hadronic interactions. Applying the cross section results on the thin target can reduce the uncertainties to a 10% level around the peak energy of T2K's neutrino beam. The cross section results on the replica target are divided into the pion production results [120] and kaon production results [121]. As the pion production is the main contribution to the T2K neutrino beam, whose energy range is about 1 GeV, applying the pion production results improves the uncertainties on hadronic interactions from 10% to 5% around that energy region. On the other hand, the kaon production contributes to higher energy regions, typically more than 2 GeV, and the uncertainties in the corresponding energy region are reduced to around 5% level from 10%. The published results [16] use the pion production results as well as the thin target results but the kaon production results, which are first applied in the updated results described in this thesis.

The neutrino flux predictions before neutrino oscillations with all the pion and kaon cross section results applied are shown in Figure 21 for both neutrino and anti-neutrino modes. The beam-intrinsic ν_e constituting an irreducible background in the neutrino oscillation analysis is 1%. The contribution from wrong-sign flavors such as $\overline{\nu}_\mu$ to ν_μ or ν_μ to $\overline{\nu}_\mu$ comes from mainly the dispersing charged pions. The fraction of the background is suppressed in the lower energy region up to 1.5 GeV thanks to the horns dispersing wrong-sign pions. In the intermediate energy region from 1.5 GeV to 3 GeV, pions that are not focused contain a larger fraction of π^- in ν_μ mode, which increases the contamination from pion backgrounds. In the high energy tail, kaon production becomes significant, which leads to $\overline{\nu}_\mu$ contamination being less significant.

Figure 22 shows the uncertainties of ν_μ or $\overline{\nu}_\mu$ enriched neutrino flux including both right-sign and wrong-sign neutrinos at the far detector. The total uncertainties around 1 GeV are around 10% level in the case of right-sign (anti-)neutrino due to the cross section results on the replica target from the NA61/SHINE experiments. The reduction has been achieved around the 2 GeV to 7 GeV region, which is thanks to the flux tuning based on the kaon production results for both right-sign and wrong-sign cases. In addition, a small reduction is seen in sub-GeV region in the updated results with respect to the published results, which is attributed to the statistical update on the NA61/SHINE thin target measurements. On the other hand, a small increase in uncertainty is seen around the 1 GeV region for the updated results. This is due to the update

on the horn field asymmetry in the JNUBEAM software [18].

(a) neutrino mode

(b) anti-neutrino mode

(c) neutrino mode

(d) anti-neutrino mode
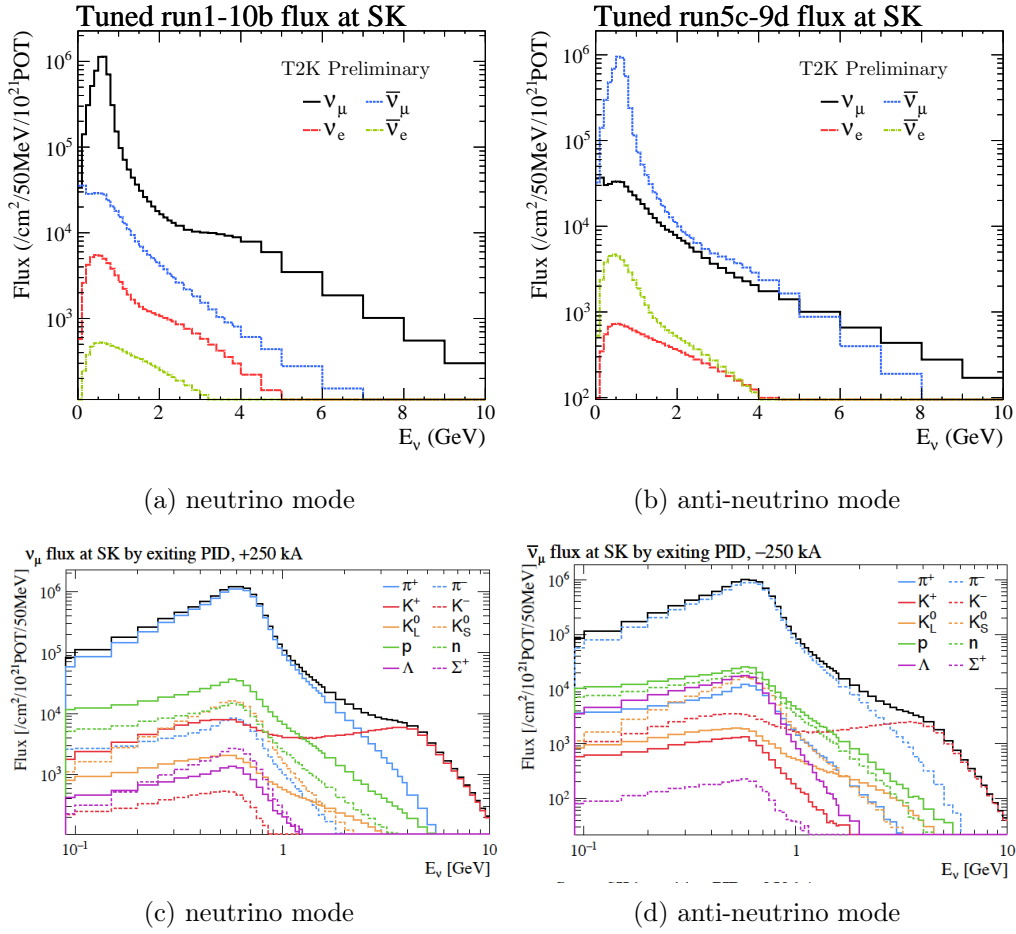
Figure 21: Unoscillated neutrino flux prediction at the far detector (SK) broken down by neutrino flavor (top) and the parent particles of the neutrinos (bottom). The flux tuning from the measurements of the thin target and the replica target was applied. For the neutrino mode (FHC), the fraction of ν_μ is 94.3% whereas that of $\overline{\nu}_\mu$ is 4.8%. For the anti-neutrino mode (RHC), the fraction of $\overline{\nu}_\mu$ is 92.7% whereas that of ν_μ is 6.5%.

---

[18] A bug in the JNUBEAM software about the magnetic field by the horns not being implemented correctly was found. After the proper implementation of the horn field gave a slight increase in the uncertainties around the peak energy of the neutrino beam. This bug fix was applied in the updated analysis.
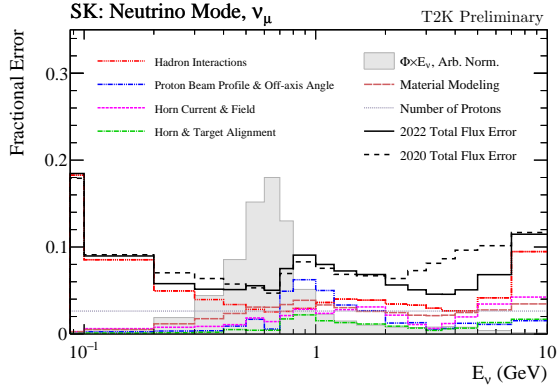
(a) Right-sign neutrino in neutrino mode
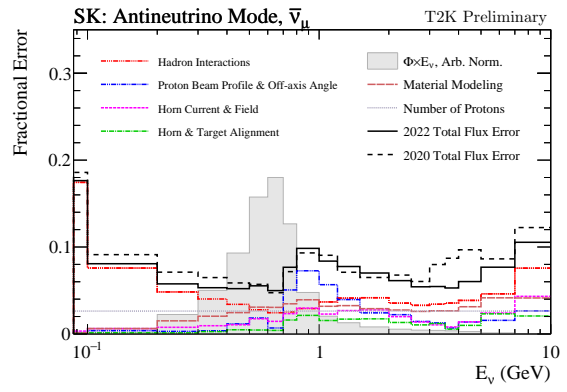
(b) Right-sign anti-neutrino in anti-neutrino mode
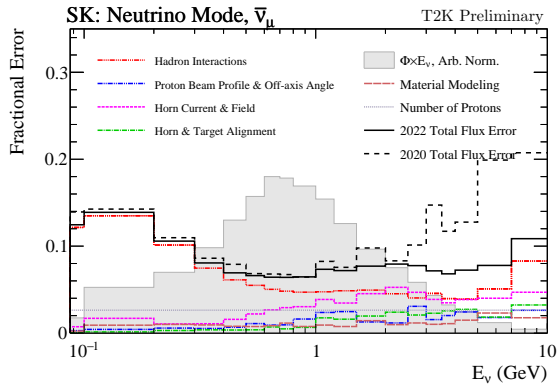
(c) Wrong-sign anti-neutrino in neutrino mode
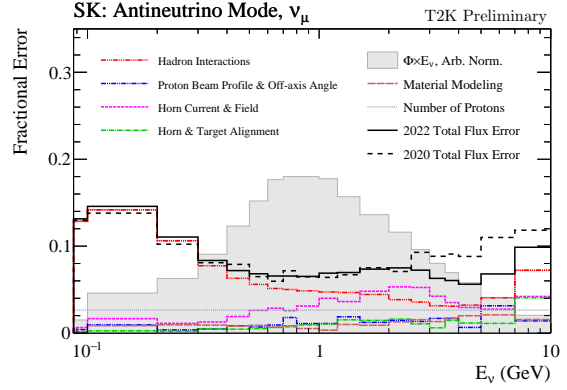
(d) Wrong-sign neutrino in anti-neutrino mode

Figure 22: Fractional uncertainties for both neutrino (upper) and anti-neutrino (lower) modes further classified into right-sign neutrinos (left) and wrong-sign neutrinos (right). Each colored line corresponds to the major sources of the flux uncertainties. Orange: "hadronic interactions" is the collective category to include uncertainties from the primary proton interactions, meson multiplicities and kinematics and the secondary interactions. Blue: It comes from the errors of the beam profile and the resulting neutrino directions. Magenta: The error comes from the fluctuation of horn current and magnetic field distortion. Green: This shows the effect of the misalignments of the horns and the carbon target. Brown: It represents the uncertainty of the water flow for the horns. Gray: The error on the protons on target, POT, is included.

6.3 Neutrino interaction modeling

Chapter 4 emphasizes the importance of comprehensive knowledge of neutrino interactions. Despite all of the efforts from theoretical and experimental approaches, no solid model of neutrino interactions is available. This requires each experiment to select a set of adequate models to simulate neutrino interactions. We developed a neutrino interaction generator to handle this situation. The generator is named NEUT, which is a program library [112] containing collective interaction models to simulate each interaction by inputting the simulated neutrino flux provided by JNUBEAM. In order to implement contemporary corrections to conventional interaction models, the libraries have been updated by modifying relevant treatments to each type of interaction [122].

6.3.1 Model selections in 1p1h interactions

If neutrinos interact with a nucleon inside a nucleus, ejecting the excited nucleon outside the nucleus, it is categorized into the 1p1h interaction. The T2K oscillation analysis focuses on charged current interactions, in particular, charged current quasi-elastic (CCQE) interaction, which is a part of the 1p1h interaction. It is important to understand the nuclear ground state for this interaction. The recent measurement [123] suggests a model called the Spectral Function (SF) is in good agreement with the data. The SF model is a shell model description of the nucleon momentum (k) and energy (E), both of which constitute the spectral function $S(E, k)$. The spectral function acts as a correction factor to the single nucleon cross section in order to factorize a fully exclusive neutrino-nucleus cross section. This is the same treatment as that used in the description of the electron scattering cross section. Both theoretical and experimental results are able to make the SF model robust for neutrino experiments. Therefore, NEUT has adopted the SF as a base model. The single nucleon component uses the BBBA05 [124] to tune the vector part of the form factor, while it adopts a simple dipole form factor for the axial part. One drawback of the SF model is the missing implementation of the FSI effect on the lepton, which has an impact on the lepton kinematics. The potential effect is simulated by another neutrino interaction generator [110], which is propagated into NEUT.

6.3.2 Model selections in 2p2h interactions (two particle two hole)

Chapter 4 mentions the discrepancies in the axial part of the form factor between the cross section measurements from the experiments [80] using the bubble chamber on deuterium target and those from MiniBooNE and T2K experiments using mainly carbon target. The inclusion of 2p2h interaction in the conventional model made them consistent. The modification to the existing model by taking 2p2h interactions into account is promising for better understanding neutrino interactions. In addition, the appropriate treatment of 2p2h interactions is important not to introduce a reconstruction bias into neutrino energy.

There are several 2p2h models, Nieves et al. [116], Martini et al. [125] and SuSAv2 [126]. Although each of them describes the experimental data in certain kinematical phase space or target material, none of them has perfect descriptions of 2p2h interactions. NEUT selects the Nieves model as its base one. In order to take the model difference into account, several kinds of systematic parameters affecting the shape and normalization of 2p2h interactions are introduced in the oscillation analysis.

6.3.3 Model selections in meson productions

Single-pion production is one of the main processes in the T2K neutrino energy region. The T2K oscillation analysis has two samples whose main interaction type is single-pion production. This interaction is necessary to understand as one of the signals as well as the significant background in CCQE-like events. The characteristic of single pion production is a pion scattering off a nucleus. The single pion production has two types of mechanism for nucleon's excitation, resonance and non-resonance. In the T2K neutrino beam energy, the resonant single pion production via Δ (1232) resonance is predominant. NEUT uses the Rein-Segal model (see Section 4.3.2) with its extension to account for lepton mass effects [127] and the modified axial form factor (C_5^A) [128] focusing on Δ (1232) resonance. [19] For the non-resonance production, NEUT only models isospin -1/2 ($I_{1/2}$) interaction, while no model for isospin -3/2 ($I_{3/2}$) channel is available. One of the bubble chamber results [89] confirmed that the effect of this channel was small. While the resonant interaction occupies the majority in the single-pion production, NEUT models the coherent interaction with the updated Rein's model (Berger-Segal model [131]).

6.3.4 Model selections in deep inelastic scattering

As the neutrino energy reaches around 5 GeV, neutrinos can interact with a quark inside a nucleon which results in breaking the nucleon (Section 4.2.3). Considering the T2K neutrino flux, the interaction is not dominant. Nevertheless, this interaction is important in order to understand the background from the high-energy tail in the neutrino flux. In calculating the DIS cross section, two Bjorken scaling variables, denoted by x, y in Section 4.2.3 have an important role in constructing Parton Distribution Functions (PDFs). Bodek-Yang corrections [132] are applied to the PDFs so as to mitigate the differences between data and MC in the low momentum transfer region, $Q^2 < 1.5$ GeV^2/c^2.

6.3.5 Implementations of nuclear medium effects

We have also developed its treatments on nuclear medium effects, in particular FSI and Coulomb corrections. The single pion production and 1p1h interaction, especially QE are largely subject to the FSI effects. In addition, a hadron exiting a nucleus may have an interaction before it is reconstructed (Secondary Interaction, SI). NEUT relies on a semi-classical intra-nuclear cascade model to simulate pion interactions to account for FSI effects. The numerical method is similar to Vicente's model described in Section 4.3.2. In order to take into account the differences in comparison with the external data or other models, the differential cross sections of $\pi^\pm - A$, where A is a various kind of nucleus, as a function of pion momentum is fitted against the external data. Six scaling factors are fitting parameters having an impact on the interaction rate for each FSI effect such as absorption, charge exchange, and so on. The best-fit parameters and their uncertainties are propagated into the oscillation analysis as prior parameters.

Coulomb corrections have an effect on decreasing (increasing) the negatively (positively) charged lepton momentum, which ends up with the shift of reconstructed neutrino energy. The key variable to understand the effect is the Coulomb potential which is proportional to the charge of the nucleus. It was extracted by the fit to electron scattering data in [133]. The main target

---

[19]There was a deficit in data for the single pion production with forward going lepton [129]. One paper [130] suggests the inclusion of non-lepton mass in the calculation of single pion production leads to the suppression of the coherent interaction in the forward-going process. This is known as the "lepton mass effect".

materials are carbon in the near detector and oxygen in the far detector. Corresponding momentum shifts are applied. The momentum shifts for neutrinos are -3.6 MeV/c (-4.3 MeV/c) on the Carbon (Oxygen) target and +2.6 MeV/c (-3.3 MeV/c) on the carbon (oxygen) target for anti-neutrinos.

6.3.6 T2K parametrization for neutrino interaction models

This section summarizes the parametrization for neutrino interaction models. When possible, theory-driven parameters are prioritized. It is necessary to introduce more degrees of freedom in order to describe available experimental neutrino-nucleus cross section results. Therefore, additional empirical-driven parameters are included.

1p1h interactions

The central value and uncertainty of M_A^{QE} (1.03 ± 0.06 GeV/c^2) are allocated to describe available experimental data and the world average of the measurements. The CCQE suppression factors based on the experimental results from MINERvA [134, 135] and T2K [136, 137]) are parametrized as a function of momentum transfer, Q^2. In the published results, parameters for both low and high Q^2 regions are used. In the updated results, low Q^2 parameters are removed and more theory-driven parameters for the Pauli-Blocking are added. Pauli Blocking is one of the nuclear medium effects to affect the cross section in the low Q^2 regions. In NEUT, the cross section for the portion of the phase space in which the pre-FSI nucleon getting involved in the primary interaction has a lower value than a certain Fermi momentum (k_F) is set to 0. The parameter k_F is 209 MeV/c for both carbon and oxygen. There is no data to give a clue of which value should be taken as k_F. This analysis assigned 30 MeV/c as the uncertainty of the k_F conservatively so that the ND fit could drive the systematic error [20].

2p2h interactions

The 2p2h interaction occurs in either nn (neutron-neutron) or pn (proton-neutron) pairs for neutrinos while it occurs in either pn or pp pairs for anti-neutrinos. This analysis takes into account the fraction between these alternative two interactions in applying the normalization. As there are three underlying 2p2h models, SuSAv2, Nieves et al., and Martini et al., which predict different fractions, the uncertainty is inflated to account for these model differences.

CC Single-Pion Production (SPP) interactions

Single resonant pion production is based on the Rein-Sehgal model. The model has three characteristic parameters, the resonant axial mass (M_A^{RES}), the axial form factor at zero transferred momentum (C_5^A) and the normalization of the $I_{1/2}$ non-resonant component. The framework to tune and compare neutrino interaction generators called NUISANCE [139] used the available bubble chamber data from ANL [88, 89], BNL [87, 140] to determine the uncertainties of those parameters. In addition, we reanalyzed data [141] to extract central values of each parameter. The normalization parameters on the CC and NC coherent cross sections are assigned with the uncorrelated 30% uncertainties based on the MINERvA data [142].

---

[20]One of the standard values obtained from the experimental result is 228 MeV/c for Carbon [138]. Therefore, 30 MeV/c with respect to 209 MeV/c is as reasonably high as being considered conservative.

DIS interactions

    The main DIS parameters are associated with the Bodek-Yang (BY) corrections. They are parametrized by the differences in the cross section between with and without corrections. The impact of the BY corrections is small at the high transferred momentum region, $Q^2 \geq 1.5$ GeV^2/c^2. At the lower transferred momentum region, the effect of the BY corrections is significant. In accordance with this behavior, two kinds of parameters as a function of the final state invariant mass, denoted by W are introduced; $W < 2$ GeV/c^2 and $W > 2$ GeV/c^2 regions.

Final state interactions (FSI)

    The published results added pion FSI parameters based on the external data from pion-nucleus measurements. They were, however, not applied to nucleon FSI. The updated analysis introduces a parameter to deal with the nucleon FSI. The parameter increases or decreases the weight of an event if the nucleon exiting from the nucleus by the neutrino interaction is found to have an FSI effect [21], otherwise, does nothing. This effect ends up making multi-nucleon CCQE more or less likely depending on the direction of the tweak of the parameter.

6.4 Near detector fit

The T2K Near Detector Complex (ND280) has measured the neutrino interactions. In the context of neutrino oscillation analyses, we utilize the ND280 measurements to add constraints to the parameters in the flux prediction and neutrino interaction modeling through the near detector fitting (ND fit). The T2K flux prediction is already well-tuned by the external experiments (NA61/SHINE), having smaller uncertainties overall. While some of the cross section parameters have theory-driven central values and uncertainties, the uncertainties of most parameters are not theory-driven or inflated to account for various neutrino cross section measurements or divergent theories. The data by ND280 have the potential to give additional constraints on the flux and neutrino interaction parameters while taking into account the correlation between these parameters. The primary purpose of the ND fit is to find out a set of central values and uncertainties for both flux and cross section parameters describing the data.

6.4.1 Analysis samples

We make the analysis samples to the ND fit. In the published results, they are categorized from three points of view, which is illustrated in Figure 23. First, the event selection requires all the events to have an interaction vertex inside the fiducial volume of either FGD1 or FGD2. Second, analysis samples are classified by the neutrino flavor candidate and neutrino beam operation mode. The T2K experiment has collected data both at neutrino and anti-neutrino enriched modes. Thanks to the charge identification by the UA1 magnet installed in ND280, it is able to distinguish neutrino interactions (ν_μ) from anti-neutrino interactions ($\overline{\nu}_\mu$) by the curvature of the muon candidate track. As the ν_e events are statistically limited, only the ν_μ or $\overline{\nu}_\mu$ interactions are selected. The analysis samples consist of the right-sign muon neutrino events at both neutrino and anti-neutrino modes and the wrong-sign muon neutrino event at the anti-neutrino mode. The ν_μ contribution in the anti-neutrino mode amounts to about 30% although the contribution of wrong-sign neutrinos in the neutrino mode is about 5% in total due to the difference in the cross

---

[21]If the particle has the same momentum after the FSI as the one before the FSI, it is tagged by "no FSI".

section between neutrinos and anti-neutrinos which is originated from the helicity suppression. Third, samples are classified by the event topology, in other words, pion multiplicity. The main analysis sample at the far detector is CCQE-like events without any pion at the final state. Correspondingly, this event topology called CC0π is the most important sample in the ND fit. When the number of pions in the final state is one in an event, it is called CC1π event, which is dominated by single-pion production. Otherwise, they are categorized into CCother events. CC1π and CCother samples are necessary to understand the contamination of background into the signal sample, CC0π.
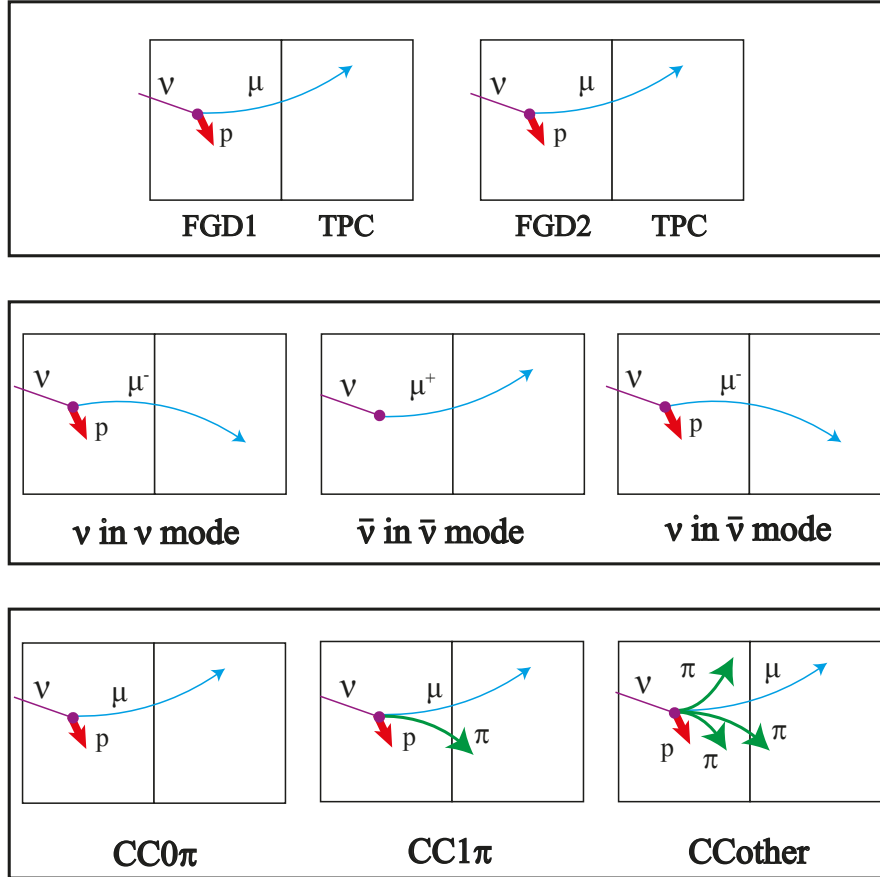
Figure 23: The classification of analysis samples in the ND fit. Vertex detector(top); Each event must include the neutrino interaction vertex inside FGD1 or FGD2. Neutrino flavor (middle); The neutrino flavor must be ν_μ or $\overline{\nu}_\mu$. The muon from the neutrino interaction is bent due to the magnetic field by the UA1 magnet. Event topology (bottom); A charged pion is tagged by the particle identification in TPC or FGD if the track is reconstructed. It is also tagged if the Michel electron tagging passes the selection.

For the purpose of better understanding of the CC0π events, we split the CC0π sample by the proton multiplicity in the updated analysis. The dominant interaction mode of the CC0π topology is CCQE. The contribution from the 2p2h interaction, where two protons are measured, is not negligible. The further classification of the CC0π sample depending on the

proton multiplicity is expected to help to disentangle these interaction modes. ND280 is capable of particle identification of proton from the energy deposit in the reconstructed momentum. According to the number of protons, the CC0π sample is split into the CC0π0p and CC0πNp, where N includes 1. The CCother samples are split into the CCother0γ and CCotherNγ based on the photon detection. This sample split has the potential to improve the purities of CCQE and the CC1π^+ for the CCother0γ sample to enhance the capability for the ND fit to constrain CCother events at the far detector. This additional classification is summarized in Figure 24. The CC1π sample in ν_μ FHC samples and $\overline{\nu}_\mu$ RHC and ν_μ FHC samples remain unchanged.
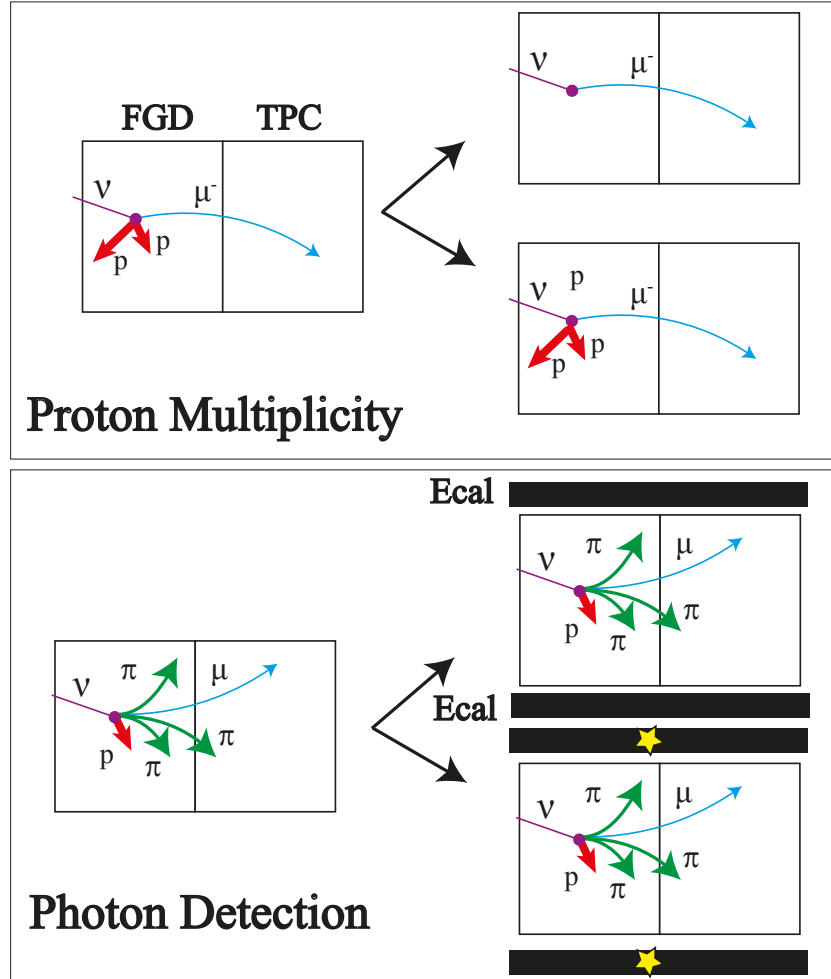
Figure 24: Illustrations of the new classification with respect to the proton multiplicity for the CC0π samples (Top) and photon detection for CCother samples (Bottom). The CC0π samples are split into the CC0π0p and CC0πNp. CCother samples are split into the CCother0γ and CCotherNγ based on the photon detection in the electro-magnetic calorimeters.

6.4.2 Fitting strategy

We developed two independent ways of fitting parameters in the ND fit. The primary approach is to explore the set of parameters such that they minimize the test statistic (χ^2) via a gradient-

decent algorithm in Minuit2 [22]. The other method relies on Markov-Chain-Monte-Carlo (MCMC) algorithm to explore the most probable parameter space in the fashion of posterior distributions. In this section, a more detailed fitting algorithm and the performance of the Minuit2 approach are shown.

Minuit2 minimizes the test statistics (χ^2). It is defined as the negative log-likelihood ($\chi^2 \equiv -2\log\mathcal{L}$) in the ND fit. The log-likelihood consists of two components given by

$$-2\log\mathcal{L} = -2\log\mathcal{L}_{\text{stat}} - 2\log\mathcal{L}_{\text{syst}}, \tag{6.1}$$

where "stat" and "syst" stand for statistic and systematic contributions, respectively. Statistical contribution is expressed with the number of events in MC and Data ($N_{\text{MC}}, N_{\text{Data}}$) as follows if the statistical fluctuation in MC is ignorable:

$$-2\log\mathcal{L}_{stat} = 2 \sum_{j}^{\text{samples}} \sum_{i}^{\text{bins}} \left(N_{\text{MC}} - N_{\text{Data}} + N_{\text{Data}} \log\frac{N_{\text{Data}}}{N_{\text{MC}}} \right). \tag{6.2}$$

Equation 6.2 represents the likelihood taking into account the statistical uncertainty based on the Poisson process. As the number of MC statistics is limited, the statistical fluctuation stemming from the limited MC samples may not be negligible. Barlow and Beeston proposed a model to include the effect in the binned likelihood [144]. The ND fit is based on the Barlow and Beeston model. Moreover, the actual likelihood reflects the approximation that J.S. Conway proposed to make the calculations feasible [145]. [23] The modified likelihood is

$$-2\log\mathcal{L}_{stat} = 2 \sum_{j}^{\text{samples}} \sum_{i}^{\text{bins}} \left[\left(N_{\text{MC}} - N_{\text{Data}} + N_{\text{Data}} \log\frac{N_{\text{Data}}}{N_{\text{MC}}} \right) + \frac{(\beta_i - 1)^2}{2\sigma_{\beta_i}^2} \right]. \tag{6.3}$$

The last term under the summation is the correction factor squeezing the effect of finite MC statistics. The variable β_i is the scaling factor (as in $N_{\text{MC}} = \beta \times N_{\text{MC}}^{\text{gen}}$, where $N_{\text{MC}}^{\text{gen}}$ is the MC truth by the amount of generated MC) in each bin and σ_{β_i} refers to the relative statistical uncertainty of β_i.

Systematic contributions are divided into flux, neutrino interaction, and detector parameters. They are given by

$$-2\log\mathcal{L}_{syst} = (\overrightarrow{x} - \overrightarrow{u})\mathbf{V}^{-1}(\overrightarrow{x} - \overrightarrow{u}). \tag{6.4}$$

Equation 6.4 forms a penalty term of the prior parameters. The variable $\overrightarrow{x}$ is the vector for the systematic parameters thrown during the fit and $\overrightarrow{u}$ refers to the central values as prior parameters. The prior values for the neutrino flux and neutrino interactions are given directly by the flux tuning results and neutrino interaction modeling described in this chapter. The covariance matrix ($\mathbf{V}$) contains the uncertainties of parameters including correlations. The prior uncertainties of detector parameters are evaluated by the dedicated control samples for the ND fit. The overall uncertainties including neutrino flux, neutrino interaction, and ND280 detector on the total event rate are around 10% for the analysis samples.

---

[22]The software tool kit named "ROOT" [143] implements this algorithm as a Fortran heritage.

[23]If one needs to apply the Barlow and Beeston model directly, additional scaling parameters whose number corresponds to the number of bins in the fit are necessary. This is unfeasible in this analysis because the ND fit introduces about 4000 bins in total. Conway's suggestion is to assume each scaling parameter follows the Gaussian distribution. The extraction of each scaling parameter is then analytical although it requires transcendent equations to solve.

6.4.3 Fit results on flux and neutrino interaction parameters

The ND fit used a data set corresponding to 19.867×10^{20} protons on target (POT), which is divided into the neutrino mode (11.531×10^{20} POT) and the anti-neutrino mode (8.336×10^{20} POT). The correlation matrix between the flux and cross section parameters and the parameter constraints are summarized in Figure 25 and Figure 26, respectively. The parameter definitions for the flux and interaction parameters are shown in Appendix A. A strong correlation between flux and cross section parameters is seen. For instance, The parameters pulling down the neutrino flux at the high energy seem to be affecting high Q^2 parameters being pulled up. The most effective parameter in 1p1h interactions, M_A^{QE}, is compatible with the model. The Pauli-Blocking parameters are pulled up against the prior values to reduce cross section in the low Q^2 region in response to the flux parameters. All of the 2p2h parameters have good compatibility with the model while newly added parameters (2p2h shape nn/np parameters) move largely to this data fit but within the prior uncertainty. For the SPP parameters, overall compatibility is good, but C_A^5 is pulled down outside the 1σ error of its prior. The data-MC differences before the fit for this sample are a major reason for this.
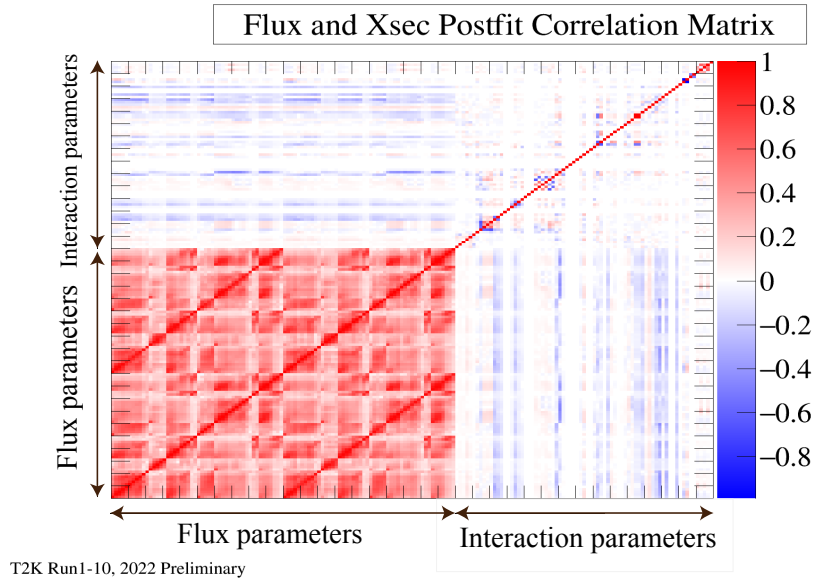
Figure 25: ND fit correlation matrix for the flux and cross section parameters. The first 100 parameters are neutrino flux parameters, and the other parameters are neutrino interaction parameters.

(a) FHC ν_μ Flux

(b) CCQE interaction

(c) 2p2h interaction

(d) CCSPP interaction
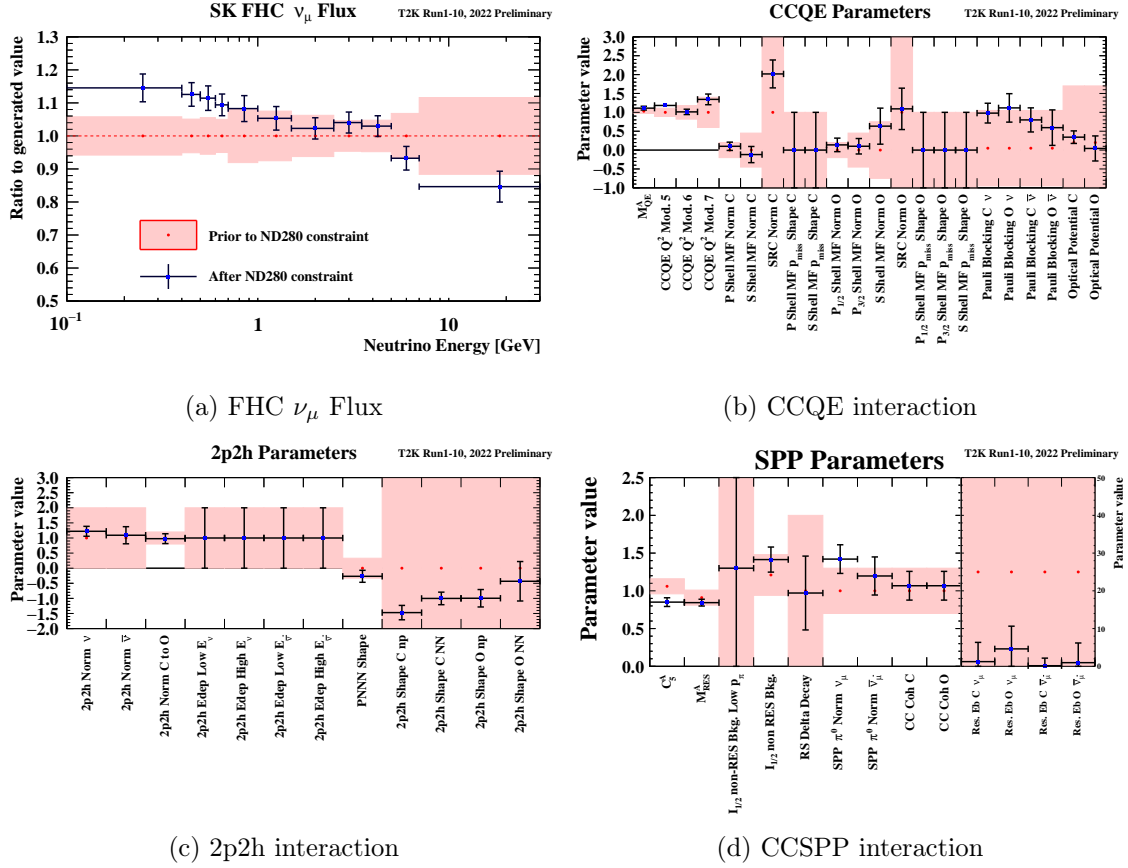
Figure 26: Parameter constraints by the ND fit on FHC ν_μ flux, CCQE, 2p2h, CCSPP parameters. The vertical axis in flux parameters refers to the "ratio" to the generated value whereas it means the actual parameter values in the interaction parameters.

6.4.4 Fit results on ND prediction

The MC predictions before and after applying the ND fit results are plotted against data to see the impact of the fit on the ND predictions. Figure 27 is one of the comparisons for the FGD1 ν_μ CC0π (CC1π) sample at ν_μ mode. The best-fit values of systematic parameters obtained by the ND fit pull up the number of events predicted by MC for the CC0π0p sample. On contrary, the MC prediction for the CC1π sample is slightly pulled down, making the agreement between data and MC better.

These comparisons showcase the ability of flux and interaction parameters to constrain CC0π and CC1π event rates for different neutrino species to account for the data to large extent. It may also indicate that mis-modelling or potential bias has a non-negligible impact on the predictions not only in the near detector but also in the far detector. Thus, the potential bias must be studied by simulated data in the context of the oscillation parameter constraints to minimize the risk of introducing that bias. The bias studies are described in Appendix C.

(a) Before applying fit results, CC0π

(b) After applying fit results, CC0π

(c) Before applying fit results, CC1π

(d) After applying fit results, CC1π
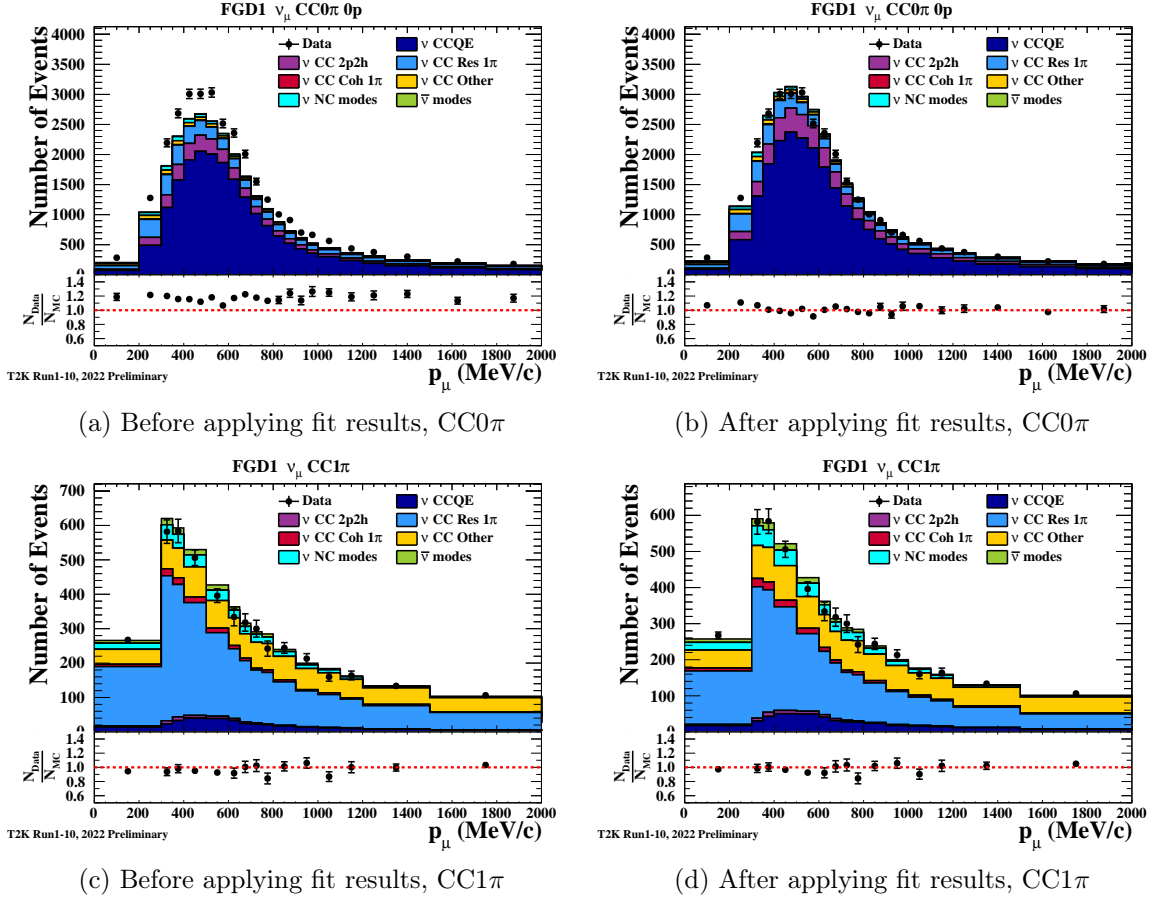
Figure 27: Comparisons of ND predictions for FGD1 ν_μ CC0π0p (upper) and FGD1 ν_μ CC1π (lower) as a function of muon momentum between before (left) and after (right) applying the fit results. The coloured histogram was the simulated events from NEUT. The black points represent data. Each distribution is broken down by the interaction type. The graphs below the comparison plots show the ratio of the number of events in data to the number of events in MC.

6.4.5 Compatibility of fit results with MC models

This analysis then performed a set of studies to ensure the validity of the fit. The goodness of the fit is assessed with a number of simulated data sets with a set of systematic parameters being varied based on the prior central values and uncertainties including their correlations among them. It is quantified by the test statistic called p-value of the probability that a toy experiment gives χ^2 being identical or exceeding the χ^2 from the data. If the test statistic gives an extremely low value, for instance, less than 0.01, it indicates the model is not compatible with the data. The threshold was set to 0.05 to evaluate the model compatibility in this analysis. The criterion is applied to the total χ^2 of likelihood. It is then applied to each likelihood contributor such as each sample, all samples with only neutrino flux parameters, and so on. Table 3 summarizes each p-value. The total p-value is 0.143, which is relatively small yet higher than the criteria (0.05), which means the fit results are compatible with the prior models. Removing the ad-hoc Q^2 parameters might be responsible for this smaller value. The p-value of the detector systematic parameter is relatively low, which indicates the overall treatment of ND280 detector systematics

should be improved in the future to guarantee reliable results from the ND fit. The p-value of the flux parameters is also lower than the threshold. Considering the strong correlations between the flux and interaction parameters, we should focus on the total p-value because it accounts for all the correlations between systematics properly.

Table 3: Results of the p-value for each likelihood contributor. This table only shows the FHC ν_μ FGD1 samples.

Likelihood contributor		p-value (*before* the fit)
FHC ν_μ CC0π at FGD1	CC0π0p	0.13
	CC0πNp	0.35
ν_μ FHC CC1π at FGD1		0.22
FHC ν_μ CCother	CCother0γ	0.86
	CCotherNγ	0.08
All samples		0.143
Neutrino flux		0.045
ND detector		0.036
Cross section		0.735

6.5 Event reconstruction of analysis samples at the far detector

6.5.1 Sample Classification

The measurement channels in the T2K oscillation analysis are ν_e appearance and ν_μ disappearance. Analysis samples can be classified into these two categories. They are further classified by interaction topologies. The dominant interaction type is the charged current quasi-elastic (CCQE) interaction while the second dominant interaction type is the single-pion production (CCSPP). We use the interaction topologies to define the signal. The main signal topology is CCQE-like event called CC0π, where there is one charged lepton but no pions in the final state. Another signal topology is CC1π, where there is only one reconstructed pion in the final state as well as one reconstructed lepton. Both ν_e appearance and ν_μ disappearance channels have two CC0π samples (ν_e 1-Ring and $\overline{\nu}_e$ 1-Ring in ν_e appearance, ν_μ 1-Ring and $\overline{\nu}_\mu$ 1-Ring in ν_μ disappearance) and one CC1π sample (ν_e CC1π^+ 1-Ring in ν_e appearance and ν_μ CC1π^+ in ν_μ disappearance). The ν_e appearance channels are sensitive to the oscillation parameters, δ_{CP}, $\sin^2\theta_{23}$, and $\sin^2 2\theta_{13}$ whereas the ν_μ appearance is sensitive to $|\Delta m^2_{32}|$ and $\sin^2 2\theta_{23}$. The ν_μ CC1π^+ sample is the sample added in the updated results. The analysis does not update the statistics, but this sample contributes to a 30% increase in muon-neutrino samples. As ν_μ CC1π^+ mainly comes from the single-pion production, the mean energy of the parent neutrino is around 1.2 GeV, which is away from the energy at the maximum oscillation probability. As the oscillation probability around 1.2 GeV is about half of the maximum probability, the oscillation effect is still visible for this sample.

The classification of these samples is summarized in Table 4. The schematic view of three samples (ν_e 1-Ring, ν_μ 1-Ring and $\overline{\nu}_e$ CC1π^+1-Ring) are shown in Figure 28 and ν_μ CC1π^+ in Figure 29.

Table 4: Classification of analysis samples at SK. The ν_μ CC1π^+ sample is added in the updated results and the other samples were already included in the published results.

Main interaction	Beam operation	Oscillation channel	Sample name
CCQE	neutrino mode	ν_e Appearance	ν_e 1-Ring
		ν_μ Disappearance	ν_μ 1-Ring
	anti-neutrino mode	ν_e Appearance	$\overline{\nu}_e$ 1-Ring
		ν_μ Disappearance	$\overline{\nu}_\mu$ 1-Ring
CCSPP	neutrino mode	ν_e Appearance	ν_e CC1π^+1-Ring
		ν_μ Disappearance	ν_μ CC1π^+
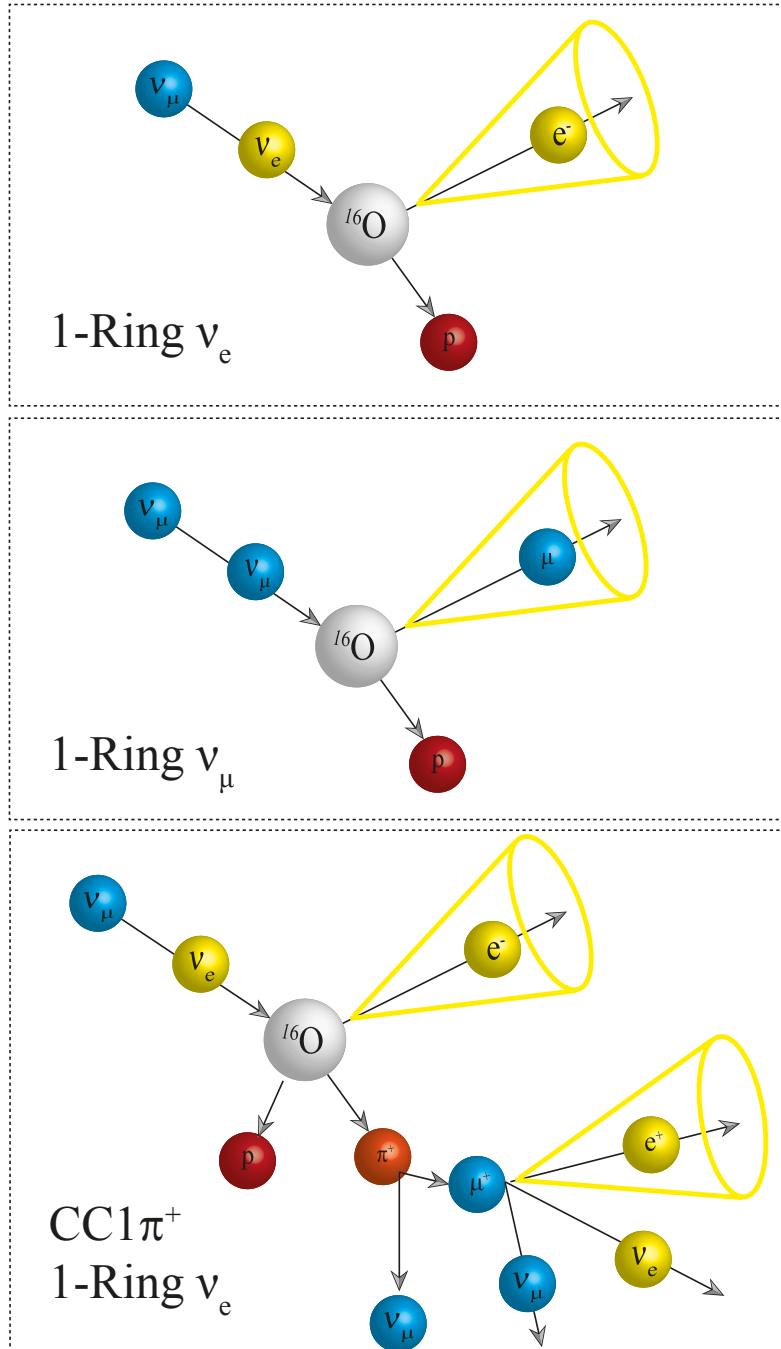
Figure 28: Schematic view of analysis samples for ν_e 1-Ring (Top), ν_μ 1-Ring (Middle) and ν_e CC1π^+1-Ring (Bottom). For the top and middle figures, they assume CCQE interaction with neutron inside ^{16}O, getting a proton outside the nucleus. With respect to the ν_e CC1π^+1-Ring sample, only π^+ is considered because π^- is highly likely to be trapped inside nucleus. The corn-like line represents a Cherenkov ring produced from each charged particle.
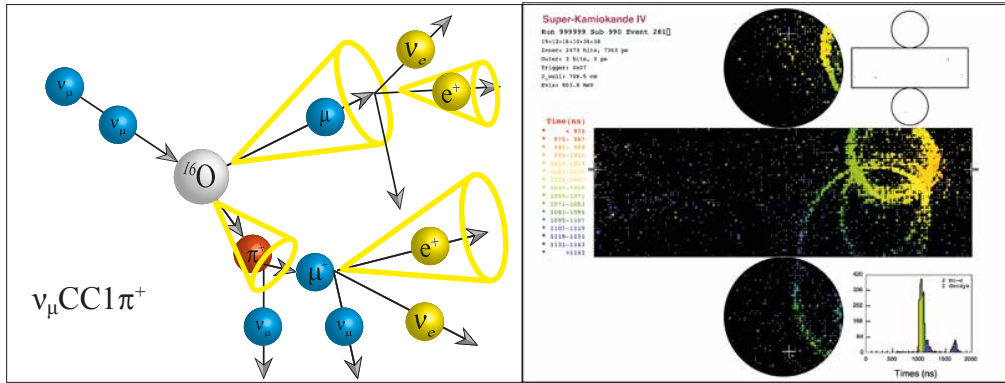
Figure 29: Illustration of the typical Multi-Ring event (left) and event display (right) for the ν_μ CC1π^+ sample from the simulation. The event display shows two rings from charged particles and two rings from the Michel electrons. The largest ring image corresponds to the ring from μ. The right top image from the outer detector guarantees this neutrino interaction happens inside the inner detector. The right bottom plot shows the time information of each ring, where the Michel electrons are delayed with respect to the charged particles.

6.5.2 Event selection

The primary event selections are a fiducial volume (FV) cut and a fully contained (FC) cut both of which are applied to all the samples. The FV cut can reject the events coming from the interactions outside the inner detector, typically cosmic-ray muons. The FC cut selects the lepton stopping inside the inner detector in order to ensure the performance of energy reconstruction and particle identification. [24] To the events after these selections, particle identification is applied to classify an electron-like (e-like) event or a muon-like (μ-like) event. The rest of the selections for e-like samples (ν_e 1-Ring, $\overline{\nu}_e$ 1-Ring, ν_e CC1π^+ 1-Ring), and μ-like samples (ν_μ 1-Ring, $\overline{\nu}_\mu$ 1-Ring, ν_μ CC1π^+) are summarized below.

Event selections for 1-Ring e-like samples after the common selections

1. The number of the reconstructed ring is one.

2. The notable contamination into 1-Ring e-like samples in the low energy region, less than 100 MeV, comes from neutral-current (NC) neutrino interaction and ν_μ interaction. The number of 1-Ring e-like events is not large in that region. In order to reject those backgrounds, a visible energy cut (E_{vis}) is applied. The parameter E_{vis} is defined as the energy of an electron that on average produces a Cherenkov ring with a total light yield equal to that of the observed ring. The cut requires E_{vis} to be larger than 100 MeV for all the 1-Ring e-like samples.

3. The distinct feature between the CC0π sample and the CC1π^+ sample is the existence of Michel electron. No Michel electron candidate is acceptable for the ν_e 1-Ring and $\overline{\nu}_e$ 1-Ring samples, while one reconstructed ring originating from Michel electron is required for the CC1π^+ sample.

---

[24] A lepton not stopping inside the tank fills up the hits inside a ring. As the SK particle identification relies on the fuzziness of the ring pattern, it has no power of particle identification to that lepton.

4. The rest of the cuts are common for all the 1-Ring e-like samples. The neutrino oscillation probability is the highest around 0.6 GeV in the configuration of the T2K experiment. The probability gradually decreases along with the increasing energy. Even though the T2K beam has a high energy tail, the oscillated ν_e spectrum has a small contribution in the high energy range, more than 1.25 GeV. Thus, the kinematic cut with respect to the reconstructed neutrino energy, $E_\nu < 1.25$ GeV is applied. If π^0 is produced in neutrino interactions, it can mimic the electron-like event without two e-like rings by two photons being reconstructed. Therefore, π^0 rejection cut is also applied based on the likelihood ratio between the electron hypothesis and the π^0 hypothesis in the reconstructed π^0 invariant mass.

Event selections for 1-Ring μ-like samples after the common selections

1. The number of the reconstructed ring is one.

2. The Cherenkov light requires a definite threshold for the particle velocity depending on the medium. [25] We cannot reconstruct any Cherenkov ring accurately if the particle is not sufficiently above the Cherenkov threshold. This analysis uses a 200 MeV/c cut for muon momentum, which corresponds to 30 MeV as the visible energy. This is large enough to reconstruct the momentum accurately.

3. Unlike the 1-Ring e-like samples, 1-Ring μ-like samples are allowed to have one Michel electron because the cut includes FC cut and the stopped muon might generate a decay electron.

4. The main background of the 1-Ring μ-like samples comes from mis-reconstruction of π^+ ring as $\mu-$ring. Therefore, π^+ rejection cut is applied.

Event selections for ν_μ CC1π^+ samples after the common selections

1. The number of the reconstructed ring and Michel electrons: A signal topology implies there would be two Michel electrons in the absence of the final state interactions (FSI). In reality, the FSI effect may prevent a pion from exiting from the nucleus due to the absorption. One-Michel-electron events are also allowed to consider such FSI effects. It should be noted that other μ-like samples are allowed to have one-Michel-electron events. In order to make this sample independent of the other 1-Ring samples, the threshold on the number of Michel electrons is associated with the number of reconstructed events. When the number of reconstructed rings is two or more, either one or two Michel electrons are required. Otherwise, two Michel electrons are mandatory.

2. Log-likelihood ratio cuts: The signal topology of the ν_μ CC1π^+ sample is defined as μ^- and π^+ being reconstructed in the final state. The main background contaminating this sample is multi-pion interaction and charged-current deep inelastic scattering (CCDIS), where two particles (in particular, one muon and another particle) are misidentified as μ^- and π^+. We prepare three kinds of log-likelihood ratios; $\mathcal{L}_e, \mathcal{L}_{\pi\pi}, \mathcal{L}_{\text{BO2R}}$. The parameter, $\mathcal{L}_e$ is the likelihood assuming the ring is produced from an electron, $\mathcal{L}_{\pi\pi}$ is the likelihood assuming the ring is produced from two $\pi^\pm$-like

---

[25]The relationship among the Cherenkov angle (θ), velocity ratio (β) and refractive index (n) is expressed $\cos\theta = 1/\beta n$. The obvious deduction is that only charged particles having the speed ($\beta > 1/n$) can create a Cherenkov light.

particles. We assume $\pi\pi$ instead of μ, π to reduce the computation time in the fit. The parameter, $\mathcal{L}_{\text{BO2R}}$ is the largest likelihood out of the 2R $ee, e\pi^{\pm}, \pi^{\pm}e$ hypotheses. The abbreviation of "BO2R" stands for "the Best Of the other 2-Ring hypothesis". For the ν_{μ} CC1π^{+} sample, $\mathcal{L}_{\pi\pi}$ is higher than the other likelihoods. We require $\ln \mathcal{L}_{\pi\pi}/\mathcal{L}_e > c_0 + c_1 p_{\pi\pi}^{\min}$ and $\mathcal{L}_{\text{BO2R}}/\mathcal{L}_{\pi\pi} < c_2$, where $p_{\pi\pi}^{\min}$ is the lowest momentum ring under the $\pi^{\pm}\pi^{\pm}$ hypothesis and c_0, c_1, c_2 are the constant parameters that are optimized using a figure of merit [26]. The figure of merit is defined as $S/\sqrt{S+B}$, where "S" is the number of signal events and "B" is the number of background events. This cut contributes to the substantial reduction in the background from CCDIS and CC multi-pi interactions.

The reconstruction of neutrino energy is performed in accordance with the interaction type. For four CCQE-like samples, the neutrino energy is calculated by

$$E_{\nu}^{\text{rec}} = \frac{(M_n - E_b) \cdot E_l - m_l^2/2 + M_n \cdot E_b - E_b^2/2 + \left(M_p^2 - M_n^2\right)/2}{M_n - E_b - E_l + p_l \cos\theta_l}, \tag{6.5}$$

where $M_{n,(p)}$ is the mass of neutron (proton), E_l, p_l, θ_l are the lepton energy, momentum, and angle, respectively. The variable E_b is the binding energy. As most interactions occur inside the nucleus ^{16}O, the binding energy of oxygen (27 MeV) is used. On the other hand, the ν_e CC1π^{+}1-Ring sample needs a different equation assuming the Δ (1232) resonance, which is the dominant interaction for the CCSPP interaction. The formula is

$$E_{\nu}^{\text{rec}} = \frac{(M_{\Delta^{++}}^2 - M_p^2 - m_X^2)/2 + M_p E_l}{M_p - E_l + p_l \cos\theta_l}. \tag{6.6}$$

Here, $M_{\Delta^{++}}$ refers to the mass of resonant delta and m_X is the mass of an electron (pion) in the case of the ν_e CC1π^{+} 1-Ring (ν_{μ} CC1π^{+}) sample.

6.6 Far detector fit

The far detector analysis (FD fit) has two fitting frameworks. One way is already mentioned in Section 6.4, which is based on the Bayesian Markov Chain Monte Carlo (MCMC) method. One of the characteristics of the MCMC fit is to be capable of simultaneous fits of the near detector and the far detector data sets. The other method is a frequentist approach by integrating all of the nuisance parameters to extract confidence intervals of the oscillation parameters of interest. The systematic part in nuisance parameters is constrained by the ND fit (Minuite2 approach). Contrary to the Bayesian analysis, the Monte Carlo integration via grid scan performs the fit in a sequential manner from the ND fit to the FD fit. In this section, the grid-scan analysis is described. [27]

6.6.1 Construction of confidence interval

The grid-scan method is based on a maximum likelihood with MC integration. A set of prior values of systematic parameters are derived from the constraints obtained from the ND fit. Nuisance parameters are marginalized in the calculation of the likelihood. The parameter space

---

[26]For 1-decay electron sample, $c_1 = -400, c_2 = 1.2, c_3 = 340$ and for 2-decay electron sample, $c_1 = -400, c_2 = 1.0, c_3 = 310$.

[27]See Appendix B for the MCMC approach.

is divided into grid points for the parameters of interest, either in one-dimension or in two-dimension. The likelihood at each grid point of oscillation parameters is calculated. The starting point of this analysis is to define the likelihood, which is

$$\mathcal{L}(N^{\text{obs}}, \boldsymbol{x}^{\text{obs}}, \boldsymbol{o}, \boldsymbol{f}) = \prod_{s\in\text{samples}} \left[\mathcal{L}_{\text{stat.}}(N_s^{\text{obs}}, \boldsymbol{x}_s^{\text{obs}}, \boldsymbol{o}, \boldsymbol{f}) \right] \times \mathcal{L}_{\text{syst.}}(\boldsymbol{f}), \tag{6.7}$$

where N^{obs} is the observed number of events, $\boldsymbol{x}^{\text{obs}}$ is the measured parameters of lepton kinematics or neutrino energy in data and variable $\boldsymbol{o}(\boldsymbol{f})$ stands for the vector of oscillation (systematic) parameters. The likelihood is divided into two contributions from the statistical part ($\mathcal{L}_{\text{stat.}}$) and the systematic part ($\mathcal{L}_{\text{syst.}}$) [28]. As the previous section describes, the far detector samples consist of six sub-samples. Correspondingly, the calculation runs over each sample. The likelihood contributor from systematic parameters does not depend on the sample classification. Therefore, it multiplies the statistical part independently. Similarly to the MCMC approach, parameter constraints on oscillation parameters are calculated in only one- or two-dimensional space. All the nuisance parameters are then marginalized. The marginal likelihood is

$$\mathcal{L}_{\text{marg}}(N^{\text{obs}}, \boldsymbol{x}^{\text{obs}}, \boldsymbol{o}) = \int d\boldsymbol{f} \, \mathcal{L}_{\text{syst.}}(\boldsymbol{f}) \mathcal{L}(N^{\text{obs}}, \boldsymbol{x}^{\text{obs}}, \boldsymbol{o}, \boldsymbol{f})$$

$$\simeq \frac{1}{N} \sum_{i=1}^{N} \frac{1}{\mathcal{L}_{\text{syst.}}(\boldsymbol{f})} \mathcal{L}(N^{\text{obs}}, \boldsymbol{x}^{\text{obs}}, \boldsymbol{o}, \boldsymbol{f})$$

$$= \frac{1}{N} \sum_{i=1}^{N} \left[\prod_{s\in\text{samples}} \mathcal{L}_{\text{stat.}}(N_s^{\text{obs}}, \boldsymbol{x}_s^{\text{obs}}, \boldsymbol{o}, \boldsymbol{f}) \right]. \tag{6.8}$$

The derivation from the first line to the second line in Equation 6.8 relies on the assumption that many parameter sets are thrown to evaluate the integral. This approximation is in principle asymptotically valid with respect to $N \to \infty$. In practice, as the sensitivity of the current analysis is limited by the statistics, the number of throws (N) should be sufficiently large such that the error originating from the N number is enough small compared to the statistical errors. It should be noted that the likelihood described in Equation 6.8 is calculated in each grid point on relevant oscillation parameters. This likelihood function is fed into the calculation of a log-likelihood ratio, given by

$$D = -2\ln\left(\frac{\mathcal{L}_{\text{marg}}(\boldsymbol{o})}{\mathcal{L}_{\text{marg}}^{\max}} \right). \tag{6.9}$$

The Wilks' theorem [146] claims the log-likelihood ratio written in Equation 6.9 asymptotically approaches the χ^2 distribution with the degree of freedoms equivalent to the number of parameter dimensions as far as the following assumptions are valid.

- The sample size is sufficiently large.

- The likelihood function can be approximated by the Gaussian distribution.

---

[28]Unlike the ND fit, the likelihood contributor from statistical fluctuation is not based on the Barlow Beeston model but calculated based on only the Poisson term. On the other hand, the likelihood contributor from systematic parameters is calculated based on the same logic as the ND fit. The corresponding covariance matrix is the post-fit one from the ND fit.

- True values of the parameters of interests are away from the physical boundaries.

When those assumptions are valid, Equation 6.9 can be rewritten by

$$D = \Delta\chi^2(\boldsymbol{o}) = -2\ln\left(\frac{\mathcal{L}_{\mathrm{marg}}(\boldsymbol{o})}{\mathcal{L}_{\mathrm{marg}}^{\max}}\right). \tag{6.10}$$

Equation 6.10 provides a way to constrain the parameter spaces in the fixed delta-chi-squared value ($\Delta\chi^2_{\mathrm{fix}}$) [29]. The interval is defined as the region of the parameter space for which the $\Delta\chi^2$ is inferior to a certain fixed value, $\Delta\chi^2_{\mathrm{fix}}$. This interval is a "confidence interval". This approach is interpreted as a frequentist method. The assumptions under Wilk's theorem are invalid for certain oscillation parameters, in particular for δ_{CP} and $\sin^2\theta_{23}$ because the likelihood function cannot be assumed to be Gaussian for both cases. In those cases, an alternative method proposed by Feldman and Cousins [147] is applied. [30] With respect to the extraction of best-fit oscillation parameters, we apply the Minuit2 algorithm in four oscillation parameter spaces ($\sin^2 2\theta_{13}$, $\sin^2 2\theta_{23}$, Δm^2_{32}, δ_{CP}) to find out the most plausible parameter set.

6.6.2 Construction of credible region

The MC integration with the grid scan approach can be utilized to construct credible regions using the marginal likelihood derived above. Here, we use the posterior probability for each oscillation parameter of interest instead of the $\Delta\chi^2$. An additional difference with respect to the construction of confidence intervals is that mass ordering is also marginalized in this analysis, where it is taken as a discrete variable with two values to which we can assign prior probabilities $P(\mathrm{NO}), P(\mathrm{IO})$. The normal ordering case corresponds to $P(\mathrm{NO}) = 1, P(\mathrm{IO}) = 0$, and inverted ordering case corresponds to $P(\mathrm{NO}) = 0, P(\mathrm{IO}) = 1$. When marginalizing over the mass ordering, we assume that both orderings are equally likely before the fit and take $P(\mathrm{NO}) = P(\mathrm{IO}) = 0.5$. The posterior density for a parameter (x) is then defined as,

$$P(x) = \alpha \times \left[\mathcal{L}_{\mathrm{marg}}(x|\mathrm{NO})P(\mathrm{NO}) + \mathcal{L}_{\mathrm{marg}}(x|\mathrm{IO})P(\mathrm{IO})\right], \tag{6.11}$$

where α is a scaling parameter to make the probability over the whole range of the parameter x equal to 1.

---

[29]$\Delta\chi^2_{\mathrm{fix}}$ depends on the number of degrees of freedom given a target coverage. With respect to the four values of target coverage (68%, 90%, 95.45%, 99.73%), they correspond to 1 (2.3), 2.71 (4.61), 4 (6.18), 9 (11.62) respectively depending on the degree of freedoms (parenthesis refers to the two degrees of freedom).

[30]Feldman and Cousins demonstrated an example to apply their method to the measurement of neutrino oscillation in the paper. In evaluating the confidence intervals, we make use of the critical χ^2 borders corresponding to each confidence level (1σ, 90%, 2σ and 3σ) instead of fixed χ^2 to extract those intervals.

7   Results of oscillation analysis

This chapter presents the updated results of the oscillation analysis [68] using 19.663×10^{20} protons on target (POT) in the ν mode and 16.344×10^{20} POT in the $\overline{\nu}$ mode. Compared to the previous results in [53], the additional statistics correspond to 4.726×10^{20} POT in the ν mode. The statistics are the same as the published results.

7.1   Systematic uncertainty

The ND fit results (Section 6.4) are used in the far detector analysis to evaluate the error sizes on each sample. Table 12 shows the size of systematic uncertainties in each sample. After the ND fit, there is a notable decrease in the systematic uncertainties. The improvement ranges from 25 to 75%. The smaller contributions from the Flux $\otimes$ Interaction than the naive quadrature sum of the Flux and Interaction contributions indicate the effect of the anti-correlation between flux and interaction parameters. In either case before or after the ND fit, the overall uncertainty in the $\overline{\nu}$ mode is larger than in the ν mode. Table 12 includes the FD-only systematic parameters that are not constrained by the ND fit. The most significant contribution of all unconstrained parameters comes from the isospin ($I_{1/2}$) non-resonant interaction with the low-momentum pion parameter. This parameter has a large impact on $\overline{\nu}$ interactions, which inflates the uncertainties in the $\overline{\nu}$ mode. The parameter value is tuned by the neutrino mode data set, but there is no available data for the anti-neutrino mode data set. Therefore, a larger uncertainty is assigned for the anti-neutrino interactions. Figure 30 demonstrates the effect of the reduction in the uncertainties and the shift in the best-fit parameters on the oscillated spectrum of each sample. The spectra for the CCQE-like samples are pulled up after the fit. This tendency reflects the fact that higher cross sections for CCQE-like interactions compared to the prediction from the nominal interaction model are favored in the ND fit [31]. Figure 30 also shows that the ND fit pulls down the predicted spectrum for the ν_e CC1π^+ 1-Ring sample, which corresponds to the movement of the CC resonant parameters in the ND fit.

Table 5: Error sizes for the systematic parameters. Numbers represent the errors *after* (*before*) the ND fit. Error budgets are divided into each contribution from neutrino flux (Flux), neutrino interaction model (Interaction), and other parameters (FD + SI + PN), where FD stands for the SK detector systematic parameters, SI stands for Secondary particle Interaction and PN stands for Photo-Nuclear effects. SI and PN are evaluated at the far detector independently of the other detector parameters. FD+SI+PN errors are calculated as the quadrature sum of these errors. The errors from Flux $\otimes$ Interaction are calculated by combining the two contributions. Total uncertainties naively correspond to the quadrature sum of "Flux $\otimes$ Interaction" and "FD+SI+PN".

| FD sample | | Error size (%) | | | Flux $\otimes$ Interaction | Total (%) |
		Flux	Interaction	FD + SI + PN		
ν_μ 1-Ring	ν mode	2.8 (5.0)	3.8 (15.8)	2.0 (2.6)	2.7	3.4 (16.7)
	$\overline{\nu}$ mode	2.9 (4.6)	4.2 (13.6)	1.7 (2.2)	2.6	3.9 (14.6)
ν_e 1-Ring	ν mode	2.8 (4.9)	4.8 (16.3)	3.1 (3.1)	2.8	5.2 (17.3)
	$\overline{\nu}$ mode	3.0 (4.6)	4.8 (13.1)	3.8 (3.9)	2.97	5.8 (14.4)
ν_e CC1π^+ 1-Ring	ν mode	2.8 (5.1)	5.0 (14.7)	13.6 (13.6)	3.4	14.3 (20.9)
ν_μ CC1π^+	ν mode	2.8 (5.2)	3.3 (10.6)	4.1 (5.0)	2.2	4.9 (12.5)

---

[31]See Section 6.4, which showed the number of data exceeds the predictions before the fit.

(a) ν_μ 1-Ring

(b) $\overline{\nu}_\mu$ 1-Ring

(c) ν_e 1-Ring

(d) $\overline{\nu}_e$ 1-Ring

(e) ν_e CC1π^+ 1-Ring

(f) ν_μ CC1π^+
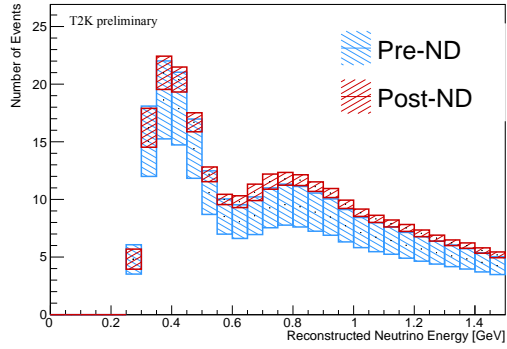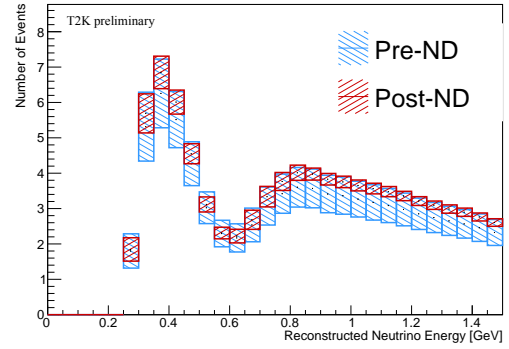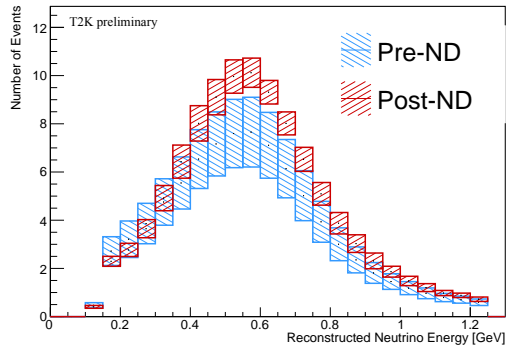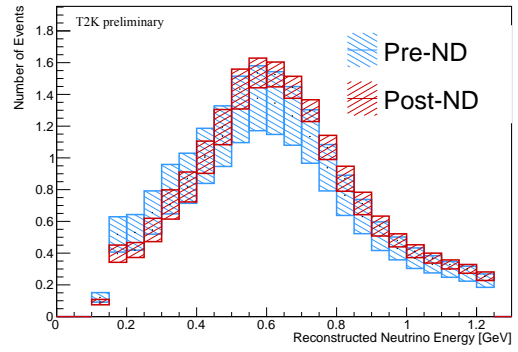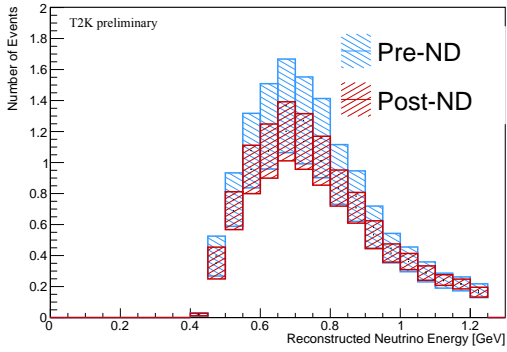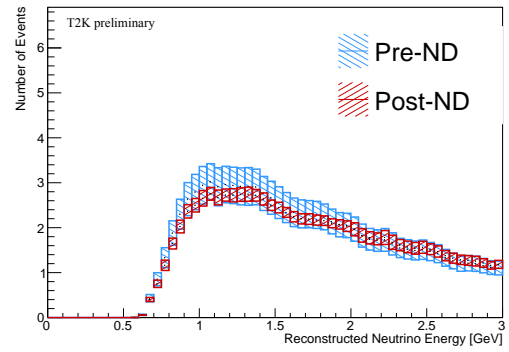
Figure 30: Distribution of reconstructed neutrino energy with (red band) or without (blue band) applying the ND fit after the oscillation. Oscillation parameters are set to the nominal values ($\Delta m_{21}^2 = 7.53 \times 10^{-5}$ eV^2/c^4, $\Delta m_{32}^2 = 2.494 \times 10^{-3}$ eV^2/c^4, $\sin^2\theta_{12} = 0.307$, $\sin^2\theta_{13} = 0.0220$, $\sin^2\theta_{23} = 0.561$, $\delta_{CP} = -1.601$). The normal mass ordering is assumed as the neutrino mass ordering.

7.2 Result of observed events

Table 6 shows the total number of observed events for each sample along with the predictions with various true $\delta_{\rm CP}$ values. The shifts in the number of events of the e-like samples clearly reflect the $\delta_{\rm CP}$ dependency of the $\nu_\mu \to \nu_e$ ($\overline{\nu}_\mu \to \overline{\nu}_e$) oscillation probabilities. It is expected that the number of events in μ-like samples is almost unchanged because the ν_μ disappearance channels do not depend on $\delta_{\rm CP}$ in the leading order [32]. There are two potential discrepancies between data and MC predictions according to Table 6. One is a "deficit" in data for the ν_μ 1-Ring sample and the other is an "excess" in data for the ν_e CC1π^+ 1-Ring sample. The MCMC method quantified the significance of these discrepancies with the p-value test using the posterior predictive distributions. The p-values using the shape (rate-only) information are calculated for the ν_μ 1-Ring and ν_e CC1π^+ 1-Ring samples, which are 0.35 (0.04) and 0.89 (0.27), respectively. The rate-only p-value is relatively small, but not significant when we consider the look-elsewhere effect with a factor of 6, which corresponds to the number of samples. It demonstrates both discrepancies are not significant considering the statistical and systematic errors and the model is compatible with the data.

Table 6: Predictions for the number of events at the far detector using oscillation parameters and systematic parameters at their best-fit values while varying $\delta_{\rm CP}$.

FD sample		True $\delta_{\rm CP}$ (rad.)				Data
		-$\pi/2$	0	$\pi/2$	π	
1-Ring μ	ν mode	358.67	358.01	358.63	359.41	318
	$\overline{\nu}$ mode	139.42	139.04	139.43	139.79	137
1-Ring e	ν mode	99.06	83.56	68.61	84.10	94
	$\overline{\nu}$ mode	17.02	19.34	21.43	19.09	16
1-Ring CC1π^+ e	ν mode	10.85	9.449	7.702	9.104	14
CC1π^+ μ	ν mode	118.53	118.01	118.50	119.02	134

The observed number of events in two-dimensional binning for each sample is shown in Figure 31. They are the results of the grid-scan method. In creating the MC predictions, the systematic parameters are set to the best-fit values from the ND fit, and the oscillation parameters are set to their best-fit values shown in the next section. The data distributions are in good agreement with the MC prediction. There seem some bins having relatively large differences between data and MC, for example, the 2nd bin for the ν_e CC1π^+ 1-Ring sample. We investigated where the observed number of data was consistent with the MC predictions by using p-value statistics. See Appendix G for details.

---

[32]See Equation 2.32,

$$P(\nu_\mu \to \nu_\mu) = 1 - \sin^2 2\theta_{13} \sin^2 \theta_{23} + \sin^2 2\theta_{23} \cos^4 \theta_{13} \sin \frac{\Delta m_{32}^2 L}{4E}.$$

(a) ν_μ 1-Ring

(b) $\overline{\nu}_\mu$ 1-Ring

(c) ν_e 1-Ring

(d) $\overline{\nu}_e$ 1-Ring

(e) ν_e CC1π^+ 1-Ring

(f) ν_μ CC1π^+
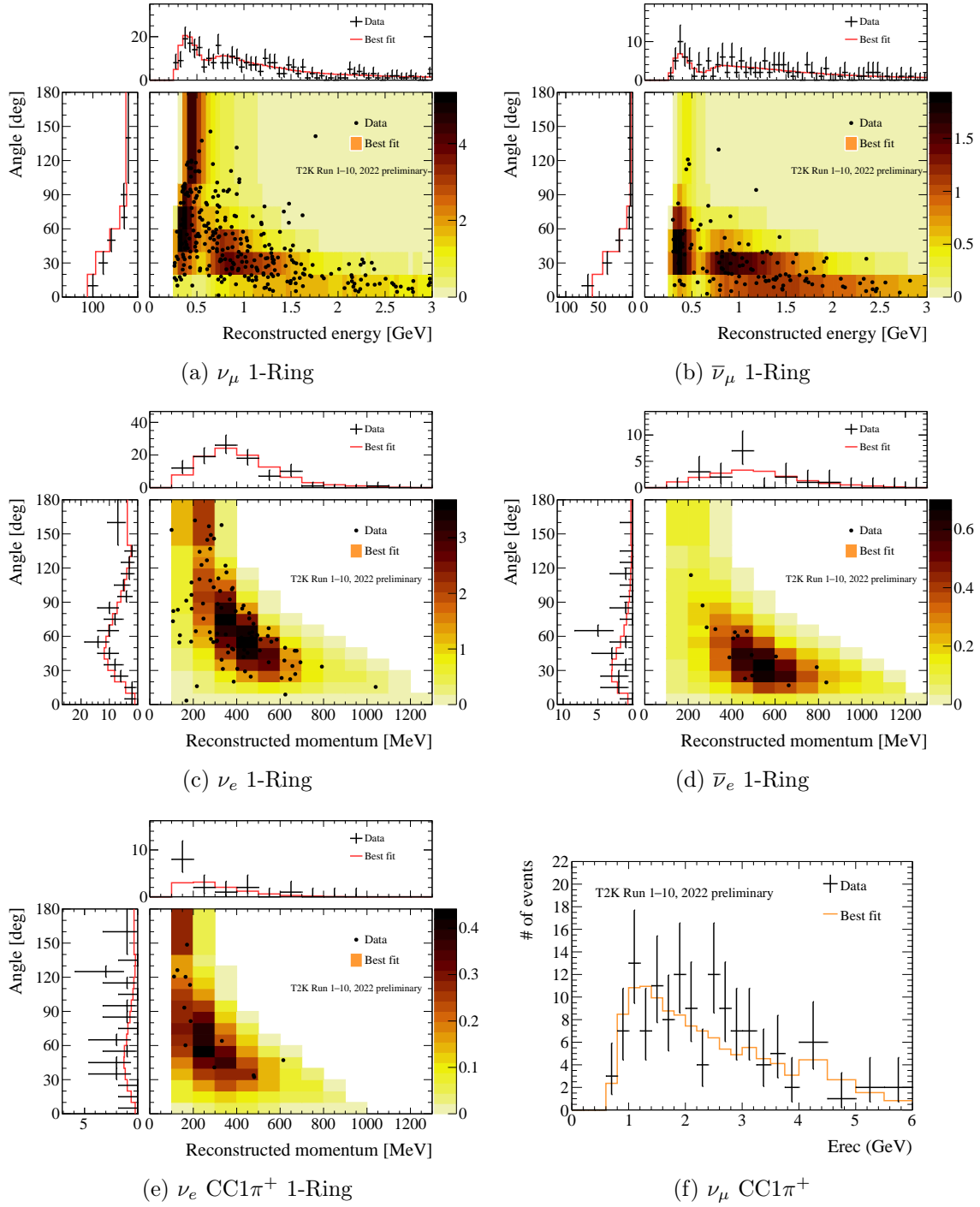
Figure 31: The number of observed events for the far detector samples. The μ-like 1 Ring samples in the top two figures are binned by the reconstructed neutrino energy and the outgoing lepton angle with respect to the incoming neutrino angle. The e-like 1 Ring samples in the middle two figures and the bottom left figure are binned by the reconstructed lepton momentum and angle. The ν_μ CC1π^+ sample in the bottom right figure is binned by the reconstructed neutrino energy. The dotted points (data), except for the ν_μ CC1π^+ sample, are plotted on the colored two-dimensional distribution of MC predictions with oscillation parameters set to their best-fit values. They are also projected onto the horizontal and vertical axis. For the ν_μ CC1π^+ sample, data points are overlaid on the one-dimensional histogram. In each one-dimensional distribution, the error bars represent the Poisson errors.

7.3 Measurements of oscillation parameters

The primary oscillation parameters to be measured in T2K are δ_{CP}, $\sin^2\theta_{23}$, Δm^2_{32} (Δm^2_{31}), and $\sin^2\theta_{13}$. The analysis with constraints on $\sin^2\theta_{13}$ from the reactor experiments enhance the sensitivity to δ_{CP} and $\sin^2\theta_{23}$. We present both results with and without the reactor constraint. When the reactor constraint is used, the prior assumption on $\sin^2\theta_{13}$ is changed from the uniform distribution $(0, 1)$ to the Gaussian distribution of its global average with the mean of 0.0861 and 1σ error of 0.0027 [50]. The constraints on the mass-squared difference parameters are smeared by the suggested value from the T2K bias studies, 3.100×10^{-5} eV^2/c^4. We extract oscillation contours using alternative simulated data sets to test the robustness of the fits and check the potential biases stemming from our interaction models. The method is described in Appendix C. We present measurements on oscillation parameters mainly from the grid-scan method. The cross-fitter comparisons were also performed, which are described in Appendix E.

7.3.1 Best fit results for oscillation parameters

Table 7 shows the best fit results with 1σ errors estimated using the fixed $\Delta\chi^2$ method. The best fit of δ_{CP} is close to $-\pi/2$, and the CP-conserving values (π and 0) are outside of the 1σ error band. The errors on δ_{CP} are significantly reduced by using the reactor constraint. The standalone measurement of $\sin^2\theta_{13}$ is consistent with the reactor measurements although the error is much smaller in the analysis with the reactor measurement. For $\sin^2\theta_{23}$, the best-fit value is in the higher octant ($\theta_{23} > \pi/4$) region when the reactor constraint is applied whereas the best-fit value is in the lower octant ($\theta_{23} < \pi/4$) region in the T2K standalone analysis.

Table 7: Results of the best-fit oscillation parameters from the data fit with or without the reactor constraint with uncertainties estimated using the fixed $\Delta\chi^2$ method.

Parameter	With reactor constraint		Without reactor constraint	
	Normal ordering	Inverted ordering	Normal ordering	Inverted ordering
δ_{CP} (rad.)	$-2.18^{+1.22}_{-0.47}$	$-1.37^{+0.52}_{-0.68}$	$-2.25^{+1.33}_{-0.74}$	$-1.25^{+0.66}_{-0.90}$
$\sin^2\theta_{13}/10^{-3}$	$22.0^{+0.76}_{-0.6}$	$22.1^{+0.74}_{-0.63}$	$26.6^{+2.5}_{-6.2}$	$29.3^{+2.7}_{-6.5}$
$\sin^2\theta_{23}$	$0.559^{+0.018}_{-0.078}$	$0.560^{+0.019}_{-0.041}$	$0.466^{+0.107}_{-0.016}$	$0.465^{+0.100}_{-0.016}$
$\Delta m^2_{32}/10^{-3}$eV^2/c^4	$2.506^{+0.047}_{-0.059}$	$2.474^{+0.050}_{-0.056}$	$2.506^{+0.048}_{-0.058}$	$2.473^{+0.051}_{-0.054}$

7.3.2 Measurement of δ_{CP}

The $\sin\delta_{\mathrm{CP}}$ dependency on the $\nu_\mu \to \nu_e$ oscillation probabilities creates two extrema at $\delta_{\mathrm{CP}} = \pm\frac{\pi}{2}$. In addition, $\sin\delta_{\mathrm{CP}}$ is a cyclic function. These characteristics of δ_{CP} make the assumption of the likelihood of the parameter in Wilk's theorem invalid. The Feldman and Cousins (FC) method is applied to evaluate the constraints. Considering the size of the significance of its constraints, the standalone analysis is based on the fixed $\Delta\chi^2$ method whereas the analysis using the reactor constraint is done with the FC method. Figure 32 shows the global data fit results of the frequentist measurement of δ_{CP} with and without the reactor constraint. The significance at each true δ_{CP} point is almost doubled with the reactor constraint. The results with the reactor constraint show the CP conserving values $(0, \pi)$ are ruled out by 90% confidence level from the grid-scan method assuming the normal ordering scenario. This is further discussed in the next chapter in the context of a comparison between the data fit results and the sensitivity. The confidence intervals for δ_{CP} are summarized in Table 8.
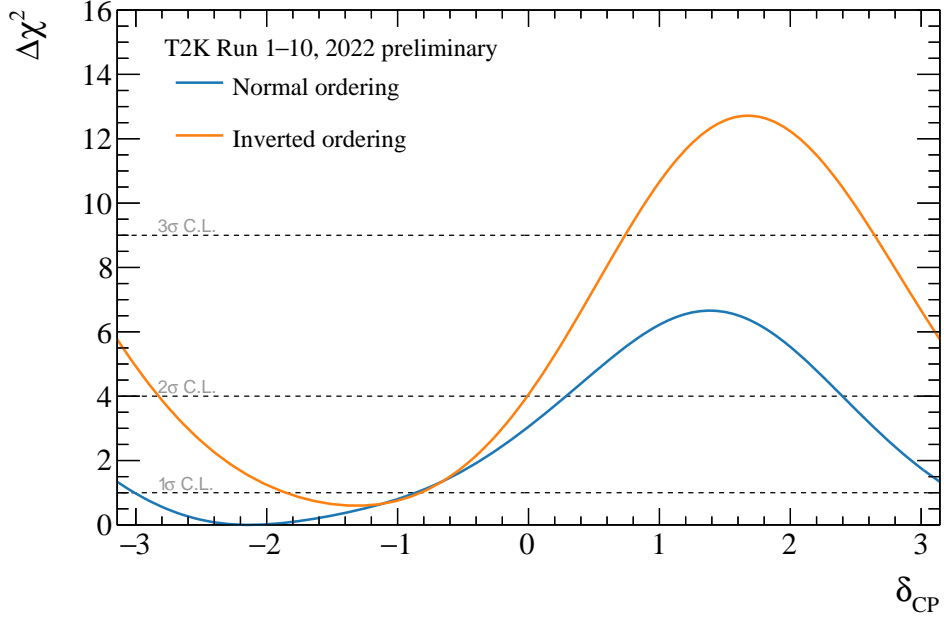
(a) Without the reactor constraint
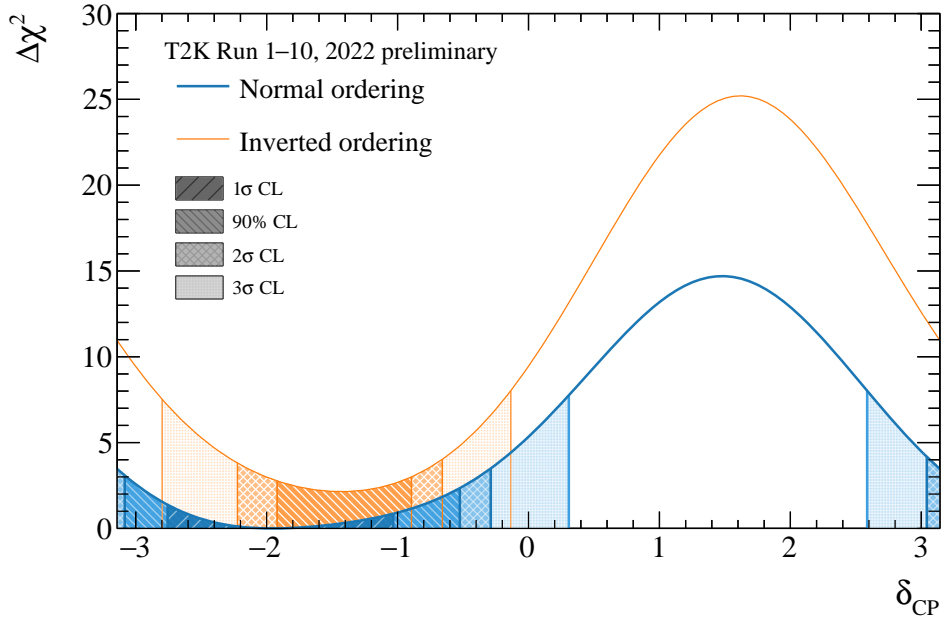
(b) With the reactor constraint

Figure 32: Results of the frequentist measurement of δ_{CP} from the analysis without (top) and with (bottom) the reactor constraint. Each of them assumes both mass ordering scenarios. Since the result without the reactor constraint is based on the fixed $\Delta\chi^2$ method, the corresponding target coverage (1σ, 2σ and 3σ) lines are shown. The analysis using the reactor constraint, on the other hand, is based on the FC method. The lines corresponding to the target coverages are determined by the critical $\Delta\chi^2$ distribution. Alternatively, the error bands to represent each target coverage are shown.

Table 8: Data fit results of confidence intervals for δ_{CP} from the grid-scan method. The results for both mass ordering scenarios (NO/IO) with the reactor constraint are shown.

Significance	normal ordering	inverted ordering
$1\,\sigma$	[-2.76, -1.03]	–
90%	[-3.08, -0.52]	[-1.92, -0.89]
$2\,\sigma$	[-π, -0.29] $\cup$ [3.04, π]	[-2.22, -0.66]
$3\,\sigma$	[-π, -0.31] $\cup$ [2.59, π]	[-2.80, -0.14]

7.3.3 Measurement of $\sin^2\theta_{23}$

The measurement of the $\nu_\mu \to \nu_\mu$ samples has the sensitivity to $\sin^2 2\theta_{23}$, whereas the measurement of the $\nu_\mu \to \nu_e$ samples has the sensitivity to $\sin^2\theta_{23}$. As a result, the likelihood for $\sin^2\theta_{23}$ does not become a Gaussian-like distribution. Therefore, the FC method is also applied to the measurement of $\sin^2\theta_{23}$ with the reactor constraint. The results are shown in Figure 33. The octant preference is different between the results with and without the reactor constraint. Assuming the normal mass ordering, the result with the reactor constraint shows a mild preference at 1σ significance for the upper octant against the lower octant. The maximum mixing scenario is rejected by 1σ significance. Table 9 summarizes the data fit results on the parameter constraints.

One way to quantify the octant preference is the Bayes factor. The MCMC obtained posterior predictive distributions of $\sin^2\theta_{23}$, which are converted to the corresponding Bayes factor to examine the preference. The result is shown in Table 10. It confirms the normal mass ordering and the upper octant are more plausible than the other scenarios. The corresponding Bayes factors are calculated by taking the fractions of each scenario, which are 2.8 as the ratio of the normal ordering to the inverted ordering and 3.0 as the ratio of the upper octant to the lower octant. Either Bayes factor is small to conclude the mass ordering and θ_{23} octant.

Table 9: Data fit results of confidence intervals for $\sin^2\theta_{23}$ from the grid-scan method. The grid-scan method gives results for both mass ordering scenarios (NO/IO) with the reactor constraint.

Significance	normal ordering	inverted ordering
$1\,\sigma$	[0.460, 0.491] $\cup$ [0.526, 0.578]	–
90%	[0.444, 0.589]	[0.525, 0.582]
$2\,\sigma$	[0.437, 0.594]	[0.459, 0.588]

Table 10: Fractions of the posterior probability from the MCMC analysis assuming the different scenarios for the mass ordering (NO/IO) and the θ_{23} octant with (without) the reactor constraint.

		$\sin^2\theta_{23}$		Sum
		< 0.5	> 0.5	
Δm_{32}^2	> 0 [NO]	0.20 (0.24)	0.54 (0.39)	0.74 (0.63)
	< 0 [IO]	0.05 (0.15)	0.21 (0.22)	0.26 (0.37)
	Sum	0.25 (0.39)	0.75 (0.61)	1.000
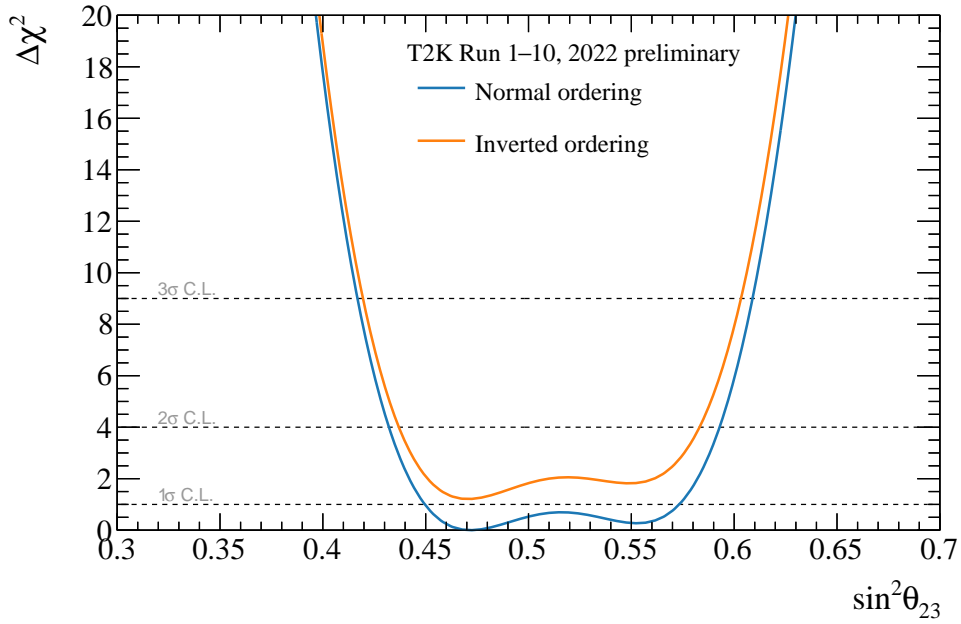
(a) Without the reactor constraint
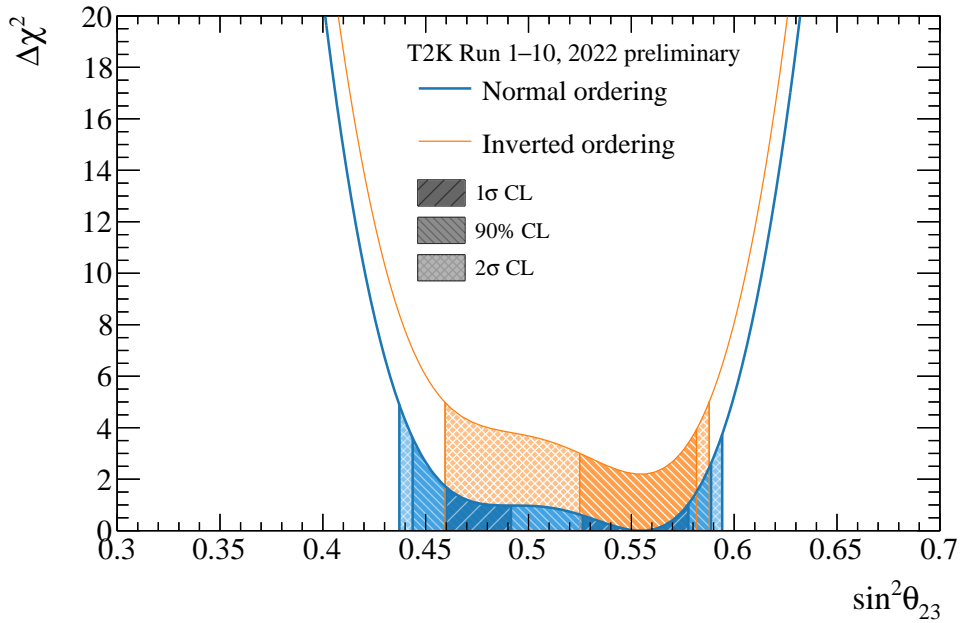
(b) With the reactor constraint

Figure 33: Results of the frequentist measurement of $\sin^2\theta_{23}$ without (top) and with (bottom) the reactor constraint. The same style as in Figure 32 is used except that the error band for 3σ coverage is missing in the FC method here.

7.3.4 Measurement of mass-squared differences (Δm^2_{32}, Δm^2_{31})

The energy of the oscillation dip in the ν_μ disappearance is sensitive to the mass-squared difference parameters. The likelihood function of these parameters can be considered as a Gaussian. The FC method is not necessary to construct the confidence intervals of the mass-squared differences paameters by the grid-scan method. The confidence intervals with the fixed $\Delta\chi^2$ method are shown in Figure 34. The fit result of the mass-squared difference is reported according to the mass ordering. When the normal ordering is assumed, Δm^2_{32} is reported. When the inverted ordering is assumed, $|\Delta m^2_{31}|$ is reported so that the value becomes positive and it corresponds to the atmospheric mass ordering. Since the inverted mass ordering is represented by $m_2 < m_1 < m_3$, $m_2 < m_1$ is the solar mass ordering and $m_1 < m_3$ is the atmospheric mass ordering in the inverted mass ordering scenario. The axis of Figure 34 has two alternative axes. The combined results do not improve the parameter constraints significantly compared to the standalone result. The μ-like samples are sensitive to the Δm^2_{32} parameters. On the other hand, the reactor constraint on $\sin^2 2\theta_{13}$ has a large effect on the e-like samples. As a result, the reactor constraint has only a small effect on the measurement of the Δm^2_{32} parameters.

7.3.5 Measurement of $\sin^2 \theta_{13}$

Figure 35 shows the results of the constraints on $\sin^2 \theta_{13}$ from the analysis with and without the reactor constraint. The result with the reactor constraint is dominated by the prior constraint from the reactor experiments.
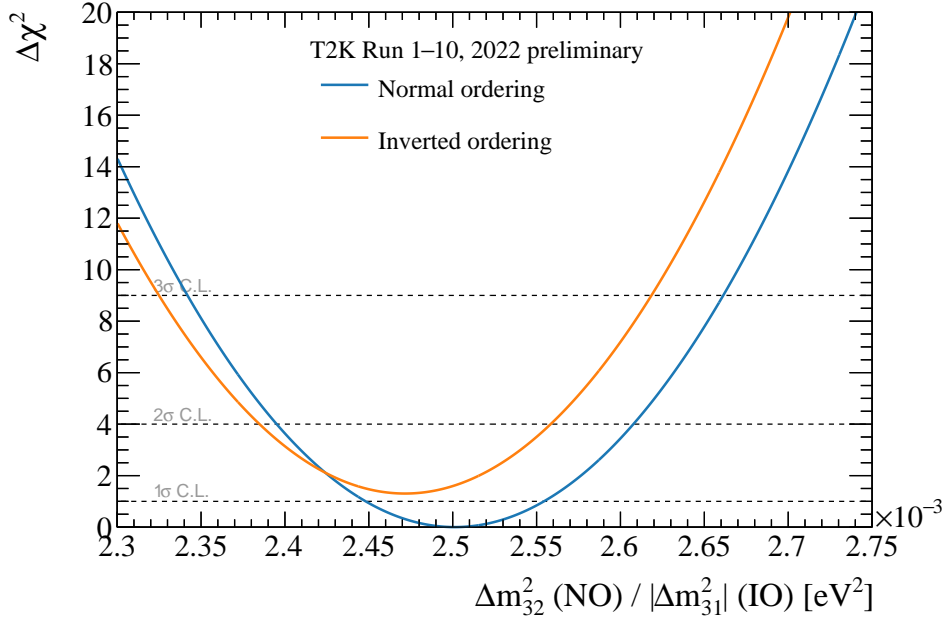
(a) Without the reactor constraint
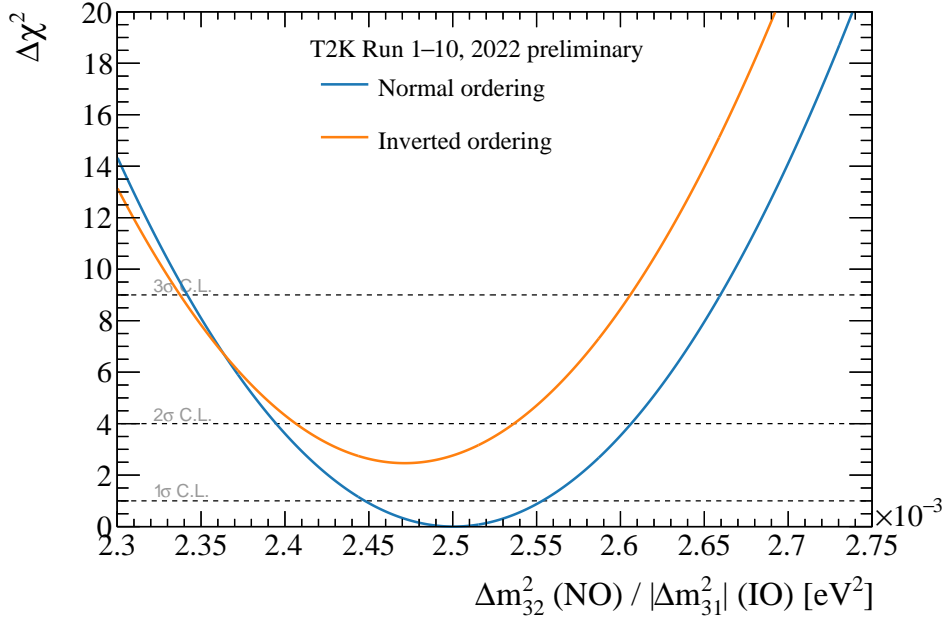
(b) With the reactor constraint

Figure 34: Results of the frequentist measurement of Δm_{32}^2 (NO) and Δm_{31}^2 (IO) without (top) and with (bottom) the reactor constraint. The horizontal axis means Δm_{32}^2 for the plot based on the assumption of NO (blue) whereas Δm_{31}^2 for the plot based on the assumption of IO (orange). Each broken line corresponds to the target coverage for 1σ, 2σ and 3σ.
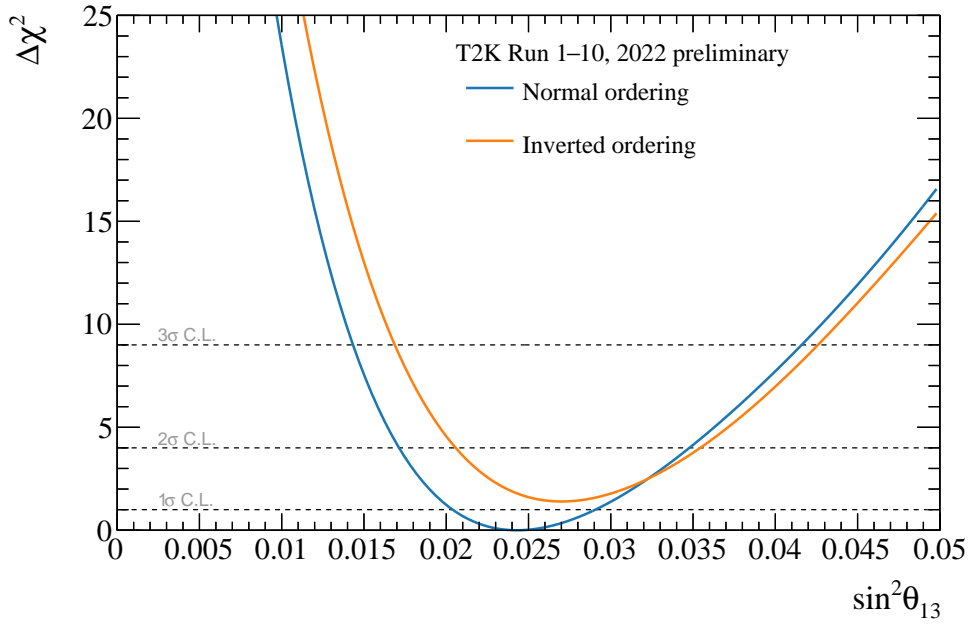
(a) Without the reactor constraint
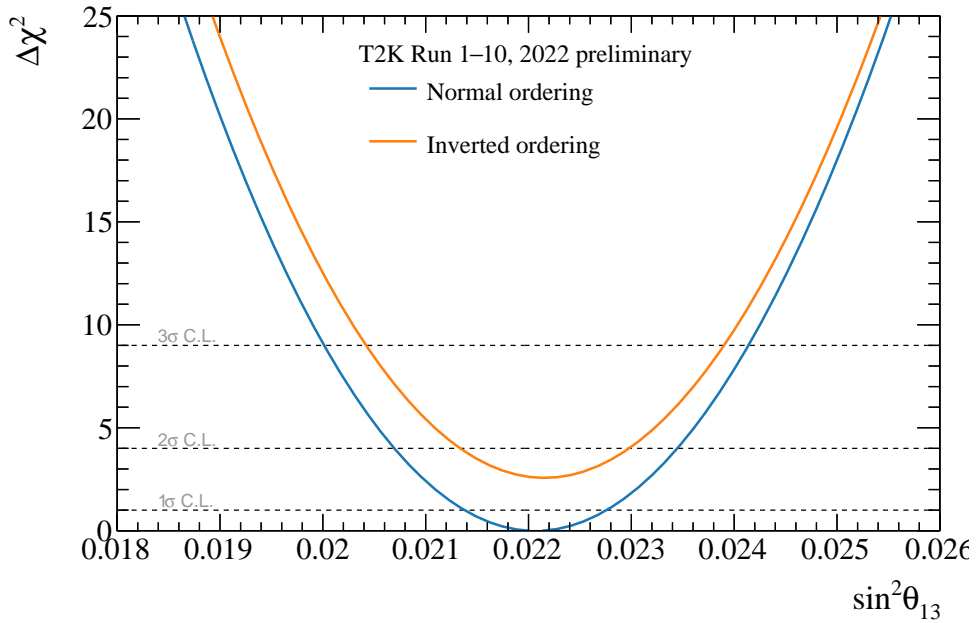
(b) With the reactor constraint

Figure 35: Results of the frequentist measurement of $\sin^2\theta_{13}$ without (top) and with (bottom) the reactor constraint. Each broken line corresponds to the target coverage for 1σ, 2σ and 3σ.

7.3.6 Measurement of Jarlskog invariant

The Jarlskog invariant is one of the indicators of whether the CP phase is violated in the leptonic sector as in the quark sector. Unlike the δ_{CP}, the measurement of the Jarlskog invariant provides a basis-independent way to verify the CP violation. The J_{CP} invariant is written down by

$$J_{CP} = c_{12}s_{12}c_{23}s_{23}c_{13}^2 s_{13} \sin\delta, \tag{7.1}$$

where c_{ij}, s_{ij} represent the cosine and sine functions for the corresponding mixing angles (θ_{ij}). The MCMC analysis using the marginalized likelihood computes all of the posterior distributions marginalizing only the mass ordering. The Jarlskog invariant is then calculated based on each set of posterior parameters with Equation 7.1. Figure 36 shows the result of the credible region of the Jarskog invariant depending on two kinds of the prior choices. The results are found to be prior-dependent, which stems from the Bayesian analysis. The CP conserving value ($J_{CP} = 0$) is rejected by 2 sigma significance for the case of the prior flat in δ_{CP}, but not for the prior flat in $\sin\delta_{CP}$.
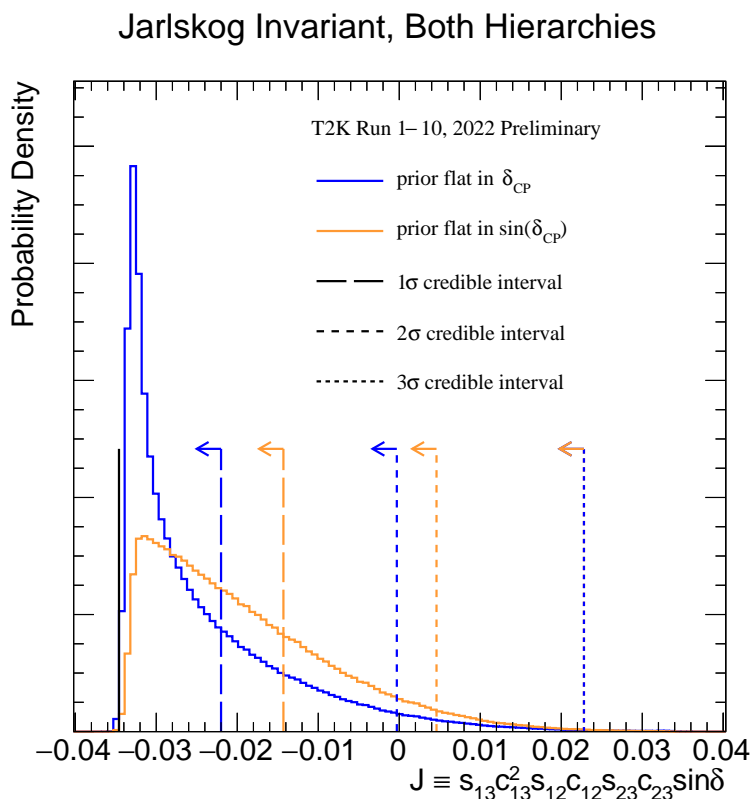
Figure 36: Probability density distributions of the Jarlskog invariant with two different prior choices with reactor constraints from the MCMC analysis. Bayesian posterior distributions can be affected by the prior distribution multiplying the likelihood. This analysis chose two alternative prior distributions, uniform distribution in δ_{CP} (blue) or uniform distribution in $\sin\delta_{CP}$ (orange).

8 Discussions on the oscillation analysis results

This chapter discusses the oscillation analysis results presented in the previous chapter in terms of the interpretations, the robustness of the analysis, the impact on neutrino physics, and future improvements.

8.1 Intepretations of the results on the oscillation parameters

We discuss the relationship between the observed number of events and the constraints on the oscillation parameters, and the preferences of the neutrino mass ordering and θ_{23} octant.

Based on the Bayesian analysis and the differences in confidence intervals between NO and IO, our data prefer the normal ordering scenario. In order to relate this to the observed number of events, we use the "Bi-probability plot", which is shown in Figure 37. It should be noted that this plot was created with the reactor constraint. The horizontal axis is the number of neutrino candidates and the vertical axis is the number of anti-neutrino candidates. The data point is overlaid on the MC prediction assuming various scenarios such as the mass ordering and θ_{23} octant. The bi-probability plot is useful to relate the number of e-like and μ-like candidates to the best-fit points of the oscillation parameters. The effect on the matter effect in T2K is not so high, which is reflected in the many overlap regions between NO and IO cases. However, our data point is near the NO region a bit away from the degeneracy region in Figure 37. This leads to the weak preference of the normal ordering in this analysis. In addition, the best-fit point is on the blue contour, which corresponds to $\sin^2\theta_{23} = 0.55$. We see the δ_{CP} of $-\pi/2$ on the blue contour being closed to the best-fit point.

We see the different best-fit points in the octant with and without the reactor constraint in Figure 33. This can be also understood by seeing the bi-probability plot. Figure 38 shows the comparison of the two bi-probability plots. One on the left is the same plot as in Figure 37. The other one is the plot without the reactor constraint, namely with a different value of $\sin^2\theta_{13}$. The best-fit point of $\sin^2\theta_{13}$ is 0.1034, which is larger than the value with the reactor constraint, 0.0869. In this case, the contours in color are shifted to the right (more e-like candidate events). Consequently, the T2K data is near the red contour, which corresponds to $\sin^2\theta_{23} = 0.45$, namely the lower octant.
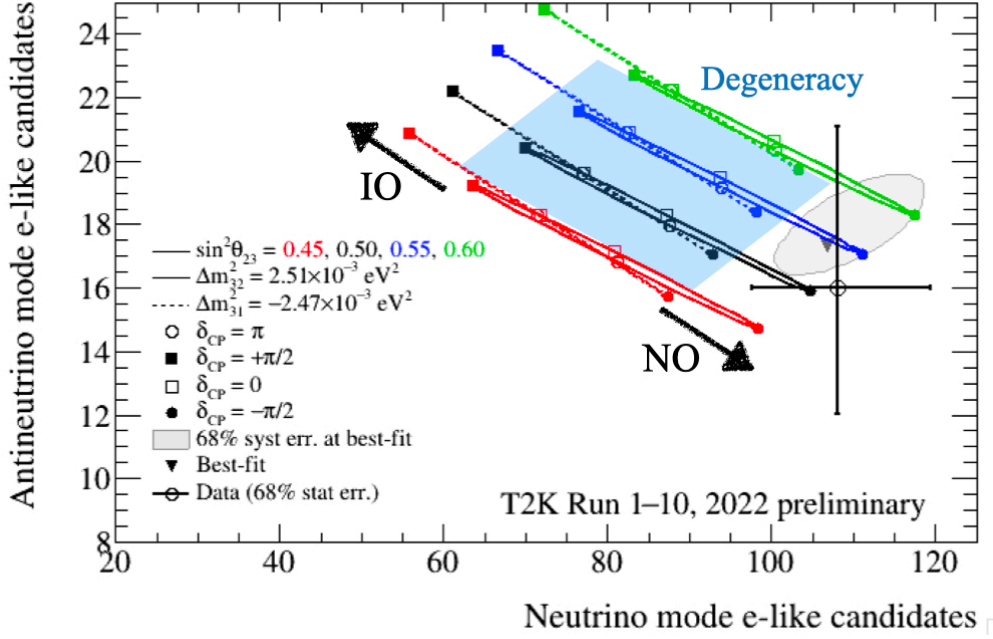
Figure 37: Bi-probability plot with the observed number of events for e-like and μ-like candidates. The solid contour refers to the "NO" case and the broken contour refers to the "IO" case. They are further divided by color depending on the value of $\sin^2 \theta_{23}$. The certain δ_{CP} values (π, $\pi/2$, 0, $-\pi/2$) are also shown as circular or rectangular points. The gray region is the 68% contour around the best-fit point taking into account the fluctuations of systematic parameters. The data is shown with the horizontal and vertical error bars.
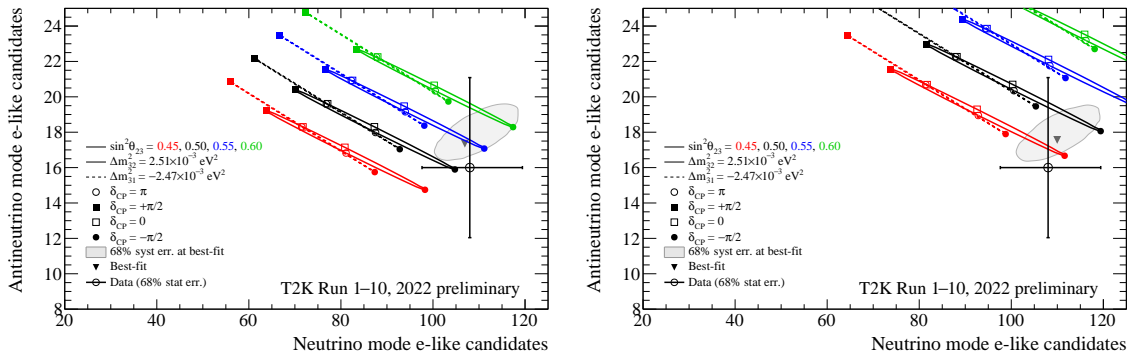
(a) with reactor constraint, $\sin^2 \theta_{13} = 0.0869$ (b) without reactor constraint, $\sin^2 \theta_{13} = 0.1034$

Figure 38: Comparison of the bi-probability plots with (left) and without (right) the reactor constraint. Correspondingly, the assumed $\sin^2 \theta_{13}$ are changed. The plotting style is the same as in Figure 37.

8.2 Comparison with sensitivity

The δ_{CP} constraint in the data fit gave a stronger constraint compared to the sensitivity results [16]. The difference between the sensitivity and the data fit was within the statistical fluctuation. There is a possibility that this difference was caused by an unknown factor to make the effect of the CP violation larger. It is worth checking if the difference is shrunk or further inflated to verify the possibility. For the sensitivity study, the oscillation parameters are set to the best-fit values obtained in this analysis (in Table 7) with the systematic parameters set to the prior values before the far detector (FD) fit. The impact of the FD fit on the systematic parameters is small due to large statistical uncertainty. We decided to use the prior values when we did the sensitivity study. The mass ordering is assumed to be the normal ordering. The frequentist grid-scan method is used to fit the MC data to extract the sensitivity.

The fit results on the parameter constraints showing the sensitivity are overlaid on the data-fit results in Figure 39. It shows two-dimensional $\Delta\chi^2$ contours for the parameters that have a large effect on the ν_μ to ν_e appearance (δ_{CP}, $\sin^2\theta_{13}$) and the parameters that have a large effect on the ν_μ disappearance (Δm_{32}^2, $\sin^2 2\theta_{23}$). They are called, appearance parameters and disappearance parameters, respectively. The data-fit results are mostly consistent with the sensitivity except for δ_{CP}. There is a relatively large discrepancy between the sensitivity and the data fit for δ_{CP}.

A Brazil band plot is used to check if the data-fit result on δ_{CP} is consistent with the MC prediction including the statistical fluctuations. It is created as follows.

1. Assume that the true mass ordering is the normal ordering and true δ_{CP} is $-\pi/2$.

2. Create 100k toy experiments with these true oscillation parameters and the nominal systematic parameters, taking statistical fluctuations into account.

3. Set the upper and lower bounds of $\Delta\chi^2$ at each δ_{CP} value by defining the interval containing all points where the density of toys per $\Delta\chi^2$ exceeds a certain threshold. Each threshold is adjusted to obtain the desired fraction of toys (68% and 95%).

The obtained error bands (Brazil bands) are plotted against the data-fit result in Figure 40. The data contour is consistent with the 68% error band of the MC prediction with the statistical fluctuation. Therefore, we have not so far seen a sign of new physics inferred from the discrepancy between the sensitivity and the data fit beyond the statistical fluctuation.
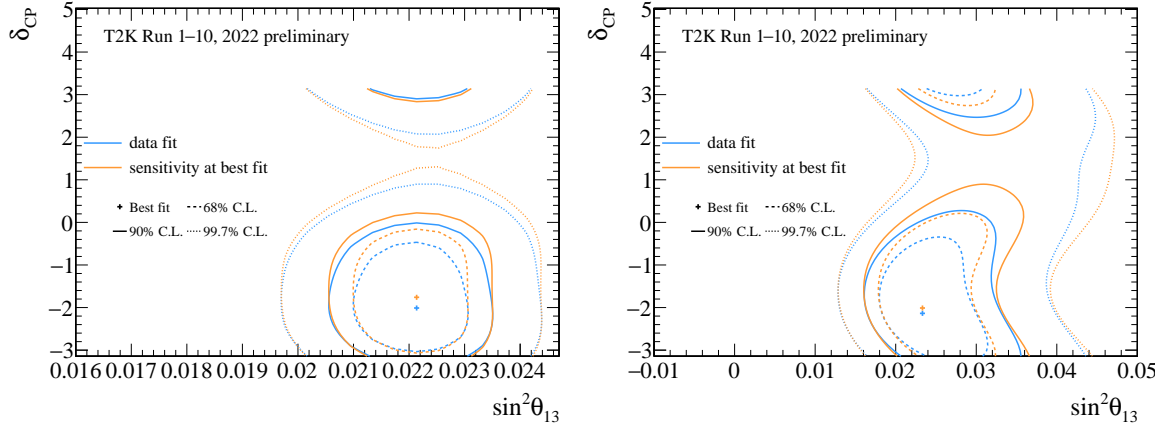
(a) Appearance parameters (δ_{CP}, $\sin^2 \theta_{13}$), with the reactor constraint

(b) Appearance parameters (δ_{CP}, $\sin^2 \theta_{13}$), without the reactor constraint
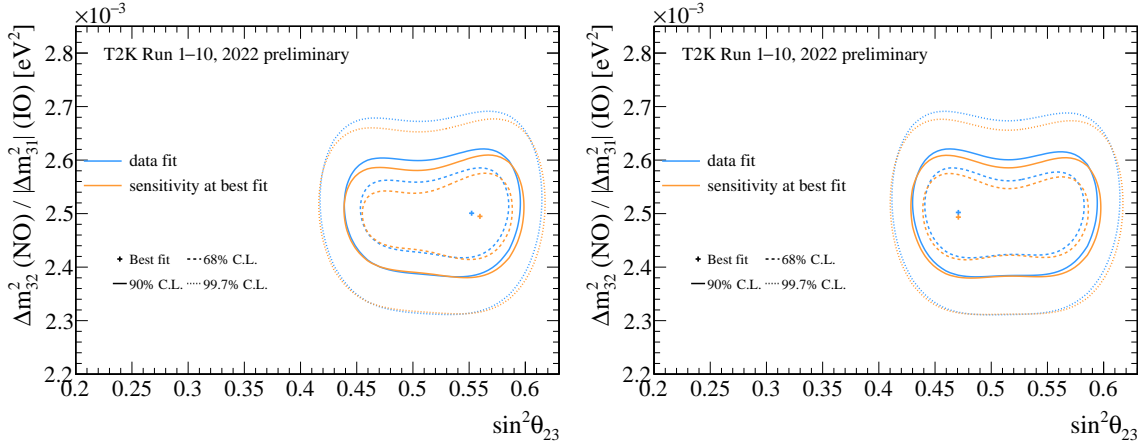
(c) Disappearance parameters (Δm_{32}^2, $\sin^2 \theta_{23}$), with the reactor constraint

(d) Disappearance parameters (Δm_{32}^2, $\sin^2 \theta_{23}$), without the reactor constraint

Figure 39: Comparisons of the two-dimensional contours between the data fit and the sensitivity for the appearance parameters (top) and the disappearance parameters (bottom). Blue: sensitivity results with the oscillation parameters set to the best-fit values. Orange: data-fit results. The left (right) figures show the results with (without) the reactor constraint.
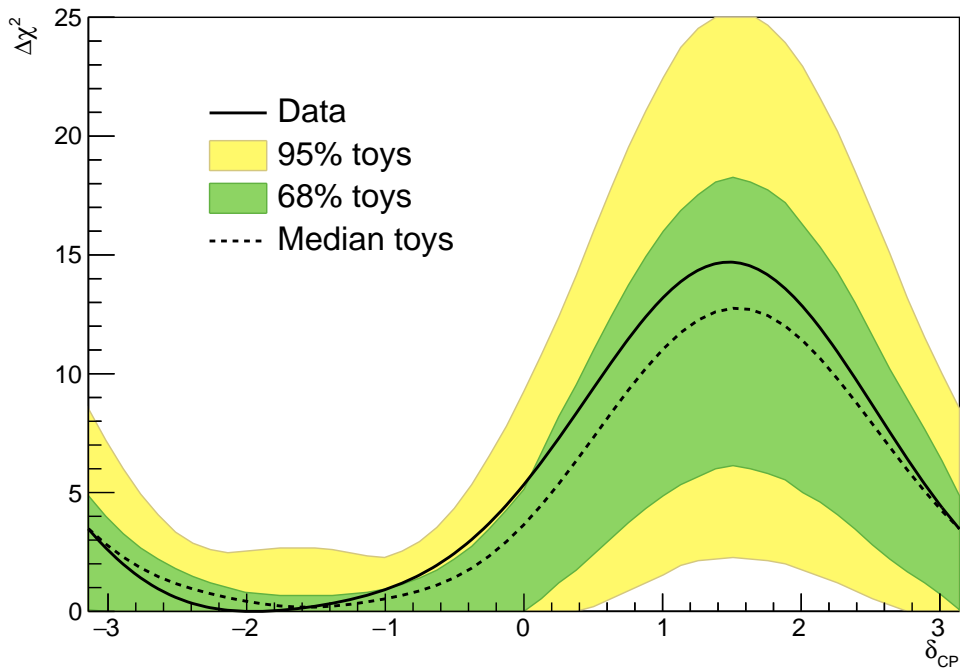
Figure 40: The error band plots along with the data fit contour assuming true normal mass ordering and true δ_{CP} being $-\pi/2$. The error band in green (yellow) contains all the points where the density of toys per $\Delta\chi^2$ exceeds 68% (95%). The dotted line is a connected line consisting of points that have median $\Delta\chi^2$ at each δ_{CP} value.

8.3 Impacts of the systematic parameters on data fit results

We performed a fit considering only the statistical fluctuation to separate the statistical and systematic uncertainties. We produce posterior probability (P) distributions for a certain oscillation parameter (o) assuming a certain mass ordering (MO), which is written by

$$P(o) = \alpha \times \left[\mathcal{L}_{\mathrm{marg}}(o|\mathrm{MO}) \right], \qquad (8.1)$$

where α is a constant such that the integral of a whole probability distribution is normalized to 1. When the mass ordering is marginalized, Equation 8.1 is then modified into

$$P(o) = \alpha \times \left[\mathcal{L}_{\mathrm{marg}}(o|\mathrm{NO})P(\mathrm{NO}) + \mathcal{L}_{\mathrm{marg}}(o|\mathrm{IO})P(\mathrm{IO}) \right]. \qquad (8.2)$$

The systematic impact on the most probable value in a one-dimensional probability distribution is evaluated by $(\mathrm{syst})^2 = (\mathrm{total})^2 - (\mathrm{stat})^2$. Table 11 shows the decompositions of the statistical and systematic errors on the most probable value of each oscillation parameter. We confirm the constraints on the oscillation parameters are statistically limited. Therefore, in order to increase the T2K's sensitivity, it is primarily important to increase the statistics. The systematic uncertainty is, however, not negligible in this analysis. It is expected that the systematic uncertainty will be reduced and the systematic uncertainty will be more important to be suppressed [68]. The reduction in the systematic uncertainties is also important to increase the discovery potential of T2K.

Table 11: Decompositions of the statistic and systematic errors on the best-fit values from the posterior distribution through the grid-scan method. These fits are performed with the reactor constraint except for $\sin^2 \theta_{13}$.

oscillation parameter	result		mass ordering
	stat. error	syst. error	
δ_{CP}	0.79	0.25	NH
$\sin^2 \theta_{23}$	0.024	0.007	NH+IH
$\Delta m^2_{32}/10^{-3}\ \mathrm{eV}^2/\mathrm{c}^4$	0.046	0.017	NH
$\sin^2 \theta_{13}/10^{-3}$	4.6	2.4	NH

8.4 Impacts of the major updates in the updated results on the contours

The major updates and their effects with respect to the published results are summarized below.

Update a: Update flux model with 2010 replica target data
Reduce the flux uncertainty at high energy regions (a few GeV).

Update b: Update neutrino interaction models
Make the interaction models more robust by changing the models, adding parameters, and replacing parameters in the models with more theory-driven uncertainties.

Update c: Add new sample in the ND fit
Categorize the CC0π samples by their proton multiplicities and classify the CC other samples based on the photon detection. This results in stronger constraints on the neutrino interaction models that are not constrained much by data.

Update d: Update the prior constraint on $\sin^2\theta_{13}$ by the reactor experiments
The prior constraint on $\sin^2 2\theta_{13}$ is updated to be 0.0220 ± 0.007 [50]. The sensitivity to the appearance parameters such as δ_{CP} is increased.

Update e: Add new sample at the FD fit
The ν_μ CC1π^+ sample is added to the FD samples. The sensitivity to the disappearance parameters, Δm_{32}^2 and $\sin^2\theta_{23}$ is increased.

Each update is sequentially applied to the published results presented in the Neutrino 2020 conference in order to pin down what effect is stronger in the context of the constraints on the oscillation parameters. We provide the contours corresponding to the following updating components.

- *Contour A = Oscillation analysis in the T2K published results*
  Contours correspond to the T2K official data release for the published results [148].

- *Contour B = A + Update a + Update b + Update c*
  The ND fit uses the improved constraints on the flux uncertainties and updated models and constraints of the neutrino interactions with the updated sample classifications. [33]

- *Contour C = B + Update d*
  The update on the PDG constraint on $\sin^2 2\theta_{13}$ (0.0220 ± 0.007 [50]) is applied.

- *Contour D = C + Update e*
  The new FD sample is added to the FD fit, making the contours reflect all the updates.

Figure 41 shows the results on each contour in two-dimensional $\Delta\chi^2$ contours with the reactor constraint. As the constraint on $\sin^2 2\theta_{13}$ is dominated by the reactor constraint, the best-fit value in this parameter is determined by the mean value of the prior. The best-fit values of $\sin^2 2\theta_{13}$ in the contours of A and B are overlapped in the upper plot in Figure 41. About the 1σ interval on δ_{CP} between the published results in blue and the updated results in red, a wider range of values for δ_{CP} is permissible in this analysis, especially near the value of π. The weaker constraint is also reflected in the errors associated with the best fit values presented in Table 7. Another comparison between the contours before and after adding the new sample at the FD tells that there does not seem a notable change in the constraints on the appearance parameters. The ν_μ CC1π^+ sample is one of the μ-like samples. It is expected to increase the sensitivity to the disappearance parameters ($\sin^2\theta_{23}$, Δm_{32}^2) instead of the appearance parameters (δ_{CP}, $\sin^2\theta_{13}$).

On the other hand, the contours for the disappearance parameters show a relatively large change, in particular between contour A pointing to the published results and contour B pointing to the published results + updates in the ND constraints. The change in Δm_{32}^2 is largely due to the updates on the smearing factor being larger than that in the published results. Besides, constraints on $\sin^2\theta_{23}$ in the updated results allow the lower octant to be more probable. The impact of adding the new sample at FD is visible by comparing contour D in red with contour C in green. The improvement in the constraint on Δm_{32}^2 is about 5% with respect to its 1σ error. The reason why the improvement is small is partly because the neutrino energy of the new sample is away from the maximum oscillation probability. The sensitivity to the disappearance parameters is weaker than that of the CCQE-like 1-Ring μ samples. More plots related to the impact of the new FD sample are shown in Appendix F.

---

[33] As the flux and interaction parameters have a strong anti-correlation, it would be difficult to see the individual effect for them. Therefore, both updates were imposed at once.
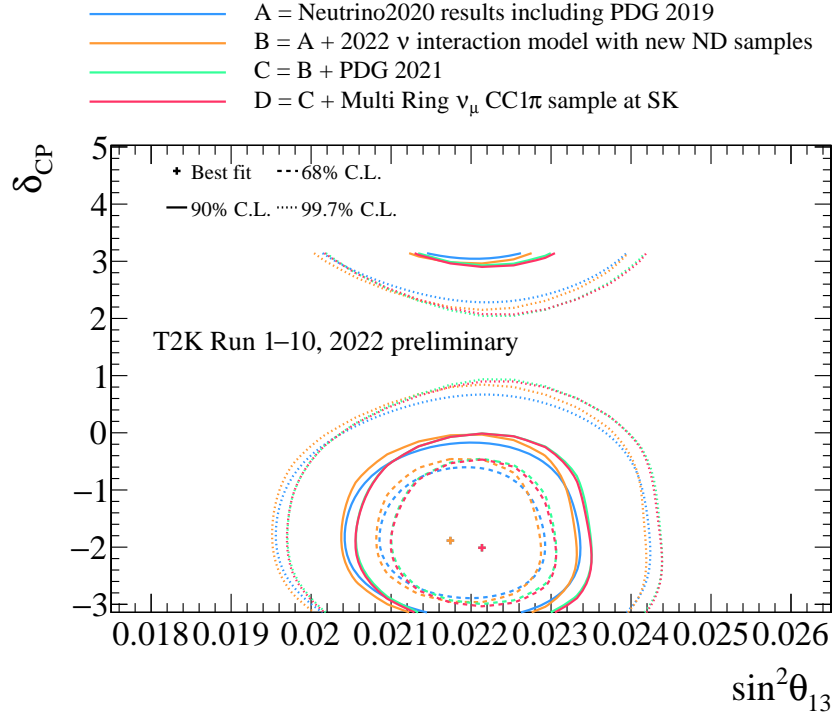
(a) Contour for $\sin^2\theta_{13}$-δ_{CP}
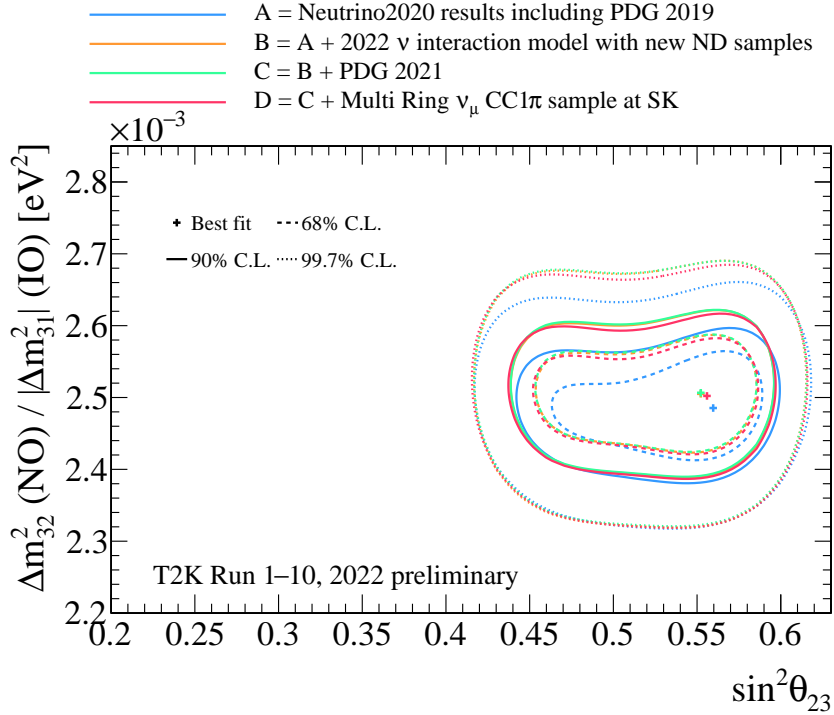
(b) Contour for $\sin^2\theta_{23}$-Δm^2_{32}

Figure 41: Two-dimensional evolution contours for the appearance parameters (top) and disappearance parameters (bottom) with the reactor constraint on $\sin^2\theta_{13}$ from the grid-scan method. Each colored line corresponds to which updates are reflected in each contour.

8.5 Comparison with other experiments

Other experiments have reported their results of constraints on the oscillation parameters recently. Their basic features are briefly described below.

Super-Kamiokande experiment

The SK detector has been used for neutrino measurements such as accelerator neutrinos and atmospheric neutrinos. Atmospheric neutrinos are produced from a similar interaction chain to that of the accelerator neutrinos except that the interactions are initiated by cosmic ray protons. The results from the SK experiment include the oscillation analysis of the atmospheric neutrinos to show the constraints on the same oscillation parameters as those from the T2K experiment [149, 150].

MINOS (MINOS+) experiment

MINOS (Main Injector Neutrino Oscillation Search) is one of the long-baseline experiments with accelerator neutrinos. MINOS+ is a second-generation program. The MINOS experiment has made use of a 120 GeV proton beam from the Fermilab NuMI accelerator to produce an intense ν_μ or $\overline{\nu}_\mu$ beam. The neutrino energy mainly ranges from 1.5 GeV to 10 GeV. The MINOS far detector [34] is located 735 km away from the target on-axis with respect to the proton beam. [35] The latest result covers the oscillation analysis with both data sets taken in the MINOS and MINOS+ experiments [151]. The result is the outcome of the combined analysis of the accelerator neutrinos and the atmospheric neutrinos.

NOvA experiment

NOνA (NuMI Off-axis ν_e Appearance) is another long-baseline (810 km) experiment using the same proton accelerator as the MINOS experiment. It adopts the off-axis neutrino beam. The peak energy of neutrinos is around 2 GeV. This experiment has a similar L/E to that of the T2K experiment. [36] The NOνA experiment reported both ν_e ($\overline{\nu}_e$) appearance and ν_μ ($\overline{\nu}_\mu$) disappearance results [152, 153], which are competitive with those from the T2K experiment.

IceCube experiment

IceCube is an experiment specialized in measurements for neutrinos coming from space in order to study astrophysics and cosmology as well as particle physics. The detector is located at the south pole to utilize a natural ice block as its target. The IceCube collaboration has reported the measurement of the atmospheric neutrinos [154].

We compared the neutrino oscillation results from this analysis with the recent measurements by those experiments in order to see the impacts of our results on neutrino physics. Comparisons of the constraints on the oscillation parameters are shown in Figures 42, 43.

---

[34]It has a sandwich structure of steel and segmented scintillator layers. The MINOS detector has particular strength in detecting charged-current ν_μ ($\overline{\nu}_\mu$) interaction. Therefore, it has a good sensitivity to ν_μ ($\overline{\nu}_\mu$) disappearance, which in turn helps the experiment to provide competitive constraints on disappearance parameters ($\sin^2\theta_{23}$ and Δm_{32}^2).

[35]Since MINOS adopted an on-axis strategy, neutrino energy is broadly spanned from 1.5 GeV to 10 GeV energy regions.

[36]Since the NOνA experiment has a longer baseline, neutrinos tend to be subject to matter effects more frequently than in the T2K experiment. This leads to the NOνA experiment being more sensitive to the neutrino mass ordering, whereas the T2K experiment is more sensitive to $\delta_{\rm CP}$. Consequently, both experiments have complementary roles in constraining those parameters.
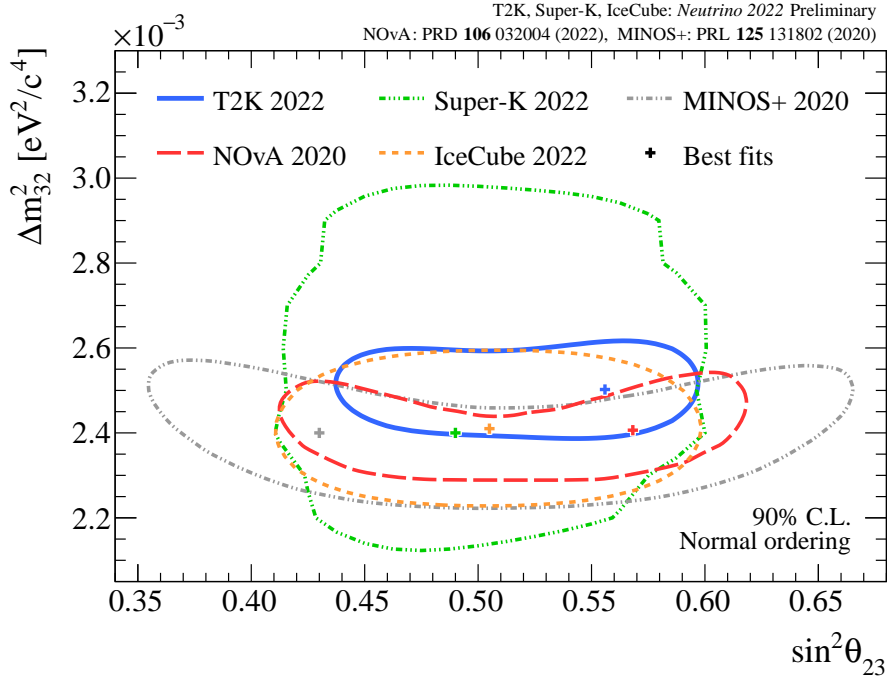
Figure 42: Comparisons of the constraints on the oscillation parameters in the $\sin^2\theta_{23}$-Δm_{32}^2 plane among the neutrino oscillation experiments. In addition to the updated result from the T2K experiment, Super-Kamiokande experiment [149,150], NOνA experiment [152,153], IceCube experiment [154] and MINOS+ experiment [151] are shown. The computing methods are different among experiments. The NOvA and IceCube constraints are produced with the Feldman and Cousins (FC) method while the constraints from the other experiments are computed with the fixed $\Delta\chi^2$ method. The treatments of the mass ordering are also different. The NOvA experiment takes the minimum over both mass orderings. On the other hand, the other experiments assume the normal mass ordering in creating these contours.
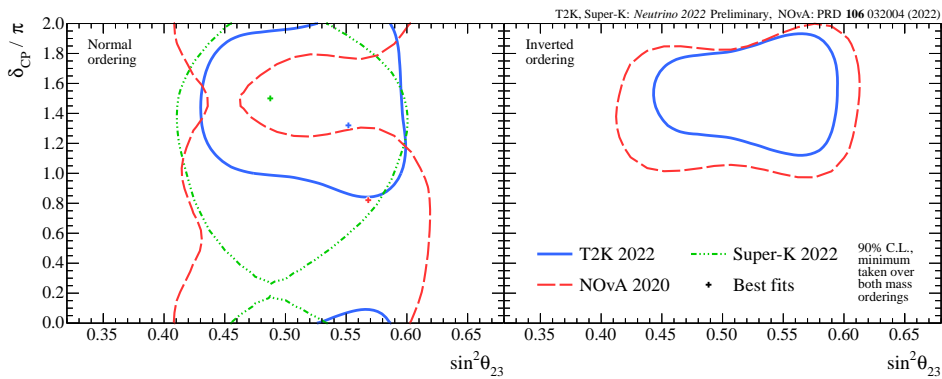
Figure 43: Comparisons of the constraints on the oscillation parameters in the $\sin^2\theta_{23}$-δ_{CP} plane among the neutrino oscillation experiments. The T2K and NOvA ([152,153]) experiments produced the contours with the FC method whilst the SK ([149,150]) experiment computed contours with the fixed $\Delta\chi^2$ method.

The updated results from the T2K experiment provide the leading constraints on these parameters. Particular attention should be paid to the distinct features of the oscillation contours in $\sin^2\theta_{23}$-δ_{CP} plane between T2K and NOνA as in Figure 43. In the normal ordering case, the T2K constraint covers the wide range of the regions around δ_{CP} being $-\pi/2$ whereas the NOνA contour shrinks around that region. In fact, the NOνA experiment favors $\pi/2$ for δ_{CP} assuming the normal ordering, which is a different indication from T2K. On the other hand, in the case of the inverted mass ordering, both contours cover a similar region with a tighter constraint by the T2K experiment. It should be noted that even in the normal ordering case, we have an overlapped region between T2K and NOνA experiments. Considering the differences in the sensitivities in the mass ordering and the δ_{CP} between these experiments, the different behaviors in contours are not surprising. Figure 44 shows the bi-probability plot obtained in the NOνA experiment. The degenerate region is much smaller than that in T2K, which is due to the longer baseline with larger matter effects in NOνA. Compared to our results, the difference in the observed number of events between anti-neutrino candidates and neutrino candidates is less in NOνA, which results in the different best-fit δ_{CP} value, $\pi/2$ from the our result, $-\pi/2$.
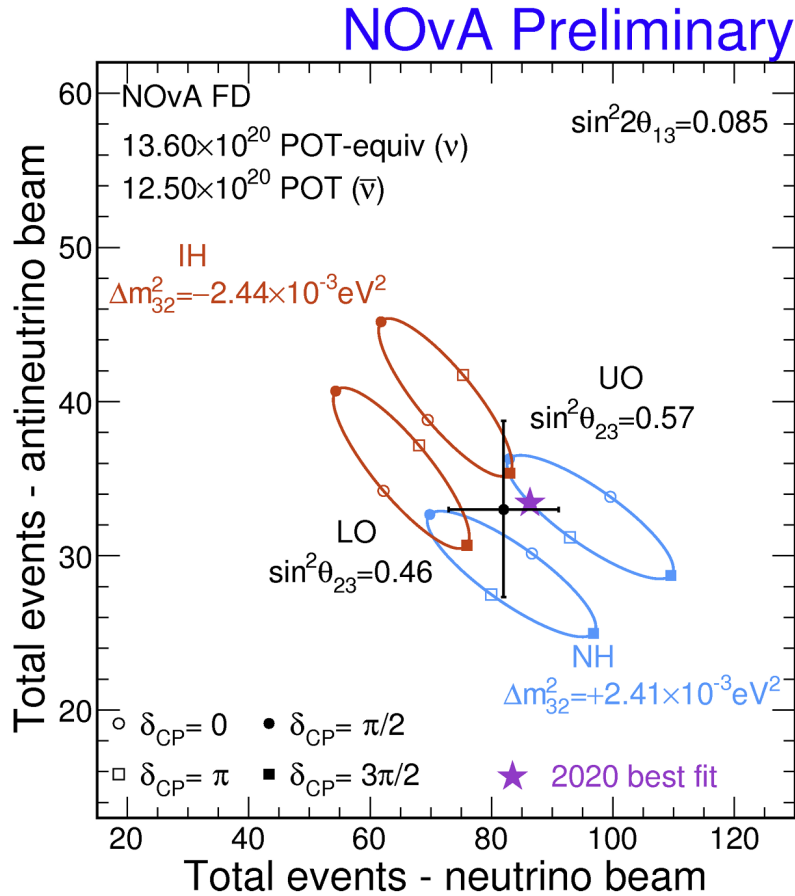
Figure 44: The bi-probability plot for the NOνA's oscillation analysis results [155]. The red contours refer to the inverted ordering case and the blue contours refer to the normal ordering case. They are further divided by θ_{23} octant, lower and upper octants. The four δ_{CP} values are placed on each contour.

8.6 Future measurements by the T2K experiment

Our analysis is statistically limited as shown in Table 11. The top priority is to increase statistics by upgrading the proton beam power in J-PARC and increasing the horn current in the T2K beamline while achieving more beam operations. Thanks to the continuous beam operations, the statistical uncertainty has been reduced and the systematic contributions has been more important. The contribution from each systematic parameter is broken down in Table 12. Overall, the dominant contributions come from the interaction parameters, which stem from the lack of understanding of neutrino interactions. For the 1-Ring $CC1\pi^+$ e sample, we see the dominant error coming from FD. This originated from the 100% uncertainties on the measured variables such as the number of ring for the NC 1π and NC other interactions. Therefore, this large uncertainty comes from the uncertainties of the neutrino interaction models.

To reduce systematic uncertainties in neutrino interactions, we need to establish a solid model to describe the experimental data. Establishing a solid model is challenging as some models can explain measurements at certain conditions, otherwise, they do not. To overcome this situation, more precise measurements to test each model are imperative. The main target of ND280 is CH while that of the FD is water. To consider the difference in the target material, the difference in cross sections between the carbon and oxygen targets is included in the systematic parameters. The recent ND280 upgrade is specialized in the improvement of measurements on the CH target while the remained water target detector lost part of the water target volume because of problems in the water containers. It is desirable to install a new detector complex consisting of water target detectors to comprehensive the difference in neutrino interactions between the carbon and oxygen targets. This is more important in the context of splitting some parameters such as Pauli-Blocking depending on the material in establishing NEUT.

The neutrino oscillation depends on the neutrino energy and the neutrino cross sections of interaction types differ depending on the neutrino energy. T2K reported that a certain neutrino interaction model can describe the $CC0\pi$ double differential cross section results on the water target for forward-going muons better while the alternative model describes the data better for high-angle muons [156]. It is difficult to pin down the energy region that causes data-MC differences seen because the T2K neutrino flux has a broad energy tail. It is important to understand neutrino-nucleus interactions at different neutrino energy to understand the ratio of neutrino interaction types to reduce the systematic uncertainties in the oscillation measurements.

Considering these issues and requirements for the ND measurements, measurements of neutrino-nucleus interactions on the water target at different neutrino energy are desirable. We developed a new detector complex and installed it in 2019. The next part of this thesis discusses the details of the measurement, presents the first result on the cross sections with the detector complex, and shows a way to apply the cross section results to the oscillation analysis.

Table 12: Error sizes for systematic parameters from the updated analysis broken down by each contribution, Flux, Interaction (NuInt.) with or without the ND constraints

FD sample		Error budget (%)				Total (%)
		Flux	NuInt. (w/ ND)	NuInt. (w/o ND)	FD + SI + PN	
1-Ring μ	ν mode	2.8	2.7	0.7	2.0	3.4
	$\bar{\nu}$ mode	2.9	3.5	2.4	1.7	3.9
1-Ring e	ν mode	2.8	3.8	2.9	3.1	5.2
	$\bar{\nu}$ mode	3.0	3.5	3.3	3.8	5.8
1-Ring $CC1\pi^+$ e	ν mode	2.8	4.1	2.8	13.6	14.3
1-Ring $CC1\pi^+$ μ	ν mode	2.8	3.0	1.4	4.1	4.9

Part III

Measurement of neutrino-nucleus cross section and applications to the oscillation analysis

9   The WAGASCI-BabyMIND detectors

We developed a new near detector complex around 280 m away from the T2K proton target, called WAGASCI-BabyMIND. This chapter describes motivations to develop this detector complex and summarizes the detector specifications and performances. At the end of this chapter, the concept of the MC simulation framework is briefly mentioned.

9.1   Motivation

We aim for measurements of neutrino-nucleus interactions on H_2O and CH targets at mean energy of neutrinos different from the one in the ND280 location with larger acceptance of detectors to muons scattering at high angles. This section elaborates on our motivations.

9.1.1   Energy dependency of neutrino interaction

The neutrino oscillation probability varies depending on the neutrino energy. Therefore, the inputs of neutrino interaction measurements in several kinds of mean neutrino energy are ideal to understand neutrino interactions affecting on the event prediction at FD. With respect to the data and model discrepancies mentioned in Section 8.6, it might be challenging for ND280 to disentangle the potential deficiencies in the model because it is unclear which energy region contributed to the discrepancies. If cross section measurements at different mean energy of neutrinos are possible, they can provide a way to disentangle the effect of energy dependency on the data-model differences. [37] In Section 3.2, we show that different angles off-axis give a different flux spectrum. It is possible to measure the neutrino interactions at different mean energy of neutrinos from that in the ND280 location if a detector complex is installed at different angles from 2.5 degrees off-axis.

Standalone measurements at different angles off-axis are valuable for the purpose of diagnosing the discrepancies between data and model. In addition, joint analyses of measurements in two different off-axis angles provide a unique way to analyze neutrino-nucleus cross sections. We can subtract one flux from another flux to cancel a high energy or low energy contribution analytically [157]. The different off-axis angles, for instance, 1.5 degrees off-axis and 2.5 degrees off-axis give different neutrino energy spectra, both of which have a similar long energy tail in higher energy regions. One way to remove the contribution from the high-energy tail is to tune the coefficient of scaling parameters of one flux at 1.5 degrees off-axis such that those high-energy tails are overlapped and subtract the flux at 2.5 degrees off-axis from the tuned flux at 1.5 degrees off-axis. This technique is shown in Figure 45. Even without the flux subtraction method, the cross section measurements at 1.5 degrees off-axis can be combined with the ND280

---

[37]The lower energy region (below 0.6 GeV) has a larger contribution from CCQE and 2p2h, whilst the higher energy region (a few GeV) has a large contribution from resonance production and deep inelastic scattering. If a measurement at a lower mean energy of neutrino shows a good agreement with a model, it indicates the discrepancies might have been coming from the higher energy region.

measurements in the ND fit. We provide a practical way to realize the combined analysis in the latter chapter.
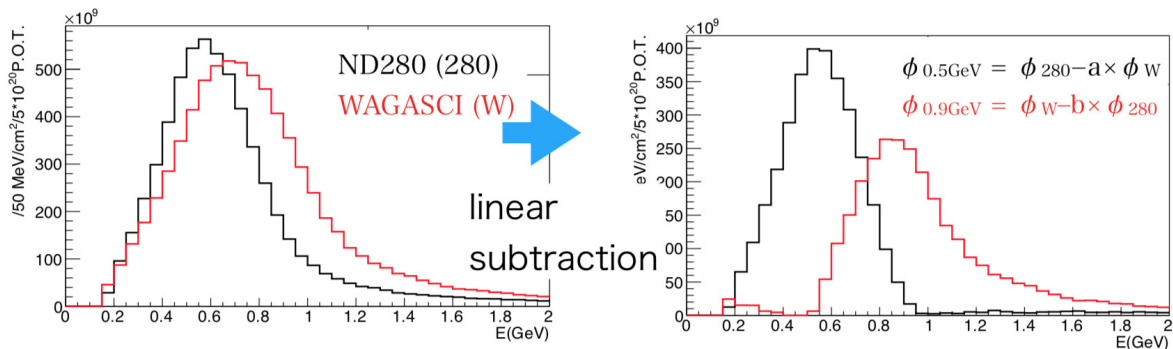
Figure 45: A flux subtraction method with two different flux spectra at different angles off-axis to obtain two kinds of fluxes having fewer contributions in low or high energy regions. The left figure shows the two flux spectra for 2.5 degrees off-axis (ND280) and 1.5 degrees off-axis (WAGASCI). The linear subtraction defined in the legend in the right figure provides two possible flux spectra to remove lower energy contribution in red and higher energy contribution in black. The coefficients, a, b are 0.35 and 0.75, respectively.

9.1.2 Target and acceptance differences between ND and FD

Since the target material of the FD is H_2O, it is important to understand the neutrino-nucleus interactions on the H_2O target. ND280 has performed the cross section measurements on the H_2O target for the CC0π sample [158]. Figure 46 shows the comparison of CC0π H_2O cross sections with two alternative models, with and without 2p2h contributions [158]. These results indicate the model with 2p2h contributions is more compatible with the data in the high scattering angle regions, but it is less compatible in the muons forward scattering regions. As discussed in the previous section, it is challenging to pin down the cause of the discrepancy because we do not know which energy region in the neutrino spectrum is responsible for this difference. More water cross section results with the different mean energy of neutrinos could have a clue to understanding this difference.

Although two of the vertex detectors in ND280 (FGD2, P∅D) have H_2O as one of the target materials, the currently ongoing project to upgrade the ND280 detector complex plans to replace the partial water-target detector (P∅D) with an intensely segmented detector made of cubic plastic scintillators [68]. [38] The upgrade project is promising to increase the performance of measurements on the CH target in ND280, but one of the downsides is that the amount of H_2O target materials is going to be smaller in ND280. In addition, the conventional ND280 detectors with the H_2O target have limited acceptance to high scattering muons, typically more than 60 degrees with respect to the neutrino beam direction. On the other hand, FD is the H_2O target detector having 4π acceptance to charged particles. As the model compatibility in Figure 46 depends on the muon scattering angle, more data in a wide range of phase space

---

[38]This upgraded detector is going to be made of six million cube-formed scintillators, each of them has the dimension of 1 cm cubic. Three wavelength-shifting fibers will be inserted through each cube to obtain three-dimensional information about a particle hit.

will be important to investigate the differences. Therefore, the detector complex capable of measurements of neutrino-nucleus cross sections on the water target in a wider range of phase space are necessary to compensate for the ND280 cross section measurements.
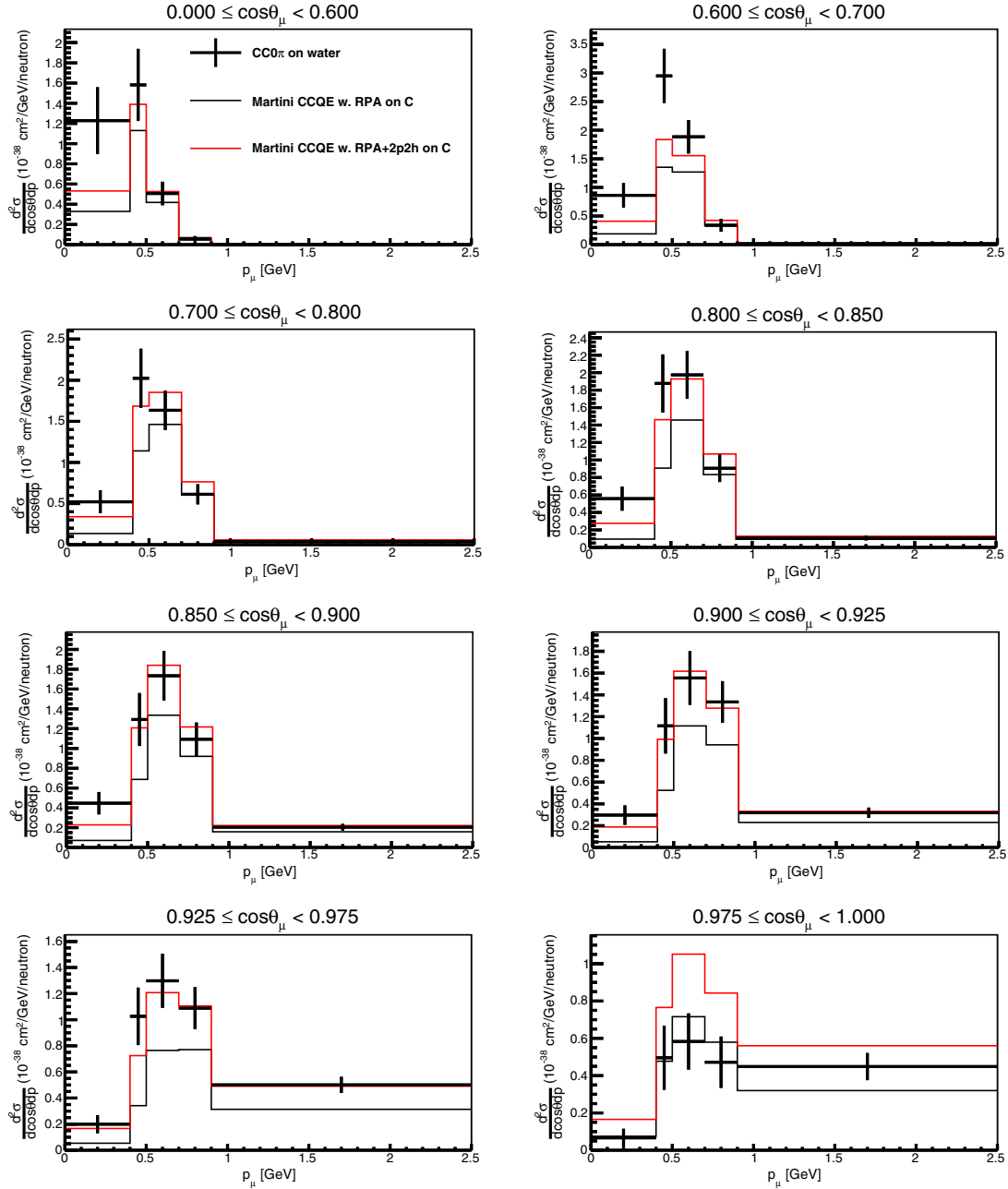
Figure 46: A comparison of the CC0π water cross section against two Martini model predictions on carbon, one with 2p2h contributions and one without [158]. The angle regions are divided into eight, where the differential cross sections as a function of muon angle and momentum are shown.

9.1.3 Target physics

One of the vital goals of this measurement is to understand neutrino interactions to verify underlying models in combination with ND280 measurements. We aim for the measurement of differential cross sections for a charged current neutrino-nucleus interactions on H_2O and CH targets as a function of muon kinematics. It is ideal to measure double differential cross sections if the statistics are enough. The available data set is not large enough to extract the meaningful result of double differential cross sections. Instead, we extract single differential cross sections as a function of muon momentum and angle.

9.2 Detector complex

The requirements mentioned in Section 9.1 are fulfilled by detector designs and their arrangement. For the measurement at the different mean energy of neutrinos, a whole detector complex was installed at 1.5 degrees off-axis. Figure 47 points to the location of the detector complex and structures of detectors. The peak energy of neutrino goes up to 0.86 GeV at this off-axis angle while it is 0.60 GeV at 2.5 degrees off-axis. The WAGASCI-BabyMIND detectors are divided into two kinds of vertex detectors and two kinds of muon range detectors. The vertex detectors detect the charged current ν_μ interactions, and the muons produced from the interactions are detected by the muon range detectors.

All of the detectors have the same signal detection method using plastic scintillators, wavelength-shifting fibers, and MPPCs. Each detector has tracking planes that are aligned with the beam axis or with the axis perpendicular to the beam axis. Tracking planes are made of plastic scintillator bars. When charged particles are incident to scintillators and interact with them, the scintillators emit scintillation light with a wavelength of around 400 nm. This wavelength is close to, but outside the lower region for the effective area of MPPC. We use wavelength-shifting fibers called Y11 [159] which absorb the scintillation light and emit the light whose wavelength is distributed with a peak around 500 nm. This wavelength is matched with the effective area of MPPC. MPPC is a semi-conductor photo sensor consisting of pixel arrays. Each pixel unit contains Geiger mode avalanche photodiodes and quenching resisters. When the charged particles are incident to the depletion layer of MPPC, electron-hole pairs are created, which are accelerated in an external electric field. In a region with a high-gradient electronic field, the accelerated electrons release more electron-hole pairs by the consecutive collision with lattice atoms. The sequential creation of electron-hole pairs is called avalanche multiplication. As each sensor works in the Geiger mode, it outputs a pulse at the same amplitude when the photon is detected in a pixel. Therefore, if the pixel density is sufficiently large with respect to the incident rate of the charged particles, the sensor is expected to have a linear response to the number of pixels with the avalanche multiplication.
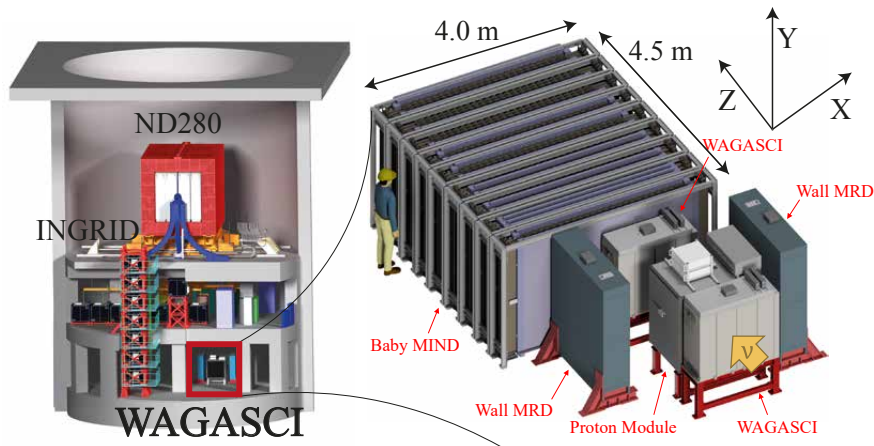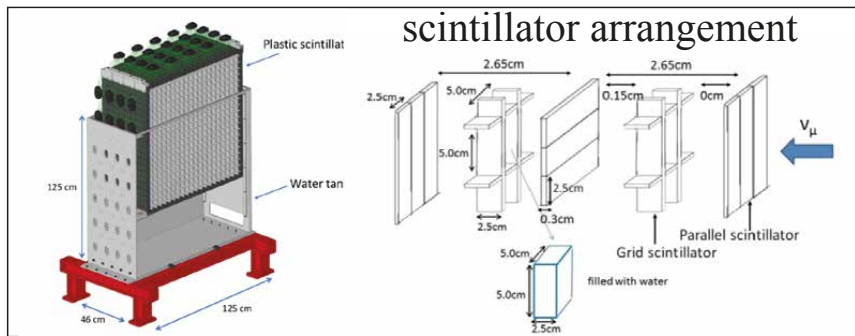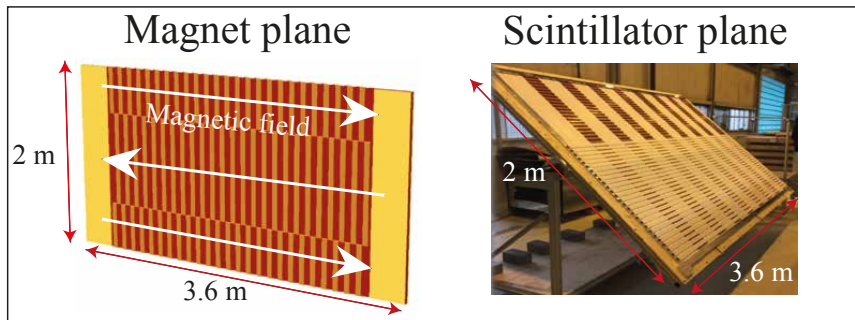
Figure 47: The location of WAGASCI-BabyMIND detector complex and detector components for the WAGASCI detector (middle) [160] and BabyMIND (bottom). The top two figures illustrate the location of a whole detector complex (left) and configuration (right). The right middle figure shows how both grid and plane scintillators are assembled to form a grid-like structure. The bottom two figures show one unit of a magnet plane (left) and a scintillator plane (right), respectively. Each magnet plane has two slits through which aluminum coils can be wound. Yellow materials on both edges in a magnet plane are flux returns to minimize stray field, which is estimated to be below 10 mT. Horizontal layers of the plane are segmented in a finer fashion than a vertical layer in order to enhance the performance of charge identification.

9.2.1 Water target detectors (WAGASCI)

Detectors to serve H_2O target in this measurement is scintillator trackers submerge in a water box, called "WAGASCI detectors" [39] in a dimension of 1.25 m × 1.25 m × 0.46 m. Each tracking plane is segmented by two kinds of scintillator bars. One type of scintillator bar, grid scintillator is 1020 mm × 25 mm × 3 mm size and has 4 mm wide slits in an interval of 32.5 mm to insert other scintillator bars, forming a grid-like structured tracking plane. The tracking plane consists of vertically aligned grid scintillators and horizontally aligned grid-scintillators. The other type of scintillator bars is in the same dimension as the grid scintillators but without any slit, called plane scintillator. A pair of vertically aligned plane scintillators and horizontally aligned plane scintillators sandwiches a tracking plane consisting of grid scintillators, being a tracking plane unit. Water fills with space segmented by these scintillators. A WAGASCI detector consists of eight tracking planes in water to act as a tracker for charged particles. In the middle in Figure 47 the scintillator assembling for the WAGASCI detector is illustrated. Grid-scintillator-based tracking planes enable this detector to enhance the detection efficiency of particles scattered at high angles, even more than 60 degrees with respect to the neutrino beam axis. We use two WAGASCI detectors whose structures are almost identical.

Each WAGASCI detector is equipped with 1280 MPPCs (S13360), whose signals are read out by Silicon PM integrated Read-Out Chip (SPIROC) [161, 162]. Collective SPIROC chips are stored in Active Sensor Unit (ASU), which conveys the analog signals from SPIROC to interface boards. The interface boards process the digital data and output them to our DAQ PCs.

9.2.2 CH target detectors (Proton Module)

To understand neutrino interactions on the CH target, we measure the cross section on the CH target. For this purpose, we deploy a detector called Proton Module [163]. [40] Proton Module is comprised of fully active scintillator tracking planes surrounded by four veto planes. The dimension is 1.42 m × 1.42 m × 0.96 m. Each tracking plane consists of 25 mm and 50 mm wide scintillator bars, both of which are about 1.2 m long. The finer scintillators are aligned around the central part of a plane while coarser ones are aligned around the marginal part to make finer segmentation around the center of this detector.

The electronics consist of Trip-t Front end Board (TFB) and Back End Board (BEB). Each MPPC is connected to the TFB, and the signal is read out by a Trip-t chip [164]. The readout signals are conveyed to BEB, where the triggers are published. The digitized signals are then output to DAQ PCs.

Both WAGASCI detectors and Proton Module contain neutrino interaction target materials. They are called "vertex detectors" hereafter.

9.2.3 Downstream muon range detector (Baby MIND)

As we aim for a single differential cross section as a function of muon kinematics, muon identification is an essential task for the detector complex. We developed two kinds of muon range detectors (MRDs) that cover different phase spaces. Muons going downstream are covered by a magnetized iron-core magnet detector, BabyMIND. The size of the detector is 4 m × 2 m × 4.5 m.

---

[39]It is the abbreviation of "WAter Grid and SCIntillator".

[40]This detector was originally designed to measure neutrino interaction as one of the on-axis detectors for the T2K experiment. We reused this detector for the off-axis neutrino interaction measurements in the WAGASCI project.

BabyMIND has 18 scintillator tracking planes to detect particles' trajectories. In addition, this downstream MRD has 33 iron-core magnet planes, each of which is 3.0 cm wide, energized by 140 A current, providing a magnetic field of 1.5 T in the X direction [165] as they are shown in Figure 47. Therefore, it is capable of identifying the charge of a particle.

The number of MPPC (S12571-025C) channels is 3996 for all of the tracking planes. We use CITIROC chips [162] to digitize the MPPC signals, which are embedded in a Front End Board (FEB). Each FEB is connected to a Master Clock Board (MCB), which receives the beam trigger and sends processed signals to the DAQ PCs.

9.2.4   Muon range detectors aside vertex detectors (WallMRD)

In order to detect muons going backwards or in the perpendicular direction with respect to the beam axis, the other type of MRD, WallMRD was designed. This detector has a sandwich structure of irons and scintillators but without a magnetic field. [41] It has alternating ten iron planes and nine scintillator planes. The number of iron planes was determined such that it is sufficient to measure the momentum of muons by their range. The total number of MPPC channels is 160. The electronics are the same as the WAGASCI one and both are integrated such that we can operate them simultaneously.

Both BabyMIND and WallMRDs are called MRDs hereafter.

9.3   Detector specification and performance

Each detector was examined if it met the fundamental requirements to perform as a tracking detector. First, the stability of the dark noise rate of MPPC must be guaranteed under the experimental environment. In addition to the stability, its effect has to be suppressed with a certain electronic threshold to separate the signal hit from dark noises of MPPC. We set the threshold to 2.5 p.e. Second, a sufficient amount of light yield for a Minimum Ionizing Particle (MIP) is necessary to ensure a high hit detection efficiency and particle identification. Our detectors achieve around 20 p.e. or more for the mean yield for MIP. Third, detectors must have a high hit detection efficiency for MIP. Even if a detector fulfills the two requirements, insufficient efficiencies are caused by a misalignment of the scintillator bar or a small gap between neighboring scintillator bars. We have to confirm that all detectors have the expected hit detection efficiency, which is more than 95%. Fourth, as a tracking detector for charged particles, a two-dimensional and three-dimensional track reconstruction efficiency must be high. We expect the reconstruction efficiency to be higher than 95% for the typical angle and momentum regions in each detector. The measurements for detector performances are described in this section.

9.3.1   Dark noise

The dark noise rate for each detector was studied by specific calibration runs. We confirmed that the dark noise rate was stable for all the detectors. Figure 48 shows the MPPC dark noise history plots for the Upstream WAGASCI during 2020 and 2021 data taking. The dark noise

---

[41]There is a reason why we designed a magnetised detector only for downstream MRD. Charge identification is specifically important for muons in terms of cross section measurements to reduce a wrong-sign component in neutrino flux. Positive muons scattered from the anti-neutrino interaction have a tendency to go forward due to helicity suppression. Consequently, wrong-sign contamination matters for mainly forward-going muons, whereas large-angle-scattering muons are likely to be negative muons from neutrino interactions. Therefore, the charge identification is more significant for the downstream MRD.

rate is drastically reduced in 2021 data taking due to the change in the hit threshold from 2.5 p.e. to 3.5 p.e. Our timing window in the beam bunch opens for about 580 ns. Therefore, 1 kHz dark noise in 2020 is expected to have a negligible impact on the contamination in signal detection.

(a) 2020 data taking
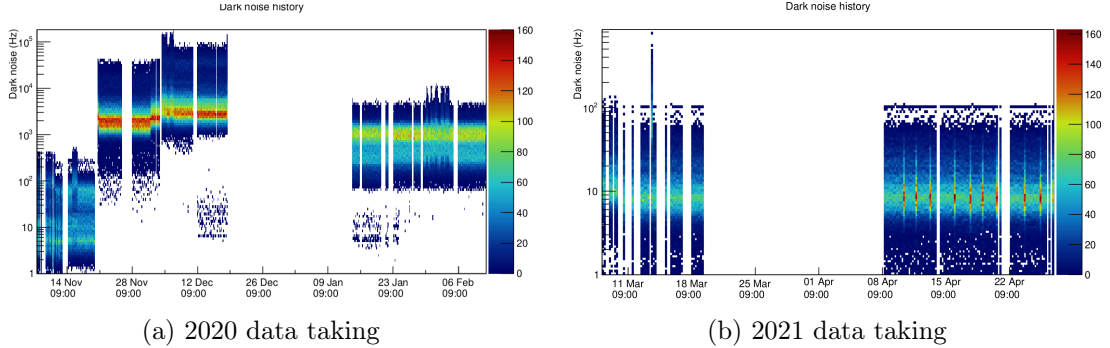
(b) 2021 data taking

Figure 48: The MPPC dark noise history of the Upstream WAGASCI in the 2020 data taking (left) and in the 2021 data taking (right).

9.3.2 Light yield

The mean light yield for each type of scintillator bars was measured by using MIP-like particles. As the light yield is proportional to the path length in each scintillator, a light yield distribution is normalized by the path length.

The mean of the light yield per unit path length (p.e./cm) is then calculated based on the distributions. The results are shown in Figures 49, 50. The absolute values of the mean light yields are high enough to detect MIP-like particles, and the comparisons between MC and data are also good enough. The differences are within around 10%.
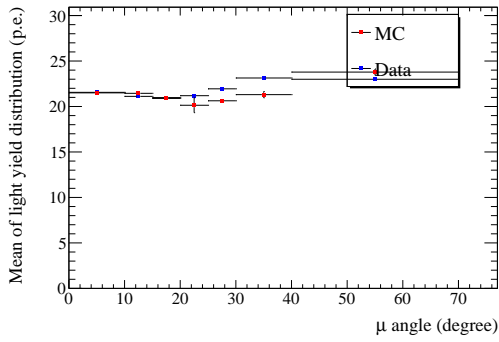
(a) INGRID type scintillator in Proton Module (b) Scibar type scintillator in Proton Module
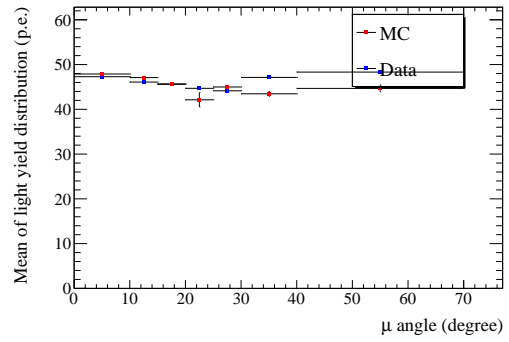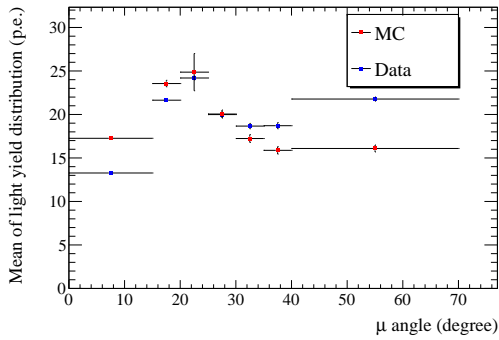
(c) Grid scintillator in Upstream WAGASCI (d) Plane scintillator in Upstream WAGASCI
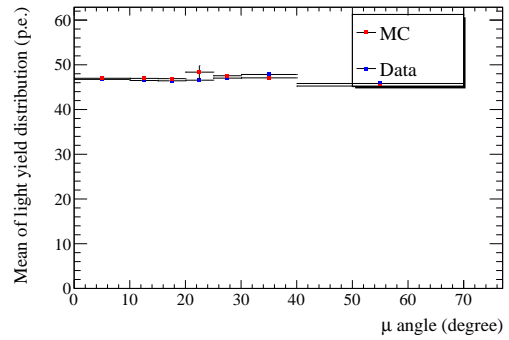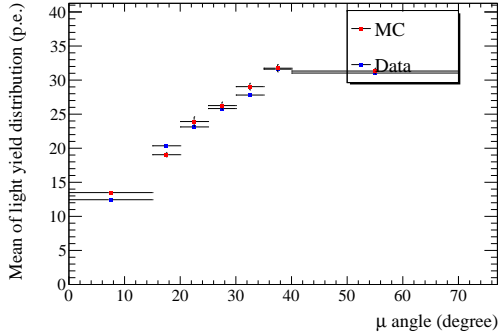
(e) Grid scintillator in Downstream WAGASCI (f) Plane scintillator in Downstream WAGASCI
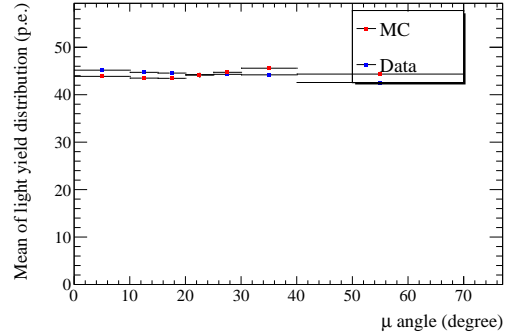
Figure 49: The mean light yield for MIP-like particles as a function of muon angle for Proton Module (top), Upstream WAGASCI (middle), and Downstream WAGASCI (bottom). Error bars represent only statistical errors. As both vertex detectors have two types of scintillator bars, the plots are divided into two for each scintillator bar (left and right).
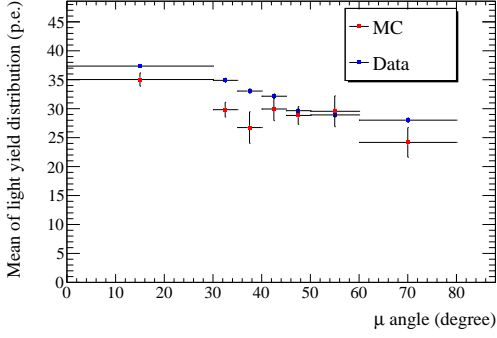
(a) Scintillator in WallMRD South
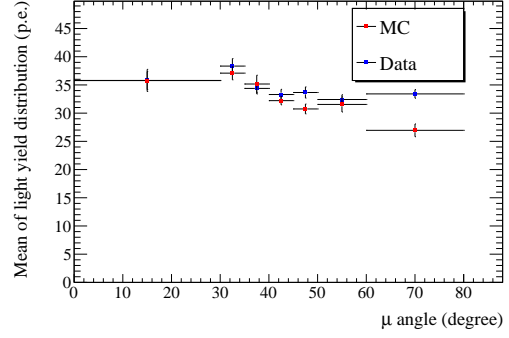
(b) Scintillator in WallMRD North
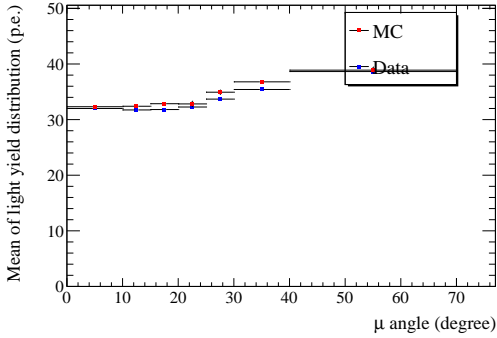
(c) Horizontal scintillator in BabyMIND
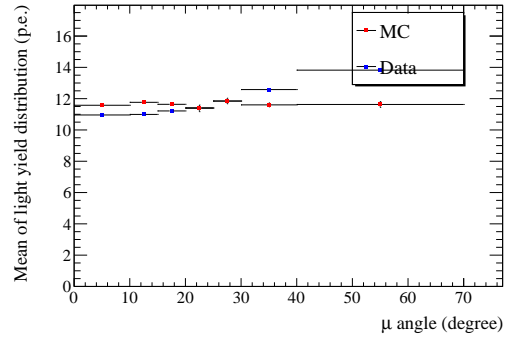
(d) Vertical scintillator in BabyMIND

Figure 50: The mean light yield for MIP-like particles as a function of the angle with respect to the initial neutrino direction for WallMRD (top) and BabyMIND (bottom). The vertical error bars represent only statistical errors on the corresponding mean light yields. The Figures 50a, 50b are the mean light yield plots for the scintillator bars of WallMRD south and WallMRD north detectors. As BabyMIND has two types of scintillator bars, Figures 50c, 50d correspond to the horizontal and vertical scintillator bars, respectively.

9.3.3 Hit detection efficiency

The hit threshold is set to 4.5 p.e. for the vertex detectors to separate signal hits from noise hits. It is necessary to confirm the threshold is not too high with respect to the mean light yield for each scintillator bar by checking the hit detection efficiency. If there is a misalignment of scintillator bars resulting in a small slit or hole between neighboring scintillators, the hit detection efficiency is reduced. We need to confirm the effect of possible misalignment is negligible.

The hit detection efficiency was evaluated with MIP-like tracks. For all the detectors except for WAGASCI detectors, plane-by-plane hit efficiency was evaluated. As WAGASCI detectors have a three-dimensional grid-like structure unlike the other detectors, a block group is defined to estimate the hit detection efficiency. Each block contains a combination of one line of plane scintillators and two lines of grid scintillators. For WAGASCI detectors, the hit detection efficiency is measured for each block. The evaluation was done in the following way.

- Collect MIP-like tracks passing through a detector of interest

- Find a plane or a block whose neighboring planes or blocks have a hit from the track

• Check if the plane (block) has a hit

Plane being evaluated   **Block being evaluated**

Pln 1 Pln 2 Pln 3 Pln 4 Pln 5   Block 1   Block 2   Block 3

Proton Module   **WAGASCI detectors**
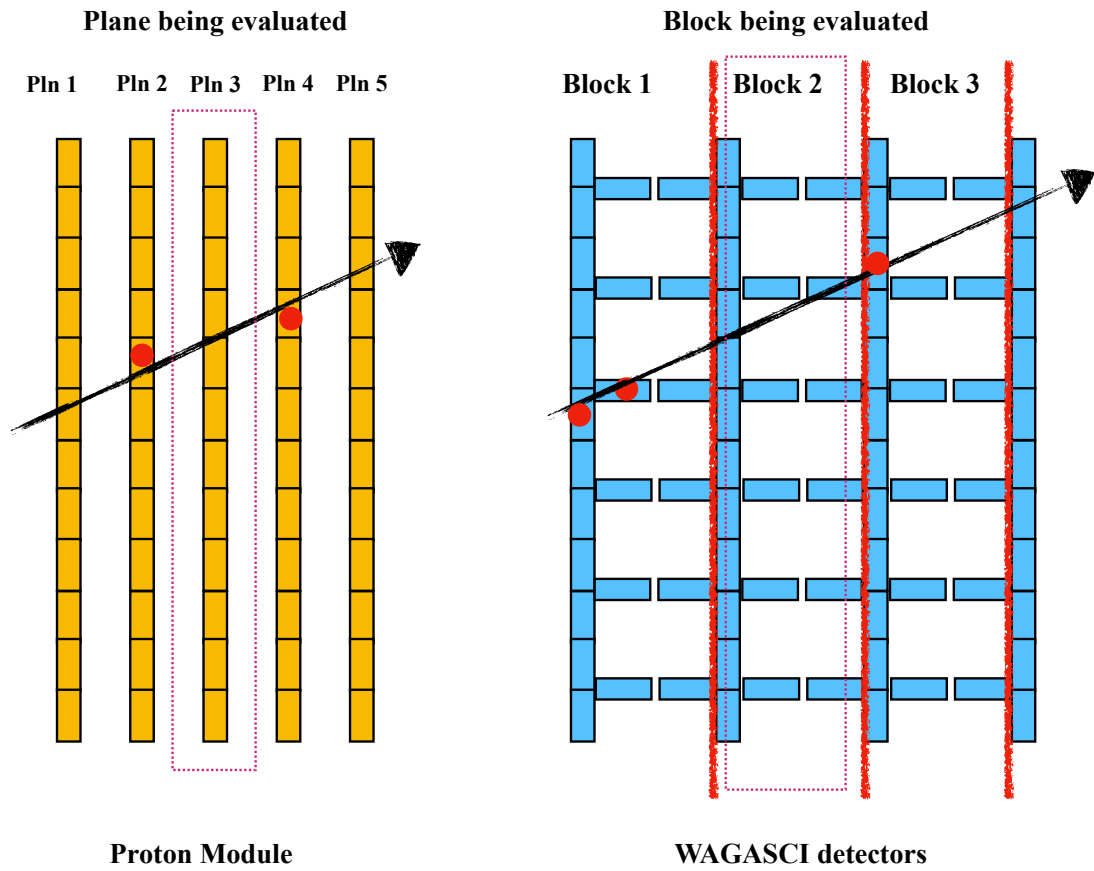
Figure 51: Illustration of the evaluation method for the hit detection efficiency. The left one shows the Proton Module case. As each plane is separated, the hit detection efficiency is evaluated plane by plane. The right one is for the WAGASCI detectors case. Each block contains a combination of one line of plane scintillators and two lines of grid scintillators. The block-by-block efficiency is calculated in this case.

The process is illustrated in Figure 51. Figure 52 shows the results for each detector. For most angle regions, the hit efficiency exceeds the 95% level. Moreover, overall differences stay within around a few % between MC and data.
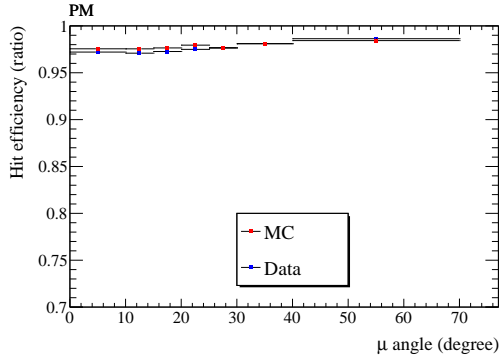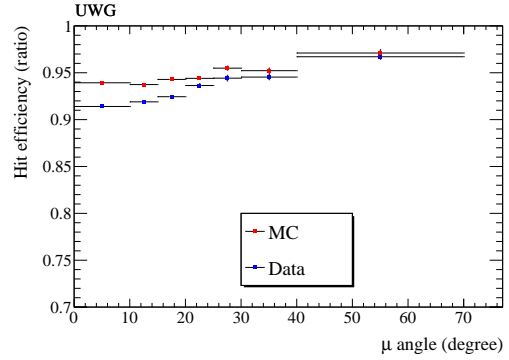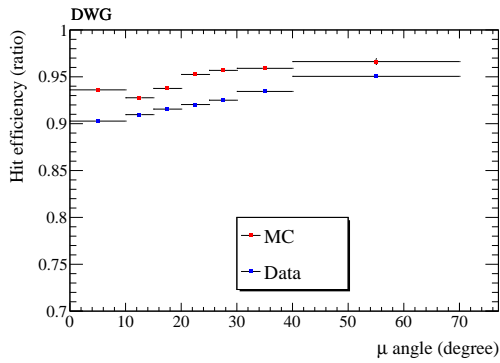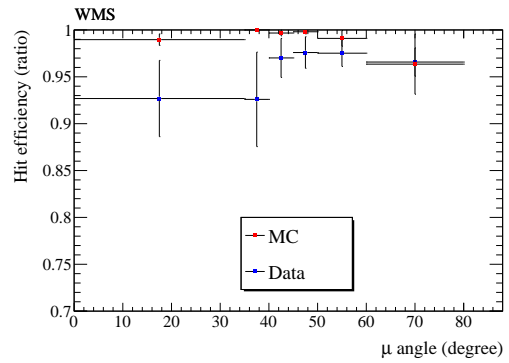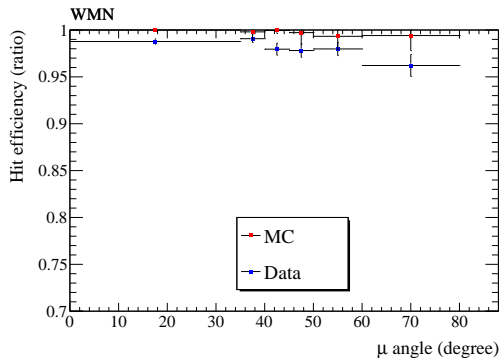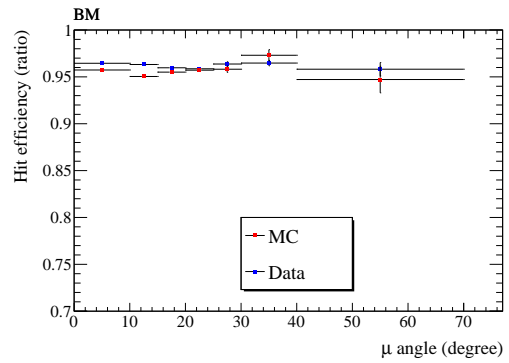
Figure 52: The results of hit detection efficiency as a function of MIP-like particles' angle with respect to the initial neutrino direction. The vertical error bars represent statistical errors in hit detection efficiencies. Each plot corresponds to the hit detection efficiency of each detector.

9.3.4 Two-dimensional tracking efficiency

Two-dimensional tracking efficiency was evaluated for the vertex detectors with the MIP-like tracks passing through either muon range detector. The evaluation was done in the following way.

- Reconstruct at least one three-dimensional track in a muon range detector.

- Extrapolate the track to the vertex detectors.

- Check if the distance between the extrapolated track line and each hit in the vertex detector is less than 200 mm.

- If the number of planes having at least one hit satisfying the conditions is four or more, check if there is a reconstructed cluster in the vertex detector. Otherwise, the event is dismissed.

This process for the Proton Module is illustrated in Figure 53. WAGASCI detectors follow the same way. The results are shown in Figure 54. The horizontal axis on the figures refers to bin numbers corresponding to the binning schemes used in this cross section measurement, which is shown in Table 13. The measured tracking efficiency in both detectors is sufficient for the cross section analysis. The efficiency in data seems to exceed the efficiency in MC for both detectors, but the difference is within a few % levels. We confirm the level of difference is acceptable because it is not expected to cause significant systematic uncertainties.

Table 13: Bin numbers for θ_μ measurement. The reconstruction efficiency for the bins from 0 to 8 is used for the signal samples in this analysis. The 9th and 10th bins are made for the reconstruction efficiency in the regions to be used for control samples in this analysis.

Bin number	0	1	2	3	4	5	6	7	8	9	10
Lower bound (degree)	0	10	15	20	25	30	35	40	50	0	20
Upper bound (degree)	10	15	20	25	30	35	40	50	70	20	70
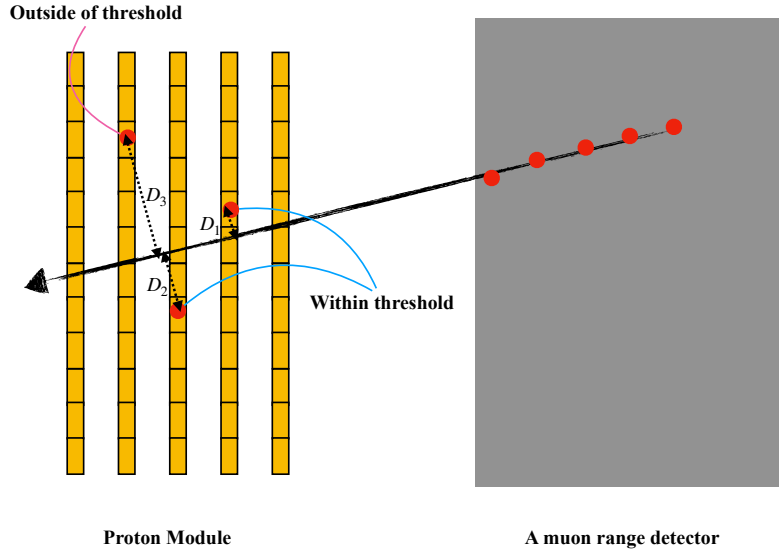
Figure 53: Illustration of the evaluation method for the tracking efficiency. Once the algorithm confirms there is at least one three-dimensional track in a muon range detector, the track is extrapolated to one of the vertex detectors, here the Proton Module. Then it checks if each hit in the vertex detector satisfies the condition on the distance between the hit point and the extrapolated line. If the event has four or more hits satisfying the conditions, the algorithm checks if there is a cluster reconstructed in the vertex detector.

(a) WAGASCI detectors
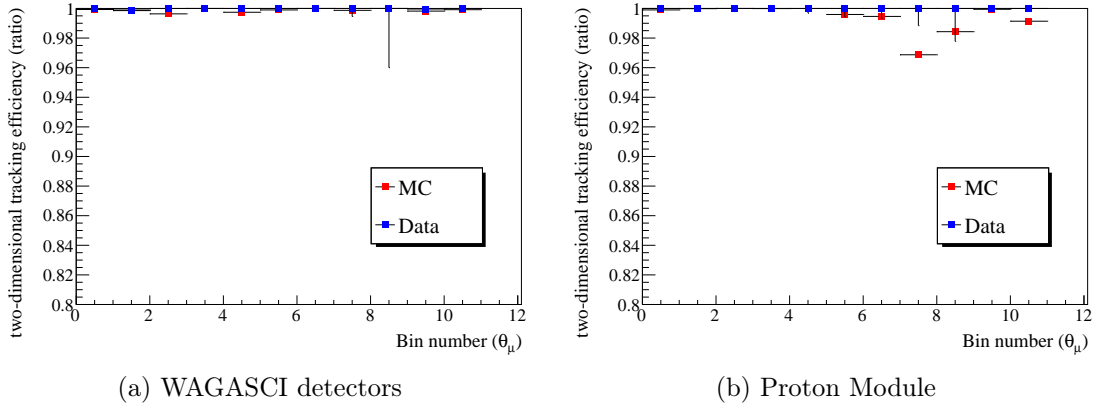
(b) Proton Module

Figure 54: The results of two-dimensional tracking efficiency for WAGASCI detectors (left) and Proton Module (right). The horizontal axis corresponds to the MIP-like particles' angle as it is shown in Table 13. The vertical error bars represent statistical uncertainties.

9.3.5 The summary of detector specification and performances

Table 14 summarizes the fundamental detectors' performances as well as their specifications. We confirm that each detector's performance is suitable for the target physics. All of the perfor-

mances shown in Table 14 were estimated by the measurement using physics data. We confirm the difference in each performance stays within a few percentages, which does not make a large systematic uncertainty.

Table 14: Performances of the vertex detectors (top) and the muon range detectors (bottom) of WAGASCI-BabyMIND. Each mean of light yields is estimated for MIP. The light yields are not corrected by the path length here. WAGASCI, Proton Module and Baby MIND have two kinds of scintillators, corresponding to two different light yields. Hit detection efficiency (Hit. eff) for each detector was estimated by using physics data. Two-dimensional tracking efficiency (Recon. eff 2D) was calculated for only the vertex detectors.

Detector		Target / Material	Light yield (p.e.)	Hit. eff	Recon. eff (2D)
Vertex	WAGASCI	$H_2O : CH = 4 : 1$	18 / 24	$\sim$95%	$\sim$100%
	Proton Module	CH	20 / 50	>95%	$\sim$100%
MRD	Wall MRD	iron and scintillator	18	$\sim$95%	–
	Baby MIND	magnet and scintillator	17 / 30	>95%	–

9.4 Monte Carlo simulation

Monte Carlo simulation (MC) begins with generating neutrino flux based on JNUBEAM (see Section 6.2). It takes into account the different off-axis angles for the flux prediction. The neutrino flux inputs are fed into NEUT (see Section 6.3) to simulate neutrino interactions on a specific target material considering neutrino kinematics. The output of the neutrino interaction simulator contains all information on the primary interactions of neutrinos and the final states of all particles from the interactions. In order to simulate detector responses and iterative interactions, secondary, tertiary, and so on, we developed Geant4-based Monte-Carlo simulation framework. A whole description of the detector complex was implemented in this framework. In addition, the detector responses in particularly to MIP-like particles are tuned based on the physics data, which are shown in Section 9.3. Thus, the output of the whole procedure above provides simulated data for the reproduction of data that are obtained in physics runs.

10 Track reconstruction

In order to study neutrino interactions, it is necessary to analyze hit patterns, find particle trajectories, reconstruct interaction vertices, and measure relevant track properties. The whole procedure from analyzing hits up to measuring relevant track properties is called reconstruction. In this analysis, the reconstruction is divided into five steps. The first step is to search for track candidates in each detector by classifying hits that are likely to come from the same particle ("Track Seeding"). The next step is to search for a pair of tracks between detectors corresponding to the same particle ("Track Matching"). The third step is to find an interaction vertex using the information in the Matching step ("Vertex Reconstruction"). The processes up to the third step are done in two-dimensional space in the XZ or YZ view. Next, we look for a pair of two-dimensional track candidates to reconstruct a three-dimensional track candidate ("Three-dimensional track reconstruction"). Lastly, the candidate is analyzed by each algorithm suitable for the measurement of its property, such as angle, momentum, particle type, particle charge, and track-per-cluster ratio. This chapter provides a principle for each procedure as well as a core algorithm used. More details are described in Appendix H.

10.1 Track Seeding

Track seeding is to analyze hit patterns in two-dimensional space to classify hits based on possible particle trajectories or noises. In most cases, particle trajectories are supposed to be straight in each detector because it is not magnetized except for the downstream MRD, BabyMIND. In addition, the particles to be detected in BabyMIND are MIP-like particles that do not produce electromagnetic showers or are not significantly subject to multiple Coulomb scattering. The track seeding is to collect hits along with a straight line which is most likely to come from a particle while rejecting random hits stemming from the dark noises. [42] Figure 55 demonstrates an attained result in the track seeding.

---

[42]We applied the same assumption of particle trajectory being straight in this clustering step although the BabyMIND is magnetized. We confirmed that this assumption is valid by loosing tolerance to connect hits in the algorithm.
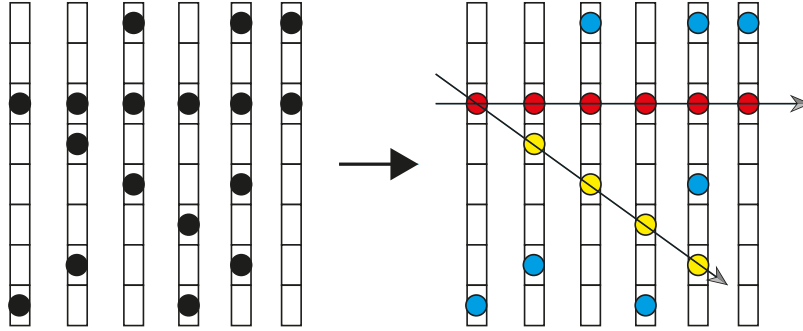
Figure 55: An illustrative example of a result of track seeding, showing hit maps before the track seeding (left) and classified hit collections after the track seeding (right). Collective hits in red and yellow represent clusters that are supposed to be different particle trajectories. Hits in blue are dissociated from the ones in red and yellow. They are most likely to come from dark noise hits.

We use the concept of the cellular automaton for the track seeding. The game of "life" [166] is one of the examples using this method. The concept of the game of "life" is to let a simple object such as a "dots pattern" in a matrix evolve spontaneously by imposing generic laws governing the game. Each dot has its own "state" at a given step. For example, the state is defined by the color (white or black) of each dot. The state is changed according to generic laws, for instance, when a dot in white is sandwiched by two black dots, the state of the dot in the middle is changed, white to black. The iteration continues until all dots are unchanged.

In order to apply this concept to the track seeding, we substitute hit patterns for dot patterns and construct generic laws to classify hits into a cluster. A unit of this algorithm is a line connecting two hits on corresponding two tracking planes in a distance of one or two planes. The unit is called "Cell". This algorithm allocates a unique "state" to each Cell. The state is an integer and initialized to 0. The state is changed according to a rule. The rule is if a chi-squared value in a linear fitting of three hits included in two Cells sharing one common hit is less than a threshold, then the state of the downstream Cell is increased by 1. This rule allows the algorithm to search for hits in a straight line. This iteration continues until the state of any Cell stays constant. Consequently, the more downstream the Cell is in a straight line, the higher state it has. In this case, picking up those hits in the order from the highest state to the lowest state ends up providing a track. After all possible pairs are chosen, the algorithm gives the result shown in Figure 55. Relevant variables such as thresholds in a linear fitting are optimized considering detector specifications. [43]

10.2 Track Matching

The previous step provides tracks in each sub-detector. Since we have six sub-detectors, connecting tracks between different sub-detectors is necessary to find a full track of a particle. The

---

[43]See Appendix H for details.

track matching step proceeds based on the tracks in a two-dimensional space. Key variables to determine whether two tracks come from the same particle are positional and angular differences. The positional difference refers to the difference between an expected position in the downstream detector extrapolated from the upstream detector and the upstream end position in a track in the downstream detector. With respect to the angular difference, we check a difference in angles obtained by the linear fitting to a pair of tracks. When both differences do not exceed thresholds defined for each combination of detectors, they are regarded as "matching tracks". The simple illustrations of the track matching step are shown in Figure 56.

10.3   Vertex Reconstruction

In this analysis, we use only events where at least one matching track is reconstructed assuming it is considered as a muon candidate. The majority of protons from the neutrino interactions in the T2K flux are fully contained. Pions should interact with particles in the iron material before reaching the tracking threshold in the step of the track seeding. Therefore, requiring one matching track, in particular with MRD, can enhance the purity of the muon candidate. An interaction vertex in each event is then determined based on the matching track. The vertex is defined as the upstream end position of the matching track. Once the vertex is found, the algorithm searches for tracks that are considered to share the vertex. This is done by comparing the vertex Z position and the upstream end position of each track in the Z axis. If the difference in the Z position is less than two planes, the track is considered to be the one starting from the same vertex as the matching track. Finding a vertex and collecting other tracks are referred to as vertexing, which is illustrated in Figure 57. It should be noted that the vertex position at this stage is in two dimensions (X, Z or Y, Z). The three-dimensional position is reconstructed in the next step.
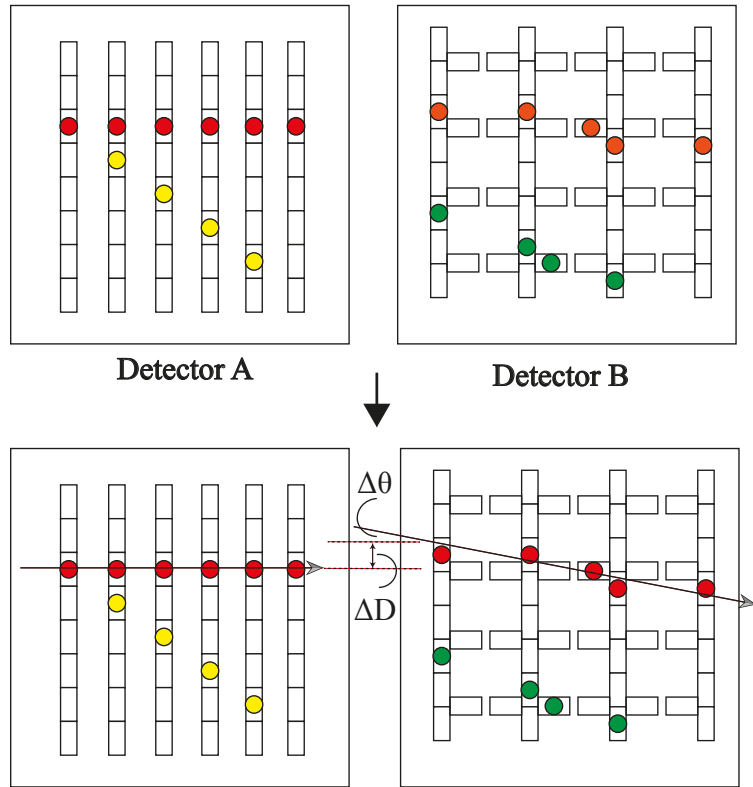
Figure 56: An illustrative example of the track matching process before (top) and after (bottom). In the bottom figure, $\Delta\theta$ and ΔD show the differences in angle and position between the two tracks. The change in colour from orange to red in Detector B between the top and bottom demonstrates the track is matched with the track in red in Detector A. On the other hand, the track in green in Detector B remains as it is because it does not satisfy the requirement.
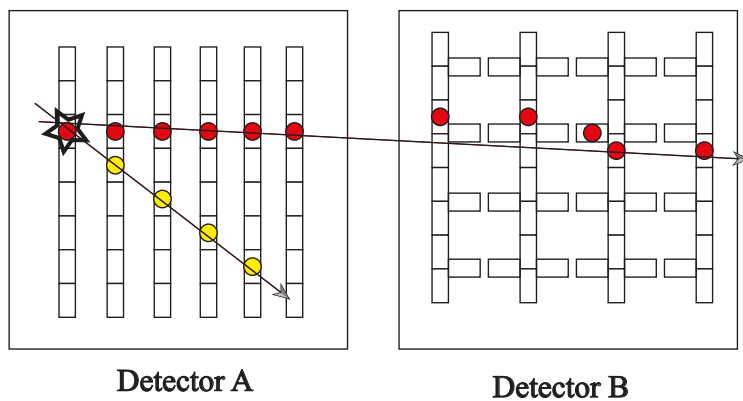
Figure 57: An illustrative example of finding an interaction vertex based on the result of track matching. A vertex indicated by a star is defined as the starting point of the matching track. Other tracks in the detector are collected if it is considered as sharing the vertex.

125

10.4 Three-dimensional track reconstruction

Now, we have two-dimensional vertices in the XZ view and YZ view that are associated with corresponding matching tracks. In this three-dimensional track reconstruction, the algorithm looks for a probable pair of matching tracks both in the XZ and YZ views, ending up reconstructing three-dimensional tracks and an interaction vertex. The pair-matching process relies on differences in the upstream and downstream end Z positions between matching tracks in each view. When the differences satisfy the requirement that the distance must be less than two planes, both tracks are matched with one another as a three-dimensional track. In addition, a three-dimensional vertex is also reconstructed using the upstream end positions of corresponding matching clusters. For the vertex Z position, the smaller position of the two is chosen because it is considered closer to the true vertex position. The process is illustrated in Figure 58.
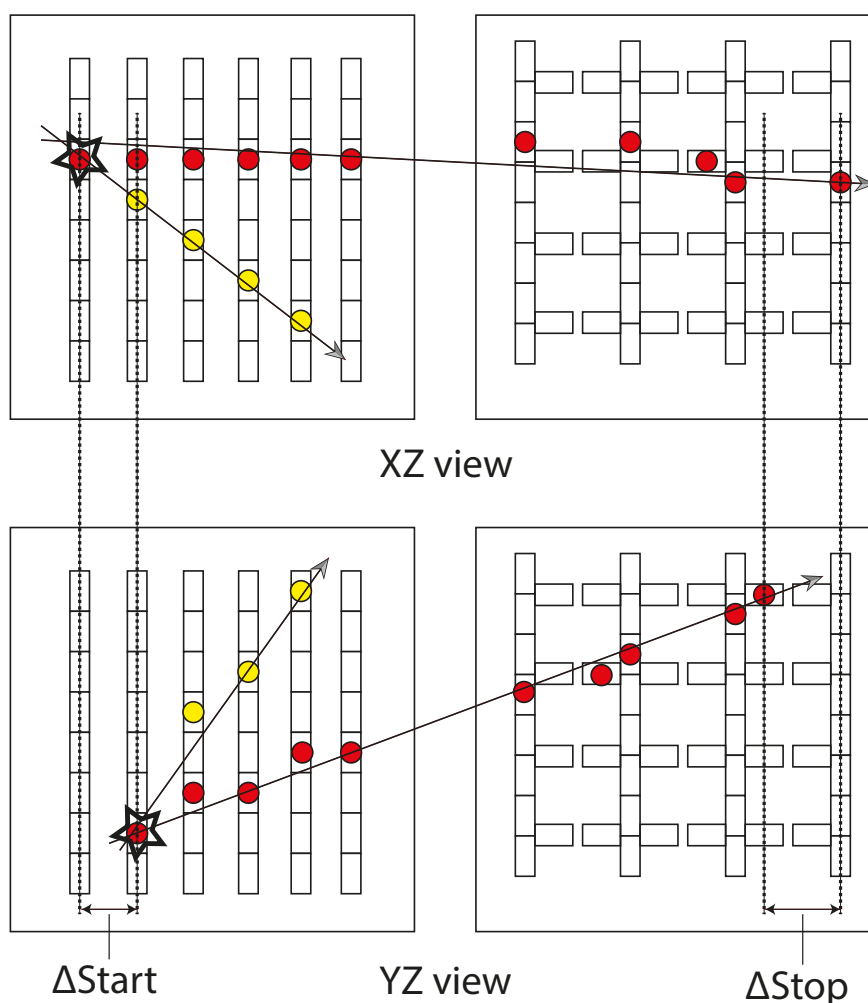
Figure 58: An illustrative example of the three-dimensional track reconstruction process with key variables (ΔStart, ΔStop) to match a pair of two matching tracks in XZ and YZ views. When they satisfy the requirement, both clusters are matched with one another as a three-dimensional track. In addition, a three-dimensional vertex is also reconstructed. With respect to the vertex Z position, the smaller position of the two is chosen.

10.5 Measurement of track properties

The obtained three-dimensional tracks in the previous step are further analyzed to measure their properties. The longest three-dimensional track is considered to be a muon candidate. We apply each algorithm to the muon candidates in order to obtain the angle, momentum, and charge. Besides the muon tracks, other tracks are also reconstructed in the previous step. We then identify the particle type of those tracks. Each algorithm is summarized in this section.

10.5.1 Angle reconstruction

The aforementioned reconstruction algorithm provides the three-dimensional track of a muon candidate. We apply a linear fitting to the track to reconstruct the angle. In practice, the hits in the track in the vertex detector are fitted in both XZ and YZ views. The two linear fittings determine slopes of the track, denoted by $\tan\theta_{XZ}, \tan\theta_{YZ}$. These slopes represent two-dimensional angles with respect to the detector coordination. We need a track angle with respect to the neutrino direction [44] to extract a differential cross section as a function of angle. The calculation formula is

$$\text{reconstructed track angle} = \arccos\left(\frac{|d_x^\nu \tan\theta_{XZ} + d_y^\nu \tan\theta_{YZ} + d_z^\nu|}{\sqrt{1 + \tan^2\theta_{XZ} + \tan^2\theta_{YZ}}}\right). \tag{10.1}$$

The standard deviation of the reconstructed angle of the muon candidate with respect to the true muon angle is calculated based on the Monte-Carlo simulation. For muons whose momentum ranges from a few hundred MeV/c to a few GeV/c with a mean angle of 20 to 30 degrees, it is estimated to be a few degrees. We take into account this information in defining kinematic binnings for the cross section measurements.

10.5.2 Momentum reconstruction

The precise measurement of the cross section as a function of muon momentum requires a reliable method achieving a sufficient resolution, less than 10% for typical momentum of around 800 MeV/c without introducing a large reconstruction bias. The bias means the difference in the mean value of residual distributions with respect to zero. We have so far established a way to use a total track range for all segmented regions. [45] The total track range is converted to the momentum based on the relationship between CSDA (Continuous-Slowing-Down Approximation) range and μ momentum [167]. The momentum resolution, defined as the standard deviation of the residual momentum distribution, is calculated with the MC simulation. The result is shown in Figure 59. The estimated resolution falls within the requirement.

---

[44]The neutrino direction is represented by $(d_x^\nu, d_y^\nu, d_z^\nu)$. In the current location of the detector complex, they are given as in

$$d_x^\nu = -0.019972, d_y^\nu = -0.079947, d_z^\nu = 0.996599$$

[45]Since the downstream MRD has a magnetic field, it is in principle possible to make use of it in calculating the momentum by its curvature. The magnetic field of the MRD was optimized for charge identification but for momentum measurement. Although there are many trials to utilize the magnetic field to calculate momentum, none of them satisfies the requirement of both resolution and reconstruction bias.
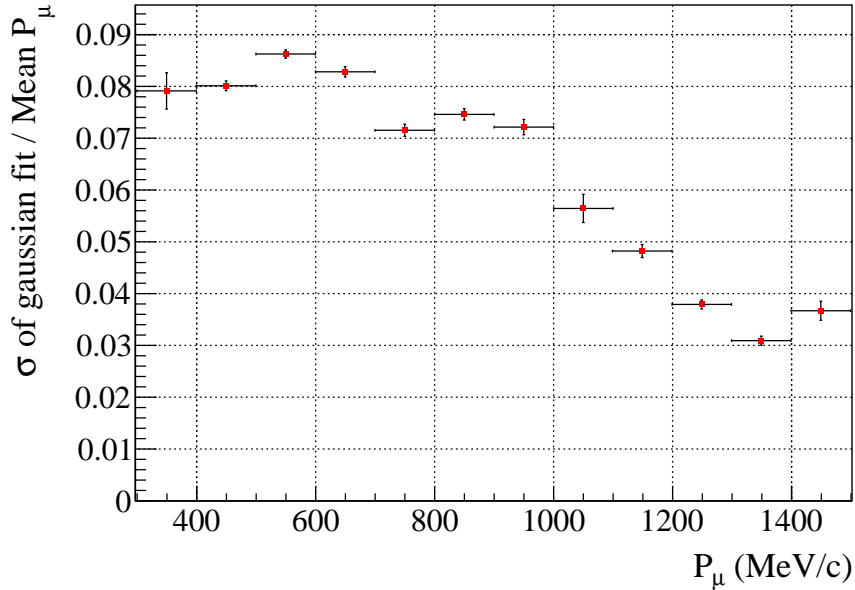
Figure 59: Resolution of reconstructed muon momentum as a function of true muon momentum. The resolution is defined as the fraction of the standard deviation of the residual momentum (reconstructed momentum - true momentum) distribution with respect to the mean momentum. Each error bar represents the error of the standard deviation divided by the mean momentum.

10.5.3 Particle charge identification

The magnetized downstream MRD, BabyMIND is capable of identifying the charge of a particle. A magnet plane has three divisions each of which has a uniform 1.5 T field in either a positive or negative direction of X. We developed a custom-made fitter to estimate the charge of a particle. The fitter predicts a true particle trajectory with varying several free parameters including the particle charge. [46] When the trajectory is compared to the measured data, the fitter calculates a chi-squared value for that trajectory. After all iterations of the free parameters, it obtains minimum chi-squared values for the positive and negative charge hypotheses. Those two values are then input to calculate a negative log-likelihood ratio for the discriminator of the particle charge. All of the descriptions including derivation about this fitter are found in Appendix I. According to the MC simulation, the selection efficiency of μ^- exceeds 95% with the purity of μ^- being larger than 96%.

10.5.4 Particle type identification

A muon candidate is determined when a track originating from a vertex detector is matched with other detectors. When there are several kinds of tracks, the longest track is assumed to be a muon candidate. If it is matched with either MRD, the probability of that track being muon

---

[46] Free parameters are comprised of an incident angle from a vertex detector (ϕ_I), an incident Y position (Y_I), a momentum (P_I) and a charge (C_I). Since this includes momentum as one of the free parameters, it can in principle be used for momentum reconstruction. The performance test, however, showed a relatively large reconstruction bias with an overall resolution of 20 to 30%. We have decided to apply this method only for charge identification.

exceeds 95%. In this case, there are not many benefits from particle identification by using the energy loss, dE/dx information. It is, however, important for other tracks originating from an interaction vertex to identify their particle types by dE/dx. Particular attention is paid to the discrimination between a MIP-like particle, typically muon and charged pion, and a proton-like particle. One of the differences between these particles is the energy deposit per unit length in each scintillator.

The discriminator is based on a dE/dx distribution for MIP-like particles for each vertex detector. The reverse cumulative function of the dE/dx distribution $(1 - \Phi(dE/dx))$ is defined as "Confidence Level (CL)" which is an indicator of the likelihood of a MIP-like particle. Provided a track contains hits in N planes, it gives N's values for the confidence level. Using all the values, the discriminator (MUon Confidence Level, MUCL) is given in

$$\text{MUCL} = P \times \sum_{i=0}^{N-1} \frac{(-\ln P)^i}{i!}, P = \prod_{i=1}^{N} CL_i, \quad (10.2)$$

where N refers to the number of planes having a hit and CL_i is each confidence level for a hit on the i-th plane. The particle identification performance was studied by using MIP-like tracks in the MC simulation. We confirmed that the purity of MIP-like particles is 85% (84%) with 95% (78%) selection efficiency and the purity of proton-like particles is 59% (58%) with 74% (85%) efficiency in WAGASCI modules (Proton Module).

10.5.5 Track-per-cluster ratio calculation

The track-per-cluster ratio is defined as the ratio of the number of hits in all the reconstructed tracks starting from the same vertex to the number of hits in all the tracks obtained in the vertex detector in the track seeding. Here, we check the tracks only in a vertex detector in each event. When all reconstructed tracks in the track seeding end up with the reconstructed tracks in the event, the ratio is 1.0. When some tracks coming from a neutrino interaction different from the one in the vertex detector are reconstructed in the track seeding and not used in the event, the ratio is lower than 1.0. Figure 60 shows the illustrative example where the track-per-cluster ratio is 0.66. This parameter is used in the event selection, which is revisited in Chapter 11.
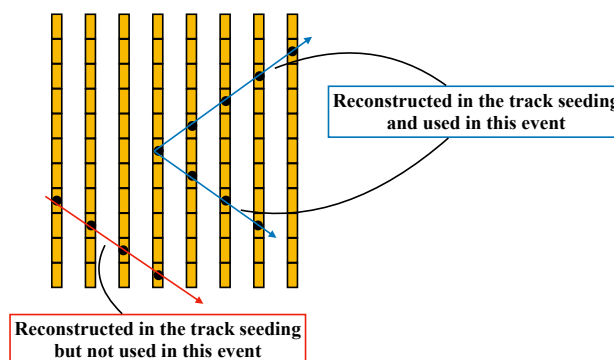
Figure 60: An illustrative example of the track-per-cluster ratio parameter. The arrows in blue represent the tracks used in the event and the arrows in red represent the reconstructed tracks in the track seeding but not used in the event.

11 Event selection and cross section analysis

This chapter is devoted to describing our analysis objects, event selection criteria, and methodology of cross section extraction. Section 11.1 introduces the definition of signal and control samples. The event selection criteria are optimized such that they provide sufficient purity and efficiency for each sample, which is discussed in Section 11.2. Outcomes of the selection criteria based on the MC simulation give a nominal data set. Alternative simulation data sets are used to validate the performances of our fitter. The simulated events include various sources of systematic uncertainties. All possible error sources are scrutinized and the sizes of uncertainties are estimated, whose results are summarized in Section 11.3. The selection outcomes and all systematic errors are then incorporated into a cross section fitting framework to produce the best-fit results of neutrino-nucleus cross sections and systematic parameters. The methodology is explained in Section 11.4.

11.1 Signal definition and Sample classification

11.1.1 Signal definition

A whole analysis using WAGASCI-BabyMIND detectors has been motivated to enhance the sensitivity of the oscillation analysis by T2K. Since the signal samples in the T2K oscillation analysis consists of mainly CCQE-like interactions, they are also primary signals for our cross section measurements. The signal is defined as a charged current muon neutrino interaction without having any charged pion in the final state, denoted by $CC0\pi^{\pm}$. As the detector complex is not equipped with an electro-magnetic calorimeter, it is unable to detect gamma-rays from neutral pion decays. Therefore, the signal is defined such that it can accept neutral pions in the final state. This is interpreted as a "topology" instead of the individual interaction type before FSI. Topology is defined based on the particles that each detector is able to measure in the final state. It mitigates the potential bias that can be introduced by an interaction model to predict initial neutrino interactions including the FSI effects. [47] Using the topology in the analysis is a way to reduce the neutrino interaction model dependency. In addition to the topology selection, the signal is also classified by the target material, H_2O or CH. The primary target is H_2O. The WAGASCI detectors have plastic scintillators with the mass fraction of 20%, whose cross section and its uncertainty are controlled by the CH measurement using the Proton Module. Each signal has two observables, muon momentum (P_μ) and angle (θ_μ), corresponding to the single differential cross section measurements.

11.1.2 Sample classification

The signal definition is based on "true" information provided by the simulation. The sample classification, on the other hand, is based on the reconstructed variables. It is defined as a combination of detectors through which the muon candidate passes. The classification is summarized in Table 15. We do not have a sufficient number of events where interactions happen in Downstream WAGASCI and produced muons go through WallMRDs. Therefore, we do not include the "DWG to WMRD" sample in the classification. Each subdetector is abbreviated in

---

[47]Defining a signal in the way of interaction type relies on each physics model to predict FSI effects. When the outcome of the particular interaction model is used as "true" information to be compared to reconstructed information, it may introduce the bias that is associated with the interaction model.

the following way; PM: Proton Module, Upstream WAGASCI: UWG, Downstream WAGASCI: DWG, WMRD: WallMRD, BabyMIND: BM.

Table 15: The sample classification for both signal and control regions. MRDs include both BabyMIND and WallMRDs.

	Sample	Target Material	Detector Topology
Signal samples	$CC0\pi^{\pm}$	CH	PM to WMRD
			PM to BM
		H_2O or CH	UWG to WMRD
			UWG to BM
			DWG to BM
Control samples	$CC1\pi^{\pm}$	CH	PM to MRDs
		H_2O or CH	WGs to MRDs
	beam-induced background	concrete	UWG, PM, DWG to BM

Table 15 describes the classification of control samples as well. They are divided into $CC1\pi^{\pm}$ and beam-induced background. $CC1\pi^{\pm}$ is a sample that has one charged pion in the final state in addition to a muon. [48] The T2K neutrino flux at 1.5 degrees off-axis has its peak around 0.86 GeV. The CCQE interaction is dominant around this energy while the CC Single Pion Production (CCSPP) is subdominant. The inclusion of $CC1\pi^{\pm}$ in the control sample is helpful to understand the $CC1\pi^{\pm}$ background contaminating in $CC0\pi^{\pm}$ in a data-driven way. On the other hand, the beam-induced background is motivated by a better understanding of interactions with the wall in the experimental hall. The detector complex is located inside an underground pit surrounded by a cylindrical wall. The thickness of the upstream wall made of concrete is 8 m. Consequently, more neutrino interactions could happen inside the wall than in the vertex detectors. When the neutrino interactions produce neutral particles such as neutrons and gamma from neutral pions, which travel into one of the vertex detectors, they could mimic a neutrino interaction inside the vertex detector. In order to reduce the uncertainty of this beam-induced external background, we have to rely on the MC simulation for the neutrino interactions in the wall. This simulation uses an approximate density of concrete, which directly causes a difference in the normalization of the wall background events. A solution to mitigate the difference is to tune the density in accordance with beam data. The beam-induced background sample is collected in both MC and data. The difference in the number of events between them is used to tune the density of the concrete.

11.2   Event selection

For each sample defined in the previous section, dedicated selection criteria were determined taking into account the balance between signal purity and efficiency. All of the selection criteria begin with the outcomes of the reconstruction. The following discussions overview criteria for all the samples.

---

[48] "One charged pion in the final state" means a pion exiting out of a nucleus. Even if it does not leave any hit inside a detector due to its secondary interaction in an event, the event is categorized as the $CC1\pi^{\pm}$ sample.

11.2.1 Selection criteria for the CC0$\pi^{\pm}$ sample

The diagram of the selection criteria for the CC0$\pi^{\pm}$ sample is shown in Figure 61. The following descriptions are the summary of each selection criterion. Complementary plots and explanations are found in Appendix J.

Pre-selection

The Pre-selection means all steps of reconstruction. In this analysis, we use events that have at least one three-dimensional reconstructed muon track candidates based on the track reconstruction methods described in Chaper 10.

Fiducial volume

We define a fiducial volume for each vertex detector to make sure of a neutrino interaction in the detector. The fiducial volume cut plays an important role in suppressing the beam-induced muon background produced in the wall. The fiducial mass of the Proton Module is 313 kg for CH and that of the WAGASCI detectors is 229 kg for H$_2$O and 62 kg for CH per module. Figure 62 shows the comparisons of the vertex distributions after the fiducial volume selections. We confirm the MC predictions and data distributions agree well except for the vertex Z distribution for the WAGASCI detectors samples. Unlike the other distributions, as vertex distributions should not reflect the neutrino interaction models we can expect good data and MC consistency. We investigated the possible causes of these differences and found no clear failure mode in our analysis. In addition, the possible impacts on the cross section analysis were also examined. Then, we found no significant impact. Since we did not find any deficit cause, we prepared one systematic parameter to take into account this difference. The details are described in the Appendix K.2.9.

Number of tracks

In the CC0$\pi^{\pm}$ sample, we expect one muon and one or two protons for the final state particles. The number of track distributions are shown in Figure 64. When the number of tracks exceeds three, the purity of the CC0$\pi^{\pm}$ events ("numuCC0pi") in the legends is small. We choose only one, two, and three tracks. The number of events coming from ν_{μ} CC other interactions dominated by DIS interactions halves thanks to this selection.

Particle identification

If the number of tracks is one, the track is selected as the muon candidate in the event. We do not apply the particle identification with MUCL that is explained in Section 10.5 to this kind of events. When the number of tracks is two or three, we apply the particle identification with MUCL to the second and third tracks and require both tracks not to be μ-like tracks. Here, the first track is the muon candidate selected in the track reconstruction. The MUCL distributions are shown in Figure 64. In this plot, the first tracks are not included because they are not used for the particle identification by MUCL. When MUCL exceeds 0.6 (0.7) for Proton Module (WAGASCI detectors) samples, the track is selected as the μ-like particle, and when it is under 0.6 (0.7), it is selected as the proton-like track. This selection is important to reject events where there is at least one charged pion in the final state.

Charge of muon

Since the signal comes from the ν_{μ} interaction, the muon candidate should be negatively charged. Therefore, charge identification is applied if the muon candidate passes through

BabyMIND. When the reconstructed charge is identified to be negative, the event is accepted. The discriminator for this selection is the log-likelihood ratio explained in Section 10.5. The distribution of the log-likelihood ratio is shown in Figure 65. When the log-likelihood ratio is less than 4, the track is selected as a negatively charged particle. This selection is useful to reject background that comes from wrong-sign neutrino interactions.

Track-per-cluster ratio

The track-per-cluster ratio parameter is explained in Section 10.5. This selection is used to reduce background that comes from the interactions outside the fiducial volume called Out Of Fiducial Volume (OOFV), in particular the interactions in the wall. For the $CC0\pi^{\pm}$ samples, the track-per-cluster ratio tends to be large and for the OOFV events, the ratio tends to be small. When the track-per-cluster ratio is larger than 0.6, it is selected as the signal sample. This is applied to only the WAGASCI events because the wall background is around 20% with respect to the total number of WAGASCI events without this selection. After this selection is applied, the contamination of the wall background is reduced to around 10%, which is a similar level to the Proton Module case. Figure 66 shows the track/cluster ratio distribution for the WAGASCI events. The difference is mostly due to the differences in the number of events between data and MC by 10%. We checked that the shape in distributions were consistent with each other.

Michel electron tagging

We search for Michel electron hits originating from a pion track in each event in order to detect a pion under the tracking thresholds. The Michel electron tagging for each neutrino event proceeds in the following way.

- Create hit clusters whose timings are outside the beam bunch and time differences between the hits are within 100 ns.
- Check the position of the hit whose timing is earliest in each cluster. Check if the positional difference between the hit and the vertex of the neutrino event is less than 150 mm in each X, Y, Z direction.
- Check the number of events for the cluster satisfying the above criteria. When the number of events exceeds two, the Michel electron is tagged in the event.

Figure 67 shows the distributions of the number of hits in hit clusters containing the Michel electron candidates. Here, we collect muon-enriched samples and require the muon candidates to stop inside the vertex detectors. The Michel electron tagging efficiency is higher in the WAGASCI detectors (see Appendix J for details). One of the strengths of the WAGASCI detectors detectors is 4π acceptance thanks to the grid-like structure to capture a Michel electron. No dead time in a time window for the Michel electron tagging, up to $1\ \mu$ second after the beam bunch timing is another strength in the WAGASCI detectors. On the other hand, Proton Module introduces a periodic 100 ns dead time per 580 ns trigger cycle, which can affect the efficiency of the Michel electron tagging. This results in the higher power of rejecting the $CC1\pi^{\pm}$ background in the WAGASCI samples.

Stop inside the MRD detectors for the momentum measurement

When we analyze the differential cross section as a function of momentum, we add a selection to require the track to stop inside MRDs in order to calculate the track momentum by range.
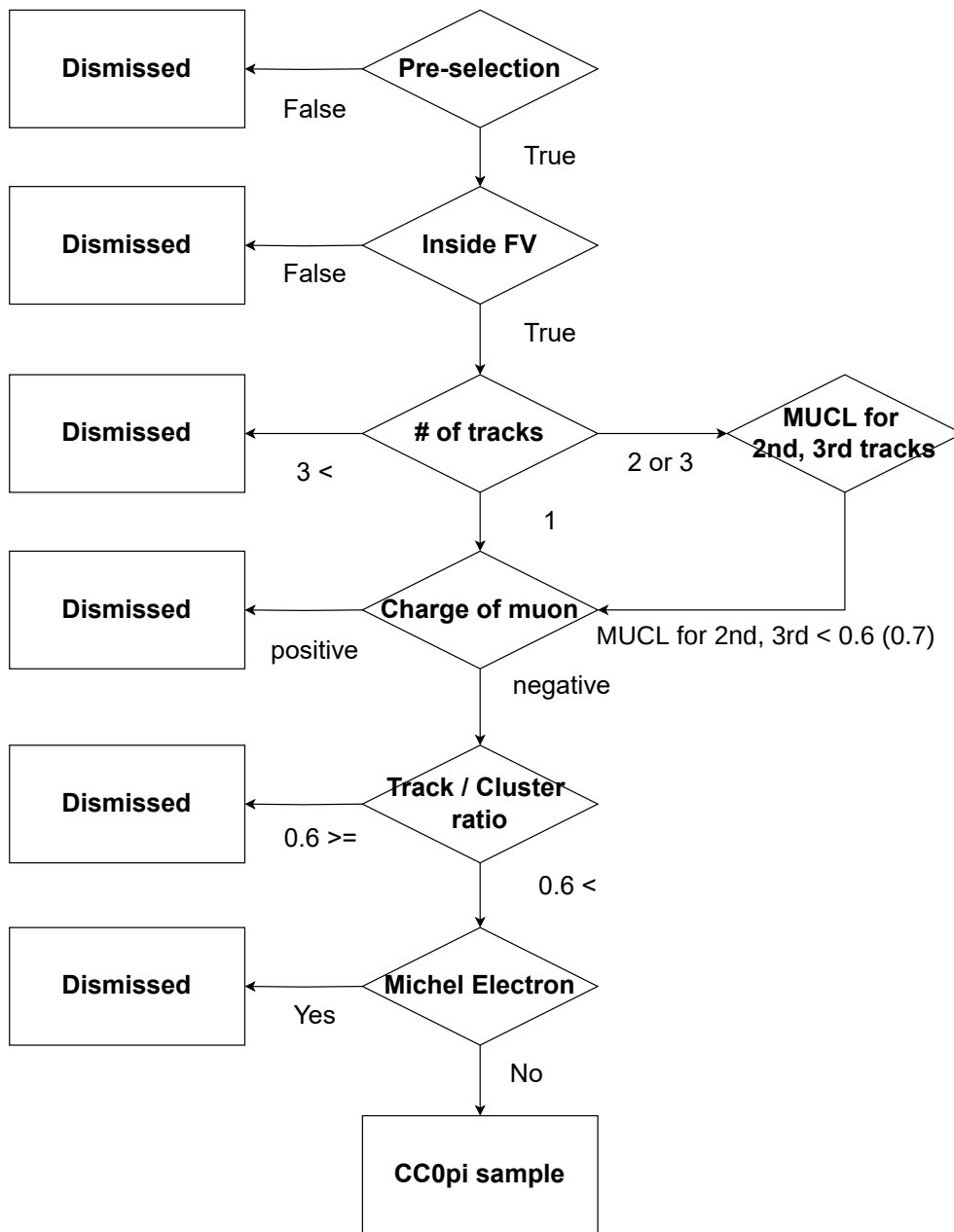
Figure 61: The diagram of the selection criteria for the CC0$\pi^{\pm}$ sample. "Pre-selection" means the three-dimensional reconstruction described in Chapter 10. "FV" is fiducial volume and "MUCL" is the parameter called MUon Confidence Level to be used for the particle identification. The thresholds for MUCL are different between Proton Module and the WAGASCI detectors. The parenthesis indicates the WAGASCI detectors case.
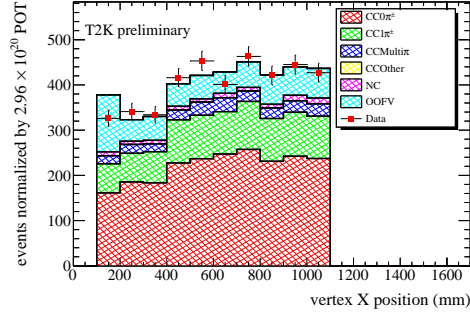
(a) Proton Module, vertex X
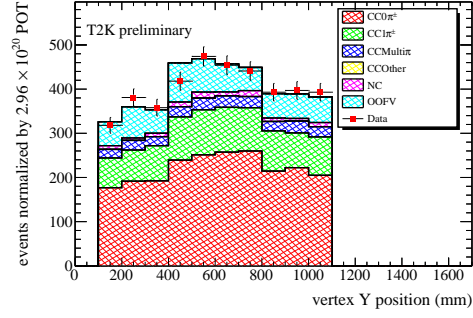
(b) Proton Module, vertex Y
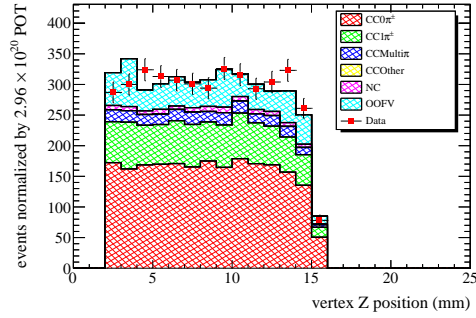
(c) Proton Module, vertex Z
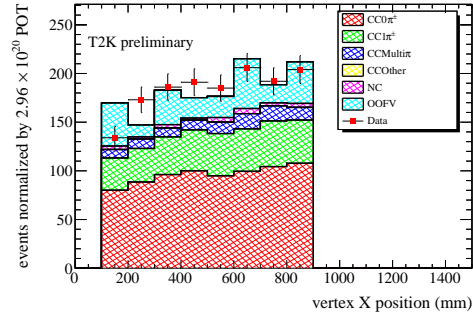
(d) WAGASCI detectors, vertex X
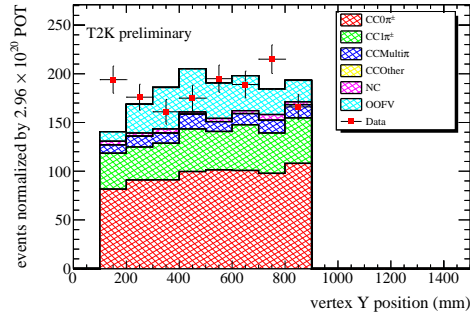
(e) WAGASCI detectors, vertex Y
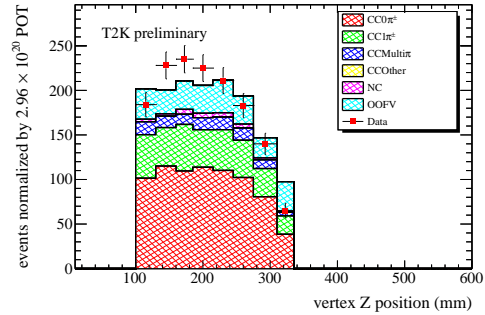
(f) WAGASCI detectors, vertex Z

Figure 62: Vertex X (top left), Y (top right), Z (middle left) distributions for the Proton Module samples, and Vertex X (middle right), Y (bottom left), Z (bottom right) distributions for the WAGASCI detectors samples inside the fiducial volumes. The red-shaded histogram shows the CC0$\pi^{\pm}$ distribution. The others are the background distributions. Data points are overlaid on the stacked histograms. The MC events are normalized by the data POT.

(a) WAGASCI detectors (b) Proton Module
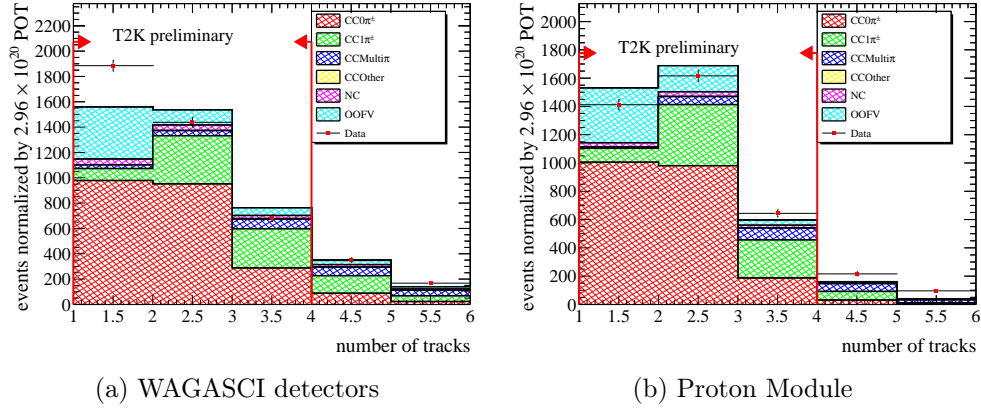
Figure 63: The number of track distributions for the events after the fiducial volume selection. The left plot shows the Upstream WAGASCI and Downstream WAGASCI events and the right plot shows the Proton Module events. The red-shaded histogram shows the CC0$\pi^{\pm}$ distribution. The others are the background distributions. The red arrows indicate the threshold on the number of tracks in the event selections. Data points are overlaid on the stacked histograms. The MC events are normalized by the data POT.

(a) WAGASCI detectors (b) Proton Module
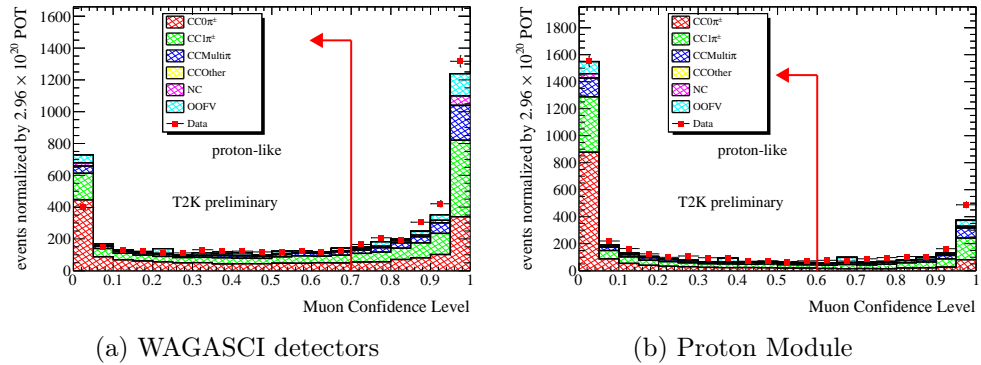
Figure 64: The MUCL distributions for the events after the fiducial volume selection. The left plot shows the Upstream WAGASCI and Downstream WAGASCI events and the right plot shows the Proton Module events. The histograms are stacked by the interaction topologies. The red arrows indicate the threshold on MUCL for proton-like in the event selections. Data points are overlaid on the stacked histograms. The MC events are normalized by the data POT.

136
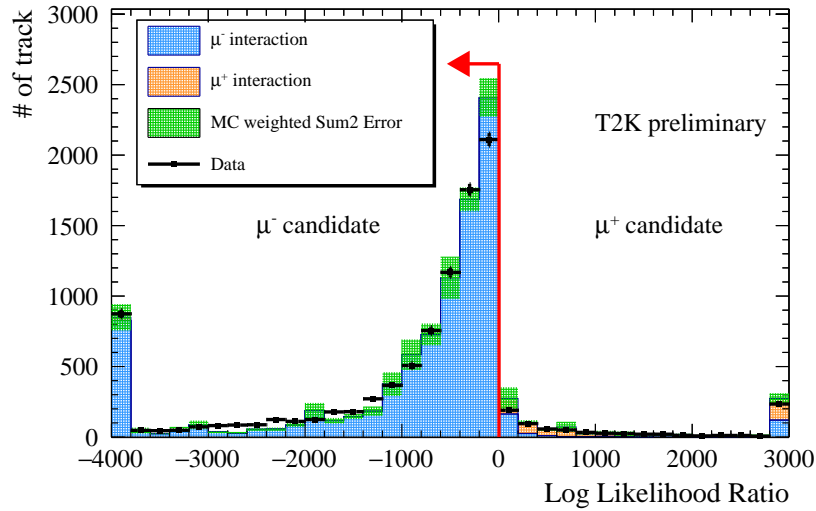
Figure 65: The log-likelihood ratio distribution for the muon-enriched sample in both MC and data. The simulated ν_μ and $\overline{\nu}_\mu$ events are represented in the shaded histograms in blue and red, respectively, The dotted points represent the data distribution. The MC distributions are normalized by the number of tracks in data.
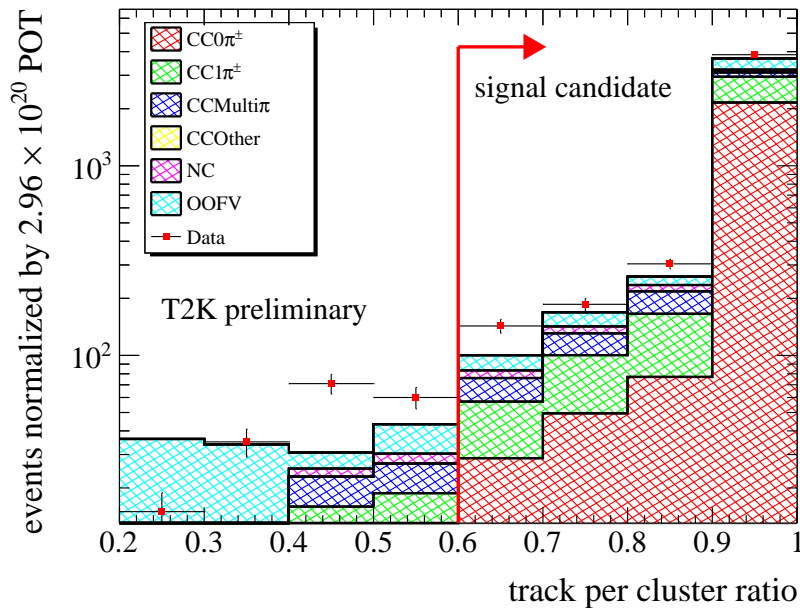
Figure 66: The distribution of the track-per-cluster ratio for the WAGASCI events after the fiducial volume selection. The red-shaded histogram shows the $CC0\pi^\pm$ distribution. The others are the background distributions. The red arrows indicate the threshold on the track/cluster ratio in the event selections. Note that the vertical axis is a log scale to emphasize the background contributions under the threshold. Data points are overlaid on the stacked histograms. The MC events are normalized by the data POT.

137

(a) Proton Module (b) WAGASCI detectors
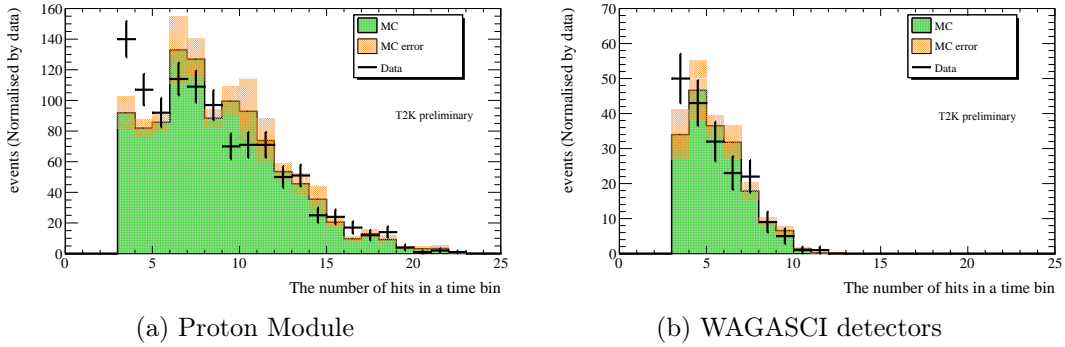
Figure 67: The distribution of the number of hits in hit clusters containing Michel electron candidates. The left plot shows the Proton Module events and the right plot shows the WAGASCI detectors events. The green-shaded histogram is the simulation results and the errors are shown by the orange bars. The dotted points represent the data distributions. The MC distributions are normalized by the number of events in data.

Table 16 shows the transition of the number of selected events with each selection criterion applied sequentially. The number of selected events in MC is normalized by the data POT. The number of events in data is 10-20% larger than that in MC after all the selections are applied.

Table 16: The transition of the number of selected events with each selection criterion applied sequentially. The table is divided into WAGASCI and Proton Module samples, each of which is further divided into the measurements for $\cos\theta_\mu$ and P_μ. The contained cut is applied before the "Pre-selection" only for the P_μ cases. The variables, $N_{\mathrm{MC}}, N_{\mathrm{Data}}$ represent the number of events in MC and Data, respectively.

Selection	WAGASCI samples				Proton Module samples			
	$\cos\theta_\mu$		P_μ		$\cos\theta_\mu$		P_μ	
	N_{MC}	N_{Data}	N_{MC}	N_{Data}	N_{MC}	N_{Data}	N_{MC}	N_{Data}
Pre-selection	141841	152510	90028	99285	58956	59778	35561	37375
Fiducial Volume	4455	4673	3043	3177	4030	4027	2564	2617
N_{track}	3861	4007	2657	2763	3814	3672	2441	2408
MUCL	2516	2789	1753	1941	3129	2920	2017	1925
log-Likelihood ratio	2274	2528	1576	1772	2867	2742	1838	1806
Track-per-cluster ratio	2223	2458	1532	1725	2867	2742	1838	1806
Michel Electron tagging	2097	2335	1442	1636	2631	2554	1673	1671

11.2.2 Selection criteria for CC1$\pi^\pm$ sample

A motivation to introduce a control sample is to understand the background in the CC0$\pi^\pm$ sample for the same phase space as that of the signal. We prepared two kinds of selection criteria where we changed (reversed) one specific cut in the CC0$\pi^\pm$ sample to for the CC1$\pi^\pm$ sample. One selection criterion requires two MIP-like particles without Michel electron candidates. Since the CCSPP interaction is expected to have two MIP-like particles (muon and pion), the number of MIP-like particles must be two accordingly. When there is more than one Michel electron candidate, it means there is more than one pion that is not reconstructed. As we already have

138

one muon and one pion candidate by the cut of the number of MIP-like particles, no other pion candidate is allowed. The other selection criteria have the same selection cuts as the one used for the $CC0\pi^{\pm}$ sample except for the Michel electron cut. This makes sure that the event has one muon candidate and one pion under the tracking thresholds. This way provides the control sample to enrich CCSPP with a similar phase space as the $CC0\pi^{\pm}$ sample. [49]

11.2.3   Selection criteria for beam-induced background sample

The beam-induced background sample is dominated by events where neutrino interactions happen outside any of the vertex detectors. In addition, this sample should contain only a muon in each event. We reverse the fiducial volume cut and require the muon candidate to pass through Upstream WAGASCI, Proton Module, Downstream WAGASCI and BabyMIND to purify the beam-induced muons from outside in this sample.

11.2.4   Summary of event selection

The performance of the event selections was evaluated with two mutually correlating variables, signal purity and efficiency. The signal purity is defined as the fraction of the true signal events to the total number of selected events. On the other hand, the signal efficiency is defined as the fraction of the selected number of events to the total number of true signal events in the true fiducial volume. The optimization of each selection criteria was done based on the figure of merit defined as $N_{\text{signal}}/\sqrt{N_{\text{signal}} + N_{\text{background}}}$, where N_{signal} and $N_{\text{background}}$ are the number of signal events and background events, respectively.

   The results of the event selections are summarized in Table 17. The selection results indicate that the total number of selected events in the Proton Module samples surpasses that in the WAGASCI samples although the fiducial mass is less in the Proton Module. This originates in the difference in acceptance of MRDs with respect to each vertex detector. The acceptance of BabyMIND is limited for the Upstream WAGASCI samples while that of the WallMRDs is limited to the Downstream WAGASCI. Both MRDs have balanced acceptance to both vertex detectors. On the other hand, the difference in the purity between the WAGASCI samples and the Proton Module samples is visible. It is due in large part to the WAGASCI detectors' superiority in the performance of the Michel electron tagging to the Proton Module. The total number of events for the momentum measurements in the left table of Table 17 is smaller than that for the angle measurement in the right table of Table 17.

---

[49]See Appendix J for details.

Table 17: Results of the selection criteria for the CC0$\pi^{\pm}$ samples to show signal purity and efficiency along with interaction topology compositions. The left column presents numbers for cross section for muon momentum and cross section for muon angle on the right. Each number refers to WAGASCI (WG) samples and one with parenthesis does to Proton Module (PM) samples. The selected number of events is normalized by the expected statistics (2.96×10^{20} protons on target).

Topology	WG(PM) samples (P_μ)		WG(PM) samples (θ_μ)	
	Selected events	Fraction (%)	Selected events	Fraction (%)
CC0$\pi^{\pm}$	1080 (1160)	74.9 (69.3)	1614 (1884)	77.0 (71.6)
CC1$\pi^{\pm}$	130.5 (207.6)	9.05 (12.4)	185.8 (344.5)	8.86 (13.1)
CC Multi-π	10.50 (28.80)	0.73 (1.72)	18.16 (51.18)	0.87 (1.95)
NC	41.80 (40.74)	2.00 (2.44)	47.73 (48.71)	2.28 (1.85)
OOFV	163.5 (221.4)	11.3 (13.2)	197.3 (261.7)	9.41 (9.95)
Wrong sign	15.41 (14.68)	1.07 (0.88)	34.58 (40.77)	1.65 (1.55)
Total	1442 (1673)	100 (100)	2097 (2631)	100 (100)
Purity (%)	74.9 (69.3)		77.0 (71.6)	
Efficiency (%)	19.4 (18.5)		29.1 (30.3)	

The corresponding plots to Table 17 including the control samples are shown in Figures 68, 69. The MC distributions are broken down by the interaction topology, CC0$\pi^{\pm}$, CC1$\pi^{\pm}$, CCMulti-π production, CCOther, Neutral Current, Out of Fiducial Volume and anti-muon neutrino interactions. From the comparison plots, we can find the following things.

CC0$\pi^{\pm}$, WAGASCI detectors samples

Discrepancies in the shape of the distributions are seen. In the momentum distribution, relatively large data-MC differences are visible in the low momentum regions (0.3 GeV/c to 0.7 GeV/c) and in the high momentum region (more than 1.5 GeV/c). On the other hand, in the angle distribution, the shape is mostly consistent. The difference in the normalization by around 10% is seen.

CC0$\pi^{\pm}$, Proton Module samples

The data and the MC prediction are consistent with each other.

CC1$\pi^{\pm}$, WAGASCI detectors samples

The total number of events in data is smaller than that in MC by approximately 20%. In particular, the difference in the shape is large in the momentum distribution.

CC1$\pi^{\pm}$, Proton Module samples

The total number of events in data is larger than that in MC by approximately 10%. The difference in the number of events in the momentum distribution can be attributed to the difference in the normalization. In the angle distribution, the number of events in data in the high angle region is smaller than that in MC, and the number of events in the low angle region is larger.

We find the difference in the number of the OOFV events in data between Figures 68a, 68b in the low momentum region. The sources of the OOFV events are different between these samples. The dominant contribution to the OOFV events in the Proton Module CC0$\pi^{\pm}$ samples comes from the neutrino interactions in either WallMRD north or south. These backgrounds

are suppressed by the Michel electron tagging. Due to the relatively low Michel electron tagging efficiency for the Proton Module, a relatively large amount of the OOFV events remain in the low energy region. On the other hand, the dominant source of the OOFV events for WAGASCI detectors comes from the wall upstream to the detector complex. These backgrounds are suppressed by the track-per-cluster ratio selection. Then the number of the OOFV background is reduced in the WAGASCI detectors. Considering the difference in the source of the OOFV backgrounds, it is reasonable to see the large fractions of the OOFV events in the high angle region in Figures 69b, 69d and to see the OOFV events almost evenly distributed in Figures 69a, 69c. When the muon produced in the WallMRD detectors stops inside the Proton Module and the event is mis-reconstructed as the neutrino interaction in the Proton Module, the reconstructed muon angle should be large. In this analysis, due to electronics problems, we cannot use the TDC information to identify the muon angle. When the problem is solved, we can reduce these OOFV backgrounds for the Proton Module in future analysis.
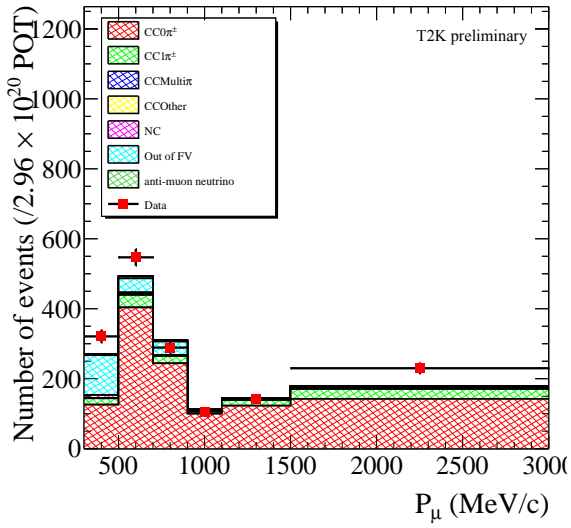
(a) CC0$\pi^{\pm}$, WAGASCI detectors samples
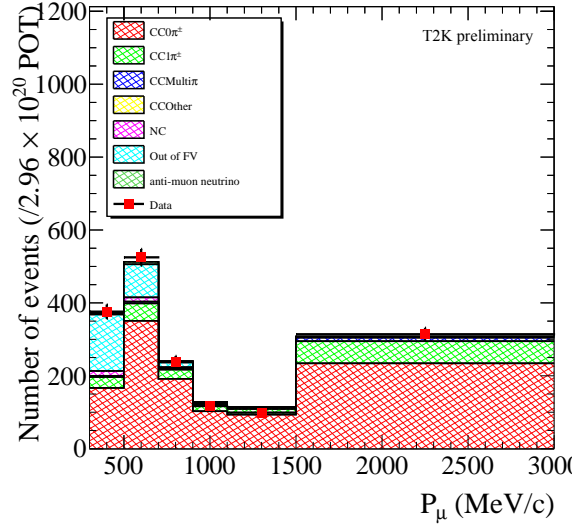
(b) CC0$\pi^{\pm}$, Proton Module samples
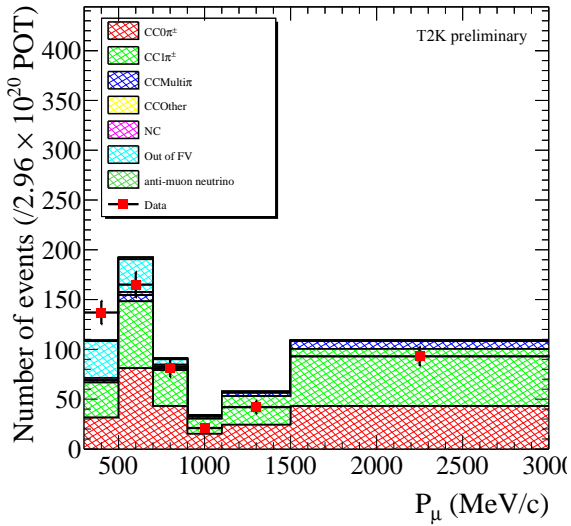
(c) CC1$\pi^{\pm}$, WAGASCI detectors samples
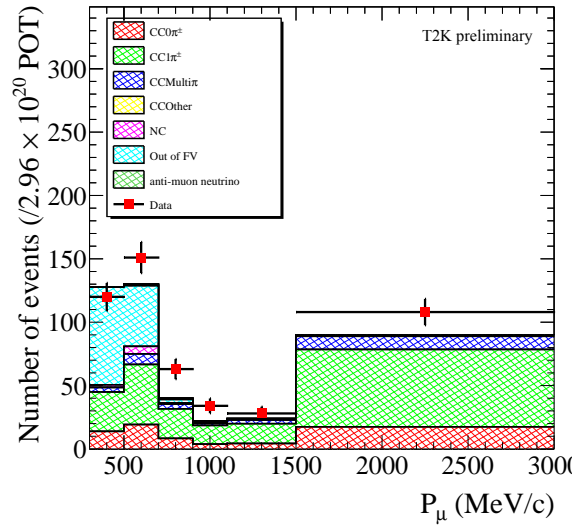
(d) CC1$\pi^{\pm}$, Proton Module samples

Figure 68: Comparisons of the momentum distributions for the WAGASCI detectors (left) and Proton Module (right) samples (68a to 68d) between data and MC in the signal (top) and control regions of CC1$\pi^{\pm}$ (bottom). The event distribution from MC is broken down by its interaction topology (CC0$\pi^{\pm}$, CC1$\pi^{\pm}$, CCMulti-π production, CCOther, Neutral Current, Out of Fiducial Volume, and anti-muon neutrino interactions), while the total number of signal events from the data is plotted as red dotted points. Error bars represent Poisson statistical fluctuation for 1σ.
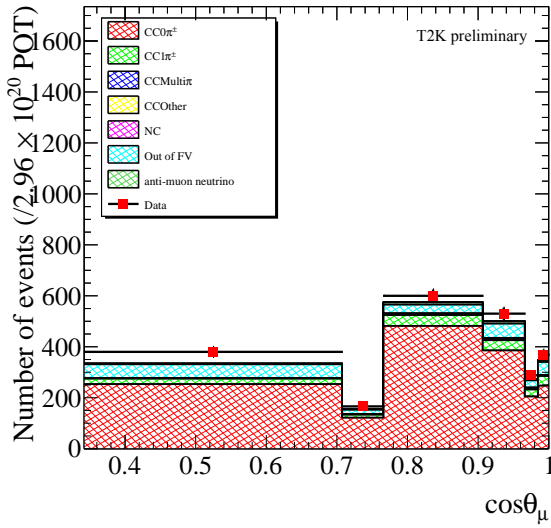
(a) CC0$\pi^{\pm}$, WAGASCI detectors samples
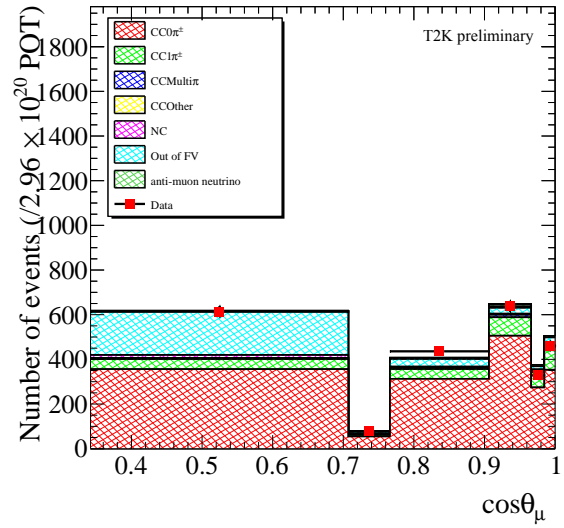
(b) CC0$\pi^{\pm}$, Proton Module samples
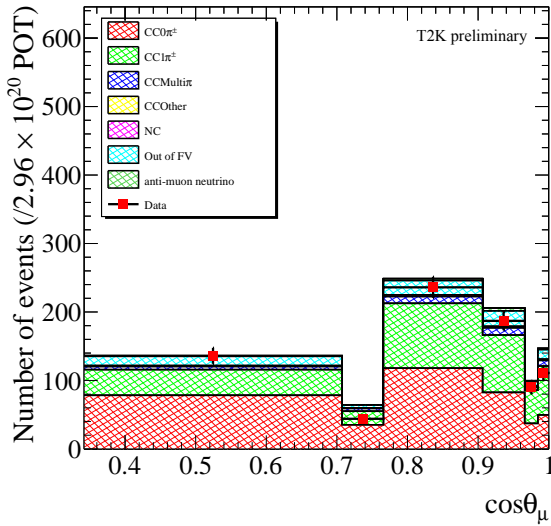
(c) CC1$\pi^{\pm}$, WAGASCI detectors samples
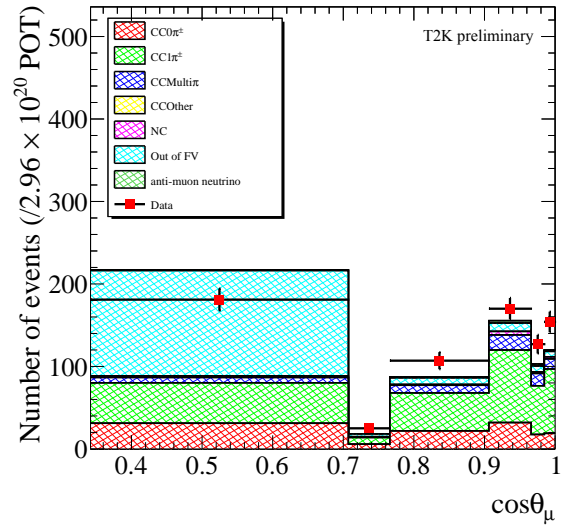
(d) CC1$\pi^{\pm}$, Proton Module samples

Figure 69: Comparisons of cosine of muon angle distributions for the WAGASCI detectors (left) and Proton Module (right) samples (69a to 69d) between data and MC in the signal region (top) and control region of CC1$\pi^{\pm}$ (bottom). The event distributions from MC are broken down by its interaction topology (CC0$\pi^{\pm}$, CC1$\pi^{\pm}$, CCMulti-π production, CCOther, Neutral Current, Out of Fiducial Volume, and anti-muon neutrino interactions), while the total number of signal events from the data is plotted as red dotted points. Error bars represent Poisson statistical fluctuation for 1σ.

11.3 Systematic parameters

The effect of systematic errors on the number of events is parametrized depending on the source. The parameters are mainly categorized into three sources, neutrino flux, neutrino interaction, and detector systematics. They are treated as nuisance parameters in our cross section fitting. Dedicated studies were conducted to understand the effects of each parameter on the number of selected events, which is overviewed in this section [50]. The way of propagating these errors into the cross section analysis is explained in the next section.

11.3.1 Neutrino flux parameters

The neutrino flux is simulated based on the JNUBEAM software. This analysis utilizes the same method as in the oscillation analysis to estimate the flux uncertainties (see Section 6.2). Although the neutrino flux is different due to the detector complex being located at the different off-axis angle, the uncertainties are similar to those for 2.5 degrees off-axis. We introduced twenty parameters in total each of which has a response to a specific range of neutrino energy spectra from 0 to 30 GeV. The uncertainty from the neutrino flux is approximately 5% in the main energy region, around 1 GeV.

11.3.2 Neutrino interaction parameters

This analysis in principle follows the interaction models that we established in the oscillation analysis. We reduced parameters to 26 as other parameters are expected to have a negligible impact considering the background compositions in this cross section measurement. The total prior uncertainty amounts to $10 \sim 15\%$ on the number of selected events.

As this analysis is capable of measurements for both H_2O and CH target, optical potential parameters for carbon and oxygen remain. The most powerful parameter to control the CCQE interaction, M_A^{QE}, also remains.

For the 2p2h interaction and the CCSPP interaction, the prior uncertainties are inflated to make these parameters more sensitive to a change in the number of events with respect to the nominal simulation based on the underlying models.

Other sub-dominant interactions such as charged-current multi-pion production and deep inelastic scattering are simplified. The only normalization parameters in response to each interaction are introduced. This is because their contribution is small enough according to Table 17. In order to make the normalization parameters more flexible to cover other shape-altering parameters in these interactions, we inflate the uncertainties from 5% to 50% level.

11.3.3 Detector parameters

We can in principle reproduce the detector complex in the Geant4-based Monte Carlo simulation only within measurement precisions. The difference in the implementation of detector parameters may potentially end up with uncertainties on the number of selected events. The detector parameters cover geometrical alignments, scintillator/MPPC/electronics responses, the magnetic field in BabyMIND and the physics models to control pion FSI interactions. They are the most fundamental parameters to provoke the data/MC differences in the end. In order to estimate the effect, we perform a lot of simulations with a specific parameter being varied and then calculate the differences in the number of selected events between the nominal value and the altered value.

---

[50]See Appendix K for detailed calculations.

These detector parameters are practically not sufficient to take into account data/MC differences given there might be missing error sources that are not implemented in the MC simulation. The different actions of the thresholds used in the track reconstruction and event selections may not be covered only by these parameters. Therefore, we introduced additional systematic errors on the data-MC differences in the variation of the number of events when the nominal threshold is altered. An illustrative example of how to calculate these additional statistics is shown in Table 18. First, we calculate the number of events with the nominal threshold and varying thresholds using MC and data. Second, we calculate the difference in the number of events between the setup of the nominal threshold and varying thresholds. Third, the data-MC differences are calculated by subtracting the differences in data from the one in MC. Finally, the mean value of the data-MC differences is allocated to one of the additional systematic uncertainties. In the analysis, this calculation is done for each bin instead of the total number of events.

Table 18: An illustrative example to calculate the additional systematics about the positional differences in the track matching taking into account the data-MC differences stemming from the thresholds defined in the track reconstruction and event selections. "Value nom" represents the nominal threshold in the track reconstruction or event selection. "Value minus" and "Value plus" mean the thresholds shifted in negative and positive directions.

		Value minus	Value nom	Value plus
Threshold (mm)		80	100	120
MC	Nominal number of events	990	1000	1010
	Difference w.r.t. nominal	-0.01	0.00	0.01
Data	Nominal number of events	880	900	920
	Difference w.r.t. nominal	-0.022	0.00	0.022
Data-MC difference		0.012	0.00	0.012
Systematic value		$(0.012 + 0.012)/2 = 0.012$ (1.2%)		

The total number of detector systematic parameters is 27, and the contribution to the total uncertainties on the number of events is around 5% for the total cross section analysis. Compared to the other systematics parameters, the total uncertainty of detector parameters is not dominant. Not only the size of total uncertainties in each bin but also the covariances between bins are calculated and stored in the covariance matrices.

11.4 Cross section analysis

We perform the cross section measurements by incorporating the outcomes of the event selections and prior constraints of the systematic parameters into a fitting framework that finds the most probable values to describe data. The outcomes of the event selections are binned in reconstructed momentum or angle for each sample. The binning scheme was determined to give a sufficient number of events in every bin. We made use of the same fitting method, Barlow-Beeston modified by J.S. Conway as the ND fitting (see Section 6.4). The fitter searches for the best-fit values for signal and background events and all fitting parameters by minimizing the defined chi-squared. In addition, the fitter gives a covariance matrix to contain the uncertainties on the cross section as well as the correlation. The obtained best-fit parameters give the cross section results and the covariance matrix provides posterior uncertainties on each differential cross section along with the covariances. This section provides information on the analysis binning scheme, the fitting framework and the calculation formula for cross sections.

11.4.1 Analysis binning

Corresponding to true signal events and reconstructed signal samples, we defined their analysis binning as in Figures 19, 20.

Table 19: Binning edges for true and reconstructed P_μ. The lower edge of the momentum, 300 MeV/c represents the phase space restriction used in this analysis.

	topology	P_μ (MeV/c)
True	CC0$\pi^\pm$	300, 500, 700, 900, 1100, 1500, 30000
Reco	CC0$\pi^\pm$ PM-BM	300, 600, 700, 900, 1100, 1500, 30000
	CC0$\pi^\pm$ PM-WMRD	300, 400, 500, 600, 30000
	CC1$\pi^\pm$ PM	300, 1100, 3000
	CC0$\pi^\pm$ UWG-WMRD	300, 500, 600, 3000
	CC0$\pi^\pm$ UWG-BM	300, 900, 1500, 30000
	CC0$\pi^\pm$ DWG-BM	300, 500, 600, 700, 900, 1100, 30000
	CC1$\pi^\pm$ WG	300, 1100, 30000

Table 20: Binning edges for true and reconstructed $\cos\theta_\mu$. The lower edge of the cosine of the angle, 0.34 represents the phase space restriction used in this analysis.

	topology	$\cos\theta_\mu$
True	CC0$\pi^\pm$	0.34, 0.71, 0.77, 0.91, 0.94, 0.97, 1.0
Reco	CC0$\pi^\pm$ PM-BM	0.34, 0.819, 0.906, 0.94, 0.966, 0.985, 1.0
	CC0$\pi^\pm$ PM-WMRD	0.34, 0.50, 0.643, 0.766, 1.0
	CC1$\pi^\pm$ PM	0.34, 0.94, 1.0
	CC0$\pi^\pm$ UWG-WMRD	0.34, 0.643, 0.766, 1.0
	CC0$\pi^\pm$ UWG-BM	0.34, 0.966, 0.985, 1.0
	CC0$\pi^\pm$ DWG-BM	0.34, 0.643, 0.819, 0.906, 0.940, 0.966, 0.985, 1.0
	CC1$\pi^\pm$ WG	0.34, 0.94, 1.0

The true binning scheme is used when the corresponding differential cross section is shown. The binning for reconstructed variables depends on the detector topology, in particular the MRD detector. Each bin width was determined such that each bin should have a sufficient number of selected events, typically 50 to 100 events at least. The lower edge of muon kinematics represents the phase space restrictions used in this analysis. The MC simulation predicts significantly small statistics outside the certain phase space with the current data. We decided to restrict the signal region above 300 MeV/c for P_μ and above 0.34 for $\cos\theta_\mu$.

11.5 Cross section fitter

The outcomes of the selection criteria are stored in histograms according to the defined binning scheme for both MC and data. We then explore the most probable parameter values to describe data. We make use of a binned likelihood approach practically using a negative log-likelihood to realize it. The likelihood is expressed as

$$-2\ln\mathcal{L}(\overrightarrow{y};\overrightarrow{\theta}) = -2\ln\mathcal{L}_{\text{stat}}(\overrightarrow{y};\overrightarrow{\theta}) - 2\ln\mathcal{L}_{\text{syst}}(\overrightarrow{y};\overrightarrow{\theta}), \tag{11.1}$$

where $\overrightarrow{y}$ is the given data and $\overrightarrow{\theta}$ is a set of parameter values.

The statistical part of the likelihood is given by

$$-2\ln\mathcal{L}_{\text{stat}}(\overrightarrow{y};\overrightarrow{\theta}) = \sum_{j}^{\text{reco bins}} 2\left(\beta_j N_j^{\text{exp}} - N_j^{\text{obs}} + N_j^{\text{obs}}\ln\frac{N_j^{\text{obs}}}{\beta_j N_j^{\text{exp}}} + \frac{(\beta_j - 1)^2}{2\sigma_j^2}\right), \qquad (11.2)$$

where j runs over each reconstructed bin for all samples and N^{exp} is the number of selected events predicted by MC and N^{obs} is the observed number of selected events in data, β is the Barlow-Beeston scaling parameter and σ is the relative Monte Carlo statistical uncertainty. [51] The expected number of events in each bin (N_j^{exp}) consists of contributions from the signal ($N_j^{\text{exp,sig}}$) and background ($N_j^{\text{exp,bg}}$). The signal contribution is calculated with the true signal events based on a detector smearing matrix or transferring matrix, denoted by t_{ij} to provide a conversion factor from the true kinematic variables to reconstructed variables. The number of events, $N_j^{\text{exp,sig}}$ is then given by

$$N_j^{\text{exp,sig}} = \sum_{i}^{\text{true}} N_i^{\text{exp,sig}} t_{ij}. \qquad (11.3)$$

We then introduce additional parameters to apply multiplicative event weights as a function of true bins to the number of selected events in MC ($N_i^{\text{MC,sig}}$), called "template parameters" denoted by c_i. $N_i^{\text{exp,sig}}$ is expressed using them in

$$N_i^{\text{exp,sig}} = c_i N_i^{\text{MC,sig}}. \qquad (11.4)$$

The template parameters are free parameters with no prior uncertainty. Therefore, they are more sensitive to the shape of the input simulation than systematic parameters are. The template parameters can mitigate the potential bias from underlying models. Equation 11.3 is written using Equation 11.4 by

$$N_j^{\text{exp,sig}} = \sum_{i}^{\text{true}} c_i N_i^{\text{MC,sig}} t_{ij}. \qquad (11.5)$$

Inclusion of the background contribution in Equation 11.5 gives

$$N_j^{\text{exp}} = \sum_{i}^{\text{true}} \left(c_i N_i^{\text{MC,sig}} + N_i^{\text{MC,bg}}\right) t_{ij}. \qquad (11.6)$$

At this point, only weights from the template parameters are taken into account. In addition, there are three systematic contributions such as neutrino flux, neutrino interaction and detector systematics. The expected number of events is weighted by these parameters. The flux parameters are binned in the true neutrino energy. The parameter values that are given in each MINUIT iteration act as multiplicative event weights to change the predicted event distributions. The neutrino interaction parameters (26 in total) have different responses, which are sensitive to specific neutrino interaction types. The relationship between interaction parameters and weights is pre-calculated and stored in the format of spline functions for interaction type, target material,

---

[51]In addition to the fact that this refers to MC statistical uncertainty, σ could be interpreted as the statistical uncertainty on the data.

and kinematic bins. The weight of each interaction parameter is calculated using splines. The detector systematic parameters (26 for P_μ, 27 for θ_μ in total) act as normalization parameters. The covariances between these parameters can be described by the detector covariance matrix. Inclusion of all systematic weights modifies Equation 11.5 to

$$N_j^{\text{exp}} = \sum_i^{\text{true}} \left[c_i \left(N_i^{\text{MC,sig}} \prod_a^{\text{int}} w(a)_{ij}^{\text{sig}} \right) + \sum_k^{\text{bg}} N_{ik}^{\text{MC,bg}} \prod_a^{\text{int}} w(a)_{ij}^{\text{bg}} \right] t_{ij} r_j \sum_n^{E_\nu} v_{in} f_n, \qquad (11.7)$$

where a runs over interaction parameters and $w(a)$ refers to each weight. They affect the number of selected events in the MC to change its shape or normalisation. The parameter r_j represents the weights from detector systematics. The integer n runs over the neutrino energy corresponding to true bin i. The v_{in} factors are weights from neutrino energy bin n and f_n factors are the weights from flux systematics.

The systematic part is given in

$$-2 \ln \mathcal{L}_{\text{syst}} = \sum_p (\overrightarrow{p} - \overrightarrow{p}_{\text{prior}})(V_{\text{cov}}^{\text{syst}})^{-1}(\overrightarrow{p} - \overrightarrow{p}_{\text{prior}}), \qquad (11.8)$$

where p runs over all systematic parameters and $V_{\text{cov}}^{\text{syst}}$ represents covariance matrices for flux, interaction, and detector parameters, denoted by $\overrightarrow{p}_{\text{prior}}$. This acts as a penalty term for moving the systematic parameters away from their nominal values. Using this method of describing all the uncertainties with a covariance matrix and calculating the penalty term approximates the uncertainties as Gaussian.

We performed various kinds of fits to verify the fitting framework and to check the sanity of the outcomes of the selection criteria and systematic priors. In addition, we assessed the potential weakness in the neutrino interaction model. In case the uncertainty of interaction models cannot be covered by the underlying systematic parameters, the potential bias stemming from the nominal model is checked by alternative simulated data sets. [52]

11.6   Cross section extraction

The cross section fitter provides the best-fit values for the template parameters (c_i) and the systematic parameters. The expected signal events are then calculated with those parameters and the inversed smearing matrix that can convert the observed number of events in the binning of the reconstructed variables to the number of true signal events in the binning of the true variables. The equation is

$$\hat{N}_i^{\text{exp,sig}} = \sum_j^{\text{recon}} \left(\hat{c}_i N_j^{\text{MC,sig}} \prod_a^{\text{int}} \hat{w}(a)_{ij}^{\text{sig}} \right) (t_{ij})^{-1} \hat{r}_j \sum_n^{E_\nu} v_{in} \hat{f}_n, \qquad (11.9)$$

where the "hat" means the best fit. When we calculate a cross section, there are multiple ways of treating neutrino flux. We took an approach of a flux-integrated cross section rather than a flux-unfolded one to avoid model dependence (or at least reduce it) in terms of the shape of the neutrino energy spectrum. The formula to calculate the differential flux-integrated cross section as a function of muon kinematics, $d\sigma/dx_i$, where σ is the total flux-integrated cross section and x is muon kinematics is

---

[52]See Appendix N,O for details.

$$\frac{d\sigma}{dx_i} = \frac{\hat{N}_i^{\text{exp,sig}}}{\epsilon_i \Phi N_{\text{nucleons}}^{\text{FV}}} \times \frac{1}{\Delta x_i}, \tag{11.10}$$

where $\epsilon, \Phi, N_{\text{nucleons}}^{\text{FV}}$, and Δx_i are the signal detection efficiency, integrated muon neutrino flux, the number of target nucleons in the fiducial volume and the bin width of true bin i, respectively. The detailed calculation of the number of nucleons and the integrated flux are shown in Appendix M. Since we report the single differential cross section as a function of muon kinematics, x refers to either muon momentum P_μ or muon angle θ_μ.

The errors on the cross section results are estimated by throwing a lot of toy experiments based on a covariance matrix with the Cholesky decomposition [168]. The method is explained in Appendix L.

12 Results of neutrino-nucleus cross sections

The results of the data fit for the neutrino cross sections of the CC0$\pi^\pm$ signal are shown in this section. We perform the cross section fit to obtain the constraints on the template parameters and the nuisance parameters. With the best fit parameters and the constraints, we extract the integrated and differential cross sections for the muon-neutrino charged-current interactions without a charged pion in the final state on H_2O and CH targets. The interpretation of those results is discussed. Then, the importance of these results and future prospects are also described.

12.1 Data Set

We present the analysis results of the differential cross section for the muon-neutrino charged-current interactions without a charged pion in the final state on H_2O and CH targets at 1 GeV energy region with the data set corresponding to 2.96×10^{20} POT taken in the neutrino mode. The data set is divided into three periods from November 2019 to April 2021, shown in Table 21. The installation of our detectors was done in 2019. The commissioning of the detectors revealed some failures in the WallMRD electronics. We found that the random noises which remain even after the 2.5 p.e. cut inside the electronics. As the electronics have limited buffers in each trigger, signal hits are sometimes lost due to the random noises. After thorough investigations, we concluded the circuits in the electronics needed to be modified during the data taking in 2019. The modification works were done after the data taking in the middle of January 2020. Since the end of January 2020, we have succeeded in operating all the detectors in good condition. Thus, the good-quality data are limited to 2.96×10^{20} POT, which are used in the data fit. The MC distributions to be compared to data are normalized by this data POT.

Table 21: The data set used in this analysis

T2K Run	Period	Delivered POT [/10^{20}]	Good-quality POT [/10^{20}]
Run10	Nov. and Dec. in 2019	2.65	0.00
Run10	Jan. and Feb. in 2020	2.12	1.38
Run11	Mar. and Apr. in 2021	1.78	1.58
Total		6.55	2.96

12.2 Results of the flux-integrated cross section

We report the flux integrated total cross section (σ_{tot}) on both targets using the samples for the angle distribution in the limited phase space. The impact of the low statistics in this analysis is small for the integrated cross section compared to the differential cross section because all data are merged in one bin. The total cross sections are calculated by the summation of the differential cross section as a function of the angle because it has higher statistics than the statistics for the differential cross section as a function of the momentum. The comparison of the integrated cross section between data and MC can be achieved with higher precision. The extracted integrated cross sections are

$$\sigma_{\text{tot},H_2O} = 1.636 \pm 0.370 \ (10^{-39} \ \text{cm}^2/\text{nucleon}) \tag{12.1}$$

$$\sigma_{\text{tot,CH}} = 1.432 \pm 0.355 \ (10^{-39} \ \text{cm}^2/\text{nucleon}). \tag{12.2}$$

On the other hand, the predicted cross sections by the neutrino interaction models in NEUT are 1.165 for H_2O and 1.197 for CH in the same unit. The size of the cross section in data is larger than that in MC but does not deviate from the MC predictions by 2σ significance.

12.3   Results of the differential cross section

The fitting method described in the previous chapter is used to extract the differential cross sections using the selected events in data and MC. The results of the differential cross section in the momentum distribution are shown in Table 22. The results in the angle distribution are shown in Table 23. The corresponding plots are also shown in Figures 70, 71. The errors on these differential cross section results include both statistical and systematic contributions. The measured differential cross section on the H_2O target is mostly consistent with our MC prediction except for the first bin in the momentum distribution (0.3 GeV/c - 0.5 GeV/c) and the fourth bin in the angle distribution ($\cos\theta_\mu$ range of 0.91 - 0.94). On the other hand, the measured differential cross section on the CH target is consistent with the MC prediction within the errors in all bins. These data-MC differences including the differences in the integrated cross sections are discussed in Section 12.4.1.

Table 22: Results of the differential cross sections in the momentum distribution. The unit of each differential cross section is $(\mathrm{cm}^2)/(\mathrm{nucleon} \cdot \mathrm{GeV/c})$.

Target Material	Range (GeV/c)	Postfit value (10^{-39})	Postfit error (10^{-39})	MC (10^{-39})
H$_2$O	0.3 - 0.5	2.367	0.675	1.225
	0.5 - 0.7	1.825	0.458	1.553
	0.7 - 0.9	1.063	0.320	1.010
	0.9 - 1.1	0.437	0.194	0.513
	1.1 - 1.5	0.099	0.127	0.259
	1.5 - 5.0	0.012	0.003	0.007
CH	0.3 - 0.5	1.274	0.402	1.227
	0.5 - 0.7	1.391	0.352	1.570
	0.7 - 0.9	0.879	0.235	1.034
	0.9 - 1.1	0.514	0.155	0.536
	1.1 - 1.5	0.227	0.076	0.266
	1.5 - 5.0	0.008	0.002	0.008

Table 23: Results of the differential cross sections in the angle distribution. The unit of each differential cross section is $(\mathrm{cm}^2)/(\mathrm{nucleon})$.

Target Material	Range $(\cos\theta_\mu)$	Postfit value (10^{-39})	Postfit error (10^{-39})	MC (10^{-39})
H$_2$O	0.34 - 0.71	1.489	0.539	0.884
	0.71 - 0.77	1.892	1.066	1.613
	0.77 - 0.91	2.815	0.652	2.329
	0.91 - 0.94	6.374	1.614	3.491
	0.94 - 0.97	5.087	1.494	4.080
	0.97 - 1.00	7.779	1.772	6.269
CH	0.34 - 0.71	1.114	0.365	0.895
	0.71 - 0.77	2.750	1.120	1.615
	0.77 - 0.91	2.845	0.721	2.357
	0.91 - 0.94	4.089	1.118	3.509
	0.94 - 0.97	5.012	1.322	4.392
	0.97 - 1.00	6.123	1.511	6.739
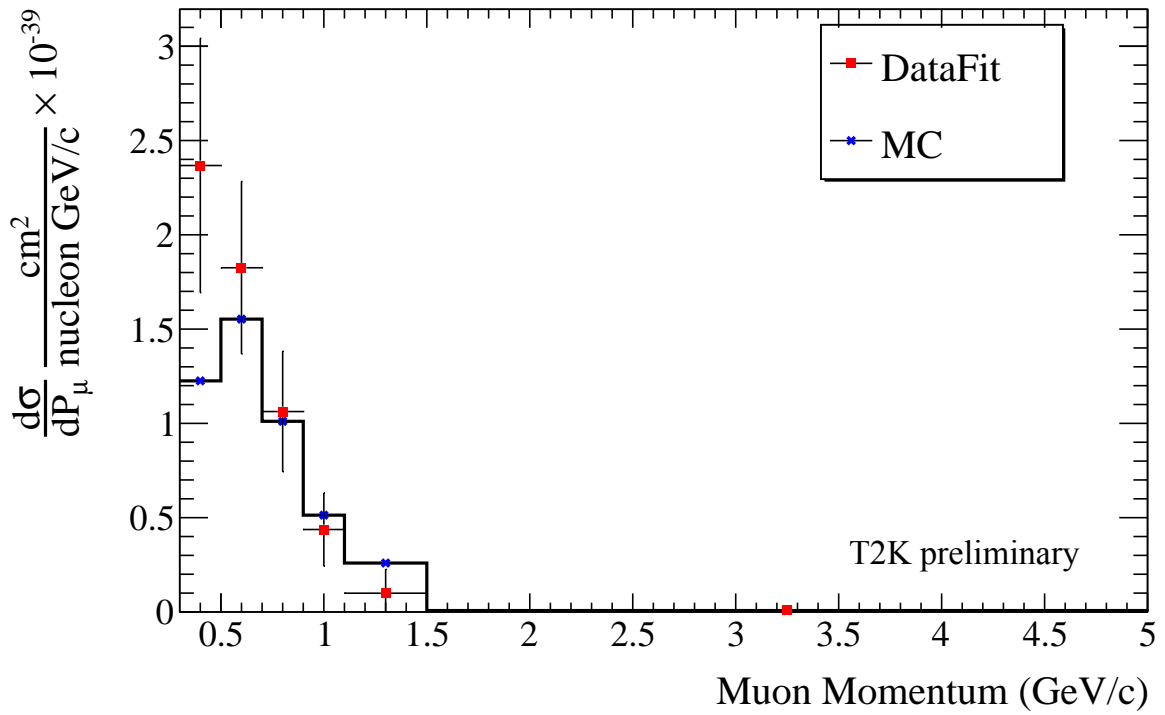
(a) H_2O target
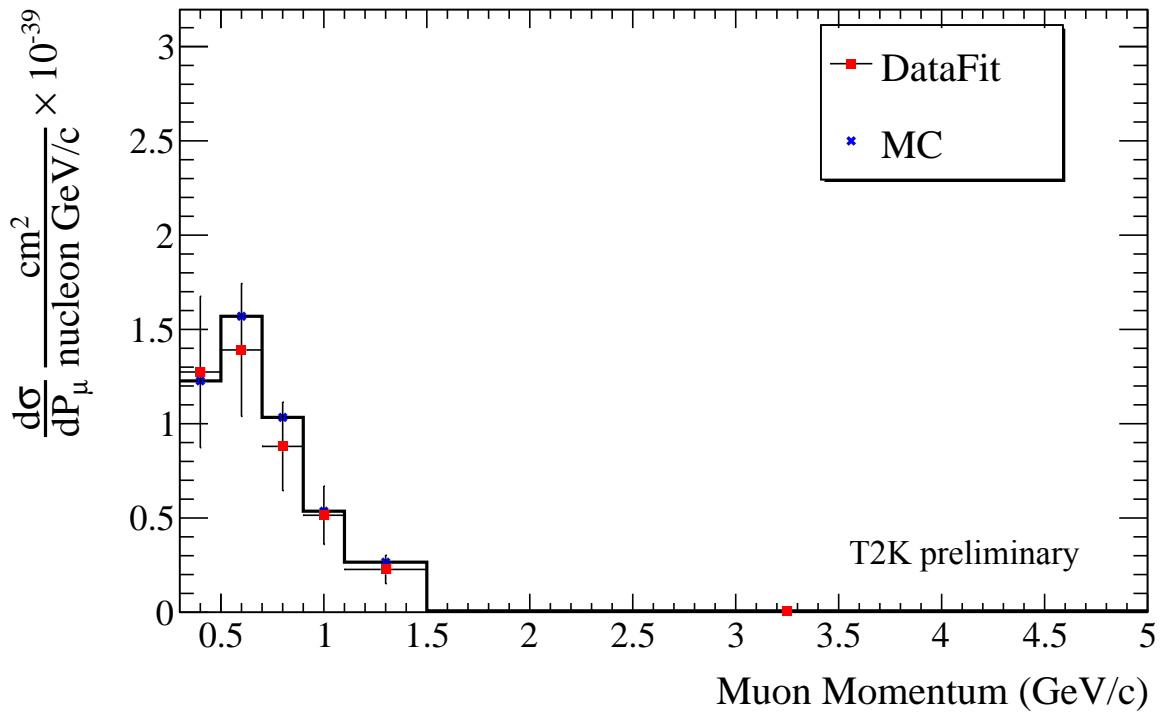
(b) CH target

Figure 70: The differential cross section results as a function of P_μ on H_2O target (top) and CH target (bottom).
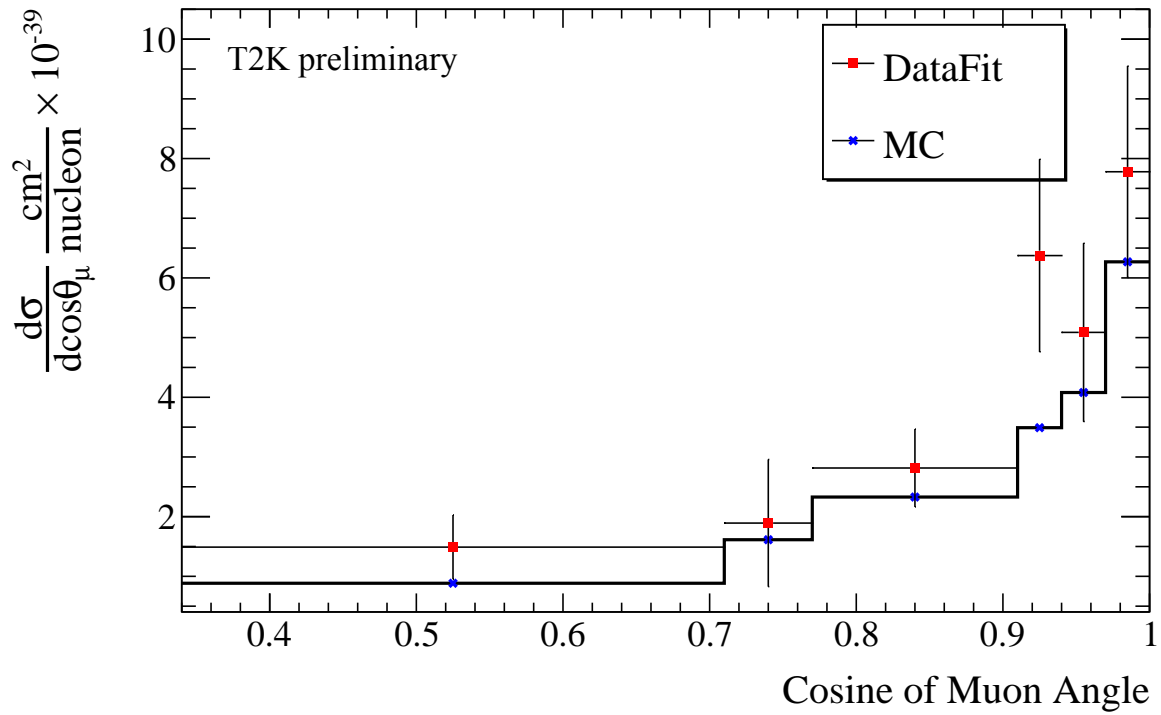
(a) H_2O target
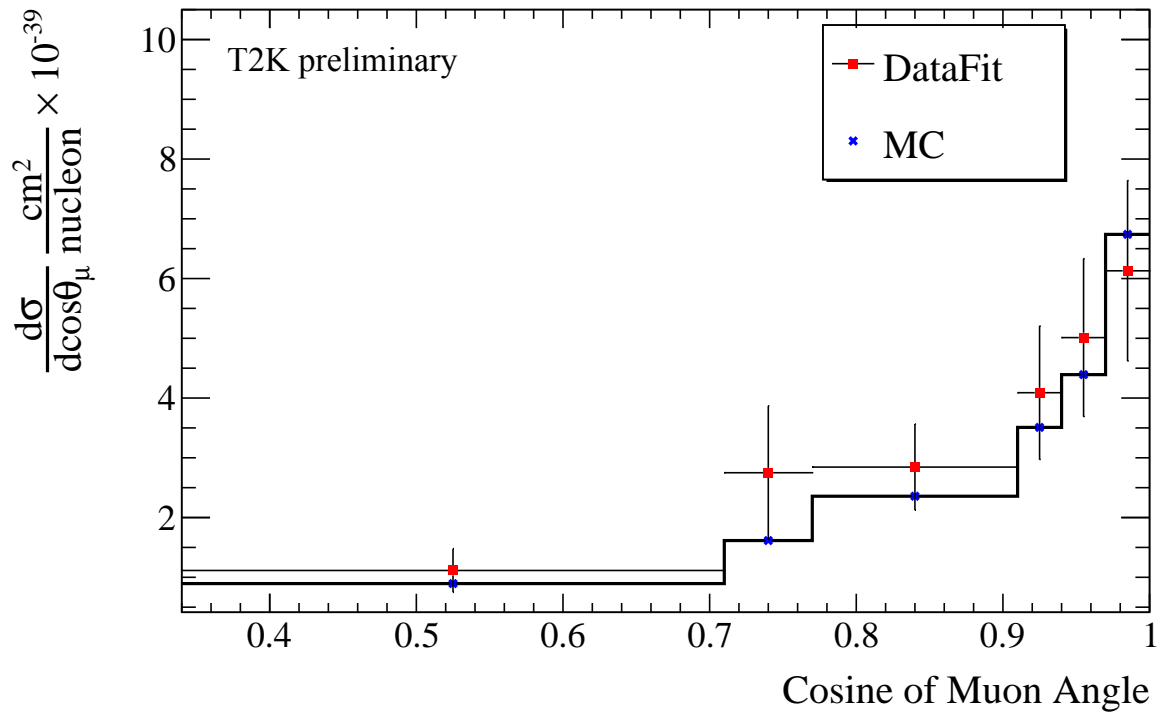
(b) CH target

Figure 71: The differential cross section results as a function of $\cos\theta_\mu$ on H_2O target (top) and CH target (bottom).

12.4 Discussions

12.4.1 Interpretation of the cross section results

We obtained the integrated cross sections larger than around 20% - 30% than the MC predictions. These are not so significant difference with respect to the size of the uncertainties. However, according to Table 16, we see the number of events in MC be almost comparable to the number of events in data for the Proton Module samples. Even for the WAGASCI samples, the difference is around 10%. We discuss how the extracted cross sections are pulled up.

In this analysis, we perform the fits to get the best-fit parameters, template, cross section, detector, and flux parameters as well as their constraints. Then, we calculate the best-fit cross sections using the parameters, signal detection efficiency, integrated flux, and the number of target nucleons. The cross section parameters have two roles; to change the expected number of events via their weights and to change the signal detection efficiency. We check the fitting formula again.

$$N_j^{\text{exp}} = \sum_i^{\text{true}} \left[c_i \left(N_i^{\text{MC,sig}} \prod_a^{\text{int}} w(a)_{ij}^{\text{sig}} \right) + \sum_k^{\text{bg}} N_{ik}^{\text{MC,bg}} \prod_a^{\text{int}} w(a)_{ij}^{\text{bg}} \right] t_{ij} r_j \sum_n^{E_\nu} v_{in} f_n. \tag{12.3}$$

The cross section parameters are denoted by $w(a)_{ij}$, which multiply the number of signal and background events. The change in the number of events by the cross section parameters will be canceled in the calculation of the cross section by the template parameters denoted by c_i in Equation 12.3. The first role of the cross section parameters is not reflected in the end. The efficiency change, however, can affect the extracted cross sections. Before discussing the efficiency change, we compare the event distributions in MC before the fit with the distributions multiplied by the best-fit parameters.

(a) WAGASCI detectors samples (b) Proton Module samples
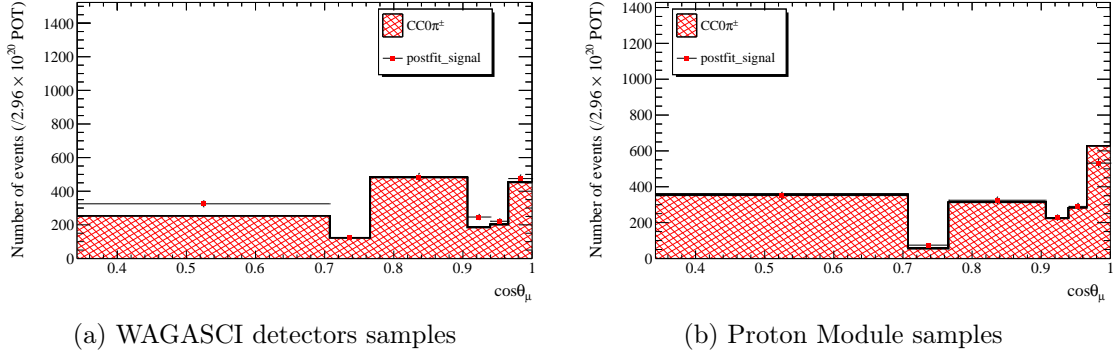
Figure 72: Comparison between the prior and post-fit $\cos\theta_\mu$ distributions only for the signal samples. The horizontal axis is $\cos\theta_\mu$ in the reconstruction space.

The WAGASCI events are pulled up by around 11% with respect to the prior distribution, while the Proton Module events are comparable to the prior distributions except for the last bin. The post-fit distributions are multiplied by all the parameters but without recon-true conversion. In the actual calculation, after the recon-true conversion, the cross sections are extracted. We compare the signal efficiencies using the best-fit parameters to the prior efficiencies. For the integrated cross section on the H_2O target, the overall efficiency is changed from 0.425 to 0.384

and on the CH target, it is changed from 0.357 to 0.301. They correspond to around 10.6% and 18.6% increases in the cross sections. The behaviors of the differential cross section shown in Figure 71 can be understood by taking into account these efficiency changes. The differential cross sections on the CH target are larger than the MC true cross sections except for the last bin, which corresponds to the distributions in Figure 72 multiplied by the increasing efficiency. In addition, the discrepancy in the 4th bin on H_2O target can be also explained by the shape in the post-fit distributions and increasing efficiency.
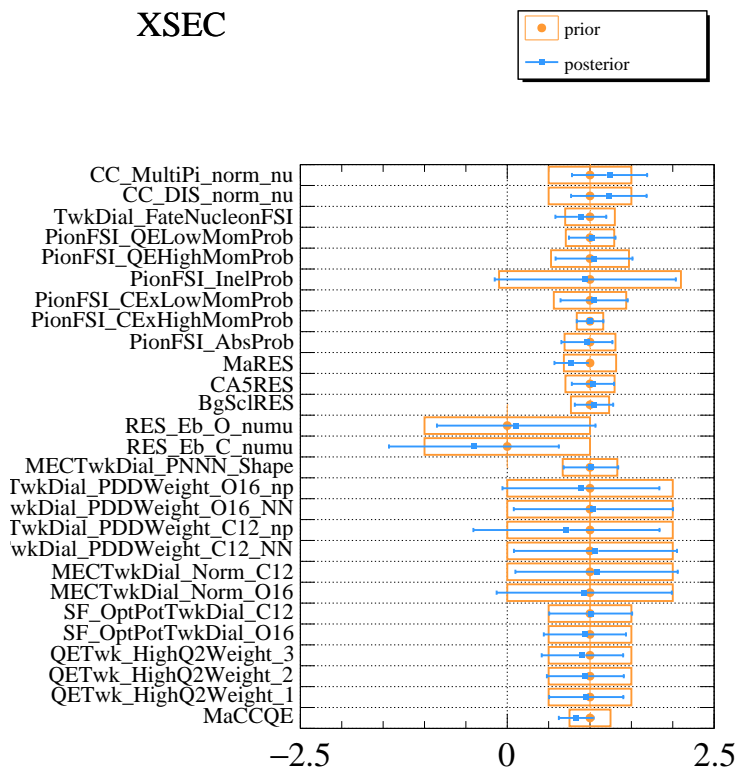
Figure 73: The best-fit and errors of the cross section parameters in the angle measurement. Orange rectangles indicate the prior constraints on the cross section parameters, and the blue dots and bars are the best-fit values and their errors. The nominal value is 1.0, and the relative value with respect to the nominal is calculated for each cross section parameter.

We assume the changes in the efficiency are caused by the post-fit cross section parameters. The constraints on the parameters are shown in Figure 73. The constraints on the other parameters are described in Appendix P. We focus on the "MaRES" and "MaCCQE" parameters which are the main parameters of CCRES and CCQE respectively. They are both decreasing, which means that the number of events for CCRES and CCQE is pulled down by these parameters. This causes the signal efficiency to decrease because those interactions are the main signal components. In order to check which reconstructed samples drive these changes, we list the χ^2 values for each likelihood contributor during the fit in Table 24. It shows the cross section parameters move so that the difference in PM CC1$\pi^{\pm}$ is reduced during the fit. The $\cos\theta_{\mu}$ distributions for CC1$\pi^{\pm}$ samples are shown in Figure 74. The shape in the PM CC1$\pi^{\pm}$ sample is different

between data and MC. In order to reduce the difference, the fitter pulls down the CCRES and CCQE components by changing the MaRES and MaCCQE parameters while pulling up the CCDIS and CCMulti-pi (CCMPI) parameters. This reduction of the MaRES is also seen even in the fit without the control samples. Figure 75 shows the comparisons of $\cos\theta_\mu$ distributions for the signal samples between data and MC. We see relatively large differences in shape for the UWG-WM (Upstream WAGASCI to WallMRDs) sample. In fact, χ^2 for this sample is reduced most in the fit without the control samples. We find CCRES events in the 1st and 3rd bins significantly larger than those in the 2nd bin. The main contributions in the CCRES events in the 1st and 3rd bins come from the Wall background events with large weights (10 15, typically less than 0.1). Therefore, these events have relatively large uncertainties. On the other hand, in the 2nd bin, the signal contribution is high without any events having this larger weight. It is reasonable for the fit to find the best fit by reducing the MaRES parameter and increasing the template parameters corresponding to the 2nd bin. By taking into account this fact, a reduction in the MaRES parameter would be the right direction considering the signal samples as well as the background samples.

Table 24: Comparison of the χ^2 for each likelihood contributor between fits with and without the cross section parameters.

Likelihood contributor	fit with the cross section parameters	fit without the cross section parameters
flux	0.006	0.112
cross section	2.27	0
detector	5.23	7.25
PM-WM	2.59	2.35
PM-BM	1.10	1.36
PM CC1$\pi^\pm$	2.82	1.09
UWG-WM	3.67	3.45
UWG-BM	1.48	0.92
DWG-BM	2.31	3.15
WG CC1$\pi^\pm$	0.146	0.33
Total	19.33	22.30
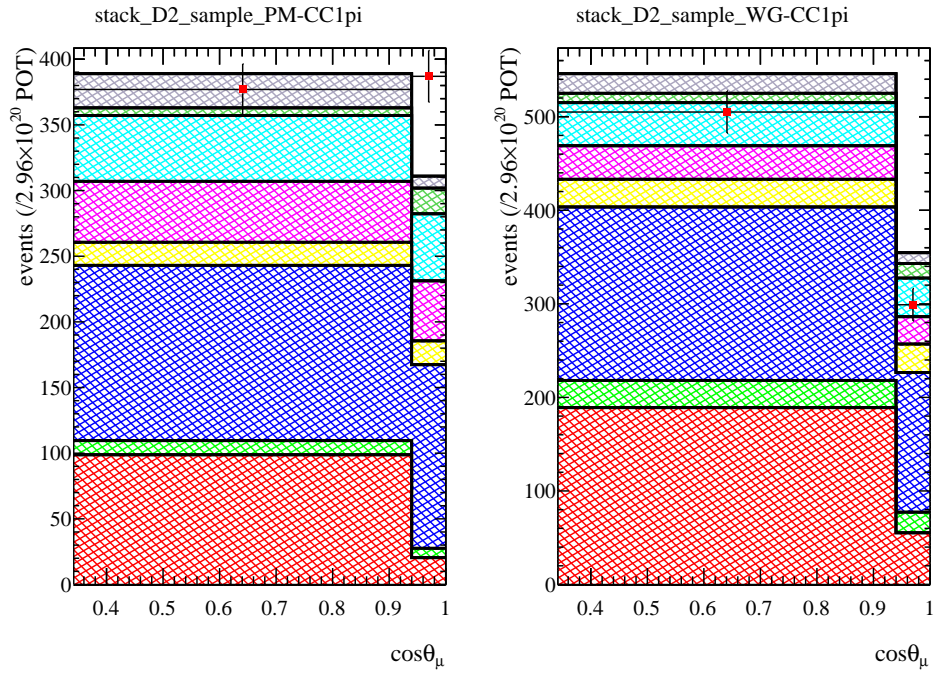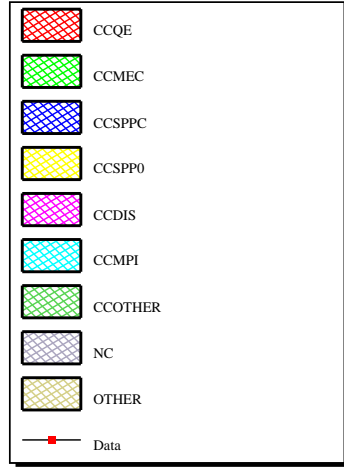
Figure 74: Comparison of CC1$\pi^{\pm}$ $\cos\theta_{\mu}$ distributions between data and MC. The histograms are stacked by the interaction types; CCQE (charged current quasi elastic), CCMEC (charged current meson exchange), CCSPPC (charged current single charged pion production), CCSPP0 (charged current single neutral pion), CCDIS (charged current deep inelastic scattering), CCMPI (charged current multi-pion production), NC (neutral current). Data points are overlaid on the histograms.
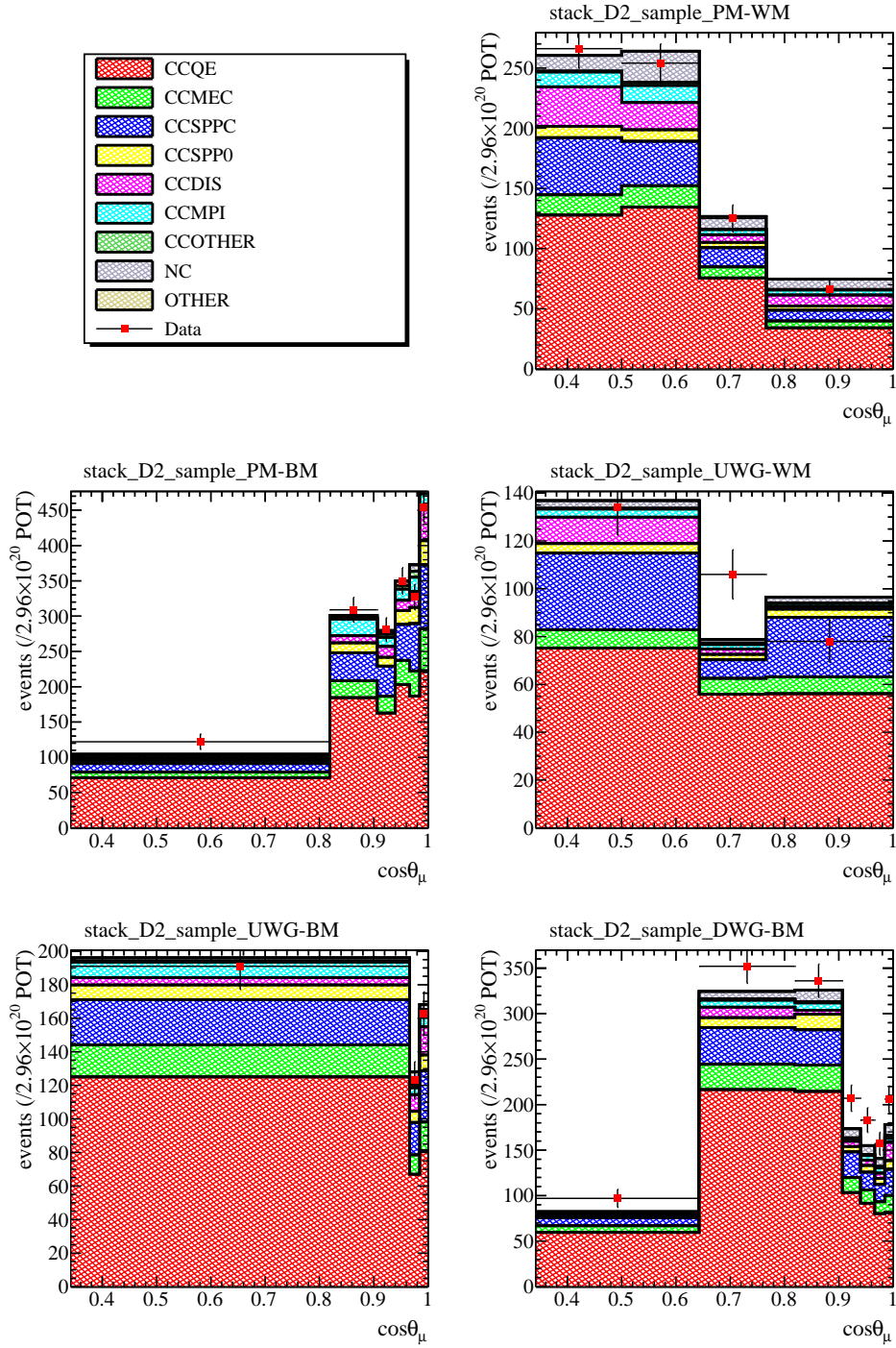
Figure 75: Comparison of CC0$\pi^{\pm}$ $\cos\theta_{\mu}$ distributions between data and MC. The histograms are stacked by the interaction types, same as in Figure 74. Data points are overlaid on the histograms.

We have discussed so far the integrated cross sections using the angle distributions. We can in principle extract the integrated cross sections using the momentum distributions. The extracted integrated cross sections by the summation of the differential cross sections as a function of muon momentum are

$$\sigma_{\text{tot},H_2O} = 1.22 \pm 0.320 \ (10^{-39} \ \text{cm}^2/\text{nucleon}) \tag{12.4}$$

$$\sigma_{\text{tot,CH}} = 0.93 \pm 0.226 \ (10^{-39} \ \text{cm}^2/\text{nucleon}). \tag{12.5}$$

The true cross sections on the H_2O and CH targets are 0.989×10^{-39} and 1.008×10^{-39} respectively. The data are consistent with the MC predictions within 1σ errors. It should be mentioned that the integrated cross sections using angle distributions are 1.636×10^{-39} on the H_2O target and 1.432×10^{-39} on the CH target. As we use the different samples between the momentum and angle distributions, some differences should be expected. In particular, the parameter MaCCQE is not so much changed with the fit using muon momentum distributions (Appendix P), while the parameter is decreased with the fit using the cosine of the muon angle distributions. This can lead to differences in signal detection efficiencies. In fact, the efficiency for the momentum distributions is increased by about 10% on the CH target, while the efficiency for the angle distributions is almost unchanged on the H_2O target. As a result, we see relatively large differences between the integrated results using momentum and angle distributions. The level of differences is still 1σ considering both measurement errors. As the statistics are higher by about 40-50% in the angle distributions, we quote the integrated cross section results using the angle distributions as the final results in this paper.

12.4.2 Importance of the measurements

We presented the differential cross sections for the muon-neutrino charged current interactions without a charged pion in the final state at a mean energy of 0.97 GeV. In the T2K publications, we have only one paper for the cross section measurement at this mean energy for the anti-muon neutrino interactions [160]. Therefore, this is the first measurement result by T2K at this energy region for muon-neutrino interactions. This will provide a new perspective to assess our neutrino interaction models. As described in Chapter 6, in the ND280 measurements, the number of events for the CC0π samples in data is larger than that in the MC. Similar yet milder differences can be seen in the data-MC comparisons of the event distributions in Figures 68a, 69a on the H_2O target. On the other hand, we can see good consistency between data and MC on the CH target. Neutrino interactions depend on neutrino energy. As the mean energy of the WAGASCI-BabyMIND measurements is different from the one in the ND280 measurements, the ratios of each interaction type in both measurements are different from each other. The measurements by WAGASCI-BabyMIND with more statistics comparable to the ND280 measurements are desirable to confirm if the observed difference between WAGASCI-BabyMIND and ND280 results is caused by the ratio of interaction types in the mean energy of neutrinos. The contribution from statistical parameters and systematic parameters is discussed in the next section.

The neutrino-nucleus interaction on the H_2O in T2K is important as described in Chapter 9. The detector with the CH target has been upgraded for ND280 whereas the H_2O target detector is not. In fact, one-third of the FGD2 water target in the ND280 is lost. Thus, the cross section measurements on the H_2O target by WAGASCI-BabyMIND are expected to cover and provide meaningful insights into the oxygen-carbon differences in neutrino interactions by the

standalone measurements and combined measurements with ND280. Our measurements are the starting point. In the future, a finer binning or two-dimensional binning scheme will be analyzed with more statistics.

12.4.3   Separation of statistical and systematic uncertainties

We evaluate the statistical and systematic uncertainties as follows.

- Perform the cross section fit using the simulated data with each event weight increased by a thousand times. When the event weights are increased by a thousand times, the statistical effect is negligible.

- Do the quadrature subtraction of the cross section errors obtained in the fit using simulated data with increasing event weights from the cross section errors obtained in the data fit. This will provide the estimated statistical uncertainty in the data fit assuming the systematic uncertainty affects both MC and data in the same manner.

The calculated statistical and systematic uncertainties are summarized in Tables 25, 26. This analysis is statistically limited. The relative statistical errors to the best fit values in the angle distribution are smaller than those in the momentum distributions. As we do not require the contained cut for the muon candidate in the angle distributions, the statistics for the differential cross section as a function of angle is almost 50% larger than as a function of momentum.

The systematic uncertainty is not negligible to the statistical uncertainty for the momentum distributions. A large contribution comes from the detector parameters. The detailed calculations of the detector parameters are described in Appendix K. For the momentum distributions, the dominant error source comes from the effect of the parameter of signal lost to take into account the potential differences between data and MC in vertex Z distributions. [53] In addition, the fiducial volume and muon contained cut in the MRDs are other large error sources. We need the muon contained cut to measure the muon momentum by range. We can reduce this error when we establish the method to reconstruct the momentum by curvature in BabyMIND. The size of the detector systematics is related to the total number of events in data because we use the data to estimate the effect of the data-MC differences. We expect the detector systematics to be reduced by increasing the statistics as well as the statistical uncertainties.

On the other hand, the systematic uncertainty is not significant to the statistical uncertainty for the angle distributions. One of the reasons is that the statistics for the angle distributions are larger by about 40% than the statistics for the momentum distributions because we do not need the muon contained cut. Besides, we do not need the detector error stemming from this cut. However, the parameter to take into account the WAGASCI vertex Z differences has relatively large contributions in this case as well. Confirming that they are accidental differences or identifying the causes of the differences would be a primary matter to deal with to achieve more precise measurements.

---

[53]We found the differences in WAGASCI vertex Z distributions between data and MC, which are described in Appendix K.2.9. After thorough investigations, we did not find any failure mode to cause these differences or significant impact on the cross section analysis. As we did not specify the cause of the differences, we added a conservative systematic parameter to take into account the potential difference.

Table 25: The impact of statistical (stat.) and systematic (syst.) uncertainties in momentum distributions. The unit of each differential cross section is $(cm^2)/(nucleon \cdot GeV/c)$. The fraction of the statistical uncertainty to each best fit value is also shown in the parenthesis.

Target Material	Range (GeV/c)	Best fit value (10^{-39})	Stat. (10^{-39})	Syst. (10^{-39})
H$_2$O	0.3 - 0.5	2.367	0.675 (28.5%)	0.261
	0.5 - 0.7	1.825	0.458 (25.1%)	0.236
	0.7 - 0.9	1.063	0.320 (30.1%)	0.173
	0.9 - 1.1	0.437	0.194 (44.4%)	0.104
	1.1 - 1.5	0.099	0.127 (128.3%)	0.067
	1.5 - 5.0	0.012	0.003 (25%)	0.001
CH	0.3 - 0.5	1.274	0.402 (31.6%)	0.282
	0.5 - 0.7	1.391	0.352 (25.3%)	0.205
	0.7 - 0.9	0.879	0.235 (26.7%)	0.225
	0.9 - 1.1	0.514	0.155 (30.2%)	0.082
	1.1 - 1.5	0.227	0.076 (33.5%)	0.045
	1.5 - 5.0	0.008	0.002 (25%)	0.001

Table 26: The impact of statistical (stat.) and systematic (syst.) uncertainties in angle distributions. The unit of each differential cross section is $(cm^2)/(nucleon)$. The fraction of the statistical uncertainty to each best fit value is also shown in the parenthesis.

Target Material	Range ($\cos\theta_\mu$)	Best fit value (10^{-39})	Stat. (10^{-39})	Syst. (10^{-39})
H$_2$O	0.34 - 0.71	1.489	0.539 (36.2%)	0.027
	0.71 - 0.77	1.892	1.066 (56.3%)	0.104
	0.77 - 0.91	2.815	0.652 (23.2%)	0.064
	0.91 - 0.94	6.374	1.614 (25.3%)	0.165
	0.94 - 0.97	5.087	1.494 (29.4%)	0.158
	0.97 - 1.00	7.779	1.772 (22.8%)	0.165
CH	0.34 - 0.71	1.114	0.365 (32.8%)	0.021
	0.71 - 0.77	2.750	1.120 (40.7%)	0.079
	0.77 - 0.91	2.845	0.721 (25.3%)	0.057
	0.91 - 0.94	4.089	1.118 (27.3%)	0.127
	0.94 - 0.97	5.012	1.322 (26.4%)	0.12
	0.97 - 1.00	6.123	1.511 (24.7%)	0.124

12.4.4 Data and MC model comparisons

The data fit results are compared to several kinds of alternative interaction models to see which models describe the results best. The agreement between the measurement and models is qualified by the χ^2 defined by

$$\chi^2 = \sum_{ij}^{N} \left(\left(\frac{d\sigma}{dx}\right)_{i,\text{data}} - \left(\frac{d\sigma}{dx}\right)_{i,\text{model}} \right) \mathbf{V_{ij}}^{-1} \left(\left(\frac{d\sigma}{dx}\right)_{j,\text{data}} - \left(\frac{d\sigma}{dx}\right)_{j,\text{model}} \right) \tag{12.6}$$

where N is the number of cross section bins, i, j are the ith and jth kinematic bin, respectively. The parameter $\mathbf{V}$ is the cross section covariance matrix. The models compared to this analysis result are briefly described as follows.

NEUT alternative version

We use another model implemented in NEUT. One difference exists in the treatments for the nuclear ground state. The alternative model does not introduce Spectral Function (SF) but treats the ground state in the Global Fermi Gas (GFG) model as shown in Figure 76. The CCQE model is the Nieves 1p1h model without the RPA correction, with M_A^{QE} being set to 1.05 GeV/c^2, compared to 1.21 GeV/c^2 in the original NEUT model. This M_A^{QE} value reflects the theoretical calculation using 2p2h excitations ($M_A = 1.049$ GeV/c^2 [100]). The expected number of CCQE events would decrease by about 15% in this model, which is the outcome of the smaller cross section.

GENIE

GENIE is a neutrino interaction simulator allowing various combinations of interaction models. [54] The CCQE model is the same as NEUT but with a different M_A^{QE} (0.99 GeV/c^2). The treatment of the ground state of a nucleus is also different. Our NEUT model utilizes the Benhar spectral function model, whereas the GENIE adopts a Relativistic Fermi Gas (RFG) model. Another difference is in the missing energy and missing momentum distributions. The relationship between the missing energy and missing momentum is described by a unique curve in the GFG while it is described with several bands corresponding to the nuclear shell states in the Benhar spectral function model.

---

[54]We used the version "G18-02".
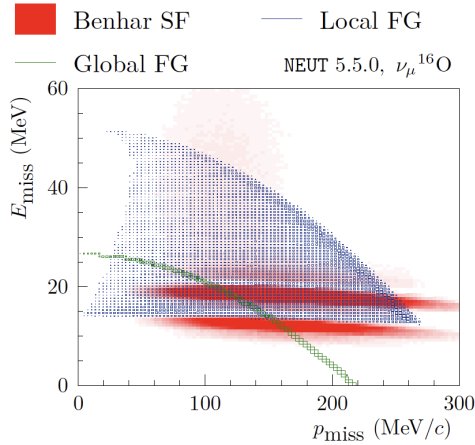
Figure 76: The reconstructed missing energy and momentum distributions for the three initial-state nuclear models implemented for the CCQE interaction in NEUT (Benhar Spectral Function in red, Local Fermi Gas model in blue, and Global Relativistic Fermi Gas model in green) [122].

Post fit by the ND fit

The best-fit interaction parameters obtained from the near detector fit in the oscillation analysis are used to weight the event distributions in the base model. CCQE-related parameters and 2p2h parameters are increased with respect to the pre-fit values whilst resonant parameters (C_A^5, M_A^{RES}) are decreased so that the best fit parameters pull up the CC0π events and pull down the CC1π events.

The comparisons of χ^2 for each model are shown in Table 27. Each model prediction on the differential cross sections is compared in Figure 77 against the data result. The degree of freedom is 12 for both momentum and angle distributions. No particular model is rejected or favored based on the fit results according to the χ^2 in this analysis due in large part to the large statistical uncertainty.

Table 27: Agreement between the data fit and the simulation based on various models as measured by the χ^2.

Model	χ^2 in momentum binning			χ^2 in angle binning		
	CH	H_2O	total	CH	H_2O	total
NEUT nominal	1.138	10.46	11.9	2.894	4.074	6.519
NEUT alternative version	1.245	10.35	11.65	2.783	5.114	7.237
GENIE	2.066	10.7	13.11	1.66	3.773	5.197
Post fit by the ND fit	1.473	10.13	12.01	2.406	4.146	5.958
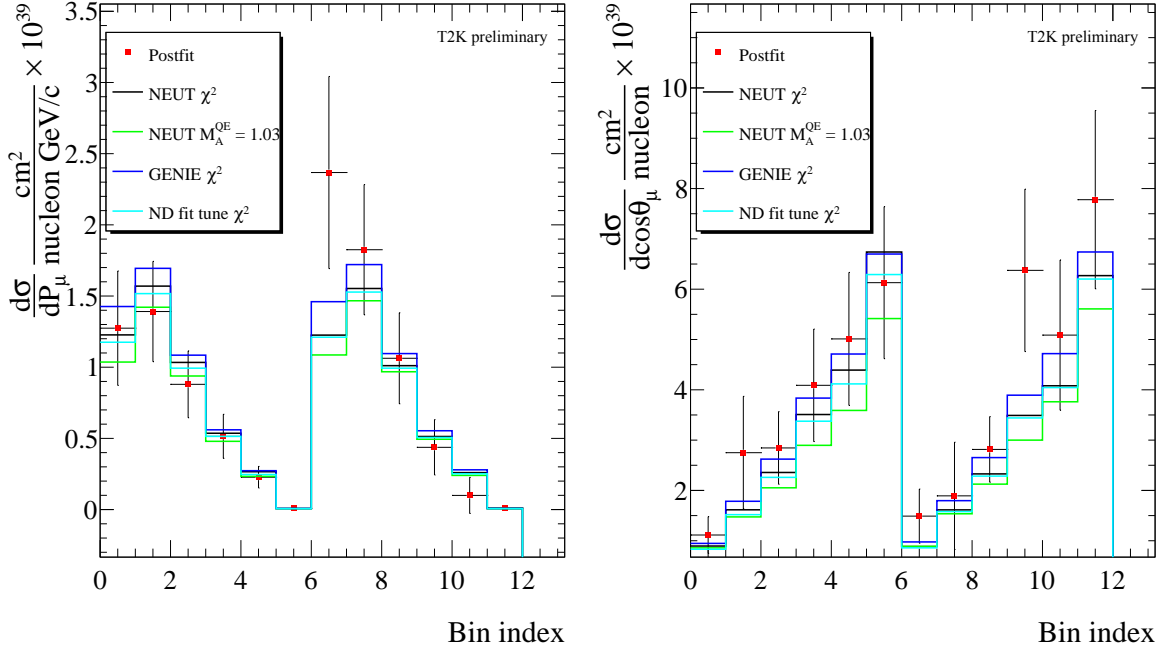
(a) As a function of muon momentum

(b) As a function of cosine of muon angle

Figure 77: Extracted differential cross section compared to nominal MC and alternative MC models as a function of momentum (left) and angle (right). The bin indices from 0 to 5 are the CH results and the bin indices from 6 to 11 are the H_2O results. The color corresponds to each model; black: the nominal NEUT version, green: the alternative version of NEUT with M_A^{QE} is set to 1.03 GeV/c^2, blue: GENIE, cyan: post-fit ND tune.

12.4.5 Future prospects

This analysis is statistically limited as was already discussed. The accelerator power supplies in the Main-Ring have been upgraded and the T2K experiment has upgraded the horn current to increase the statistics for the cross section measurements and the oscillation measurements. Assuming the beam upgrade plan proposed in [68], T2K is going to accumulate 1.5×10^{21} POT in a one-year operation on average until 2027. The expected statistics until 2027 correspond to about five times larger than what we used for the first result. When the statistics reach about 10 times larger than the current statistics for WAGASCI-BabyMIND, we will be able to measure the double differential cross sections in a similar binning scheme used in the ND280 measurements. It will be possible to compare the results with those from ND280 and discuss the cause of differences that we have seen between data and MC as shown in Figure 46 in Chapter 9. The update of the statistics and the binning scheme will increase the precision of the measurements to constrain the neutrino flux and interaction parameters, which are eventually used in the oscillation analysis by T2K. In order to apply the WAGASCI-BabyMIND measurements, we can perform the ND280 and WAGASCI-BabyMIND joint fit analysis to provide better constraints on the flux and interaction parameters. This is further discussed in the next chapter.

13 Application of cross section results to the oscillation analysis

This chapter shows a way to apply cross section results by WAGASCI-BabyMIND detectors to the oscillation analysis. Quantitative studies in terms of an expected increase in T2K's sensitivity are also shown.

13.1 A joint fit of ND280 and WAGASCI-BabyMIND measurements to give better constraints on systematic parameters

The frequentist far detector fit makes use of the near detector constraints on the nuisance parameters. Tighter constraints on the nuisance parameters will give the far detector fit a higher potential to constrain the oscillation parameters. We expect the WAGASCI-BabyMIND measurements will provide additional constraints on the current near detector fit, which may eventually reduce the systematic uncertainties at the far detector analysis. So far we have not utilized the joint fit of ND280 and WAGASCI-BabyMIND in the data analysis because the WAGASCI-BabyMIND measurements are statistically limited. The joint fit analysis is then performed using the simulated SK data instead of the physics data to check the impact of the WAGASCI-BabyMIND samples on the constraints.

The future sensitivity of the joint fit analysis is discussed in this section assuming the statistics currently available for the ND280 measurements and future statistics for the WAGASCI-BabyMIND measurements. The assumed statistics are shown in Table 28. For the WAGASCI-BabyMIND samples, we introduced only muon neutrino samples because we have not established the event selection for anti-muon neutrino samples. In the current T2K's proposal, the accumulated POT will be 7.3×10^{21} at the end of 2027 [68]. The binnings for the WAGASCI-BabyMIND samples are changed to two-dimensional binnings that are different from what was used for the data fit. The two-dimensional binning scheme was determined so that the number of events in each bin is at least around 100 events. The sample classification for the WAGASCI-BabyMIND samples is the same as that in the data fit (Table 15). The ND280 samples and binnings are exactly the same as that used in the oscillation analysis (Figures 23, 24).

To evaluate an improved sensitivity in the oscillation analysis, first, we perform the joint fit to constrain the nuisance parameters. Then, we utilize the resulting central values and the covariance matrix to perform the far detector fit. We use simulated data for both near and far detector fits.

Table 28: The statistics assumed in the sensitivity study for the ND280 and WAGASCI-BabyMIND joint fit analysis. The statistics for the WAGASCI-BabyMIND samples are the expected amount of data assuming T2K continues to take data until 2027.

Detectors	neutrino mode	Statistics (POT [$/10^{21}$])
ND280	neutrino	1.9867
	anti-neutrino	1.1531
WAGASCI-BabyMIND	neutrino	7.3
	anti-neutrino	0

The nuisance parameters for the near detector fit are divided into flux parameters at 1.5 and 2.5 degrees off-axis, neutrino interaction parameters, and the detector systematic parameters. For the priors of the flux parameters, the same covariance matrix as the WAGASCI-BabyMIND

data fit is used for the flux parameters at 1.5 degrees off-axis, and the same matrix as the updated oscillation analysis is used for those at 2.5 degrees off-axis without modifying them or adding another matrix. We do not take into account the correlation between neutrino flux at 1.5 and 2.5 degrees off-axis although they have strong correlations. Regarding the priors of the neutrino interaction parameters and the detector systematic parameters for ND280, the same covariance matrix in the updated oscillation analysis is used. With respect to the detector systematic parameters for the WAGASCI-BabyMIND samples, we adopt the same priors as that used in the cross section measurement with the WAGASCI-BabyMIND detectors.

Figure 78 shows comparisons of the nuisance parameter constraints for the flux at 2.5 degrees off-axis and neutrino interactions with and without the WAGASCI-BabyMIND samples in the near detector fit. For most of the parameters, the impact of the ND280 samples on those constraints is dominant. The constraints on the neutrino flux parameters for muon neutrinos and electron neutrinos are improved by at most 10% thanks to the addition of the WAGASCI-BabyMIND samples. In addition, the constraints on the normalization parameters and the Pion FSI parameters in the neutrino interaction models are improved by around 10 - 30%. The T2K FD cannot measure the final state interactions. We minimize the effect of the mis-reconstruction in the FD by using the Pion FSI parameters. The stronger constraints of these parameters can reduce the systematic uncertainty of the FSI interactions and increase the sensitivity of the oscillation analysis. In addition, as the T2K oscillation analysis includes the $CC1\pi^{\pm}$ samples in both μ and e ring samples, the understanding of the Pion FSI interactions is more and more important.

There are several factors that make these improvements. The dominant effect should come from the increasing statistics used in the near detector fit by combining the both ND280 and the WAGASCI-BabyMIND samples. As the WAGASCI-BabyMIND samples include both $CC0\pi^{\pm}$ and $CC1\pi^{\pm}$ samples, $CC0\pi$ and $CC1\pi$ samples in the ND280 measurements are similar to those samples in the WAGASCI-BabyMIND measurements. There is an effect of the increasing statistics for those samples. According to Figure 78, the impact on the oxygen parameters is larger than that on the carbon parameters. This indicates that the carbon parameters are already constrained by the ND280 samples well whereas there is room to improve the constraints on the oxygen parameters. Thanks to the addition of the WAGASCI-BabyMIND H_2O samples, the sensitivity to the oxygen parameters is increased. The better constraints on the Pion FSI parameters should be explained by the addition of both $CC0\pi^{\pm}$ and $CC1\pi^{\pm}$ samples that are affected by these parameters.

The sensitivity to muon-neutrino flux parameters and an intrinsic nue parameter are increased. This might be due to the strong correlation between flux and interaction parameters. As some of the interaction parameters for neutrinos are better constrained, neutrino flux parameters are also affected. Reducing the errors on the oxygen parameters, in particular the CCQE normalization and 2p2h norm parameters, is important because their 1σ errors are relatively large. The joint fit is promising to improve this situation.
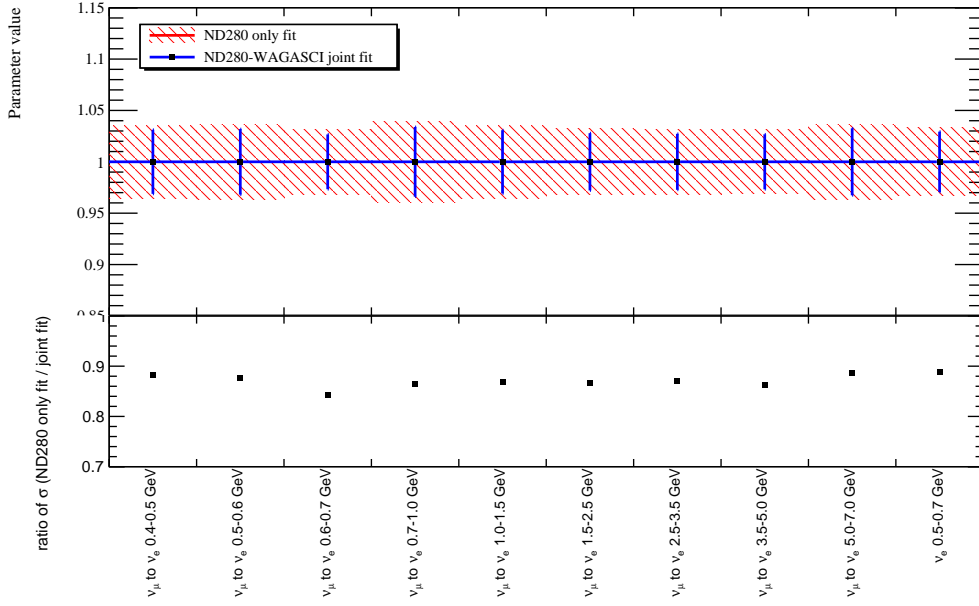
(a) Flux parmeters
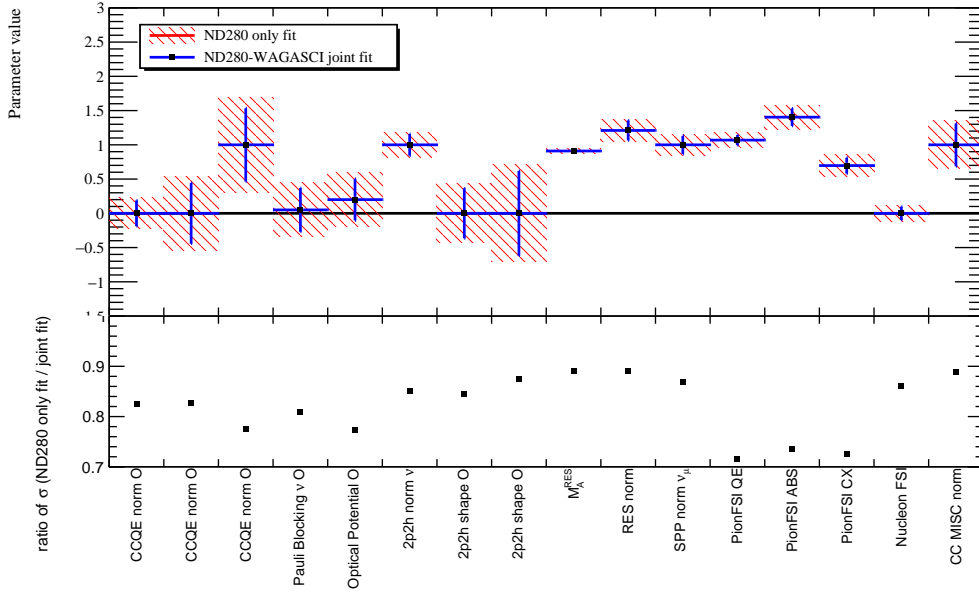
(b) Neutrino interaction parameters

Figure 78: Comparisons of the constraints on the flux parameters (top) and the neutrino interaction parameters (bottom) between with and without the WAGASCI-BabyMIND samples. The abbreviation of "O", "QE", "ABS", and "CX" means "Oxygen", "Quasi Elastic", "Absorption", and "Charge eXchange" respectively. "CC MISC" refers to the charged current diffractive pion production. The plot below the comparison plots shows the fraction of the uncertainties from the joint fit to those from the standalone ND fit.

13.2 A potential improvement in constraints on the oscillation parameters using the updated near detector constraints

In this analysis, we perform the far detector fits by using the ND fit with only the ND280 samples and both ND280 and WAGASCI-BabyMIND samples. Both constraints on the δ_{CP} are compared with each other to see the potential improvement in the oscillation parameters constraints. The MC integrated marginalization method (Section 6.6) is used in the far detector fit. The statistics for the far detector event samples are the same in the oscillation analysis shown in this thesis (Chapter 7). The prior values of the oscillation parameters are shown in Table 29. Here in this study, we only present the results with the reactor constraint on $\sin^2 \theta_{13}$.

Figure 79 shows the comparison of 1σ errors for the reconstructed neutrino energy distributions in the far detector with and without adding the WAGASCI samples in the near detector fit. Overall improvement in 1σ error is very limited, but slight improvements are visible for the samples in the neutrino mode.

Table 29: Prior values for the far detector fit

Parameters	Prior
Δm^2_{21}	$7.53 \times 10^{-5} \, \mathrm{eV}^2/\mathrm{c}^4$
Δm^2_{32} (NH) / $|\Delta m^2_{31}|$ (IH)	$2.494 \times 10^{-3} \, \mathrm{eV}^2/\mathrm{c}^4$
$\sin^2 \theta_{23}$	0.561
$\sin^2 \theta_{12}$ ($\sin^2 2\theta_{12}$)	0.307 (0.851)
$\sin^2 \theta_{13}$ ($\sin^2 2\theta_{13}$)	0.0220 (0.0861)
δ_{CP}	-1.601
Mass ordering	Normal

(a) ν_μ 1-Ring

(b) $\overline{\nu}_\mu$ 1-Ring

(c) ν_e 1-Ring

(d) $\overline{\nu}_e$ 1-Ring

(e) ν_e CC1π^+ 1-Ring

(f) ν_μ CC1π^+
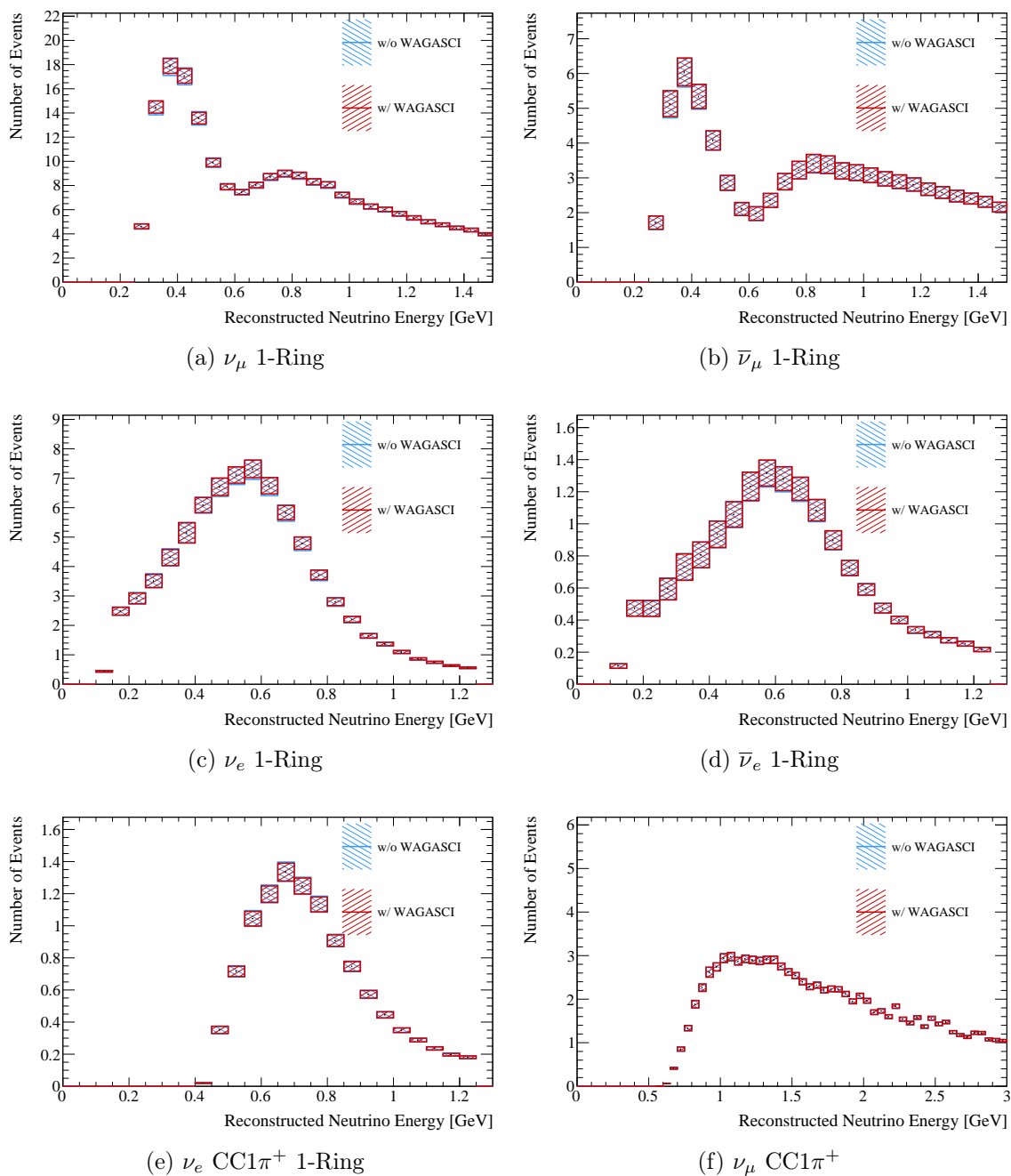
Figure 79: Comparisons of 1σ errors for the reconstructed neutrino energy distributions in the far detector with (red band) or without (blue band) using the WAGASCI samples in the near detector fit. The error bands represent 1σ error from flux parameters and neutrino interaction parameters.

The results of the one-dimensional contours on δ_{CP} with the reactor constraint on $\sin^2 \theta_{13}$ are shown in Figure 80. There is no visible improvement in the constraints on the oscillation parameter as expected from the error band plots shown in Figure 79.

One of the possible causes of the weak impact on the far detector fit is that the correlations between flux parameters at 1.5 degrees off-axis and 2.5 degrees off-axis were not taken into account in the sensitivity study. The flux and cross section parameters have strong correlations in T2K, which was clearly visible in the oscillation analysis. Once the correlations in the flux parameters are fully treated in the near and far detector fit, the sensitivity is expected to be improved. In addition, we assume the statistical update only for the WAGASCI-BabyMIND muon-neutrino samples in the near detector fit. There are several neutrino interaction parameters in the ND fit that are sensitive to only anti-muon neutrino samples, such as Pauli Blocking oxygen $\overline{\nu}_\mu$ and 2p2h norm oxygen $\overline{\nu}_\mu$ parameters. The current result did not have any improvement on these parameters. When the constraints on those parameters are improved after adding anti-muon neutrino samples, the constraints of the oscillation parameters are expected to be improved. On the one hand, we added both WAGASCI CC0$\pi^\pm$ and CC1$\pi^\pm$ samples to the near detector fit. When other samples such as the charged current multi-pion samples are added, the constraints on the nuisance parameters will be improved.

It is imperative for the T2K experiment to continue to take data in order to get closed to the discovery of the CP-violation. At the same time, it is important to reduce the systematic uncertainty to achieve the discovery earlier. In the current T2K analysis, the systematic error from the uncertainty of the neutrino interactions has a large contribution. In this thesis, a new way of improving the constraints on the neutrino interaction parameters was introduced. The expected improvement is not large. Nevertheless, we have opened a path towards incorporating results from the new detector complex into the oscillation analysis, leveraging a different mean neutrino energy from that seen at the conventional near detectors. There is a possibility that it will help T2K to discover the CP violation, determine the neutrino mass ordering, and solve the octant problem.
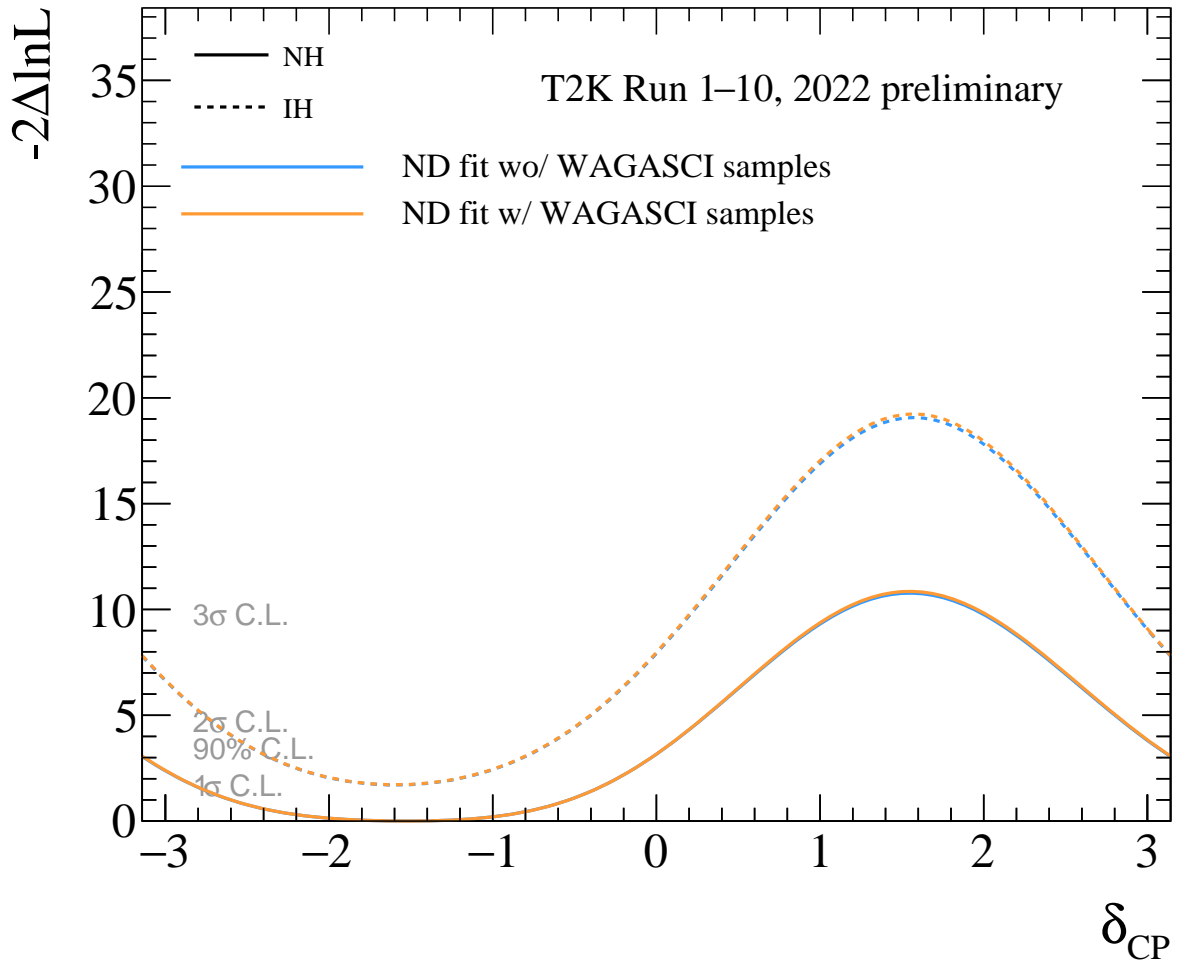
Figure 80: The contours on δ_{CP} by the far detector fit using the near detector constraints with (orange) and without (blue) the WAGASCI samples. The contour in orange almost overlays the contour in blue.

Part IV

Summary

14 Conclusion

One of the unresolved problems in physics is the matter-antimatter asymmetry in the universe. There has been no solid answer to this question. One promising solution called the leptogenesis scenario was proposed, where the baryon asymmetry has been generated originally by lepton asymmetry. One of the leptogenesis scenarios assumes the effect of CP violation is visible in neutrino oscillations. We have not confirmed this CP violation though we have already verified the neutrino oscillations. Observing CP violation in the neutrino oscillations has an important role in verifying this leptogenesis scenario. We need precise measurements of neutrino oscillation parameters to discover CP violation. In this thesis, we tackled the CP violation. We also considered the neutrino mass ordering and the octant problem.

We measured the neutrino oscillations in the T2K experiment, which is a long-baseline neutrino oscillation experiment. T2K is sensitive to the CP-violating phase (δ_{CP}) and other neutrino oscillation parameters such as Δm_{32}^2, $\sin^2 \theta_{23}$, and $\sin^2 \theta_{13}$.

The analysis has a statistical update, which corresponds to 4.726×10^{20} POT (approximately 30% increase) in the neutrino mode. We maintain the neutrino beam directed to the T2K far detector with the muon monitor (MUMON). The profile measurements with MUMON confirmed the good quality of the neutrino beam for 99.996% of all the spills collected in the period. For updates on the analysis, we split samples in the near-detector fit using the proton multiplicity and photon detection in addition to updates on the neutrino flux and interaction models. In addition, a new sample (ν_μ CC1π^+) in the far detector fit was added. Adding the new sample increased the statistics of neutrino events in the neutrino mode by 30%.

CP conservation was rejected at the 90% confidence level. The 2σ confidence interval for δ_{CP} was [-π, -0.29] $\cup$ [3.04, π] in the normal ordering case. The constraint on δ_{CP} was stronger than our sensitivity, but consistent within the statistical fluctuation. The 1σ confidence interval on $\sin^2 \theta_{23}$ was [0.460, 0.491] $\cup$ [0.526, 0.578] for the normal ordering. Both octants were allowed within the 1σ confidence intervals in this analysis. The upper octant is weakly preferred with a Bayes factor of 3.0. The result of Δm_{32}^2 using constraints on $\sin^2 2\theta_{13}$ from the reactor experiments is $2.506^{+0.047}_{-0.059} \times 10^{-3}$ eV^2/c^4 assuming the normal ordering and $|\Delta m_{31}^2|$ was $2.474^{+0.050}_{-0.056} \times 10^{-3}$ eV^2/c^4 assuming the inverted ordering. The normal ordering was preferred with a Bayes factor of 2.8, which was a weak preference. The large impact on the constraints on the oscillation parameters was the combination of the updates on the neutrino interaction models and new samples in the near detector fits.

We do not discover CP violation in the leptonic sector in this analysis. To discover the CP violation, we primarily need more statistics on neutrino oscillations because the current analysis is statistically limited. When the statistical uncertainty is comparable to the systematic uncertainty, the reduction in systematic uncertainties is also important to achieve T2K's goal. The reduction in the systematic uncertainty coming from the uncertainty of neutrino interaction models is important for T2K.

We performed cross section measurements to provide inputs to understand interaction models more precisely with the newly installed detector complex at J-PARC, called WAGASCI-BabyMIND. We defined the signal as charged current muon neutrino interactions with no charged pions in the final state. We extracted the integrated cross section and differential cross section

as a function of muon momentum and cosine of muon angle on the CH and H_2O targets with a peak neutrino energy of 0.86 GeV. Both integrated and differential cross section results were mostly consistent with our MC model. The integrated cross section in limited phase space ($P_\mu > 300$ MeV/c, $\cos\theta_\mu > 0.34$) were measured to be

$$\sigma_{\text{tot},H_2O} = 1.636 \pm 0.370 \ (10^{-39} \ \text{cm}^2/\text{nucleon}) \tag{14.1}$$

$$\sigma_{\text{tot,CH}} = 1.432 \pm 0.355 \ (10^{-39} \ \text{cm}^2/\text{nucleon}). \tag{14.2}$$

The MC predicted cross sections were 1.165 for H_2O and 1.197 for CH with the same units. The pulled up integrated cross sections are due to the changes in the signal detection efficiency on both targets, which are driven by the decreasing parameters of MaRES and MaCCQE parameters. The differential cross section on the H_2O target in the momentum range of (0.3 - 0.5 GeV/c) and that in the range of the cosine of the angle (0.91 - 0.94) deviated from the MC prediction by more than 1 sigma but less than 2 sigma. We then compared the results with the predictions of other neutrino interaction models. Due to the limited statistics of the neutrino interaction samples, this analysis was unable to discern between these models. We continue the operation of WAGASCI-BabyMIND detectors, which is expected to provide more statistics to pin down a proper interaction model describing data.

Finally, we considered the application of measurements by the WAGASCI-BabyMIND detectors to the T2K oscillation analysis. A joint fit of the ND280 and the WAGASCI-BabyMIND detectors was performed assuming future statistics with simulated data. We aimed for additional constraints on the flux and neutrino interaction parameters. According to the joint fit results, better constraints on these parameters were visible. The size of the improvements was at most 30% with respect to the fit without adding WAGASCI-BabyMIND samples. The fit results were then utilized in the far detector analysis. The impact of the joint fit on the oscillation parameter constraints was modest in the current fit configuration. Nevertheless we have opened a path towards incorporating results from the new detector complex to the oscillation analysis, leveraging a different mean neutrino energy from that seen at the conventional near detectors.

In this thesis we have searched for leptonic CP violation using measurements of neutrino oscillations with the T2K experiment and the results indicate that CP is violated at the 90% confidence level. To achieve more precise measurements, this thesis also proposed a novel approach to reducing systematic uncertainties in the neutrino interaction and flux models using measurements of neutrino interactions from T2K's new detector complex. We have established a method to apply these results to T2K neutrino oscillation analysis which may offer a valuable method to enhance T2K's potential to discover leptonic CP violation in future.

Appendices

A   PartII: The definition of fitting parameters in the ND fit

A.1   Neutrino flux parameters

The neutrino flux parameters are divided into ND and FD parts, each of which consists of 25×2 (FHC and RHC) parameters. The followings are the bin edges for the neutrino mode.

FHC ν_μ + RHC $\overline{\nu}_\mu$
   E_ν^{true} (GeV): 0, 0.4, 0.5, 0.6, 0.7, 1, 1.5, 2.5, 3.5, 5, 7, 30

FHC $\overline{\nu}_\mu$ + RHC ν_μ
   E_ν^{true} (GeV): 0, 0.7, 1, 1.5, 2.5, 30

FHC ν_e + RHC $\overline{\nu}_e$
   E_ν^{true} (GeV): 0, 0.5, 0.7, 0.8, 1.5, 2.5, 4.0, 30

FHC $\overline{\nu}_e$ + RHC ν_e
   E_ν^{true} (GeV): 0, 2.5, 30

   The total flux parameters consist of "FHC ND", "RHC ND", "FHC FD", and "RHC FD". The total number of parameters is 100.

A.2   Neutrino interaction parameters

The neutrino interaction parameters in the ND fit are divided into 75 parameters in total, which are summarized in Table 30.

Table 30: The neutrino interaction parameters used in the ND fit. MF: Mean Field, SPP: Single Pion Production.

Number	Parameter name	Interaction	Comment
0	FEFQE	Any π	PionFSI QE, low momentum
1	FEFQEH	Any π	PionFSI QE, high momentum
2	FEFINEL	Any π	PionFSI pion production
3	FEFABS	Any π	PionFSI pion absorption
4	FEFCX	Any π	PionFSI charge exchange, low momentum
5	FEFCXH	Any π	PionFSI charge exchange, high momentum
6	Nucleon FSI	Any π	Nucelon FSI
7	MAQE	CCQE	Axial vector mass in the CCQE interactions
8	Q2 norm 5	CCQE	Q^2 normalization (0.25 to 0.5 GeV^2/c^2)
9	Q2 norm 6	CCQE	Q^2 normalization (0.5 to 1.0 GeV^2/c^2)
10	Q2 norm 7	CCQE	Q^2 normalization (above 1.0 GeV^2/c^2)
11	PShell MF Norm C	CCQE	Normalization for P shell MF contributions
12	SShell MF Norm C	CCQE	Normalization for S shell MF contributions
13	SRC Norm C	SPP	Normalization for the Short-Range Correlated nucleons (SRC) on the carbon target
14	PShell MF PMissShape C	CCQE	Change kinematics for P shell MF contributions
15	SShell MF PMissShape C	CCQE	Change kinematics for S shell MF contributions
16	P1 2Shell MF Norm O	CCQE	Normalization for P1/2 shell MF contributions
17	P3 2Shell MF Norm O	CCQE	Normalization for P3/2 shell MF contributions
18	SShell MF Norm O	CCQE	Normalization for S Shell MF contributions
19	SRC Norm O	SPP	Normalization for the Short-Range Correlated nucleons (SRC) on the oxygen target
20	P1 2Shell MF PMissShape O	CCQE	Change shape of missing momentum distribution for P1/2 shell MF contributions
21	P3 2Shell MF PMissShape O	CCQE	Change shape of missing momentum distribution for P3/2 shell MF contributions
22	SShell MF PMissShape O	CCQE	Change shape of missing momentum distribution for S shell MF contributions
23	Pauli Blocking C nu	CCQE	Change the Fermi momentum, k_F on the carbon target for ν interactions
24	Pauli Blocking O nu	CCQE	Change the Fermi momentum, k_F on the oxygen target for ν interactions
25	Pauli Blocking C nubar	CCQE	Change the Fermi momentum, k_F on the carbon target for $\overline{\nu}$ interactions
26	Pauli Blocking O nubar	CCQE	Change the Fermi momentum, k_F on the oxygen target for $\overline{\nu}$ interactions
27	Optical Potential C	CCQE	Normalization for q_0, q_3 parameters for the carbon target
28	Optical Potential O	CCQE	Normalization for q_0, q_3 parameters for the oxygen target
29	2p2h norm nu	2p2h	Normalization for 2p2h ν interaction

30	2p2h norm nubar	2p2h	Normalization for 2p2h $\overline{\nu}$ interaction
31	2p2h norm CtoO	2p2h	Normalization for 2p2h ν interaction covering difference between carbon and oxygen
32	2p2h Edep lowEnu	2p2h	Neutrino energy-dependent difference in the region of $E_\nu < 600$ MeV for ν
33	2p2h Edep highEnu	2p2h	Neutrino energy-dependent difference in the region of $E_\nu > 600$ MeV for ν
34	2p2h Edep lowEnubar	2p2h	Neutrino energy-dependent difference in the region of $E_\nu < 600$ MeV for $\overline{\nu}$
35	2p2h Edep highEnubar	2p2h	Neutrino energy-dependent difference in the region of $E_\nu > 600$ MeV for $\overline{\nu}$
36	PNNN Shape	2p2h	Change in ratio of "pn" to "nn" pairs
37	2p2h shape C np	2p2h	Changing 2p2h kinematics on the carbon target from np contributions
38	2p2h shape C NN	2p2h	Changing 2p2h kinematics on the carbon target from NN contributions
39	2p2h shape O np	2p2h	Changing 2p2h kinematics on the oxygen target from np contributions
40	2p2h shape O NN	2p2h	Changing 2p2h kinematics on the oxygen target from NN contributions
41	CA5	SPP	Form factor to parametrize MARES
42	MARES	SPP	Axial vector mass in the resonance interactions
43	ISO BKG LowPPi	SPP	The iso-spin 1/2 backgrounds, low momentum pion
44	ISO BKG	SPP	The iso-spin 1/2 backgrounds,
45	RES Eb C numu	SPP	Binding energy in resonance interactions on the carbon target for ν interactions
46	RES Eb O numu	SPP	Binding energy in resonance interactions on the oxygen target for ν interactions
47	RES Eb C numubar	SPP	Binding energy in resonance interactions on the carbon target for $\overline{\nu}$ interactions
48	RES Eb O numubar	SPP	Binding energy in resonance interactions on the oxygen target for $\overline{\nu}$ interactions
49	RS Delta Decay	SPP	Rein-Sehgal (RS), delta resonance decay
50	SPP Pi0Norm numu	SPP	Normalization for SPP (neutral pion) in ν interactions
51	SPP Pi0Norm numubar	SPP	Normalization for SPP (neutral pion) in $\overline{\nu}$ interactions
52	CC Coh C	CCCoherent	Normalization for CC coherent interaction on the carbon target
53	CC Coh O	CCCoherent	Normalization for CC coherent interaction on the oxygen target
54	MPi Multi TotXSec	Multipi	Multi-pion total cross section (TotXSec)
55	Mpi BY Vector	Multipi	Bodek-Yang (BY) corrections for vector part contributions
56	Mpi BY Axial	Multipi	Bodek-Yang (BY) corrections for axial part contributions
57	Mpi Multi Shape	Multipi	Change kinematics for Multi pion interactions
58	CC BY DIS	DIS	Bodek-Yang (BY) corrections for CC DIS
59	CC DIS MultiPi Norm Nu	DIS	Normalization for CCDIS and CCMultiPi in ν interactions
60	CC DIS MultiPi Norm Nubar	DIS	Normalization for CCDIS and CCMultiPi in $\overline{\nu}$ interactions
61	CC Misc	Misc	Normalization for CC diffractive pion production
62	NC Coh	NCCoherent	Normalization for NC coherent interactions
63	NC 1gamma	NC 1gamma	Normalization for NC 1gamma interactions
64	NC other near	NC other	Normalization for NC other interactions for ND
65	NC other far	NC other	Normalization for NC other interactions for FD
66	CC norm nu	CC	Normalization for all the ν_μ CC interactions
67	CC norm nubar	CC	Normalization for all the $\overline{\nu}_\mu$ CC interactions
68	nue numu	–	Normalization between ν_e and ν_μ cross sections
69	nuebar numubar	–	Normalization between $\overline{\nu}_e$ and $\overline{\nu}_\mu$ cross sections
70	Eb bin C nu	–	Binding energy (Eb) for carbon in ν interactions
71	Eb bin C nubar	–	Binding energy (Eb) for carbon in $\overline{\nu}$ interactions
72	Eb bin O nu	–	Binding energy (Eb) for oxygen in ν interactions
73	Eb bin O nubar	–	Binding energy (Eb) for oxygen in $\overline{\nu}$ interactions
74	Eb alpha	–	$\Delta E_{\mathrm{rmv}} = \delta + \alpha(mq_3 + c)$, where ΔE_{rmv} is the removal energy

B PartII: Fitting method for Bayesian Markov Chain Monte Carlo

B.1 Fitting algorithm

Bayesian analysis is one of the statistical approaches to exploring the most probable parameter spaces to describe data with a set of prior knowledge. The probability density after the fit (so-called posterior probability, $P(\boldsymbol{\theta}|D)$) is expressed by

$$P(\boldsymbol{\theta}|D) \propto \mathcal{L}(D|\boldsymbol{\theta}) \times \pi(\boldsymbol{\theta}), \tag{B.1}$$

where $\boldsymbol{\theta}$ is a vector consisting of both systematic and oscillation parameters, $\pi(\boldsymbol{\theta})$ is a likelihood, D is data and $\mathcal{L}(D|\boldsymbol{\theta})$ stands for the likelihood. The analysis addresses about 750 parameters from each sample at ND and FD, systematic and oscillation parameters. An analytical calculation would not be feasible. Instead, this analysis introduced Markov Chain Monte Carlo to evaluate the posterior probability. The algorithm is the Metropolis-Hastings one [169] to generate a set of parameters. [55] The key part of the MCMC method is the acceptance function, which is expressed in the Metropolis-Hastings algorithm by

$$\alpha = \min\left[1, \frac{p(\boldsymbol{\theta}_{t+1})}{p(\boldsymbol{\theta}_t)}\right], \tag{B.2}$$

where t is the step number and the function p refers to the target probability function. A parameter $\boldsymbol{\theta}_t$, except $\boldsymbol{\theta}_0$, is selected by a proposal function ($q(\boldsymbol{\theta}_{t+1}|\boldsymbol{\theta}_t)$). One of the features of the Metropolis-Hastings algorithm is the acceptance function does not depend on the proposal function explicitly. Therefore, almost any proposal function can be chosen. The basic procedure of the MCMC is to propose a parameter, calculate the acceptance function, decide on a parameter set [56] and repeat this round of steps. In order to make the parameter sets obtained by these iterations follow the posterior distribution, we defined the probability function as

$$p(\boldsymbol{\theta}_t) \equiv \mathcal{L}(D|\boldsymbol{\theta_t}) \times \pi(\boldsymbol{\theta_t}). \tag{B.3}$$

Although this analysis has to cope with about 750 parameters in the fit, one-dimensional or two-dimensional posterior distributions on oscillation parameters would be important to see their constraints. We then use a marginalization method by integrating all the nuisance parameters. The marginal likelihood is

$$\mathcal{L}_{\mathrm{m}}(D|\boldsymbol{\phi}) = \int \mathcal{L}(D|\boldsymbol{\phi},\boldsymbol{\psi}) \times \pi(\boldsymbol{\psi})d\boldsymbol{\psi}, \tag{B.4}$$

where $\boldsymbol{\phi}$ ($\boldsymbol{\psi}$) is a set of parameters of interest (nuisance parameters). The output of the MCMC is the plenty number of sets of parameters to follow the most probable posterior distributions to describe the data. They in turn can be used to determine the regions that will have a given probability of containing the true value of a parameter. The credible regions are given by solving

$$1 - \alpha = \int_{\phi_{\mathrm{lower\ bound}}}^{\phi_{\mathrm{upper\ bound}}} p(\phi|D)d\phi. \tag{B.5}$$

---

[55]The orthodox algorithm would be the accept-rejection algorithm. This is not suitable for this analysis because of the low efficiency to accept a proposed parameter, which originates from a large number of dimensions.

[56]$\boldsymbol{\theta}_t$ if the proposed parameter is rejected, otherwise, $\boldsymbol{\theta}_{t+1}$

Equation B.5 assumes the case of one-dimension as the parameter of interest. The credible region is then defined by "$(\phi_{\text{lower bound}}, \phi_{\text{upper bound}})$" given the credibility, α. The best-fit values are naturally transcended by this marginalization of likelihood. The most probable value of each oscillation parameter in two-dimensional parameter spaces (Δm^2_{32}-$\sin^2\theta_{23}$ or $\sin^2\theta_{13}$-δ_{CP}) is assigned to the best fit.

B.2 Comparison of two methods

Both analyses share a few common parts in their fitting procedures. Firstly, they limit target neutrino flavors. The neutrino oscillations involving ν_τ and $\overline{\nu}_\tau$ are negligible under the T2K neutrino flux because most of them cannot undergo CC interactions due to the small contribution of the high-energy tail. In addition, $\nu_e \rightarrow \nu_\mu$ and the corresponding anti-neutrino oscillation are also ignorable because of the combination of small oscillation probability and tiny contribution from ν_e in the flux. Otherwise, all combinations of neutrino oscillations are considered. Secondly, they share the common prior values for oscillation parameters. Both $\sin^2 2\theta_{13}$ and $\sin^2 2\theta_{23}$ have a uniform distribution of (0, 1). The prior value of δ_{CP} is the uniform distribution of ($-\pi$, π). Both mass difference parameters are uniformly distributed from 0 to ∞. The prior value of $\sin^2 2\theta_{13}$ is based on the way of reporting the results. When the T2K experiment reports its standalone analysis, the flat prior (0, 1) is used. When the T2K results are combined with the reactor experiment, the prior is assumed to be the gaussian distribution whose mean and error correspond to the world-average constraints of $\sin^2 2\theta_{13}$. This analysis uses the PDG2019 result [170] (the best-fit value is 0.0853 and the 1σ error is 0.0027).

Besides each algorithm, a few differences are acknowledged between the two analysis approaches. The MCMC analysis is capable of simultaneous fits using both ND and FD analysis samples, whilst the grid-scan approach relies on the ND fit for the constraints on systematic parameters. It results in a difference in the treatment of systematic parameters. On top of that, the binning scheme depends on each framework. The MCMC analysis uses the reconstructed energy of neutrino for μ-like samples while e-like samples are binned by the neutrino energy and lepton angle. On the other hand, the grid-scan method uses the reconstructed energy of neutrino and lepton angle for μ-like samples while e-like samples are binned by the lepton angle and momentum.

The difference in systematic parameter constraints is not expected to end up with a significant difference in the constraints on oscillation parameters because the two fit results from Minuite2 and the MCMC methods are mostly consistent with each other. The binning differences might result in a difference in parameter constraints. However, we have not seen a significant difference in the constraints of oscillation parameters (See Appendix D for details.).

C PartII: Bias studies for the neutrino oscillation analysis

In order to test the robustness of the fits, we extract oscillation contours using alternative simulated data sets and check the potential biases stemming from our interaction models. These bias studies investigate the potential impact of alternative interaction models and data-driven tunes at both ND and FD.

We determine the size of the bias, and criteria for adding additional smearing to data contours based on the result, as follows:

1. A bias to the center of the 2σ confidence interval is calculated. We set the threshold of the shift to 50% relative to the size of the 1σ interval.

2. A new requirement on the change in size (total integrated area) of the confidence intervals including both the statistical and systematic uncertainties is included. We set the threshold of the change to 10%.

3. For $\delta_{\rm CP}$, the bias in the contours is used to assess the impact on the $N\sigma$ CP violation boundaries from the data fit.

Criteria 1 and 2 are applied to $\sin^2\theta_{23}$ and Δm^2_{23}. We used a similar suite of data sets used in the published results [67]. We added several data sets associated with the new FD sample, ν_μ CC1π^+. The new data sets that alter the pion-production modes, such as using the Martini 1π model [125, 171] are included to validate the analysis with the new FD sample. Additional data sets to investigate nuclear modeling effects, such as Hartree-Fock Continuum Random Phase Approximation (HF CRPA) [172, 173], are included to validate the new proton-tagged ND samples.

In total 19 alternative data sets were analyzed and the new HF CRPA alteration showed the most significant impact as presented in Table 31. Since the bias on Δm^2_{23} for the HF CRPA and non-CCQE data sets is found to be larger than our criteria, we smeared the Δm^2_{23} contour, which has a near-parabolic likelihood, after the data fit using the quadrature sum of all data sets ($\Delta m^2_{32} = 3.1 \times 10^{-5}$ eV^2). No other actions are taken since criteria 2 and 3 are satisfied by all alternative data sets. The results of 2 and 3 are shown in Table 31 and Table 32, respectively.

Table 31: Differences in the oscillation parameter constraints observed in the five alternative data sets with the largest effect. The bias is calculated as the shift to the center of the 2σ confidence interval relative to their total and systematic uncertainties. The simulated datasets are produced based on the nominal oscillation parameters ($\Delta m_{21}^2 = 7.53 \times 10^{-5} \text{eV}^2/\text{c}^4$, $\Delta m_{32}^2 = 2.494 \times 10^{-3} \text{eV}^2/\text{c}^4$, $\sin^2 \theta_{12} = 0.307$, $\sin^2 \theta_{13} = 0.0220$, $\sin^2 \theta_{23} = 0.561$, $\delta_{\text{CP}} = -1.601$).

Simulated data set	Type	$\sin \theta_{23}$	Δm_{32}^2	δ_{CP}	Ref.
	Total	-0.5%	-9.5%	-0.5%	
CCQE z-exp high	Syst.	-1.0%	-24.1%	-2.2%	
	Size	-1.8%	-5.4%	-1.9%	
	Total	-11.7%	33.8%	-2.8%	
HF CRPA*	Syst.	-25.1%	84.9%	-11.2%	[172, 173]
	Size	2.0%	-5.4%	1.0%	
	Total	-1.5%	-7.3%	-0.4%	
Martini 1π	Syst.	-3.2%	-18.5%	-1.7%	[125, 171]
	Size	-0.2%	-1.0%	2.0%	
	Total	4.9%	-30.0%	-0.1%	
Non-CCQE	Syst.	10.4%	-76.3%	-0.5%	
	Size	3.0%	-0.1%	-3.0%	
	Total	-4.83%	20.3%	0.47%	
Pion SI	Syst.	-10.1%	51.6%	2.13%	
	Size	$< 1\%$	-0.6%	3%	

Table 32: Shifts of 90% confidence interval boundaries of δ_{CP} in radians derived in each data set. The values in the top row are the lower and upper boundaries of the 90% allowed interval derived from the data fit. The values for the simulated studies are the difference in the boundaries when the effects of the simulated datasets are taken into account.

Alternative data sets	Change to 90% C.L. of δ_{CP}	
	-3.10	-0.45
CCQE z-exp high	0.01	-0.01
HF CRPA	-0.03	-0.03
Martini 1π	-0.02	0.01
Non-CCQE	0.05	-0.05
Pion SI	-0.03	0.05

D PartII: Impacts of the binning variables on the oscillation analysis

It should be worth noting here our primary binning scheme is p_l–θ for the 1 Ring e samples, E_{rec}–θ for the 1Ring μ samples, and E_{rec} for the ν_μ CC1π^+. We present data-fit results with different sets of the binning scheme from the nominal one. One of the reasons why we show the data-fit results with the different binning from the primary one is to disentangle the two main differences to the Bayesian results. The fits with the different binning schemes are not to be considered the final results but alternative fits to study the impact of binning differences for the cross check with the other fitter.

D.1 Best-fit results with E_{rec}–θ binning for the e samples, E_{rec} binning for the μ samples

Table 33 shows the best fit results with this alternative binning. Compared to the main results from our fitter shown in Table 33, there are no major differences seen except δ_{CP} best fit values for the normal ordering being slightly shifted to lower.

Table 33: Results of the fit to the T2K run 1–10 data using E_{rec}–θ for the e-like samples, E_{rec} for the μ-like samples. They are not considered to be the main results in this analysis.

Parameter	Best fit			
Data	T2K only		T2K + reactor	
Mass ordering	Normal	Inverted	Normal	Inverted
$\sin^2(2\theta_{13})$	0.101	0.109	0.0861	0.0864
$\sin^2(\theta_{13})$	25.9×10^{-3}	28.0×10^{-3}	22.0×10^{-3}	22.1×10^{-3}
δ_{CP}	-2.37	-1.57	-2.31	-1.30
Δm^2_{32} (NH)/$|\Delta m^2_{31}|$ (IH) [eV^2/c^4]	2.450×10^{-3}	2.463×10^{-3}	2.500×10^{-3}	2.468×10^{-3}
$\sin^2(\theta_{23})$	0.473	0.472	0.552	0.553
$-2\ln L$	570.459	571.042	570.54	571.158
$-2\Delta\ln L$	0	0.583	0	0.618

D.2 Comparisons of $\Delta\chi^2$ distributions and fixed $\Delta\chi^2$ confidence regions with E_{rec}–θ binning for the e-like samples, E_{rec} binning for the μ-like samples

Comparisons of the 1D and 2D data-fit contours with E_{rec} binning for the μ-like samples and E_{rec}–θ binning for the e-like samples are shown in Figs. 81–88.

As expected, no large change is observed for $\sin^2\theta_{13}$ and δ_{CP}. However, the E_{rec}–θ binning for the μ-like samples have relatively large effects on $\sin^2\theta_{23}$ that are to move away from maximal mixing and give less preference on the inverted mass ordering.

(a) without the reactor constraint   (b) with the reactor constraint
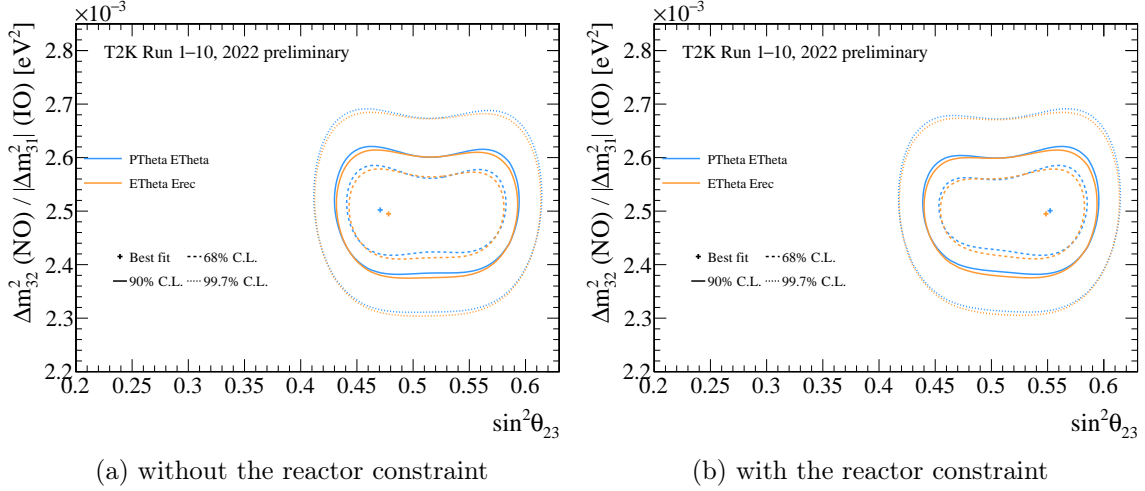
Figure 81: Comparisons of data-fit 2D confidence level contours in Δm_{32}^2 vs. $\sin^2 \theta_{23}$ in normal ordering between (p_l–θ (e samples) + E_{rec}–θ (μ samples)) and (E_{rec}–θ (e samples) + E_{rec} (μ samples)) binning variables. A smearing factor (3.100×10^{-5} [eV^2]) on Δm_{32}^2 is applied based on the bias studies. For the results without the reactor constraint, the contours were produced with 1M throws instead of 100k throws to reduce the errors coming from the number of throws.

(a) without the reactor constraint   (b) with the reactor constraint
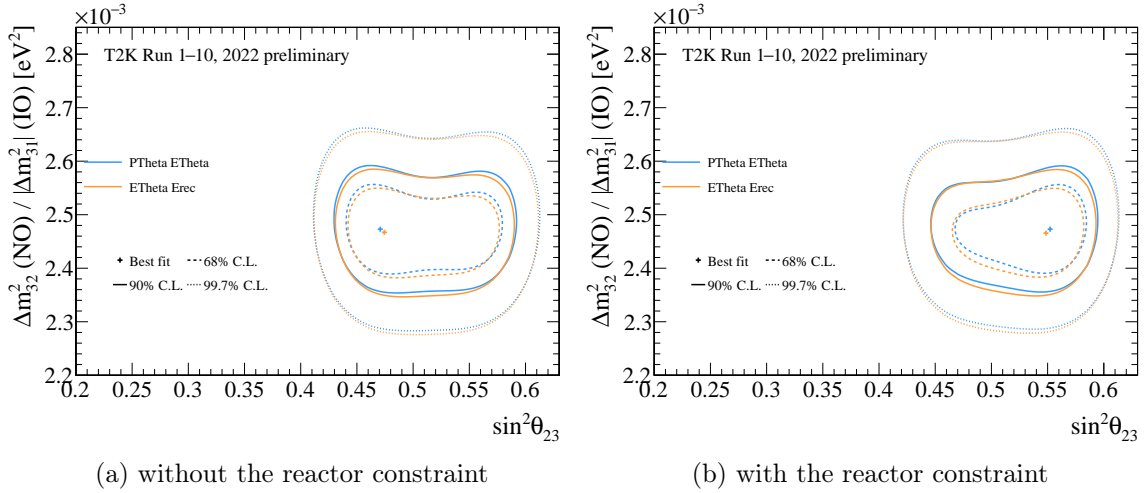
Figure 82: Comparisons of data-fit 2D confidence level contours in $|\Delta m_{31}^2|$ vs. $\sin^2 \theta_{23}$ in inverted ordering between (p_l–θ (e samples) + E_{rec}–θ (μ samples)) and (E_{rec}–θ (e samples) + E_{rec} (μ samples)) binning variables. A smearing factor (3.100×10^{-5} [eV^2]) on Δm_{32}^2 is applied based on the bias studies. For the results without the reactor constraint, the contours were produced with 1M throws instead of 100k throws to reduce the errors coming from the number of throws.

(a) without the reactor constraint

(b) with the reactor constraint
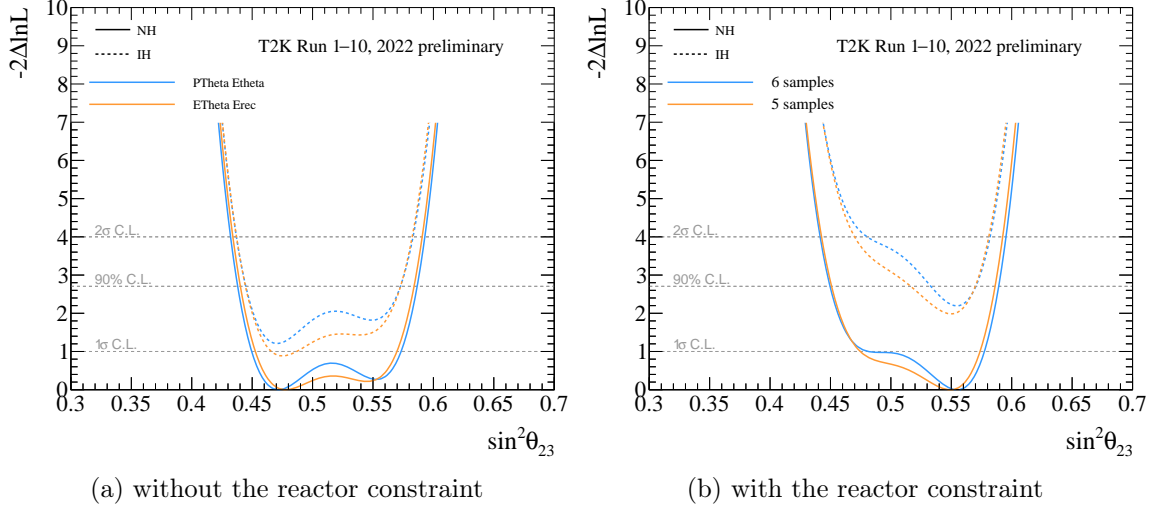
Figure 83: Comparisons of data-fit 1D $\Delta\chi^2$ in $\sin^2\theta_{23}$ between (p_l–θ (e samples) + E_{rec}–θ (μ samples)) and (E_{rec}–θ (e samples) + E_{rec} (μ samples)) binning variables. For the results without the reactor constraint, the contours were produced with 1M throws instead of 100k throws to reduce the errors coming from the number of throws.

(a) without the reactor constraint

(b) with the reactor constraint
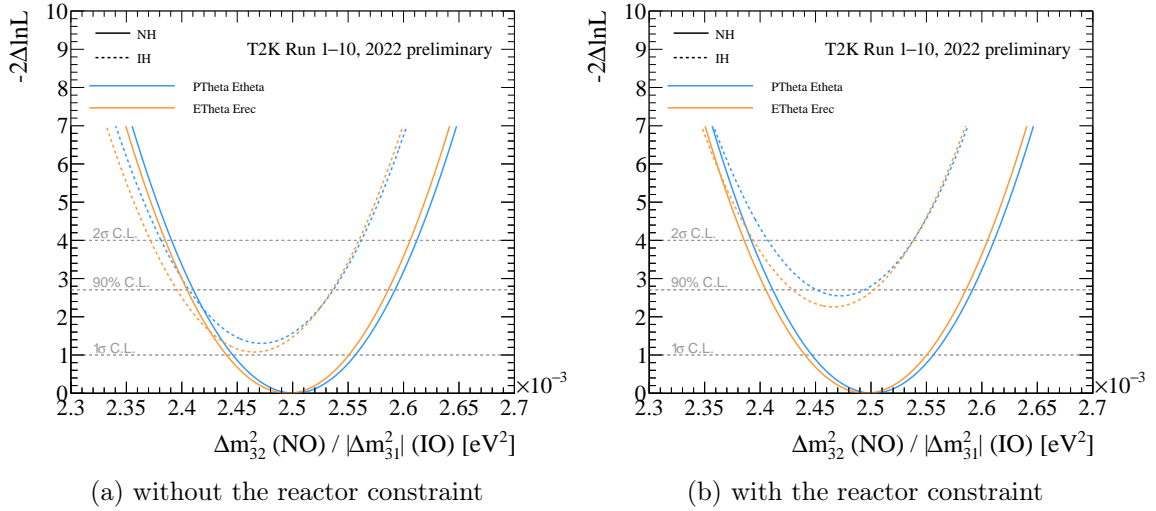
Figure 84: Comparisons of data-fit 1D $\Delta\chi^2$ in Δm^2_{32} ($|\Delta m^2_{31}|$ for inverted between (p_l–θ (e samples) + E_{rec}–θ (μ samples)) and (E_{rec}–θ (e samples) + E_{rec} (μ samples)) binning variables. A smearing factor (3.100×10^{-5} [eV^2]) on Δm^2_{32} is applied based on the bias studies. For the results without the reactor constraint, the contours were produced with 1M throws instead of 100k throws to reduce the errors coming from the throws.

(a) without the reactor constraint

(b) with the reactor constraint
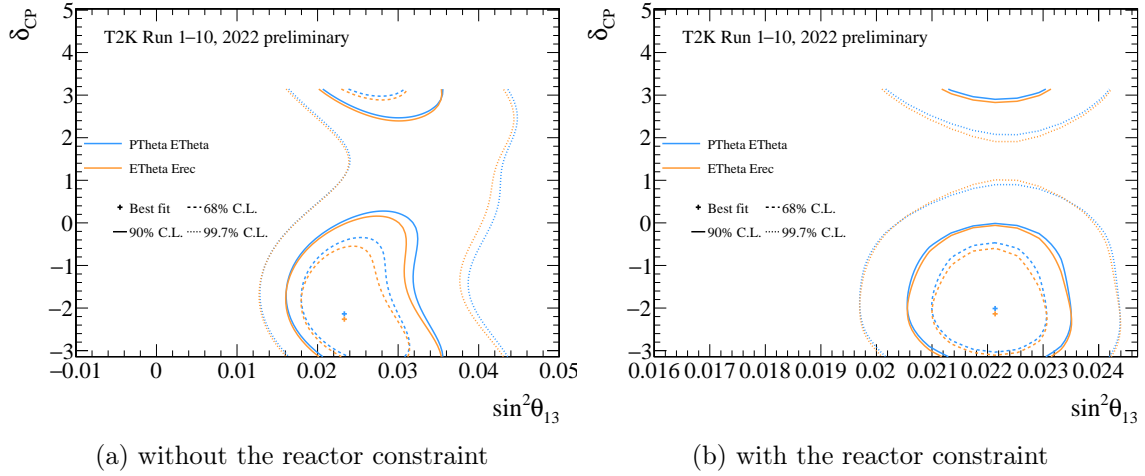
Figure 85: Comparisons of data-fit 2D confidence level contours in δ_{CP} vs. $\sin^2\theta_{13}$ in normal ordering between (p_l–θ (e samples) + E_{rec}–θ (μ samples)) and (E_{rec}–θ (e samples) + E_{rec} (μ samples)) binning variables. For the results without the reactor constraint, the contours were produced with 1M throws instead of 100k throws to reduce the errors coming from the number of throws.

(a) without the reactor constraint

(b) with the reactor constraint
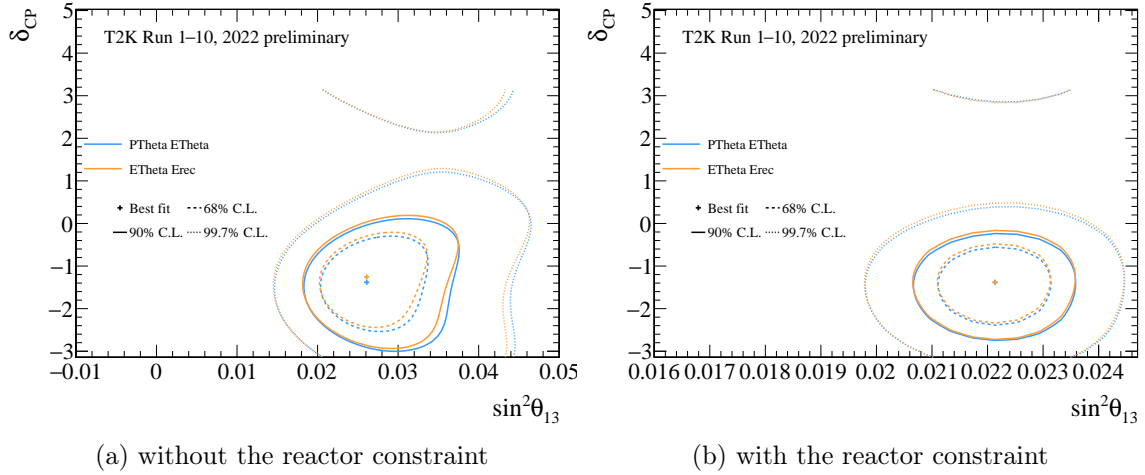
Figure 86: Comparisons of data-fit 2D confidence level contours in δ_{CP} vs. $\sin^2\theta_{13}$ in inverted ordering between (p_l–θ (e samples) + E_{rec}–θ (μ samples)) and (E_{rec}–θ (e samples) + E_{rec} (μ samples)) binning variables. For the results without the reactor constraint, the contours were produced with 1M throws instead of 100k throws to reduce the errors coming from the number of throws.

184

(a) without the reactor constraint

(b) with the reactor constraint
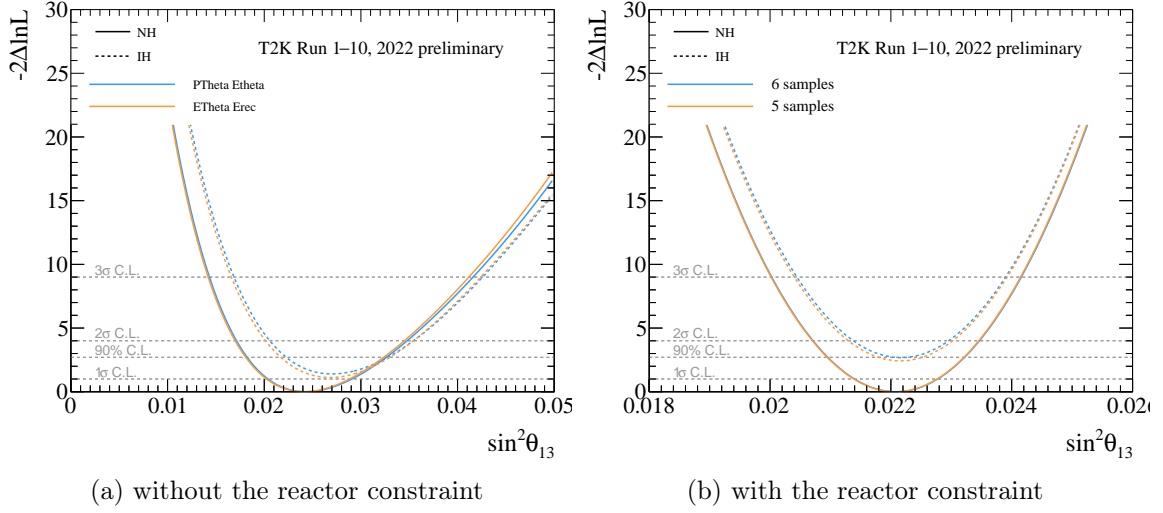
Figure 87: Comparisons of data-fit 1D $\Delta\chi^2$ in $\sin^2\theta_{13}$ between (p_l–θ (e samples) + E_{rec}–θ (μ samples)) and (E_{rec}–θ (e samples) + E_{rec} (μ samples)) binning variables. For the results without the reactor constraint, the contours were produced with 1M throws instead of 100k throws to reduce the errors coming from the number of throws.

(a) without the reactor constraint

(b) with the reactor constraint
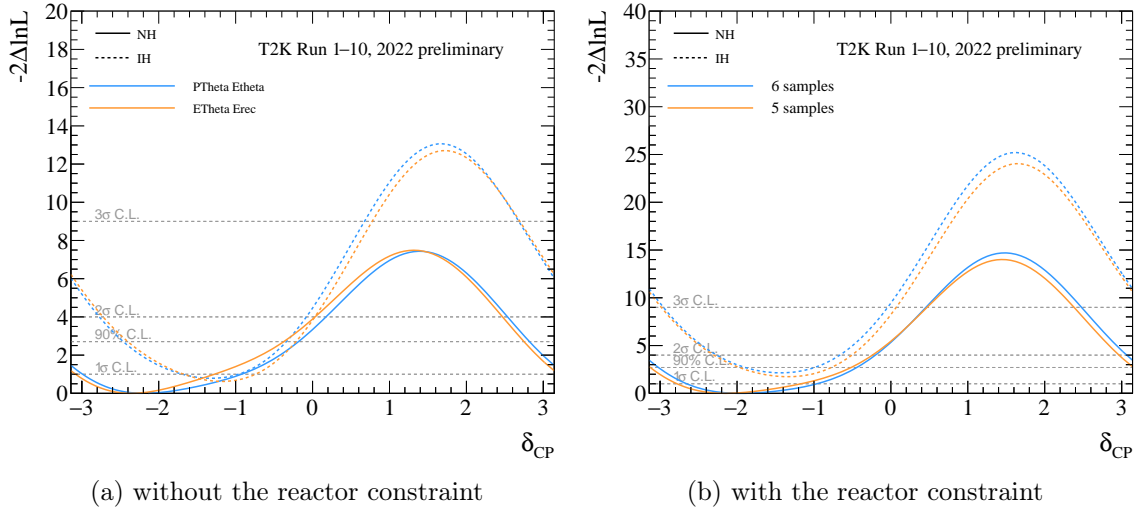
Figure 88: Comparisons of data-fit 1D $\Delta\chi^2$ in δ_{CP} between (p_l–θ (e samples) + E_{rec}–θ (μ samples)) and (E_{rec}–θ (e samples) + E_{rec} (μ samples)) binning variables. For the results without the reactor constraint, the contours were produced with 1M throws instead of 100k throws to reduce the errors coming from the number of throws.

E PartII: Cross fitter validation for the oscillation analysis results

The fitter differences between the MCMC and the frequentist grid-scan methods are summarized below [57].

- The algorithm; the MCMC method uses a Bayesian Markov Chain Monte-Carlo method, and the grid-scan method uses the MC marginalization.

- The constraints on the nuisance parameters; the grid-scan method uses the near detector fit whereas the MCMC method uses the simultaneous fit to the data from the near and far detectors.

- The far detector one-ring samples binned in different kinematic parameters; shown in Table 34.

Table 34: Variables used in the distributions for the far detector samples. The variables E_{rec}, θ_{lepton}, P_{lepton} represent reconstructed neutrino energy, an outgoing lepton angle, and a outgoing lepton momentum, respectively.

Sample	variables for the grid-scan method	variables for the MCMC method
ν_e 1-Ring	P_{lepton} and θ_{lepton}	E_{rec} and θ_{lepton}
ν_μ 1-Ring	E_{rec} and θ_{lepton}	E_{rec}
$\overline{\nu}_e$ 1-Ring	P_{lepton} and θ_{lepton}	E_{rec} and θ_{lepton}
$\overline{\nu}_\mu$ 1-Ring	E_{rec} and θ_{lepton}	E_{rec}
ν_e CC1π^+1-Ring	P_{lepton} and θ_{lepton}	E_{rec} and θ_{lepton}
ν_μ CC1π^+	E_{rec}	E_{rec}

For the purpose of the fitter comparisons, we perform three types of fits; the MCMC nominal fit, the grid-scan nominal fit, and the grid-scan MCMC-like fit. To perform the grid-scan MCMC-like fit, we use the constraints on the systematic parameters from the MCMC fit instead of the near detector fit. In addition, the grid-scan method changes its nominal kinematic variables for the MCMC-like fit to the same one as the MCMC kinematic variables. Figure 89 shows the results of two-dimensional $\Delta\chi^2$ contours for the appearance and disappearance parameters. The constraints on the appearance parameters agree well between the MCMC method and the grid-scan method for all of the fits, whereas the constraints on the disappearance parameters by the grid-scan method are weaker than those by the MCMC method. On the other hand, changing the constraints on the systematic parameters and the kinematic parameters used in the distributions in the grid-scan approach makes the agreement better. The difference in the kinematic parameters is less likely to cause this difference in contours [58]. The difference in the contours for the disappearance parameters, therefore, is likely to be due to the differences in the constraints on the systematic parameters. Nevertheless, the size of the difference is not significant with respect to the size of uncertainty on $\sin^2\theta_{23}$, which confirms the sanity of both fitters' analyses.

---

[57] See Appendix B.2 for the details.
[58] See Appendix D for the details.
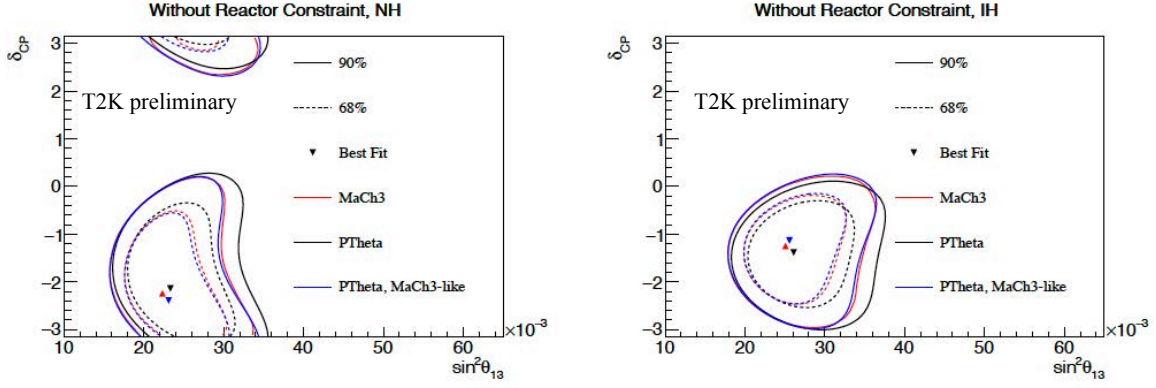
(a) Appearance parameters (δ_{CP}, $\sin^2\theta_{13}$)
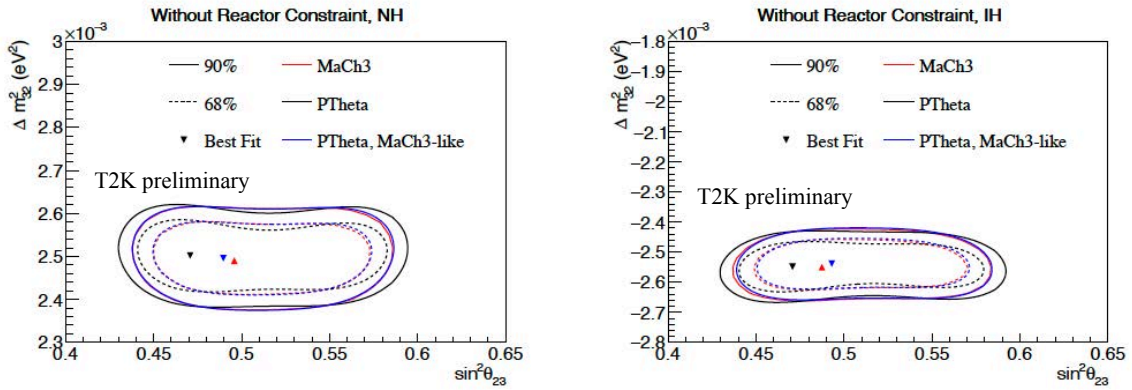
(b) Disappearance parameters (Δm_{32}^2, $\sin^2\theta_{23}$)

Figure 89: Cross fitter comparisons between the MCMC method and the grid-scan method for the two-dimensional contours for the appearance and disappearance parameters for the normal ordering (left) and the inverted ordering scenarios (right). Three kinds of fits are performed. MaCh3: the MCMC nominal fit. P-Theta: the grid-scan approach. P-Theta, MaCh3-like: the grid-scan MCMC-like fit. The reactor constraint is not applied to all of the fits. The normal ordering is assumed in those fits.

F PartII: Impacts of the new FD sample

Comparisons of the 1D and 2D data-fit contours with the 6 samples including the new sample, ν_μ CC1π^+, and conventional 5 samples are shown in Figs. 92–99 to check the impact of the multi-ring sample on the constraints of oscillation parameters. As expected, $\sin^2\theta_{13}$ and δ_{CP} contours are not affected by this change so much. A slight improvement on $\sin^2\theta_{23}$ contours is seen in the comparison of the nominal sensitivities. In particular for Δm_{32}^2 contours, the improvement is estimated to be 5% with respect to the size of the 1σ error.

(a) without the reactor constraint

(b) with the reactor constraint
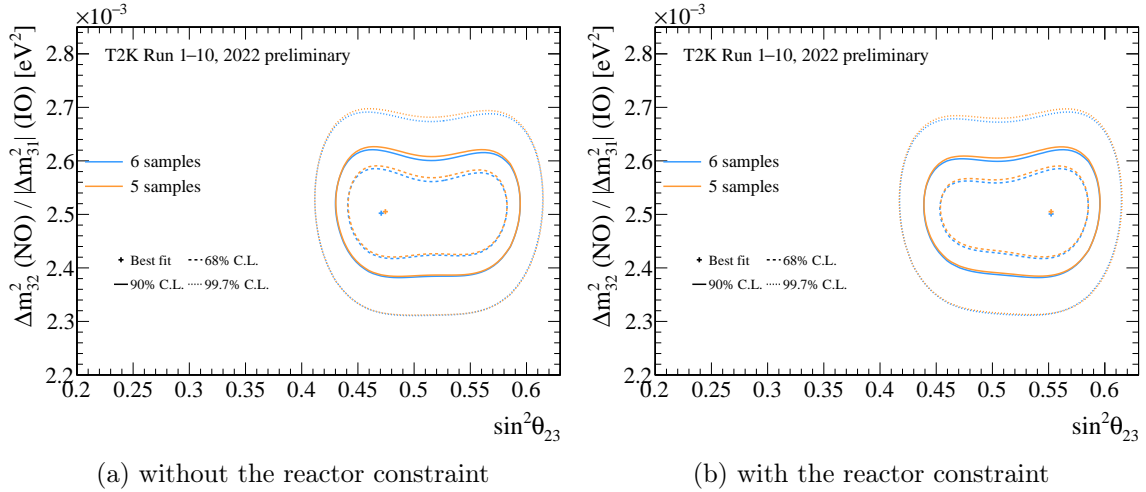
Figure 90: Comparisons of data-fit 2D confidence level contours in Δm_{32}^2 v.s. $\sin^2\theta_{23}$ in the normal ordering between with the ν_μ CC1π^+ sample (6 samples) and without the ν_μ CC1π^+ sample. A smearing factor (3.100×10^{-5} [eV^2]) on Δm_{32}^2 is applied based on the bias studies. For the results without the reactor constraint, the contours were produced with 1M throws instead of 100k throws to reduce the errors coming from the number of throws.

(a) without the reactor constraint

(b) with the reactor constraint
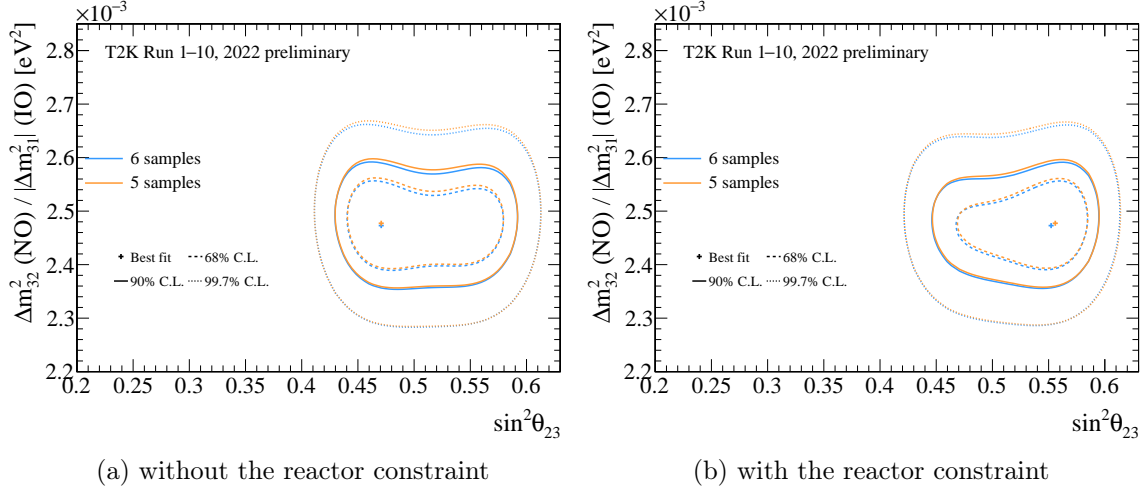
Figure 91: Comparisons of data-fit 2D confidence level contours in $|\Delta m_{31}^2|$ v.s. $\sin^2 \theta_{23}$ in the inverted ordering between with the ν_μ CC1π^+ sample (6 samples) and without the ν_μ CC1π^+ sample. A smearing factor (3.100×10^{-5} [eV^2]) on Δm_{32}^2 is applied based on the bias studies. For the results without the reactor constraint, the contours were produced with 1M throws instead of 100k throws to reduce the errors coming from the number of throws.

(a) without the reactor constraint

(b) with the reactor constraint
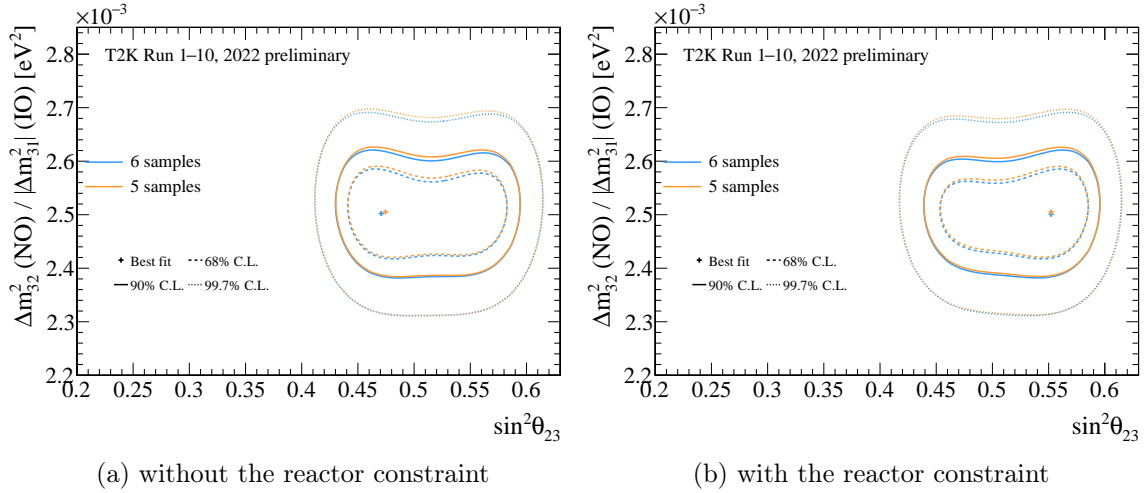
Figure 92: Comparisons of data-fit 2D confidence level contours in Δm_{32}^2 v.s. $\sin^2 \theta_{23}$ in the normal ordering between with the ν_μ CC1π^+ sample (6 samples) and without the ν_μ CC1π^+ sample. A smearing factor (3.100×10^{-5} [eV^2]) on Δm_{32}^2 is applied based on the bias studies. For the results without the reactor constraint, the contours were produced with 1M throws instead of 100k throws to reduce the errors coming from the number of throws.

(a) without the reactor constraint

(b) with the reactor constraint
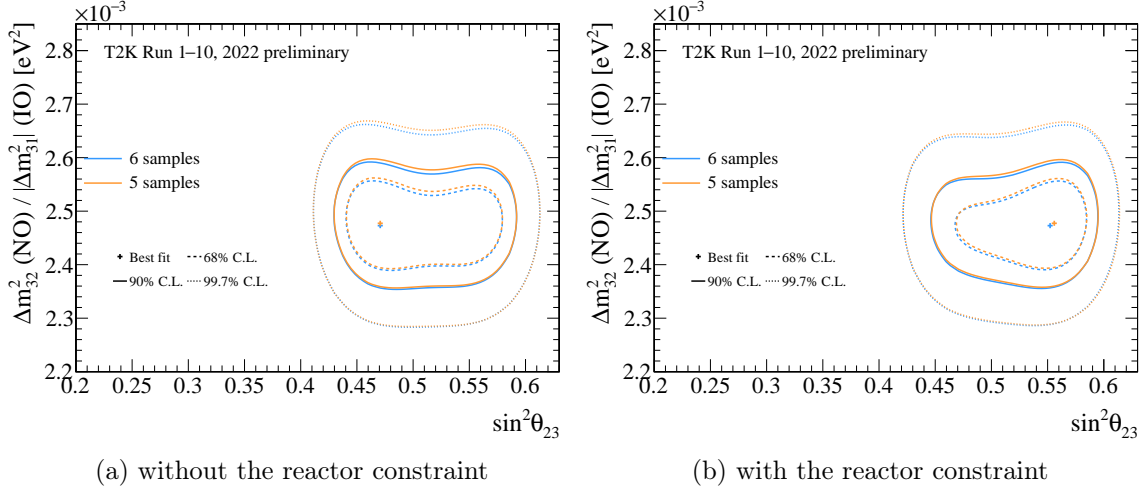
Figure 93: Comparisons of data-fit 2D confidence level contours in $|\Delta m_{31}^2|$ v.s. $\sin^2 \theta_{23}$ in the inverted ordering between with the ν_μ CC1π^+ sample (6 samples) and without the ν_μ CC1π^+ sample. A smearing factor $(3.100 \times 10^{-5} \ [\text{eV}^2])$ on Δm_{32}^2 is applied based on the bias studies. For the results without the reactor constraint, the contours were produced with 1M throws instead of 100k throws to reduce the errors coming from the number of throws.

(a) without the reactor constraint

(b) with the reactor constraint
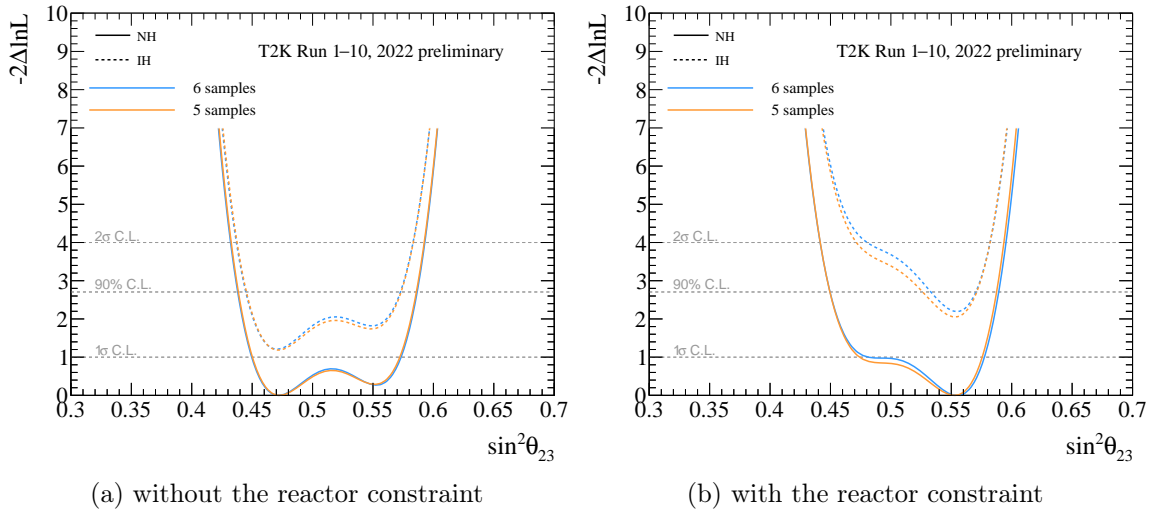
Figure 94: Comparisons of data-fit 1D $\Delta\chi^2$ in $\sin^2 \theta_{23}$ between with the ν_μ CC1π^+ sample (6 samples) and without the ν_μ CC1π^+ sample. For the results without the reactor constraint, the contours were produced with 1M throws instead of 100k throws to reduce the errors coming from the number of throws.

190

(a) without the reactor constraint

(b) with the reactor constraint
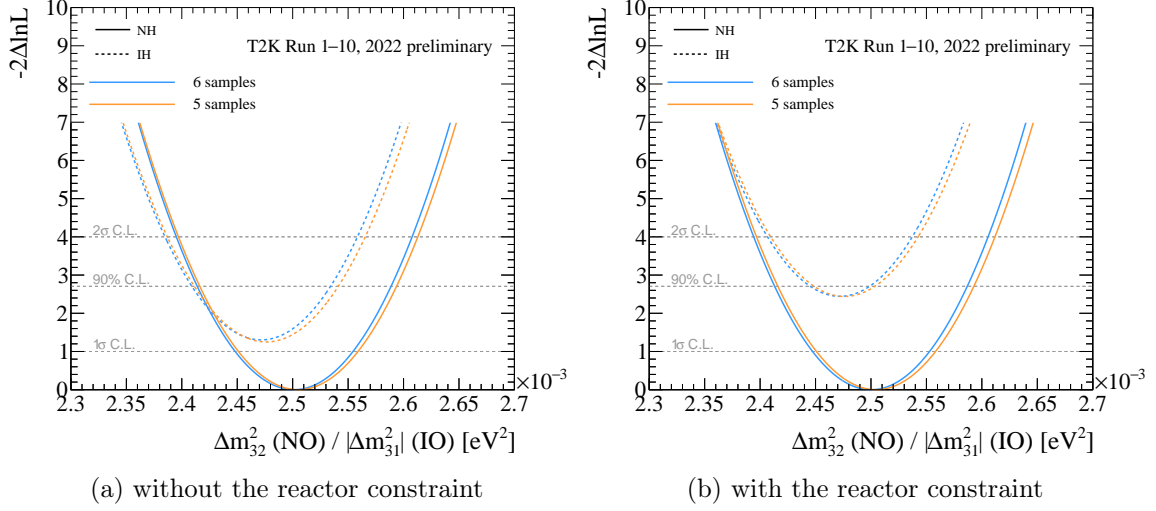
Figure 95: Comparisons of data-fit 1D $\Delta\chi^2$ in Δm_{32}^2 ($|\Delta m_{31}^2|$ for inverted) between with the ν_μ CC1π^+ sample (6 samples) and without the ν_μ CC1π^+ sample. For the results without the reactor constraint, the contours were produced with 1M throws instead of 100k throws to reduce the errors coming from the number of throws.

(a) without the reactor constraint

(b) with the reactor constraint
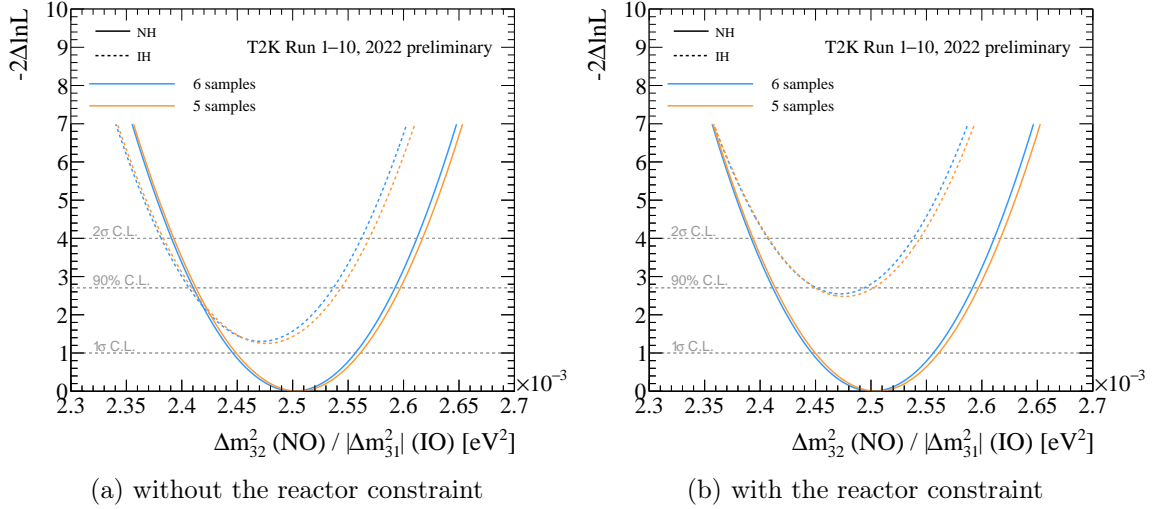
Figure 96: Comparisons of data-fit 1D $\Delta\chi^2$ in Δm_{32}^2 ($|\Delta m_{31}^2|$ for inverted) between with the ν_μ CC1π^+ sample (6 samples) and without the ν_μ CC1π^+ sample. A smearing factor (3.100×10^{-5} [eV^2]) on Δm_{32}^2 is applied based on the bias studies. For the results without the reactor constraint, the contours were produced with 1M throws instead of 100k throws to reduce the errors coming from the throws.

(a) without the reactor constraint   (b) with the reactor constraint
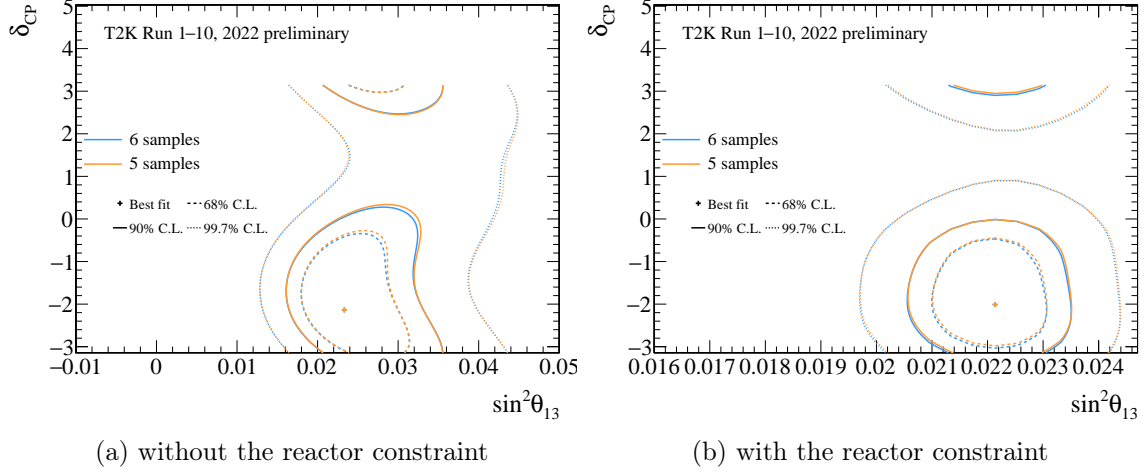
Figure 97: Comparisons of data-fit 2D confidence level contours in δ_{CP} v.s. $\sin^2\theta_{13}$ in the normal ordering between with the ν_μ CC1π^+ sample (6 samples) and without the ν_μ CC1π^+ sample. For the results without the reactor constraint, the contours were produced with 1M throws instead of 100k throws to reduce the errors coming from the number of throws.

(a) without the reactor constraint   (b) with the reactor constraint
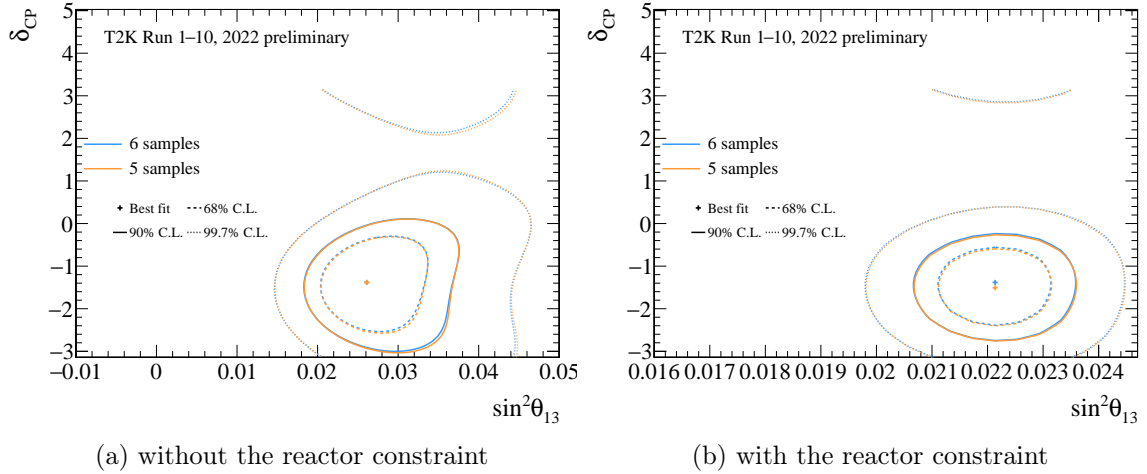
Figure 98: Comparisons of data-fit 2D confidence level contours in δ_{CP} v.s. $\sin^2\theta_{13}$ in the inverted ordering between with the ν_μ CC1π^+ sample (6 samples) and without the ν_μ CC1π^+ sample. For the results without the reactor constraint, the contours were produced with 1M throws instead of 100k throws to reduce the errors coming from the number of throws.

(a) without the reactor constraint

(b) with the reactor constraint
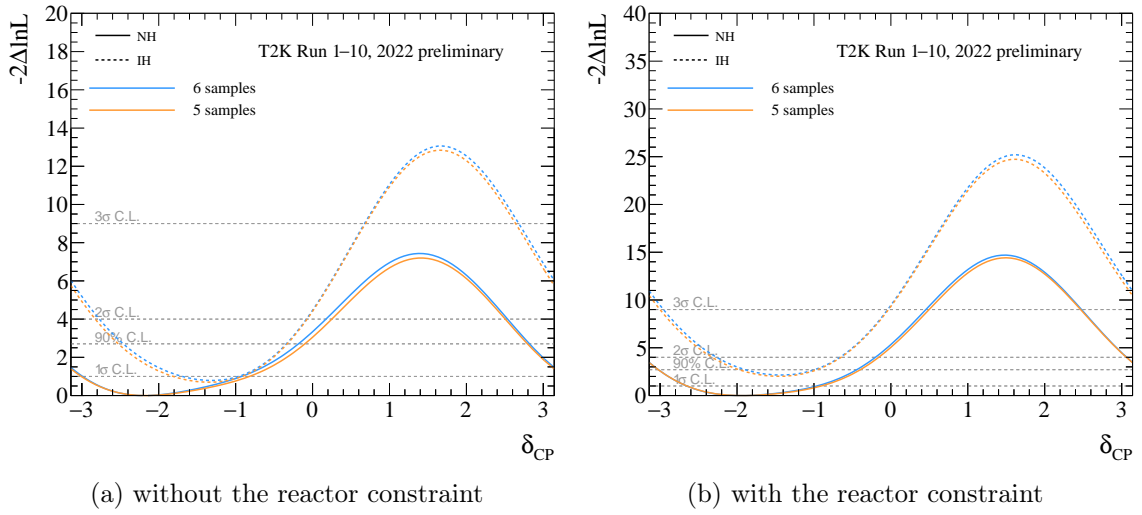
Figure 99: Comparisons of data-fit 1D $\Delta\chi^2$ in δ_{CP} between with the ν_μ CC1π^+ sample (6 samples) and without the ν_μ CC1π^+ sample. For the results without the reactor constraint, the contours were produced with 1M throws instead of 100k throws to reduce the errors coming from the number of throws.

G   PartII: P-value calculations at FD

The data distributions for the FD samples are compared to the MC predictions with the best-fit oscillation parameters in Figure 31. The data is apparently consistent with the MC predictions. On the other hand, we see a small deficit in data for the ν_μ 1-Ring sample and a small excess in data for the ν_e CC1π^+ 1-Ring sample as shown in Table 6. Here, we discuss the data-MC consistency for each sample in a quantitative way.

G.1   Rate-only p-value

In this simplest case, we compare the number of events observed in the ν_μ 1-Ring sample to the expectations for the different sets of true values of the oscillation parameters at the nominal MC. Those sets of parameters are shown in Table 35.

Table 35: Reference values of the neutrino oscillation parameters for two oscillation parameter sets and earth matter density.

Parameters	nominal MC	BestFit
Δm^2_{21}	7.53×10^{-5} eV^2	
Δm^2_{32} (NH) / $|\Delta m^2_{31}|$ (IH)	2.494×10^{-3} eV^2	2.506×10^{-3} eV^2
$\sin^2 \theta_{23}$	0.561	0.559
$\sin^2 \theta_{12}$ ($\sin^2 2\theta_{12}$)	0.307 (0.851)	
$\sin^2 \theta_{13}$ ($\sin^2 2\theta_{13}$)	0.0220 (0.08604)	
δ_{CP}	-1.601	-2.18
Mass ordering	Normal	

The expectations in each case are evaluated by generating 100k toy experiments with the oscillation parameters fixed to their values in the set considered, and the systematic parameters varied according to their prior probabilities using the results of the near detector fit for the parameters constrained by this fit. The expectations are compared to the number of events in data in Figure 100, and the obtained p-value for the ν_μ 1-Ring sample, in this case, is 0.00514.

There are six samples in the T2K analysis, and we should consider a trial factor by evaluating the probability of having such a low p-value in at least one of the 6 samples. This probability is not necessarily equal to 6 times the p-value obtained for the ν_μ 1-Ring sample as there are correlated systematics between the samples. To evaluate it, we determined for each sample the number of events corresponding to the p-value for the ν_μ 1-Ring sample and then counted the fraction of toy experiments for which at least one of the samples has a number of observed events above or equal to this threshold. The results are 4.7 $\times 10^{-2}$ and 5.3 $\times 10^{-2}$ for the nominal MC and best-fit parameters, respectively. Both p-values indicate no significant deficit in data.

Tables 36, 37 show p-values for each sample with the oscillation parameters either at the nominal MC or the best fit. Both have quite consistent results. These numbers indicate no clear deficit or excess in data regarding our predictions although the ν_μ 1-Ring sample has a relatively small p-value. In addition to the p-values for the individual samples, merged samples are also studied to check the event migration effects between samples. Here we show two cases, "ν_μ 1-Ring + ν_μ CC1π^+ " and "ν_e 1-Ring + ν_e CC1π^+ 1-Ring ". Results are summarized in Table 38. Both p-values are modest compared to individual ones.
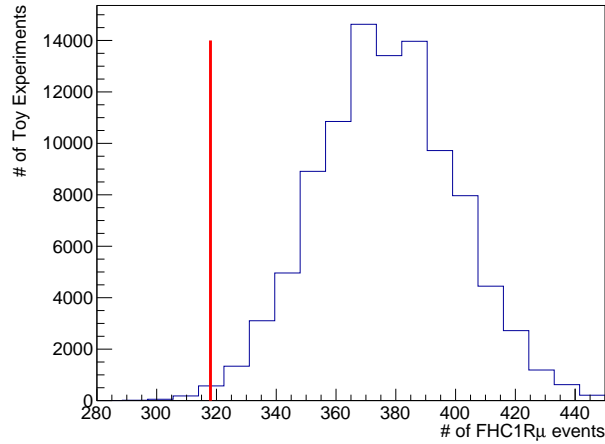
Figure 100: Expected distributions of the number of events in the ν_μ 1-Ring sample for the nominal set of the oscillation parameters. A red line is shown in the middle of the bin corresponding to the 318 events observed in data.

Table 36: Rate only p-values obtained for each sample without considering a look elsewhere effect with the nominal oscillation parameters. Conversion to sigmas is done using the formula for the Gaussian case.

	ν_μ 1-Ring	$\overline{\nu}_\mu$ 1-Ring	ν_e 1-Ring	$\overline{\nu}_e$ 1-Ring	ν_e CC1π^+ 1-Ring	ν_μ CC1π^+
P-value	5.14×10^{-3}	2.50×10^{-1}	2.23×10^{-1}	3.97×10^{-1}	1.69×10^{-1}	9.53×10^{-2}
z-score (σ)	2.56	0.67	0.84	0.75	0.96	1.31

Table 37: Rate only p-values obtained for each sample without considering a look elsewhere effect at the best fit. Conversion to sigmas is done using the formula for the Gaussian case.

	ν_μ 1-Ring	$\overline{\nu}_\mu$ 1-Ring	ν_e 1-Ring	$\overline{\nu}_e$ 1-Ring	ν_e CC1π^+ 1-Ring	ν_μ CC1π^+
P-value	5.71×10^{-3}	2.59×10^{-1}	3.09×10^{-1}	3.73×10^{-1}	1.42×10^{-1}	9.15×10^{-2}
z-score (σ)	2.52	0.64	0.50	0.32	1.03	1.33

Table 38: Rate only p-values obtained for the combined samples without considering a look elsewhere effect. Conversion to sigmas is done using the formula for the Gaussian case.

	ν_μ 1-Ring + ν_μ CC1π^+	ν_e 1-Ring + ν_e CC1π^+ 1-Ring
P-value	6.01×10^{-2}	3.52×10^{-1}
z-score (σ)	1.55	0.379

195

G.2 Rate+Shape p-value

For a more robust analysis of p-values, shape information will be taken into account. The nominal binning scheme in the grid-scan method for this sample is E_{rec}–θ, but other binning schemes like 1D-E_{rec} and 1D-θ are also tested. A test statistic used here is defined as follows.

$$L = \prod_{i=1}^{\mathrm{nbins}} \frac{\mathrm{Poisson}(N_{\mathrm{obs}}^i, N_{\mathrm{pred}}^i)}{\mathrm{Poisson}(N_{\mathrm{pred}}^i, N_{\mathrm{pred}}^i)}, \tag{G.1}$$

where the predictions for bin i, N_{pred}^i, are given by our usual model for the set of values of the oscillation parameters considered, and the default values of the systematic uncertainties. According to the rate-only analysis, both results with the oscillation parameters at the nominal MC point and with the oscillation parameters at the best fit are consistent. Therefore, we use only the oscillation parameters at the best fit in this section. The predicted distributions of the test statistics are obtained using 20k toy experiments in each case. Those values and the p-values are shown in Table 39. The results show there is a relatively large difference between binning choices, in particular p-value for ν_μ 1-Ring sample in θ is small. It might indicate there is a possibility that the 1D-θ shape in ν_μ 1-Ring sample has the largest discrepancy with the prediction compared to other binning schemes.

For the comparison of p-values from the grid-scan and MCMC methods, Figure 40 summarizes each p-value taken from the MCMC analysis. It should be noted that the p-values from the grid-scan method were calculated with the systematic parameters at pre-fit but at post-fit for the MCMC method. Even though we have a known difference in the systematic parameters between the grid-scan method and the MCMC method, the p-values from the grid-scan method in E_{rec} binning are more or less consistent with the MCMC p-values for all samples.

Table 39: Rate+shape p-values obtained for each sample without considering a look elsewhere effect at the best fit. Conversion to sigmas is done using the formula for the Gaussian case.

	Binning	ν_μ 1-Ring	$\overline{\nu}_\mu$ 1-Ring	ν_e 1-Ring	$\overline{\nu}_e$ 1-Ring	ν_e CC1π^+ 1-Ring	ν_μ CC1π^+
P-value	θ	3.20×10^{-2}	6.14×10^{-1}	8.95×10^{-1}	3.27×10^{-1}	1.09×10^{-1}	–
z-score (σ)		1.85	-0.290	-1.25	0.448	1.23	–
P-value	E_{rec} (μ-like), P (e-like)	3.16×10^{-1}	8.50×10^{-1}	1.96×10^{-1}	2.37×10^{-1}	1.65×10^{-1}	9.55×10^{-1}
z-score (σ)		0.479	-1.04	0.856	0.716	0.974	-1.70
P-value	E_{rec} (e-like)	–	–	8.05×10^{-2}	8.68×10^{-1}	8.36×10^{-1}	–
z-score (σ)		–	–	1.40	-1.12	-0.98	–
P-value	E_{rec}–θ (μ-like), p_l–θ (e-like)	6.79×10^{-1}	9.80×10^{-1}	8.20×10^{-1}	7.60×10^{-1}	1.28×10^{-1}	–
z-score (σ)		-0.464	-2.05	-0.915	-0.706	1.14	–

Table 40: P-values from the MCMC data analysis

	Binning	ν_μ 1-Ring	$\overline{\nu}_\mu$ 1-Ring	ν_e 1-Ring	$\overline{\nu}_e$ 1-Ring	ν_e CC1π^+ 1-Ring	ν_μ CC1π^+
P-value	E_{rec}	3.5×10^{-1}	8.4×10^{-1}	1.3×10^{-1}	6.3×10^{-1}	8.9×10^{-1}	9.6×10^{-1}

H PartIII: Details of the track reconstruction algorithm

The track reconstruction algorithm was already overviewed in Section 10. More detailed descriptions are written in this Appendix.

H.1 Two-dimensional track reconstruction (Track seeding)

We have the same format to contain data for our simulation and data. By using the common format having fundamental information associated with detector responses such as light yield, TDC, hit position, and so on, hits are categorized into groups called "clusters". As particle tracks are supposed to be straight or slightly curved lines due to the magnetic field in BabyMIND, clusters shape a similar line. The hit positions are key components to constructing a cluster. We chose Celluler automaton tracking (CAT) as an algorithm to do this cluster reconstruction. We call this reconstruction "Track seeding".

H.1.1 Celluler automaton tracking (CAT)

This algorithm, CAT, was originally invented to analyze a liquid motion by considering a liquid as a group of discrete units and calculating the motion of each based on its neighbors' behaviors. It has been widely known since an article named "Game of Life" [174] was published in 1970. Settings in this algorithm are simple, just requiring grid spaces having a finite state that could be evolved in time spent under the specific rules. Considering the structure of scintillator trackers, each hit can be considered to be on each two-dimensional grid point defined by scintillator positions. If we choose an appropriate definition of "time" and "rules" for evolving "state", it can be applied to track seeding. To make each definition clear, several kinds of terms are also defined here.

Cell
 A line connecting a hit to another hit. Cell is a unit of this algorithm.

Neighbourhood
 A pair of two cells having one common hit.

Time
 An iteration to check each state of cells. The initial time is set to 0.

State
 A number incremented based on a certain rule. The initial state is set to 0.

In this analysis, a state is evolved based on the following rules.

1. Check if there is at least one Neighbourhood having the same State. If yes, proceed with this iteration. Otherwise, this iteration is ended.

2. Check χ^2 values obtained by a linear fitting to three hits included in the Neighbourhoods.

3. If the χ^2 is lower than a threshold (depending on a combination of scintillator bars, typically 500 for scintillator bars in Proton Module), we call those Neighbourhoods "True" Neighbourhoods otherwise "False" Neighbourhoods.

4. States of upstream cells of True Neighbourhoods are incremented by 1. Also, Time is incremented by 1.

5. Steps 1 to 4 continue until none of the Cells change their states.

Figure 101 shows a schematic view to illustrate each definition by drawings.

(a) Setting   (b) Example of two Cells   (c) Example of Neighbourhood
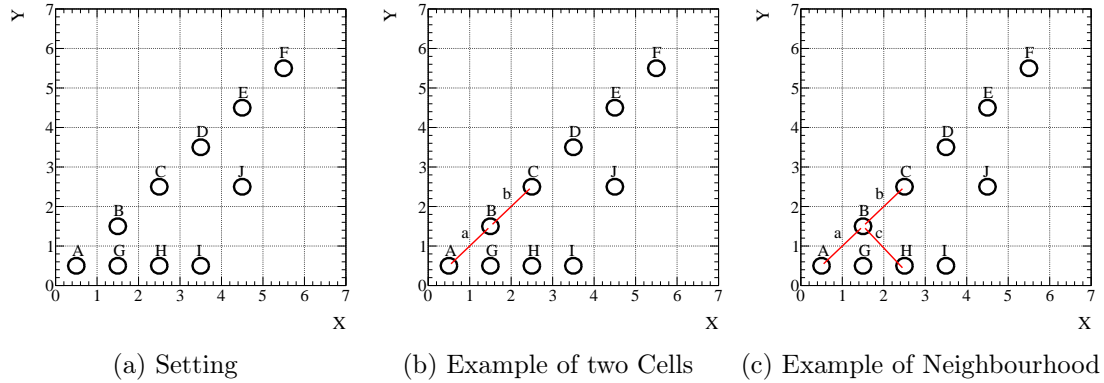
Figure 101: An illustration of the overview of the CAT algorithm. A simple setting is shown in Figure 101a. Each hit is denoted by a capital alphabet. Two cells are indicated by red arrows in Figure 101b denoted by small alphabets (a, b). Figure 101c shows a True Neighbourhood (a, b) and a False Neighbourhood (a, c).

In addition, the following rules are applied in constructing cells.

- Plane differences between two hits are less than 3. For the WAGASCI detectors, the minimum allowed plane differences is 0, otherwise 1,

- Position X, Y differences between two hits are less than 300 mm.

The reason why different thresholds for minimum plane differences are defined between the WAGASCI detectors and Proton Module is that WAGASCI detectors have three-dimensional grid structures which were designed to detect a particle going in the perpendicular direction to the detector coordinates while Proton Module has scintillator tracking planes aligned in parallel which are insensitive to those particles. When this method is applied to hit data, two additional steps are added to make clustering more robust.

Time clustering

All the hits are placed in the order of TDC and a hit is put into a time cluster one by one. If the difference in the TDC time between two neighboring hits is more than 100 ns, a hit is put into another cluster from the other hit.

Hit clustering

There can be two neighboring hits in the X or Y direction mainly due to cross-talks between scintillators. To make an algorithm simpler, those hits are put into a hit cluster. For the WAGASCI detectors, this hit clustering is disabled considering the more complicated scintillator structure compared to other detectors. WAGASCI tracking planes are combinations of plane and grid scintillators and it is not obvious which hits to be merged.

Figure 102 shows how each cell evolved based on these rules.

(a) Hit clusters on scintillators   (b) Cell construction   (c) After the first iteration

(d) After all the iterations   (e) Draw track lines   (f) Result of track seeding
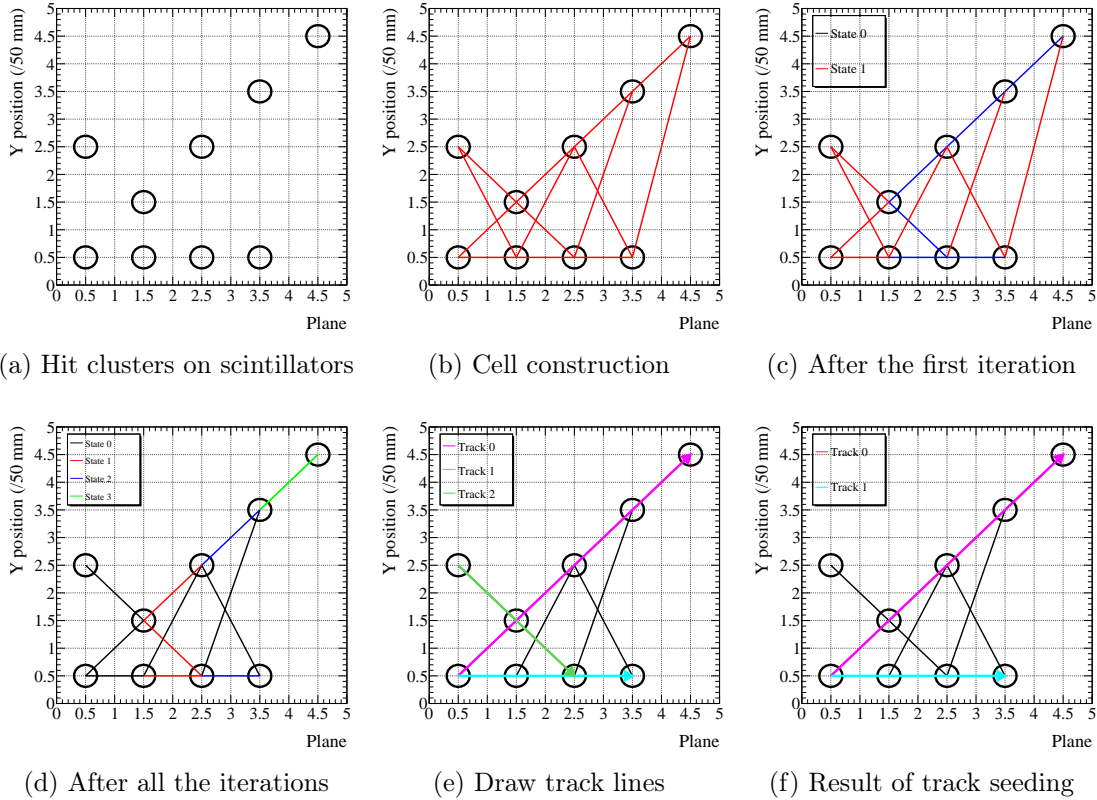
Figure 102: Illistrations of how the track seeding is processed with CAT. Figure 102a shows an example hit cluster map typically found in neutrino events. Then each cell is constructed (Figure 102b). For simplicity of the illustration, each cell is drawn only in the case the plane differences equal 1. Otherwise, cells are dismissed in these drawings. Once all cells are constructed, each state of a cell is automatically updated based on the rules until all the iterations are ended. Figure 102c is the result of the first iteration and Figure 102d is the result of all the iterations. Each track candidate can be reconstructed by tracking cells from a higher state to a lower state. In this example, three candidates are recovered (Figure 102e). Each candidate is prioritized based on the track-likeliness which is defined by the number of hits included in each candidate. As the number of hits is larger, it is considered to be more highly likely to be a particle track. After selecting track candidates, check how many isolated hits (not shared by more than one track candidate) it has. If the isolated hits are less than shared hits, it is not considered to be a particle track anymore. The track candidate 2 in this example have 1 isolated hits and 2 shared hits, therefore, it ƒs dismissed in the final step of this algorithm. Finally, we have two track candidates from this example as shown in Figure 102f.

199

H.2 Three dimensional track reconstruction

Now that all the hits in each event are reconstructed into clusters in two-dimensional space, pairs of two-dimensional clusters in XZ and YZ views have to be converted into three-dimensional tracks. After all three-dimensional tracks are reconstructed, the neutrino interaction vertex is reconstructed. Track reconstruction process here proceeds in the following steps.

1. Track matching in two-dimensional space and in three-dimentional space

2. Vertexing

3. Track reconstruction in three-dimensional space for other tracks

4. Check hits in YASU trackers

H.2.1 Track matching in two-dimensional space and in three-dimensional space

Track seeding in two-dimensional space gives reconstructed clusters in the YZ view and XZ view. All analyses ongoing in the WAGASCI-BabyMIND group aim to extract the cross section for charged current interactions. And most of the physics targets of our measurements are the differential cross section with respect to μ kinematics. Thus, the first priority in the three-dimensional reconstruction is to reconstruct a 3D track for μ candidate. In this analysis, events where neutrino interaction happens in a detector and none of the tracks are matched with another subdetector will not be used because a fraction of backgrounds in that kind of event overweighs the signal. A track matching algorithm has been developed based on this philosophy.

Figure 103 shows the overview of the track matching algorithm. As our main analysis samples include a muon candidate whose track is matched with a muon range detector, the algorithm starts from clusters in BabyMIND or WallMRD. If there is at least one cluster in either Baby-MIND or WallMRD, then the algorithm looks at clusters in the vertex detectors. If there are clusters in at least one vertex detector, it tries to check if there is a combination of clusters satisfying matching conditions. The algorithm follows the same manner in the case where there is at least one cluster in a vertex detector while there is no cluster in BabyMIND and WallMRD. Matching conditions are mainly divided into two parts, angle differences of the two clusters and position differences of an extrapolated position of a cluster from an upstream detector and a starting position of a cluster from a downstream detector. Both conditions depend on the combination of two detectors because each detector has different position and angle resolutions. Also, those conditions are determined by taking distances between two detectors into account.

Conditions for the angle differences are summarized in Table 41 and in Table 42 for the position differences. In this analysis, no requirement for TDC within each bunch is applied. After the iteration of both views, If there is no candidate of a matching cluster in an event, the event is dismissed. Otherwise, it proceeds with the three-dimensional track matching. The algorithm ensures that there is at least one pair of matched tracks in both views. The algorithm tries to check if both upstream edge position differences and downstream edge position differences satisfy a three-dimensional matching condition, which is shown in Table 43.
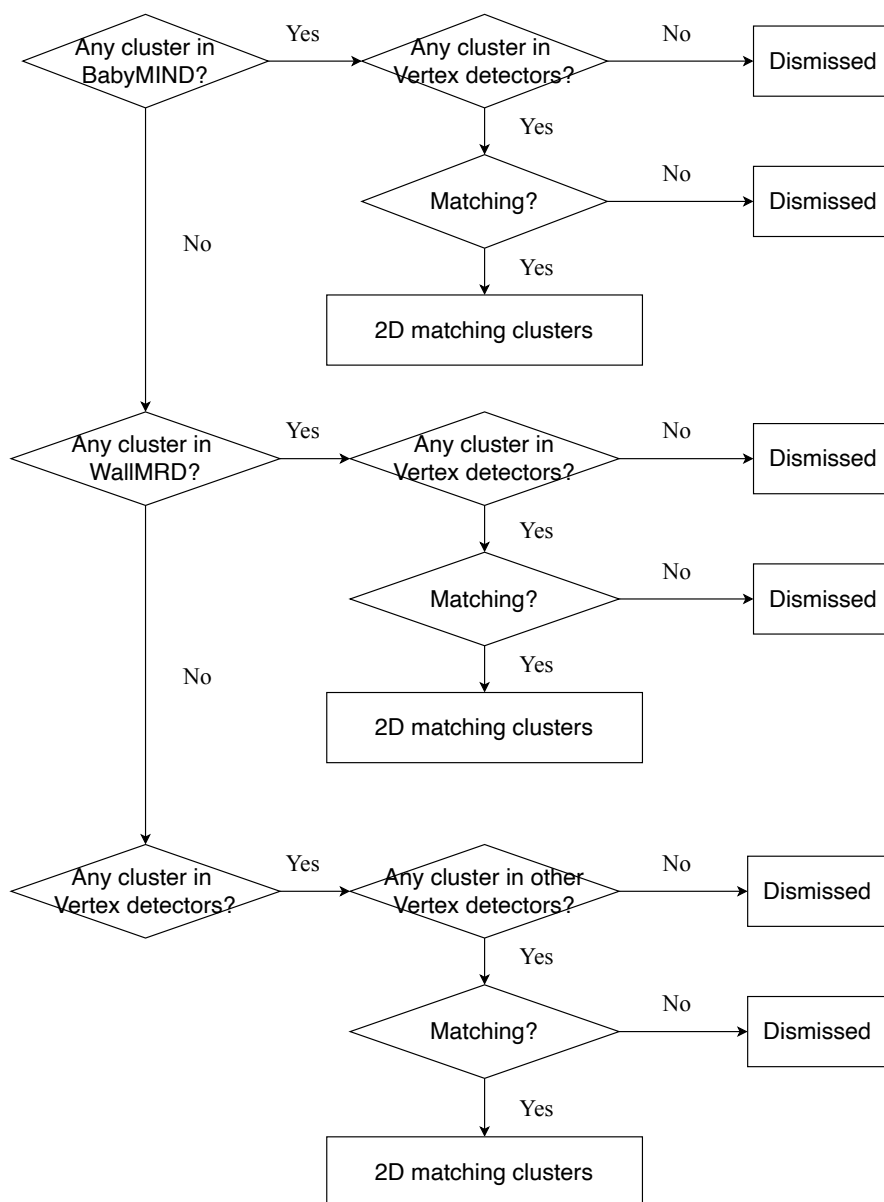
Figure 103: An algorithm for a track matching between subdetectors. In the selection of "Any cluster in Vertex detectors", clusters in all kinds of vertex detectors (Proton Module and WA-GASCI upstream and WAGASCI downstream) are covered. If there are clusters in more than 1 vertex detector in this selection, it tries to check if all clusters are matched with each other in the next "Matching" selection.

Table 41: Matching conditions for the angle differences. WMRD: WallMRD, BM: BabyMIND

Upstream detector	Downstream detector	view	Threshold (angle)
a vertex detector	BM	YZ	25
a vertex detector	BM	XZ	30
a vertex detector	WMRD	XZ	25
a vertex detector	a vertex detector	both	25

Table 42: Matching conditions for the position differences. WMRD: WallMRD, BM: BabyMIND, PM: ProtonModule, UWG: Upstream WAGASCI, DWG: Downstream WAGASCI

Upstream detector	Downstream detector	view	Threshold (mm)
PM or DWG	BM	YZ	250
UWG	BM	YZ	300
PM or DWG	BM	XZ	300
UWG	BM	XZ	300
a vertex detecor	WMRD	XZ	500
PM	DWG	both	200
UWG	DWG	both	300
UWG	PM	both	200

Table 43: Conditions of three-dimensional track matching

Detector at upstream edge	Threshold on position differences (mm)
Any vertex detector	150
Detector at downstream edge	**Threshold on position differences (mm)**
WallMRD	200
BabyMIND	350

H.2.2 Vertexing

The next step after the three-dimensional track matching is to reconstruct a neutrino interaction vertex because the matched track is supposed to be a μ candidate whose starting position in a vertex detector is expected to give a vertex position. Vertex X and Y positions are taken from the start positions from the three-dimensional matching track. Vertex Z position is defined as the more upstream position of matched tracks in both views. As planes in both views are aligned in parallel on the Z-axis, the upstream position is more likely to be an interaction point. Then the algorithm tries to look for other clusters that are expected to start from the vertex point. Suppose differences in the start Z position and start X/Y position are $\Delta Z, \Delta X/Y$, the following conditions are required for clusters in both vertex detectors.

$$\Delta Z \leq 80 \text{ mm}, \Delta XY \leq 80 \text{ mm} \tag{H.1}$$

If the cluster does not satisfy the conditions above, it can be simply ignored while the event is not rejected. It should be noted that if some of the clusters are found to be matched with

clusters in another detector in the first step and they satisfy this condition, then clusters will be treated as a matching track (but not a μ candidate). This process is conducted in each view separately and a three-dimensional track reconstruction for those clusters will be performed in the next step.

H.2.3 Track reconstruction in three-dimensional space for other tracks

The final step is to reconstruct a three-dimensional track for the clusters having the same vertex of a μ candidate. The algorithm checks if differences in the starting positions and differences in the stopping positions satisfy thresholds which are the same as shown in Figure 43. There are often cases where a track in either view cannot match any track satisfying the conditions in the other view. For example, when we assume two tracks are produced in a vertex position, there is a possibility that two tracks are visible in the YZ view but in the XZ view both tracks are overlapped as if it was one track. In order to take the effect into account, the cluster is reconstructed in the event as a two-dimensional track sharing the same vertex point as a μ candidate even if it has no candidate in the other view. The number of tracks in an event can be defined by the maximum number of tracks in both views.

H.2.4 Check hits in YASU trackers

Two scintillator planes (YASU trackers) were installed between three successive iron planes in the first block of BabyMIND to detect relatively low-energy muons, otherwise, they could stop inside the iron modules and then cannot be detected. In order to take advantage of these trackers in the sense of increasing efficiency, we check track matching between BabyMIND and another subdetector by comparing extrapolated position from a vertex detector and each hit in a YASU tracker plane. The threshold of the Y position difference is set to 300 mm. Then we check if a track from a vertex detector does not match a hit in the 2nd and 3rd planes located downstream of the YASU trackers to make sure that the event is not double-counted. It can be considered that either a track is a matching track with more than one detector or a track in one vertex detector. If it is a matching track, vertexing can be done in the same way that was described in the previous sections. If it is a track in one vertex detector, it is necessary to reconstruct a three-dimensional track and decide the vertex position.

I PartIII: Details of the analysis on the track properties

This research aims to extract the single differential cross section of neutrino-nucleus scattering with respect to muon angle and muon momentum. As this analysis focuses on a CC0π sample in the neutrino mode, particle identification, and charge identification are also essential. Each analysis method to reconstruct those four kinds of track variables is described in this Appendix.

I.1 muon angle
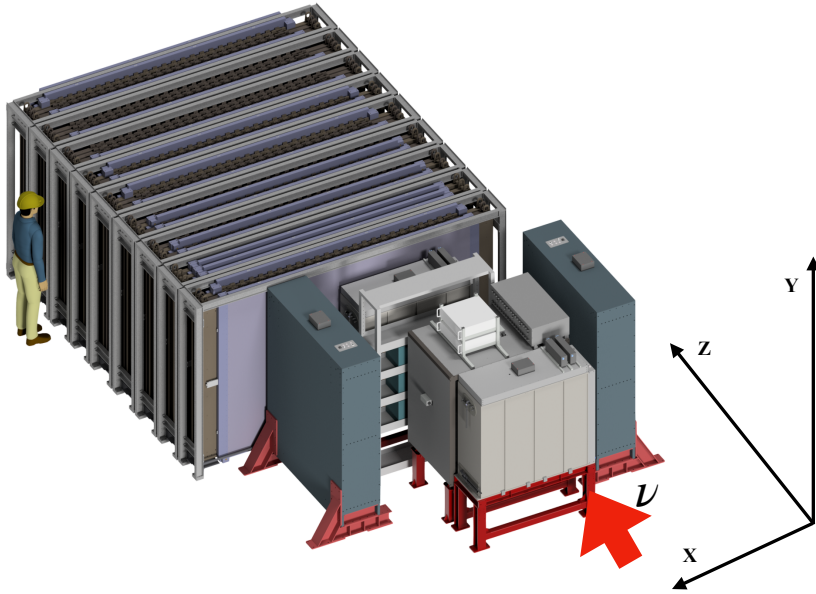
Figure 104: The definition of each axis in the detector coordinate system. The Z-axis is stretched along with the tracking planes. The Y-axis is perpendicular to the ground. The X-axis is perpendicular to both Y and Z axis.

Here we use a detector coordinate for each X, Y, and Z-axis as shown in Figure 104. The three-dimensional track reconstruction ensures there is at least one matching track which is a muon candidate if a neutrino vertex is reconstructed. Some events also have another three-dimensional track, but this analysis only needs an angle for the muon candidate. We can choose either hits in all subdetectors or hits in only vertex detectors to reconstruct an angle. The reconstruction performance of the angle is not so much improved even if hits inside WallMRD or BabyMIND are used because the position resolution in WallMRDs is worse than the one of each target detector and a little difficult to do the angle reconstruction for BabyMIND due to the magnetic field. We decided to use hits in only vertex detectors. If a neutrino interaction happens in Upstream WAGASCI or Proton Module and the matching track goes through one or two vertex detectors, all of those hits information is used. As there is no magnetic field in the vertex detectors, the angle reconstruction is simply performed by a two-dimensional linear fitting in both XZ and YZ views. Assuming each slope is $\tan\theta_{XZ}, \tan\theta_{YZ}$ (where θ is an angle with respect to the neutrino beam direction), a reconstructed angle of the matching track is given by the following formula in the unit of degree.

$$\text{reconstructed angle} = \arccos\left(\frac{|d_x^\nu \tan\theta_{XZ} + d_y^\nu \tan\theta_{YZ} + d_z^\nu|}{\sqrt{1 + \tan^2\theta_{XZ} + \tan^2\theta_{YZ}}}\right) \times \frac{180}{\pi}, \tag{I.1}$$

where $d_x^\nu = -0.019972, d_y^\nu = -0.079947, d_z^\nu = 0.996599$.
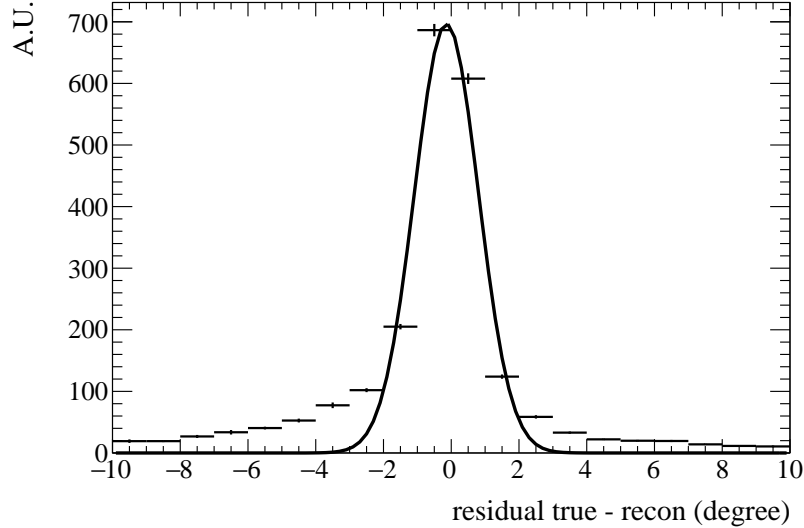
Figure 105: A residual plot of μ candidate.

We used simulated charged current inclusive events with one reconstructed track that has tracks in Upstream WAGASCI and BabyMIND to make sure this method works well for the neutrino interactions. The selection is described below.

- Three-dimensional track reconstruction

- Vertexing

- Fiducial Volume cut

- Event includes only one track which is matched with one of the MRD detectors

Figure 105 shows the residual plot of the angle.

I.2 muon momentum

WAGASCI-BabyMIND detectors are potentially capable of momentum measurements either by track curvature in BabyMIND or by track range in all subdetectors. Although there have been several trials to reconstruct momentum by curvature, none of them is validated in this analysis. We decided to use the range method for this purpose. In that case, it is required to reconstruct momentum in a reasonable way that the particle should stop inside either muon range detector. It implies statistics is essentially decreased compared to the angle measurement. For future improvement, developing a sophisticated method to reconstruct momentum by curvature will be important not to reduce the statistics for the differential cross section as a function of muon momentum.

We have six kinds of subdetectors introduced in this measurement and one set of detectors that comes from the NINJA experiment. As one of the NINJA detectors has a few cm of iron planes in total length, the energy loss there is not negligible. Thus, this energy deposit is also considered as well as the ones in our subdetectors. Dominant materials to be concerned to calculate a total energy loss are iron ($\rho = 7.874$ g/cm^3), scintillator ($\rho = 1.032$ g/cm^3) and water ($\rho = 1.002$ g/cm^3), and the energy loss is normalized by iron taking corresponding density ratio. A reconstructed momentum value is calculated using a spline (Figure 106) having the relationship between CSDA (Continuous-Slowing-Down Approximation) range and momentum for muons. The spline is produced based on a table [175] provided by Particle Data Group. The performance of this method is checked with the MC simulation for CC inclusive events where there is only a muon candidate going from Downstream WAGASCI and BabyMIND. We checked the momentum resolution in the regions separated every 100 MeV/c. A resolution is defined by the standard deviation of the Gaussian fitting in each momentum range and its error is calculated simply by dividing by the mean momentum in each region.
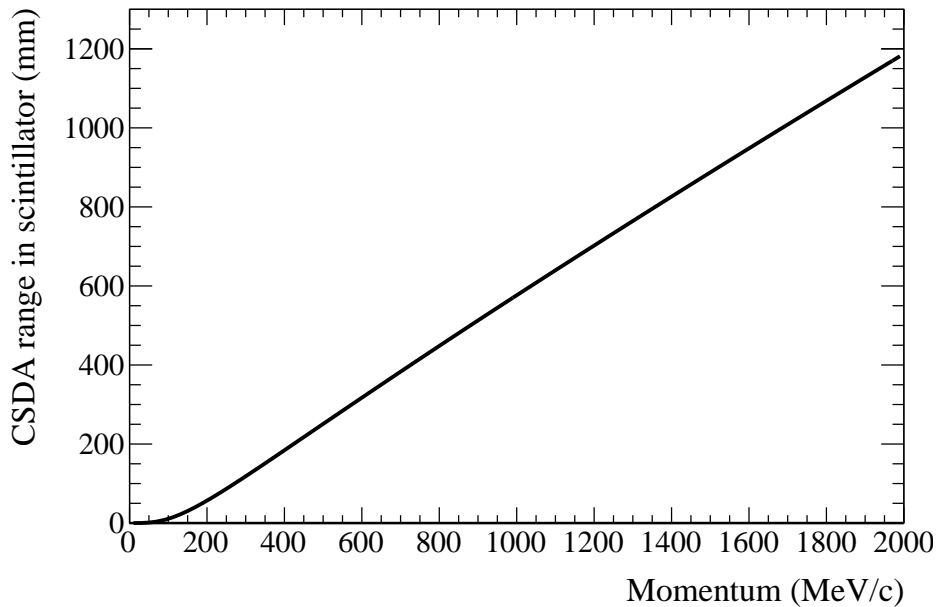
Figure 106: A spline of relationship between CSDA range in iron and μ momentum
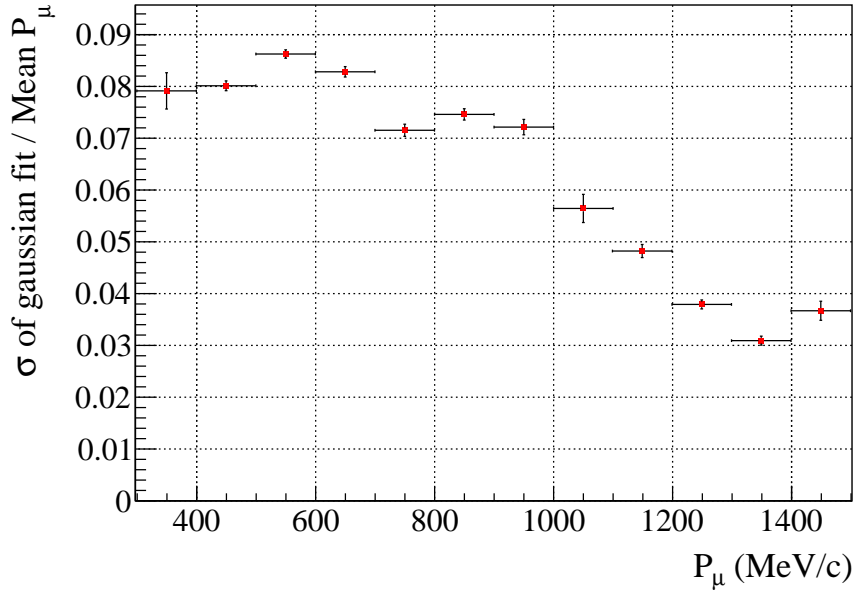
Figure 107: Momentum resolution by range in each momentum region. A resolution is defined by the standard deviation of the Gaussian fitting in each momentum range and its error is calculated simply by dividing by the mean momentum in each region.

Figure 107 shows the momentum resolution for the BabyMIND case. The resolution is more or less about 10% or less in the regions of interest which is expected from the brief calculation of the ideal resolution of BabyMIND.

I.2.1 Particle identification

For the CC0π analysis, it would be better to identify each particle, especially for muons, pions, and protons. However, even the full set of detectors in WAGASCI-BabyMIND is not capable of fully separating those particles. The most prominent thing about particle identification in terms of CC0π measurements is to separate μ-like particles (typically muons and pions) from p-like particles because the most significant background comes from single pion production where two μ-like particles are likely to be found. We use the following variable named "MUCL (muon confidence level)" for the discriminator of the particle identification.

$$\mathrm{MUCL} = P \times \sum_{i=0}^{n-1} \frac{(-\ln P)^i}{i!}, P = \prod_{i=1}^{n} CL_i, \tag{I.2}$$

where n refers to the number of planes having a hit and CL_i are the confidence levels for hits on the ith plane, which are defined by a cumulative function of dE/dx distribution for each detector.
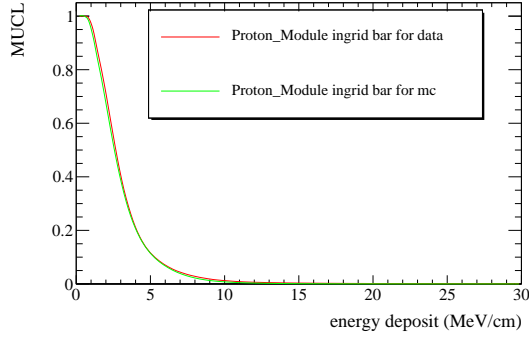
(a) INGRID scintillators in Proton Module
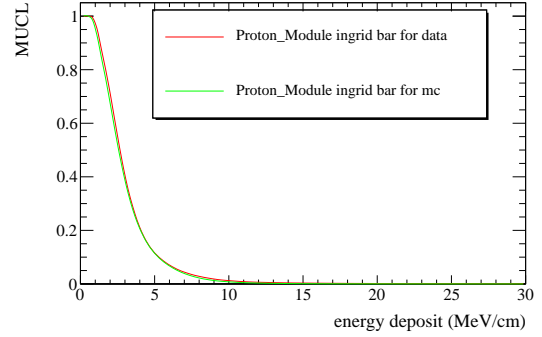
(b) Scibar scintillators in Proton Module
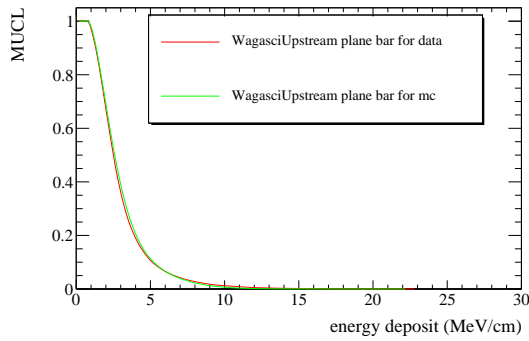
(c) Plane scintillators in Upstream WAGASCI
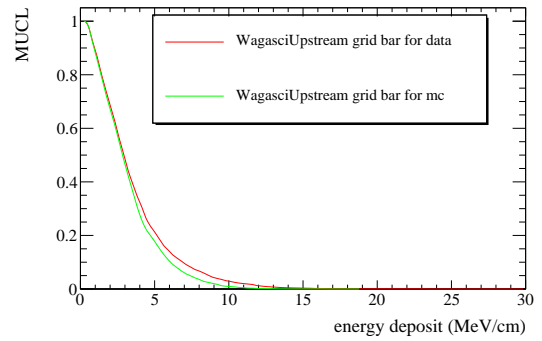
(d) Grid scintillators in Upstream WAGASCI
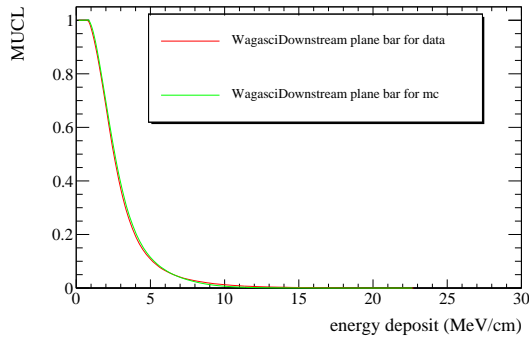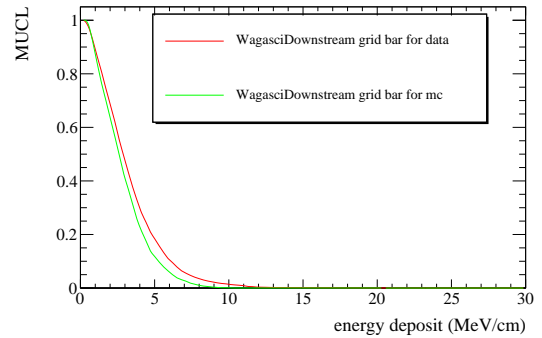
(e) Plane scintillators in Downstream WAGASCI (f) Grid scintillators in Downstream WAGASCI

Figure 108: Splines for the muon confidence level functions. Figure 108a, Figure 108b show the splines for two kinds of scintillators (INGRID and Scibar scintillators) used in Proton Module. Figure 108c, Figure 108d show the splines for two kinds of scintillators (plane scintillators and grid scintillators) used in Upstream WAGASCI. The rest of the two figures (Figure 108e, Figure 108f) are the splines for Downstream WAGASCI.

Figure 108 shows splines to calculate each confidence level (CL_i) for MC and Data. The differences between data and MC in these splines are taken into account as one of the systematic uncertainties in the late stage of this analysis.

We check the performance of the particle identification for both μ-like particles and p-like particles. The μ-like particles can be easily collected by taking a sand muon sample which is appropriate to validate this method. On the other hand, it would be difficult to obtain a p-like particles enriched sample because there is no other way to identify protons in this analysis. So we decided to use a CC inclusive sample to validate the performance for p-like particles because the sample is supposed to have a sufficient amount of p-like particles even though the purity is not nearly 100%. This inclusive sample was chosen by requiring the following conditions.

- Three-dimensional track reconstruction

- Vertexing

- Fiducial Volume cut

- At least one track matched with one of MRD detectors (supposed to be μ track)

In this validation, only the Run11 data set was used because this data set has the highest quality which is most appropriate to check performances of the method.

The validation results of μ-like particles are summarized in Figure 109 and p-like particles in Figure 110. The agreement level is good and we decided to use this method to select μ-like particles in the event selections.
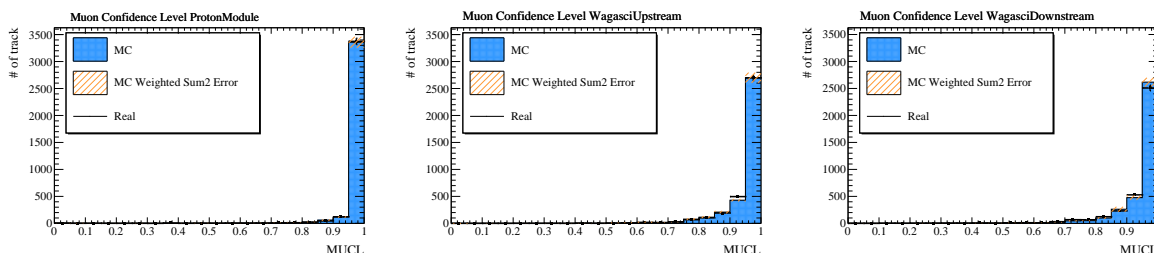
(a) μ-like particles for Proton Module

(b) μ-like particles for Upstream WAGASCI

(c) μ-like particles for Downstream WAGASCI

Figure 109: Comparisons of muon confidence level distibutions for μ-like particles.
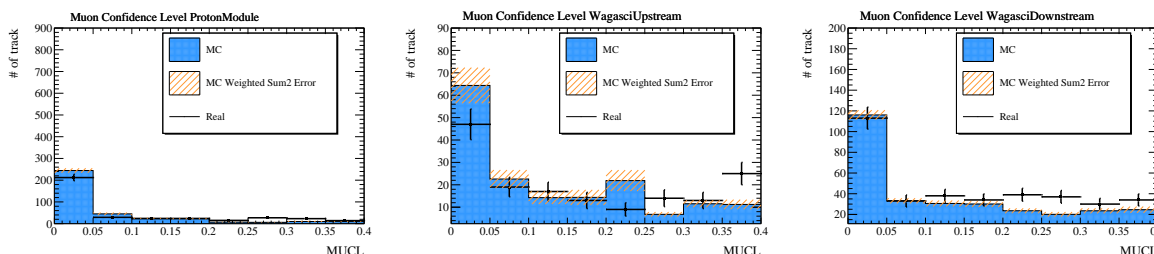
(a) p-like particles for Proton Module

(b) p-like particles for Upstream WAGASCI

(c) p-like particles for Downstream WAGASCI

Figure 110: Comparisons of muon confidence level distibutions for p-like particles.

209

I.3 Charge identification

As we aim for the measurements of ν_μ interactions, $\overline{\nu}_\mu$ interactions are among the backgrounds that can be suppressed by imposing a charge identification of muons. We need to identify the charge of only the matching track which is a muon candidate. In this section, the method of charge identification is explained in detail.

One of the muon range detectors, BabyMIND, has a magnetic field whose directions are different depending on Y positions as shown in Figure 111. There are two different kinds of regions where the magnetic field has different orientations on the X-axis.

(a) Magnetic field X direction   (b) Magnetic field Y direction   (c) Magnetic field Z direction
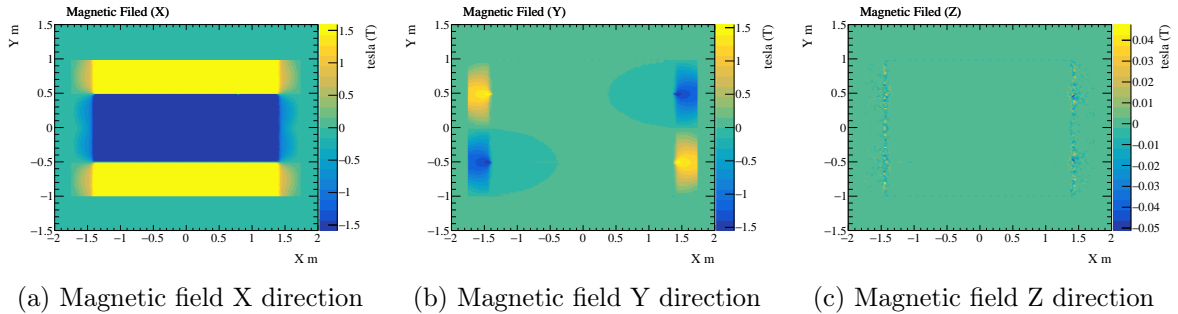
Figure 111: The orientations of the magnetic fields inside the iron planes of BabyMIND. These schematic views are seen from the neutrino beam eye. Each axis is on the detector coordinate shown in Figure 104. The geometry of BabyMIND iron planes is approximately 4 m × 2 m in the XY view. Charged particles are mostly affected by the X component of the magnetic field.

Due to the magnetic field, charged particles bend downward or upward depending on the region where they are. The method used in this analysis focuses on the track curvature only in the YZ view because it is the most sensitive to charge identification based on this structure of magnetic fields. We introduced a sequential fitter in order to reconstruct a charge with the curved tracks in the YZ view by a negative log-likelihood approach. The fitter needs to know the values of at least four parameters to get a reference track by this fitting, an incident angle from a vertex detector (ϕ_I)[59], an incident Y position (Y_I), a momentum (P_I), and a charge (C_I). These four parameters are set to free parameters in the fitting. Once these parameters are given, a reference track is obtained by taking into account the Lorenz force and energy deposit. Then, χ^2 is calculated with data points both in this reference track and in a reconstructed track assuming both hypotheses that the particle charge is negative (μ^- hypothesis) and that the particle charge is positive (μ^+ hypothesis). This calculation gives two sets of minimum χ^2 values that are fed into the calculation of the log-likelihood ratio. Table 44 shows how four free parameters are binned in a fit.

In each iteration in the fit, a particle position in each scintillator is estimated in the following way.

1. Calculate a Y position difference between the next scintillator and the current scintillator.

2. Estimate a Y position in the next scintillator.

---

[59]As a muon candidate always have a track in a vertex detector, it can be extrapolated from the detector to BabyMIND, therefore, the incident angle is roughly estimated. However, it is left as one of the free parameters because it can be estimated more accurately.

Table 44: The number of bins and width for four free parameters

Parameter	The number of bins	bin width
ϕ_I	40	0.01
Y_I	20	2 (mm)
P_I	200	12.5 (MeV/c)
C_I	2	+1 / -1

3. Calculate an energy deposit while passing to the next scintillator.

4. Calculate a momentum in the next scintillator

5. Repeat 1 to 4 until the algorithm reaches the last scintillator where there is a hit in data.

The Y position difference between the next scintillator and the current scintillator can be calculated by the Lorenz force. Figure 112 shows the example case where there are three iron planes between two successive scintillators. The Y position difference is determined by the Lorenz force if the particle passes through the iron planes assuming the multiple scattering effects are negligible. If the particle passes through the air, it feels no magnetic field.

We have another assumption that the change in the radius denoted by R_1 between two neighboring scintillators is negligible, namely $R_1 \simeq R_2$. On these assumptions, we can calculate ΔY_i, which is the Y position difference between the i-th scintillator plane and the (i+1)-th scintillator plane, by the following formula.

$$\Delta Y_i = l_{i,0} \tan \phi_i + \sum_{k=1}^{n} \left(L \tan \left(\phi_{i,k} + \frac{\theta_{i,k}}{2} \right) + l_{i,k} \tan \phi_{i,k} \right), \theta_{i,k} = \arcsin \left(\frac{L + R \sin \phi_{i,k}}{R} \right) - \phi_{i,k},$$
(I.3)

where L is the length of an iron plane, $l_{i,k} (0 \leq k \leq n)$ are the length of the air region between two successive planes. The parameter $\phi_{i,k}$ are the incident angles in the current scintillator, $\theta_{i,k}$ are the opening angles between the center point of the Lorenz force and each hit position in scintillators and n is the number of pairs of an air region and an iron region between two successive scintillator planes ($n = 3$ in the example shown in Figure 112).

As there are two kinds of orientations for the magnetic fields and two kinds of signs of the particle angle, we need to consider four kinds of cases to calculate the ΔY_i positions. Figure 112 and Equation I.3 are valid just for the case where both directions oriented by Lorentz force and incident angle are positive (upward). The following equations are corresponding to the other three cases.

$$\Delta Y_i = l_{i,0} \tan \phi_i + \sum_{k=1}^{n} \left(L \tan \left(\phi_{i,k} - \frac{\theta_{i,k}}{2} \right) + l_{i,k} \tan \phi_{i,k} \right), \theta_{i,k} = \arcsin \left(\frac{L - R \sin \phi_{i,k}}{R} \right) + \phi_k,$$
(I.4)

$$\Delta Y_i = (-1) \times \left(l_{i,0} \tan \phi_i + \sum_{k=1}^{n} \left(L \tan \left(\phi_{i,k} + \frac{\theta_{i,k}}{2} \right) + l_{i,k} \tan \phi_{i,k} \right) \right), \theta_{i,k} = \arcsin \left(\frac{L + R \sin \phi_{i,k}}{R} \right) - \phi_{i,k},$$
(I.5)
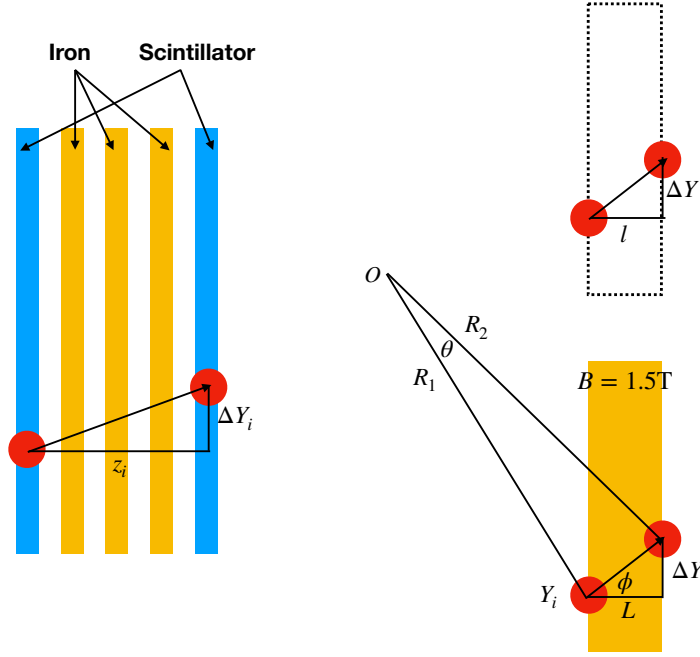
Figure 112: The example case charged particles (indicated by red circles) are on the region where there are three iron planes (indicated by yellow rectangles) between two successive scintillators (indicated by blue rectangles). The parameter z_i are the Z position differences of those two scintillators. The parameter Y_i are the current Y positions of the particle and ΔY_i are the net values between the next scintillator and the current scintillator. The parameter ϕ is the particle angle. BabyMIND has a uniform magnetic field strength of 1.5 T in iron planes, denoted by "B" in this figure. And the length of iron is 3 cm (L). The point, O is the center of the Lorentz force generated by this magnetic field. The radius of the Lorentz force in each position is denoted by R_1, R_2, respectively.

$$\Delta Y_i = (-1) \times \left(l_{i,0} \tan \phi_i + \sum_{k=1}^{n} \left(L \tan \left(\phi_{i,k} - \frac{\theta_{i,k}}{2} \right) + l_{i,k} \tan \phi_{i,k} \right) \right), \theta_{i,k} = \arcsin \left(\frac{L - R \sin \phi_{i,k}}{R} \right) + \phi_{i,k},$$
(I.6)

where Equation I.4 for the case the orientation of Lorentz force is positive (upward) and the orientation of an incident angle is negative (downward), Equation I.5 is the inverted case to Equation I.3 and Equation I.6 is the inverted case to Equation I.4. In that region where there is no iron plane between two successive scintillators, the Y position in the next scintillator is calculated by the extrapolation from the current position without the effect of the Lorentz force.

Now that the algorithm can calculate the ΔY_i in every case, a hit position in each scintillator can be estimated in a sequential way.

$$Y_{i+1} = Y_i + \Delta Y_i, P_{i+1} = P_i - \Delta P_i, R_i = \frac{P_i}{0.3[\text{m/s}] \times 1.5[\text{T}]},$$
(I.7)

$$Y_{i+1} = Y_i + \phi_i \times z_i, P_{i+1} = P_i - \Delta P_i, R_{i+1} = \frac{P_{i+1}}{0.3[\text{m/s}] \times 1.5[\text{T}]}, \tag{I.8}$$

where z_i are the Z position differences between two successive scintillator planes. Equation I.7 is used if there is at least one iron plane in two successive scintillator planes and Equation I.8 for the case there is no iron plane. The parameter ϕ_{i+1} are also calculated depending on the configuration of the two successive scintillator planes.

$$\phi_{i+1} = \phi_{i,n} + \frac{\theta_{i,n}}{2}, \tag{I.9}$$

where $\theta_{i,n}$ are the same ones defined in Equation I.3 to Equation I.6. Equation I.9 corresponds to the case for Equation I.7, otherwise the angle ϕ_{i+1} is the same as ϕ_i.

Once the four free parameters are specified iteratively following the binning scheme shown in Figure 44, those sequential formulae given in Equation I.7, Equation I.8, and Equation I.9 provide an estimation of sets of a hit position in each scintillator. Each fitted point in the i-th scintillator is written by $f_i(\phi_I, Y_I, P_I, C_I)$. A likelihood function is defined with these fitted points and data points $(Y_{D,i})$.

$$L(\phi_I, Y_I, P_I, C_I | D) = \prod_i^N \frac{1}{\sigma_i} \exp\left\{ \left(-\frac{1}{2} \sum_i \frac{(Y_{D,i} - f_i(\phi_I, Y_I, P_I, C_I))^2}{\sigma_i^2} \right) \right\}, \tag{I.10}$$

where N is the last plane where there is a hit in data. To make a numerical calculation simple, we use a log-likelihood approach.

$$-2 \ln L(\phi_I, Y_I, P_I, C_I | D) = 2 \sum_i \ln \sigma_i + \sum_i \frac{(Y_{D,i} - f_i(\phi_I, Y_I, P_I, C_I))^2}{\sigma_i^2}. \tag{I.11}$$

The log-likelihood ratio is used to get a discriminator for a particle charge because a charge parameter has only two discrete variables.

$$R = \sum_i \frac{(Y_{D,i} - f_i(\phi_I, Y_I, P_I, C_I = -1))^2}{\sigma_i^2} - \sum_i \frac{(Y_{D,i} - f_i(\phi_I, Y_I, P_I, C_I = +1))^2}{\sigma_i^2}. \tag{I.12}$$

The parameter R will be used as a discriminator of a particle charge.

Sand muon sample from the Run11 data set is used to validate the charge identification performance in the same way as the validation of the method of particle identification. The plot is already shown in Figure 65.

J PartIII: Supplemental materials for the event selections

This appendix provides supplemental materials that are not given in Section 11.2 on the event selections.

J.1 Selection criteria for the signal samples

J.1.1 Track / Cluster ratio

Figure 113 shows the data-MC comparison of this parameter with the CC inclusive sample that was also used in the validation of particle identification. The consistency between data and MC was assessed by the standard χ^2 metric, which is defined by

$$\chi^2 = \sum_{i=1}^{k} \frac{(N_{\text{data}} - N_{\text{MC}})^2}{N_{\text{MC}}} \tag{J.1}$$

where k is the number of bins, N_{data} and N_{MC} are the number of events in data and MC. As this y-axis is log-scale, discrepancies in the Proton Module sample are rather obvious between data and MC while the level of agreement in the WAGASCI detectors sample is better. The power of rejecting the background from the wall is significant for the WAGASCI detectors sample. We have decided to use this parameter only for the WAGASCI detectors sample to keep consistency between data and MC.
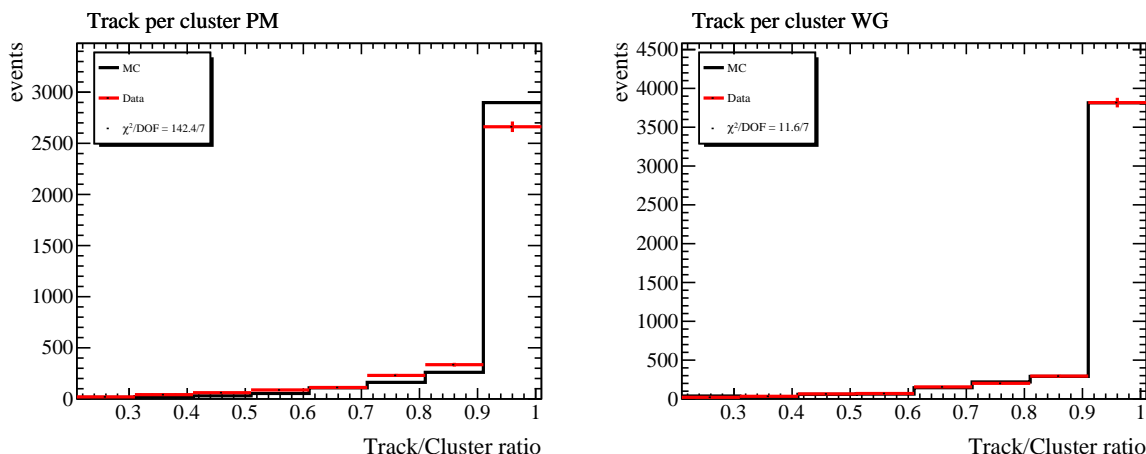
Figure 113: Data/MC comparisons of the track per cluster ratio for the Proton Module sample (left) and WAGASCI detectors samples (right). The χ^2 is defined in Equation J.1

J.1.2 Michel electron tagging

The method to tag the Michel electrons is explained in Section 11.2. Here, we show one of the validation results for the Michel electron tagging by using partial data taken in 2021 which corresponds to 1.5×10^{20} P.O.T. Sand muon samples were used in this validation. For the WAGASCI detectors sample, each sand muon is supposed to go through the Upstream WAGASCI and Proton Module before it stops inside the Downstream WAGASCI. For Proton Module sample, track matching between Upstream WAGASCI and Proton Module is required and it should stop

inside Proton Module. Contained volume for both Downstream WAGASCI and Proton Module are summarized in Table 45.

Table 45: Contained volume for stopping muons

Sample	X limit	Y limit	Z limit
downstream WAGASCI	±450	±450	±150
Proton Module	±450	±450	±250

The potential difference between MC and data related to the Michel electron tagging should come from the existence of dead time in data. The current MC does not handle the dead time in the same way as data acquisition although there is a 100 ns dead time between each trigger cycle corresponding to each bunch width (580 ns) for Proton Module. In this validation, a simple implementation is adapted by just masking hits in MC if their TDC time falls in the corresponding dead time.

Table 46 show the number of Michel electron candidates with efficiency as well as the number of selected events. The total number of events between MC and data does not correspond to the ratio of statistics expected from POT, which is expected from the previous WAGASCI analysis. It seems tagging efficiency between both MC and data agrees well with each other.

Table 46: Efficiency of Michel electron tagging for both WAGASCI and Proton Module

Detector	MC (1.0×10^{21} POT)		Data (0.15×10^{21} POT)	
	Tagging efficiency	selected events	Tagging efficiency	selected events
WAGASCI	30.3%	2913	32.8%	567
Proton Module	22.1%	23287	22.3%	4815

J.1.3 Contained Volume cut

As we use the range method to reconstruct a muon momentum, the contained volume cut in each MRD was applied only for the cross section measurement in the momentum binning. Table 47 shows the defined contained volume regions.

Table 47: Range of the Contained Volume

Selection cut	WallMRD nominal	BabyMIND nominal
Contained Volume (Lower) (mm)	(-170, –, -750)	(-1300, -900, 2nd pln)
Contained Volume (Upper) (mm)	(170, –, 750)	(1300, 900, 17th pln)

As WallMRD does not have YZ planes, any regions cannot be defined along with the Y axis. As for the X and Z axis, the region was defined by excluding the outer layer of the scintillator planes. For BabyMIND, the outer layer was excluded along with the X and Z axis in the same way as the WallMRD. As for the Y axis, the distance between channels is rather short (20 mm), we need to choose which range would be reasonable. The efficiency of choosing events where muons stop at the true level was used to evaluate the boundary of the Y position. Figure 114 shows the efficiency transition for the boundary Y with other ranges defined in the way that is

shown in Table 47. In order to make the range reasonable, we choose the range which gives 90% efficiency based on the Figure 114.
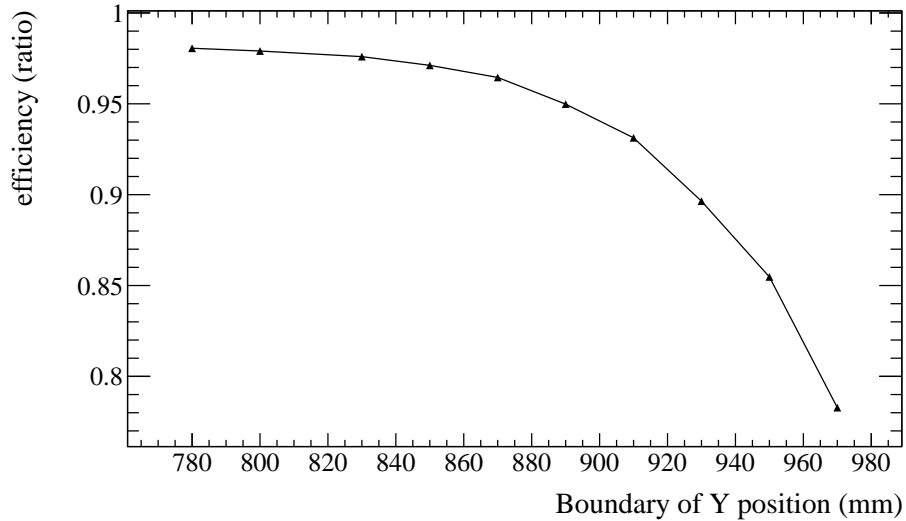
Figure 114: The efficiency of choosing events where muons stop at the true level to the selected number of events for the Proton Module samples with other ranges defined in the same way that is shown in Table 47.

J.1.4 Performance of the selection criteria

To check how each selection criterion has a positive impact on the selection performance, the reconstructed angle distributions based on the selection criteria except for a specific selection, are compared to the nominal angle distribution. Figures 115, 116 show WAGASCI and Proton Module samples, respectively. Most of the selections work in terms of the reduction in background contamination. The number of tracks cut has little effect on an increase in signal purity because the number of events with more than three tracks is a small fraction of selected events.
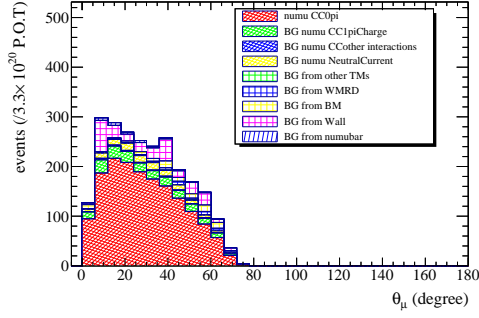
(a) all selection applied
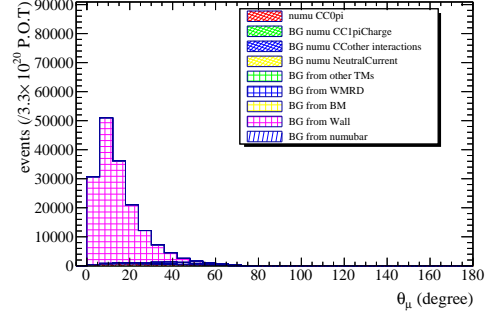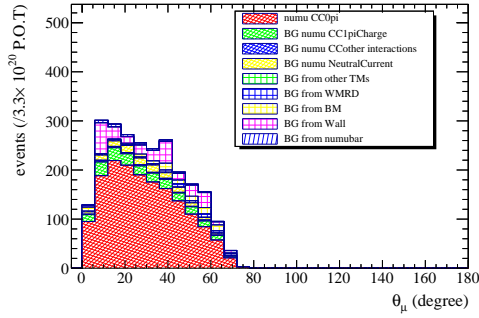
(b) without the fiducial volume cut.

(c) without the number of track cut.
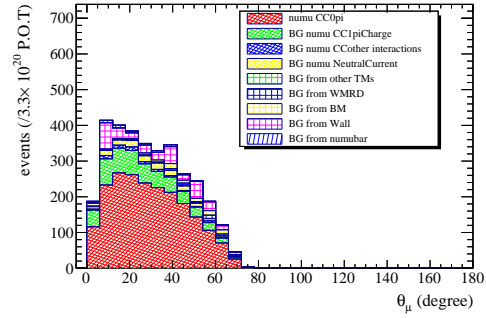
(d) without the muon confidence level cut.
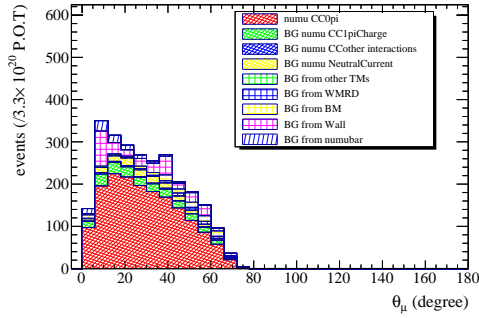
(e) without the charge id cut.
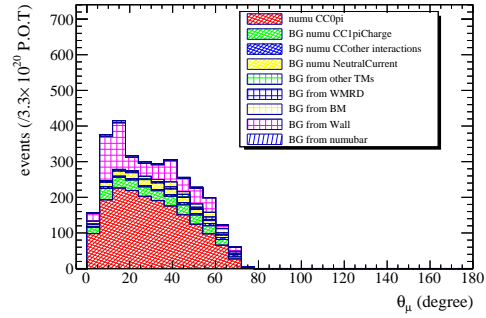
(f) without the track/cluster ratio cut.
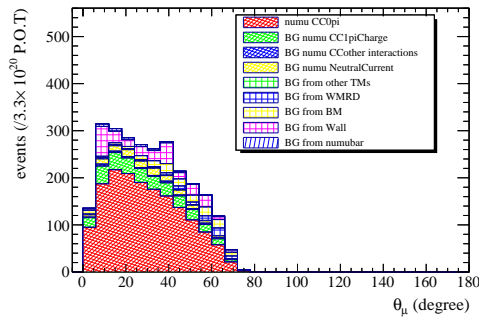
(g) without the Michel electron cut.

Figure 115: The reconstructed μ angle distribution for the WAGASCI samples without a certain selection (115b to 115g), otherwise unchanged. The signal purity is 77.0%, 4.07%, 52.5%, 57.5%, 67.5%, 71.6%, and 72.7% respectively.
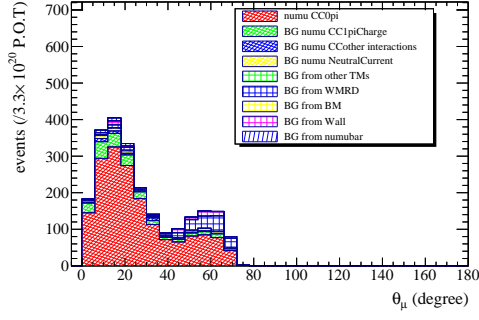
(a) all selection applied
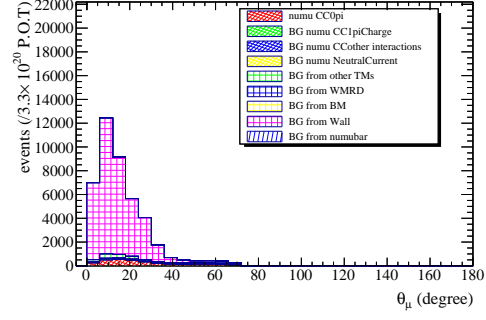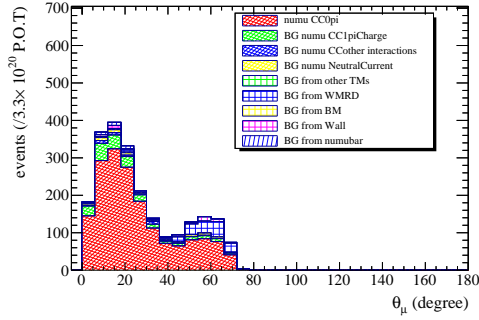
(b) without the fiducial volume cut.

(c) without the number of track cut.
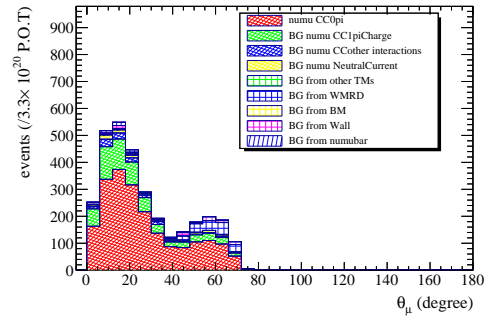
(d) without the muon confidence level cut.
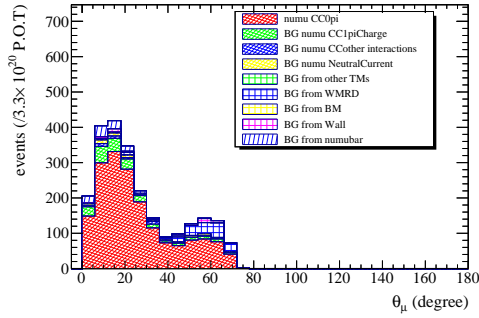
(e) without the charge id cut.
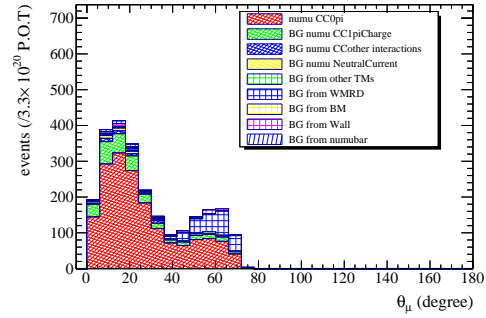
(f) without the Michel electron cut.

Figure 116: The reconstructed μ angle distribution for the Proton Module samples without a certain selection (116b to 116f), otherwise unchanged. The signal purity is 71.6%, 5.73%, 54.8%, 57.0%, 64.0% ,and 65.9% respectively.

J.2   Selection criteria for side-band samples

J.2.1   CC1$\pi^{\pm}$ sample

Figure 117 shows the whole CC1$\pi^{\pm}$ selection criteria. Each component has been already mentioned in the main section (Section 11.2) while some conditions are reversed for selecting this sample efficiently. Selections are divided into two paths depending on whether a pion can be reconstructed in a track or not. The first path is prepared to find the CC1$\pi^{\pm}$ sample when a pion track is under the tracking threshold. The whole selection criteria in this path have the same scheme to select the CC0$\pi^{\pm}$ sample except for reverting the final cut on Michel electron tagging. If the Michel electron is found in an event, the event can be considered to have a pion track and counted as the CC1$\pi^{\pm}$ event. The other path is introduced to find a pion track which should be over the tracking threshold. A pion track can be considered to be more like a μ-like track than a p-like track in terms of its MUCL value. So it would provide a pion selection to reverse the MUCL cut applied to the CC0$\pi^{\pm}$ selection. Then charge cut is applied in order to reduce wrong-sign backgrounds.
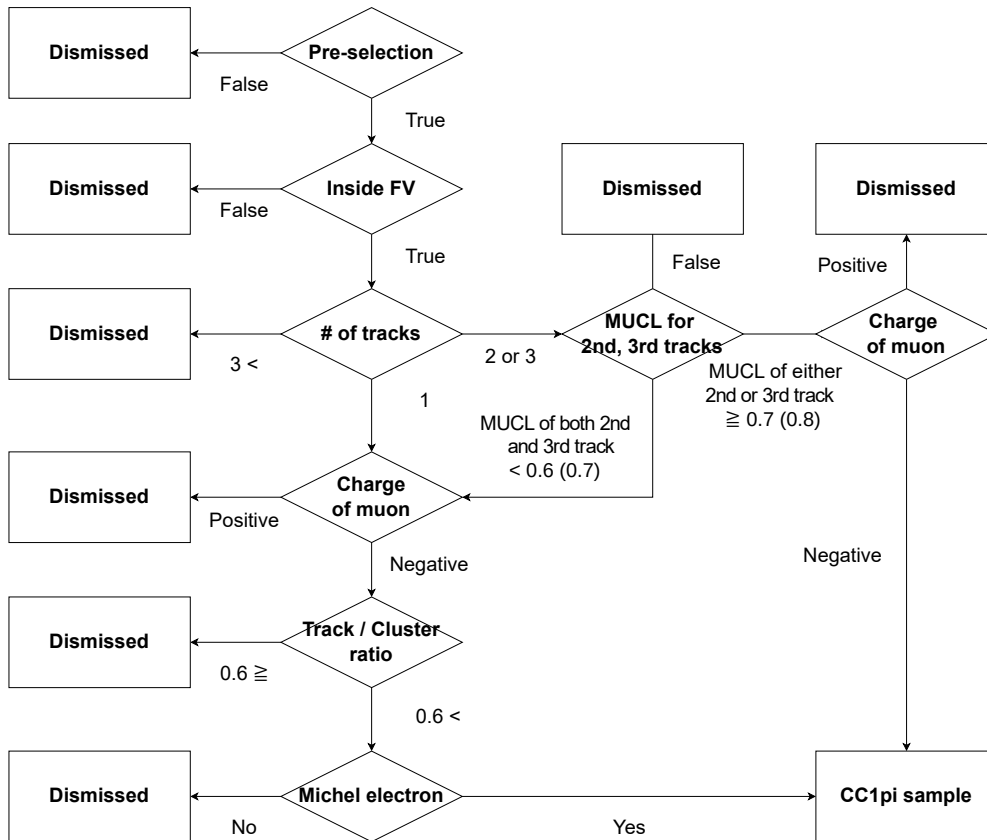
Figure 117: Event selection criteria for numu CC1$\pi^{\pm}$. As for "MUCL for 2nd, 3rd tracks" and "Track / Cluster ratio", thresholds are different between WAGASCI and Proton Module. Parenthesis indicates WAGASCI detectors case.

J.2.2 Sand muon sample

When neutrino interactions happen in the upstream wall to the experimental location, muons from the charged current interactions go to the detector complex. These muons are called "sand muon", which can be used to check the basic performance of the detector such as timing and light yield measurements. Here, we use the sand muon sample to understand the background from the neutrino interactions in the wall. Figure 118 shows the whole selection criteria for the sand muon sample. Criteria are rather simple for this sample. For events passing Pre-selection, it requires a vertex point to be outside the fiducial volume. As sand muon events are supposed to have just one track from μ, the number of tracks cut is applied in order to make sure each event has one track. The track has to come from outside all subdetectors, it would be sensible to add a selection to require a hit in the 1st plane in upstream WAGASCI, which is the most upstream detector. Finally, it checks if the track goes to one of the muon range detectors which is expected to play a role in reducing pion contamination into this sample.
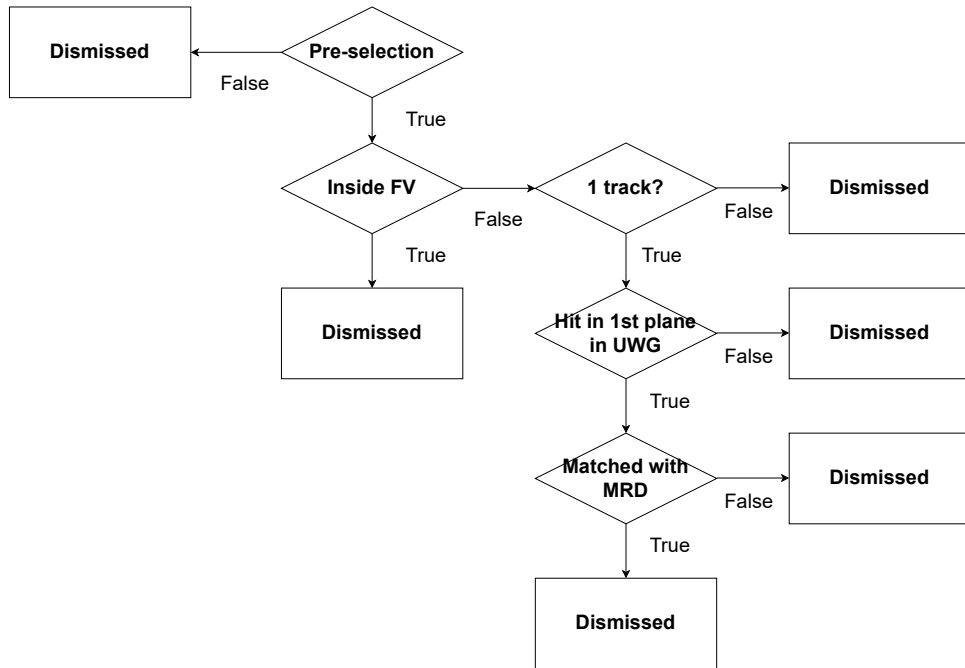
Figure 118: Event selection criteria for sand muon sample.

K PartIII: Studies of neutrino flux and detector systematic uncertainties

K.1 neutrino flux

The neutrino flux uncertainties are evaluated using the same method as that for the ND280 and SK. The uncertainty of the neutrino flux has been given in the binning format summarized in Table 48. This binning was chosen so that a fair amount of events are selected in each bin. Figures 119, 120 show the covariance matrix and correlation matrix on the neutrino flux at the position of the Downstream WAGASCI. Figures 121, 122 show the total systematic uncertainties at the position of the Downstream WAGASCI.

Table 48: Energy binning for flux uncertainty evaluation

Energy range	Number of bins	Energy width per bin
0.0-3.0 GeV	15	0.2 GeV
3.0-4.0 GeV	1	1.0 GeV
4.0-10.0 GeV	3	2.0 GeV
10.0-30.0 GeV	1	20.0 GeV
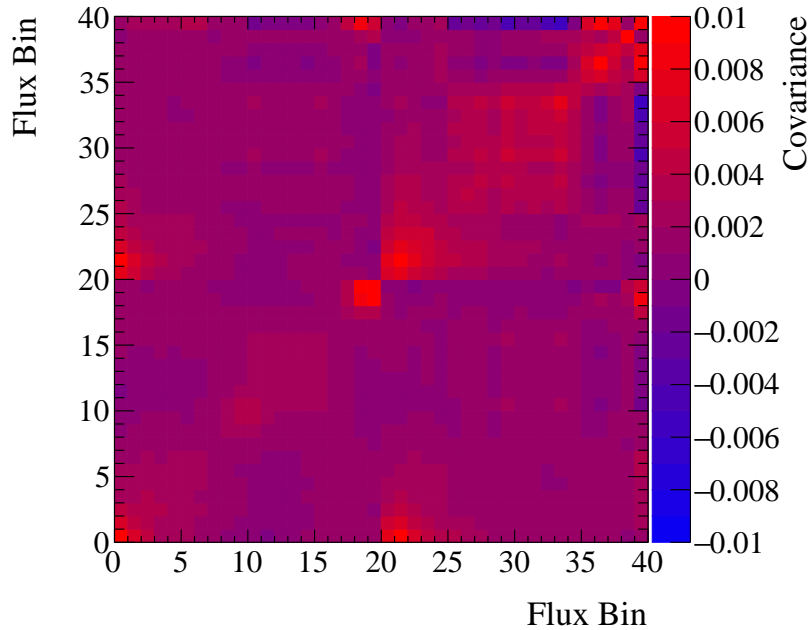
Figure 119: The covariance matrix for the total uncertainty due to neutrino beam flux on WAGASCI with the FHC mode. The bins 0-19 correspond to ν_μ fraction, and bins 20-39 correspond to $\overline{\nu}_\mu$ fraction.
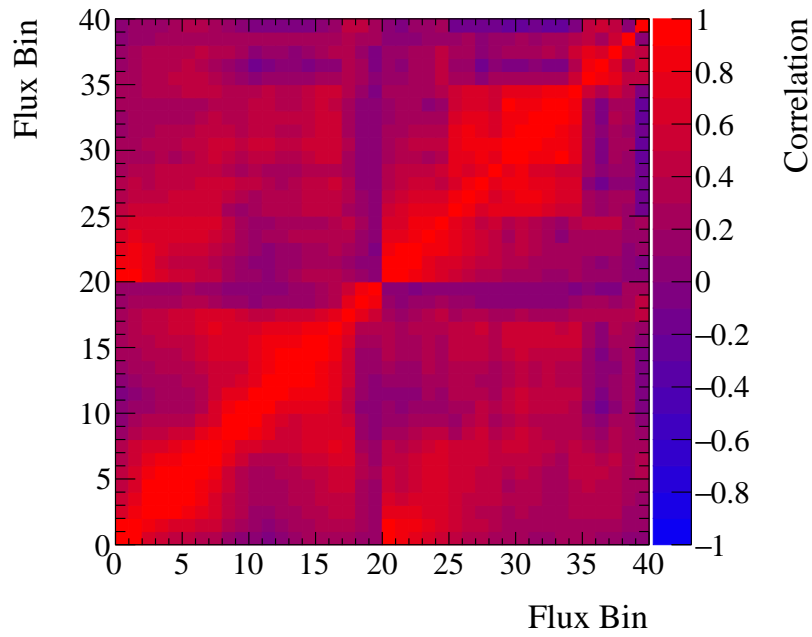
Figure 120: The correlation matrix for the total uncertainty due to neutrino beam flux on WA-GASCI with the FHC mode. The bins 0-19 correspond to ν_μ fraction, and bins 20-39 correspond to $\overline{\nu}_\mu$ fraction.
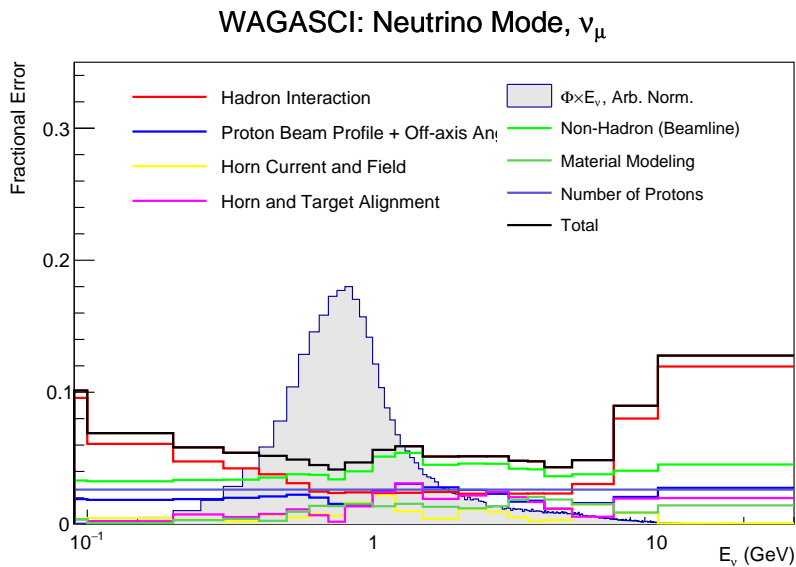
Figure 121: Total systematic uncertainties for ν_μ in FHC mode at the WAGASCI position.
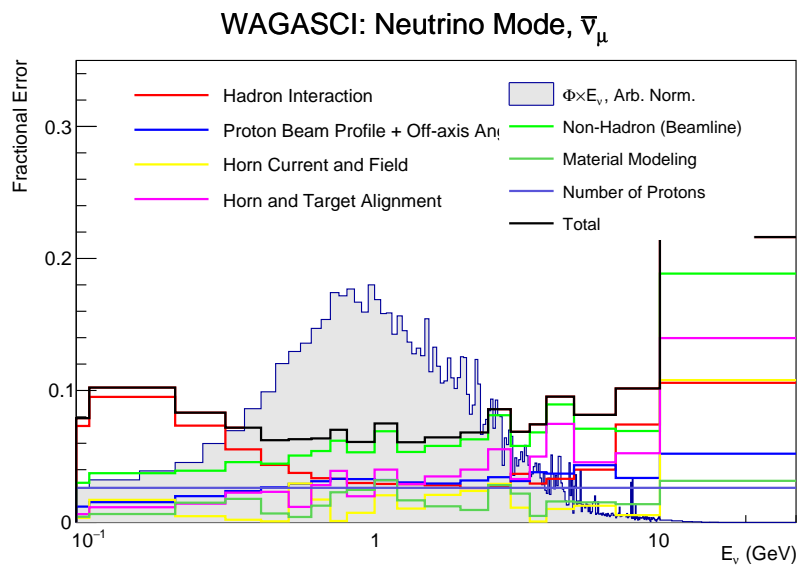
Figure 122: Total systematic uncertainties for ν_μ in FHC mode at the WAGASCI position.

K.2   detector systematics

Our analysis framework consists of three bodies, Geant4-based Monte Carlo simulation, track reconstruction and sample selections. All descriptions in our MC were relying on the nominal settings that were measured in the experimental places and using physics data. As there is measurement precision for each setting, each deviated value from the nominal setting was treated as an error source. These error sources are categorized into detector-related parameters in this section. In the track reconstruction, we have introduced many kinds of tracking thresholds in each process as described in Section H. Each threshold was set to a certain value so that we make sure it covers the sufficient range to get proper reconstruction done. In order to take a difference between MC and data into account, we intentionally shifted these thresholds one by one. And the difference in changes in the number of selected events between MC and data are considered error sources (track-reconstruction-related parameters). For sample-selections-related parameters, the data and MC differences are taken into account by shifting each nominal selection threshold. The procedure to evaluate each systematic parameter is summarized in Figure 123.
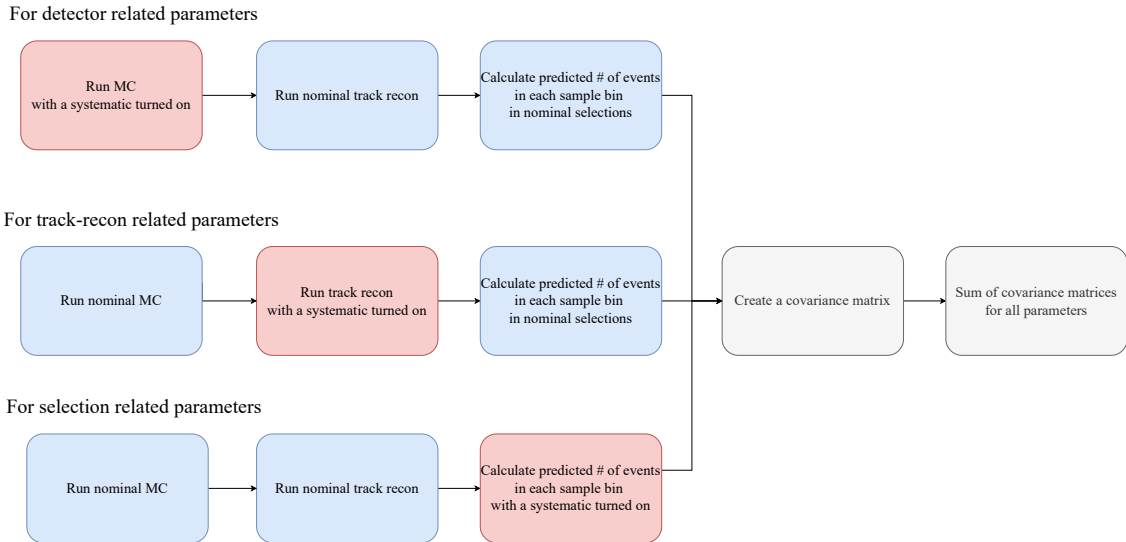
Figure 123: A diagram to show the procedure to calculate each covariance matrix. The red colour indicates a process where a systematic parameter is turned on for each category. The blue colour marked a process for nominal MC or reconstruction or event selection being used.

K.2.1   Magnetic field strength

BabyMIND detector has the magnetic field in iron planes, whose strength is supposed to be 1.5T in any region. The design of the electric coil in BabyMIND is complicated so that it minimizes the leak field outside. In order to estimate the field strength, we had a two-dimensional simulation for the magnetic field, which was implemented in the MC framework. Figure 124 shows the measurement result for a module in BabyMIND. We operated the magnet power supply at 140 A in our data taking. The fluctuation of the power supply is less than 0.1 A, which is negligible. The estimated error of the field strength is about 0.4 T according to Figure 124 and the magnetic

field is saturated at 1.57 T. We have chosen ±0.5 T for the systematic uncertainty of magnetic field strength to take it into account the effect of magnetic-field modelling in the MC. The covariance of the detector systematics is calculated as follows.

$$V_{ij} = \frac{1}{2}\frac{(\phi^i_{\text{nom}} - \phi^i_+)(\phi^j_{\text{nom}} - \phi^j_+)}{\phi^i_{\text{nom}}\phi^j_{\text{nom}}} + \frac{1}{2}\frac{(\phi^i_{\text{nom}} - \phi^i_-)(\phi^j_{\text{nom}} - \phi^j_-)}{\phi^i_{\text{nom}}\phi^j_{\text{nom}}} \tag{K.1}$$

where V_{ij} is the (i,j) element of the covariance matrix, ϕ^i_{nom} is the number of selected events in the nominal setting in the i-th bin while ϕ^i_+ and ϕ^i_i refer to the number of selected events in the fluctuations in the i-th bin (for +0.5 T and -0.5 T respectively).
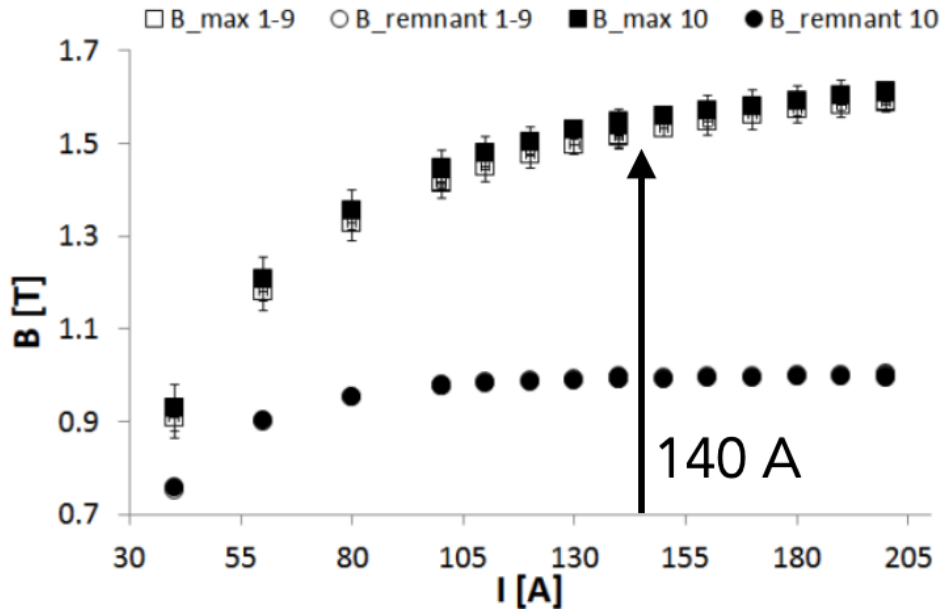
Figure 124: B-I curve of ARMCO (iron material) measured on one magnet module in Baby-MIND [176]

Figs. 125, 126 show the fractional uncertainty along with the nominal predictions.

(a) P_μ binning

(b) θ_μ binning
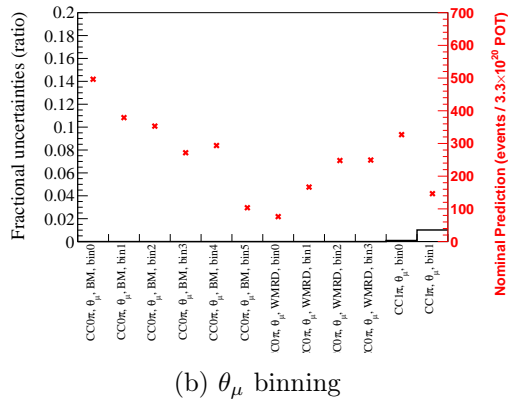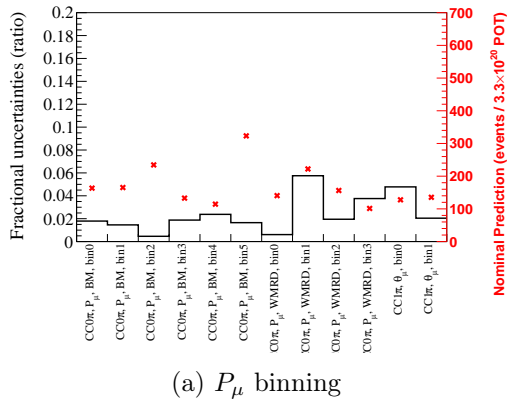
Figure 125: Systematic uncertainty of magnetic field strength for the Proton Module samples

(a) P_μ binning

(b) θ_μ binning
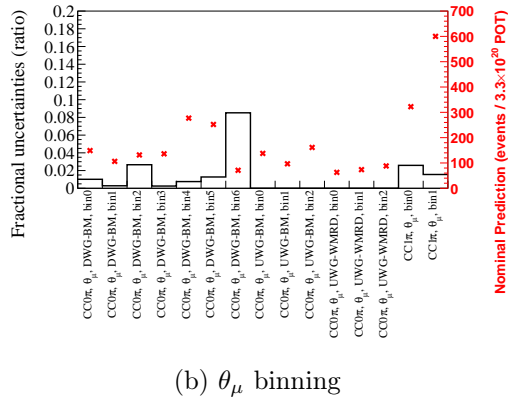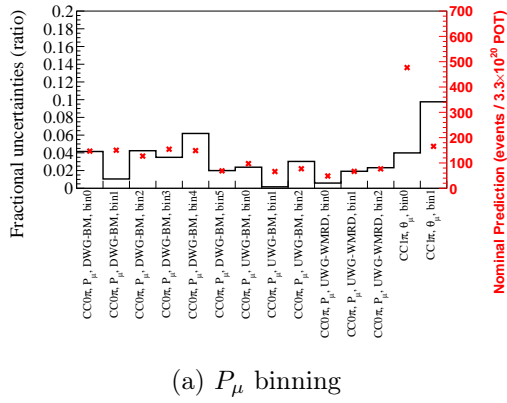
Figure 126: Systematic uncertainty of magnetic field strength for the WAGASCI samples

K.2.2 Pion SI in Monte-Carlo simulation

Final state interactions (FSI) and secondary interactions (SI) are the major nuclear medium effects which potentially affect CC0$\pi^\pm$ topology if some pions are trapped inside nucleus and cannot get out of the nucleus due to these effects. The underlying physics model used in the Geant4 simulation is "QGSP Bertini" model, which has some discrepancies in the $\pi^\pm$-A cross section. Various kinds of models are compared with data to extract the best fit parameters along with their uncertainties. Interaction channels are divided into five.

- Absorption (ABS): No pions in the final state

- Quasi-elastic Scattering (QE): Only one pion in the final state of the same charge as the incident beam

- Single Charge Exchange (CX): Only one π^0 in the final state

- Absorption + Single Charge Exchange (ABS + CX): Sum of ABS and CX

- Reactive: Sum of ABS + CX + QE, Double Charge Exchange and Hadron Production. Double Charge Exchange is defined as final states with one pion in the final state with opposite charge as the incident beam. Hadron production is defined as final states with more than pion.

In this analysis, QE, ABS and CX are closely relevant channels to consider these effects. The size of pion SI related effects are basically determined by the uncertainty of $\pi^\pm$-A cross section. The uncertainty matters in two kinds of context. The first will appear in somewhat interaction probability function (P1 = $\exp\{(-n\sigma x)\}$, where n is the number of scattering center of nucleus in mm^3, σ is the cross section and x is the travelling length before the interaction) and another is the uncertainty of its just cross section (P2). Considering the background components of CC0$\pi^\pm$, P2 will be dominant. Just in case this analysis considers these two factors following the ND280 analysis. So the weight factor for this systematic is given by the product of both weights $w_{P_1} \times w_{P_2}$. Unlike ND280 analysis method, this analysis estimates the averaged weight factor to the total number of selected pion background contaminating into the signal instead of taking into account each weight on an event-by-event basis. In order to calculate the weight factor for P1 in each background event, the following formula was used.

$$w_{P_1} = \prod_{i=1}^{i=n_\pi} \exp\left\{\left(-\sigma^j x_i^j\right)\right\} = \exp\left\{\left(\sigma^j x_i^j\right)\right\} \simeq \exp\{(n_\pi \langle\sigma\rangle\langle x\rangle)\} \tag{K.2}$$

where $\langle\sigma\rangle$ is the weighted cross section of QE+ABS+CX channels and $\langle x\rangle$ is the interaction length of the pion in a certain nucleus (^{12}C in this analysis). The same weighted cross section was used for the factor P2, and then the weight factor can be calculated with these values. It should be noted that the P1 weight is multiplied by the number of all pion backgrounds while P2 weight is multiplied by the number of pion background having the interaction inside the vertex detector. If the pion goes through the vertex detector, it wasn't taken into account in this calculation.

The weighted cross section was calculated with the digitized values of these plots and the true momentum distribution of the pion background contaminating into this selection. Also, each 1 σ error on the corresponding best fit value of the cross section value is digitized and weighted error is calculated for both QE and ABS+CX. The total uncertainty of this parameter was given by the quadrature sum of the number of events obtained by two weight factors (P1, P2).
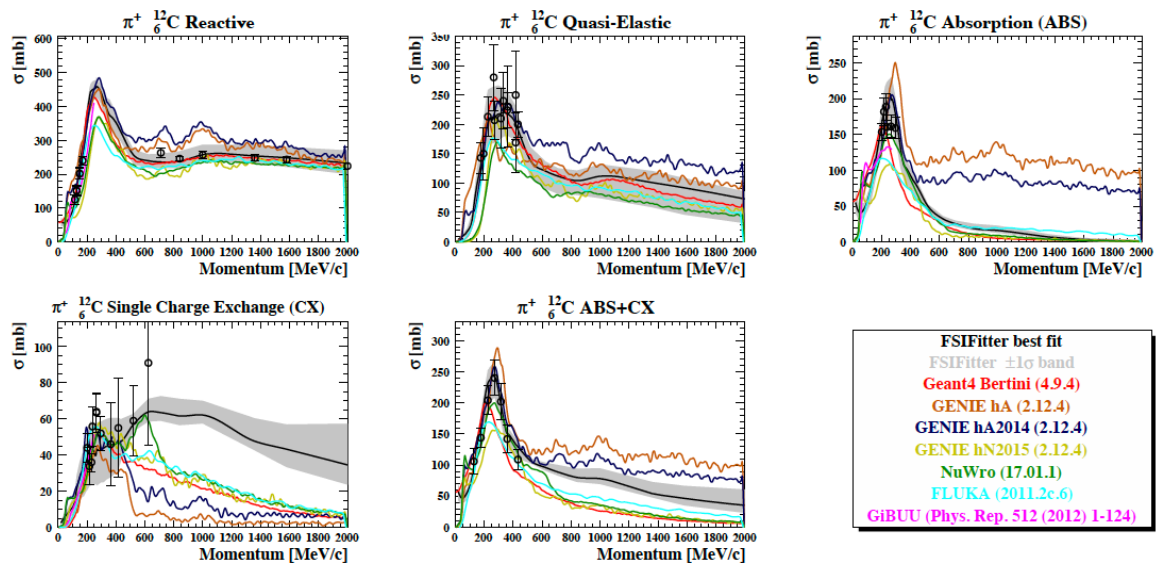
Figure 127: Comparison of the available π^+-C cross section external data with the FSIFitter best fit and its 1σ band, and other models.

K.2.3 MPPC noise

MPPC accidental noise hits sometimes result in misreconstruction of vertices or two-dimensional tracks, which vary the selected number of events. MPPC noise rates for each detector were measured using off-beam data. For conservative choices of this systematic uncertainty, both twice higher noise rate and zero noise rate were chosen as the fluctuation from the measured noise rate. The covariance of the detector systematics is calculated as follows.

$$V_{ij} = \frac{1}{2} \frac{(\phi_{\mathrm{nom}}^i - \phi_+^i)(\phi_{\mathrm{nom}}^j - \phi_+^j)}{\phi_{\mathrm{nom}}^i \phi_{\mathrm{nom}}^j} + \frac{1}{2} \frac{(\phi_{\mathrm{nom}}^i - \phi_-^i)(\phi_{\mathrm{nom}}^j - \phi_-^j)}{\phi_{\mathrm{nom}}^i \phi_{\mathrm{nom}}^j} \tag{K.3}$$

where "+" refers to twice higher noise rate and "-" refers to zero noise rate.

Figs. 128, 129 show the fractional uncertainty along with the nominal predictions.

(a) P_μ binning
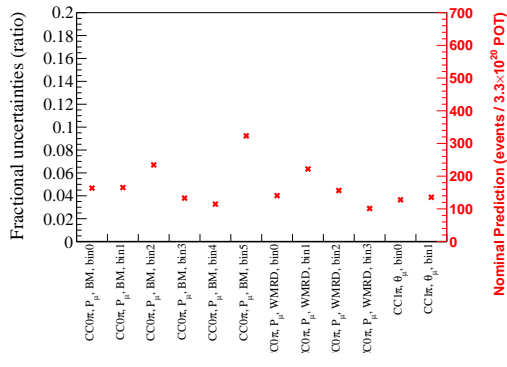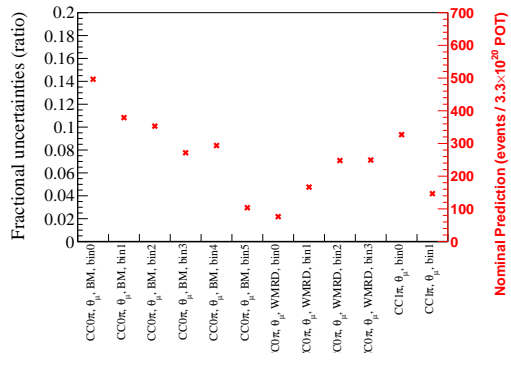
(b) θ_μ binning

Figure 128: Systematic uncertainty of MPPC noise for the Proton Module samples

(a) P_μ binning
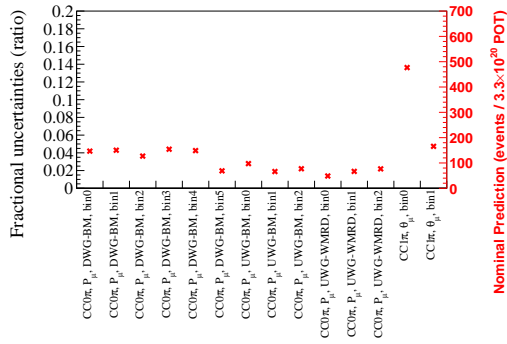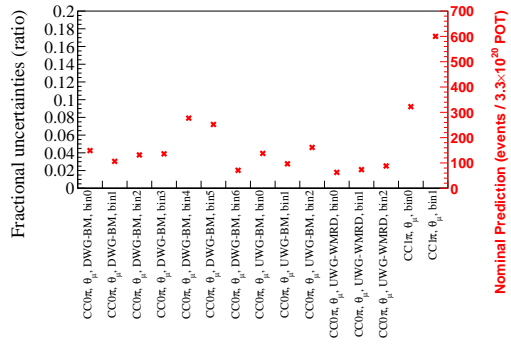
(b) θ_μ binning

Figure 129: Systematic uncertainty of MPPC noise for the WAGASCI samples

K.2.4 scintillator cross talk

The effect of scintillator cross talk was taken into account only for WAGASCI modules because it was confirmed to be negligible for Proton Module in the past analyses. Crosstalk occurs between the grid scintillators in the x view and the y view through the cross point of the slits. Its uncertainty should be estimated because the cross talk sometimes results in mis-vertexing and track mis-reconstruction. As we have already measured the effect of crosstalk for both WAGASCI modules which were done in the previous analysis [160], we can use the same results to show the relation of the light yield between grid-x and grid-y scintillator (Figure 130, Figure 131). In the MC framework, when a grid scintillator has a hit, crosstalk hits are generated on the grid scintillator in the opposite view within 5 cm distance from the hit point. The size of the light yield of the crosstalk hit is determined based on the Poisson distribution with a mean value calculated as follows.

$$\text{observed p.e. of the initial hit } \times \text{crosstalk rate} \tag{K.4}$$

where the crosstalk rate was determined based on the slope of Figs. 130, 131. The variation of the crosstalk effect is assumed to be 10%. (The previous analyses assume 1% variation, but we used previous measurements on the crosstalk rate. Conservatively, the uncertainty is assumed to be 10%) The covariance of the detector systematics is calculated as follows.

$$V_{ij} = \frac{(\phi^i_{\text{nom}} - \phi^i_+)(\phi^j_{\text{nom}} - \phi^j_+)}{\phi^i_{\text{nom}} \phi^j_{\text{nom}}} \tag{K.5}$$

where "+" refers to the 1% variation of the measured values for both modules.
Figs. 132, 133 show the fractional uncertainty along with the nominal predictions.
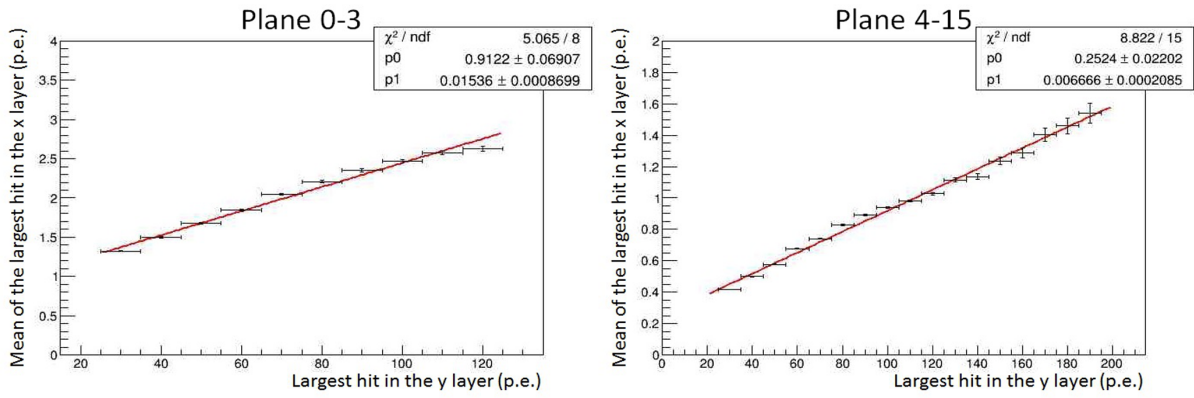
Figure 130: Relation of the light yield between grid-x and grid-y scintillator for Upstream WA-GASCI
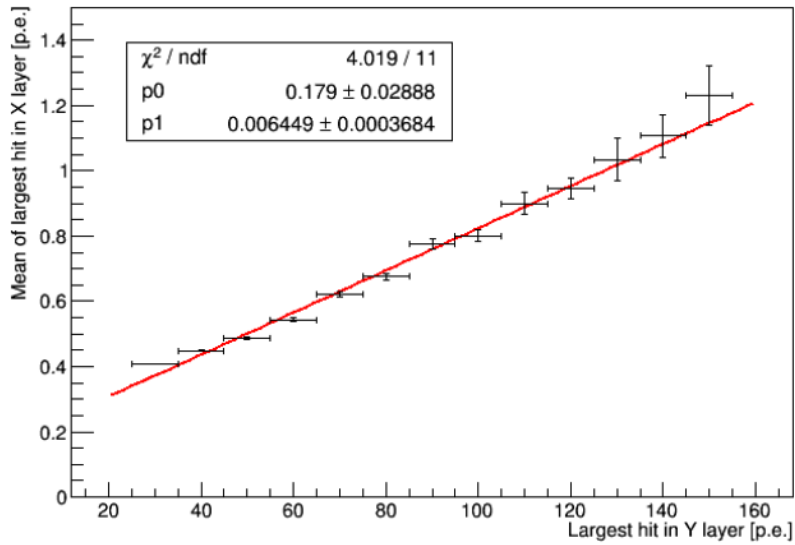
Figure 131: Relation of the light yield between grid-x and grid-y scintillator for Downstream WAGASCI

(a) P_μ binning
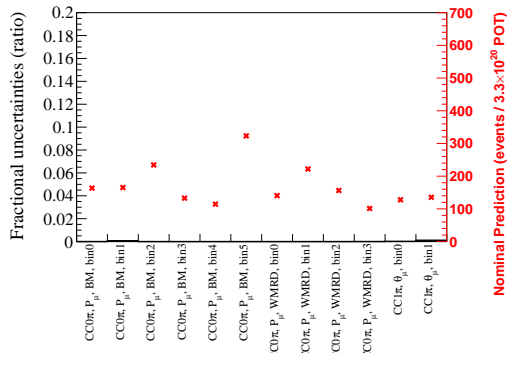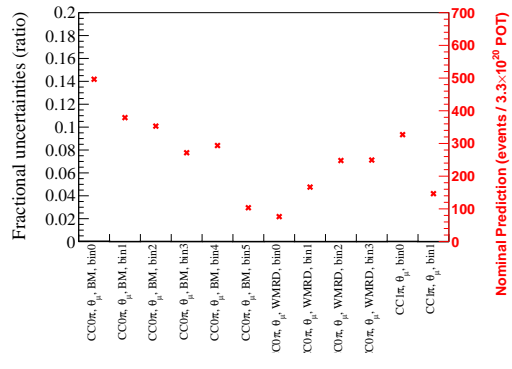
(b) θ_μ binning

Figure 132: Systematic uncertainty of cross talk for the Proton Module samples

(a) P_μ binning
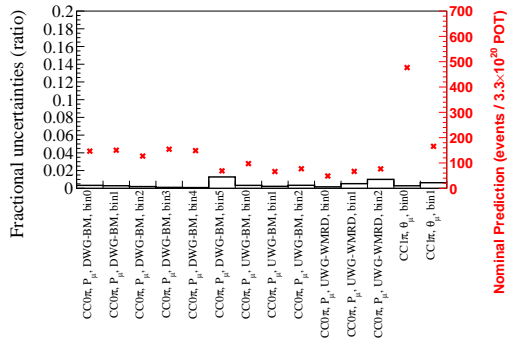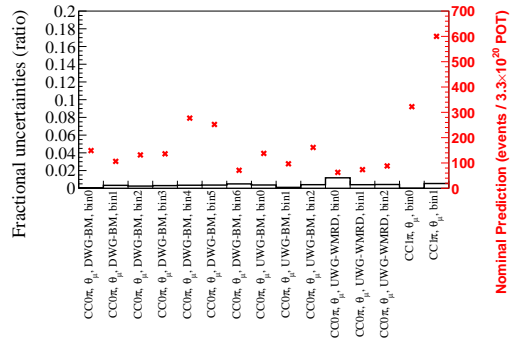
(b) θ_μ binning

Figure 133: Systematic uncertainty of cross tallk for the WAGASCI samples

K.2.5 Light yield

Light yield is supposed to have an effect on the hit threshold, which is the cause of mis-reconstruction in the two-dimensional clustering process. The light yield for each detector module was measured with sand muon samples. And variation of parameters to determine the light yield in the MC framework was decided to cover differences observed in light yield distribution between MC and data. Figure 134 shows the example cases for vertex modules, and Figure 135 for MRDs.. Each variation is summarized in Table 49. The covariance of the detector systematics is calculated as follows.

$$V_{ij} = \frac{1}{2} \frac{(\phi^i_{\text{nom}} - \phi^i_+)(\phi^j_{\text{nom}} - \phi^j_+)}{\phi^i_{\text{nom}}\phi^j_{\text{nom}}} + \frac{1}{2} \frac{(\phi^i_{\text{nom}} - \phi^i_-)(\phi^j_{\text{nom}} - \phi^j_-)}{\phi^i_{\text{nom}}\phi^j_{\text{nom}}} \tag{K.6}$$

where "+" refers to plus variation and "-" refers to minus variation.

Table 49: Variation of light yield

Detector	"+" Variation	"-" Variation
Proton Module	+5%	-5%
WAGASCI modules	+5%	-5%
WallMRDs	+10%	-10%
BabyMIND	+5%	-5%

Figs. 136, 137 show the fractional uncertainty along with the nominal predictions.
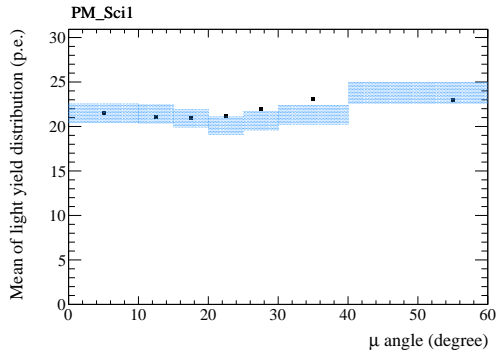
(a) Variation of light yiled for Proton Module scibar scintillator
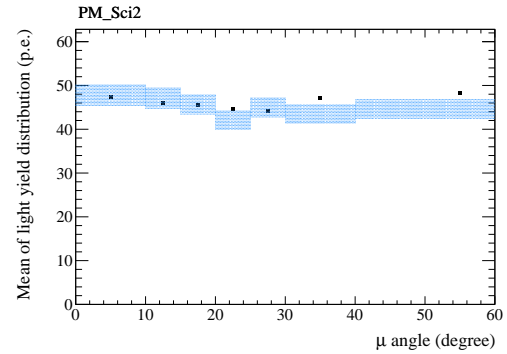
(b) Variation of light yiled for Proton Module ingrid scintillator
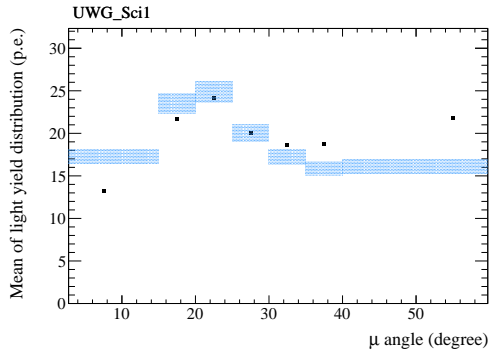
(c) Variation of light yiled for WAGASCI upstream plane scintillator
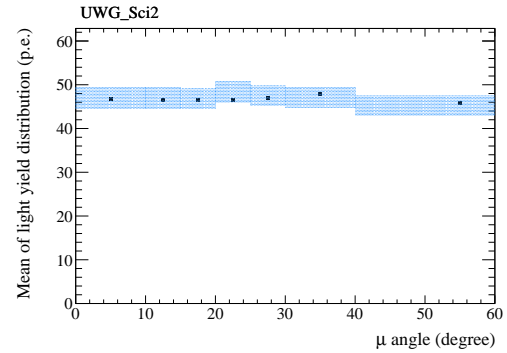
(d) Variation of light yiled for WAGASCI upstream plane scintillator
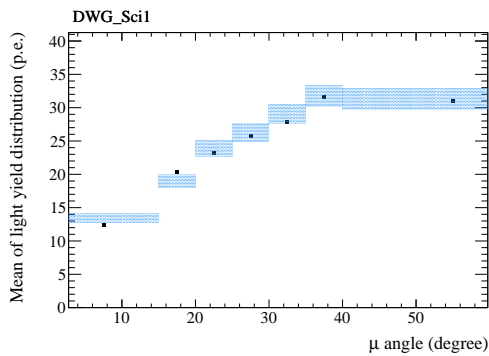
(e) Variation of light yiled for WAGASCI downstream plane scintillator
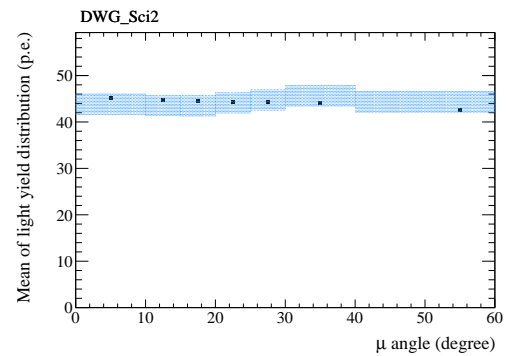
(f) Variation of light yiled for WAGASCI downstream plane scintillator

Figure 134: Variation of light yield for vertex detectors.

235
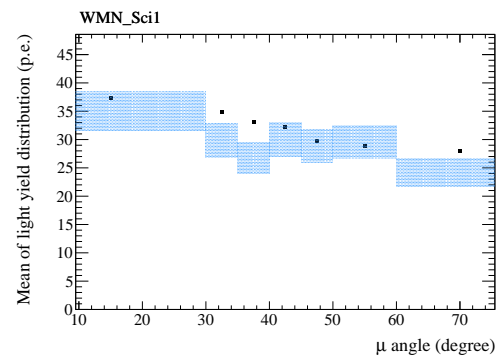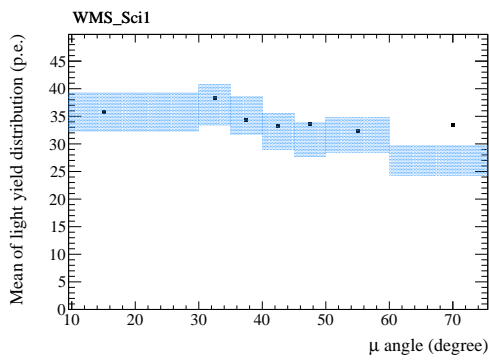
(a) Variation of light yiled for WallMRD south scintillator

(b) Variation of light yiled for WallMRD north scintillator
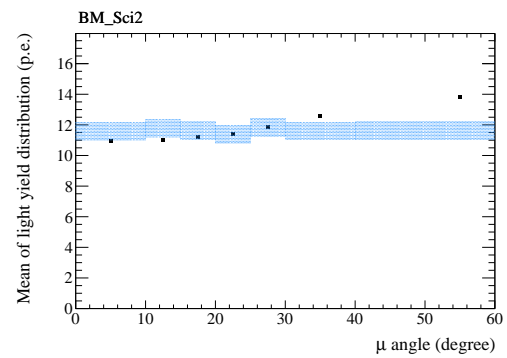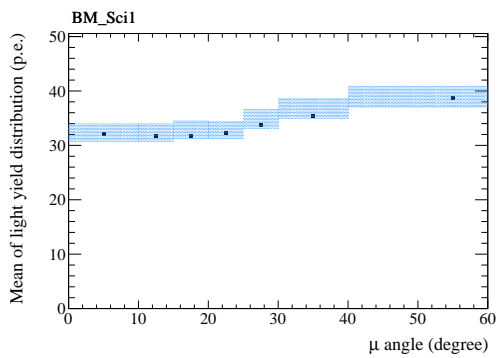
(c) Variation of light yiled for WAGASCI upstream plane scintillator

(d) Variation of light yiled for WAGASCI upstream plane scintillator

Figure 135: Variation of light yield for muon range detectors.

(a) P_μ binning
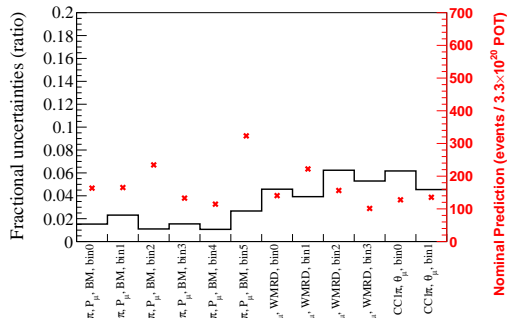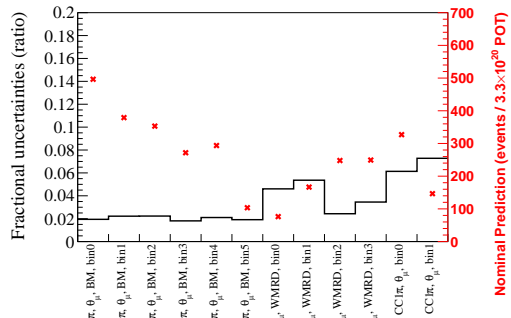
(b) θ_μ binning

Figure 136: Systematic uncertainty of Light yield for the Proton Module samples

(a) P_μ binning
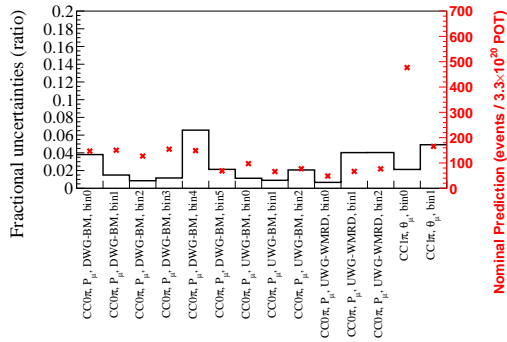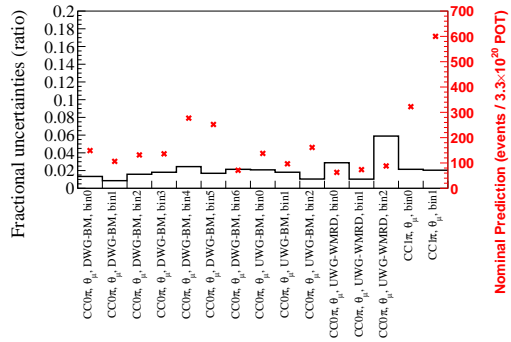
(b) θ_μ binning

Figure 137: Systematic uncertainty of Light yield for the WAGASCI samples

K.2.6 Hit efficiency

Related to the light yield systematics, the hit efficiency has to be considered to be one of the systematic uncertainties because it is supposed to directly affect the result of track reconstruction in particular two-dimensional clustering. In this analysis, the effect of hit efficiency was estimated by varying the hit threshold in the two-dimensional track reconstruction process. Analogous to the previous subsection, each variation of the hit threshold for the detector was decided based on hit efficiency results with sand muon samples for lower angles and with CC inclusive samples whose vertex is either in Proton Module or Upstream WAGASCI module for higher angles. CC inclusive samples were collected by imposing the only fiducial volume cut for the events passing the pre-selection. Figure 138 shows the variations covering measured data points. The blue shaded area represents the errors estimated by varying the hit threshold according to its variation. It should be noted that the errors were calculated by the sum of the square root of statistical errors and these variational errors. Each variation is summarized in Table 50.

Table 50: Variation of hit efficiency

Detector	"+" Variation	"-" Variation
Proton Module	+1.0 p.e.	0.0 p.e.
WAGASCI modules	+1.5 p.e.	0.0 p.e.
WallMRDs	+1.5 p.e.	0.0 p.e.
BabyMIND (XZ view)	+1.0 p.e.	-0.5 p.e.
BabyMIND (YZ view)	+1.0 p.e.	-0.5 p.e.

The covariance of the detector systematics is calculated as follows.

$$V_{ij} = \frac{1}{2} \frac{(\phi^i_{\text{nom}} - \phi^i_+)(\phi^j_{\text{nom}} - \phi^j_+)}{\phi^i_{\text{nom}} \phi^j_{\text{nom}}} + \frac{1}{2} \frac{(\phi^i_{\text{nom}} - \phi^i_-)(\phi^j_{\text{nom}} - \phi^j_-)}{\phi^i_{\text{nom}} \phi^j_{\text{nom}}} \tag{K.7}$$

where "+" refers to plus variation and "-" refers to minus variation.
Figs. 139, 140 show the fractional uncertainty along with the nominal predictions.
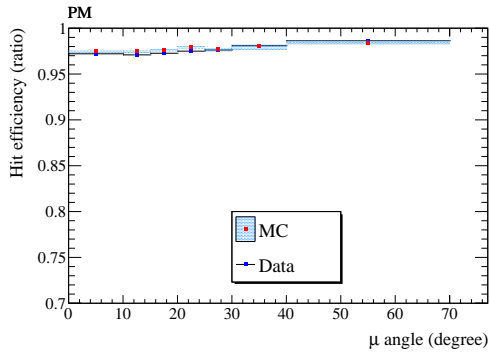
(a) Proton Module
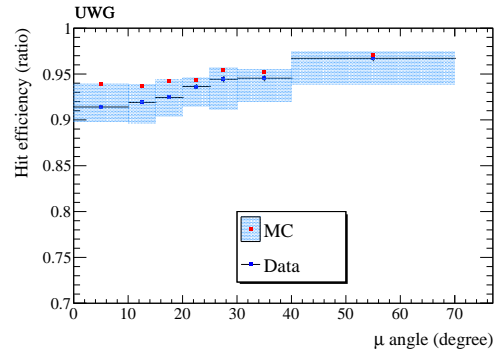
(b) WAGASCI upstream
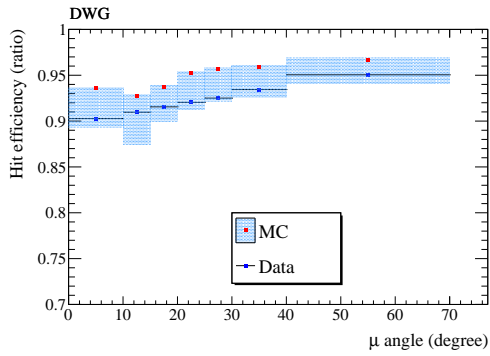
(c) WAGASCI downstream
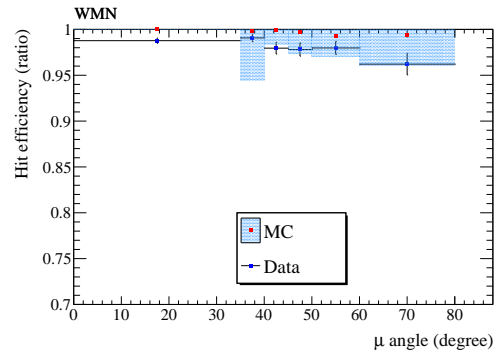
(d) WallMRD north
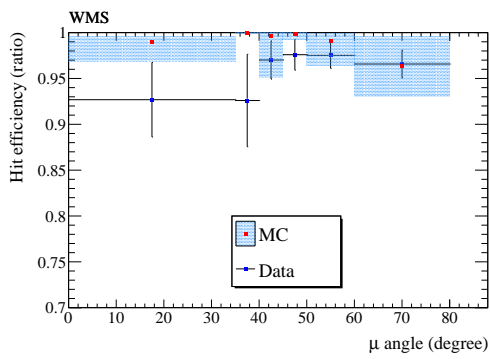
(e) WallMRD south
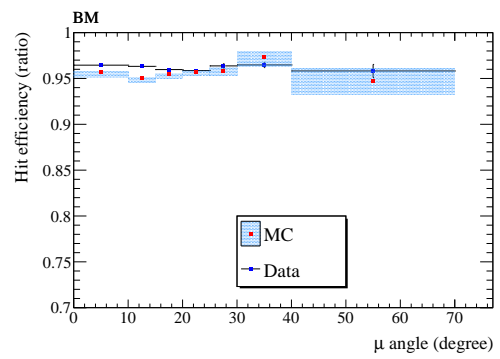
(f) BabyMIND

Figure 138: Variation of hit efficiency for each detector.

(a) P_μ binning

(b) θ_μ binning
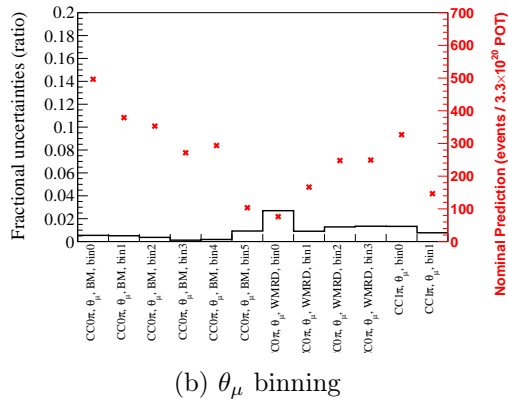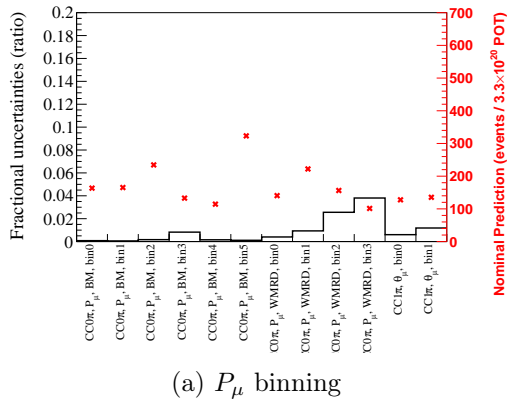
Figure 139: Systematic uncertainty of Hit threshold for the Proton Module samples

(a) P_μ binning

(b) θ_μ binning
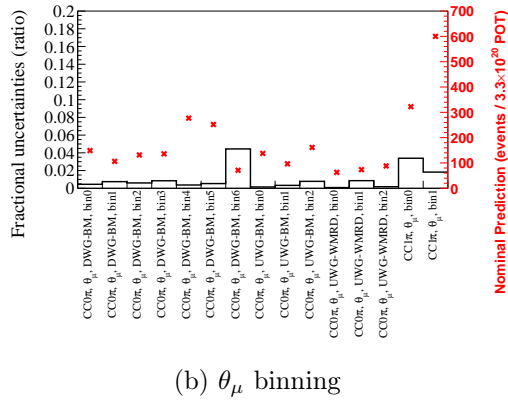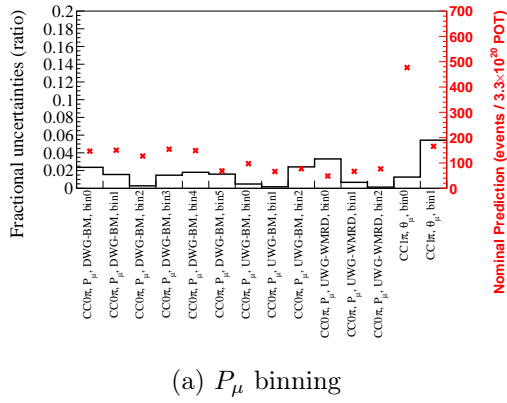
Figure 140: Systematic uncertainty of Hit threshold for the WAGASCI samples

K.2.7 Scintillator distortion in BabyMIND

We found detector modules in BabyMIND have been distorted as illustrated in Figure 141.
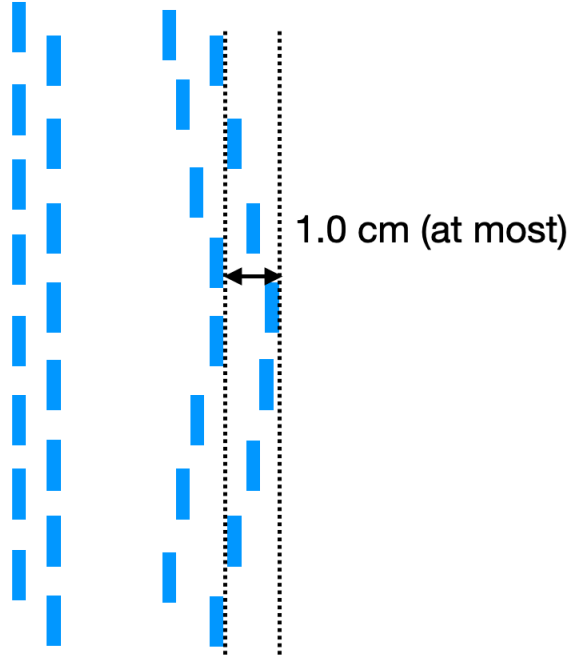
Figure 141: Illustration of how a detector module in BabyMIND is distorted from the top (XZ) view. The left one is the nominal configuration. The right one shows the distortion.

The maximum distortion is about 1.0 cm which should not be neglected because it would cause a difference in reconstruction between MC and data. In order to reproduce this kind of distortion in the MC framework, the displacement of each vertical module was applied depending on the X position so that the maximum distortion was 1.0 cm in the middle. The covariance of the detector systematics is calculated as follows.

$$V_{ij} = \frac{(\phi^i_{\text{nom}} - \phi^i_+)(\phi^j_{\text{nom}} - \phi^j_+)}{\phi^i_{\text{nom}} \phi^j_{\text{nom}}} \tag{K.8}$$

where "+" refers to applying this distortion in the MC framework.
Figs. 142, 143 show the fractional uncertainty along with the nominal predictions.

(a) P_μ binning

(b) θ_μ binning
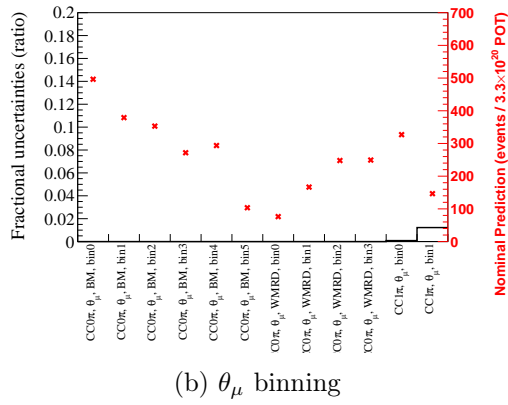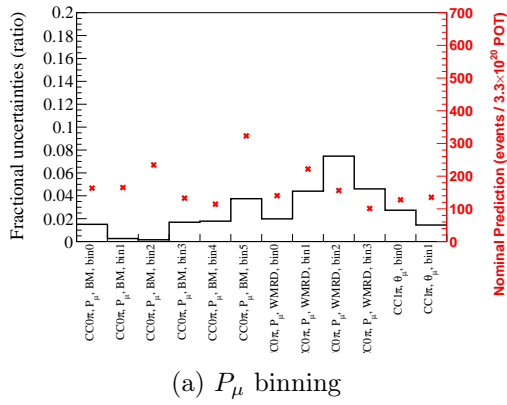
Figure 142: Systematic uncertainty of Scintillator distortion for the Proton Module samples

(a) P_μ binning

(b) θ_μ binning
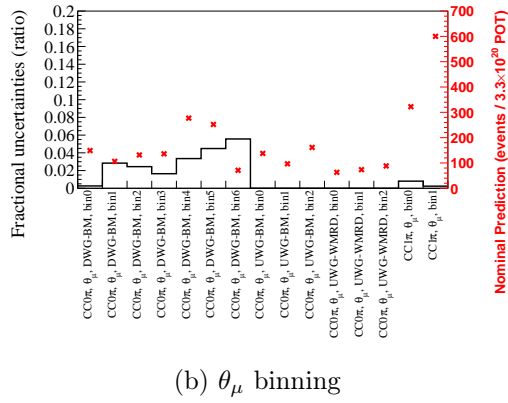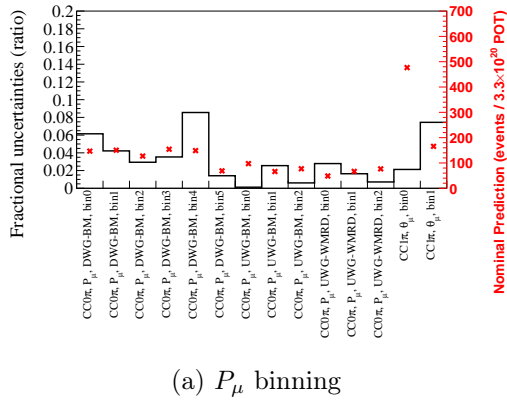
Figure 143: Systematic uncertainty of Scintillator distortion for the WAGASCI samples

K.2.8 Scintillator alignment

Aside from the scintillator distortion in BabyMIND, each detector module has a few centimetre alignment errors on the Y position. This could have an effect on the curvature of a reconstructed track because the method relies on the Y position strongly. So this effect was taken into account by assuming the worse scenario where the Y position is shifted to -0.5 cm for odd number planes while the Y position is shifted to +0.5 cm for even number planes. This couldn't be the worst scenario but it would be a reasonably worse scenario compared to the ideal situation. The covariance of the detector systematics is calculated as follows.

$$V_{ij} = \frac{(\phi^i_{\text{nom}} - \phi^i_+)(\phi^j_{\text{nom}} - \phi^j_+)}{\phi^i_{\text{nom}}\phi^j_{\text{nom}}} \tag{K.9}$$

where "+" refers to applying this mis-alignment in the MC framework.

Figs. 144, 145 show the fractional uncertainty along with the nominal predictions.

(a) P_μ binning
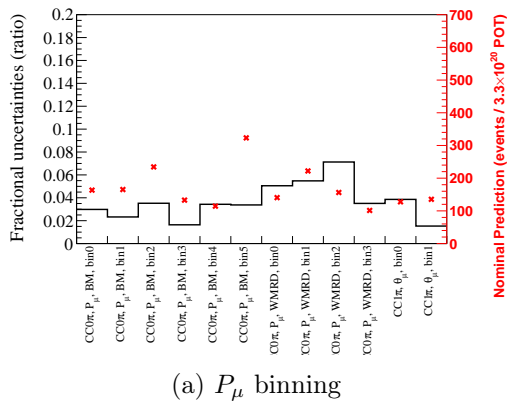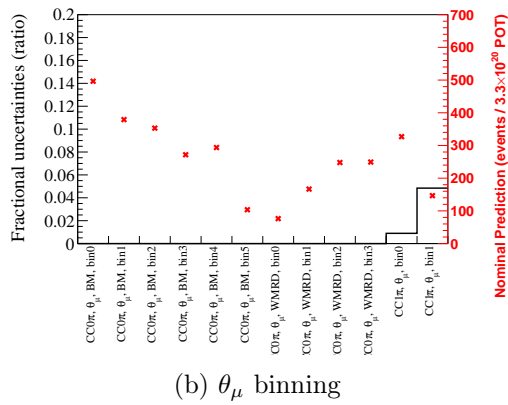
(b) θ_μ binning

Figure 144: Systematic uncertainty of Local alignment for the Proton Module samples

(a) P_μ binning
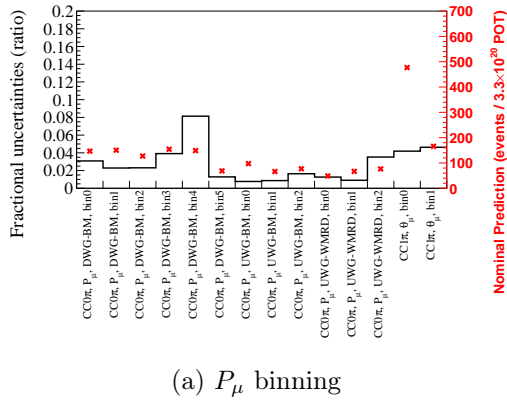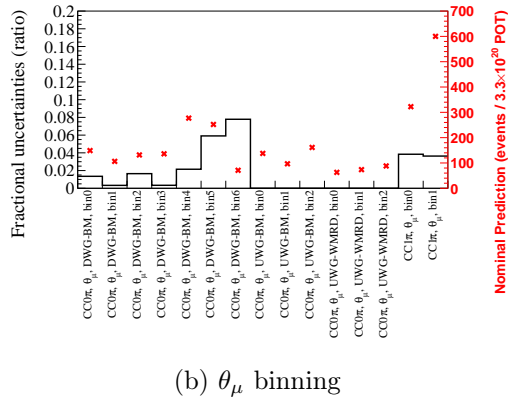
(b) θ_μ binning

Figure 145: Systematic uncertainty of Local alignment for the WAGASCI samples

K.2.9 Signal Lost

On the way to unblinding data, we observed a non-negligible difference between data and MC in the reconstructed vertex Z position for WAGASCI samples. Figure 146 shows the data-MC comparison separated for each data-taking period. The discrepancy in the Downstream WAGASCI case is moderate, however, we could see a data-MC difference in vertex Z position for the Upstream WAGASCI samples. We tried to nail down the possible causes of the discrepancy by scrutinizing the selection outputs and calibration results. We found no solid culprit contributing to the observed difference.
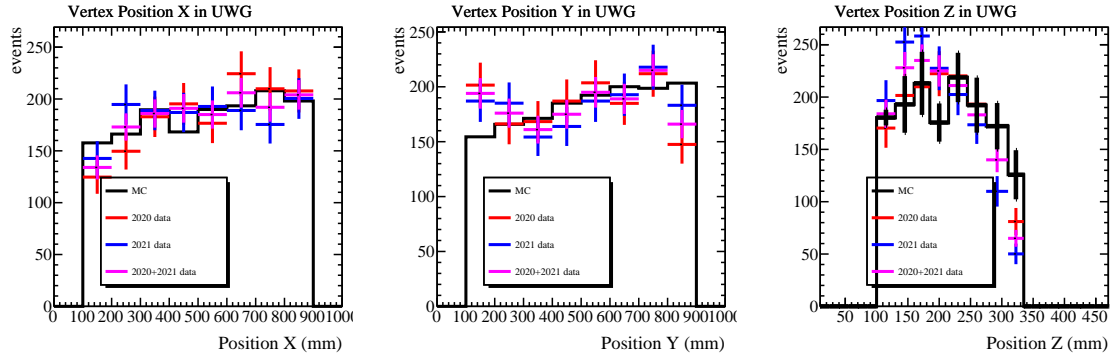
(a) Upstream WAGASCI sample
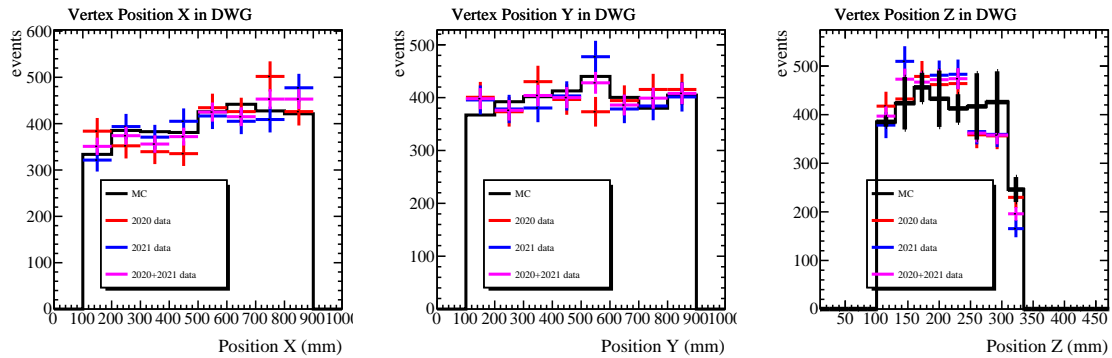
(b) Downstream WAGASCI sample

Figure 146: Comparison of the vertex distributions for WAGASCI samples (top: Upstream WAGASCI samples, bottom: Downstream WAGASCI samples). The data points are separated for the 2020 data set (red), 2021 data set (blue), and 2020 + 2021 merged data set (magenta). The data error bars represent only statistical uncertainty while the MC error bars include both MC statistic errors and detector systematic errors. The number of events in MC is area-normalized by the statistics (2020 + 2021).

Then ad-hoc systematic parameter is added in order to take into account the effect of the observed differences. If there had been signal hits (in particular the 6th plane) lost before being recorded in electronics, this kind of difference could have happened. In the simulation, the signal hits (grid scintillators) in the sixth plane are lost at random by a certain probability. This probability is taken as a systematic parameter. In this analysis, the probability is fixed at 50%. The selection outputs from this modified MC give more consistent results with data in terms of vertex Z distributions (Figure 147). It should be mentioned that this systematic parameter is only applied for WAGASCI samples.
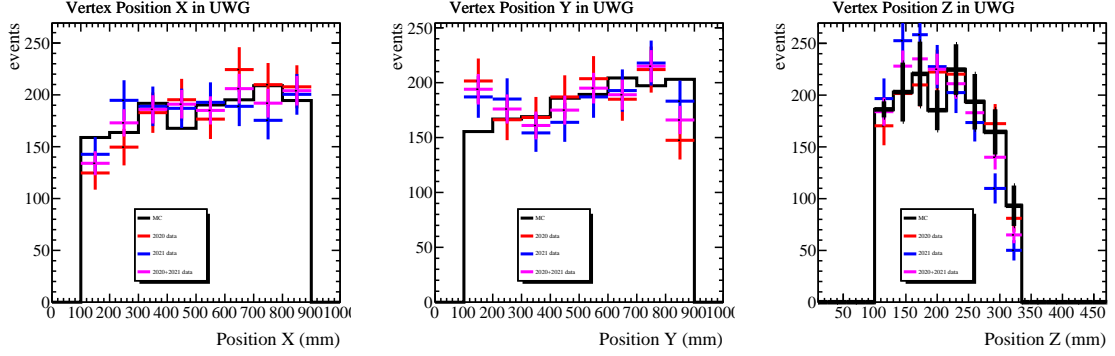
(a) Upstream WAGASCI sample
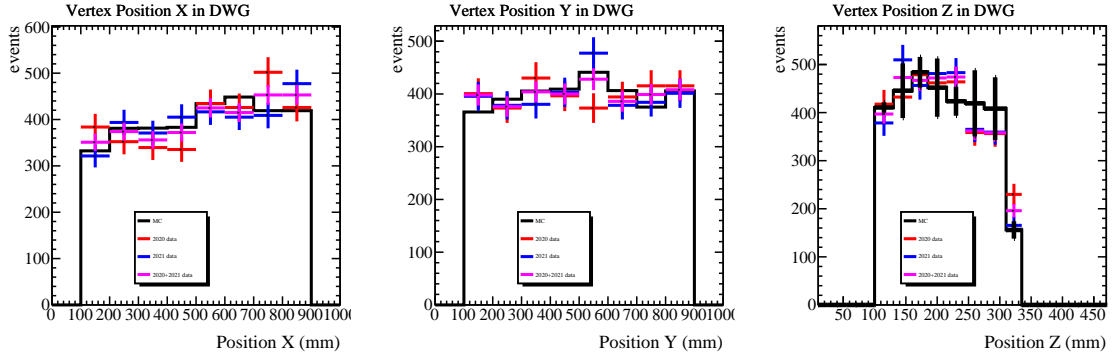
(b) Downstream WAGASCI sample

Figure 147: Comparison of vertex distribution for WAGASCI samples (top: Upstream WAGASCI samples, bottom: Downstream WAGASCI samples). The data points are separated for the 2020 data set (red), 2021 data set (blue), and modified MC with signal lost (magenta). The data error bars represent only statistical uncertainty while the MC error bars include both MC statistic errors and detector systematic errors. The number of events in MC is area-normalized by the statistics (2020 + 2021).

$$V_{ij} = \frac{(\phi^i_{\mathrm{nom}} - \phi^i_+)(\phi^j_{\mathrm{nom}} - \phi^j_+)}{\phi^i_{\mathrm{nom}} \phi^j_{\mathrm{nom}}} \tag{K.10}$$

where "+" refers to the simulation where the signal hits are lost.

Figure 148 shows the fractional uncertainty along with the nominal predictions.

(a) P_μ binning
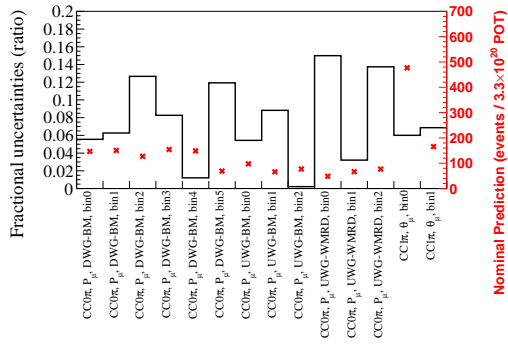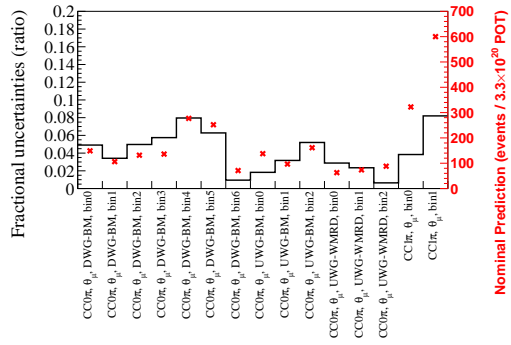
(b) θ_μ binning

Figure 148: Systematic uncertainty of Signal Lost for the WAGASCI samples

K.2.10 Target Mass

In the extraction of cross section, the target mass is one of the factors in the multiplications. As the effect of the target mass for Proton Module and WAGASCI modules has been already studied in past studies. Each effect on the number of selected events is summarized in Table 51. In the covariance matrices, a full correlation between bins is assumed.

Table 51: Effect of target mass on the number of selected events

	Effect to CH in PM	Effect to CH in WAGASCI	Effect to H_2O in WAGASCI
Total	0.56%	1.09%	0.8%

K.2.11 Event pileup

No correlation is applied to the events on either WAGASCI or the Proton Module because of the low statistics and small effect of the pileup due to the small mass. In order to estimate the systematic errors due to this effect, however, the difference of the number of selected events in the double bunched data (Nsel2) and the number of selected events with normal bunch structure (Nsel1) is calculated. The difference between Nsel1 and Nsel2, 0.5% is taken as 1σ systematic uncertainty conservatively for all reconstructed angle bins with full correlation.

K.2.12 Beam-related background

The uncertainty of the beam-related background is here specific to the background from the B2 wall in the experimental place. The normalization of the number of the generated background from wall causes this uncertainty. This uncertainty was estimated with sand muon samples. The selection criteria for this sample are the following.

1. Pre-selection

2. Reconstructed vertex is the out-of-fiducial volume in the upstream WAGASCI

3. Only one track in the event, which should be muon candidate

4. The muon candidate has a partial track in the Proton Module, WAGASCI downstream and BabyMIND

The partial data set (1.5×10^{20} POT) were used. The difference in the number of selected events between Data and MC was taken into account as this uncertainty, which is 13% (data: 39864 events, MC: 45632 events) with respect to data. Figure 149 shows the comparison of angle distributions for this sample between data and MC. Before getting the error on this background, the selected events from Wall interactions were scaled based on this difference, namely, divided by 1.13 because the difference is expected to be caused by the density or composition of the wall. Then errors were given by the product of the scaled number of selected binned events and the data-MC difference (0.13).
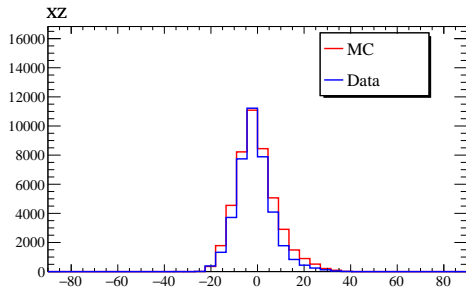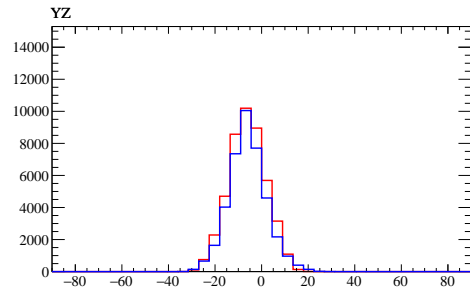
(a) XZ view   (b) YZ view

Figure 149: Comparison of three-dimensional angle distributions in XZ view (left) and in YZ view (right) for the sand muon sample between data and MC. Both MC distributions were normalized by the integral of data.

Figs. 150, 151 show the fractional uncertainty along with the nominal predictions.

(a) P_μ binning
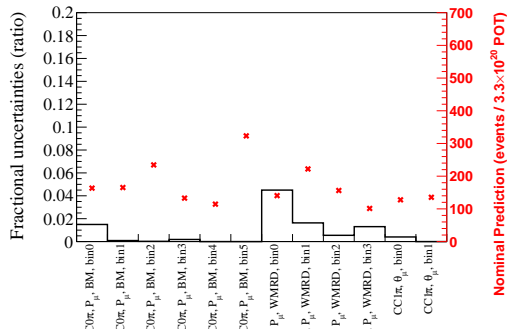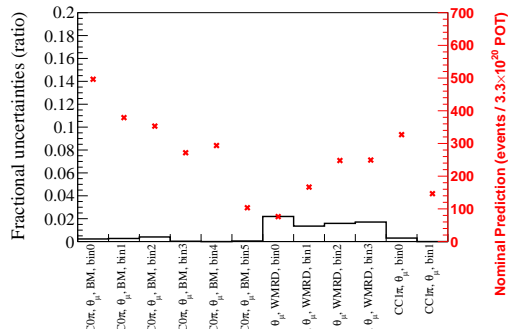
(b) θ_μ binning

Figure 150: Systematic uncertainty of Beam-related background for the Proton Module samples

(a) P_μ binning
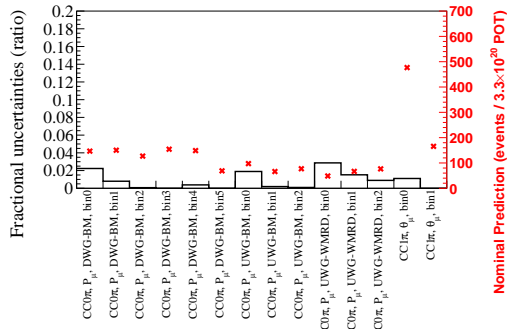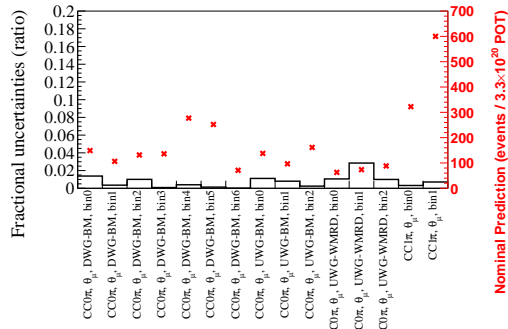
(b) θ_μ binning

Figure 151: Systematic uncertainty of Beam-related background for the WAGASCI samples

K.2.13 Two-dimensional tracking

The efficiency of the track reconstruction is estimated using the reconstructed angle of the Baby-MIND as described in Appnedix H. The efficiency is compared to data and the Monte Carlo simulation to test the gap of the scintillators and physics processes such as multiple scattering of muons and secondary interactions. The difference was taken into account to estimate the effect of this uncertainty. The covariance element is calculated as follows.

$$V_{ij} = \text{difference}_i \times \text{difference}_j \tag{K.11}$$

where difference$_i$ means the difference in the two-dimensional tracking efficiency between data and MC, namely, it can be calculated by

$$\text{difference}_i = \text{efficiency}_i^{\text{MC}} - \text{efficiency}_i^{\text{Data}} \tag{K.12}$$

As the efficiency was calculated as a function of angle, the uncertainties of this parameter for momentum binning can't be treated in the same way. Assuming this two-dimensional tracking efficiency doesn't depend on the particle momentum significantly compared to the angular dependence, we can simply derive the binned efficiency as a function of momentum by the following formula.

$$\epsilon_{\text{momentum}}^i = \sum_{j=0}^{n} w_j^i \times \epsilon_{\text{angle},j} \tag{K.13}$$

where i runs over the momentum binning, j runs over the angle binning and ϵ refers to the efficiency. w_j means each weight from the angle distribution for each momentum slice for binning i. Figure 152 shows the differences between data and MC for both Proton Module and WAGASCI modules.

(a) Proton Module (b) WAGASCI modules
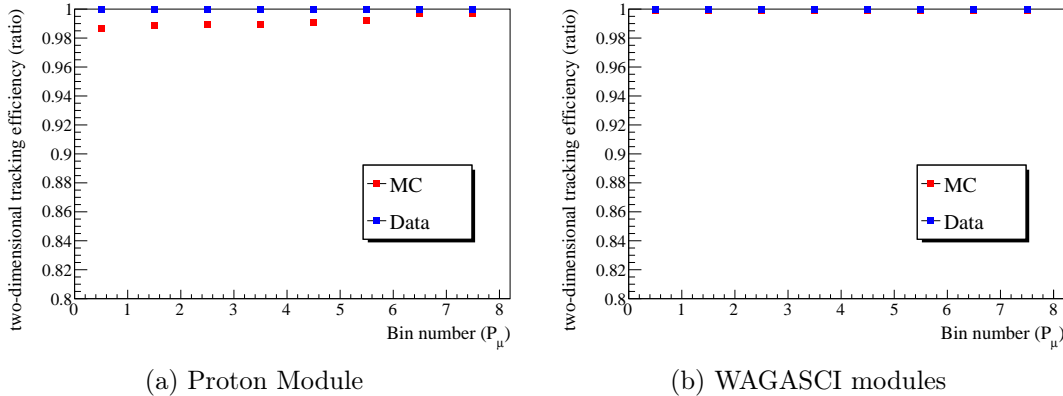
Figure 152: Comparison of two-dimensional tracking efficiency as a function of momentum between Data and MC for Proton Module (left) and WAGASCI modules (right).

Figs. 153, 154 show the fractional uncertainty along with the nominal predictions.

(a) P_μ binning
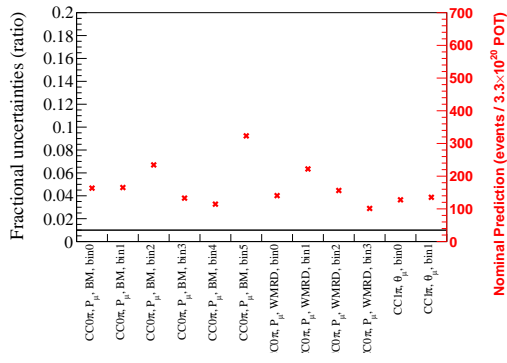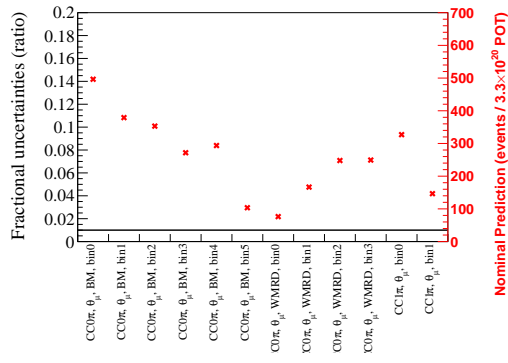
(b) θ_μ binning

Figure 153: Systematic uncertainty of Two dimensional tracking efficinecy for the Proton Module samples

(a) P_μ binning
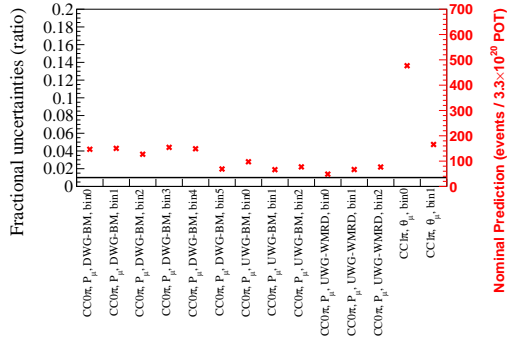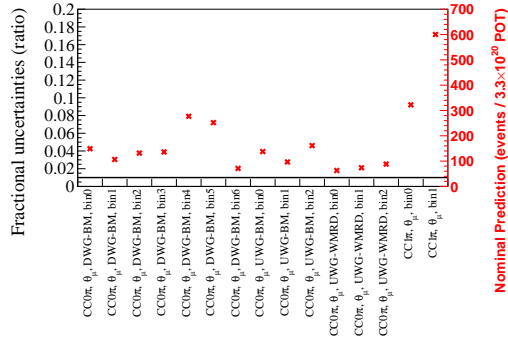
(b) θ_μ binning

Figure 154: Systematic uncertainty of Two dimensional tracking efficiency for the WAGASCI samples

K.2.14 Track matching between detectors

In order to take the difference between MC and data from other effects that were mentioned so far into account, we added other error sources on threshold values which were used in the reconstruction process. In the first step of finding a neutrino vertex, we required each track satisfying with track matching thresholds depending on detectors. If there were no difference between MC and data, there would be the same changes in both MC and data with different threshold values. The ratio of the changes in the selected number of events to the number of events at the nominal threshold is taken as the systematic uncertainty. The variation of the thresholds is summarized in Table 52.

Table 52: Variation of the thresholds for trackmatching depending on detectors

Detector combination	angle threshold (degree)	distance threshold (cm)
Proton Module - WallMRDs	$45 \rightarrow 40$	$500 \rightarrow 450$
Proton Module - WAGASCI downstream	$25 \rightarrow 20$	$200 \rightarrow 150$
Proton Module - BabyMIND	$35 \rightarrow 30$	$300 \rightarrow 250$
WAGASCI upstream - WallMRDs	$40 \rightarrow 35$	$500 \rightarrow 450$
WAGASCI upstream - Proton Module	$25 \rightarrow 20$	$300 \rightarrow 250$
WAGASCI downstream - BabyMIND	$30 \rightarrow 25$	$250 \rightarrow 200$

The element of each covariance matrix is calculated as follows. It should be noted that the calculation formula is modified compared to the detector-related systematics because for reconstructed-related parameters, data and MC difference has to be taken into account.

$$V_{ij} = \text{difference}_i \times \text{difference}_j \tag{K.14}$$

where difference_i is the difference of the variation of the selected events in the i-th reconstructed angle or momentum bin between the data and Monte Carlo, namely, it can be calculated by

$$\text{difference}_i = \frac{N_i^{\text{MC,nominal}} - N_i^{\text{MC,variation}}}{N_i^{\text{MC,nominal}}} - \frac{N_i^{\text{Data,nominal}} - N_i^{\text{Data,variation}}}{N_i^{\text{Data,nominal}}} \tag{K.15}$$

N_i^{nominal} refers to the nominal number of events in i bin.

The last three systematics parameters will not be used for the Proton Module sample because they are relatively irrelevant to the sample whereas the first three parameters will not be used for WAGASCI samples likewise.

Figs. 155 to 166 show the fractional uncertainty along with the nominal predictions.

(a) P_μ binning
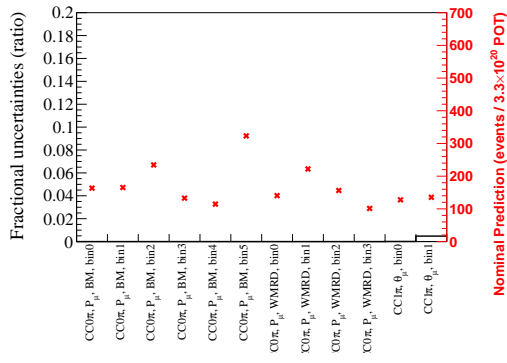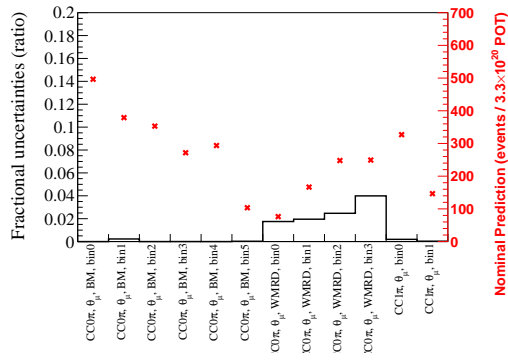
(b) θ_μ binning

Figure 155: Systematic uncertainty of Track matching between Proton Module to WallMRD for the Proton Module samples

(a) P_μ binning
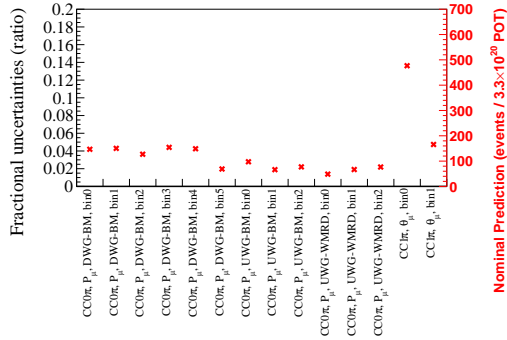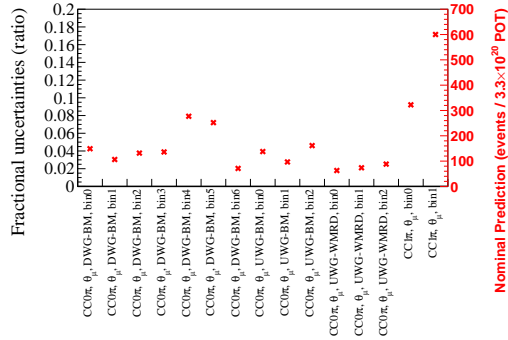
(b) θ_μ binning

Figure 156: Systematic uncertainty of Track matching between Proton Module to WallMRD for the WAGASCI samples

(a) P_μ binning
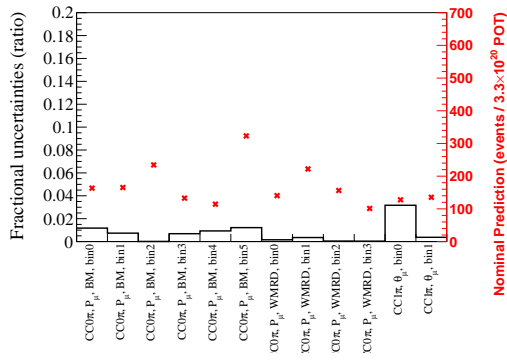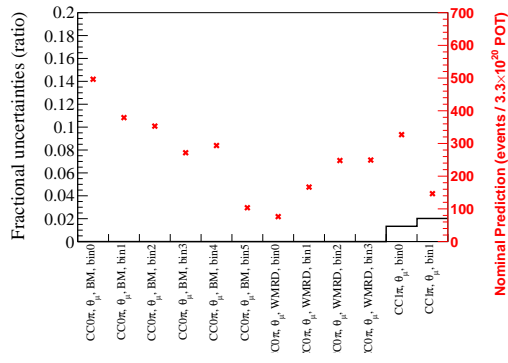
(b) θ_μ binning

Figure 157: Systematic uncertainty of Track matching between Proton Module to Downstream WAGASCI for the Proton Module samples

(a) P_μ binning
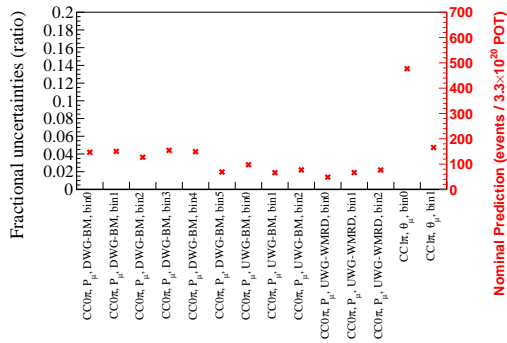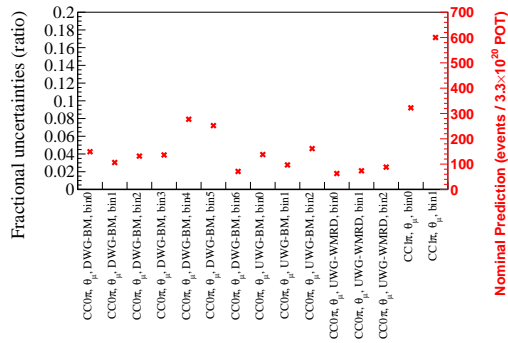
(b) θ_μ binning

Figure 158: Systematic uncertainty of Track matching between Proton Module to Downstream WAGASCI for the WAGASCI samples

(a) P_μ binning
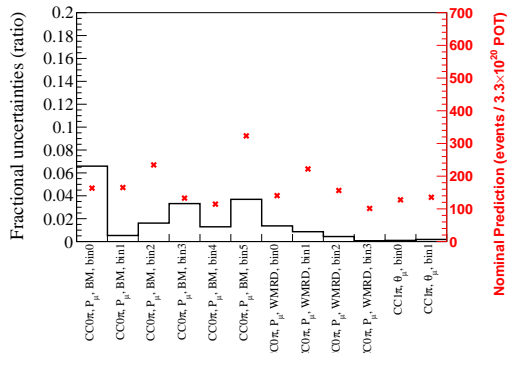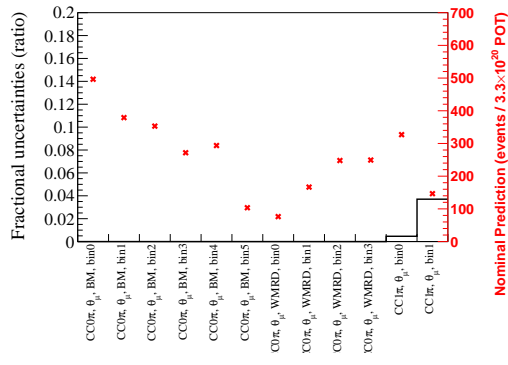
(b) θ_μ binning

Figure 159: Systematic uncertainty of Track matching between Proton Module to BabyMIND for the Proton Module samples
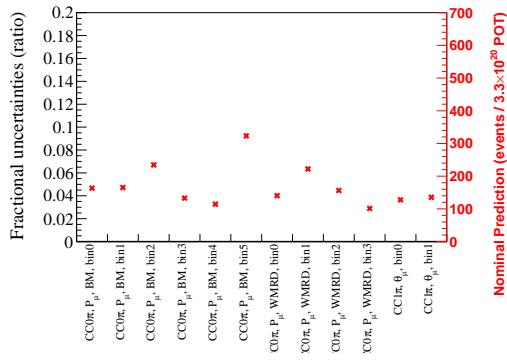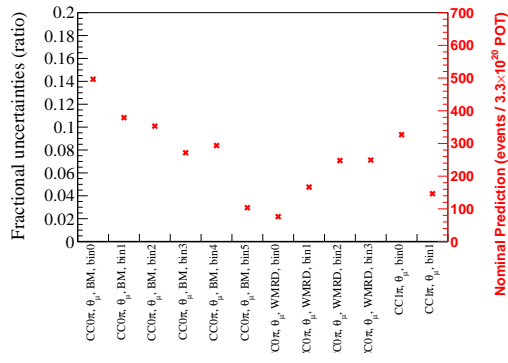
(a) P_μ binning
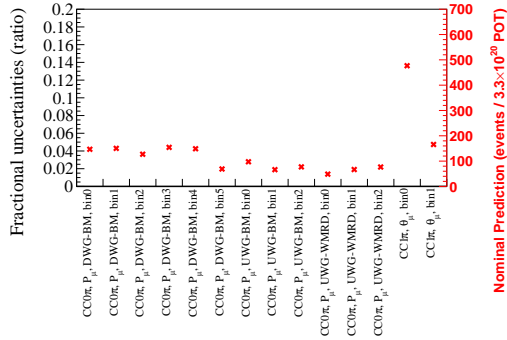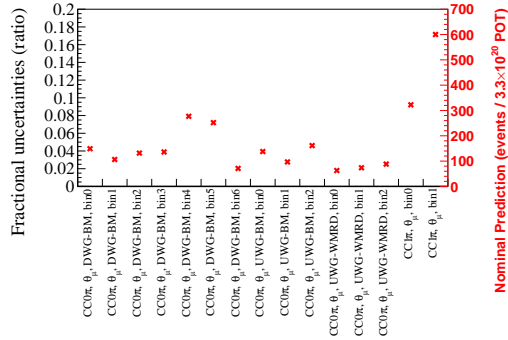
(b) θ_μ binning

Figure 160: Systematic uncertainty of Track matching between Proton Module to BabyMIND for the WAGASCI samples

(a) P_μ binning

(b) θ_μ binning

Figure 161: Systematic uncertainty of Track matching between WAGASCI upstream to Proton Module for the Proton Module samples

(a) P_μ binning
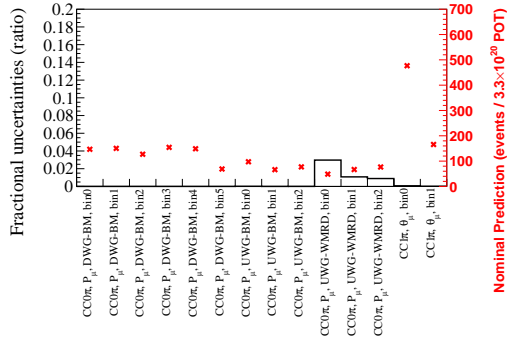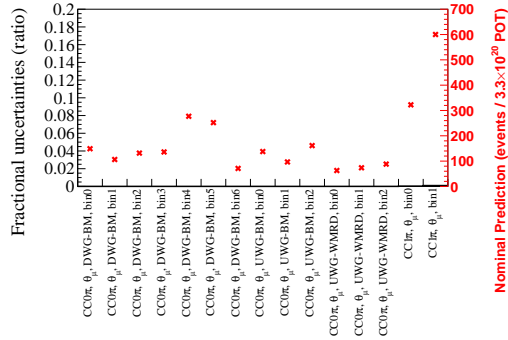
(b) θ_μ binning

Figure 162: Systematic uncertainty of Track matching between WAGASCI upstream to Proton Module for the WAGASCI samples

(a) P_μ binning
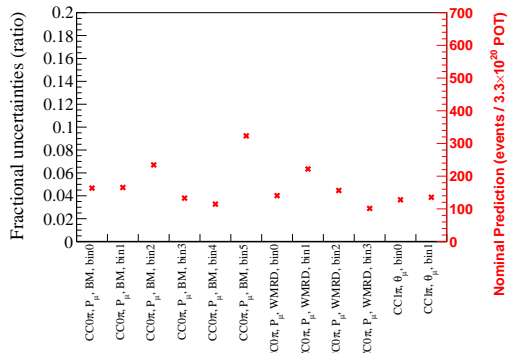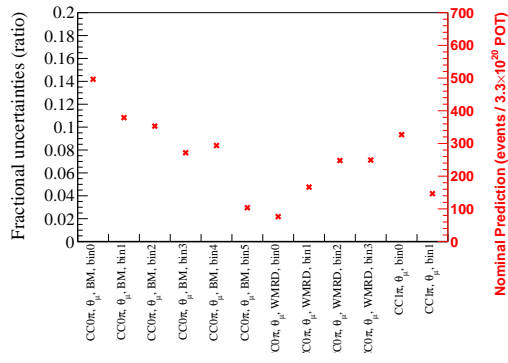
(b) θ_μ binning

Figure 163: Systematic uncertainty of Track matching between WAGASCI upstream to WallMRD for the Proton Module samples

(a) P_μ binning
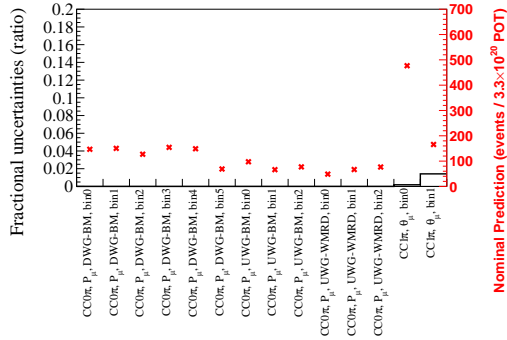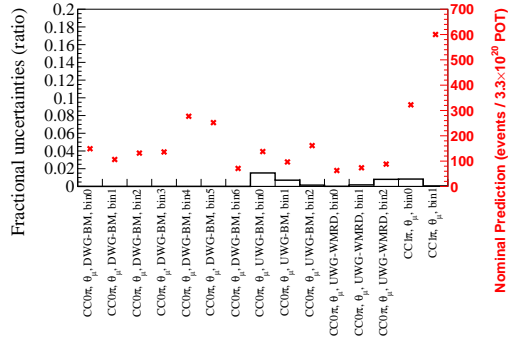
(b) θ_μ binning

Figure 164: Systematic uncertainty of Track matching between WAGASCI upstream to WallMRD for the WAGASCI samples

(a) P_μ binning
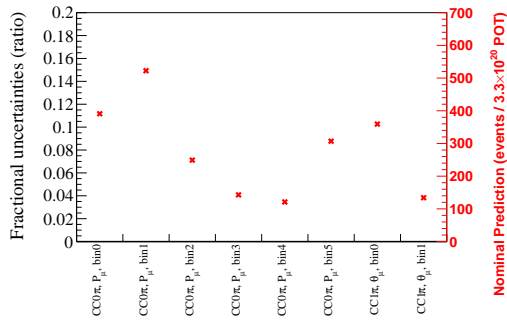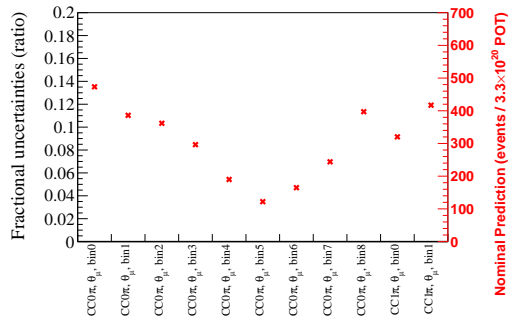
(b) θ_μ binning

Figure 165: Systematic uncertainty of Track matching between WAGASCI downstream to Baby-MIND for the Proton Module samples

(a) P_μ binning
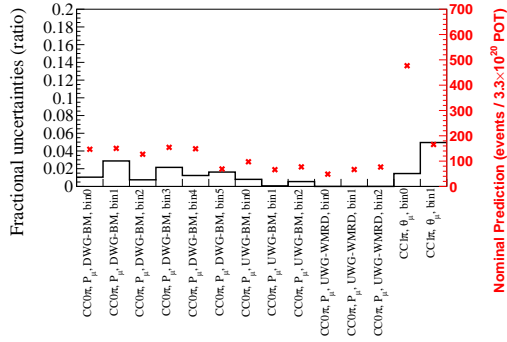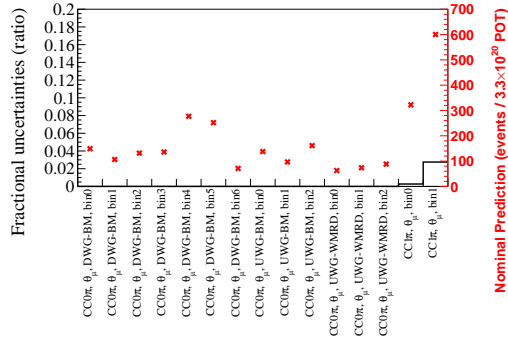
(b) θ_μ binning

Figure 166: Systematic uncertainty of Track matching between WAGASCI downstream to Baby-MIND for the WAGASCI samples

K.2.15 Vertexing

Analogous to the systematic uncertainty of track matching, the threshold of vertexing which might affect the number of tracks in each event. As we applied the maximum tolerance of XY and Z differences for each track, corresponding thresholds vary in order to estimate the effect. The variation is summarized in Table 53.

Table 53: Variation of the thresholds for vertexing depending on detectors

Detector	XY difference (cm)	Z difference (cm)
Proton Module	$110 \to 80$	$110 \to 80$
WAGASCI modules	$125 \to 95$	$125 \to 95$

The element of each covariance matrix is calculated as follows.

$$V_{ij} = \text{difference}_i \times \text{difference}_j \tag{K.16}$$

where difference_i is the difference of the variation of the selected events in the i-th reconstructed angle or momentum bin between the data and Monte Carlo, namely, it can be calculated by

$$\text{difference}_i = \frac{N_i^{\text{MC,nominal}} - N_i^{\text{MC,variation}}}{N_i^{\text{MC,nominal}}} - \frac{N_i^{\text{Data,nominal}} - N_i^{\text{Data,variation}}}{N_i^{\text{Data,nominal}}} \tag{K.17}$$

Figs. 167, 168 show the fractional uncertainty along with the nominal predictions.

(a) P_μ binning
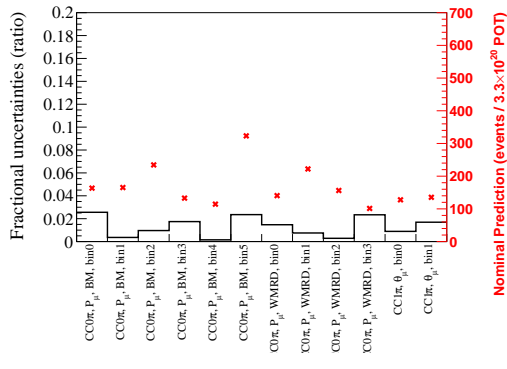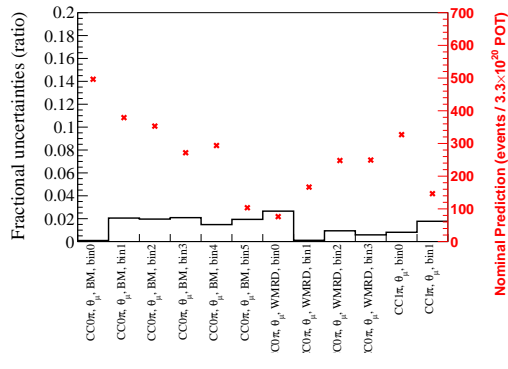
(b) θ_μ binning

Figure 167: Systematic uncertainty of Vertexing for the Proton Module samples

(a) P_μ binning
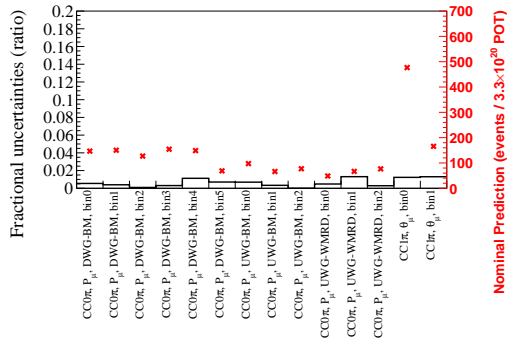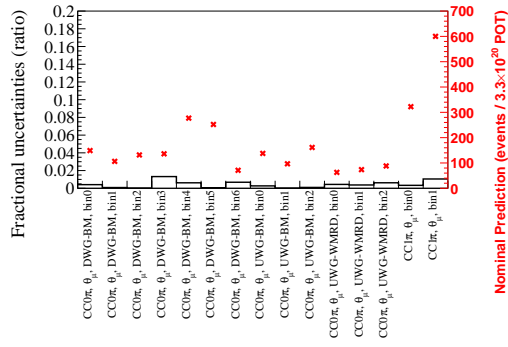
(b) θ_μ binning

Figure 168: Systematic uncertainty of Vertexing for the WAGASCI samples

K.2.16 Three-dimensional tracking

After finding a candidate for neutrino vertex, the algorithm tries to find a combination of both two-dimensional tracks. In this searching process, the maximum tolerance of the start Z position and stop Z position is defined, which should be considered to be one of systematic uncertainty because it could affect the number of selected events. The threshold values were different depending on the MRDs, so they vary accordingly for the stop position. The variation is summarized in Table 54.

Table 54: Variation of the thresholds for three-dimensional tracking depending on MRDs

MRD	start difference (cm)	stop difference (cm)
WallMRDs	$150 \rightarrow 100$	$200 \rightarrow 150$
BabyMIND	$150 \rightarrow 100$	$350 \rightarrow 300$

The element of each covariance matrix is calculated as follows.

$$V_{ij} = \text{difference}_i \times \text{difference}_j \tag{K.18}$$

where difference$_i$ is the difference of the variation of the selected events in the i-th reconstructed angle or momentum bin between the data and Monte Carlo, namely, it can be calculated by

$$\text{difference}_i = \frac{N_i^{\text{MC,nominal}} - N_i^{\text{MC,variation}}}{N_i^{\text{MC,nominal}}} - \frac{N_i^{\text{Data,nominal}} - N_i^{\text{Data,variation}}}{N_i^{\text{Data,nominal}}} \tag{K.19}$$

Figs. 169, 170 show the fractional uncertainty along with the nominal predictions.

(a) P_μ binning

(b) θ_μ binning
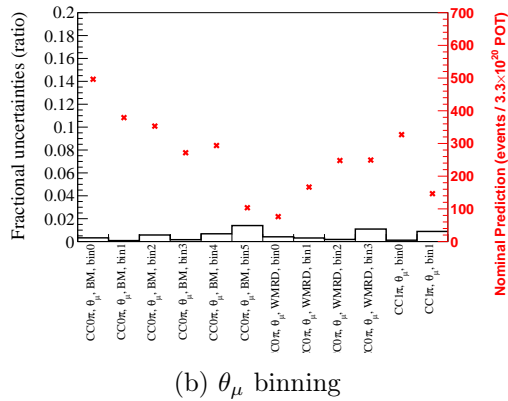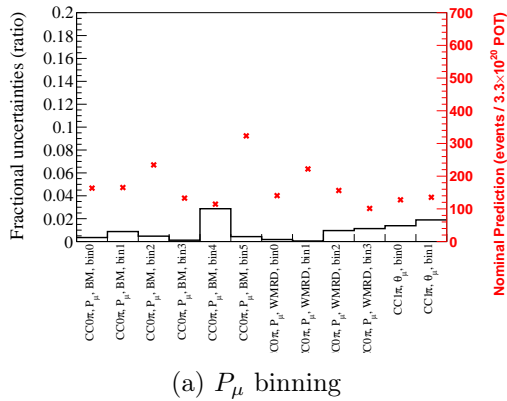
Figure 169: Systematic uncertainty of Three-dimensional tracking for the Proton Module samples

(a) P_μ binning

(b) θ_μ binning
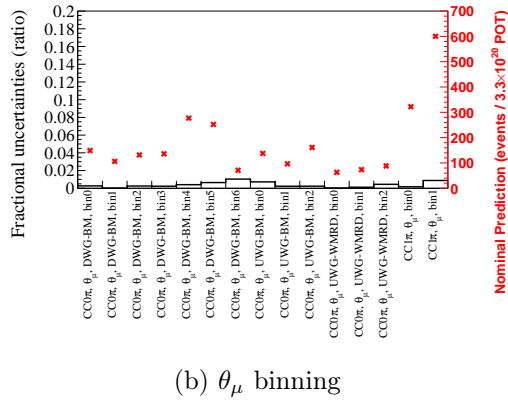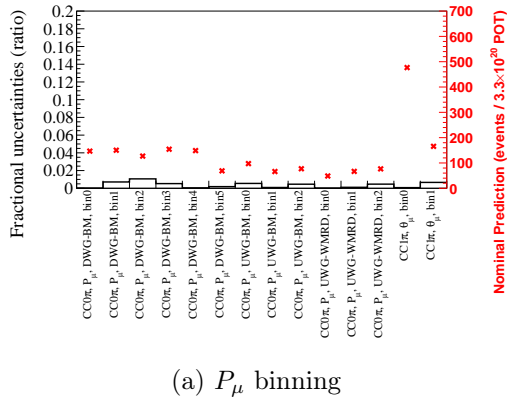
Figure 170: Systematic uncertainty of Three-dimensional tracking for the WAGASCI samples

263

K.2.17 Fiducial volume cut

Along with the systematic uncertainties in the track reconstruction, we also studied systematic uncertainties for each selection criteria. The calculation formula to estimate the effect of each uncertainty is the same as the one used for reconstruction-related parameters. The tentative threshold values are defined for each selection cut to calculate the ratio of change in the number of selected events for both data and MC. Then the difference between data and MC is considered for each systematic uncertainty. The selection cut applied first is the fiducial volume cut. The variations of fiducial volume cut are summarized in Table 55 depending on the vertex module. Each variation along with X, Y, and Z axis corresponds to the distance of one scintillator plane (in Proton Module) or one scintillator block of plane and grid scintillators (in WAGASCI module).

Table 55: Variation of the thresholds for fiducial volume cut

Selection cut	Proton Module		WAGASCI modules	
	nominal	variation	nominal	variation
Fiducial Volume (Lower) (mm)	(-500, -500, 2nd pln)	(-450, -450, 3rd pln)	(-380, -385, -105)	(-330, -335, -80)
Fiducial Volume (Upper) (mm)	(500, 500, 15th pln)	(450, 450, 14th pln)	(400, 400, 115)	(350, 350, 90)

The element of the covariance matrix is calculated as follows.

$$V_{ij} = \text{difference}_i \times \text{difference}_j \tag{K.20}$$

where difference$_i$ is the difference of the variation of the selected events in the i-th reconstructed angle or momentum bin between the data and Monte Carlo, namely, it can be calculated by

$$\text{difference}_i = \frac{N_i^{\text{MC,nominal}} - N_i^{\text{MC,variation}}}{N_i^{\text{MC,nominal}}} - \frac{N_i^{\text{Data,nominal}} - N_i^{\text{Data,variation}}}{N_i^{\text{Data,nominal}}} \tag{K.21}$$

Figs. 171, 172 show the fractional uncertainty along with the nominal predictions.

(a) P_μ binning
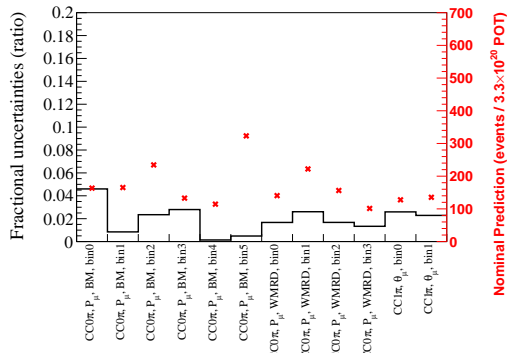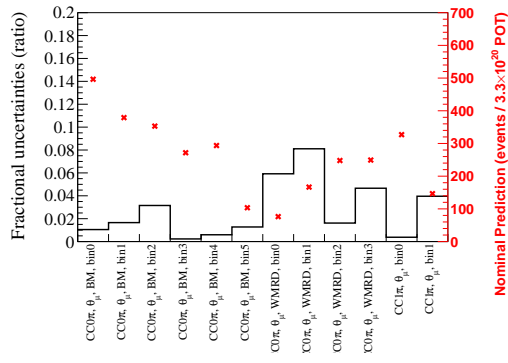
(b) θ_μ binning

Figure 171: Systematic uncertainty of Fiducial Volume for the Proton Module samples

(a) P_μ binning
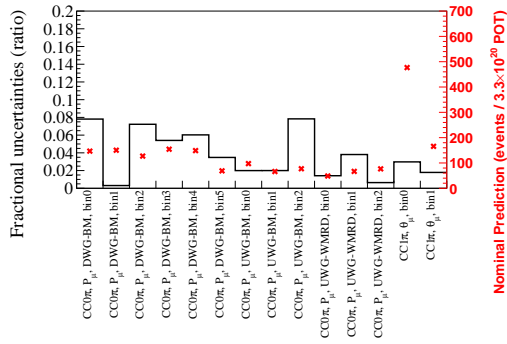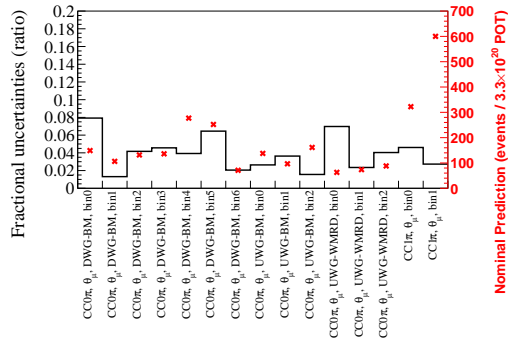
(b) θ_μ binning

Figure 172: Systematic uncertainty of Fiducial Volume for the WAGASCI samples

K.2.18 Contained volume cut

For the momentum measurement, we use the range method to estimate momentum, which requires a contained volume cut. In order to minimize the background contamination from escaping muons while studying this uncertainty, only the narrower tentative volume is defined. The variations are summarized in Table 56 depending on the type of MRD. The variations for the X and Z axis correspond to the one scintillator bar distance for both WallMRD and BabyMIND. The variation for the Y axis doesn't correspond to one scintillator bar distance yet three scintillator bar distances to see the effect of reduced volumes. As the contained volume cut was only applied to momentum binning, there is no impact on angle binning.

Table 56: Variation of the thresholds for contained volume cut

Selection cut	WallMRDs		BabyMIND	
	nominal	variation	nominal	variation
Contained Volume (Lower) (mm)	(-170, –, -750)	(140, –, -550)	(-1300, -900, 2nd pln)	(-1100, -850, 3rd pln)
Contained Volume (Upper) (mm)	(170, –, 750)	(140, –, 550)	(1300, 900, 17th pln)	(1100, 850, 16th pln)

The element of the covariance matrix is calculated as follows.

$$V_{ij} = \text{difference}_i \times \text{difference}_j \tag{K.22}$$

where difference_i is the difference of the variation of the selected events in the i-th reconstructed angle or momentum bin between the data and Monte Carlo, namely, it can be calculated by

$$\text{difference}_i = \frac{N_i^{\text{MC,nominal}} - N_i^{\text{MC,variation}}}{N_i^{\text{MC,nominal}}} - \frac{N_i^{\text{Data,nominal}} - N_i^{\text{Data,variation}}}{N_i^{\text{Data,nominal}}} \tag{K.23}$$

Figs. 173, 174 show the fractional uncertainty along with the nominal predictions.

(a) P_μ binning
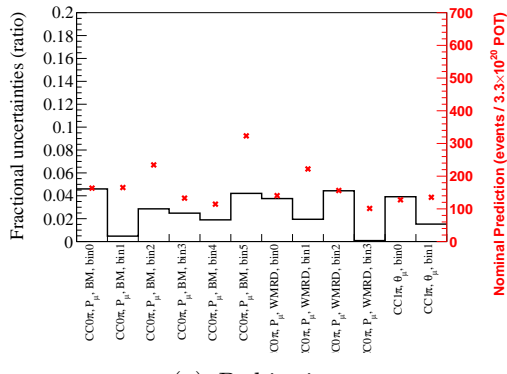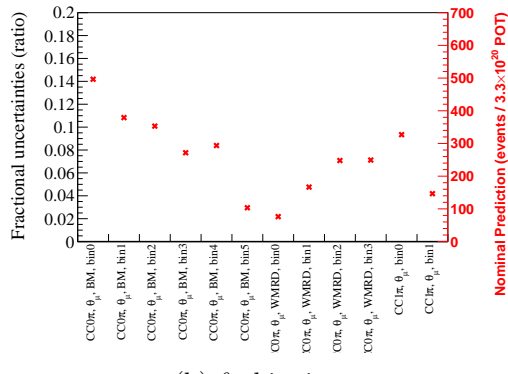
(b) θ_μ binning

Figure 173: Systematic uncertainty of Contained Volume for the Proton Module samples

(a) P_μ binning
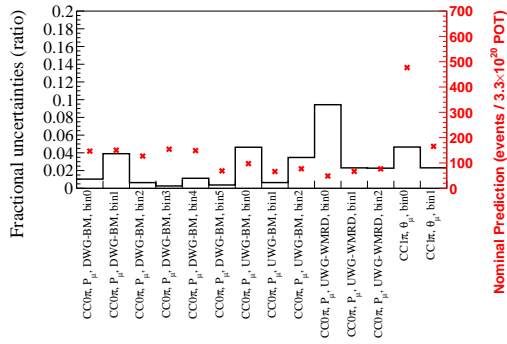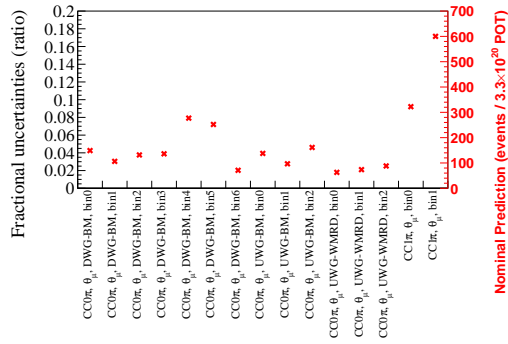
(b) θ_μ binning

Figure 174: Systematic uncertainty of Contained Volume for the WAGASCI samples

K.2.19 MUon Confidence Level (MUCL) cut

MUCL cut was applied to discriminate the CC0$\pi^{\pm}$ sample from the CC1$\pi^{\pm}$ sample by selecting a proton-like particle except for the first track. As the performance of the particle ID is different between Proton Module and WAGASCI modules, different thresholds are applied in this analysis. In order to estimate the effect of this uncertainty, the tentative MUCL thresholds are defined, which are found in Table 57.

Table 57: Variation of the thresholds for muon confidence level cut

Selection cut	Proton Module		WAGASCI modules	
	nominal	variation	nominal	variation
MUCL threshold (+ variation)	0.2	0.3	0.7	0.8
MUCL threshold (- variation)	0.2	0.1	0.7	0.6

The element of the covariance matrix is calculated as follows.

$$V_{ij} = \sum_k \text{difference}_i^k \times \text{difference}_j^k \qquad (K.24)$$

where k runs through the type of variation and difference$_i$ is the difference of the variation of the selected events in the i-th reconstructed angle or momentum bin between the data and Monte Carlo, namely, it can be calculated by

$$\text{difference}_i = \frac{N_i^{\text{MC,nominal}} - N_i^{\text{MC,variation}}}{N_i^{\text{MC,nominal}}} - \frac{N_i^{\text{Data,nominal}} - N_i^{\text{Data,variation}}}{N_i^{\text{Data,nominal}}} \qquad (K.25)$$

Figs. 175, 176 show the fractional uncertainty along with the nominal predictions.

(a) P_μ binning

(b) θ_μ binning
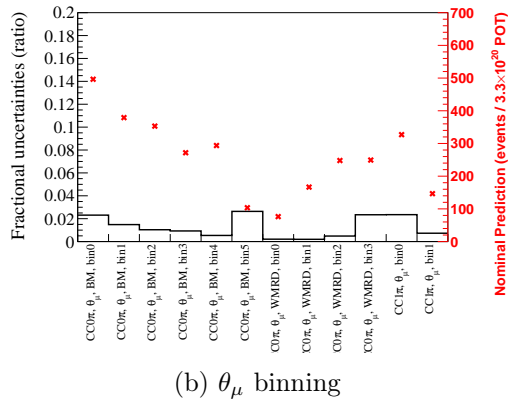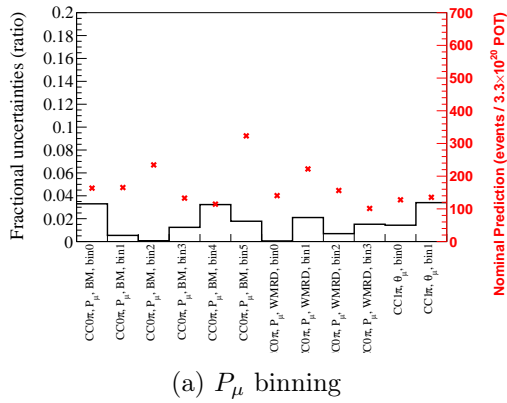
Figure 175: Systematic uncertainty of Particle ID for the Proton Module samples

(a) P_μ binning

(b) θ_μ binning
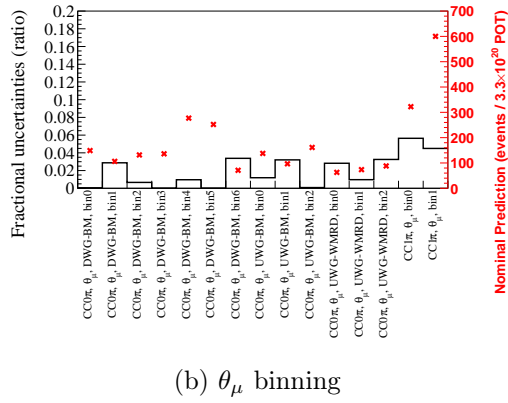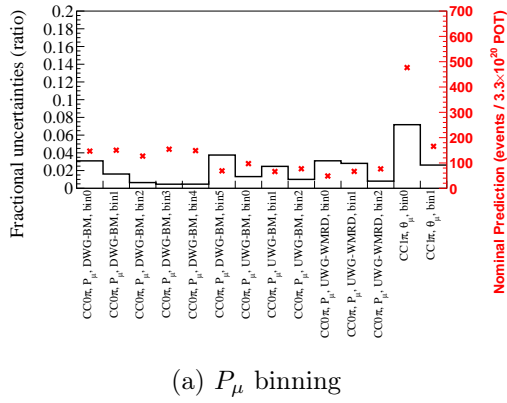
Figure 176: Systematic uncertainty of Particle ID for the WAGASCI samples

K.2.20 Charge ID cut

Charge ID cut was applied to select ν_μ interactions by using the log-likelihood ratio based on the curvature of a track in BabyMIND. The performance of charge ID depends on only tracking in BabyMIND regardless of the vertex position. So the same nominal value and tentative value are used for Proton Module and WAGASCI modules. The variation is found in Table 58.

Table 58: Variation of the thresholds for charge ID cut

Selection cut	Proton Module		WAGASCI modules	
	nominal	variation	nominal	variation
Threshold on log-likelihood ratio (+ variation)	(-99999, 4)	(-99999, 8)	(-99999, 4)	(-99999, 8)
Threshold on log-likelihood ratio (- variation)	(-99999, 4)	(-99999, 0)	(-99999, 4)	(-99999, 0)

The element of the covariance matrix is calculated as follows.

$$V_{ij} = \sum_k \text{difference}_i^k \times \text{difference}_j^k \tag{K.26}$$

where k runs through the type of variation and difference$_i$ is the difference of the variation of the selected events in the i-th reconstructed angle or momentum bin between the data and Monte Carlo, namely, it can be calculated by

$$\text{difference}_i = \frac{N_i^{\text{MC,nominal}} - N_i^{\text{MC,variation}}}{N_i^{\text{MC,nominal}}} - \frac{N_i^{\text{Data,nominal}} - N_i^{\text{Data,variation}}}{N_i^{\text{Data,nominal}}} \tag{K.27}$$

Figs. 177, 178 show the fractional uncertainty along with the nominal predictions.

(a) P_μ binning
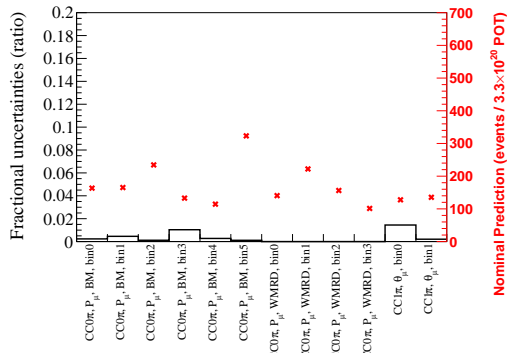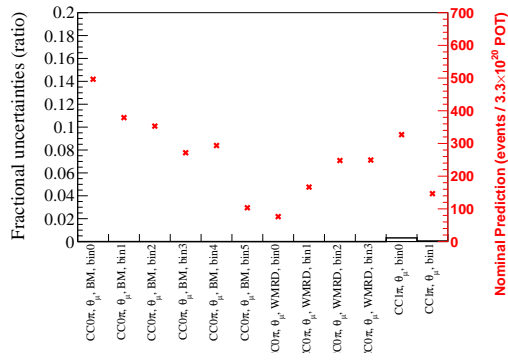
(b) θ_μ binning

Figure 177: Systematic uncertainty of Charge ID for the Proton Module samples

(a) P_μ binning
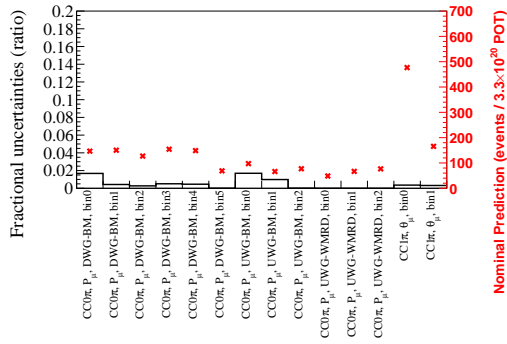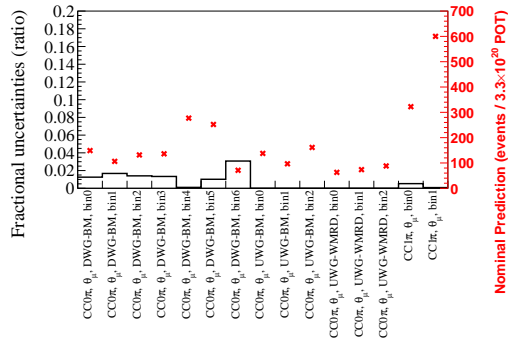
(b) θ_μ binning

Figure 178: Systematic uncertainty of Charge ID for the WAGASCI samples

K.2.21　Track/Cluster ratio cut

The track/cluster ratio cut was applied to reject the background contamination from Wall interactions. The distribution of track/cluster ratio depends on the detector configuration in the experimental place. So the threshold values differ depending on vertex modules. The variation is summarized in Table 59.

Table 59: Variation of the thresholds for the track/cluster ratio cut

Selection cut	Proton Module		WAGASCI modules	
	nominal	variation	nominal	variation
Threshold on track/cluster ratio (+ variation)	–	–	0.6	0.7
Threshold on track/cluster ratio (- variation)	–	–	0.6	0.4

The element of the covariance matrix is calculated as follows.

$$V_{ij} = \sum_k \text{difference}_i^k \times \text{difference}_j^k \tag{K.28}$$

where k runs through the type of variation and difference$_i$ is the difference of the variation of the selected events in the i-th reconstructed angle or momentum bin between the data and Monte Carlo, namely, it can be calculated by

$$\text{difference}_i = \frac{N_i^{\text{MC,nominal}} - N_i^{\text{MC,variation}}}{N_i^{\text{MC,nominal}}} - \frac{N_i^{\text{Data,nominal}} - N_i^{\text{Data,variation}}}{N_i^{\text{Data,nominal}}} \tag{K.29}$$

Figs. 179, 180 show the fractional uncertainty along with the nominal predictions.

(a) P_μ binning

(b) θ_μ binning

Figure 179: Systematic uncertainty of Track cluster ratio for the Proton Module samples

(a) P_μ binning
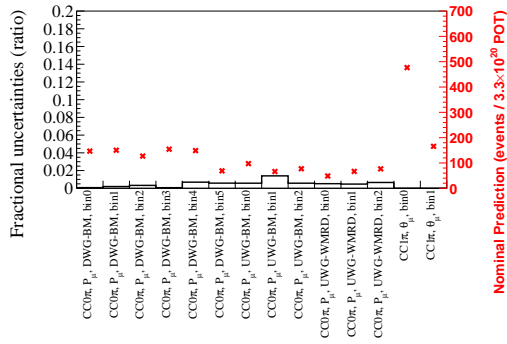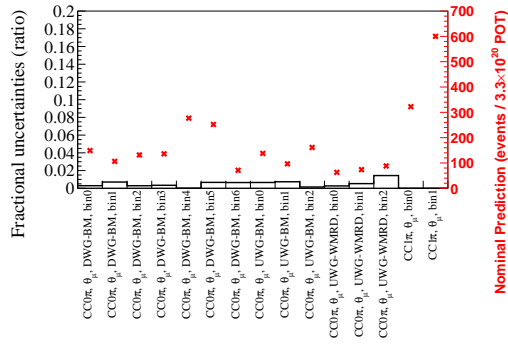
(b) θ_μ binning

Figure 180: Systematic uncertainty of Track cluster ratio for the WAGASCI samples

K.2.22 Michel electron cut

Michel electron tagging is applied to have additional power to reject CC1$\pi^{\pm}$ sample. The most significant parameter to estimate the effect of this uncertainty is the number of hits in delayed timebins for each event. The nominal threshold is set to 3. The comparison between data and MC related to the performance of Michel electron tagging was already discussed in Appendix J. And the result says that if the number of hits is less than 3 in the delayed timebins, the comparison between data and MC is much worse. So the tentative threshold to estimate the effect is set to only a higher value, namely 4. Then the element of the covariance matrix is calculated as follows.

$$V_{ij} = \text{difference}_i \times \text{difference}_j \qquad (K.30)$$

where difference$_i$ is the difference of the variation of the selected events in the i-th reconstructed angle or momentum bin between the data and Monte Carlo, namely, it can be calculated by

$$\text{difference}_i = \frac{N_i^{\text{MC,nominal}} - N_i^{\text{MC,variation}}}{N_i^{\text{MC,nominal}}} - \frac{N_i^{\text{Data,nominal}} - N_i^{\text{Data,variation}}}{N_i^{\text{Data,nominal}}} \qquad (K.31)$$

Figs. 181, 182 show the fractional uncertainty along with the nominal predictions.

(a) P_μ binning
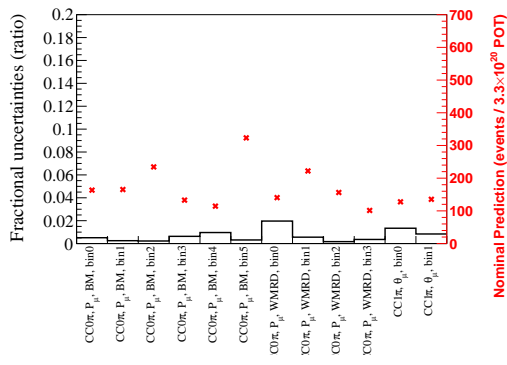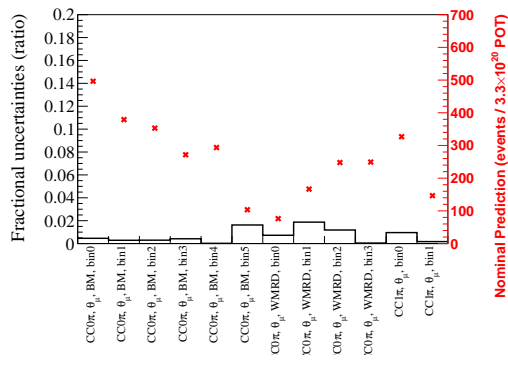
(b) θ_μ binning

Figure 181: Systematic uncertainty of Michel Electron for the Proton Module samples

(a) P_μ binning
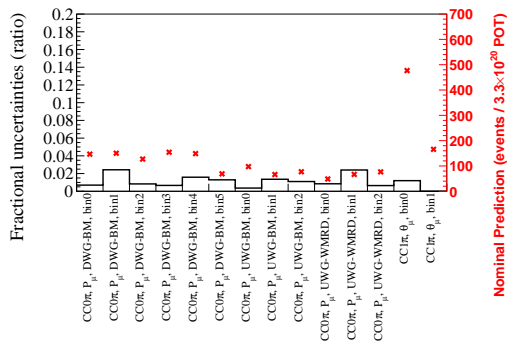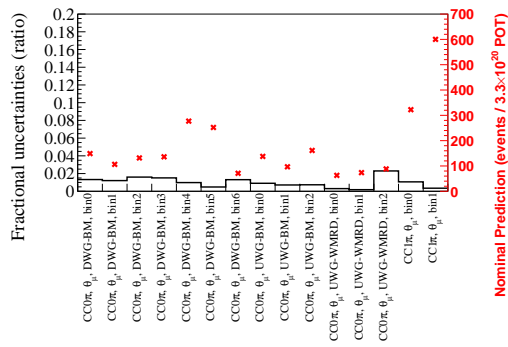
(b) θ_μ binning

Figure 182: Systematic uncertainty of Michel Electron for the WAGASCI samples

K.2.23 beam timing cut

There is a probability that some neutrino events are lost with the timing selection because of the finite resolution of beam timing. The beam timing cut in this analysis was applied for only Proton Module data. Hits falling in the outside region of ± 250 ns of bunch timing were initially removed from data construction. In order to estimate this uncertainty, the number of selected events is compared with and without the beam timing cut. And the element of the covariance matrix is calculated as follows. We expect the contribution from this uncertainty to be very trivial considering how the cut works.

$$V_{ij} = \text{difference}_i \times \text{difference}_j \tag{K.32}$$

where difference$_i$ is the difference of the variation of the selected events in the i-th reconstructed angle or momentum bin between data with timing cut and data without timing cut, namely, it can be calculated by

$$\text{difference}_i = \frac{N_i^{\text{wo/timingcut}} - N_i^{\text{w/timingcut}}}{N_i^{\text{w/timingcut}}} \tag{K.33}$$

Figs. 183, 184 show the fractional uncertainty along with the nominal predictions.

(a) P_μ binning

(b) θ_μ binning
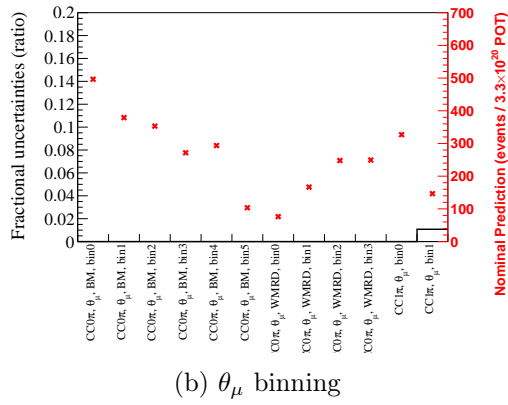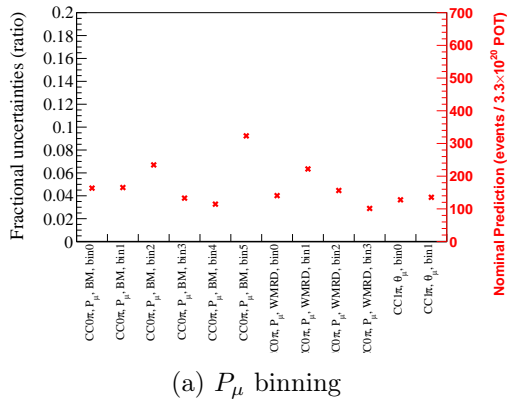
Figure 183: Systematic uncertainty of Timing Cut for the Proton Module samples

(a) P_μ binning

(b) θ_μ binning
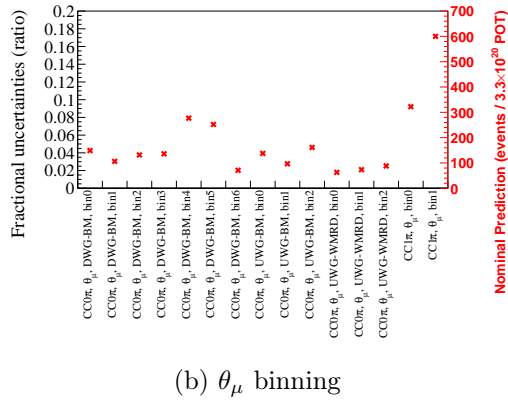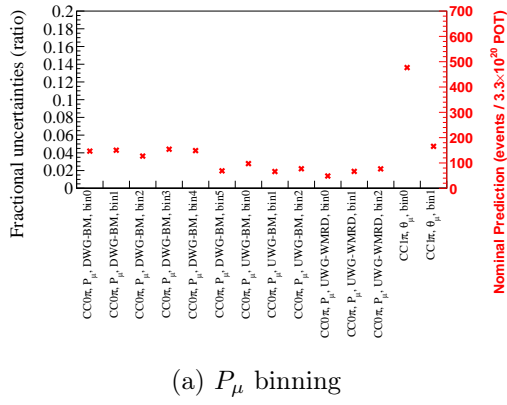
Figure 184: Systematic uncertainty of Timing Cut for the WAGASCI samples

K.2.24 The effect of resolution for angle and momentum measurements

It is in practice impossible to either perfectly understand detector performance or implement every single property in the analysis framework at 100% accuracy. This results in the uncertainty of measurement for each kinematic variable such as momentum and angle. Thus, each variable includes the effect of detector resolution. The resolution can be estimated by Monte Carlo simulation, which is propagated into the measurement with data suppose the resolution wouldn't be different as far as the same analysis method is used and detector properties are reasonably reflected in the simulation. The effect of resolution matters if some resolutions estimated in the simulation can't be valid in data. Here in this section, we focus on the resolution for angle and momentum. The direct impact of the resolution will be seen in the binning migration for the selection outputs. As we have introduced many detector systematic parameters to account for the effect of binning migration related to the angle and momentum, these parameters can cover the effect of angle or momentum resolution to large extent unless we're missing the unexpected or unknown parameters to have an impact on the resolutions. Thus, we shouldn't take care of additional parameters stemming from the resolutions of kinematic variables unless the estimated resolutions are far from those for measurement in data.

In order to check the difference in resolution between MC and data, we took the CC inclusive sample having an interaction point in Proton Module as the control sample. Then the following method is applied.

1. Choose events where the muon candidate pass through both Proton Module and Downstream WAGASCI detectors.

2. Reconstruct angle from hits in Proton Module (θ_{pm}) and angle from hits in Downstream WAGASCI (θ_{dwg}). And this step is done for MC and data.

3. Compare θ_{pm} - θ_{dwg} in MC with the one in data.

In this study, θ_{pm} - θ_{dwg} is supposed to correspond to resolution, and then it makes the comparison of the "resolutions" in MC and data possible. Figure 185 shows the results of each distribution of θ_{pm} - θ_{dwg}. When the width of those distributions is evaluated by their RMS values, they are 4.69 degrees in MC and 4.52 degrees in data respectively. This result indicates that there wouldn't be significant discrepancies in resolution between MC and data. In addition, we checked the effect of resolution discrepancy in the usual techniques applied to other systematic parameters when smearing is applied to the reconstructed angle. In this case, the smearing factor is chosen to be 2.0 degrees which corresponds to the angle resolution on average (Figure 105). Figure 186 shows the fractional uncertainties for this angular smearing, which also ensures the effect is not significant.

On the other hand, with the current data set, it is challenging to collect a reasonable control sample to check the consistency of the resolution of momentum measurement between MC and data [60]. Analogous to the logic applied to the angle measurement, it is likely that the discrepancy in momentum resolutions between MC and data should not be larger than the current detector

---

[60] If we had conducted the beam test to check the momentum resolution with monochromatic beam, or we had other detectors to measure the momentum at good precision (of the order of 5%), it's possible to check the consistency. In fact, we did neither of them. One possible way to do this is to measure the momentum for the events where the muon candidate stops on the same detector plane in BabyMIND. The problem is that the momentum spread would be the same or larger than the expected resolution, which could paper over the difference in resolution between MC and data.

systematics can cover. Just in case, we checked the impact of a potential difference in momentum resolution by simply applying the gaussian smearing to each momentum based on the momentum resolution on average (7%, Figure 107) and evaluating the systematics. This corresponds to the assumption that the resolution estimated by the simulation is smaller by one-second than that in data, which could be an over-conservative choice. Even though the smearing to the reconstructed momentum can be over-conservative, the result (Figure 187) shows they will not have a significant impact on the binning migration compared to other systematic uncertainties. Thus, we determined to assume that the potential effect of the difference in resolution between MC and data is negligible, which is not considered as one of the detector's systematic parameters.

(a) MC

(b) Data
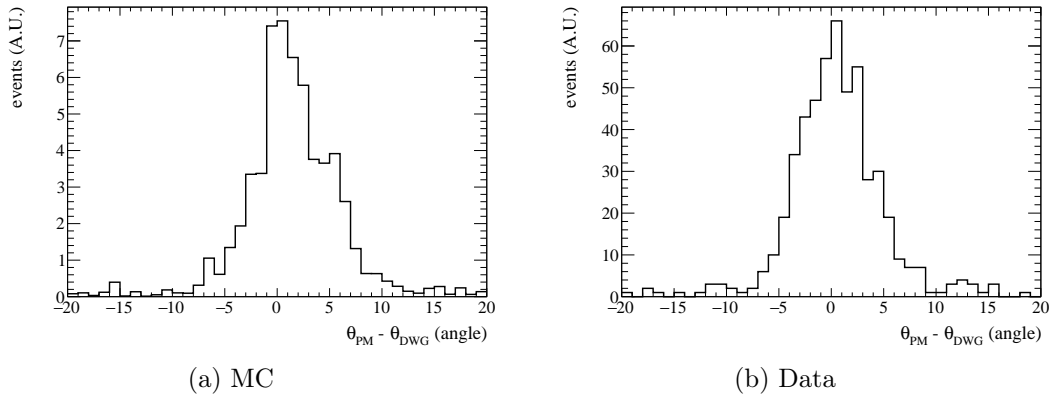
Figure 185: The residual distributions for both MC and data. The horizontal axis represents the angle difference between the two vertex detectors, θ_{pm} - θ_{dwg}
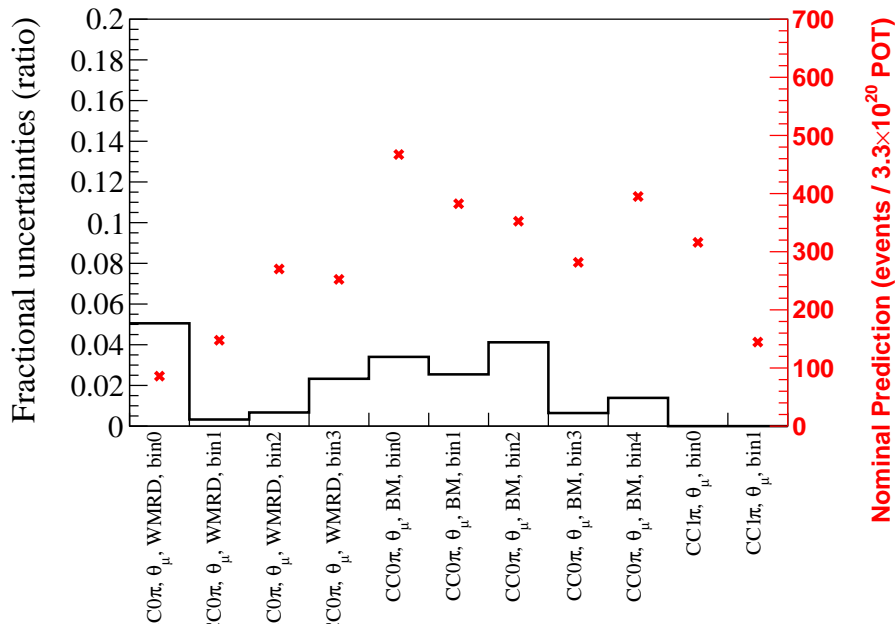
Figure 186: The effect of angle smearing for Proton Module sample in θ_μ binning

279
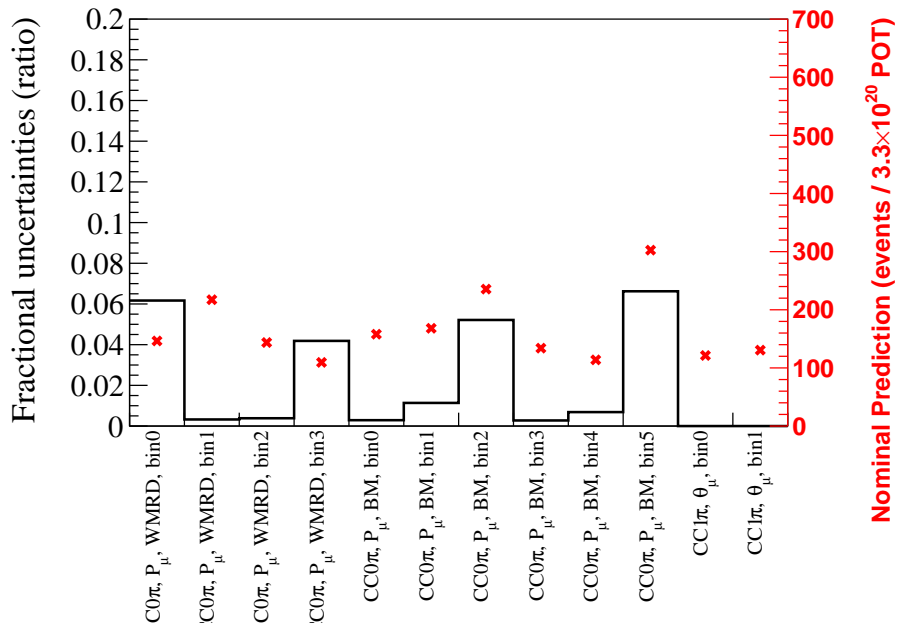
Figure 187: The effect of momentum smearing for Proton Module sample in P_μ binning

K.2.25 Summary of detector systematics

Figure 188 shows the results of total covariance matrices. Also, total correlation matrices are shown in Figure 189.

(a) WAGASCI P_μ binning

(b) WAGASCI θ_μ binning

(c) Proton Module P_μ binning

(d) Proton Module θ_μ binning
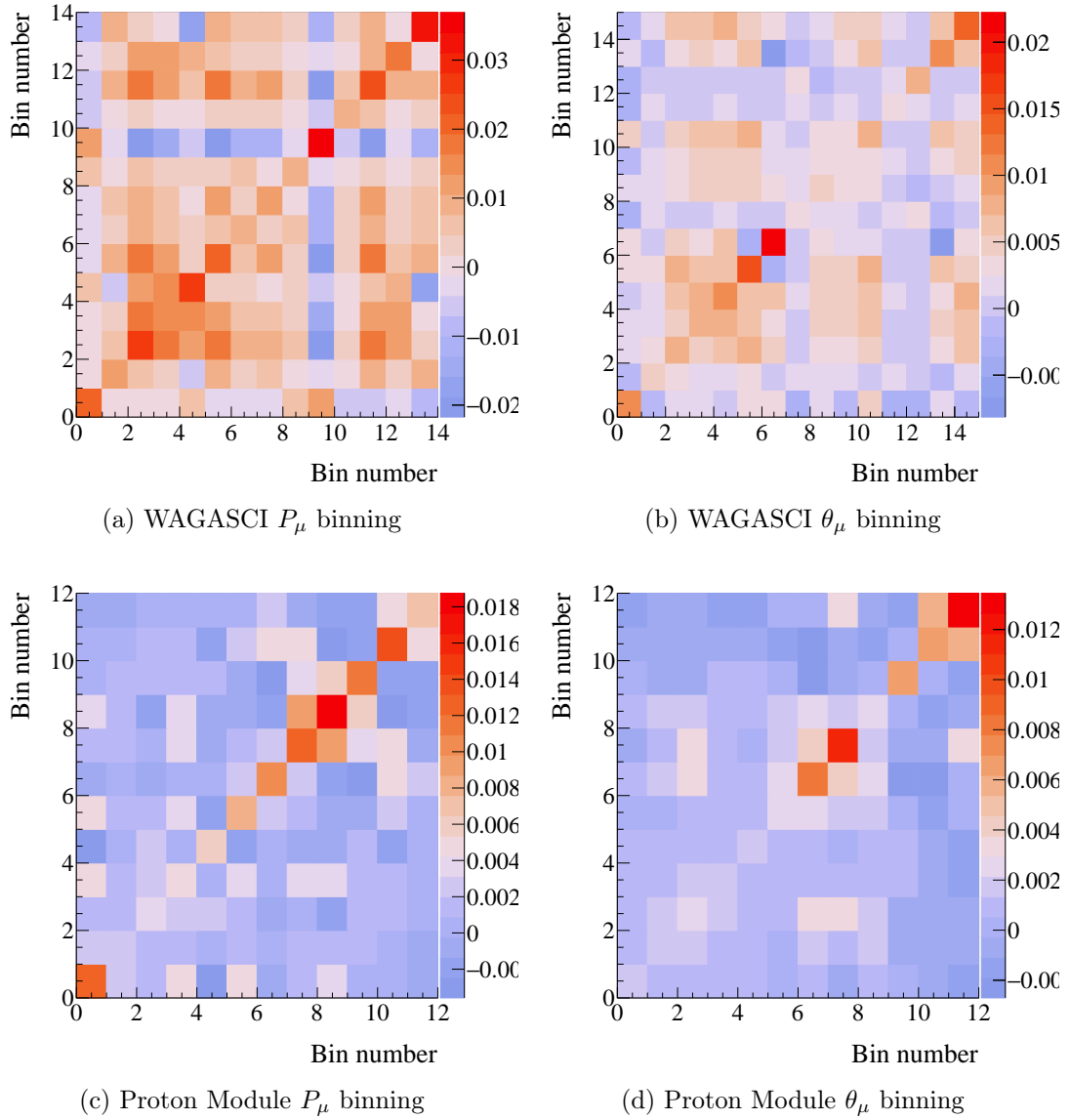
Figure 188: Total covariance matrices for the detector systematic uncertainties on the number of selected events.

(a) WAGASCI P_μ binning

(b) WAGASCI θ_μ binning

(c) Proton Module P_μ binning

(d) Proton Module θ_μ binning
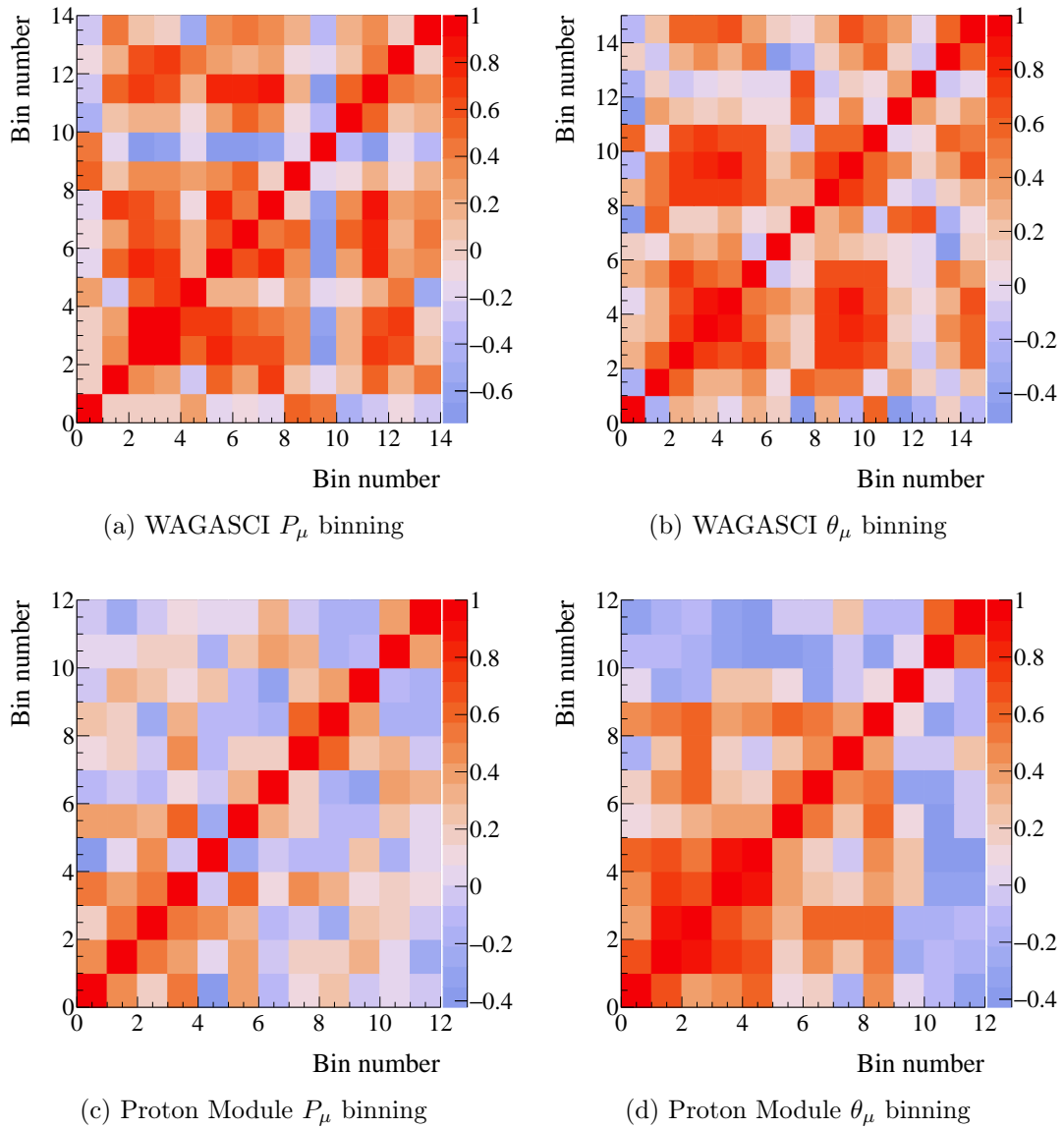
Figure 189: Total correlation matrices for the detector systematic uncertainties on the number of selected events.

Fractional errors are also calculated based on the diagonal elements in corresponding covariance matrices. Figs. 190 to 195 show the fractional systematic errors due to detector systematics. All detector systematic parameters are categorized into three groups, detector performance-related parameters, track reconstruction-related parameters and event selection-related parameters. Table 60 shows how those parameters are divided. Figs. 196, 197 show the total fractional uncertainties along with the one of each category of systematic parameters.

Table 60: Three categories depending on the type of detector systematic parameters

Parameter	Category
targetmass	Detector performance
magnet	Detector performance
localalignment	Detector performance
mppcnoise	Detector performance
scintillatordistortion	Detector performance
lightyield	Detector performance
hitthreshold	Detector performance
crosstalk	Detector performance
signal lost (WG)	Detector performance
Pion SI interaction	Detector performance
two-dimensional-trackeff	Track reconstruction
trackmatching-PM-to-WM	Track reconstruction
trackmatching-PM-to-DWG	Track reconstruction
trackmatching-PM-to-BM	Track reconstruction
trackmatching-UWG-to-WM	Track reconstruction
trackmatching-UWG-to-PM	Track reconstruction
trackmatching-DWG-to-BM	Track reconstruction
vertexing-PM	Track reconstruction
vertexing-WG	Track reconstruction
3dtracking	Track reconstruction
timingcut	Event Selection
fiducialvolume	Event Selection
containedvolume	Event Selection
particleid	Event Selection
chargeid	Event Selection
trackclusterratio	Event Selection
michelelectron	Event Selection
pileup	Event Selection
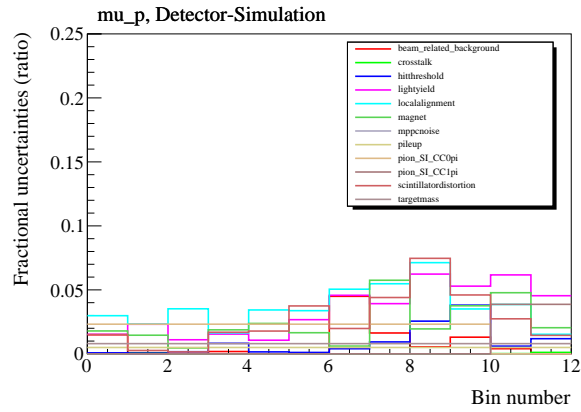
Figure 190: The fractional errors for the detector simulation category in the P_μ binning with Proton Module samples
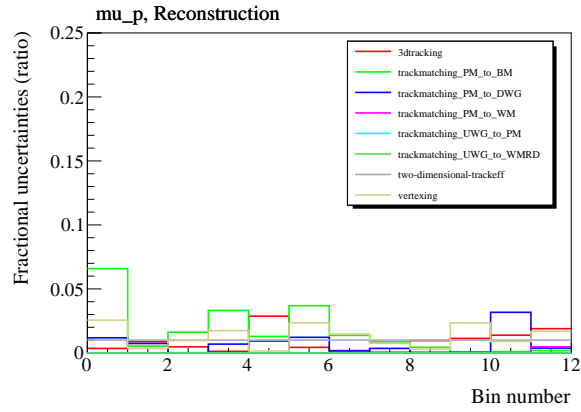
Figure 191: The fractional errors for the reconstruction category in the P_μ binning with Proton Module samples
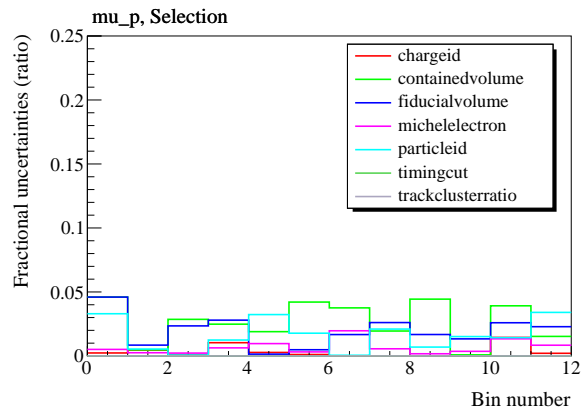
Figure 192: The fractional errors for the selection category in the P_μ binning with Proton Module samples
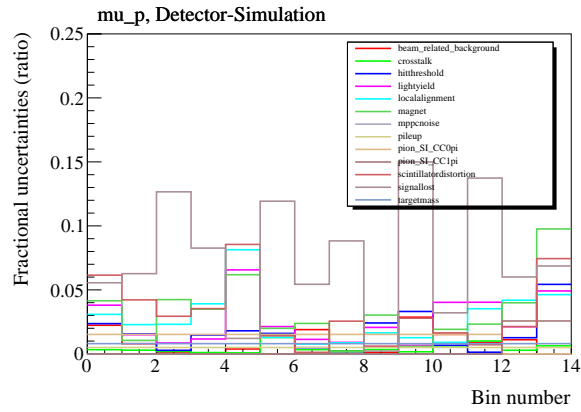
Figure 193: The fractional errors for the detector simulation category in the P_μ binning with WAGASCI detectors samples
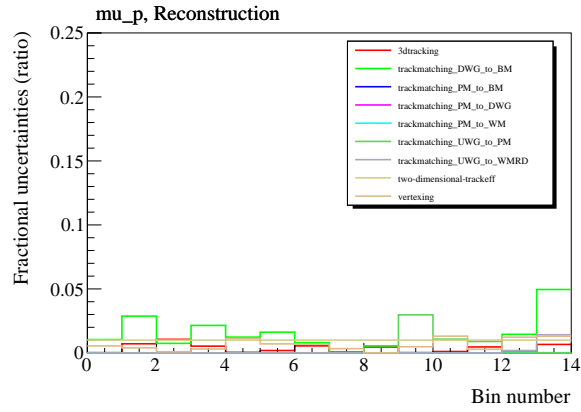
Figure 194: The fractional errors for the reconstruction category in the P_μ binning with WAGASCI detectors samples
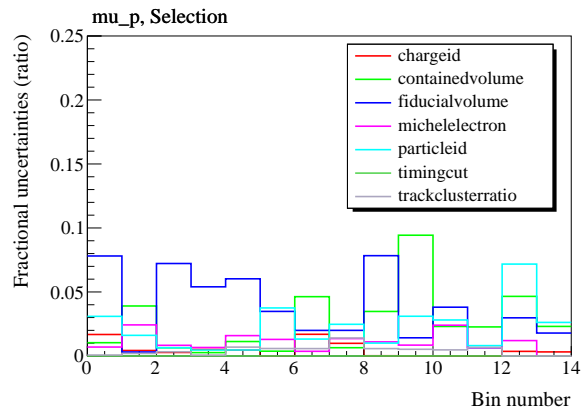
Figure 195: The fractional errors for the selection category in the P_μ binning with WAGASCI detectors samples

(a) P_μ binning
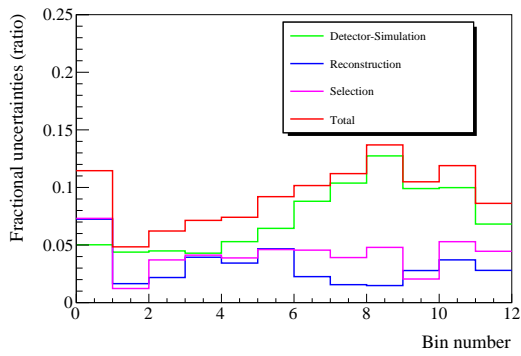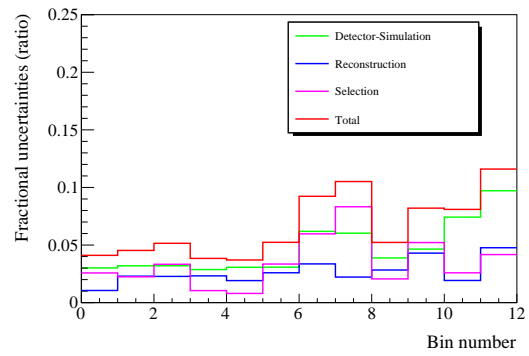
(b) θ_μ binning

Figure 196: Fractional errors due to the detector systematic uncertainties on the number of selected events for the Proton Module samples.

(a) P_μ binning
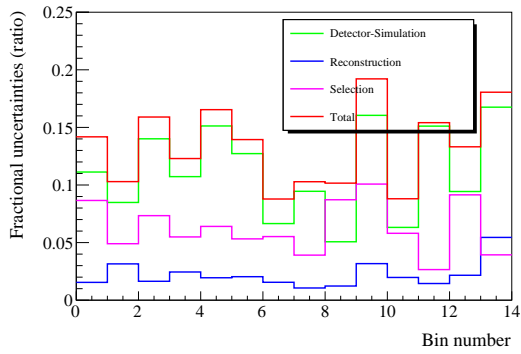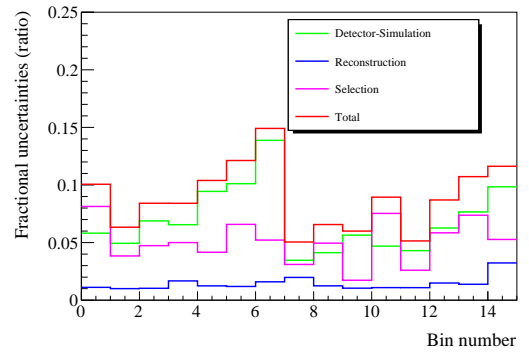
(b) θ_μ binning

Figure 197: Fractional errors due to the detector systematic uncertainties on the number of selected events for the WAGASCI detectors samples.

L   PartIII: Error propagation

It is difficult to mathematically formulate the errors on a cross section in general because there are too many parameters having correlations with each other. A useful technique to estimate error distributions is to throw a lot of toy experiments based on a covariance matrix with the Cholesky decomposition [168]. Each toy experiment from the Cholesky decomposition preserves the original parameter correlations. A fair amount of toy throws (typically 10,000 throws) can statistically take into account the effect of systematic parameters. The procedure of the Cholesky decomposition is described in the following. As the covariance matrix is symmetric and positive-definite [61], the matrix can be decomposed in

$$\Sigma = LL^* = LL^\mathsf{T} \tag{L.1}$$

where L is a lower triangular matrix (L^* is a corresponding conjugate matrix), which preserves all correlations included in the original matrix (Σ) [168]. The second equation is valid only if the matrix Σ is real, which is the case here. Assuming the systematic variations follow the Gaussian distributions, matrix (L) multiplied by a random value vector following Gaussian distribution with $\mu = 0, \sigma = 1$ gives random fluctuations around the best-fit values according to the post-fit covariance matrix (Σ). Then each thrown value ($\overrightarrow{\theta_t}$) is defined as

$$\overrightarrow{\theta_t} = \overrightarrow{\theta_f} + (L \times \overrightarrow{r_t}), \tag{L.2}$$

where $\overrightarrow{\theta_f}$ is the best-fit parameters. Once each toy throw ($\overrightarrow{\theta_t}$) is obtained, all the events are reweighted according to each systematic parameter, giving the corresponding cross section for the toy throw. Assuming the best-fit differential cross section is expressed by $\overline{x_i}$ and the variant cross section in each toy throw (t) is $x_{i,t}$ in a template bin i, the resulting covariance matrix (V) based on many toy throws (N throws) is given by

$$V_{ij} = \frac{1}{N} \sum_t (x_{it} - \overline{x_i})(x_{jt} - \overline{x_j}). \tag{L.3}$$

It should be noted that the errors related to flux integral, signal efficiency, and the number of target nucleons are also varied in each toy throw, which in turn the matrix (V) includes those kinds of uncertainties. The matrix contains all posterior uncertainties for the relevant parameters.

---

[61] All the eigenvalues are positive. In practice, if the eigenvalues are negative but extremely small, adding a small value such as $O(10^{-7})$ to the diagonal element is acceptable as far as it has little impact on the analysis.

M PartIII: The number of target nucleons and flux integral

The cross section extraction in this analysis requires accurate constants for the number of target nucleons and the flux integral. This section provides the process to calculate these values.

M.1 The number of target nucleons

Since we required fiducial volume events in the selection, the total number of target nucleons inside a fiducial volume is to be calculated. Proton Module and WAGASCI detectors, which are vertex detectors in the WAGASCI project, have their own fiducial volumes. They are defined in each view of XZ or YZ, which is shown in Figure 198.

(a) Proton Module, XZ view   (b) Proton Module, YZ view

(c) WAGASCI detectors, XZ view   (d) WAGASCI detectors, YZ view
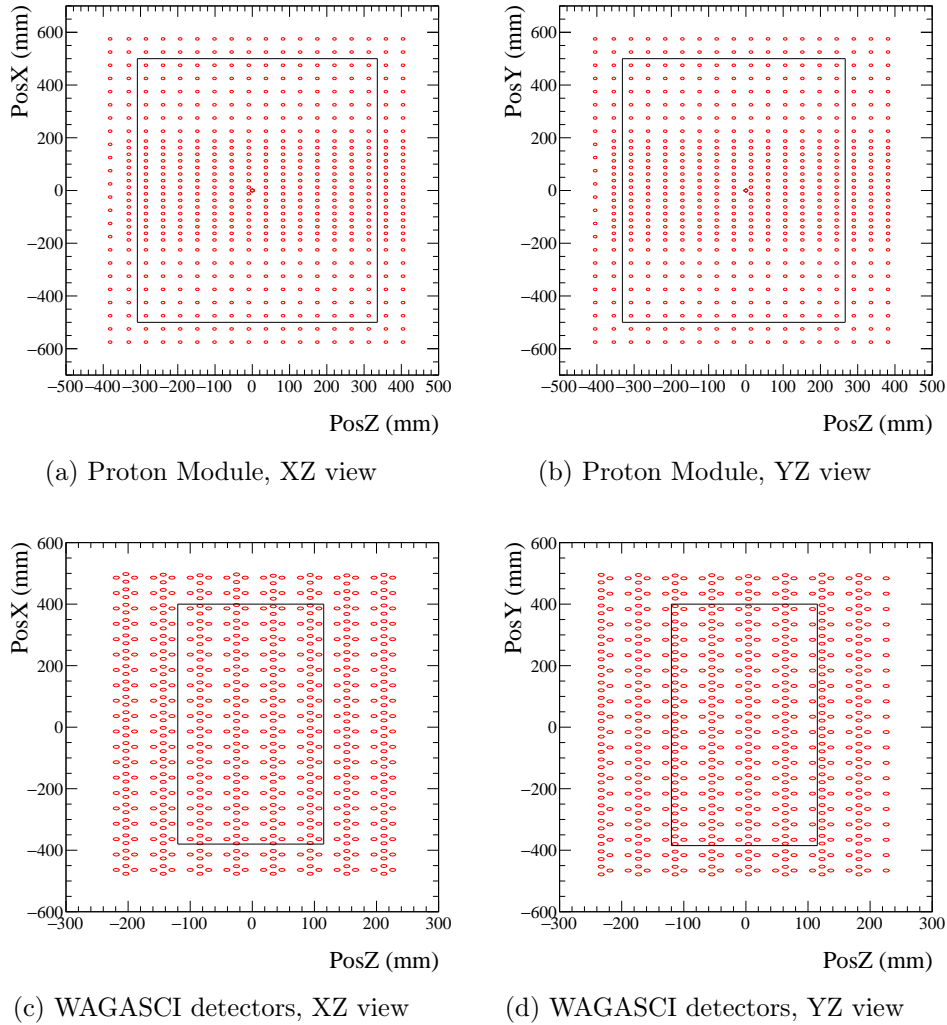
Figure 198: The definition of a fiducial volume in each detector in each view. A black solid line represents the border of fiducial volume. Circles in red point to the center of the scintillator bars. The exact border lines for WAGASCI detectors are a bit deviated from these illustrations. They are defined by the length between the most upstream (upper) position of the scintillator bars and the most downstream (lower) position of the scintillator bars inside the fiducial volume.

288

For the Proton Module case, the target nucleus in the air is neglected. Therefore, the number of nucleons inside scintillator bars is taken into account. On the other hand, scintillator bars in the WAGASCI detectors are filled in water. Materials inside both scintillator bars and water have to be taken into account. In this calculation, the length of the fiducial volume in each axis for the WAGASCI detectors is defined as the length between the most upstream (upper) position of the scintillator bars and the most downstream (lower) position of the scintillator bars.

Each vertex detector has different fractions of elements. Proton Module predominantly contains CH as a target material, while the WAGASCI detectors contains H_2O and CH by the mass fraction of 4:1. As a reminder, both detectors consist of two kinds of scintillator bars. It is necessary to examine the accurate fraction of the nucleus in each scintillator bar. Table 61 shows the elemental compositions of each scintillator bar and water. The multiplication of the number of scintillator bars (water volume), the weight per scintillator bar (water density) and each fraction of the target materials provide the measured value for target nucleons. Every number is summarized in Table 62.

Table 61: Elemental compositions of each scintillator bar and water. Hydrogen and Oxygen atoms are differentiated from each of them in a H_2O molecule. The column of "Mean weight (Error)" shows the weight for each scintillator bar or water per litre (g/L). The error refers to the 1σ fluctuation of each measurement.

	Scintillator bar	Mean weight (Error)	H	C	N	O	Ti	Si	H_2O
PM	scintillator (INGRID)	601.2 (1.21) g	7.59%	90.74%	0.07%	0.69%	0.91%	0.00%	0.00%
	scintillator (Scibar)	392.2 (2.02) g	7.63%	91.22%	0.07%	0.48%	0.59%	0.00%	0.00%
UWG	scintillator (plane)	77.56 (0.435) g	7.40%	88.3%	0.3%	2.7%	1.2%	0.2%	0.00%
	scintillator (grid)	74.55 (0.526) g	7.40%	88.0%	0.4%	2.9%	1.1%	0.1%	0.00%
	water	998.3 (0.00) (g/L)	0.00%	0.03%	0.02%	0.0%	0.0%	0.0%	99.95%
DWG	scintillator (plane)	79.25 (0.435) g	7.40%	87.9%	0.7%	2.7%	1.2%	0.1%	0.00%
	scintillator (grid)	75.44 (0.526) g	7.30%	87.7%	0.7%	2.9%	1.1%	0.1%	0.00%
	water	998.3 (0.00) (g/L)	0.00%	0.03%	0.02%	0.0%	0.0%	0.0%	99.95%

Table 62: The number of target nucleons inside the fiducial volume for each vertex detector. Each number refers to the number of nucleons (proton and neutron) in a target material of CH or H_2O.

Target material		Number of target nucleons	
		Mean (10^{28})	Error (10^{28})
PM	CH	18.66	0.045
	H_2O	0.00	0.00
UWG	CH	1.76	0.0079
	H_2O	6.90	0.035
DWG	CH	1.78	0.0078
	H_2O	6.87	0.034
WG total	CH	3.64	0.011
	H_2O	13.77	0.048

N   PartIII: Validations of the cross section fitter

When we have all selection outputs and the fitter to analyze cross sections, it is important to check the validity of the method and sanity of prepared inputs by feeding well-understood simulated data (pseudo data) to the fitter. The pseudo data were chosen depending on what kind of validations were necessary. For instance, the most fundamental one is the pseudo data that are identical to the selection outputs based on the nominal model. The fitter outcome of the fit can help us to check whether the level of uncertainty of each parameter is reasonable and whether each input works as expected. The fit results can give the sensitivity of our analysis. Another example is the pseudo data that are created by tweaking a specific parameter (for instance, M_A^{RES}), otherwise, unchanged. In this case, the number of events varies for the specific interactions having the response to the tweaked parameter. Then we need to check whether the fitter is able to recover the true value of the parameter.

In addition to the validation, we are motivated to test pseudo data by re-weighting events based on the suggestion provided by an alternative model. This is the test to make sure that we do not introduce a severe bias in the analysis. If there is no significant bias in the analysis, the fitter is in principle able to recover the true cross-section value based on the fit to the selected samples. In the final step of this simulated data study, we feed a full MC data set using an alternative-based model in NEUT or a full MC data set using another neutrino generator such as GENIE. The purpose of this fit is the same as the previous step, which is to check whether the fit is able to find the true cross section from the alternative model within the error. These items are further discussed in the next Appendix O.

Table 63 shows the list of simulated data studies that were performed in this analysis.

Table 63: The list of simulated data studies. The upper part of these studies is more like tests to check whether the fitter performs the fit as expected based on all inputs. The lower part of the studies is the tests to make sure whether we have not introduced severe selection bias into this analysis.

Name of simulated data study	Descriptions of pseudo data
AsimovFit	Data set is based on the nominal selection, systematic parameters and NEUT models.
Altered signal events (overall)	Alter all true signal events by +20%.
Altered signal events (individual)	Alter all true signal events on CH (H_2O) target by +20% (-20%).
Tweaked MaRES	MaRES parameter is tweaked by +2 sigma ($0.95 \to 1.25$).
Statistical fluctuation	The same configuration in AsimovFit but statistical fluctuation is applied.
Systematic parameter variation	All systematic parameters are thrown based on their covariance matrices.
Coverage	Create 1000 toy experiments in systematic variations with statistical fluctuation
Alternate RPA model (BeRPA)	Reweight CCQE events based on the BeRPA model.
Low Q^2 suppression	Reweight CCRES events based on Q^2.
Alternate neutrino generator	Run full GENIE MC (version 3.02).
post-BANFF tuned events	Reweight all events based on the post-BANFF tune in OA2022
Alternative NEUT model	Nieves 1p1h model without SF function ($M_A^{\mathrm{QE}} = 1.05$)

In each pseudo data fit shown in Figure 63, we check the systematic parameter constraints from the fit, the post-fit and pre-fit event distribution for sample by sample and the difference of post-fit cross section results with respect to the true cross section from the model. The difference in event distribution between post-fit and pre-fit and that in cross section values between post-fit and true should be assessed with some metrics to check the performance of the fit. We introduce appropriate χ^2 values for this purpose. For the difference in event distributions, χ^2 is defined as

$$\chi^2_{\text{evdis}} = \sum_{i=1}^{N} 2 \left(N_i^{\text{fit}} - N_i^{\text{obs}} + N_i^{\text{obs}} \ln \frac{N_i^{\text{obs}}}{N_i^{\text{fit}}} \right), \tag{N.1}$$

by taking only statistical contribution into account. N_i^{fit} are the expected number of events for bin i from a fit result, which form a post-fit event distribution. N_i^{obs} are the observed number of events (from pseudo data in the context of this validation) for bin i. On the other hand, the difference in cross sections is evaluated by

$$\chi^2_{\text{xsec}} = \sum_{i=1}^{N} \left((\sigma_i^{\text{fit}} - \sigma_i^{\text{true}}) V_{\text{fit}}^{-1} (\sigma_i^{\text{fit}} - \sigma_i^{\text{true}}) \right), \tag{N.2}$$

where $\sigma_i^{\text{fit}}(\sigma_i^{\text{true}})$ are post-fit (true) cross sections for the true bin i, and V is a covariance matrix that is obtained by the error propagation.

N.1 AsimovFit

AsimovFit is defined as the fit with the pseudo data where all the systematic parameters are set to their nominal values returning to the weight of 1. In other words, the fit is done against the nominal data set based on the underlying model adopted in this analysis. The outcome of AsimovFit provides a sensitivity result in terms of the parameter constraints because the data is not subject to statistical uncertainty unlike the real data fit. Considering these features, we expect the fit to recover the nominal value for all the nuisance parameters including the template parameters.

The results are shown in Figures 199, 200 in the momentum distribution and Figures 201, 202 in the angle distribution. Figure 199 shows all the post-fit parameters are overlaid on the pre-fit parameters, which means the fitter is able to recover the expected values in the fit. With respect to the parameter constraints in particular for the interaction parameters, we do not see a lot of improvements except for the normalization parameters. The current sensitivity is limited by the smaller statistics that result in a relatively coarser binning scheme in one dimension. Figure 200 presents two kinds of comparisons for the bin-by-bin event distributions and cross sections along with the true cross sections from the pseudo data and nominal data set. The post-fit event distribution is identical to the pre-fit distribution, which can be confirmed by our metrics. In terms of cross section, the bottom plot in Figure 200 confirms the fitter is able to find expected differential cross section, which is supported by χ^2_{xsec}. Since the pseudo data is identical to the nominal data set, both true cross sections are exactly overlaid. The error bars correspond to the 1σ region of the cross section distribution from 1000 toy experiments.

(a) template parameters

(b) detector parameters

(c) flux parameters

(d) interaction parameters
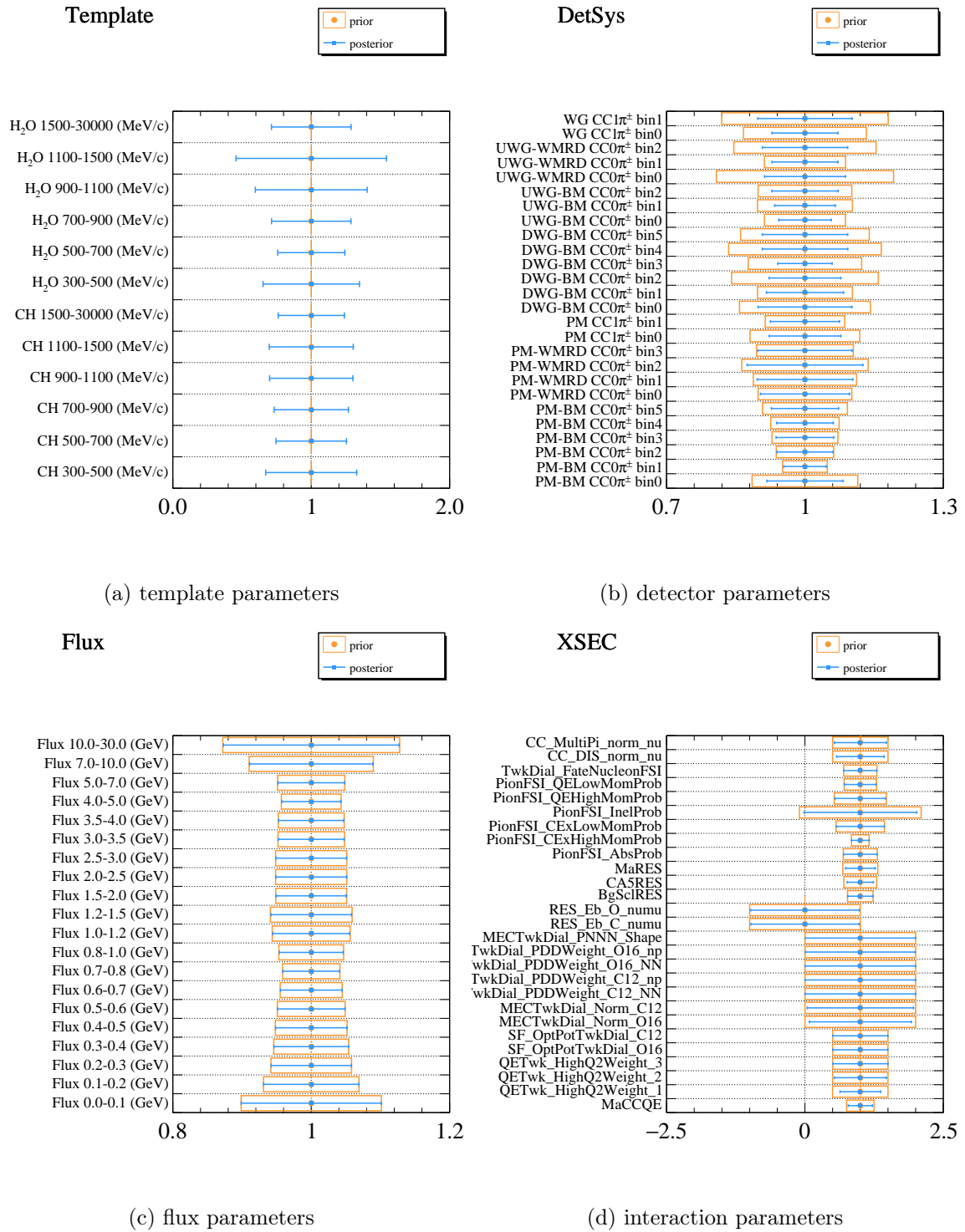
Figure 199: The parameter constraints from the FDS of AsimovFit in the momentum distribution. Each posterior result is presented by a best-fit point and error bar (blue dot and line) against its prior parameter in orange rectangular. The error is calculated based on the gaussian assumption of each parameter distribution.
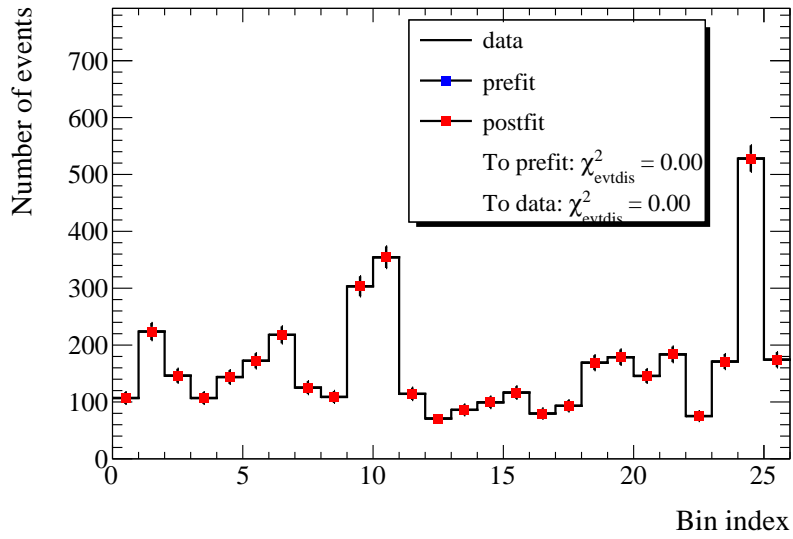
(a) Comparison of event distributions
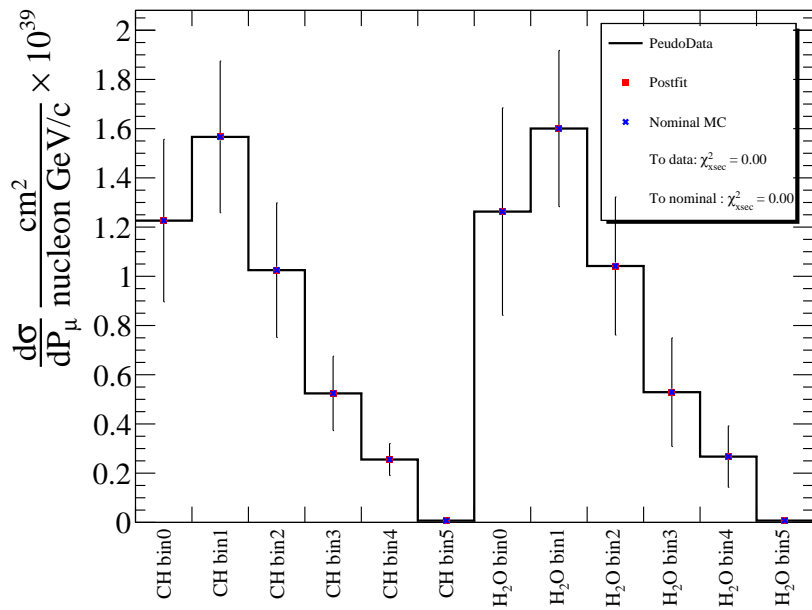
(b) Comparison of cross section fit results

Figure 200: Comparisons of bin-by-bin event distributions between post-fit and pre-fit (top) and the post-fit cross sections overlaid on the true cross sections from pseudo data and nominal data set (bottom) as results of the FDS of AsimovFit in the momentum distribution. Both plots include corresponding χ^2 values as metrics defined in Equations N.1, N.2.

(a) template parameters

(b) detector parameters

(c) flux parameters

(d) interaction parameters
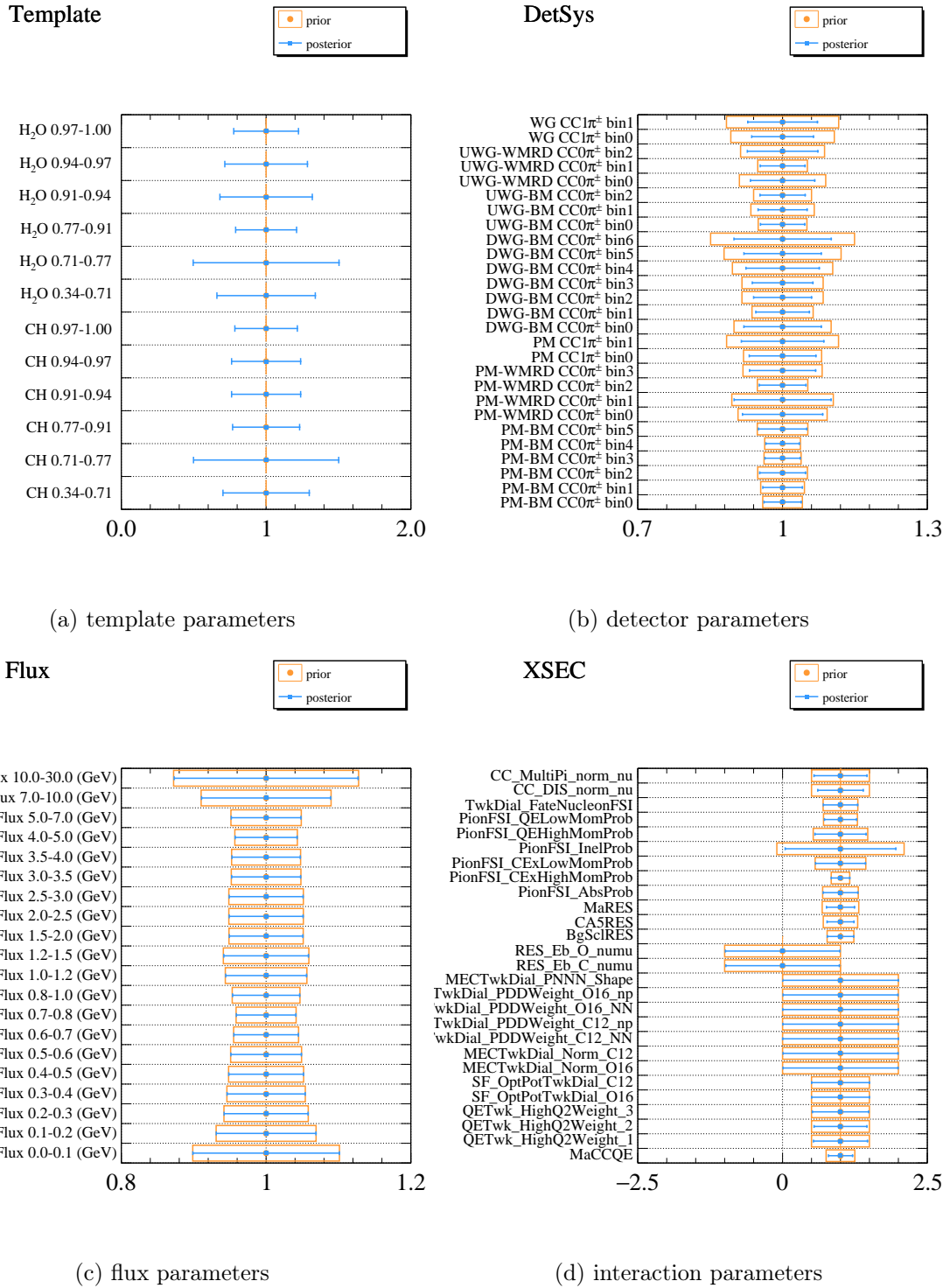
Figure 201: The parameter constraints from the FDS of AsimovFit in the angle distribution. Each posterior result is presented by a best-fit point and error bar (blue dot and line) against its prior parameter in orange rectangular. The error is calculated based on the gaussian assumption of each parameter distribution.
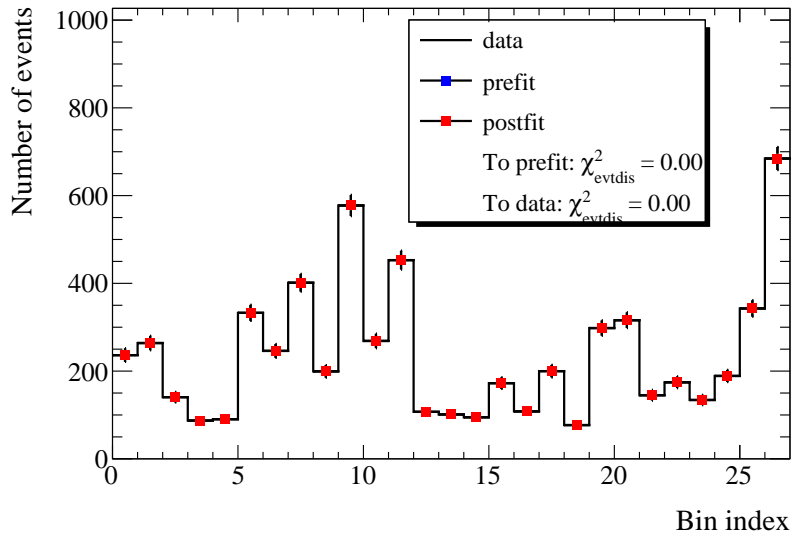
(a) Comparison of event distributions
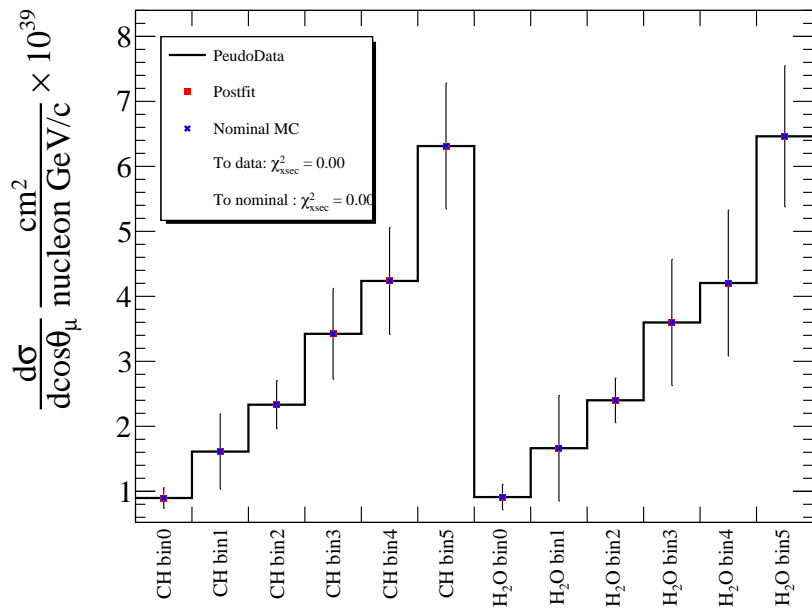
(b) Comparison of cross section fit results

Figure 202: Comparisons of bin-by-bin event distributions between post-fit and pre-fit (top) and the post-fit cross sections overlaid on the true cross sections from pseudo data and nominal data set (bottom) as results of the FDS of AsimovFit in the angle distribution. Both plots include corresponding χ^2 values as metrics defined in Equations N.1, N.2.

N.2 Altered signal events (overall)

We change the number of signal events in both selected and true events by $+20\%$ overall to create this pseudo data. The change acts as a normalization of signal events. Since template parameters are capable of catching up with the normalization of signal events and have no penalty term unlike the other nuisance parameters, the expected performance would be that the fitter is able to minimize χ^2 by moving only the template parameters by the exact same amount of original change.

The results are shown in Figures 203, 204 in the momentum distribution and Figures 205, 206 in the angle distribution. The left top plot in Figure 203 presents the best-fit (posterior) values and constraints of the template parameters. All posterior values move by exactly 20% in the "right" direction with respect to the pseudo data set, while other parameters are unchanged from their prior values. The top plot in Figure 204 shows the comparison of event distribution between post-fit and pre-fit. The χ^2 metric getting exactly 0 with respect to data confirms the shift of the template parameters recovers the event distribution in pseudo data. Post-fit cross sections are compared in the bottom plot in Figure 204. It confirms the fitter is able to find out the true cross section parameters precisely.

(a) template parameters

(b) detector parameters

(c) flux parameters

(d) interaction parameters
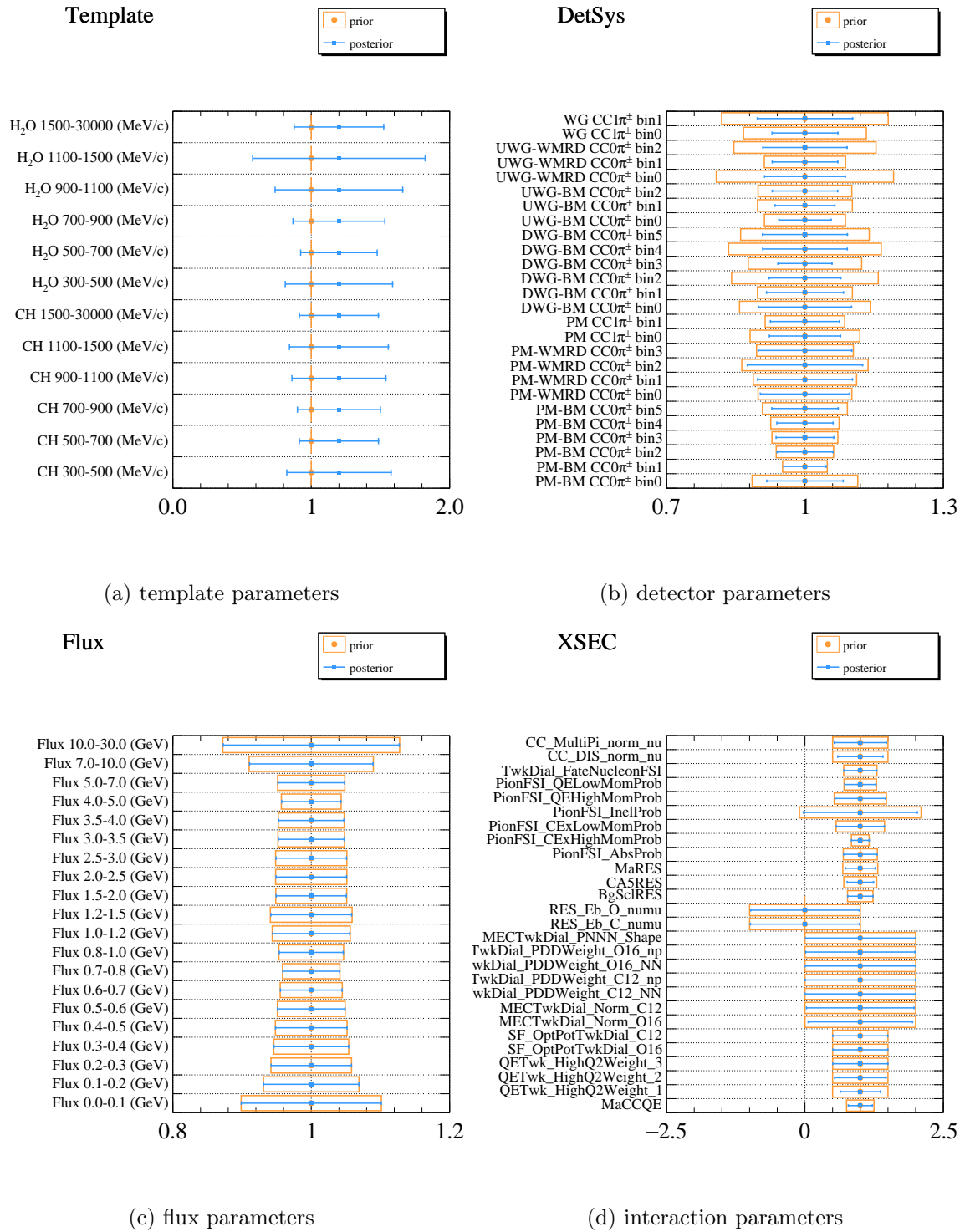
Figure 203: The parameter constraints from the FDS of Altered signal events (overall) in the momentum distribution. Each posterior result is presented by a best-fit point and error bar (blue dot and line) against its prior parameter in orange rectangular. The error is calculated based on the gaussian assumption of each parameter distribution.
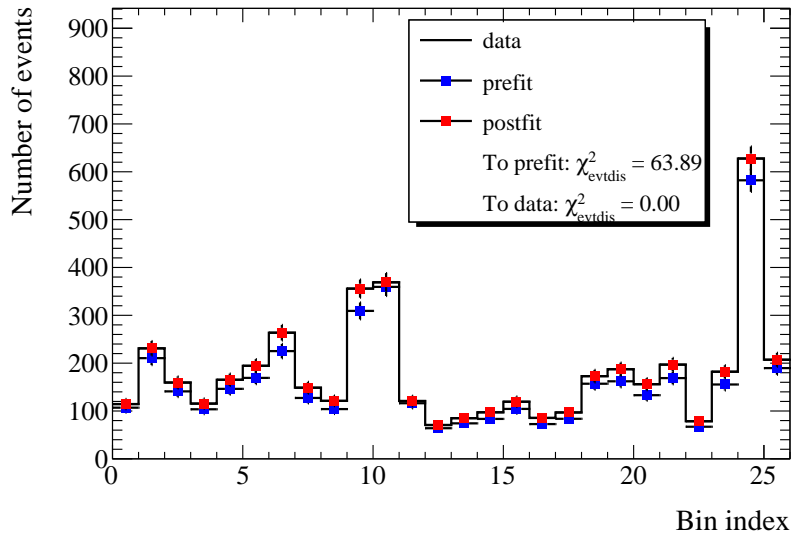
(a) Comparison of event distributions
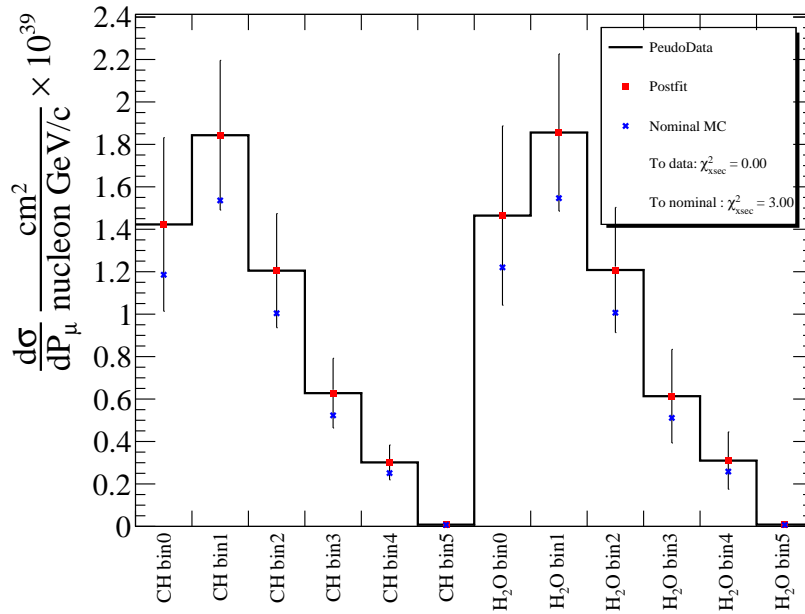
(b) Comparison of cross section fit results

Figure 204: Comparisons of bin-by-bin event distributions between post-fit and pre-fit (top) and the post-fit cross sections overlaid on the true cross sections from pseudo data and nominal data set (bottom) as results of the FDS of Altered signal events (overall) in the momentum distribution. Both plots include corresponding χ^2 values as metrics defined in Equations N.1, N.2.
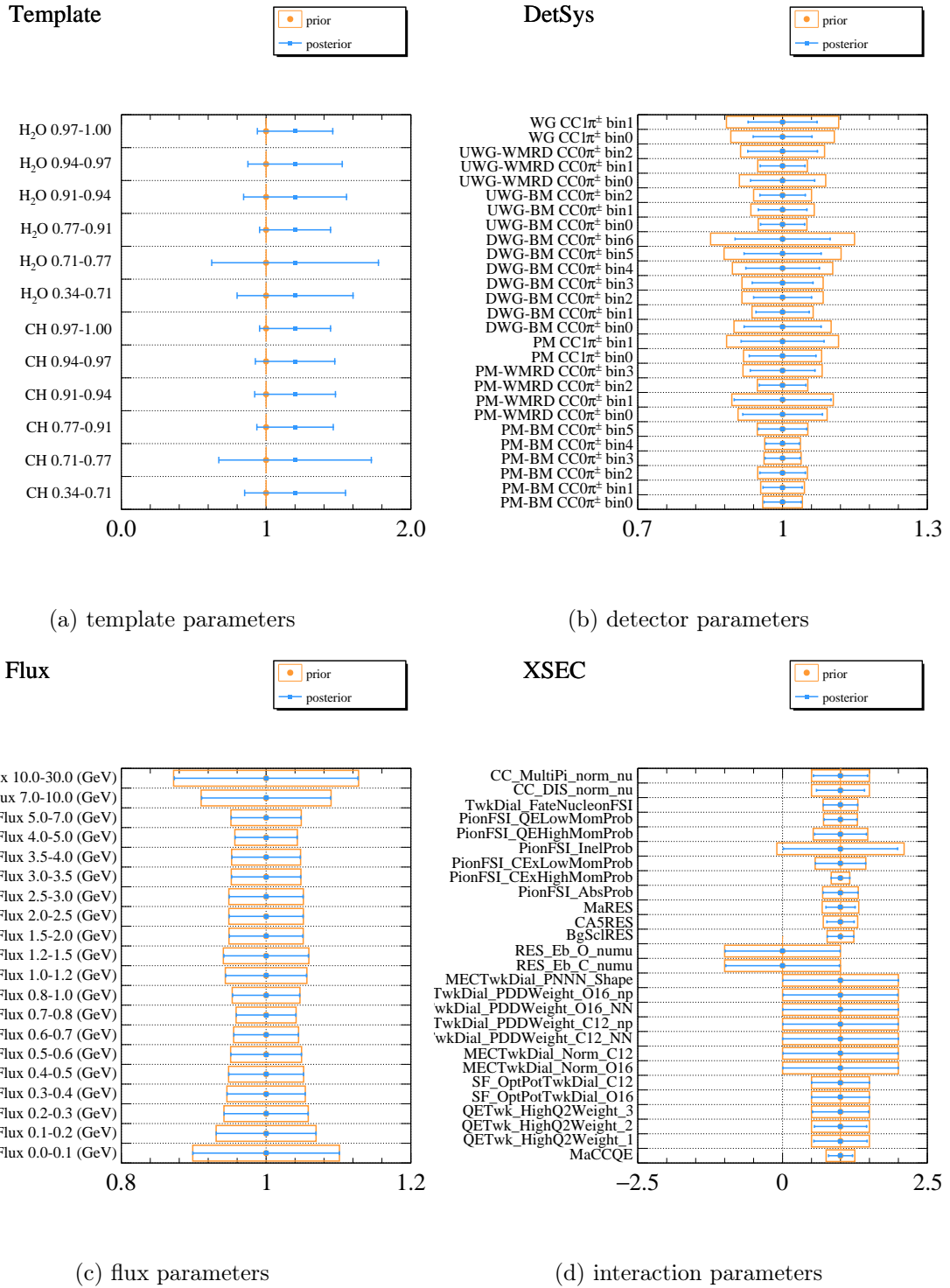
Figure 205: The parameter constraints from the FDS of Altered signal events (overall) in the angle distribution. Each posterior result is presented by a best-fit point and error bar (blue dot and line) against its prior parameter in orange rectangular. The error is calculated based on the gaussian assumption of each parameter distribution.
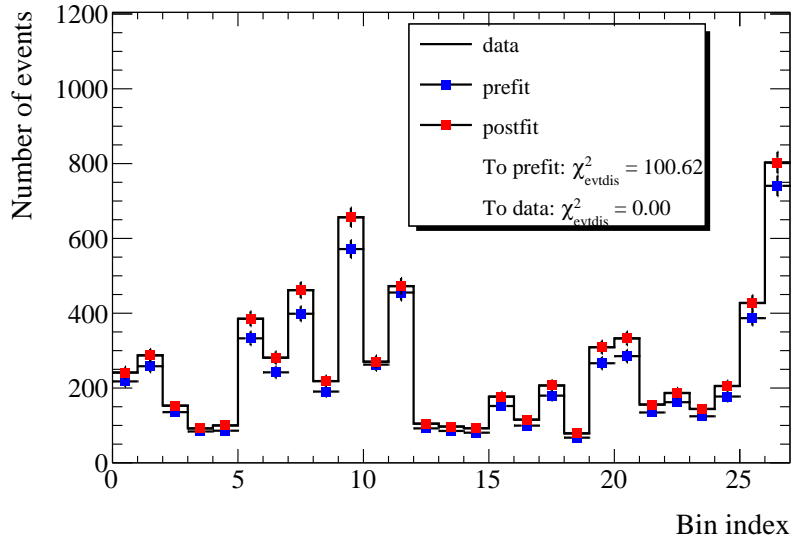
(a) Comparison of event distributions
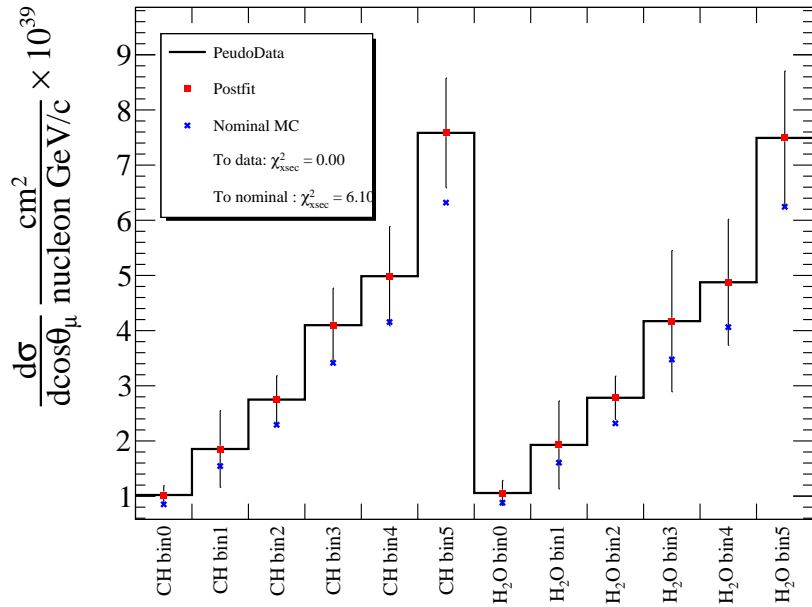
(b) Comparison of cross section fit results

Figure 206: Comparisons of bin-by-bin event distributions between post-fit and pre-fit (top) and the post-fit cross sections overlaid on the true cross sections from pseudo data and nominal data set (bottom) as results of the FDS of Altered signal events (overall) in the angle distribution. Both plots include corresponding χ^2 values as metrics defined in Equations N.1, N.2.

N.3 Altered signal events (individual)

Similar to the previous altered signal events, the pseudo data was produced with the signal events on CH target increased by 20%, but with those on H_2O target decreased by 20%. We then check whether the fitter is able to recover the true value by moving template parameters individually for CH and H_2O target events.

The results are shown in Figures 207, 208. Figures 209, 210. As expected, the template parameters for the CH target decreases by -20% and those for the H_2O target increases by +20% as in the left top plot in Figure 207. Similar to the previous study, the fit was able to minimize χ^2 by moving only the template parameters, other parameters remain pre-fit values. Figure 207 also shows the expected fitter performance where we can see the same change in event distributions and cross sections as we expect from the pseudo data.

(a) template parameters

(b) detector parameters

(c) flux parameters

(d) interaction parameters
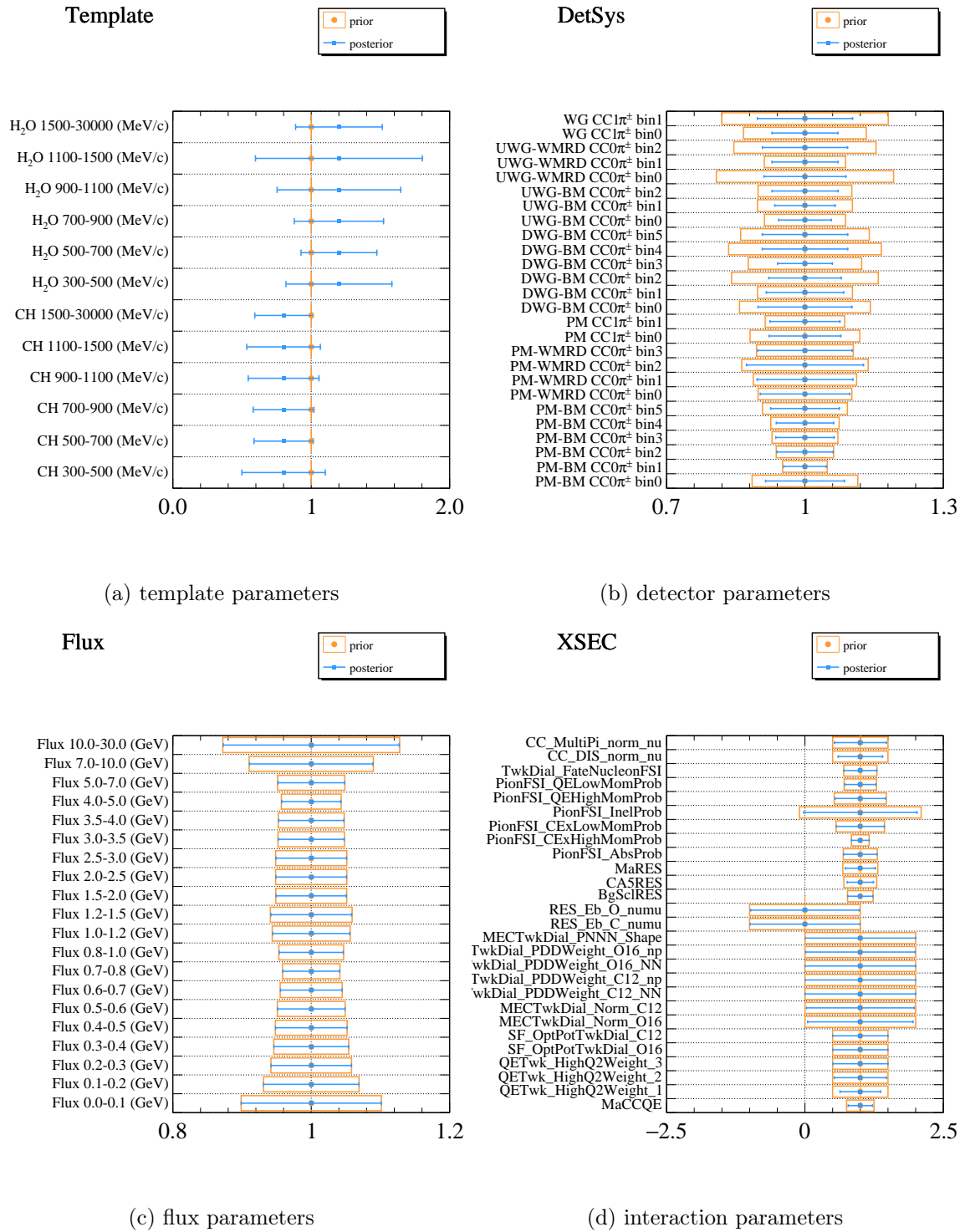
Figure 207: The parameter constraints from the FDS of Altered signal events (individual) in the momentum distribution. Each posterior result is presented by a best-fit point and error bar (blue dot and line) against its prior parameter in orange rectangular. The error is calculated based on the gaussian assumption of each parameter distribution.
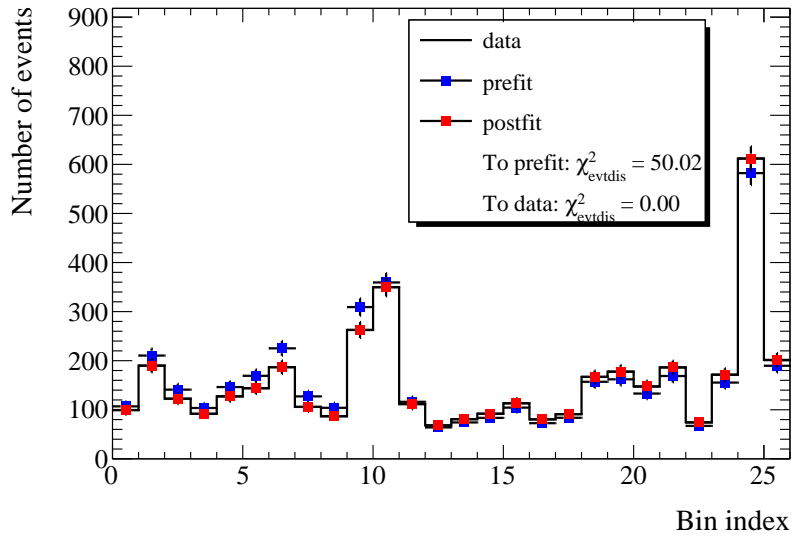
(a) Comparison of event distributions
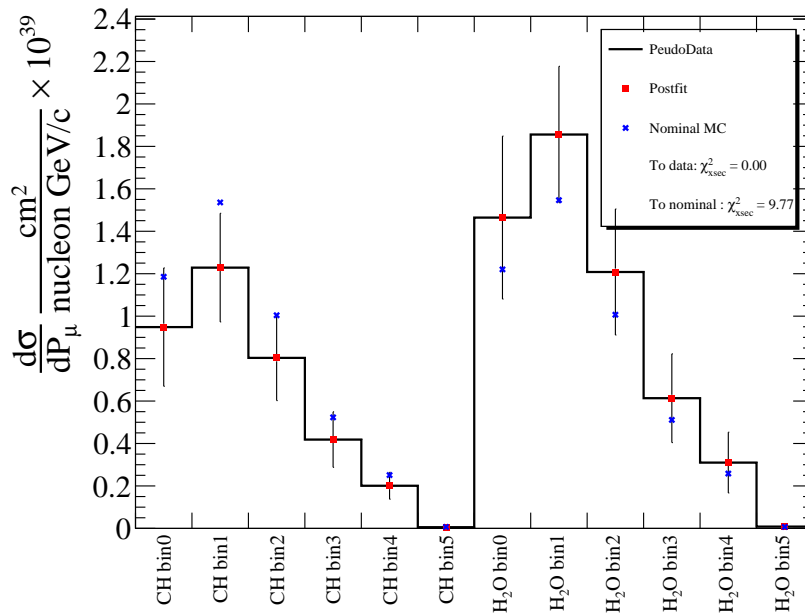
(b) Comparison of cross section fit results

Figure 208: Comparisons of bin-by-bin event distributions between post-fit and pre-fit (top) and the post-fit cross sections overlaid on the true cross sections from pseudo data and nominal data set (bottom) as results of the FDS of Altered signal events (individual) in the momentum distribution. Both plots include corresponding χ^2 values as metrics defined in Equations N.1, N.2.

(a) template parameters

(b) detector parameters

(c) flux parameters

(d) interaction parameters
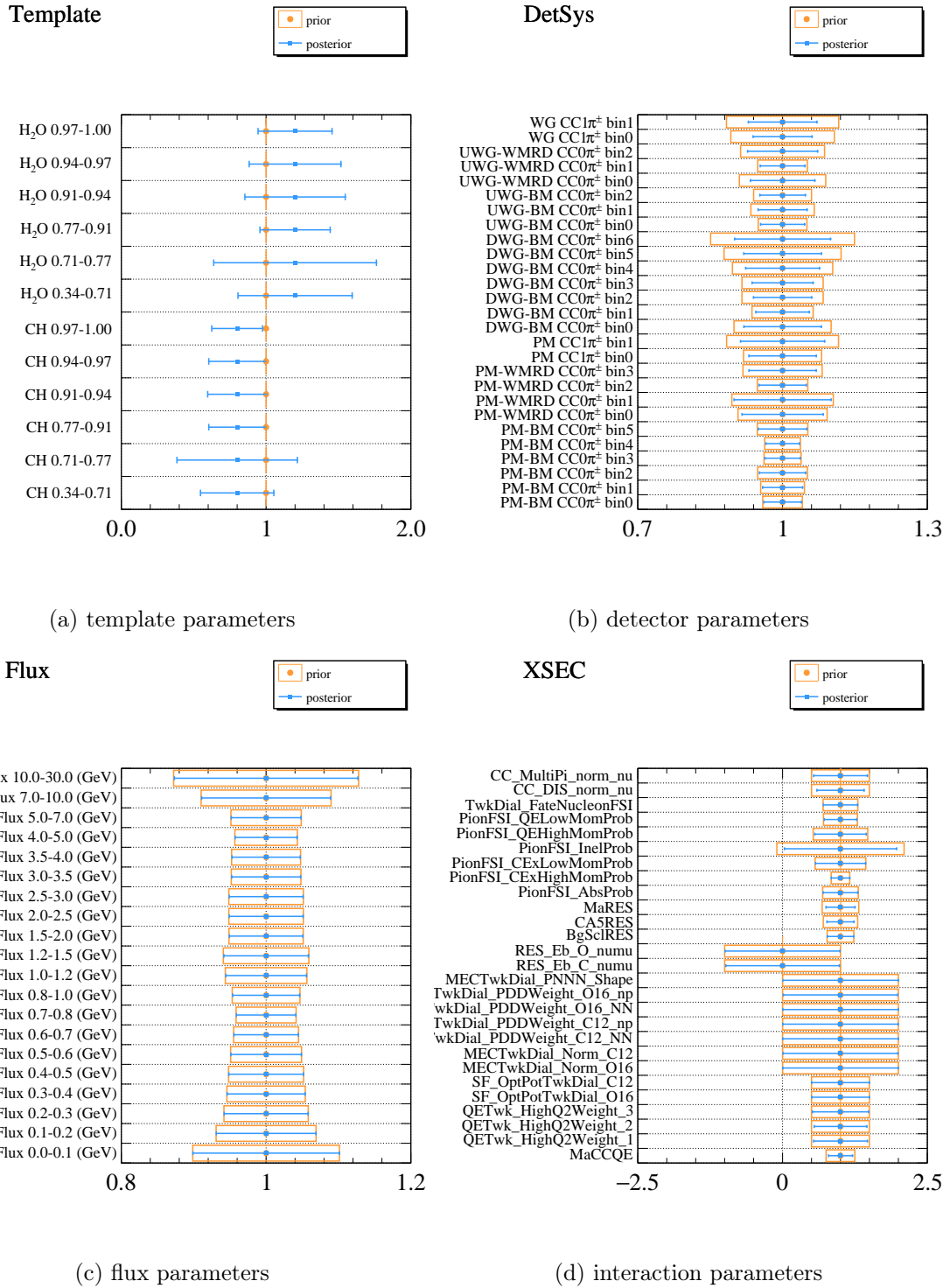
Figure 209: The parameter constraints from the FDS of Altered signal events (individual) in the angle distribution. Each posterior result is presented by a best-fit point and error bar (blue dot and line) against its prior parameter in orange rectangular. The error is calculated based on the gaussian assumption of each parameter distribution.
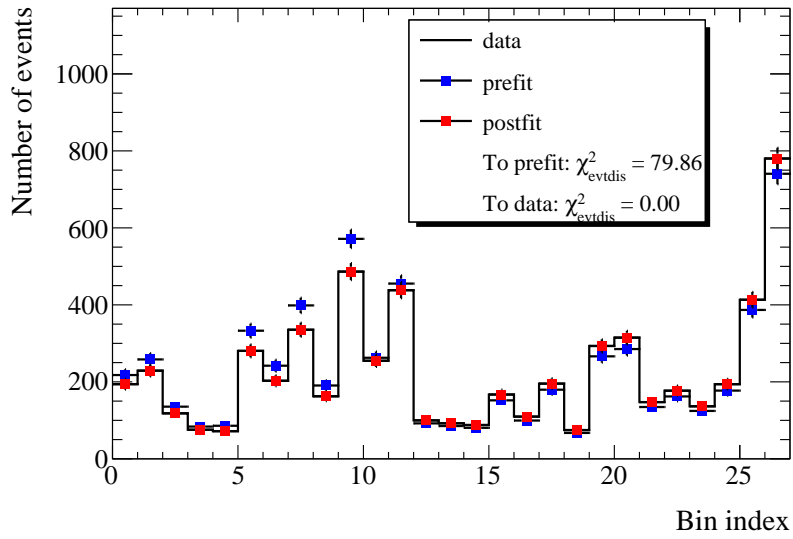
(a) Comparison of event distributions
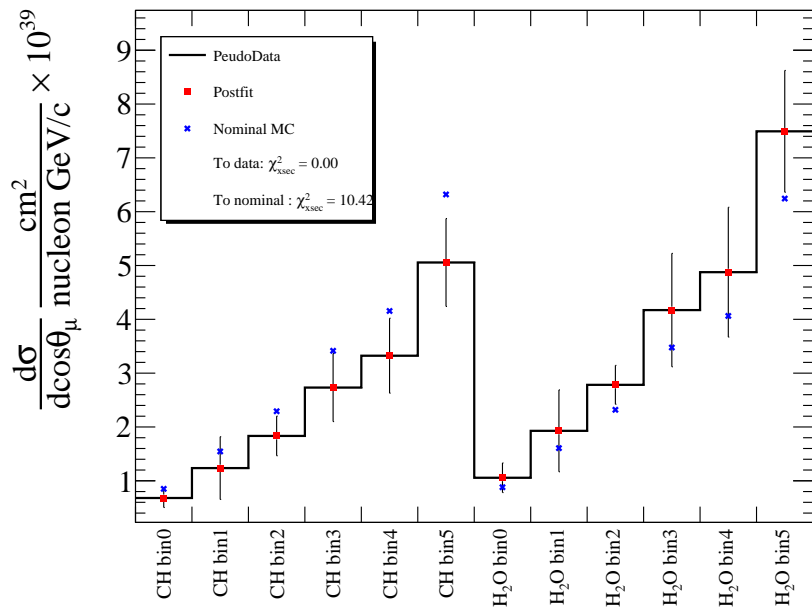
(b) Comparison of cross section fit results

Figure 210: Comparisons of bin-by-bin event distributions between post-fit and pre-fit (top) and the post-fit cross sections overlaid on the true cross sections from pseudo data and nominal data set (bottom) as results of the FDS of Altered signal events (individual) in the angle distribution. Both plots include corresponding χ^2 values as metrics defined in Equations N.1, N.2.

N.4   Tweaked MaRES

The pseudo data for this study was created with the M_A^{RES} tweaked by $+2\sigma$ ($0.95 \rightarrow 1.25$), otherwise unchanged compared to nominal. This parameter has a response to single-pion production. The fraction of the interaction in the number of selected events is inflated. The results are shown in Figures 211, 212 in the momentum distribution and Figures 213, 214 in the angle distribution. The primary point of this study is how the fitter finds the best-fit values.

Focusing on the interaction parameters, we see increases in the resonant interaction related parameters (M_A^{RES}, C_A^5). As this analysis adopts a relatively coarser one-dimensional binning scheme, resonant parameters act more like "normalization" than like changing "shape". Therefore, both resonant parameters (M_A^{RES}, C_A^5) have a similar response to a change in the event distributions. Consequently, these parameters are shifted in a synonymous fashion. In addition, the normalization parameters for the multi-pion production and DIS (deep inelastic scattering) interactions are subject to being shifted to higher values. This behaviour is understandable considering the true resonant events are sometimes reconstructed as signal events, which may inflate (at least change) the background distribution. Those normalization parameters could have compensated for this change. When we take a look at the template parameters in the left top plot in Figure 211, a noticeable change is seen in the low momentum bins "300 MeV to 500 MeV" for both samples. This is due in large part to the background contamination from resonant interactions being large in low momentum bins, where muons pass through WallMRD instead of BabyMIND. This change in template parameters dilutes the shift in the resonant interaction parameters.

The post-fit event distributions (shown in the top plot in Figure 212) are in line with the distribution based on the pseudo data, which is supported by the drastic improvement of χ^2 metric. The comparison of cross sections (shown in the bottom plot in Figure 212) shows that there is a good agreement between post-fit cross sections and cross sections from the pseudo data. A little deviation in the low-momentum bins reflects the change in template parameters mentioned above, which does not have a significant impact on the χ^2 value.

(a) template parameters

(b) detector parameters

(c) flux parameters

(d) interaction parameters
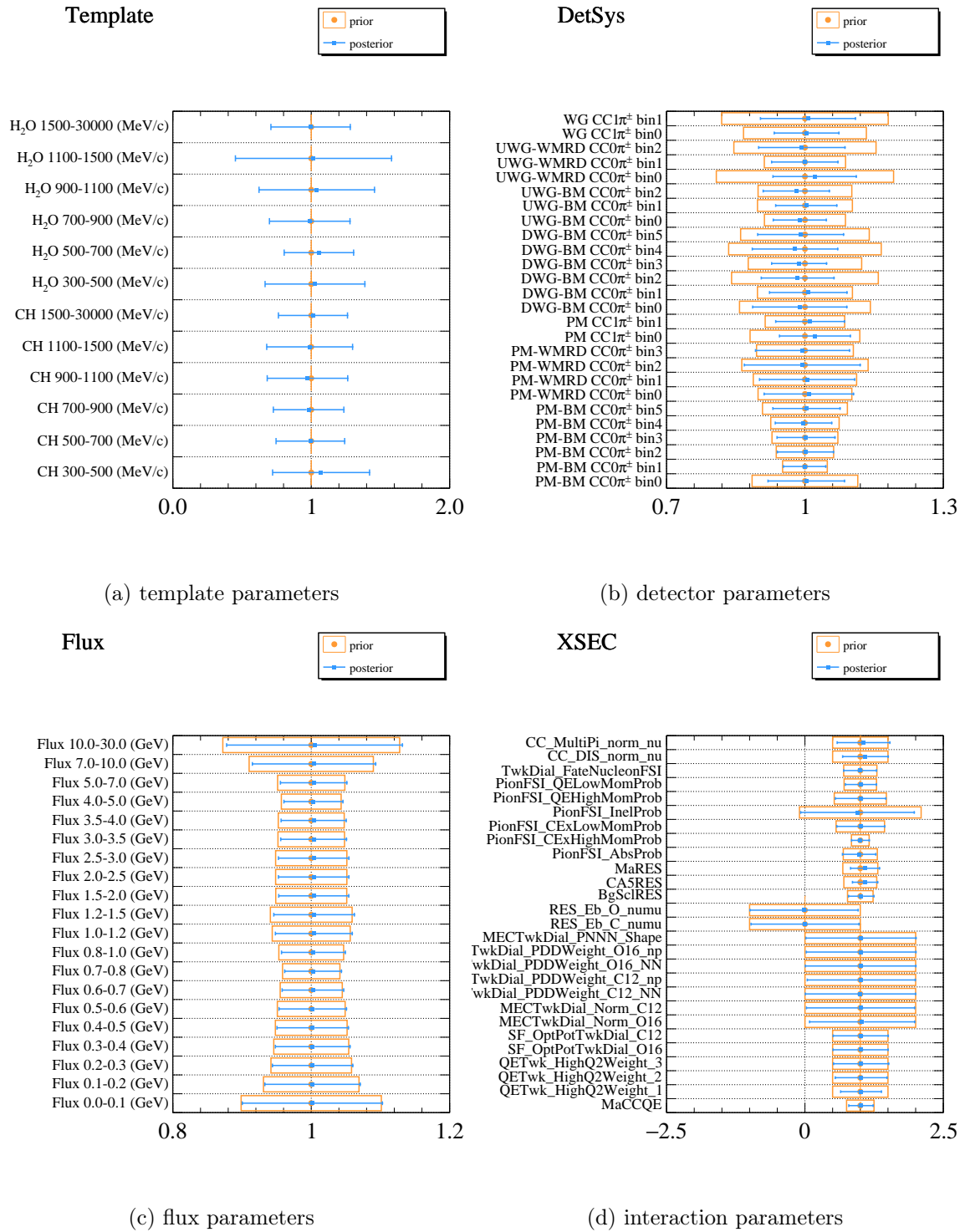
Figure 211: The parameter constraints from the FDS of Tweaked MaRES in the momentum distribution. Each posterior result is presented by a best-fit point and error bar (blue dot and line) against its prior parameter in orange rectangular. The error is calculated based on the gaussian assumption of each parameter distribution.
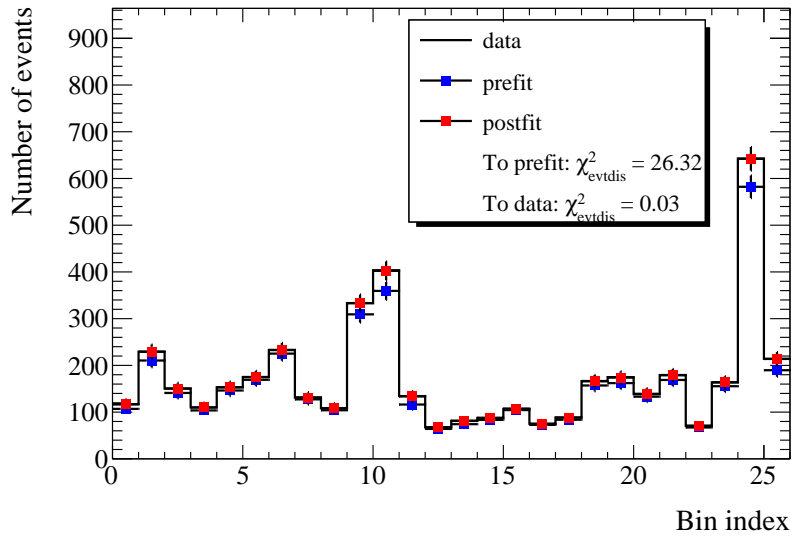
(a) Comparison of event distributions
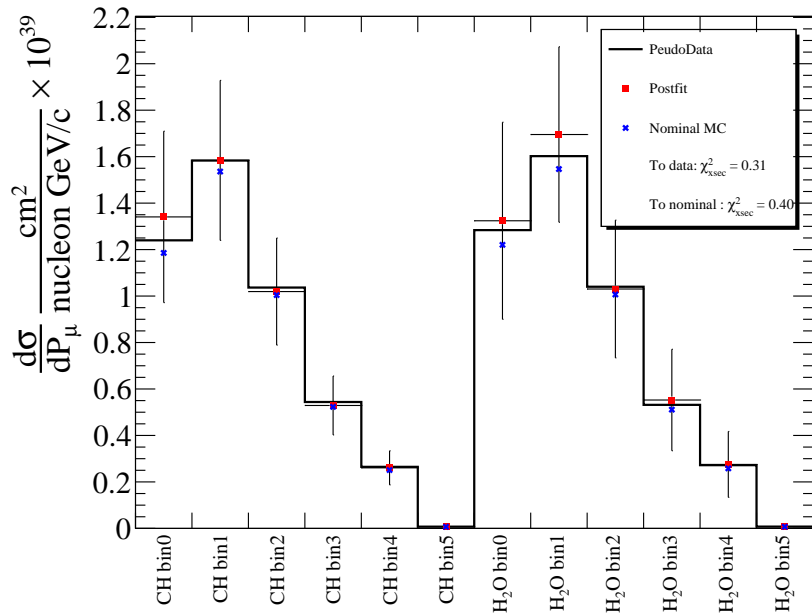
(b) Comparison of cross section fit results

Figure 212: Comparisons of bin-by-bin event distributions between post-fit and pre-fit (top) and the post-fit cross sections overlaid on the true cross sections from pseudo data and nominal data set (bottom) as results of the FDS of Tweaked MaRES in the momentum distribution. Both plots include corresponding χ^2 values as metrics defined in Equations N.1, N.2.

(a) template parameters

(b) detector parameters

(c) flux parameters

(d) interaction parameters
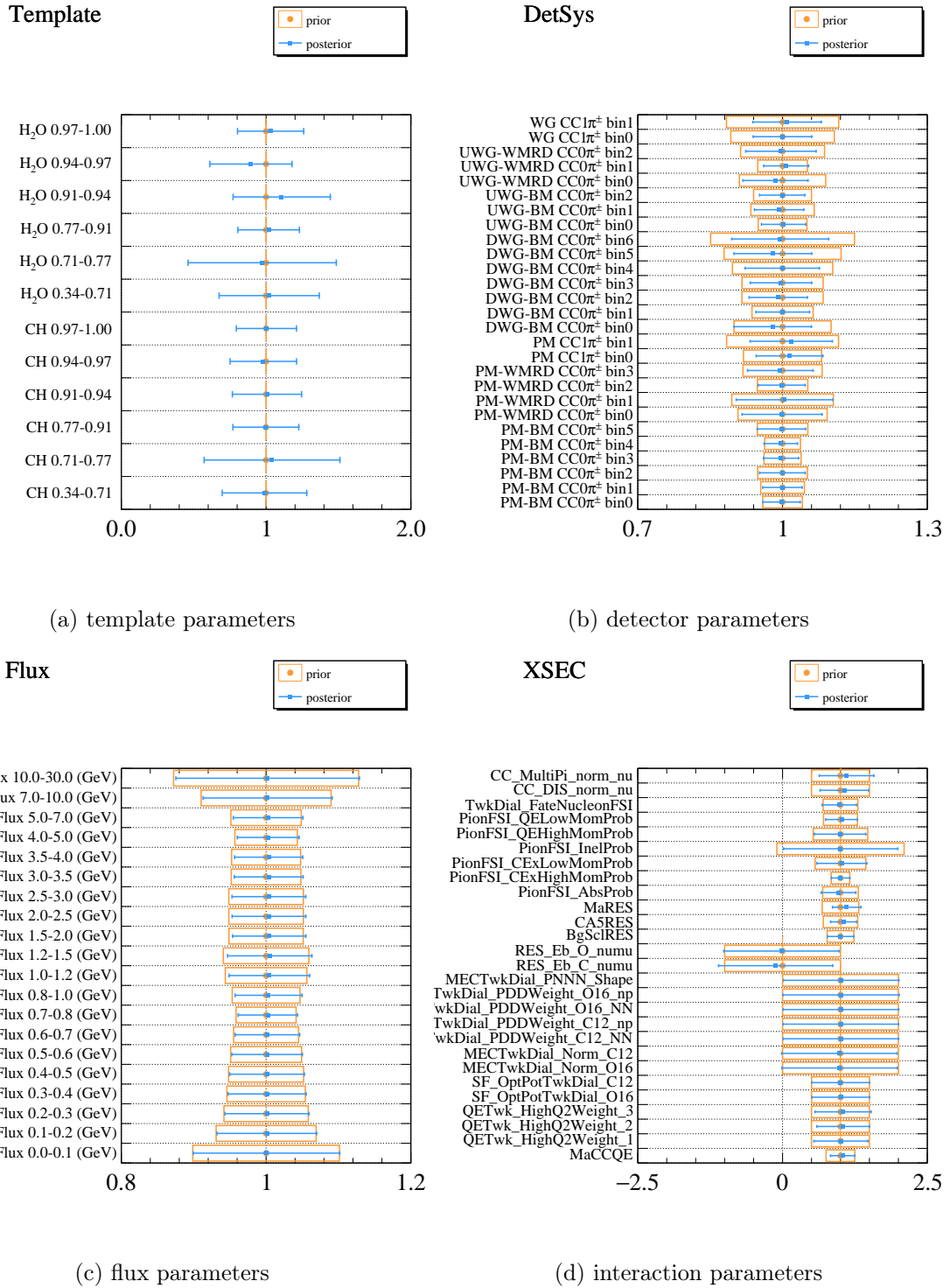
Figure 213: The parameter constraints from the FDS of Tweaked MaRES in the angle distribution. Each posterior result is presented by a best-fit point and error bar (blue dot and line) against its prior parameter in orange rectangular. The error is calculated based on the gaussian assumption of each parameter distribution.
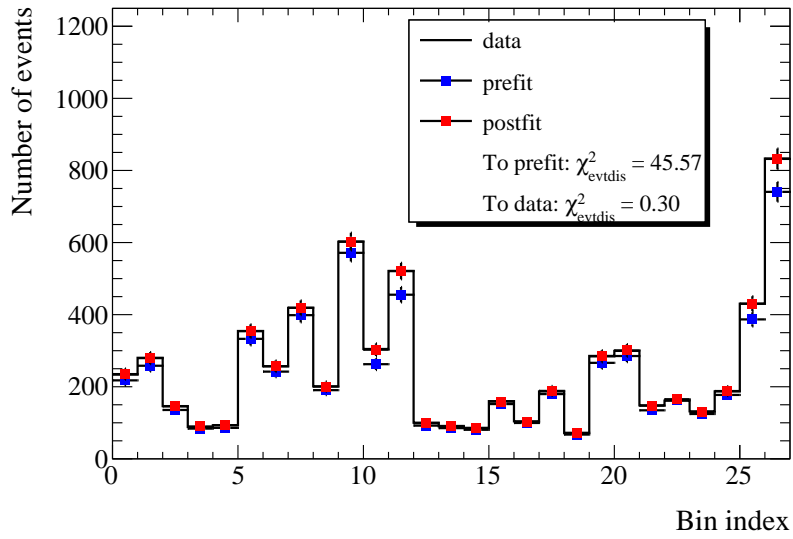
(a) Comparison of event distributions
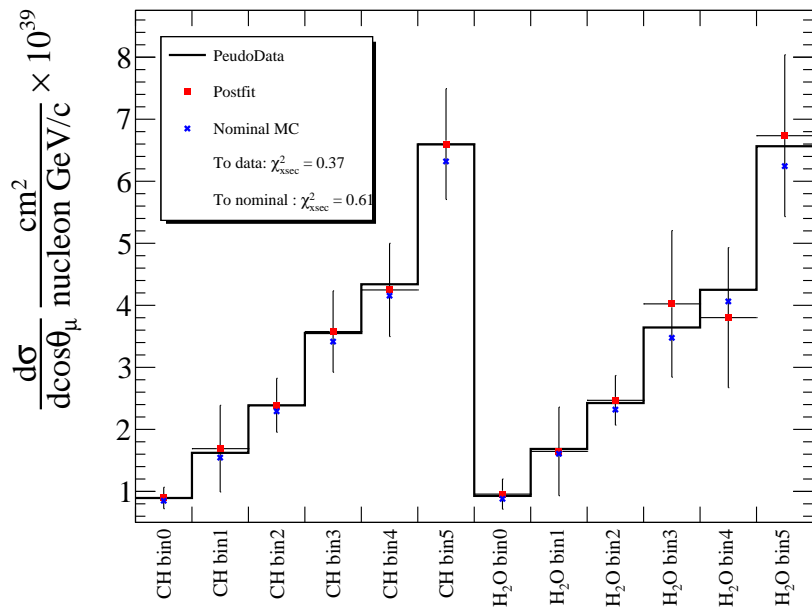
(b) Comparison of cross section fit results

Figure 214: Comparisons of bin-by-bin event distributions between post-fit and pre-fit (top) and the post-fit cross sections overlaid on the true cross sections from pseudo data and nominal data set (bottom) as results of the FDS of Tweaked MaRES in the angle distribution. Both plots include corresponding χ^2 values as metrics defined in Equations N.1, N.2.

N.5 Statistical fluctuation

The base data set for this study is the same as AsimovFit (all systematic parameters are set to their nominal values). The bin-by-bin statistical fluctuations are applied to the base data based on the Poisson distribution with the mean value of the number of events in each bin. The pseudo data, therefore, is not identical to the nominal one. As the statistical fluctuation changes the true cross section value unpredictably, the post-fit χ^2 results in a non-zero yet minimized value if the fit is converged.

The results are presented in Figures 215, 216. The statistical fluctuation makes the true values of nuisance parameters unknown. It is not so important how each parameter behaves during this fit. That being mentioned, Figure 215 shows the post-fit parameters stay within their 1σ error of prior values, which confirms no unexpected behaviour is observed from the fit. The important point in this study is to check the fitter performance to obtain posterior event distributions and see the impact of the fluctuations on the extracted cross sections. The top plot in Figure 216 shows the χ^2 is considerably improved after the fit. The fact that the value is not getting close to 0 compared to other fits is due in large part to the statistical fluctuation. We can see a relatively large impact on bin0 for the CH target, which should stem from the lower statistics. Otherwise, the deviation is at the expected level.

(a) template parameters

(b) detector parameters

(c) flux parameters

(d) interaction parameters
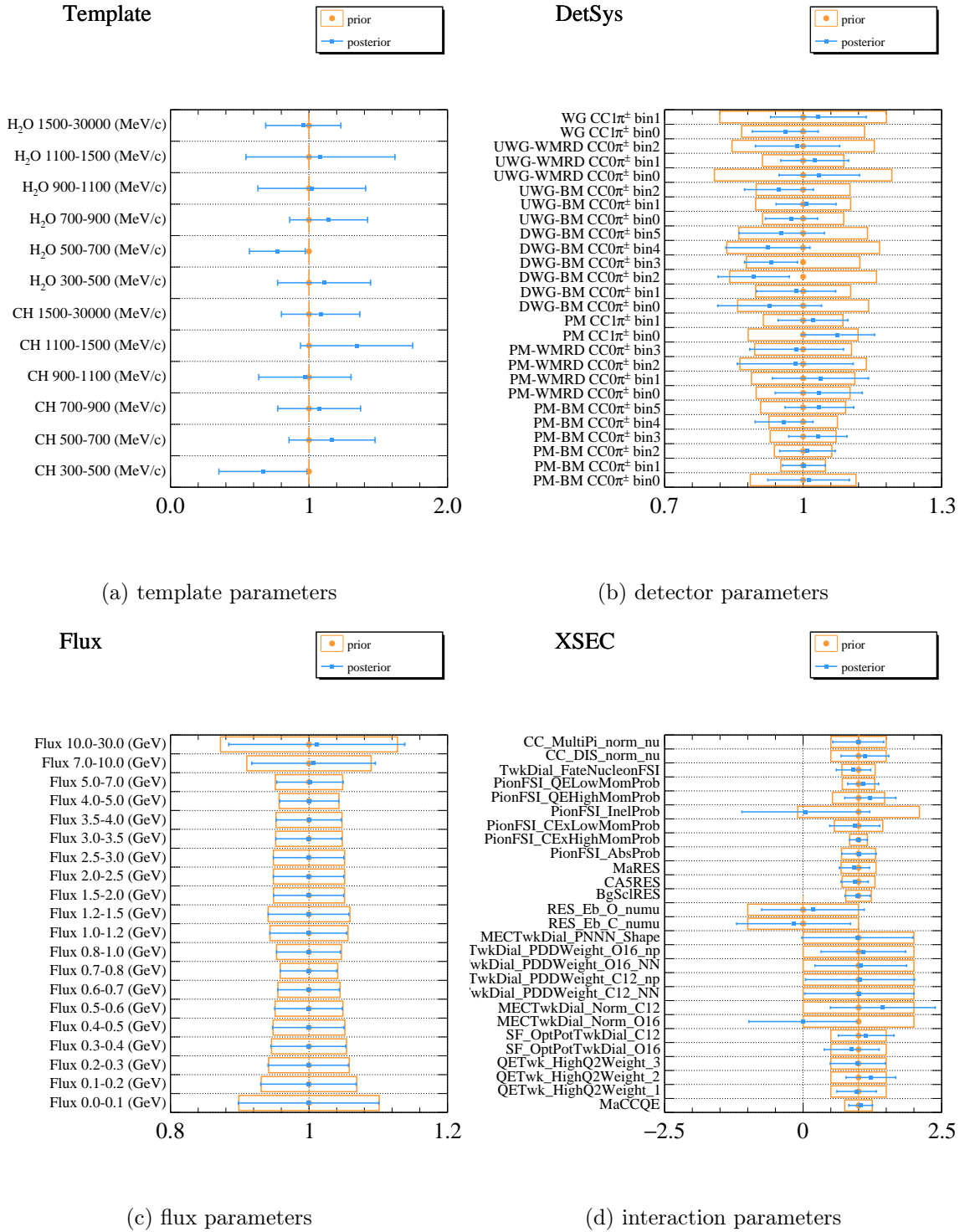
Figure 215: The parameter constraints from the FDS of Statistical fluctuation in the momentum distribution. Each posterior result is presented by a best-fit point and error bar (blue dot and line) against its prior parameter in orange rectangular. The error is calculated based on the gaussian assumption of each parameter distribution.
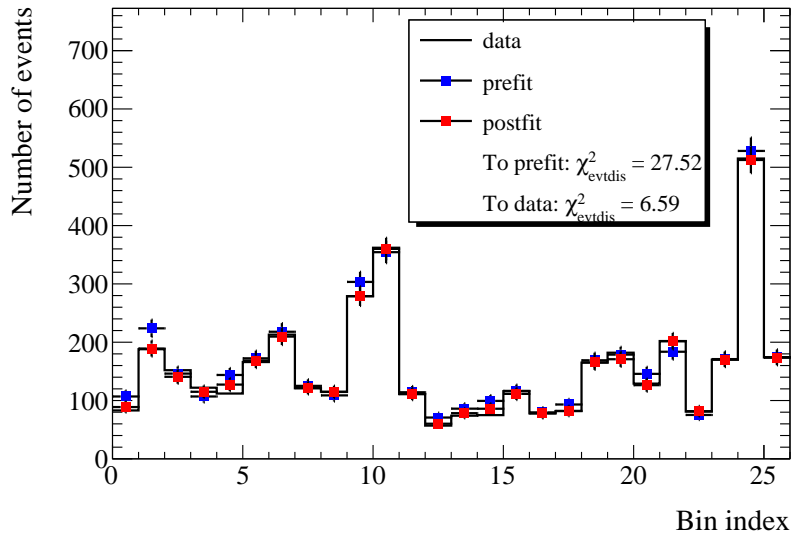
(a) Comparison of event distributions
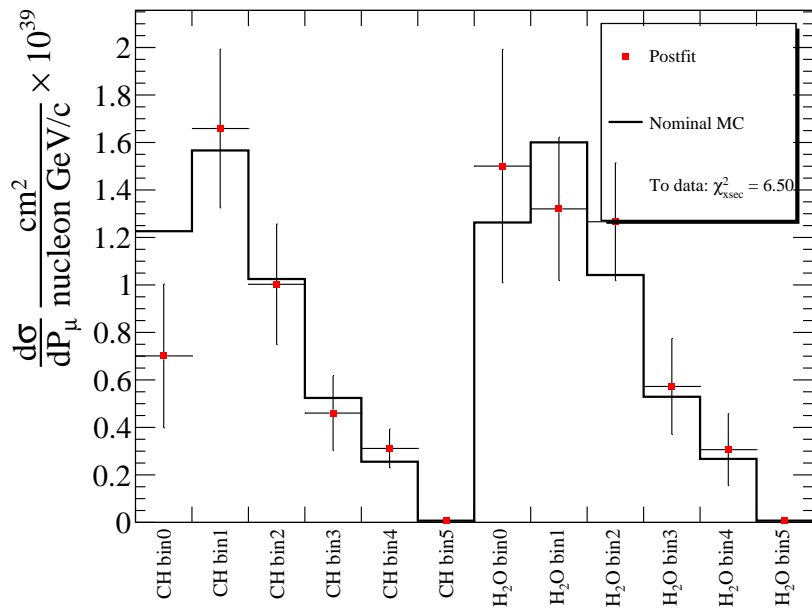
(b) Comparison of cross section fit results

Figure 216: Comparisons of bin-by-bin event distributions between post-fit and pre-fit (top) and the post-fit cross sections overlaid on the true cross sections from pseudo data and nominal data set (bottom) as results of the FDS of Statistical fluctuation in the momentum distribution. Both plots include corresponding χ^2 values as metrics defined in Equations N.1, N.2. As we lose information on statistical fluctuation in the calculation of cross section, the bottom plot shows only true cross section from nominal MC and corresponding χ^2 metric.

(a) template parameters

(b) detector parameters

(c) flux parameters

(d) interaction parameters
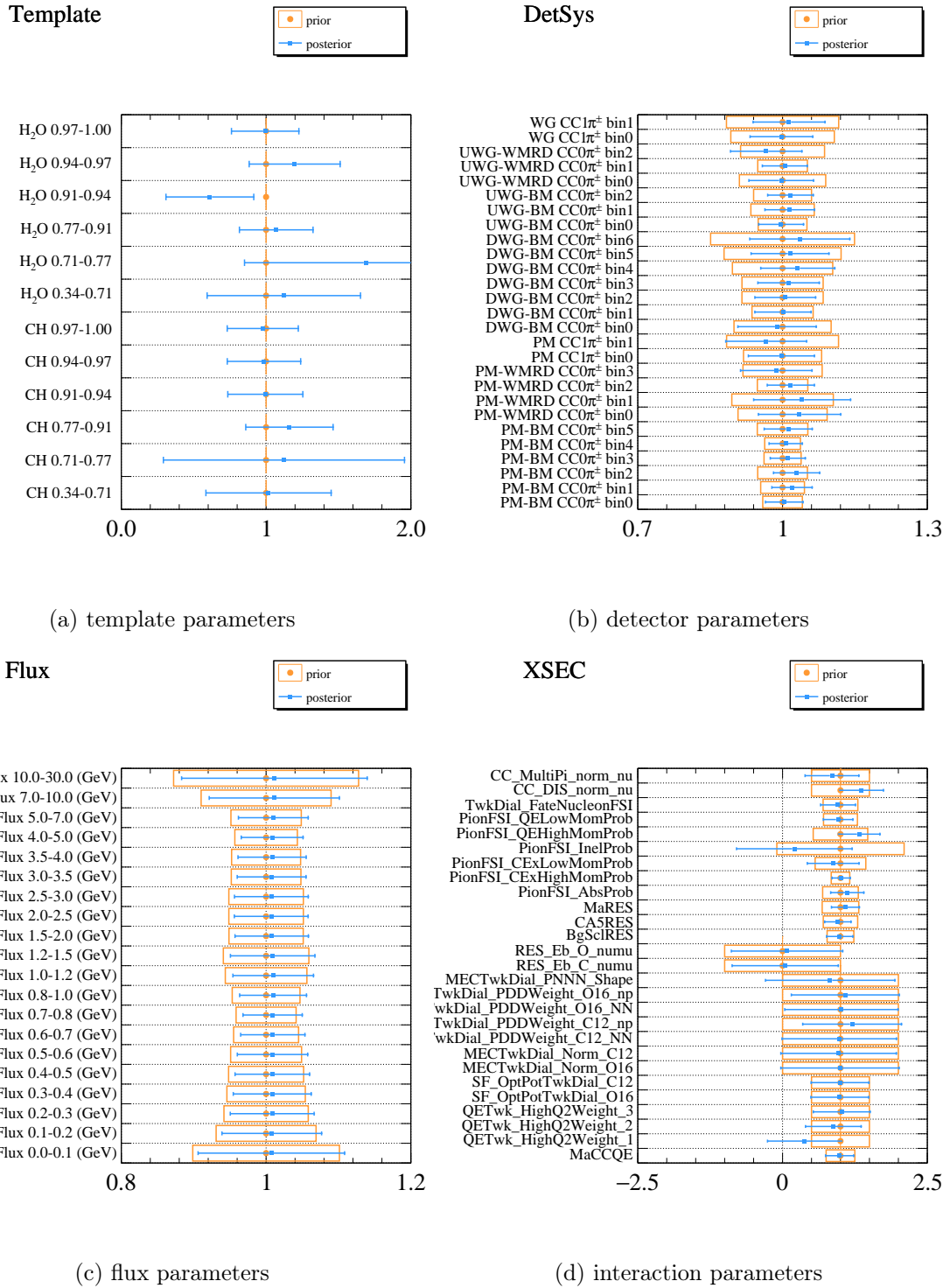
Figure 217: The parameter constraints from the FDS of Statistical fluctuation in the angle distribution. Each posterior result is presented by a best-fit point and error bar (blue dot and line) against its prior parameter in orange rectangular. The error is calculated based on the gaussian assumption of each parameter distribution.
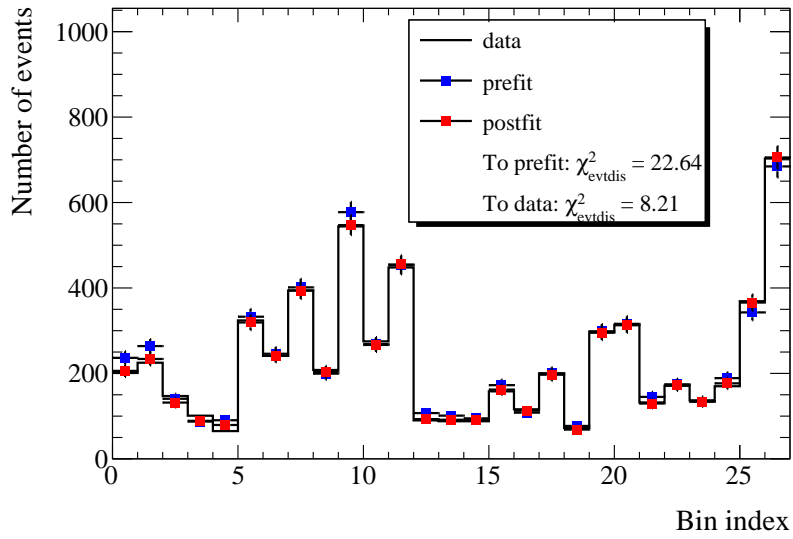
(a) Comparison of event distributions
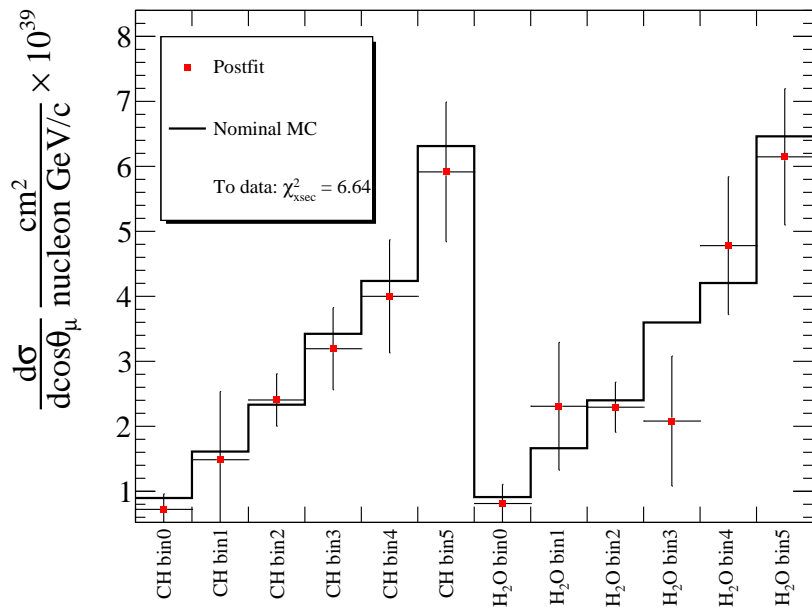
(b) Comparison of cross section fit results

Figure 218: Comparisons of bin-by-bin event distributions between post-fit and pre-fit (top) and the post-fit cross sections overlaid on the true cross sections from pseudo data and nominal data set (bottom) as results of the FDS of Statistical fluctuation in the angle distribution. Both plots include corresponding χ^2 values as metrics defined in Equations N.1, N.2. As we lose information on statistical fluctuation in the calculation of cross section, the bottom plot shows only true cross section from nominal MC and corresponding χ^2 metric.

N.6 Systematic variation (with statistical fluctuation)

In addition to the statistical fluctuation, we applied a systematic variation to the nominal data set in order to create the pseudo data in this study. Each systematic parameter is described by its covariance matrix (flux, interaction or detector). Each covariance matrix is decomposed and the resulting lower triangular matrix is multiplied by a random value vector following Gaussian distribution with $\mu = 0, \sigma = 1$, which gives a set of thrown parameters reflecting their correlations. The fitter re-weights all selected and true events based on this particular set of parameters as well as statistical fluctuations before the fit. It then performs the fit against the pseudo data. As the statistical fluctuations are applied in this study, the effect of systematic parameters on the number of events would not be directly reflected in the fit result. The primary purpose of this fit is to check whether the post-fit event distributions (and resulting post-fit cross section) are matched with that from the pseudo data compared to the nominal data set within their error bars.

The results are shown in Figures 219, 220 in the momentum distribution and Figures 221, 222 in the angle distribution. Although the importance of parameters having responses to changes is not that significant compared to the studies up to the altered signal events or a certain tweaked interaction parameter, the detector systematic parameters and interaction parameters move at least in the "right direction" with respect to the true parameters set in this study. Most of the 2p2h shape parameters ("TwkDial") remained unchanged in this fit due in part to the smaller responses compared to the norm parameters. [62] On the other hand, most flux parameters do not have correct responses to the true values. The effect of flux parameters is less competitive with the template parameters or the detector systematic parameters. Therefore, the changes in event distributions coming from the flux parameters are compensated by other normalization parameters.

The more important thing to check in this study is the post-fit event distributions shown in the top plot in Figure 220. Unlike the other studies without statistical fluctuations, the χ^2 values are not very excellent. The post-fit distribution, however, sufficiently agrees with the distribution from the pseudo data. The bottom plot in Figure 220 is the comparison of cross section. It should be mentioned that the pseudo data line (black solid line) does not correspond to the cross section from the true values of systematic variations. Since true events include all neutrino interactions (even events without tracks), it is not, in principle, possible to apply the detector parameters to all true events. Moreover, the information on statistical fluctuation is lost after the fit. As a result, the pseudo data reflects variations for only flux and interaction parameters. Nevertheless, the post-fit cross section is closer to the pseudo data compared to nominal MC in the sense of χ^2 metric.

---

[62]This is again, related to the coarser binning of this analysis, which in turn makes the shape parameters act as more normalization. Therefore, the effect is not as apparent as that of those normalization parameters.

(a) template parameters

(b) detector parameters

(c) flux parameters

(d) interaction parameters
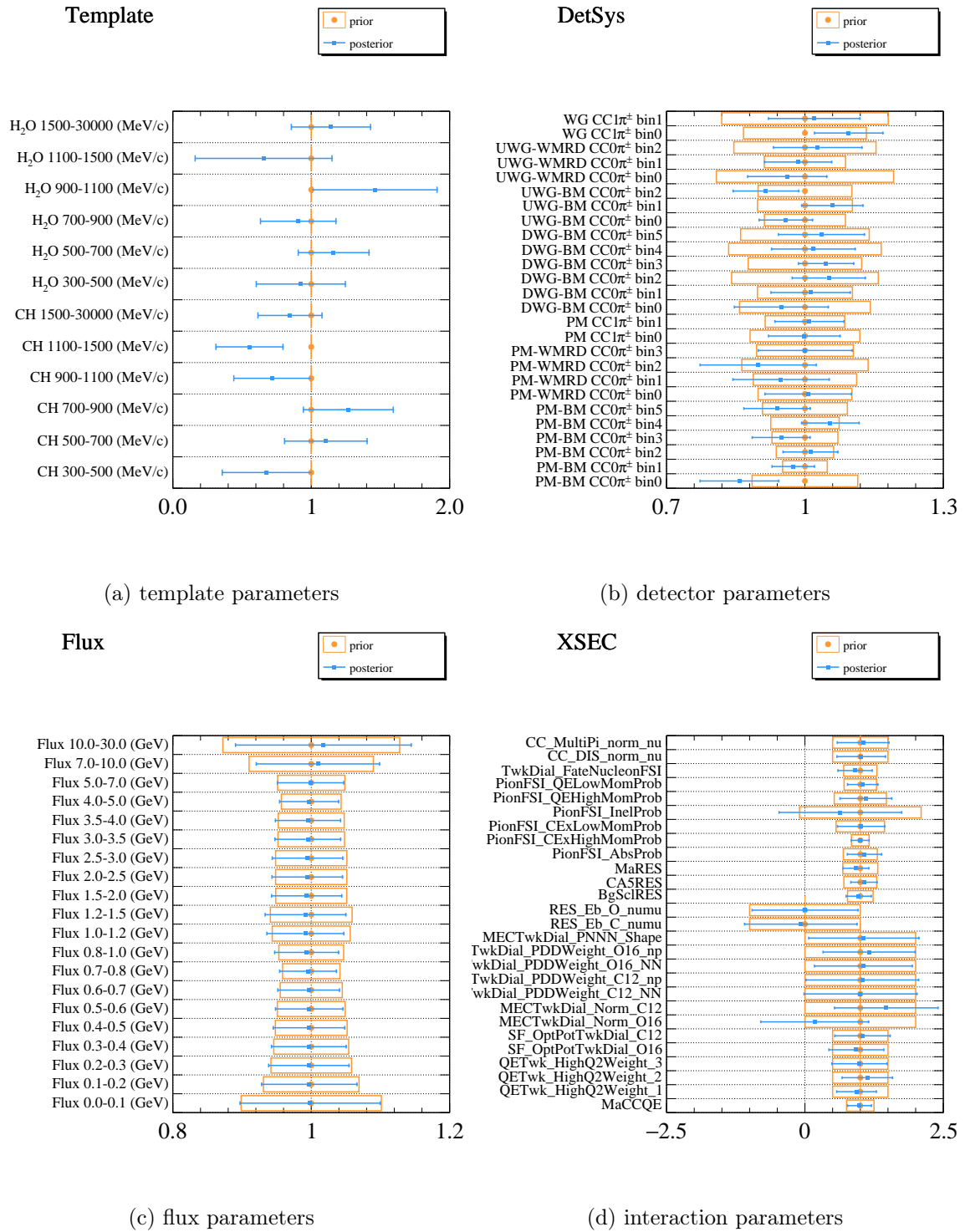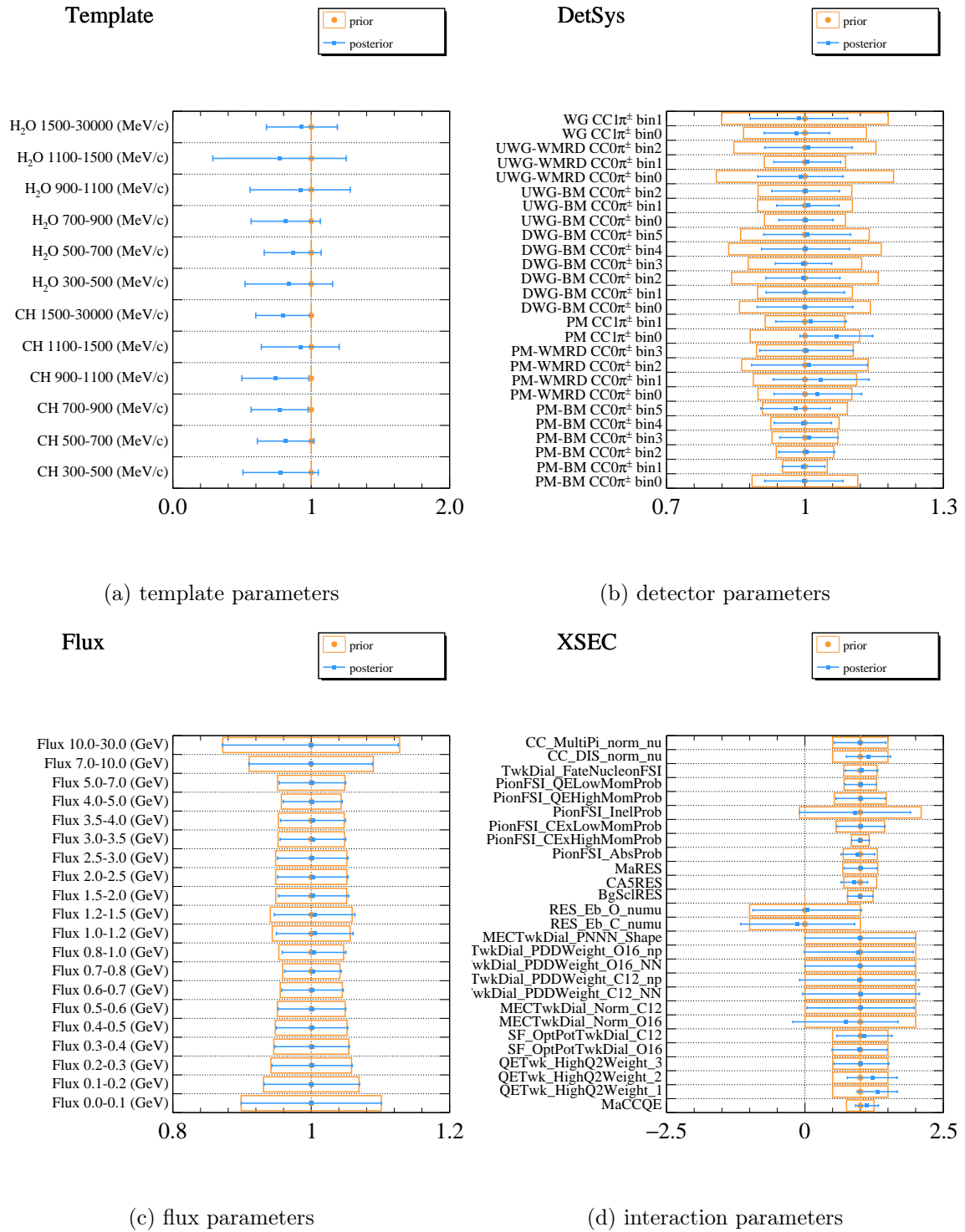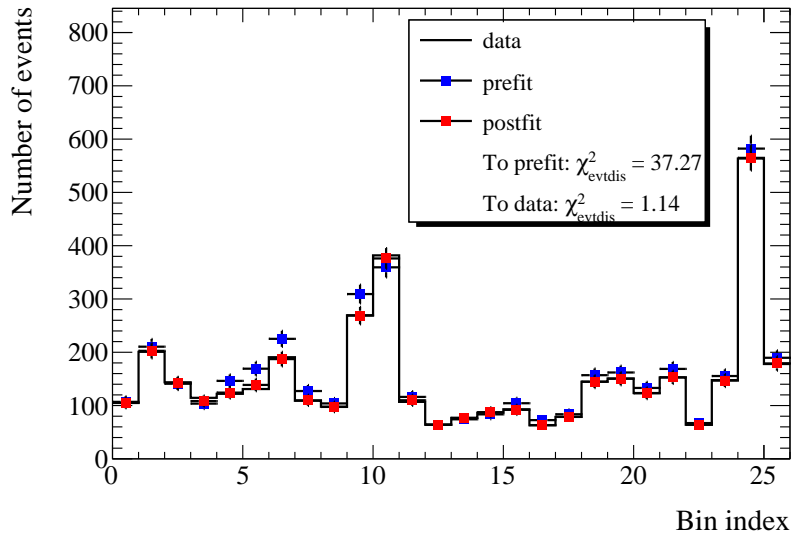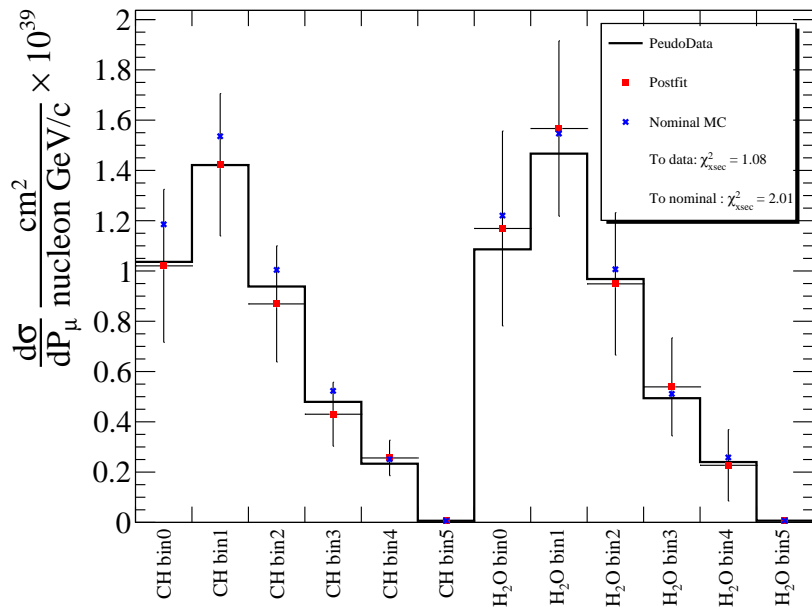
Figure 219: The parameter constraints from the FDS of Systematic variation in the momentum distribution. Each posterior result is presented by a best-fit point and error bar (blue dot and line) against its prior parameter in orange rectangular. The error is calculated based on the gaussian assumption of each parameter distribution. Green dots represent the true values in the systematic variations of a certain toy.
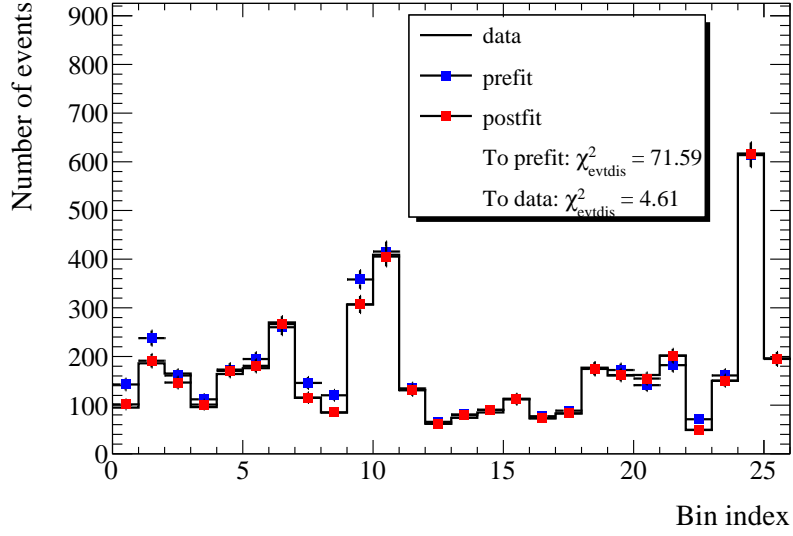
(a) Comparison of event distributions
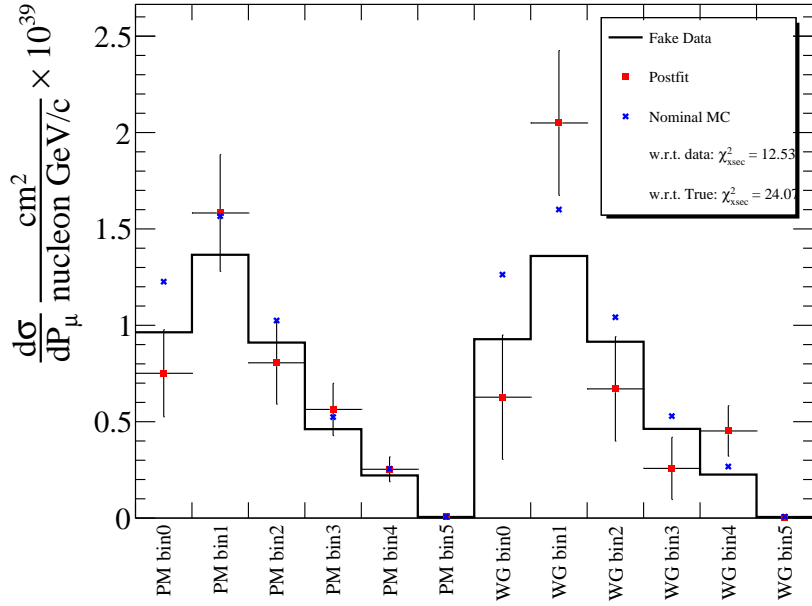
(b) Comparison of cross section fit results

Figure 220: Comparisons of bin-by-bin event distributions between post-fit and pre-fit (top) and the post-fit cross sections overlaid on the true cross sections from pseudo data and nominal data set (bottom) as results of the FDS of Systematic variation in the momentum distribution. Both plots include corresponding χ^2 values as metrics defined in Equations N.1, N.2. "Fake Data" line corresponds to the true cross section reflecting variations only for flux and interaction parameters because detector systematic parameters cannot be applied to the true events and the information of statistical fluctuation is no longer available after the fit. In order to show the improvement of the fitter, two kinds of χ^2 were given with respect to the pseudo data and nominal MC.

(a) template parameters

(b) detector parameters

(c) flux parameters

(d) interaction parameters

Figure 221: The parameter constraints from the FDS of Systematic variation in the angle distribution. Each posterior result is presented by a best-fit point and error bar (blue dot and line) against its prior parameter in orange rectangular. The error is calculated based on the gaussian assumption of each parameter distribution. Green dots represent the true values in the systematic variations of a certain toy.
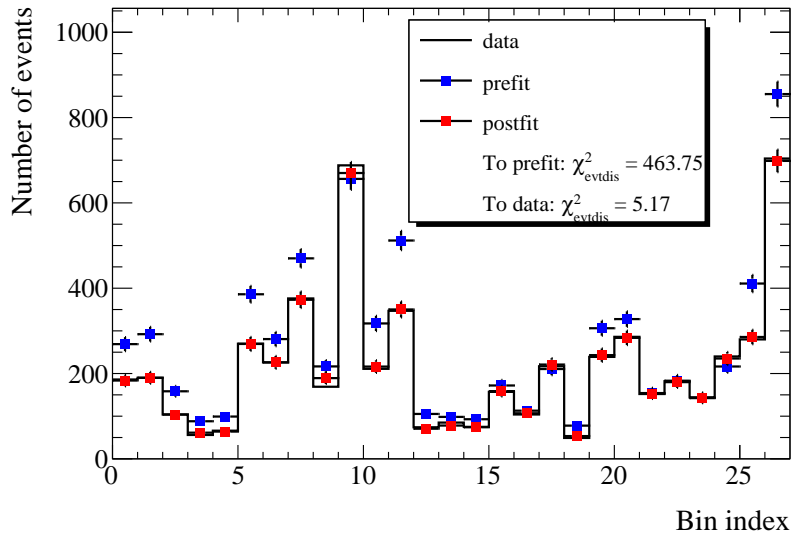
(a) Comparison of event distributions
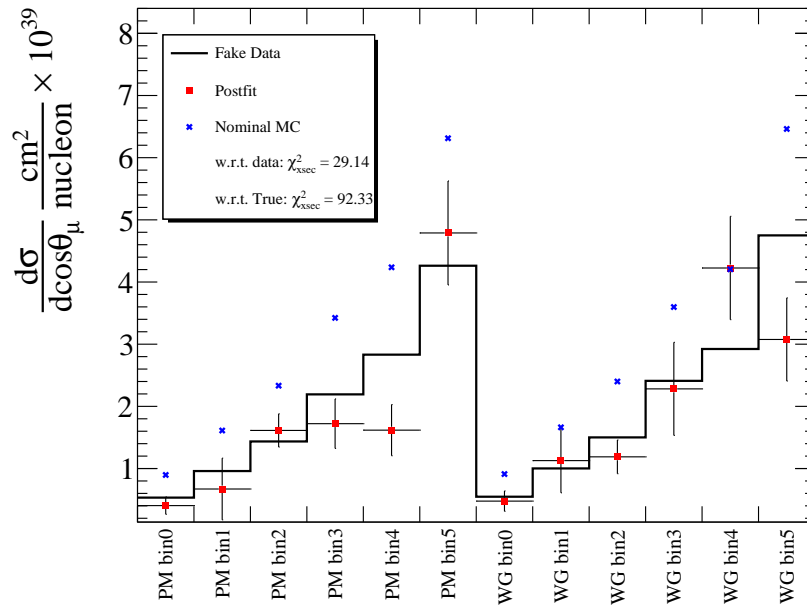
(b) Comparison of cross section fit results

Figure 222: Comparisons of bin-by-bin event distributions between post-fit and pre-fit (top) and the post-fit cross sections overlaid on the true cross sections from pseudo data and nominal data set (bottom) as results of the FDS of Systematic variation in the angle distribution. Both plots include corresponding χ^2 values as metrics defined in Equations N.1, N.2. "Fake Data" line corresponds to the true cross section reflecting variations only for flux and interaction parameters because detector systematic parameters cannot be applied to the true events and the information of statistical fluctuation is no longer available after the fit. In order to show the improvement of the fitter, two kinds of χ^2 were given with respect to the pseudo data and nominal MC.

N.7 Coverage

The coverage test aims to confirm the plausible range of event distributions and cross section by varying systematic parameters based on their prior uncertainties and by applying statistical fluctuations. If the underlying model is compatible with the data fit, the χ^2 in the data-fit would fall inside the range obtained in this test. We make use of the same technique as in the study for the systematic variations, but using 1000 sets of toy throws. Each fit against a pseudo data corresponding to each throw gives its χ^2 considering both systematic and statistical contributions. We then fill the value in a histogram and compare it to the theoretical χ^2 probability distribution. The behaviour χ^2 probability distribution (PDF) depends on the degree of freedom (DOF) in the fit. It is calculated by subtraction of the number of all data bins (26 in our case) from the number of free parameters (i.e. template parameters, 12 in this case). Therefore, we use the χ^2 PDF with DOF of 14.

The result of the χ^2 distribution is shown in Figure 223. The χ^2 distributions have a great agreement with the theoretical probability functions. Therefore, we confirm the fitter properly performs the fit in terms of getting posterior distributions in an expected manner.

We utilize the same 1000 toy throws to examine the plausible range of cross sections and their relative errors. These results are summarized in candle plots as in Figures 224, 225. A good sign of the cross section candle plot is that each mean value is more or less matched with the median. As we calculate a relative error of cross section assuming the cross section distribution from toy experiments follows the gaussian distribution, the gaussianity should be validated. The mean value being matched with the median indicates the assumption is reasonable. The number of outliers in the top plot is moderate for all the bins except for the low-momentum bin (bin0 for both templates). A similar tendency is found in the bottom plot, where, in addition to the number of outliers being larger, the spread of the distribution is relatively larger too. Moreover, for H_2O target cross section results, the higher momentum bin (WG bin4) has a similar tendency to bin0. This tendency reflects the lower statistics for these bins, which causes a wider spread of cross section from toy experiments originally stemming from statistical fluctuation.
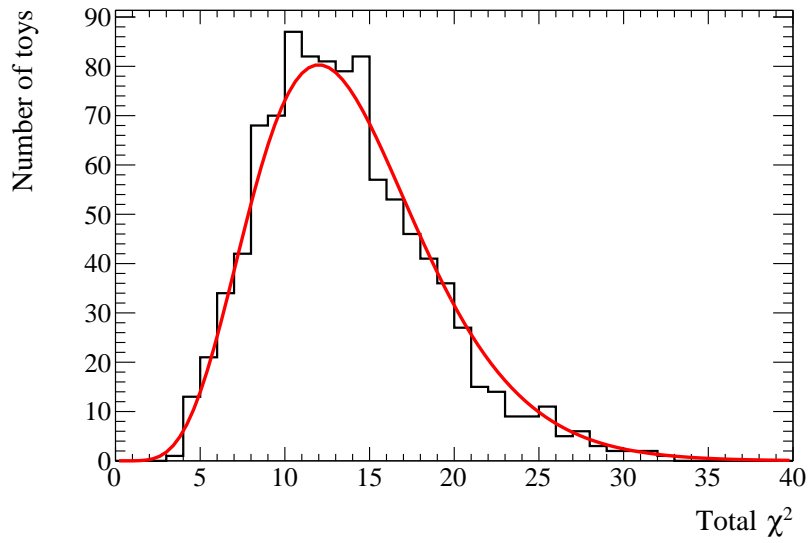
(a) Momentum distribution
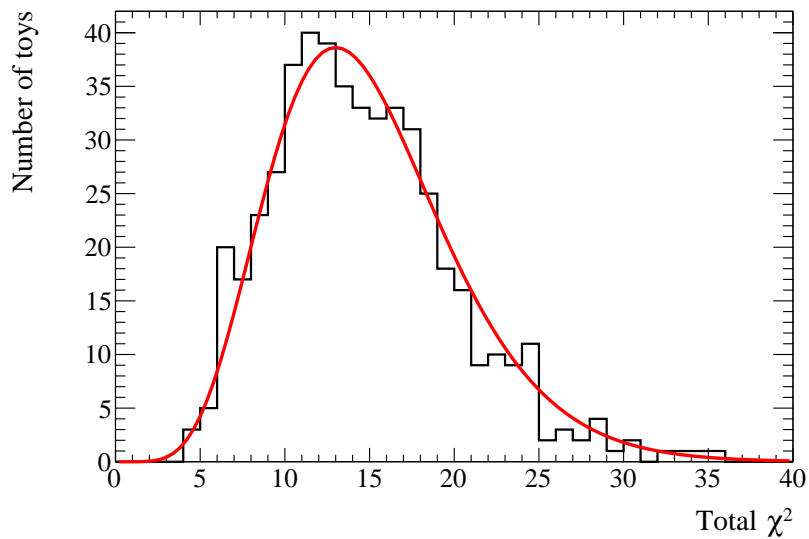
(b) Angle distribution

Figure 223: χ^2 distributions (black line) from the 1000 toy throws for the FDS of systematic parameters' variation with statistical fluctuation in the momentum distribution (top) and the angle distribution (bottom) compared to the theoretical χ^2 probability function (red line) with DOF of 14 for momentum distribution and 15 for angle distribution. The χ^2 includes both statistical and systematic contributions.
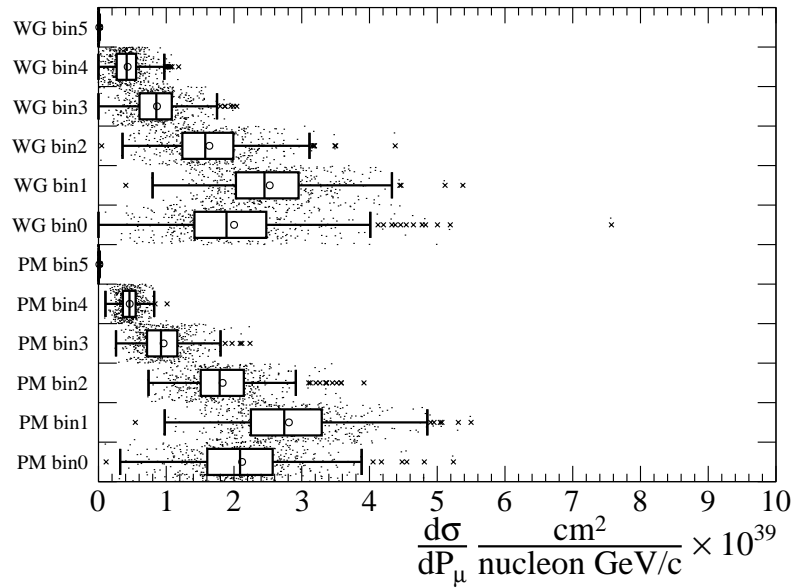
(a) Differential cross section as a function of momentum in momentum distribution
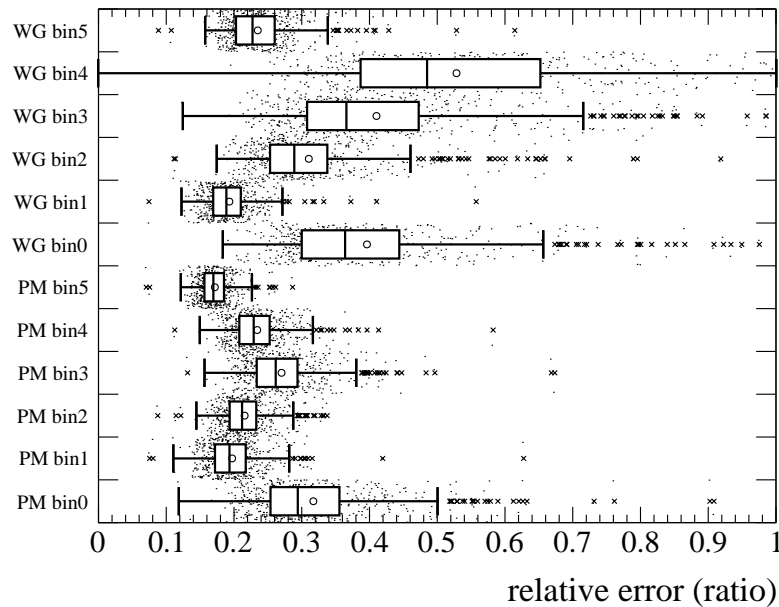
(b) Relative error of differential cross section in momentum distribution

Figure 224: Candle plots for the differential cross sections as a function of momentum (top) and its error (bottom). Each "box" represents 25% quantile for lower and upper directions with respect to the medium value (a solid vertical line in the box). A circle in a box refers to the mean value in each bin. A whisker is then extended to a 1.5 times larger range of the inner quantile. The data points that are not covered by the whiskers are described as outliers (cross points). Besides, all data points (dotted points) are plotted in these plots.
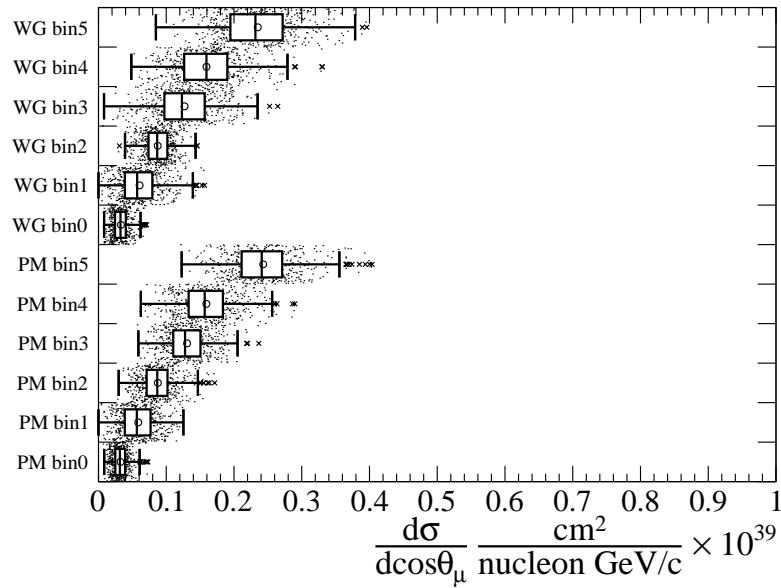
(a) Differential cross section as a function of momentum in angle distribution
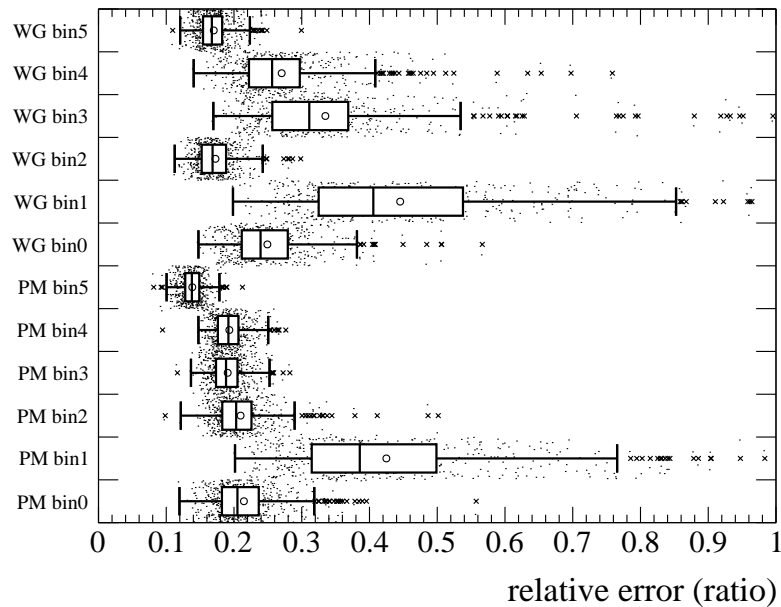
(b) Relative error of differential cross section in angle distirbution

Figure 225: Candle plots for differential cross section as a function of angle (top) and its error (bottom). Each "box" represents 25% quantile for lower and upper directions with respect to the medium value (a solid vertical line in the box). A circle in a box refers to the mean value in each bin. A whisker is then extended to a 1.5 times larger range of the inner quantile. The data points that are not covered by the whiskers are described as outliers (cross points). Besides, all data points (dotted points) are plotted in these plots.

N.8 Alternative CCQE model (BeRPA)

We tested several kinds of scenarios before the previous sections while keeping the based NEUT model to create each pseudo data. Now that we confirm the fitter shows the expected performance for those artificially created pseudo data, it is then necessary to see how the fitter is able to handle a change in true signal events based on a physically motivated re-weight factor. As our signal consists of mainly CCQE interactions, an alternative CCQE model is used to create pseudo data. The model is Nieves et al. model with RPA correction [177]. Instead of running a full MC simulation, we take an approach to re-weight CCQE events to mimic the shape of the cross section predicted by this model. The re-weight factor is parametrized by

$$w(Q^2) = \begin{cases} A(1-x')^3 + 3B(1-x')^2 x' + 3C(1-x')x'^2 + Dx'^3 & \text{if } x < U \\ 1 + (D-1)\exp(-E(x-U)) & \text{if } x \geq U \end{cases} \tag{N.3}$$

$$C = D + \frac{1}{3}U \times E \times (D-1), \tag{N.4}$$

where A, B, C, D, E, U are coefficients to vary the shape of the distribution and $x = Q^2, x' = Q^2/U$.[63] This alternative model mostly affects the true CCQE events. Besides, it can also have an impact on the background distributions via FSI effects. The re-weight behaviour is visualized in Figure 226. The lower Q^2 region (corresponds to muons having a lower angle with respect to the incident neutrino direction) is subject to the suppression from this factor.
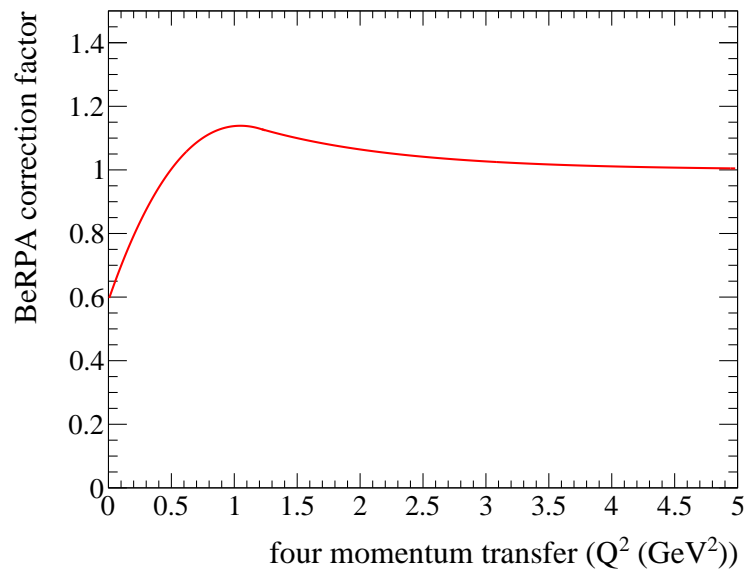
Figure 226: The re-weight function of BeRPA model based on the formula written in Equation N.3.

---

[63] This parametrization is called "BeRPA" model, which comes from the Bernstein polynomials to construct the polynomial form used for the $x < U$ case. Each coefficient is defined as

$$A = 0.59, B = 1.05, D = 1.13, E = 0.88, U = 1.20. \tag{N.5}$$

These values are the same ones used in the T2K oscillation analysis in 2020.

The results of the fit are shown in Figures 227, 228 and Figures 229, 230. Template parameters are more or less decreased by 20% with respect to their nominal values (in the left top plot in Figure 227), which are associated with the changes in the number of events in particular for BabyMIND sample where Q^2 is lower because muons are scattered at a lower angle (in the top plot in Figure 228). As the WallMRD samples have events having rather higher Q^2 values, it is predictable that the event distribution is close to the nominal one. Other parameters are more or less unchanged except for high Q^2 parameters. They are shifted to higher values, which makes the number of events in high Q^2 regions inflate. This is the expected behaviour of the fitter to counteract the changes in template parameters for those regions. Taking a look at the bottom plot in Figure 228, we see a large improvement of the χ^2 (1.24 from 4.64) after the post-fit. The post-fit cross section agrees with the true cross section suggested from this alternative model within its error bar.

(a) template parameters

(b) detector parameters

(c) flux parameters

(d) interaction parameters
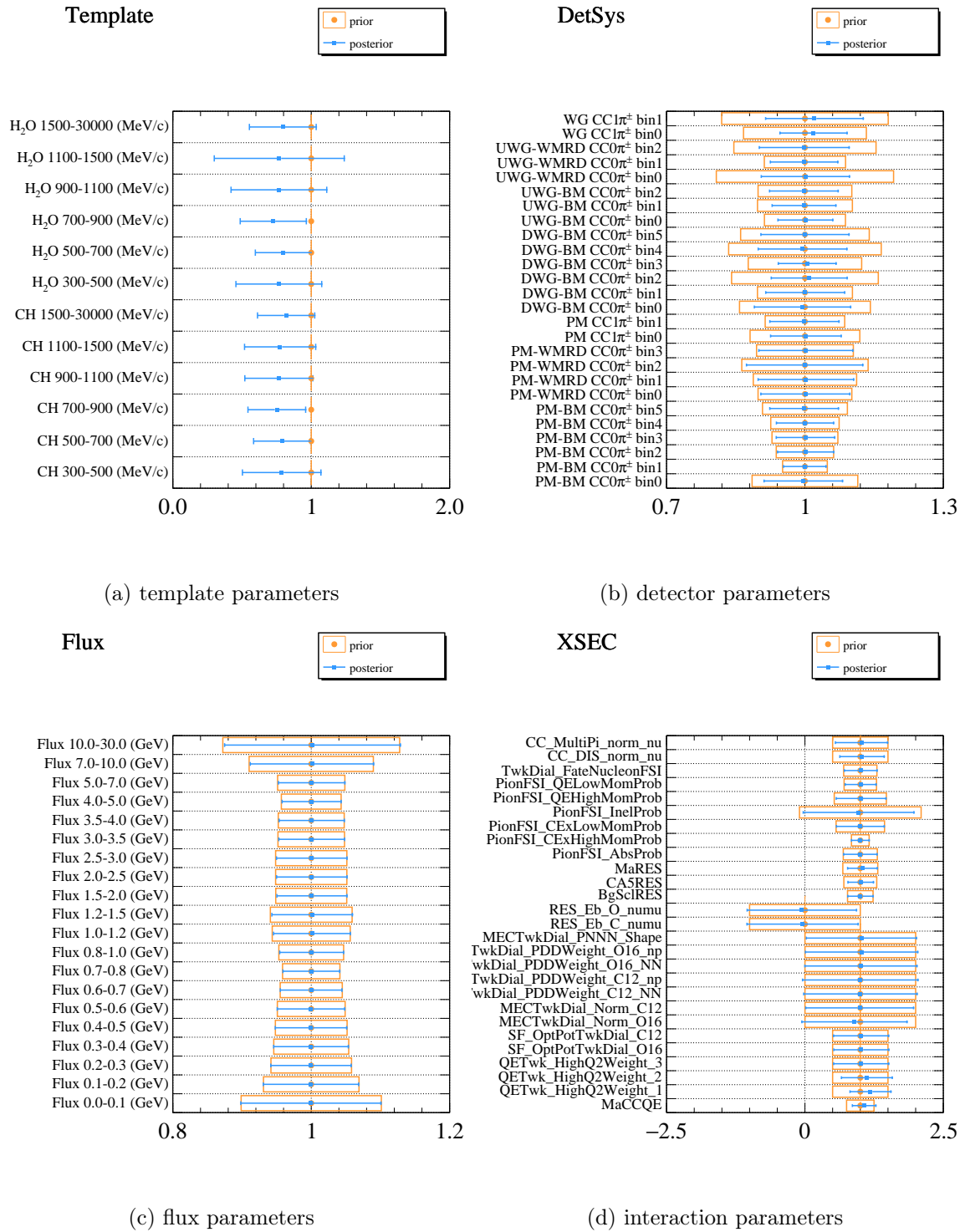
Figure 227: The parameter constraints from the FDS of Alternative CCQE model (BeRPA reweight) in the momentum distribution. Each posterior result is presented by a best-fit point and error bar (blue dot and line) against its prior parameter in orange rectangular. The error is calculated based on the gaussian assumption of each parameter distribution.
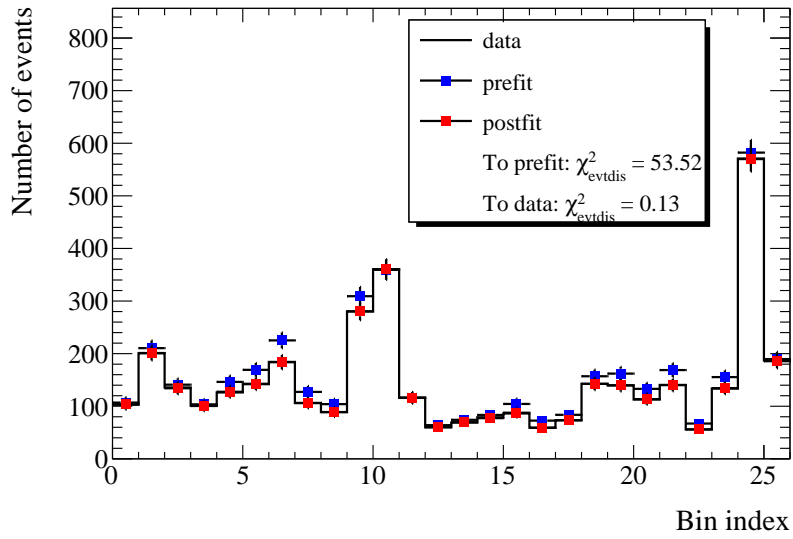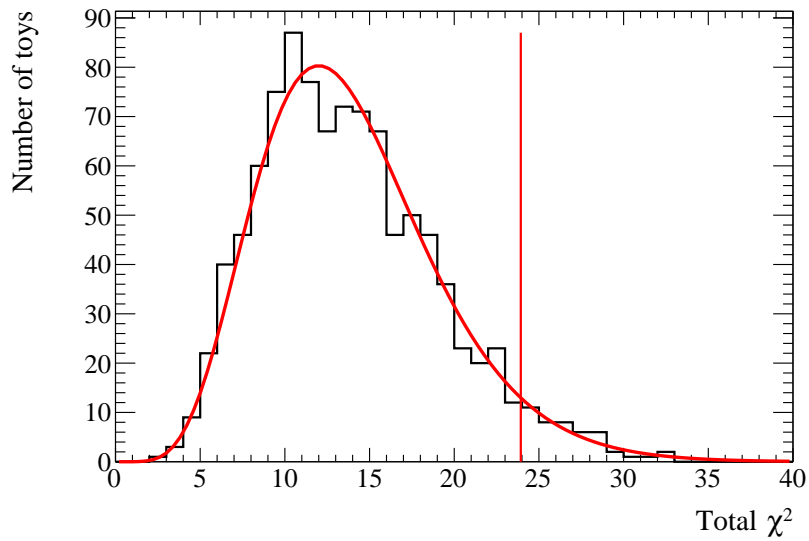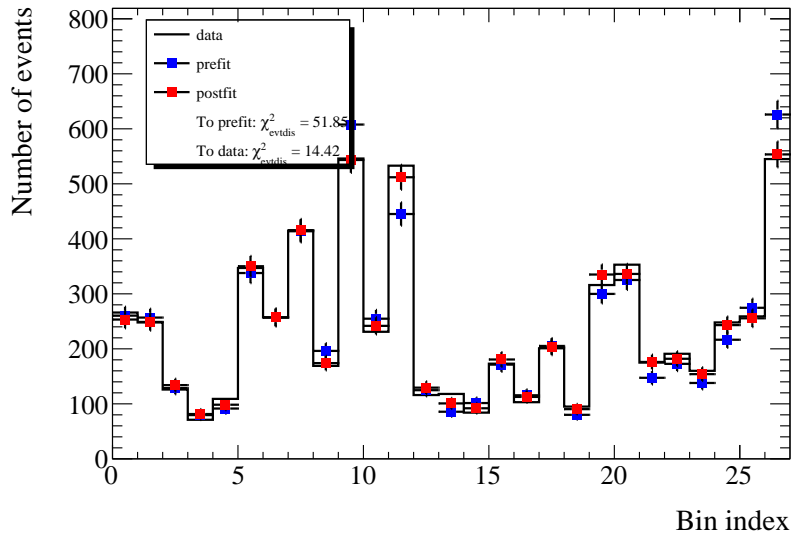
(a) Comparison of event distributions
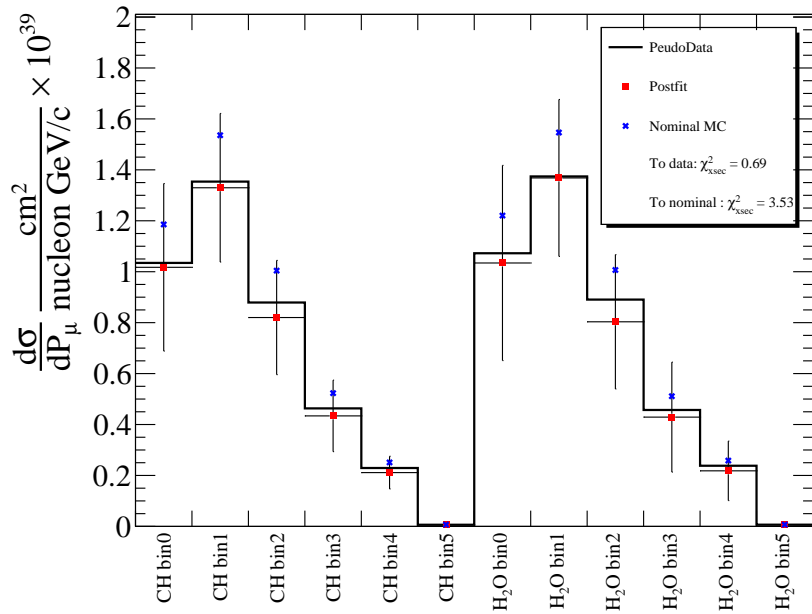

(b) Comparison of cross section fit results

Figure 228: Comparisons of bin-by-bin event distributions between post-fit and pre-fit (top) and the post-fit cross sections overlaid on the true cross sections from pseudo data and nominal data set (bottom) as results of the FDS of Alternative CCQE model (BeRPA reweight) in the momentum distribution. Both plots include corresponding χ^2 values as metrics defined in Equations N.1, N.2.

Template

(a) template parameters

DetSys

(b) detector parameters

Flux

(c) flux parameters

XSEC

(d) interaction parameters
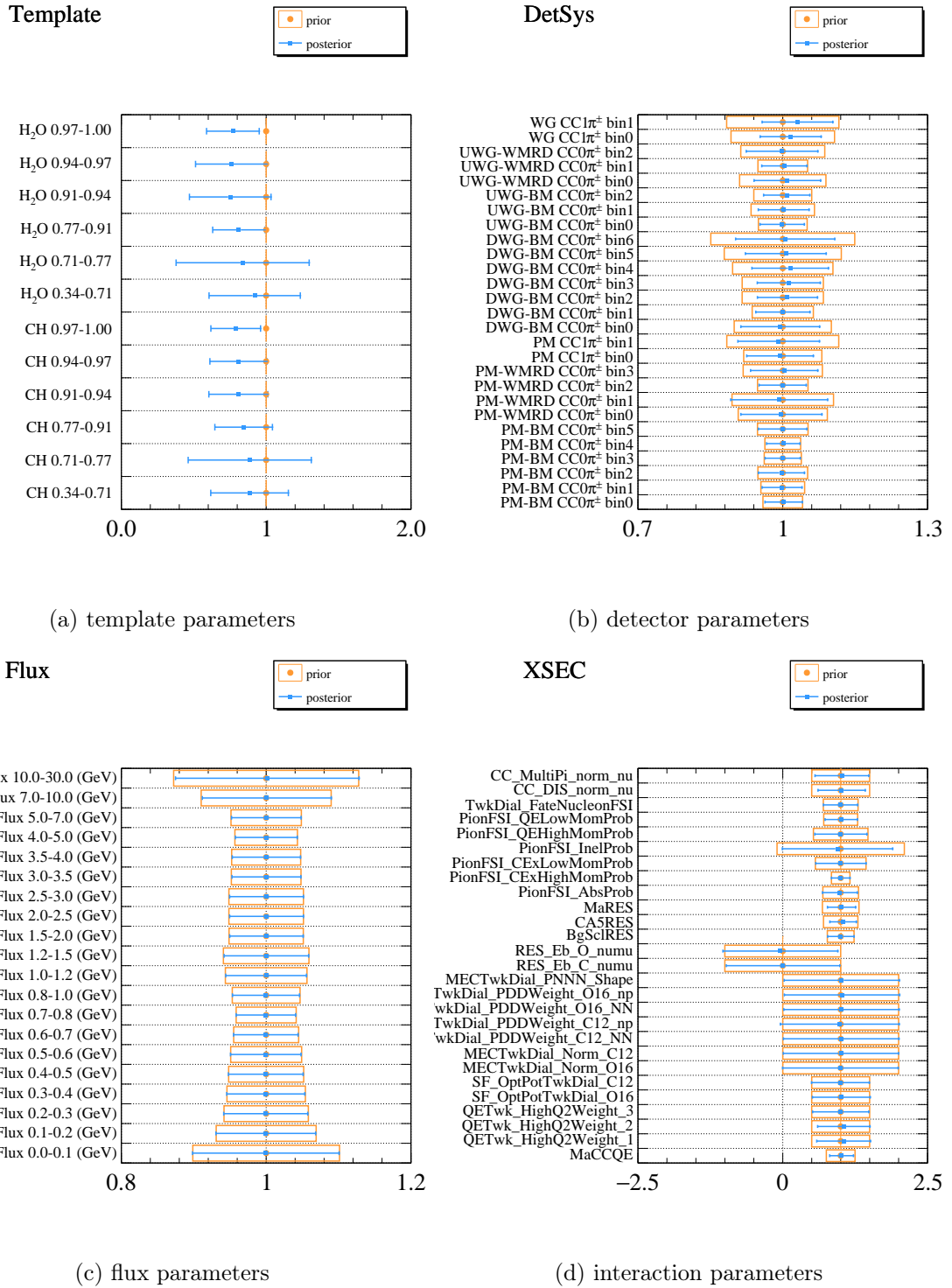
Figure 229: The parameter constraints from the FDS of Alternative CCQE model (BeRPA reweight) in the angle distribution. Each posterior result is presented by a best-fit point and error bar (blue dot and line) against its prior parameter in orange rectangular. The error is calculated based on the gaussian assumption of each parameter distribution.
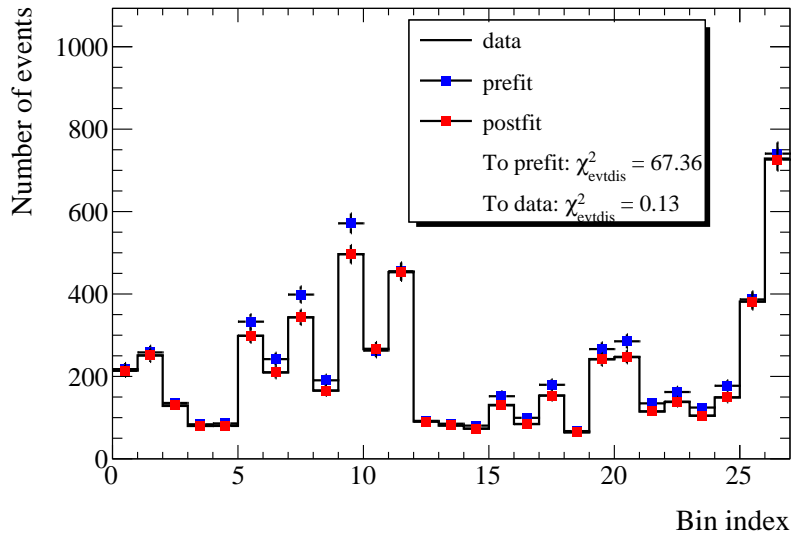
(a) Comparison of event distributions
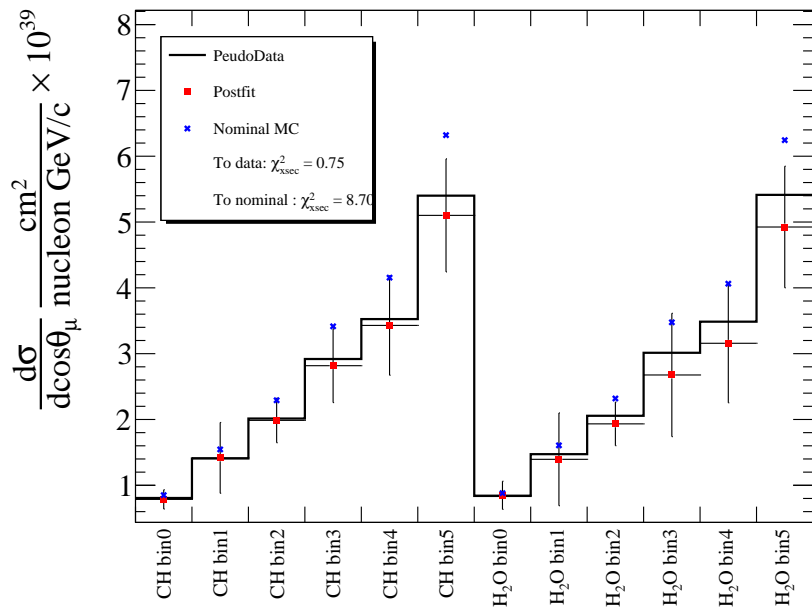
(b) Comparison of cross section fit results

Figure 230: Comparisons of bin-by-bin event distributions between post-fit and pre-fit (top) and the post-fit cross sections overlaid on the true cross sections from pseudo data and nominal data set (bottom) as results of the FDS of Alternative CCQE model (BeRPA reweight) in the angle distribution. Both plots include corresponding χ^2 values as metrics defined in Equations N.1, N.2.

N.9 CCRES low Q^2 suppression

We need to test the flexibility of the fitter about whether it can cope with a change in the background distributions. One of the main backgrounds in this analysis is events coming from charged current pion production via $\Delta^{++}(1232)$ resonance. Therefore, we decided to perform the fit with pseudo data where we change true resonant events based on an alternative model. The alternative model is motivated to account for the difference between data and MC reported by the MINERvA experiment [178] and MINOS experiment [179]. The difference emerges in the low-energy transfer region (sub-GeV), where the data was smaller than the MC prediction. In order to take this effect into account, we make use of the formula provided by [179] to re-weight each resonant event. The formula is written by

$$w(Q^2) = \frac{1.01}{1 + \exp\left(1 - \sqrt{Q^2}/0.156\right)} \text{ if } Q^2 < 0.7 \text{ GeV}^2/\text{c}^4, \tag{N.6}$$

where Q^2 is energy transfer. This re-reweight factor acts as the suppression of resonant events. The corresponding function is plotted in Figures 231, 232.
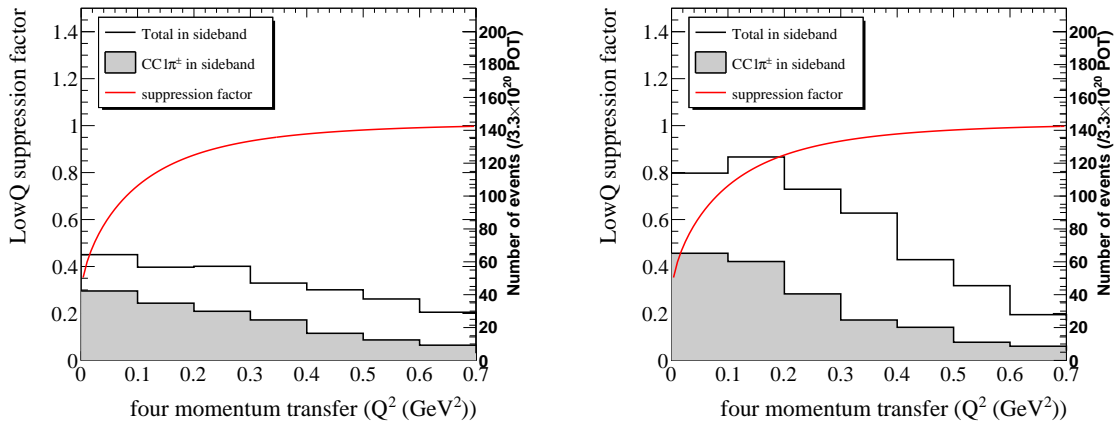
(a) CC1$\pi^{\pm}$ in the CH sideband sample overlaid   (b) CC1$\pi^{\pm}$ in the H$_2$O sideband sample overlaid

Figure 231: The re-weight function of Low Q^2 suppression based on the formula written in Equation N.6, where CC1$\pi^{\pm}$ distribution in the CH sideband (left) and in the H$_2$O sideband in momentum distribution are overlaid.
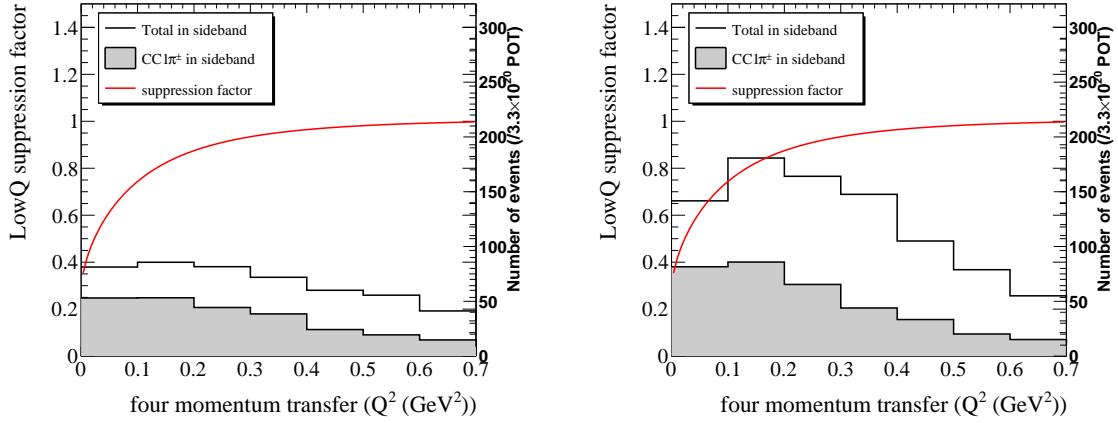
(a) CC1$\pi^{\pm}$ in the CH sideband sample overlaid   (b) CC1$\pi^{\pm}$ in the H$_2$O sideband sample overlaid

Figure 232: The re-weight function of Low Q^2 suppression based on the formula written in Equation N.6, where CC1$\pi^{\pm}$ distribution in the CH sideband (left) and in the H$_2$O sideband in the angle distribution are overlaid.

The results are presented in Figures 233, 234 and Figures 235, 236. All results of parameter constraints, event distributions and post-fit cross section are not drastically changed with respect to their nominal values. Noticeable changes are seen only in CC resonant-related parameters and distributions. $M_A^{\mathrm{RES}}, C_A^5$ parameters move to lower values (in the right bottom plot in Figure 233) in response to the decrease in the event distribution (see bin11 and bin24 in the top plot in Figure 234). These changes are expected when we consider the pseudo data is subject to suppression of resonant events (ending up with suppression of CC1$\pi^{\pm}$ sample). In the bottom plot in Figure 234, a slight improvement is seen in post-fit cross section with respect to true cross section from the pseudo data. This pettiness is due in large part to the fact that true cross section from the pseudo data is not much deviated from the true cross section from the nominal MC.

(a) template parameters

(b) detector parameters

(c) flux parameters

(d) interaction parameters
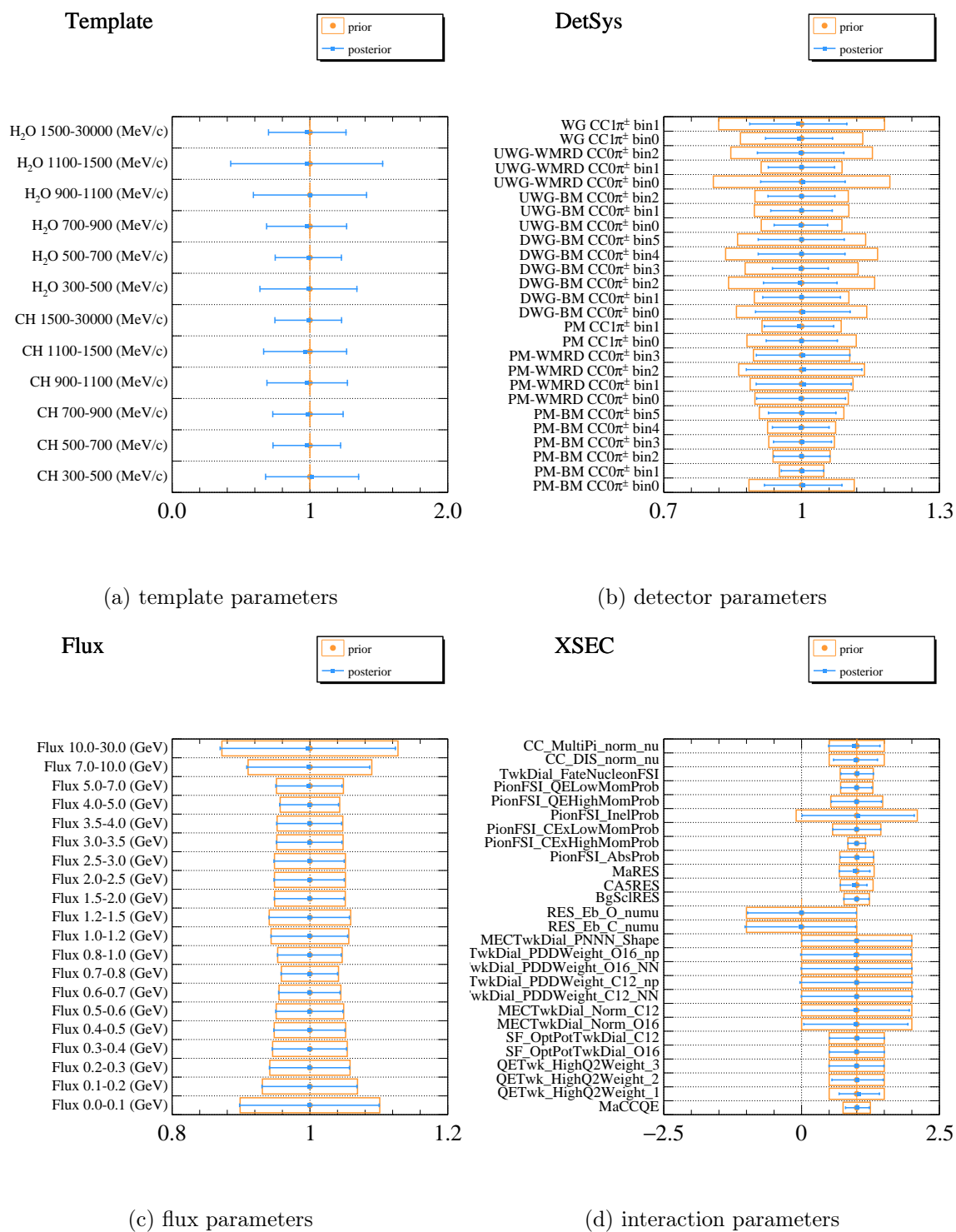
Figure 233: The parameter constraints from the FDS of Low Q^2 suppression in the momentum distribution. Each posterior result is presented by a best-fit point and error bar (blue dot and line) against its prior parameter in orange rectangular. The error is calculated based on the gaussian assumption of each parameter distribution.
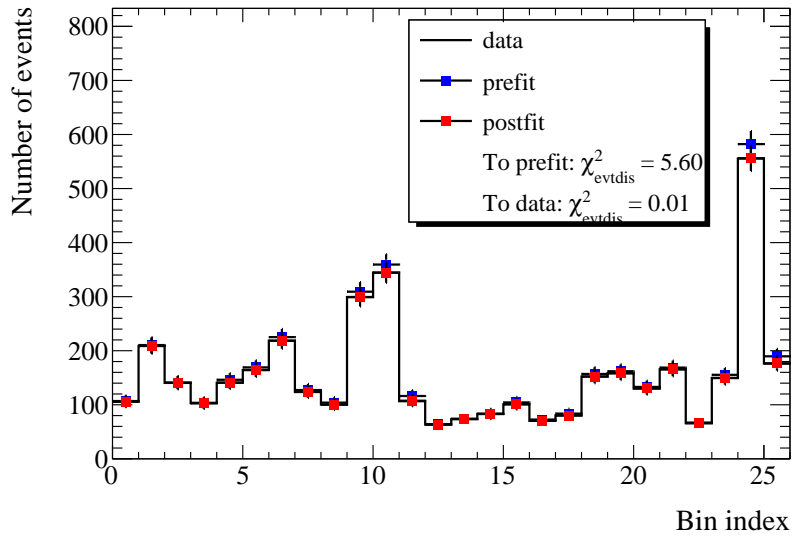
(a) Comparison of event distributions
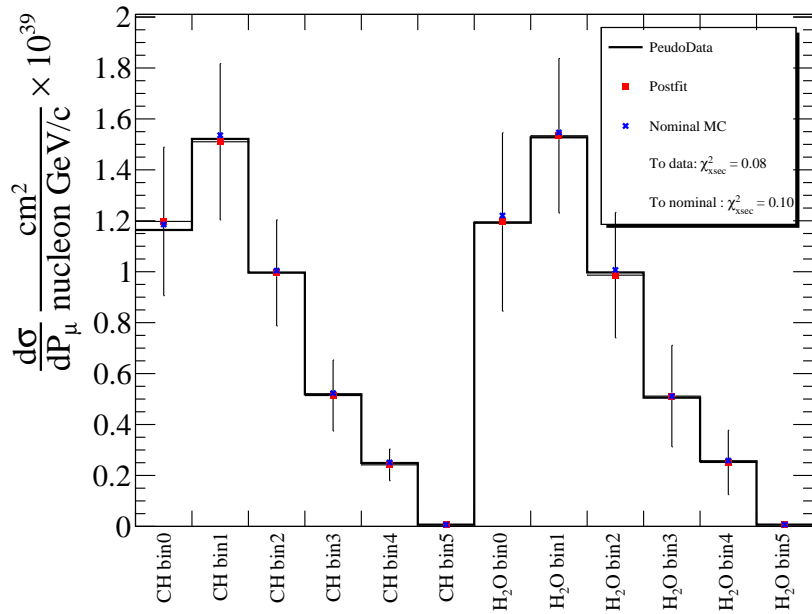
(b) Comparison of cross section fit results

Figure 234: Comparisons of bin-by-bin event distributions between post-fit and pre-fit (top) and the post-fit cross sections overlaid on the true cross sections from pseudo data and nominal data set (bottom) as results of the FDS of Low Q^2 suppression in the momentum distribution. Both plots include corresponding χ^2 values as metrics defined in Equations N.1, N.2.

(a) template parameters

(b) detector parameters

(c) flux parameters

(d) interaction parameters
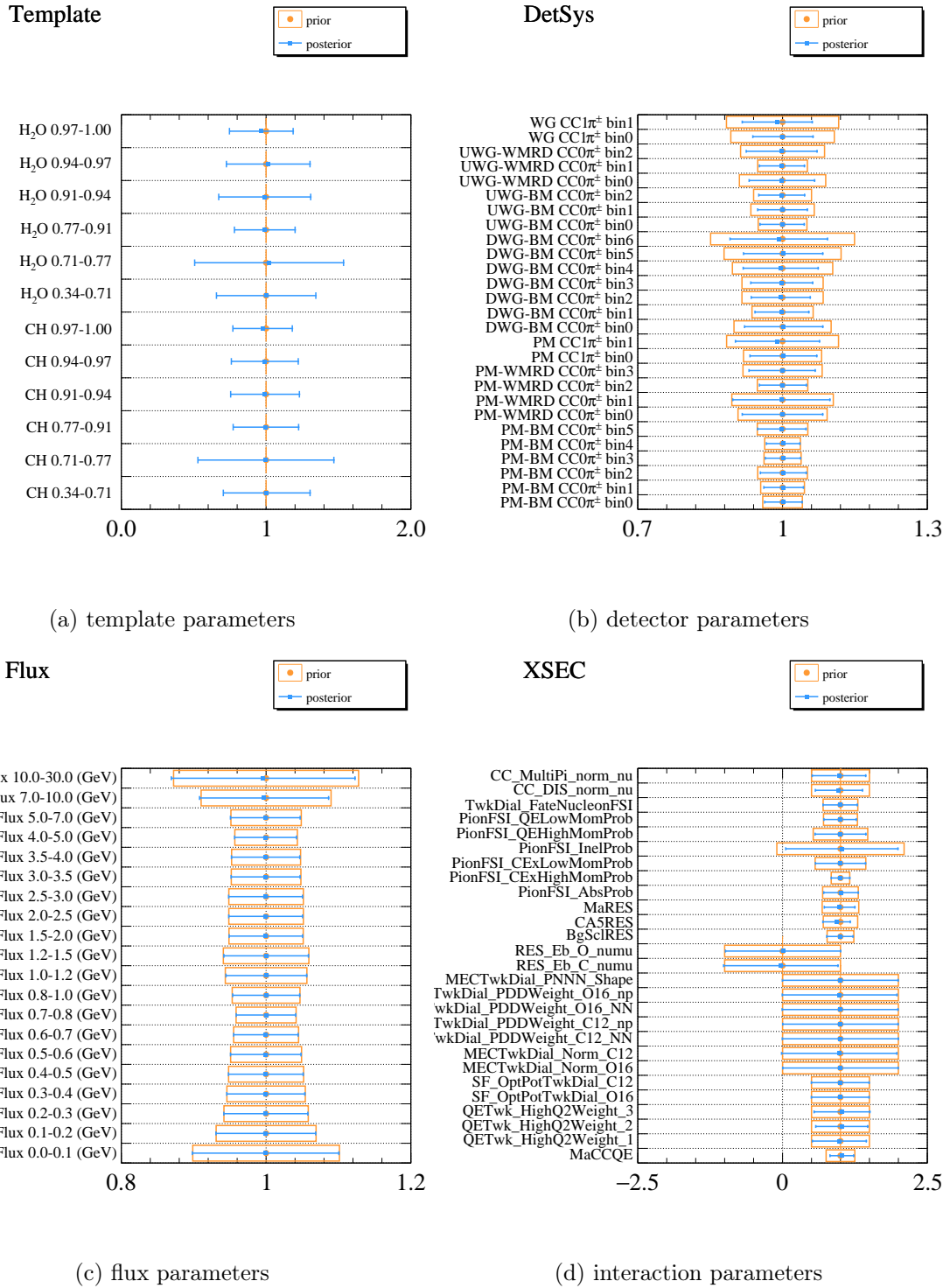
Figure 235: The parameter constraints from the FDS of Low Q^2 suppression in the angle distribution. Each posterior result is presented by a best-fit point and error bar (blue dot and line) against its prior parameter in orange rectangular. The error is calculated based on the gaussian assumption of each parameter distribution.
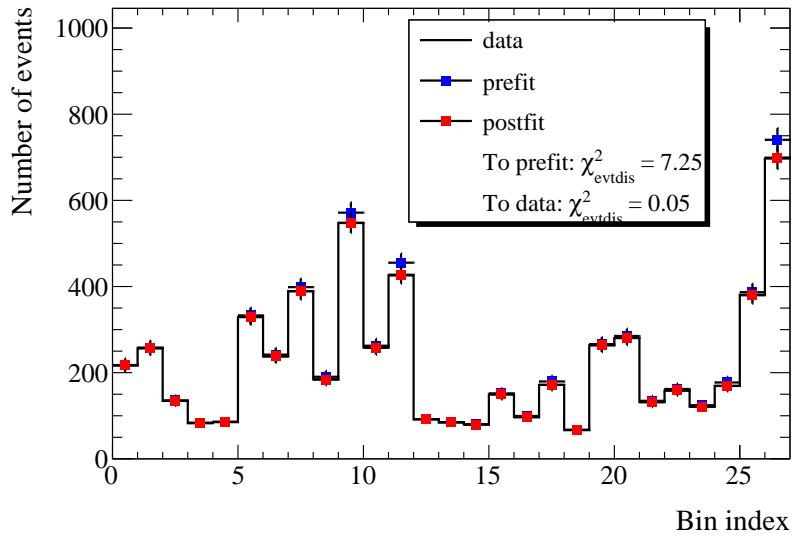
(a) Comparison of event distributions
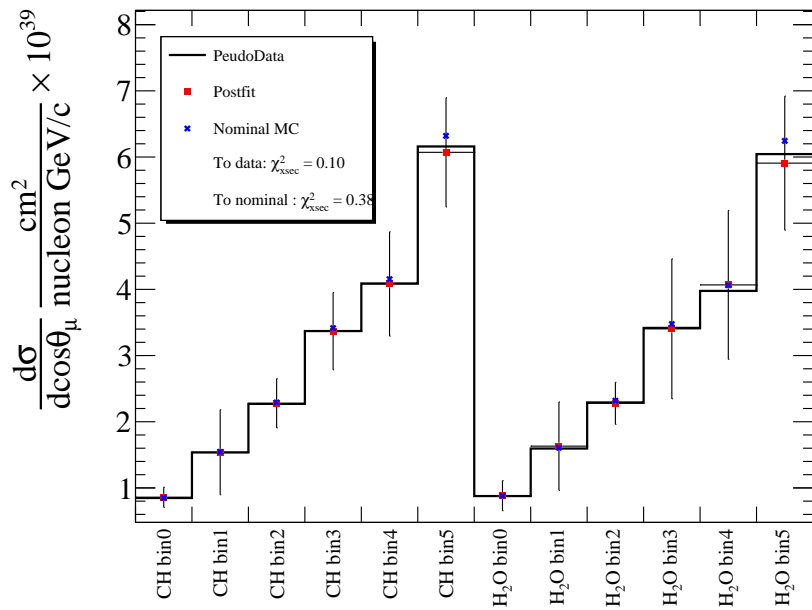
(b) Comparison of cross section fit results

Figure 236: Comparisons of bin-by-bin event distributions between post-fit and pre-fit (top) and the post-fit cross sections overlaid on the true cross sections from pseudo data and nominal data set (bottom) as results of the FDS of Low Q^2 suppression in the angle distribution. Both plots include corresponding χ^2 values as metrics defined in Equations N.1, N.2.

O PartIII: Simulated data studies for the cross section measurements

This appendix is the extension of another one describing the fitter validation, yet, deals with investigations of whether the analysis introduces a potential bias, which might come from the process of our simulation, track reconstruction, or event selections. The procedure is the same as the one written in "fitter validation". We substitute the alternative signal model provided by GENIE [111] or another based model from NEUT. Given there is no significant bias, when we start from the NEUT simulation as a nominal data set and feed the simulated data set, the fit should be able to recover the true cross section from the alternative model. The goal of this study is to verify this expectation.

O.1 GENIE signal + NEUT background

We alternatively use the GENIE neutrino generator which has been on market since 2003. As GENIE provides many options for users to choose appropriate underlying models, we need to choose a specific one. The combination of interaction models that we have chosen is summarized in Table 64.

Table 64: Combination of interaction models used in GENIE for main interaction channels for the T2K experiment.

	Object	Model
Interaction	Quasi elastic scattering	Llewellyn-Smith formalism, with dipole form factor ($M_A^{\mathrm{QE}} = 0.99 \; GeV$)
	2p2h	Dytman model [180]
	resonance	Rein Segal model (2020 tuned)
	DIS	Bodek Yang model (2020 tuned)
Others	FSI	effective model [181]
	Ground state	Relativistic Fermi Gas model

In comparison with the NEUT base model that we use, the CCQE model is the same but with a different nominal value (0.99 v.s.1.21). This would end up with a 20% decrease in CCQE events if there were no other difference between GENIE and NEUT. The base models for 2p2h interactions are different. NEUT adopted Nieves et al. model [116] whereas Dytman model was implemented in this version of GENIE. Both models are tuned to be matched with MINERvA data [99]. For resonance and DIS, there are no significant differences between GENIE and NEUT as their base models but GENIE updated them based on the 2020 tune results. With respect to FSI, Figure 237 compares both implementations of π^+ cross section on carbon target. Although both generators use different models, underlying cross section values for π^+-carbon is similar to each other. The treatment of the ground state of a nucleus is also different. The nominal NEUT utilizes the Benher spectral function model, whereas, on the other hand, the GENIE adopts a relativistic fermi gas model. The difference in missing energy and missing momentum distributions are shown in Figure 238.

NEUT FSI

GENIE FSI
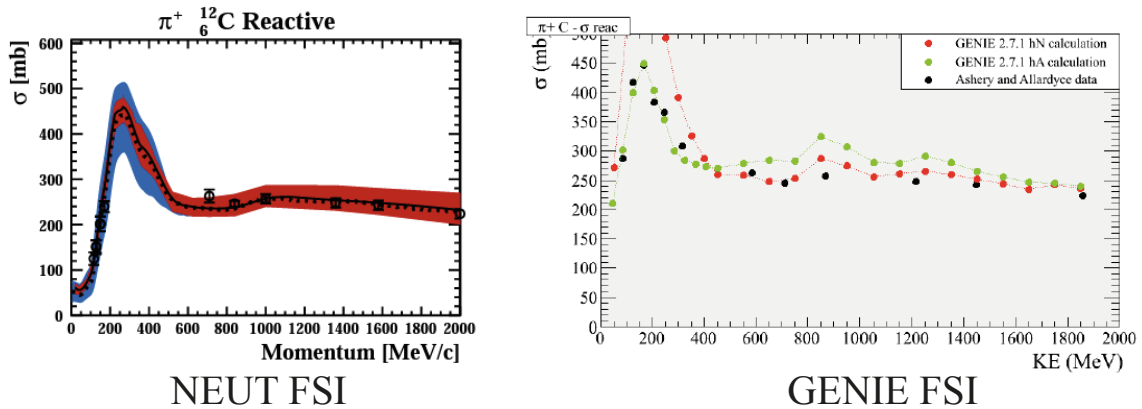
Figure 237: Comparison of the sum of non-elastic interaction cross section for π^+-carbon interaction between NEUT (left) and GENIE (right) from [181]. In the left plot, the black solid line represents the best-fit cross section with the red band referring to the 1σ errors. (The blue band represents the 1σ errors obtained in the previous analysis.) In the right plot, green dotted points show the FSI model that is used in this analysis while red dotted one refers to the alternative model in GENIE. (Black dotted points represent experimental data.) It should be noted that the horizontal labels are different between them. (pion momentum in the left plot and pion kinematic energy in the right plot.)
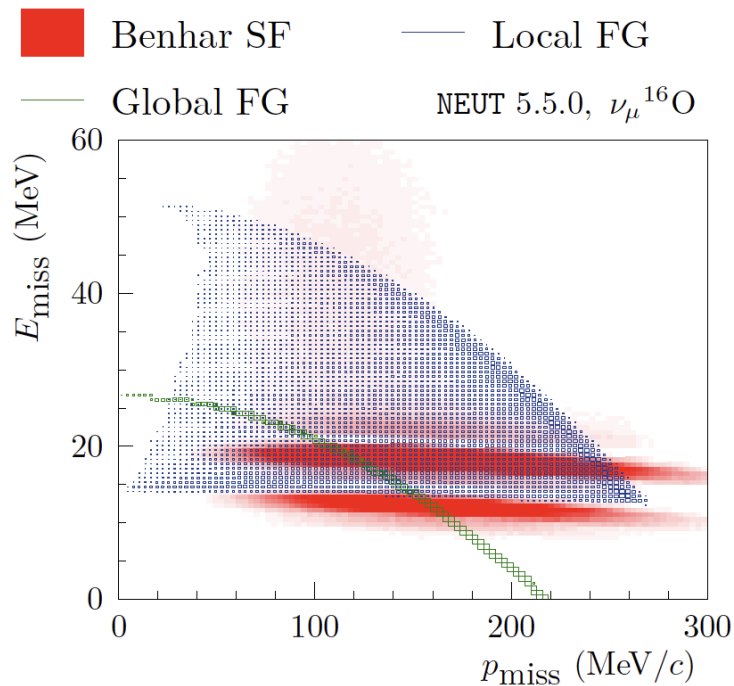
Figure 238: The reconstructed missing energy and missing momentum distributions for the three initial-state nuclear models implemented for the CCQE interaction in NEUT (Benhar Spectral Function in red, Local Fermi Gas model in blue and Global Relativistic Fermi Gas model in green).

We compared the selection outputs for true CC0$\pi^\pm$ events obtained from our nominal NEUT and GENIE as in Figures 239, 240. In the current study, true CC0$\pi^\pm$ events in the signal region were replaced by GENIE events whilst all events in the sideband region remained the same as in nominal MC.

(a) CH target

(b) H$_2$O target
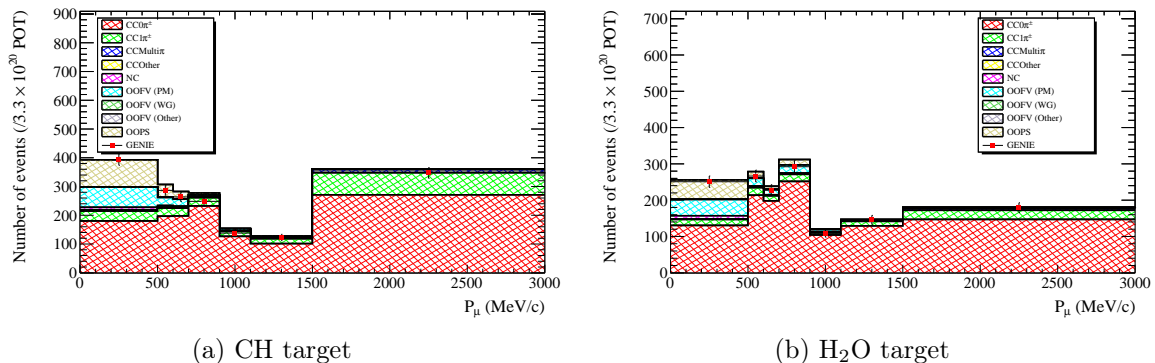
Figure 239: Comparisons of the true CC0$\pi^\pm$ momentum distributions between nominal NEUT and the GENIE for the only signal region. The distributions from NEUT are broken down by their interaction type, while the total number of signal events from GENIE is plotted as red dotted points. Error bars represent Poisson statistical fluctuation for 1σ.

(a) CH target

(b) H$_2$O target
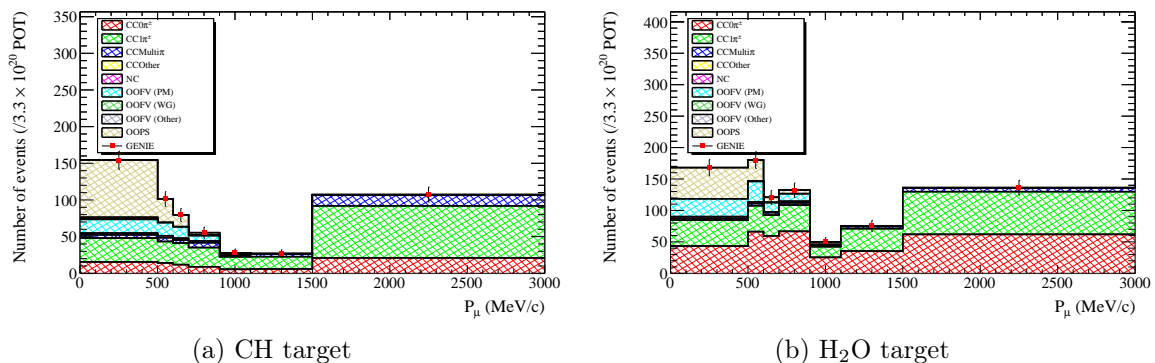
Figure 240: Comparisons of the true CC0$\pi^\pm$ momentum distributions between nominal NEUT and the GENIE the only control region of CC1$\pi^\pm$. The event distribution from NEUT is broken down by its interaction type, while the total number of signal events from GENIE is plotted as red dotted points. Error bars represent Poisson statistical fluctuation for 1σ.

The fit results are shown in Figures 241, 242 in the momentum distribution and in Figures 243, 244 in the angle distribution. The results for parameter constraints seen in Figures 241, 243 show normalization parameters such as template parameters and detector systematic parameters have a larger response in particular for PM samples to these changes whilst cross section parameters are mostly unaltered. This behavior is expected from the selection outputs from GENIE in Figure 239, where we can see similar shapes between NEUT and GENIE but a slight decrease in PM samples from GENIE MC compared to NEUT nominal.

With respect to the post-fit event distribution shown in the top in Figure 241, although the

χ^2 is a bit away from 0, it is improved significantly compared to the pre-fit event distribution. Moreover, the resulting post-fit cross section is in good agreement with true cross section from the GENIE data set.

(a) template parameters

(b) detector parameters

(c) flux parameters

(d) interaction parameters
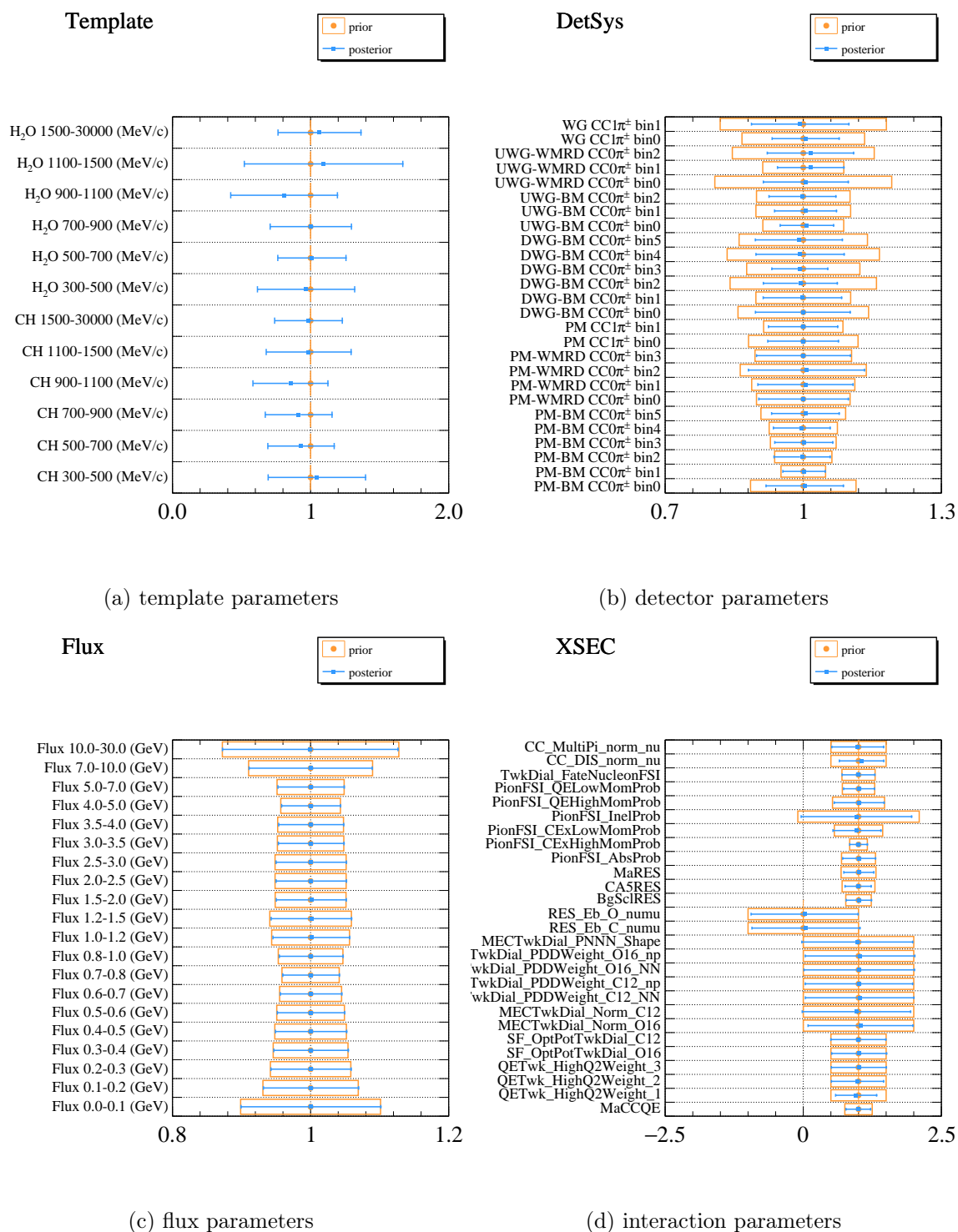
Figure 241: The parameter constraints from the FDS of GENIE in the momentum distribution. Each posterior result is presented by a best-fit point and error bar (blue dot and line) against its prior parameter in orange rectangular. The error is calculated based on the gaussian assumption of each parameter distribution.
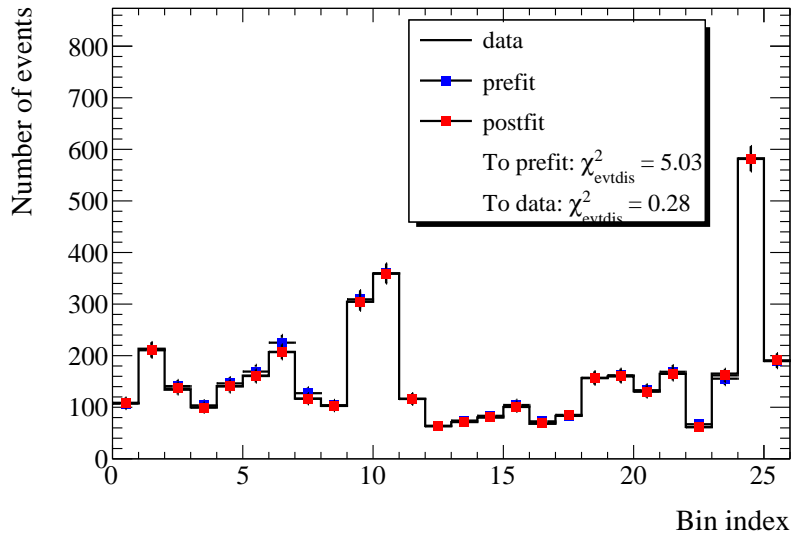
(a) Comparison of event distributions
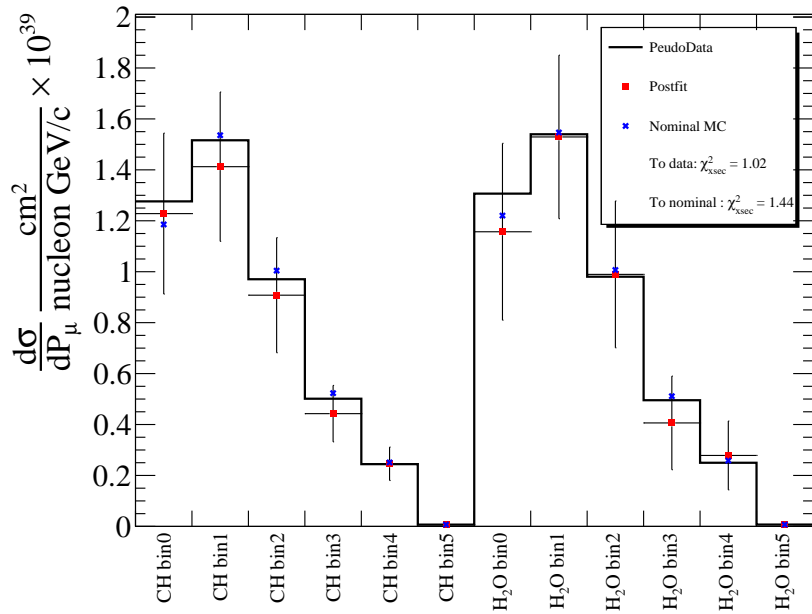
(b) Comparison of cross section fit results

Figure 242: Comparisons of bin-by-bin event distributions between post-fit and pre-fit (top) and the post-fit cross sections overlaid on the true cross sections from pseudo data and nominal data set (bottom) as results of the FDS of GENIE in the momentum distribution. Both plots include corresponding χ^2 values as metrics defined in Equations N.1, N.2.

(a) template parameters

(b) detector parameters

(c) flux parameters

(d) interaction parameters
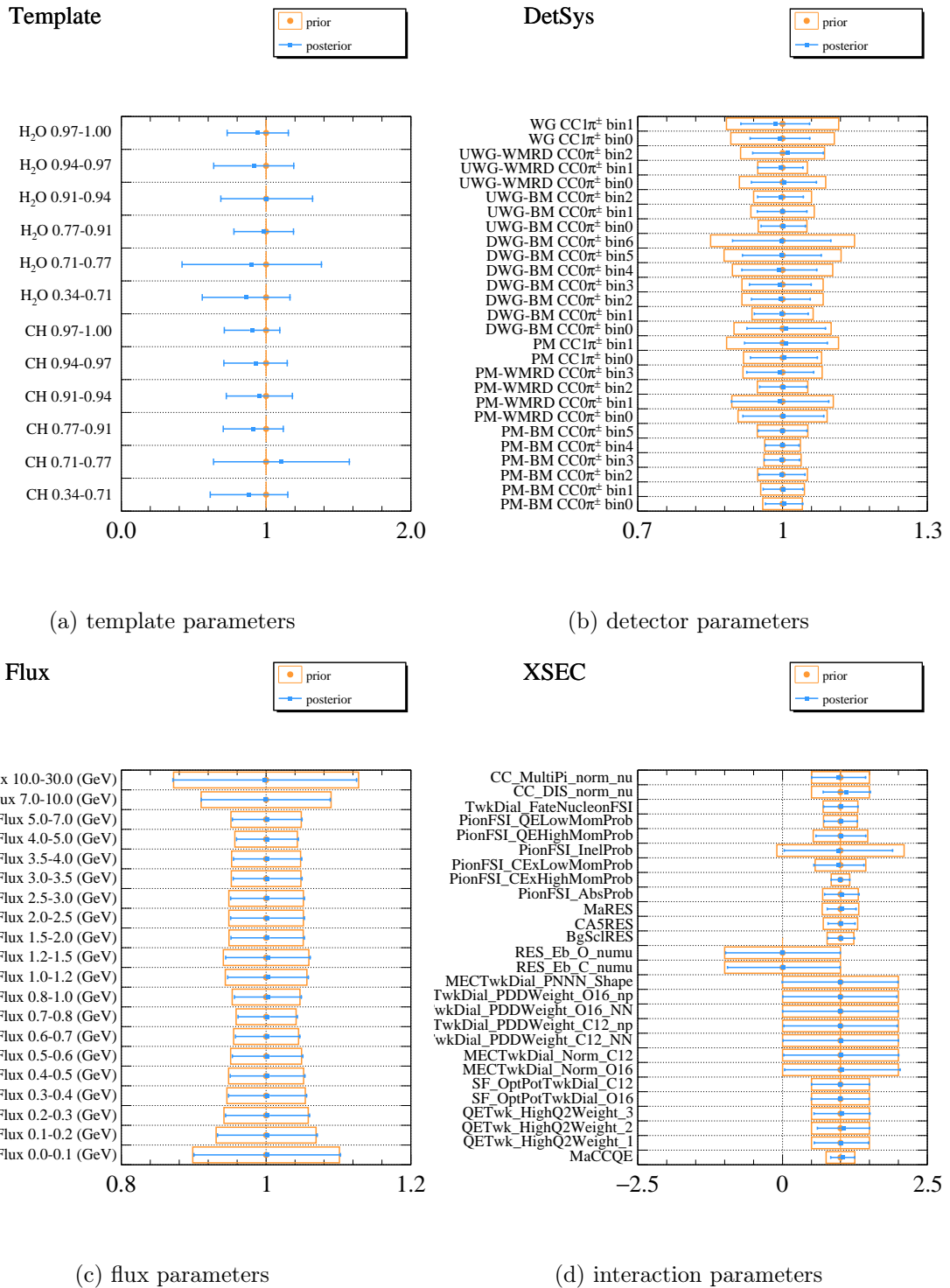
Figure 243: The parameter constraints from the FDS of GENIE in the angle distribution. Each posterior result is presented by a best-fit point and error bar (blue dot and line) against its prior parameter in orange rectangular. The error is calculated based on the gaussian assumption of each parameter distribution.
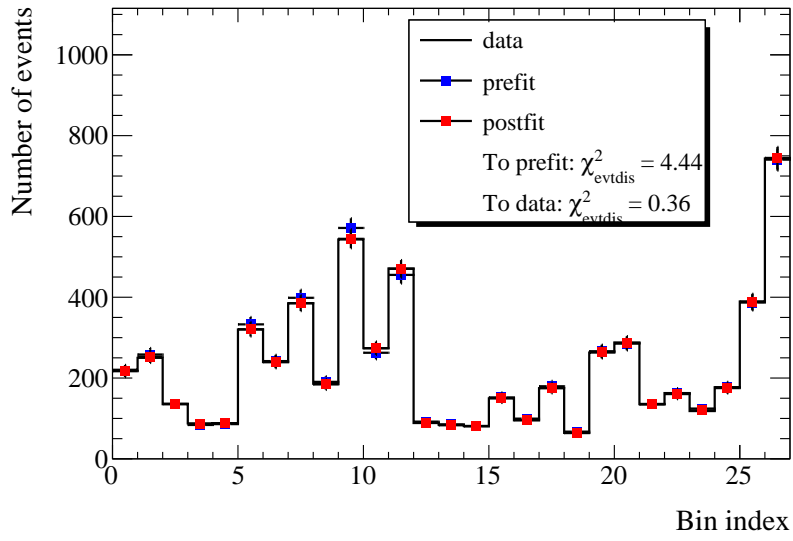
(a) Comparison of event distributions
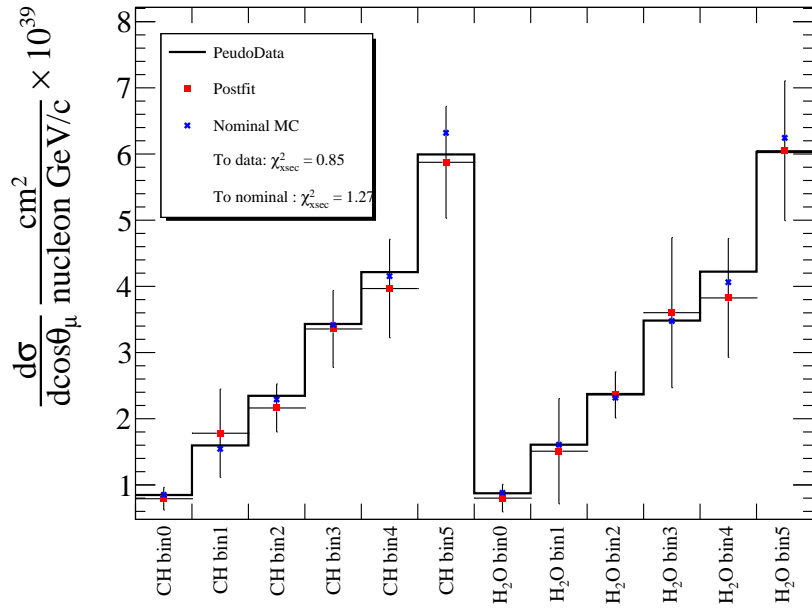
(b) Comparison of cross section fit results

Figure 244: Comparisons of bin-by-bin event distributions between post-fit and pre-fit (top) and the post-fit cross sections overlaid on the true cross sections from pseudo data and nominal data set (bottom) as results of the FDS of GENIE in the angle distribution. Both plots include corresponding χ^2 values as metrics defined in Equations N.1, N.2.

O.2 Alternative NEUT model (without Spectral Function, Nieves 1p1h model)

We alternatively use another model implemented in NEUT. This model adopts the simple Fermi gas model proposed by Smith-Moniz with the correction from BBBA(05) parametrization, which is the same as the nominal version that this analysis relies on. The distinct part is the treatment for the nuclear ground state. The alternative model does not introduce Spectral Function (SF) but treats it in the global Fermi gas model. The CCQE model is the Nieves 1p1h model without RPA correction, with M_A^{QE} being set to 1.05. As the nominal NEUT model in this analysis set the parameter value to 1.21, the expected number of CCQE events would naively decrease by about 15% level, which ends up being smaller cross section. If the fitter works as expected without introducing any bias, it is expected to find relatively smaller cross section compared to the nominal cross section. Figure 245 presents the comparison between nominal prediction and that from the alternative version of NEUT. The predicted number of selected events in the alternative NEUT seems lower than that in the nominal configuration, which is expected.

(a) CC0$\pi^\pm$, CH target

(b) CC0$\pi^\pm$, H$_2$O target

(c) CC1$\pi^\pm$, CH target

(d) CC1$\pi^\pm$, H$_2$O target
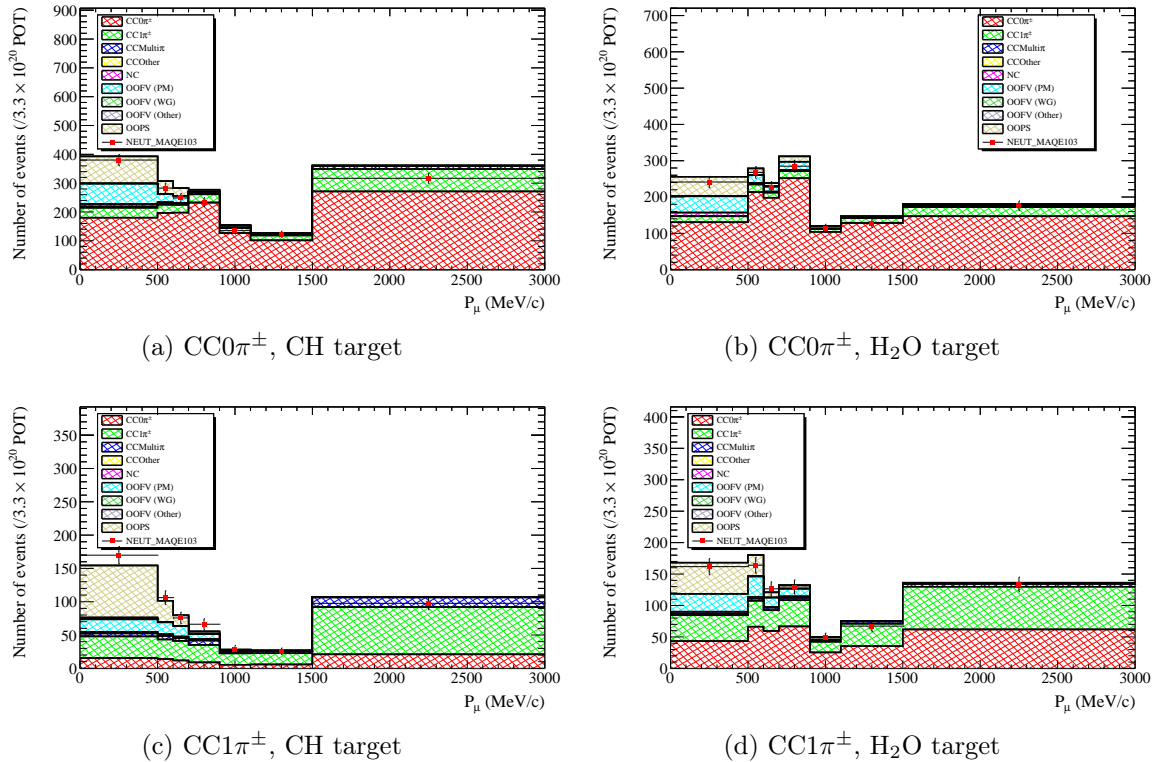
Figure 245: Comparison of selected event distributions on CH (left) and H$_2$O (right) target in the momentum distribution between nominal NEUT and the alternative NEUT ($M_A^{QE} = 1.05$) in the signal region (top) and control region of CC1$\pi^\pm$ (bottom). The event distribution from NEUT is broken down by its interaction type, while the total number of signal events from the alternative NEUT is plotted as red dotted points. Error bars represent Poisson statistical fluctuation for 1σ.

The fit results are presented in Figures 246, 247 in the momentum distribution and Figures 248, 249 in the angle distribution.

(a) template parameters

(b) detector parameters

(c) flux parameters

(d) interaction parameters

Figure 246: The parameter constraints from the FDS of Alternative version of NEUT in the momentum distribution. Each posterior result is presented by a best-fit point and error bar (blue dot and line) against its prior parameter in orange rectangular. The error is calculated based on the gaussian assumption of each parameter distribution.

(a) Comparison of event distributions

(b) Comparison of cross section fit results

Figure 247: Comparisons of bin-by-bin event distributions between post-fit and pre-fit (top) and the post-fit cross sections overlaid on the true cross sections from pseudo data and nominal data set (bottom) as results of the FDS of Alternative version of NEUT in the momentum distribution. Both plots include corresponding χ^2 values as metrics defined in Equations N.1, N.2.

(a) template parameters

(b) detector parameters

(c) flux parameters

(d) interaction parameters
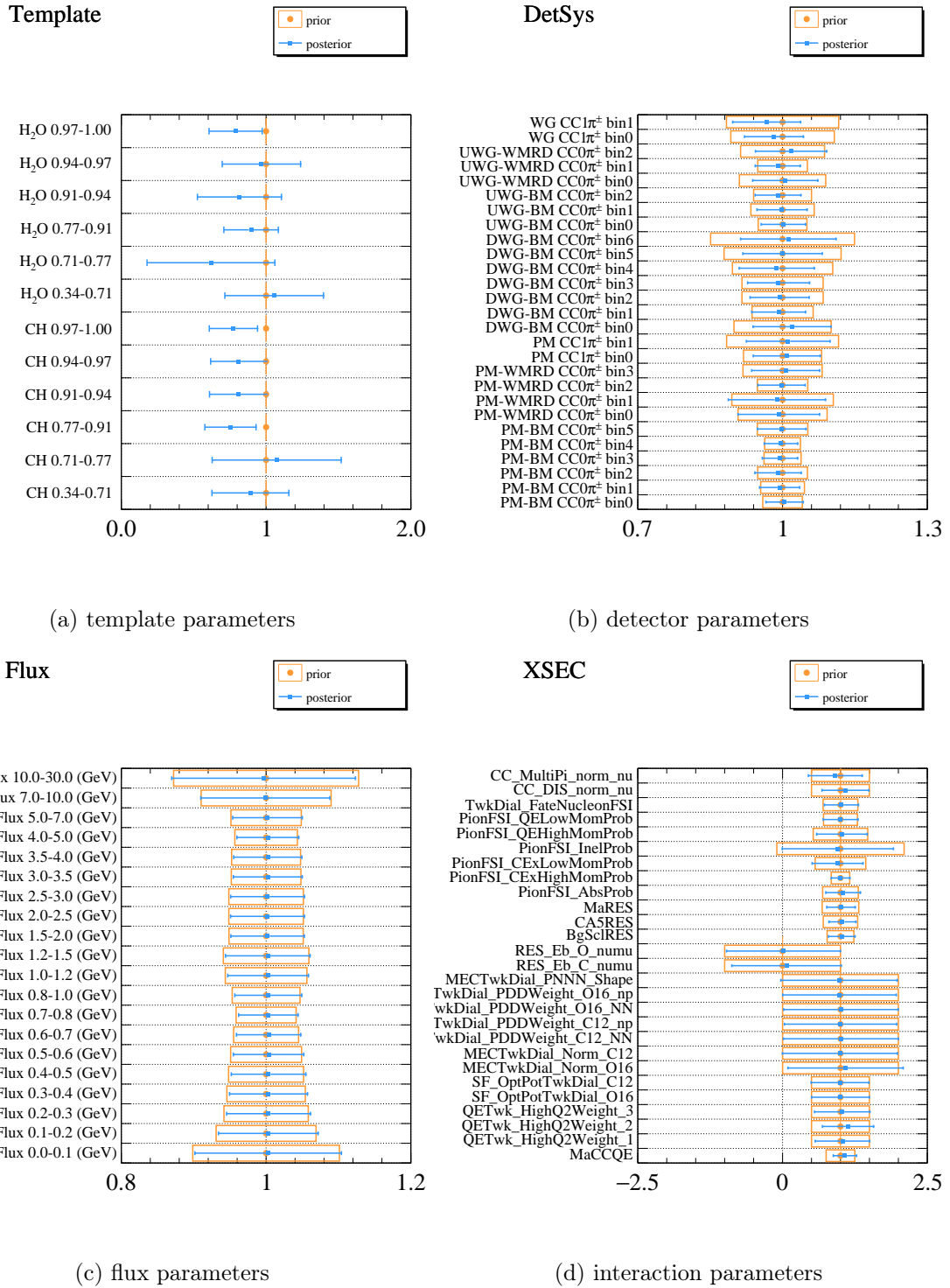
Figure 248: The parameter constraints from the FDS of Alternative version of NEUT in the angle distribution. Each posterior result is presented by a best-fit point and error bar (blue dot and line) against its prior parameter in orange rectangular. The error is calculated based on the gaussian assumption of each parameter distribution.
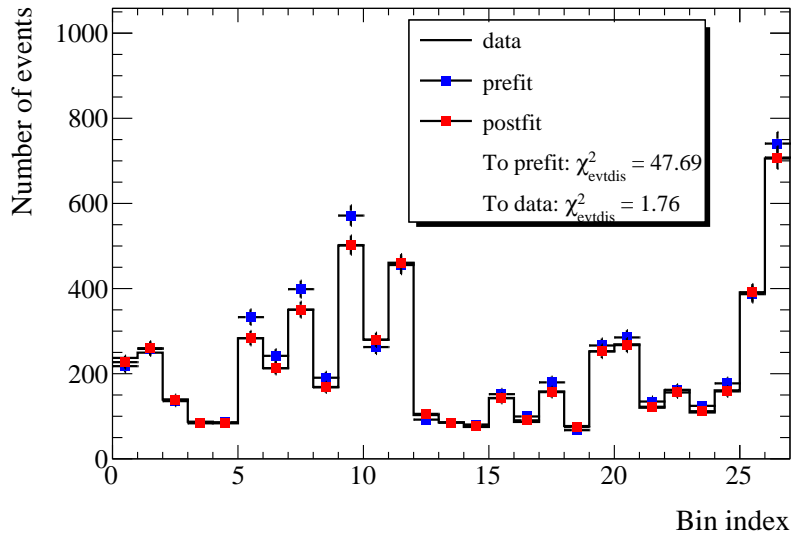
(a) Comparison of event distributions
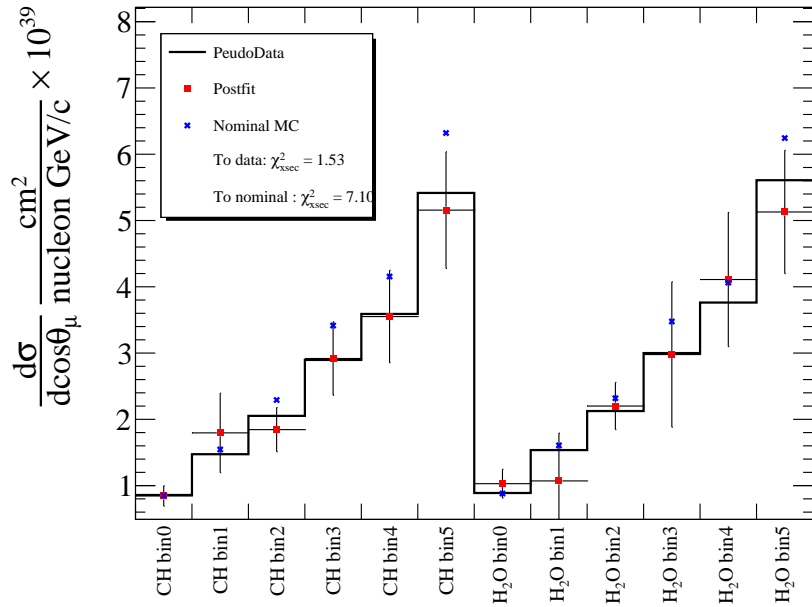
(b) Comparison of cross section fit results

Figure 249: Comparisons of bin-by-bin event distributions between post-fit and pre-fit (top) and the post-fit cross sections overlaid on the true cross sections from pseudo data and nominal data set (bottom) as results of the FDS of Alternative version of NEUT in the angle distribution. Both plots include corresponding χ^2 values as metrics defined in Equations N.1, N.2.

O.3 Reweight events based on Post-BANFF tuned in OA2022

The T2K Near detector (ND280) has performed the fit to provide parameter constraints for neutrino interaction-related systematic parameters. The post-fit results by the NDfit are referred to as "Post-BANFF" tuned parameters. In order to check the compatibility of this analysis with the Post-BANFF parameters, we perform the fit with the pseudo data where all events are re-weighted by those best-fit parameters given by Post-BANFF. The post-fit parameter values are presented in Table 65. The hallmark of ND280 parameter constraints is to pull up the CC0π events and pull down the CC1π events. As in Table 65, CCQE related parameters and 2p2h parameters are increased with respect to the pre-fit values while resonant parameters (C_A^5, M_A^{RES}, RS Delta Decay) are decreased. This feature is visible in the comparison of selected event distributions as in Figure 250. The number of CC0$\pi^{\pm}$ events on both targets is clearly inflated while that of CC1$\pi^{\pm}$ is decreased.

Table 65: Parameter constraints from T2K ND fit in OA2022 compared to the pre-fit values for the cross section parameters

	Parameter	Pre-fit	Post-fit
CCQE	M_A^{QE}	1.03	1.11136
	Q^2 norm 5	1	1.18253
	Q^2 norm 6	1	1.01229
	Q^2 norm 7	1	1.34333
	Optical Potential ^{12}C	0	0.342335
	Optical Potential ^{16}O	0	0.0431339
2p2h	2p2h norm ν	1	1.22216
	2p2h norm $\bar{\nu}$	1	1.09123
	2p2h norm others	1	0.977541
	2p2h shape ^{12}C np	0	-1.47095
	2p2h shape ^{12}C NN	0	-1.00136
	2p2h shape ^{12}O np	0	-0.99571
	2p2h shape ^{12}O NN	0	-0.433141
FSI	FEFQE	1.069	1.0004
	FEFQEH	1.824	1.71212
	FEFINEL	1.002	1.11281
	FEFABS	1.404	1.04038
	FEFCX	0.697	0.572102
	FEFCXH	1.8	1.94583
RES	C_A^5	1.06	0.850416
	M_A^{RES}	0.91	0.843586
	RES Eb ^{12}C ν_μ	25	1.24115
	RES Eb ^{16}O ν_μ	25	4.61816
	RS Delta Decay	1	0.970967

(a) CC0$\pi^{\pm}$, CH target

(b) CC0$\pi^{\pm}$, H$_2$O target

(c) CC1$\pi^{\pm}$, CH target

(d) CC1$\pi^{\pm}$, H$_2$O target
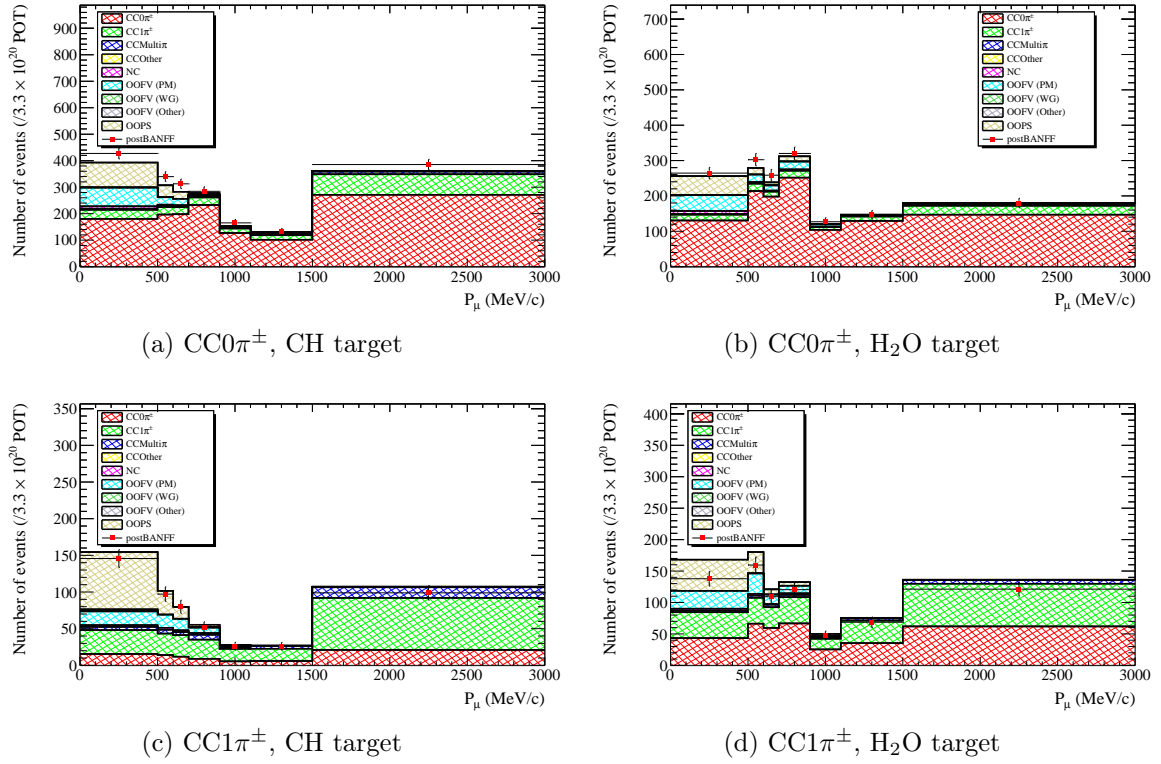
Figure 250: Comparisons of selected event distributions on CH (left) and H$_2$O (right) target in the momentum distribution between nominal NEUT and postBANFF tune in the signal region (top) and control region of CC1$\pi^{\pm}$ (bottom). The event distributions from NEUT are broken down by their interaction type, while the total number of signal events from the postBANFF tune is plotted as red dotted points. Error bars represent Poisson statistical fluctuation for 1σ.

The fit results are presented in Figures 251, 252 in momentum distribution and Figures 253, 254 in the angle distribution.

(a) template parameters

(b) detector parameters

(c) flux parameters

(d) interaction parameters
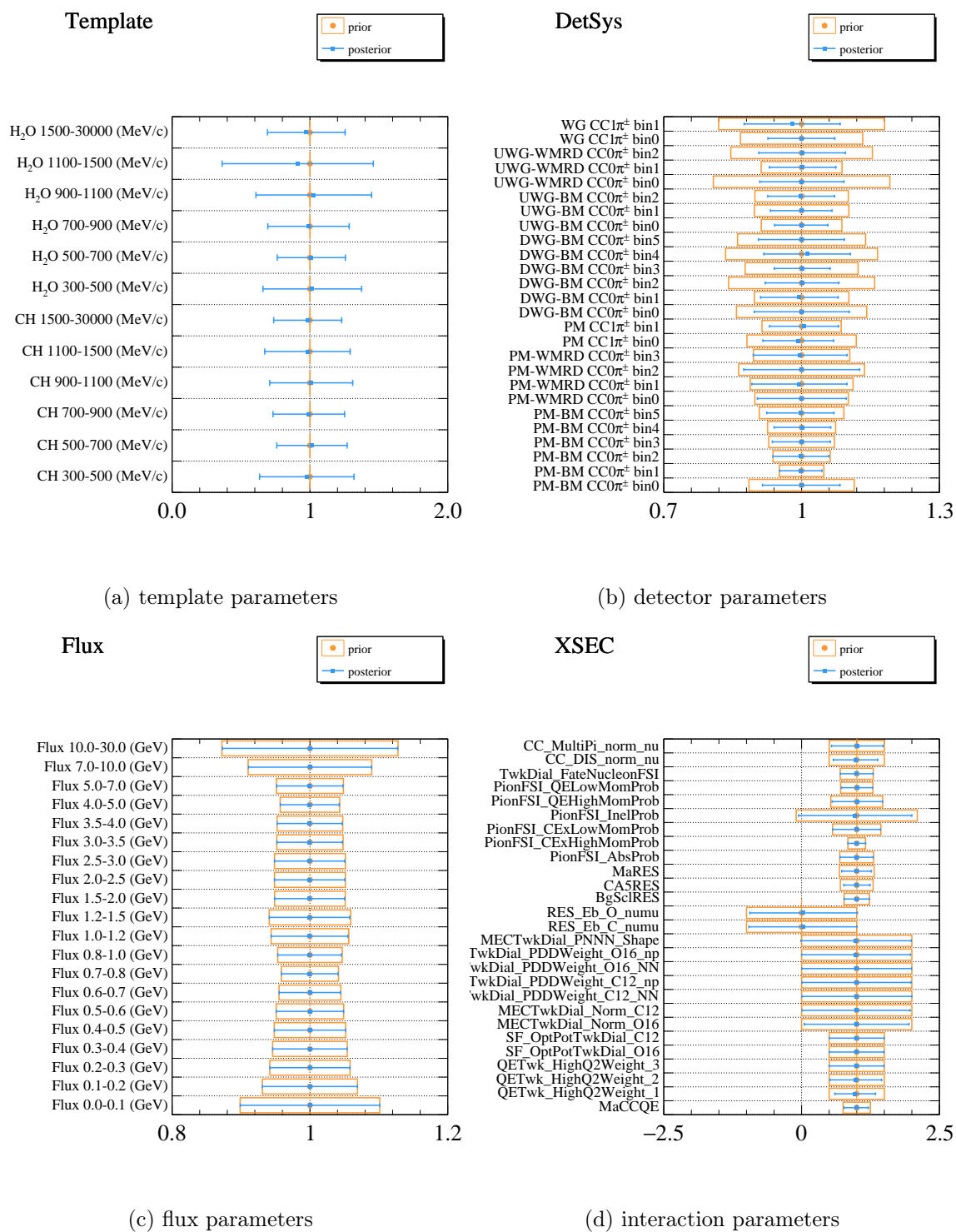
Figure 251: The parameter constraints from the FDS of Post-BANFF tune in the momentum distribution. Each posterior result is presented by a best-fit point and error bar (blue dot and line) against its prior parameter in orange rectangular. The error is calculated based on the gaussian assumption of each parameter distribution.
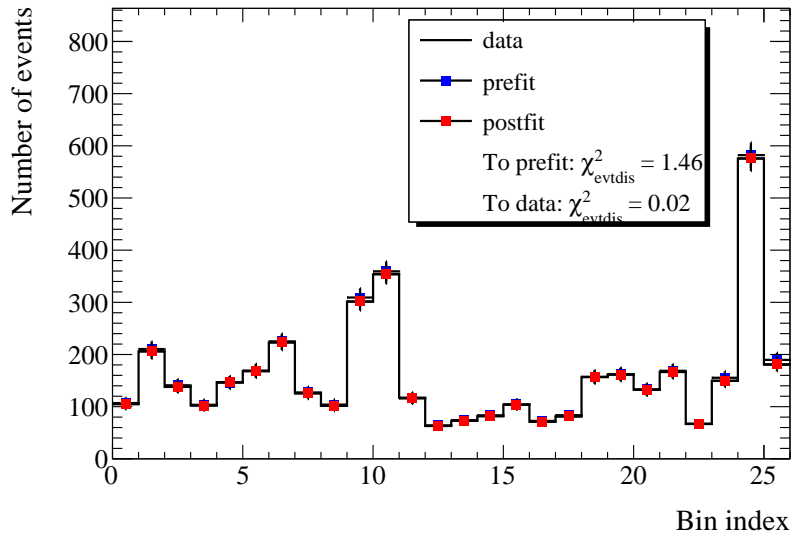
(a) Comparison of event distributions
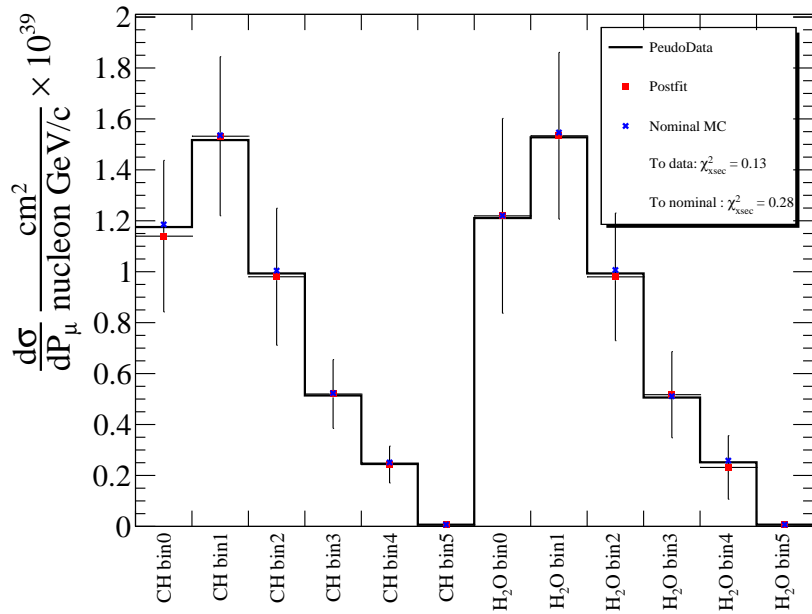
(b) Comparison of cross section fit results

Figure 252: Comparisons of bin-by-bin event distributions between post-fit and pre-fit (top) and the post-fit cross sections overlaid on the true cross sections from pseudo data and nominal data set (bottom) as results of the FDS of Post-BANFF tune in the momentum distribution. Both plots include corresponding χ^2 values as metrics defined in Equations N.1, N.2.

(a) template parameters

(b) detector parameters

(c) flux parameters

(d) interaction parameters
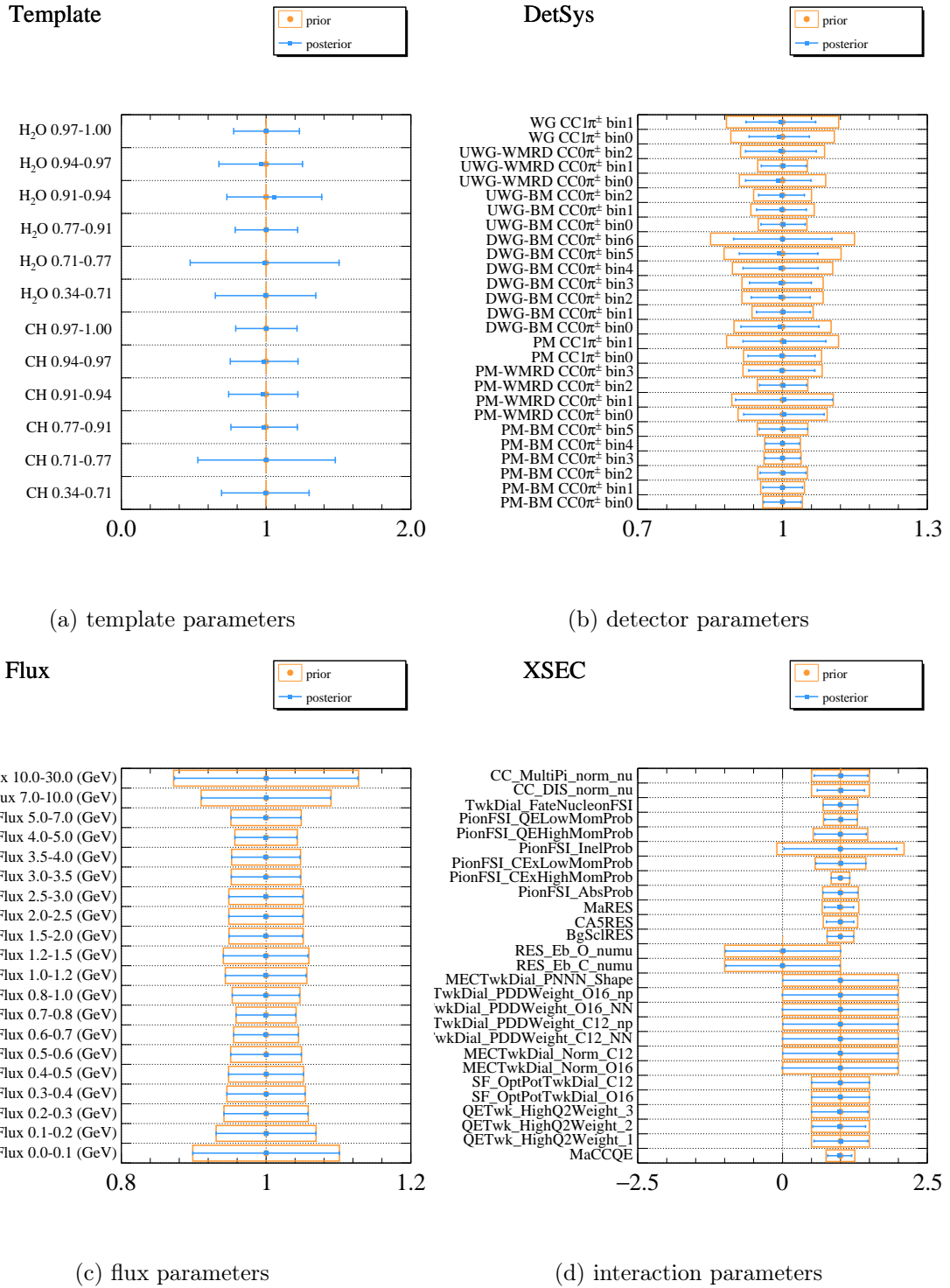
Figure 253: The parameter constraints from the FDS of Post-BANFF tune in the angle distribution. Each posterior result is presented by a best-fit point and error bar (blue dot and line) against its prior parameter in orange rectangular. The error is calculated based on the gaussian assumption of each parameter distribution.
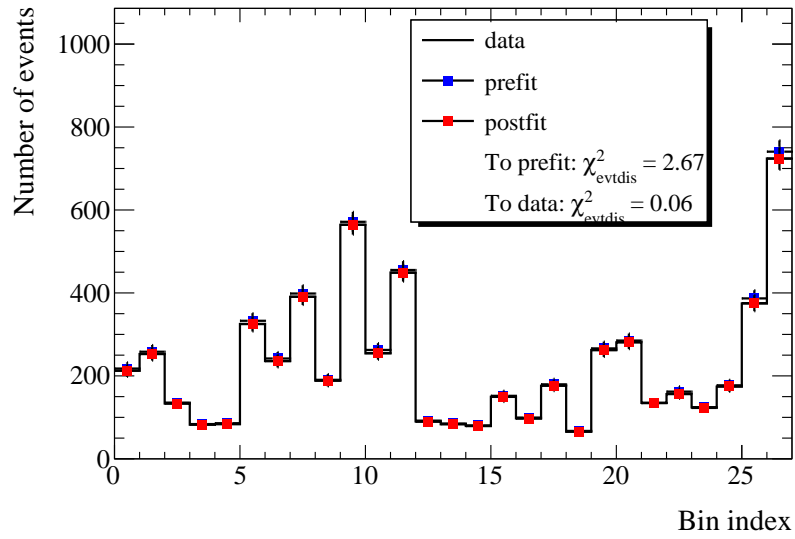
(a) Comparison of event distributions
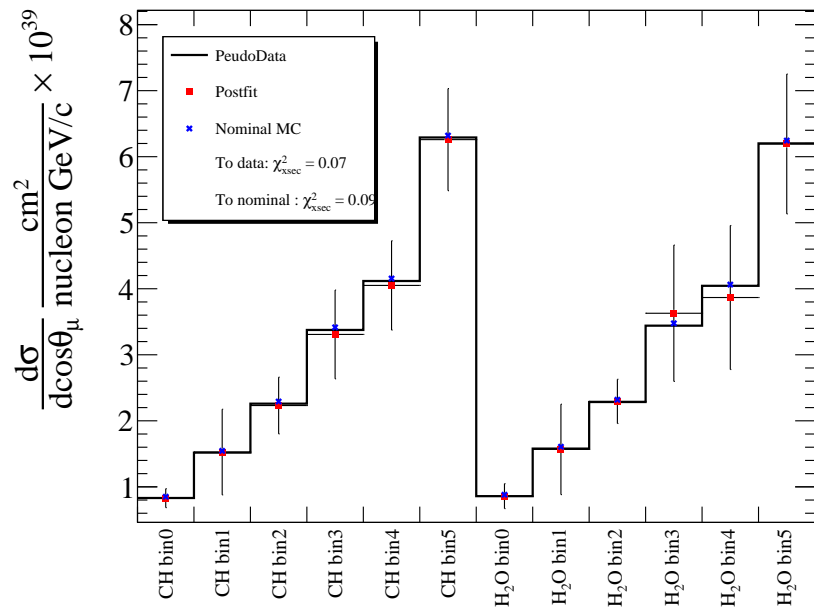
(b) Comparison of cross section fit results

Figure 254: Comparisons of bin-by-bin event distributions between post-fit and pre-fit (top) and the post-fit cross sections overlaid on the true cross sections from pseudo data and nominal data set (bottom) as results of the FDS of Post-BANFF tune in the angle distribution. Both plots include corresponding χ^2 values as metrics defined in Equations N.1, N.2.

P   PartIII: Constraints on fitting parameters in the data fit

P.1 χ^2 metric to asses the fit results

We present the comparisons of post-fit and pre-fit event distributions for sample by sample as one of the results. The differences in event distributions between post-fit and pre-fit should be assessed with some metrics to check the performance of the fit. We introduce appropriate χ^2 for this purpose, which is defined as

$$\chi^2_{\text{evdis}} = \sum_{i=1}^{N} 2 \left(N_i^{\text{fit}} - N_i^{\text{obs}} + N_i^{\text{obs}} \ln \frac{N_i^{\text{obs}}}{N_i^{\text{fit}}} \right), \tag{P.1}$$

by taking only statistical contribution into account. N_i^{fit} is the expected number of events for bin i from a fit result, which form a post-fit event distribution. N_i^{obs} is the observed number of events (from pseudo data in the context of this validation) for bin i. The χ^2 is presented on the plots for the comparisons between post-fit and pre-fit event distributions.

P.2   Results of the parameter constraints

The fit results are presented in Figs 255, 256, 257 for the momentum distribution and Figs 258, 259, 260 for the angle distribution. The parameter constraints are presented in Figures 255, 258. The detector parameters in the CC1$\pi^{\pm}$ region particularly move away from the nominal value. This is due in part to the anti-correlation between the template and detector parameters as in Figures 256, 259. The size of the movement in template parameters is larger for WAGASCI samples than that for Proton Module samples. This behavior should reflect the size of data-MC differences shown in Figures 68, 69. The post-fit distributions are shown in Figures 257, 260. The χ^2 to the data distributions get much less than that to the nominal distributions, which means the post-fit parameters work well. The p-values for both results (0.047 for the momentum distribution and 0.11 for the angle distribution) are higher than the threshold (0.01). This indicates that our MC models describe the data well.

(a) template parameters

(b) detector parameters

(c) flux parameters

(d) interaction parameters
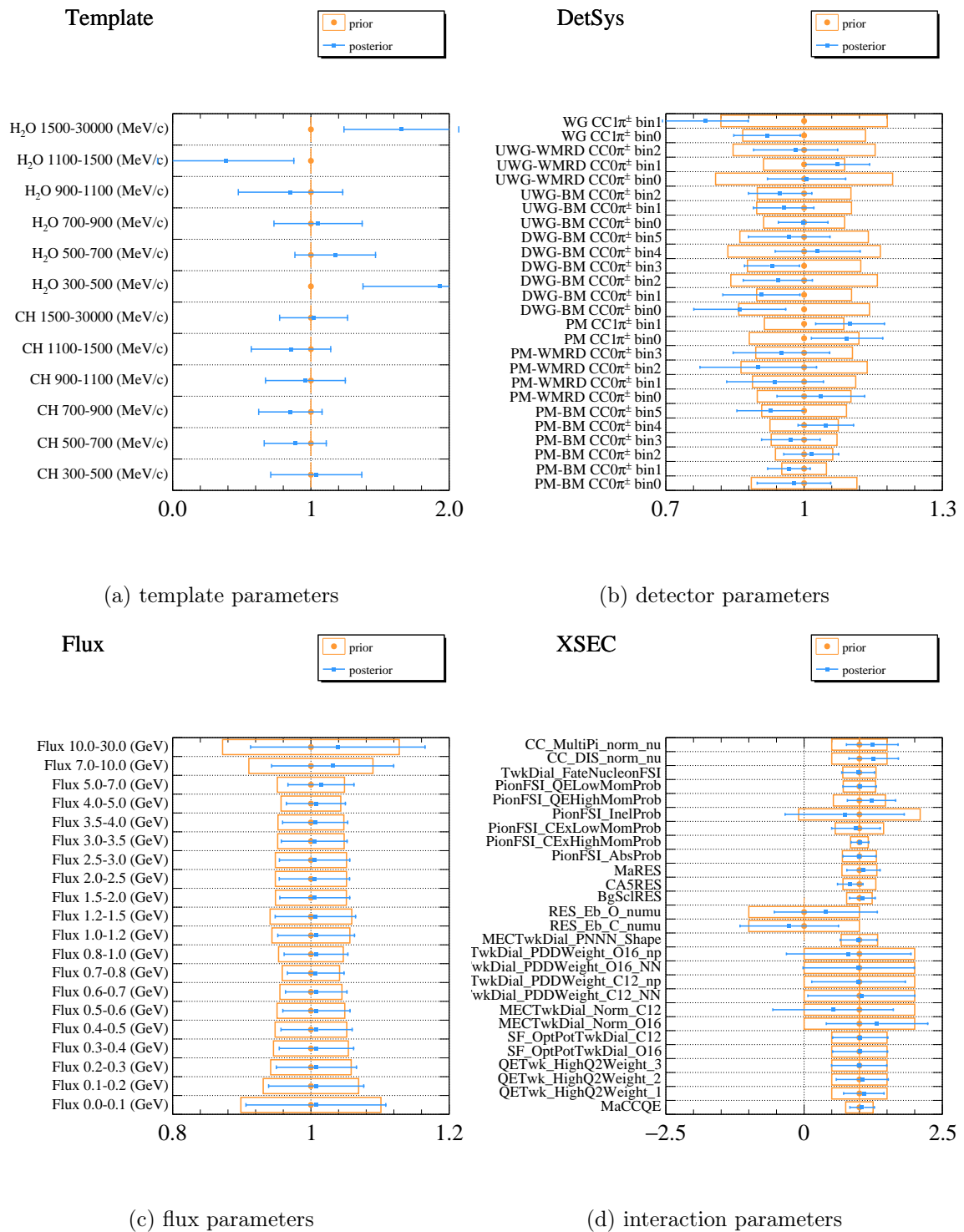
Figure 255: The parameter constraints from the Data fit in the momentum distribution. Each posterior result is presented by a best-fit point and error bar (blue dot and line) against its prior parameter in orange rectangular. The error is calculated based on the gaussian assumption of each parameter distribution.
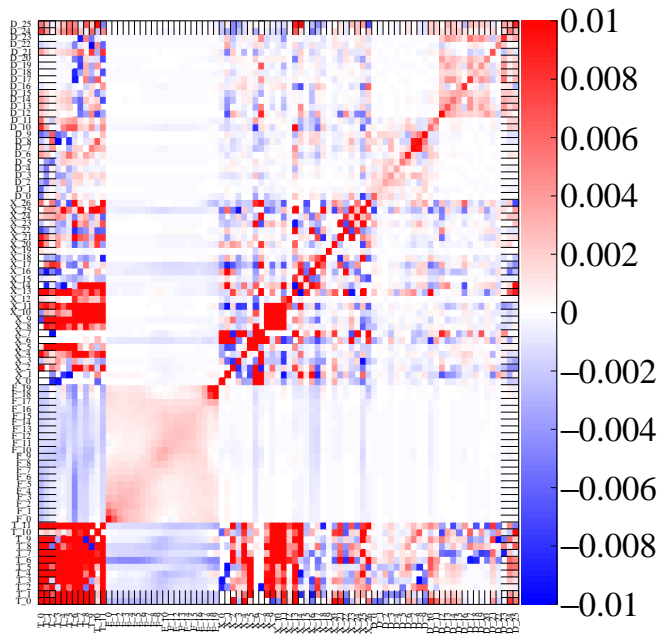
(a) Covariance matrix
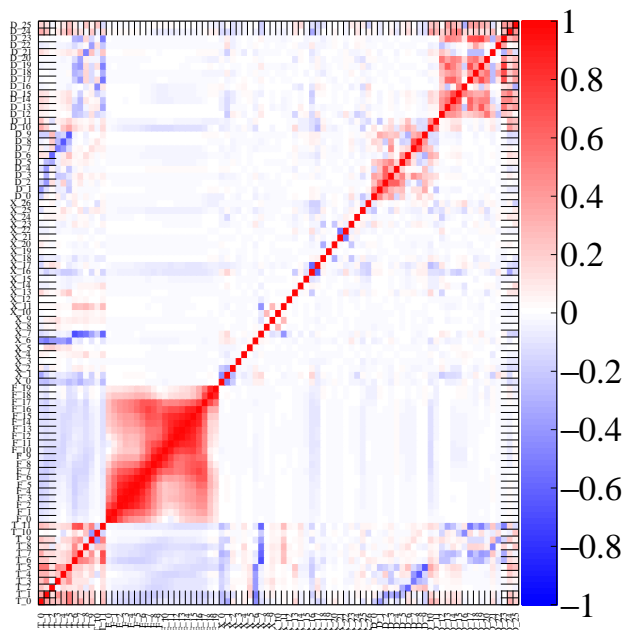
(b) Correlation matrix

Figure 256: Post-fit covariance and correlation matrices for the momentum distribution. The horizontal and vertical axis refers to fitting parameter ID; "T", "F", "X", "D" refer to "Template", "Flux systematic", "Xsec systematic", "Detector systematic" parameters.

358
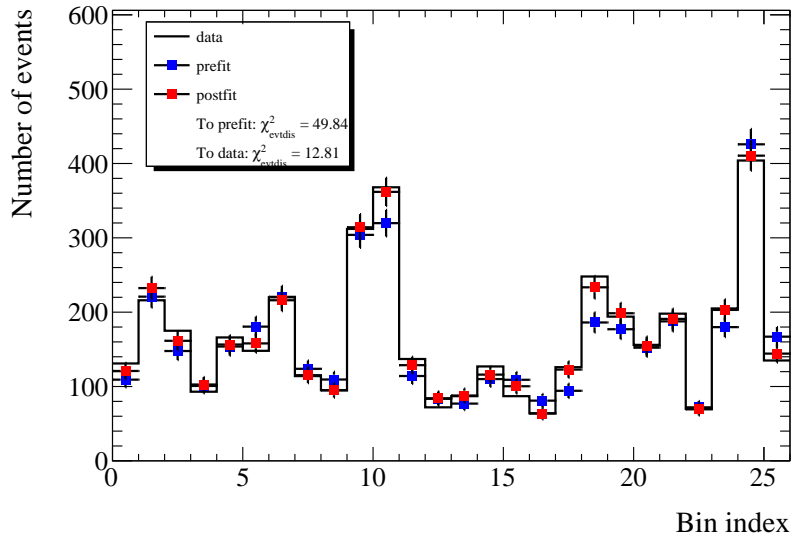
(a) Comparison of event distributions

(b) p-value test

Figure 257: Comparisons of bin-by-bin event distributions between post-fit and pre-fit (top) and the coverage plot along with the total χ^2 for the data fit in the momentum distribution. The upper plot includes the corresponding χ^2 as metrics defined in Equation P.1. For the coverage plot, the data χ^2 is overlaid in the vertical red line.

(a) template parameters

(b) detector parameters

(c) flux parameters

(d) interaction parameters
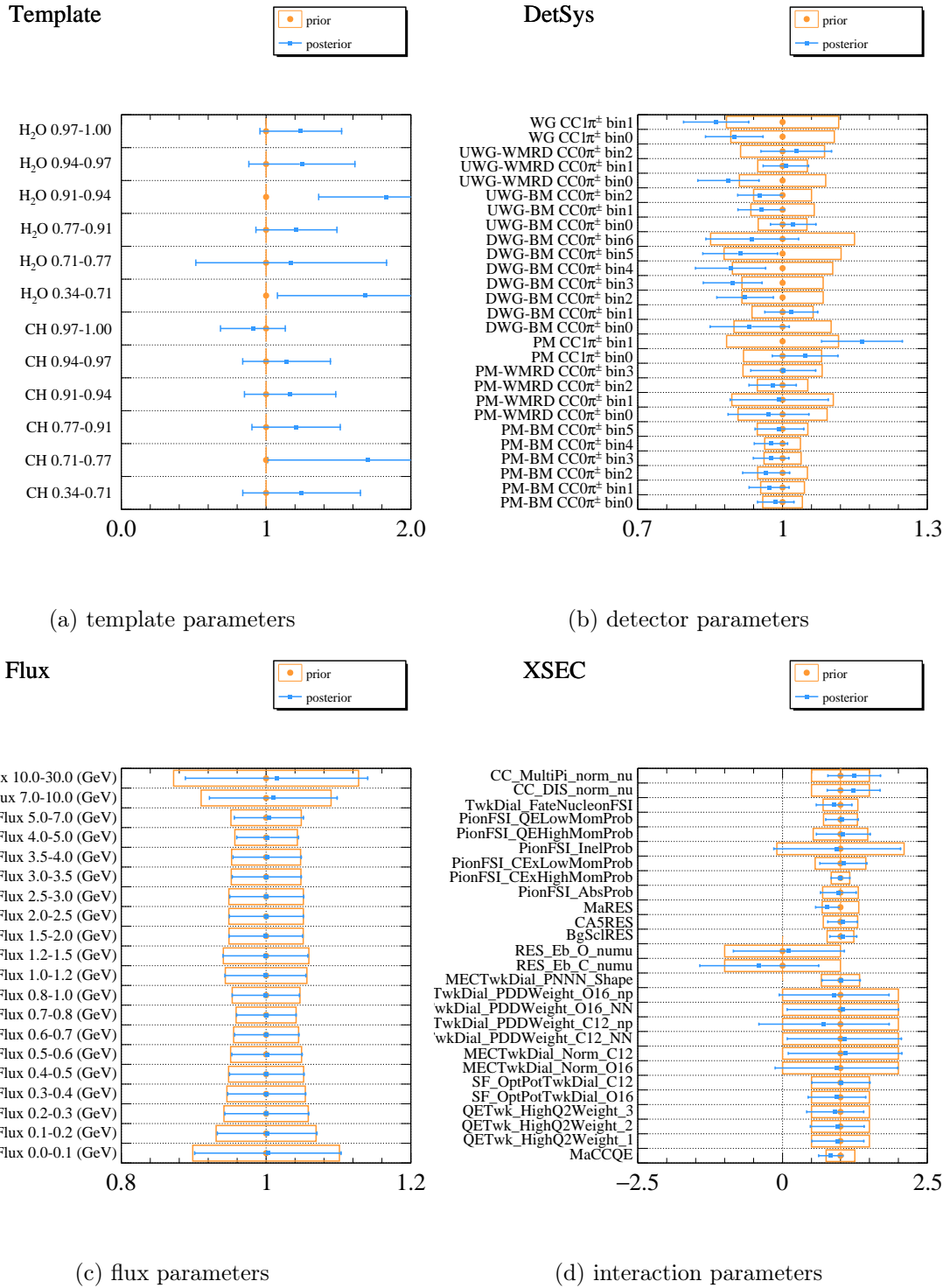
Figure 258: The parameter constraints from the Data fit in the angle distribution. Each posterior result is presented by a best-fit point and error bar (blue dot and line) against its prior parameter in orange rectangular. The error is calculated based on the gaussian assumption of each parameter distribution.
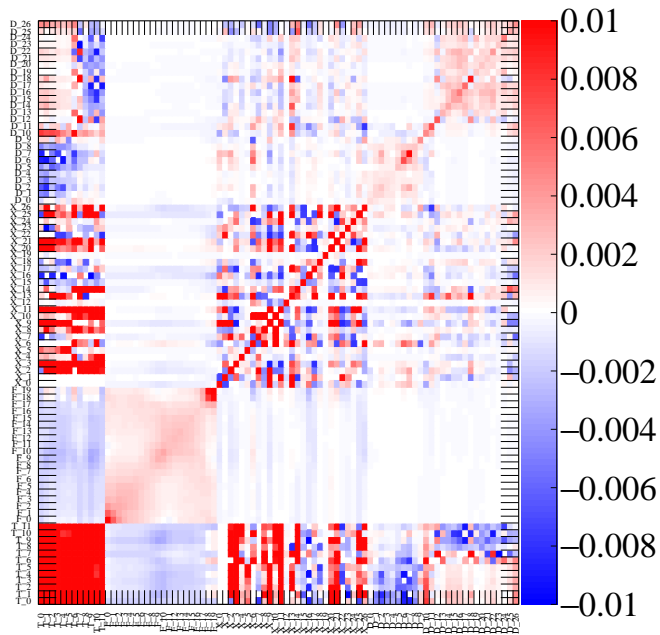
(a) Covariance matrix
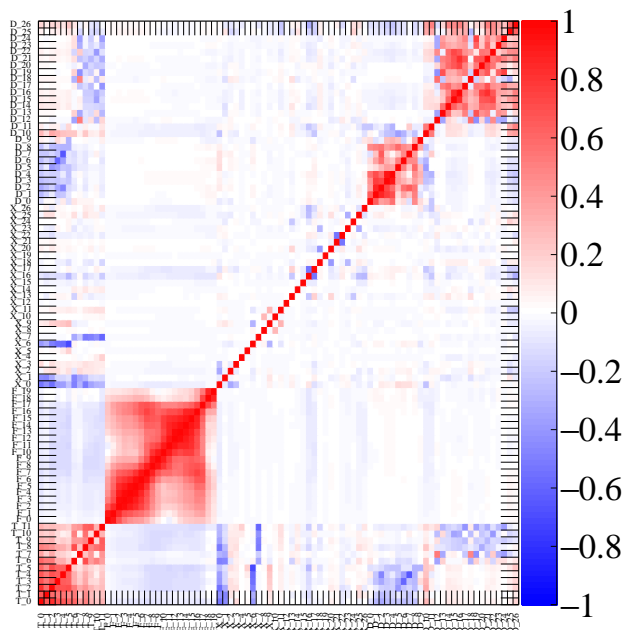
(b) Correlation matrix

Figure 259: Post-fit covariance and correlation matrices for the angle distribution. The horizontal and vertical axis refers to fitting parameter ID; "T", "F", "X", "D" refer to "Template", "Flux systematic", "Xsec systematic", "Detector systematic" parameters.

(a) Comparison of event distributions
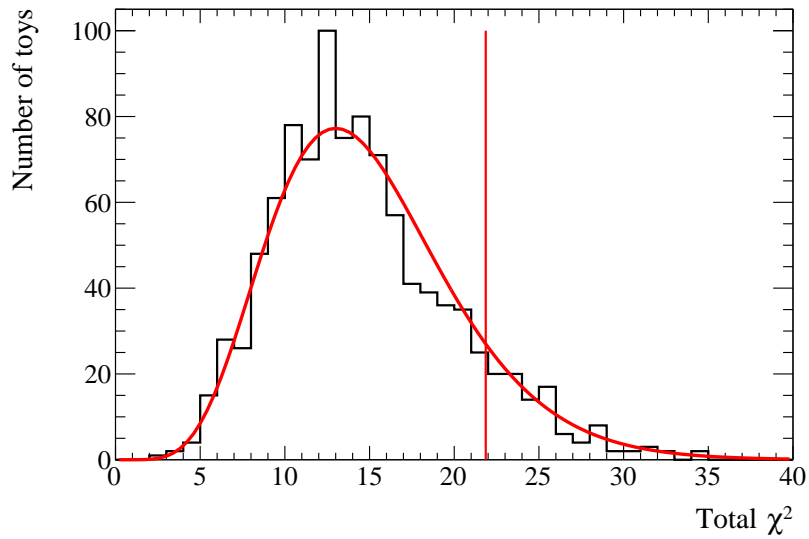
(b) p-value test

Figure 260: Comparisons of bin-by-bin event distributions between post-fit and pre-fit (top) and the coverage plot along with the total χ^2 for the data fit in the angle distribution. The upper plot includes the corresponding χ^2 as metrics defined in Equation P.1. For the coverage plot, the data χ^2 is overlaid in the vertical red line.

List of Tables

List of Figures

370

References

[1] W. Pauli. Dear radioactive ladies and gentlemen [1930]. *Phys.Today*, 31N9(27), 1978.

[2] F. Reines C.L.Cowan et al. Detection of the Free Antineutrino. *Phys. Rev.*, 117(1), January 1960.

[3] G. Danby et al. OBSERVATION OF HIGH ENERGY NEUTRINO REACTIONS AND THE EXISTENCE OF TWO KINDS OF NEUTRINOS. *Phys. Rev. L*, 9(1), July 1962.

[4] K. Kodama et al. (DONUT collaboration). Observation of tau neutrino interactions. *Phys. Lett. B*, 504:218–244, 2001.

[5] Y. Fukuda et al. (Super-Kamiokande Collaboration). Evidence for oscillation of atmospheric neutrinos. *Phys. Rev. L*, 81(1562), August 1998.

[6] B.T. Cleveland et al. Measurement of the solar electron neutrino flux with the HOMESTAKE chlorine detector. *Astrophys. J.*, 496(505), March 1998.

[7] K.S.Hirata et.al. Observation of ^{8}B Solar Neutrinos in the Kamiokande-II Detector. *Phys. Rev. L*, 63(16), April 1989.

[8] J.N.Abdurashitova et al. Results from SAGE (the Russian-American gallium solar neutrino experiment). *Phys. Lett. B*, 328(1-2):234–248, May 1994.

[9] Q. R. Ahmad et al. (SNO Collaboration). Direct Evidence for Neutrino Flavor Transformation from Neutral-Current Interactions in the Sudbury Neutrino Observatory. *Phys. Rev. L*, 89(011301), June 2002.

[10] Y. Nakajima et al. (Super-Kamiokande Collaboration). Recent results and future prospects from Super-Kamiokande. *The XXIX International Conference on Neutrino Physics and Astrophysics (NEUTRINO2020)*, 2020.

[11] T. Araki et al. (KamLAND Collaboration). Measurement of Neutrino Oscillation with KamLAND: Evidence of Spectral Distortion. *Phys. Rev. L*, 94(081801), March 2005.

[12] F. P. An et al. Observation of Electron-Antineutrino Disappearance at Daya Bay. *Phys. Rev. L*, 108(171803), April 2012.

[13] J. K. Ahn et al. (RENO collaboration). Observation of Reactor Electron Antineutrinos Disappearance in the RENO Experiment. *Phys. Rev. L*, 108(191802), May 2012.

[14] Y. Abe et al. Measurement of θ_{13} in Double Chooz using neutron captures on hydrogen with novel background rejection techniques. *JHEP*, 01(163), January 2016.

[15] M jiang et al. (Super-Kamiokande Collaboration). Atmospheric neutrino oscillation analysis with improved event reconstruction in Super-Kamiokande IV. *PTEP*, 2019(5), May 2019.

[16] K. Abe et al. (T2K Collaboration). Improved constraints on neutrino mixing from the T2K experiment with 3.13×10^{21} protons on target. *Phys. Rev. D*, 103(112008), June 2021.

[17] K. Abe et al. (T2K Collaboration). T2K measurements of muon neutrino and antineutrino disappearance using 3.13×10^{21} protons on target. *Phys. Rev. D*, 103(L011101), 2021.

[18] H. Burkhardt et al. (CERN-Dortmund-Edinburgh-Mainz-Orsay-Pisa-Siegen Collaboration). First evidence for direct CP violation. *Phys. Lett. B*, 206(1):169–176, May 1988.

[19] M. Tanabashi et al. (Particle Data Group). Review of particle physics. *Phys. Rev. D*, 98(030001), 2018.

[20] Plank collaboration: N. Aghanium et al. Plank 2018 results. *A & A*, 641(A6), 2020.

[21] A.D. Sakharov. Violation of CP Invariance, C asymmetry, and baryon asymmetry of the universe. *Pisma Zh.Eksp.Teor.Fiz.*, 5:32–35, 1967.

[22] M.Fukugita T.Yanagida. Baryogenesis without Grand Unification. *Phys. Lett. B*, 174(1), June 1986.

[23] W. Buchmuller. Leptogenesis: Theory Neutrino & Masses. *Nuclear Physics B Proceedings Supplement*, 00:1–7, 2018.

[24] Yuta Hamada Ryuichiro Kitano. Primordial Lepton Oscillations and Baryogenesis. *arXiv*, 1609(05028), October 2016.

[25] Pablo F. de Salas Stefano Gariazzo Olga Mena Christoph A Ternes and Mariam Tórtola. Neutrino Mass Ordering From Oscillations and Beyond: 2018 Status and Future Prospects. *In Astronomy and Space Sciences*, 5(36), 2018.

[26] Julien Lesgourgues and Sergio Pastor. Neutrino Mass from Cosmology. *Advances in High Energy Physics*, 2012(608515):34, 2012.

[27] Antony Lewisa Anthony Challinor. Weak gravitational lensing of the CMB. *Physics Reports*, 429:1–65, 2006.

[28] Yashar Akrami F. Arroja M. Ashdown J. Aumont C. Baccigalupi et al. Planck 2018 results: X. constraints on inflation. *A & A*, 641, 2020.

[29] Zhi zhong Xing Zhen-hua Zhao. A review of mu-tau flavor symmetry in neutrino physics. https://arxiv.org/abs/1512.04207v2, 2016.

[30] P. F. Harrison W.G. Scott. $\mu - \tau$ reflection symmetry in lepton mixing and neutrino oscillations. *Phys. Lett. B*, 547(3-4), November 2002.

[31] R. N. Mohapatr S.Nasri Hai-boYu. Leptogenesis, $\mu - \tau$ symmetry and θ_{13}. *Phys. Lett. B*, 615(3-4):231–239, June 2005.

[32] Jiro Arafune Masafumi Koike and Joe Sato. CP violation and matter effect in long baseline neutrino oscillation experiments. *Phys. Rev. D*, 56(3093), September 1997.

[33] Kai Zuber. *Neutrino Physics*. CRC Press, third edition edition, 2020.

[34] L. Wolfenstein. Neutrino oscillations in matter. *Phys. Rev. D*, 17(9), May 1978.

[35] A.Yu. Mikheev, S.P.; Smirnov. Resonance amplification of oscillations in matter and spectroscopy of solar neutrinos. *Yadernaya Fizika*, 17(24):1441–1448, 1985.

[36] John F. Beacom Shaomin Chen et al. Solar models and solar neutrino oscillations. *New Journal of Physics*, 6(63), 2004.

[37] V.N.Gavrina et al. Solar neutrino results from SAGE. *Nucl. Phys. B*, 91(1-3):36–43, January 2001.

[38] J. N. Abdurashitov et al. Measurement of the solar neutrino capture rate with gallium metal. III. Results for the 2002–2007 data-taking period. *Phys. Rev. C*, 80(015807), July 2009.

[39] P. Anselmann et al. Gallex results from the first 30 solar neutrino runs. *Phys. Lett. B*, 327(377), May 1994.

[40] P. Anselmann et al. Gallex solar neutrino observations: Complete results for gallex II. *Phys. Lett. B*, 357(237), 1995.

[41] W. Hampel et al. Gallex solar neutrino observations: Results for gallex III. *Phys. Lett. B*, 388(2), 1996.

[42] M. Altmann. Complete results for five years of GNO solar neutrino observations. *Phys. Lett. B*, 616(174), April 2005.

[43] S. Fukuda et al. (Super-Kamiokande Collaboration). Solar ^{8}B and hep Neutrino Measurements from 1258 Days of Super-Kamiokande Data. *Phys. Rev. L*, 86(5651), June 2001.

[44] S. Fukuda et al. (Super-Kamiokande Collaboration). Determination of solar neutrino oscillation parameters using 1496 days of Super-Kamiokande-I data. *Phys. Lett. B*, 539(179), July 2002.

[45] J. P. Cravens et al. (Super-Kamiokande Collaboration). Solar neutrino measurements in Super-Kamiokande-II. *Phys. Rev. D*, 78(032002), August 2008.

[46] K. Abe et al. (Super-Kamiokande Collaboration). Solar neutrino results in Super-Kamiokande-III. *Phys. Rev. D*, 83(052010), March 2011.

[47] J. Hosaka et al. (Super-Kamiokande Collaboration). Solar neutrino measurements in Super-Kamiokande-I. *Phys. Rev. D*, 73(112001), June 2006.

[48] B. Aharmim et al. (SNO collaboration). Combined analysis of all three phases of solar neutrino data from the Sudbury Neutrino Observatory. *Phys. Rev. C*, 88(025501), August 2013.

[49] C. Arpesella et al. (Borexino Collaboration). Direct Measurement of the ^{7}Be Solar Neutrino Flux with 192 Days of Borexino Data. *Phys. Rev. L*, 101(091302), August 2008.

[50] PDG. *PDG live.* https://pdglive.lbl.gov/.

[51] M. Apollonio et al. Limits on Neutrino Oscillations from the CHOOZ Experiment. *Phys. Lett. B*, 8466(415), July 1999.

[52] B. Achkar et al. Search for neutrino oscillations at 15, 40 and 95 meters from a nuclear power reactor at Bugey. *Nucl. Phys. B*, 434(503), 1995.

[53] K. Abe et al. (T2K Collaboration). Constraint on the matter–antimatter symmetry-violating phase in neutrino oscillations. *Nature*, 580:339–344, June 2020.

[54] Ivan Esteban Ivan Esteban et al. The fate of hints: updated global analysis of three-flavor neutrino oscillations. *Journal of High Energy Physics*, 09(178), September 2020.

[55] High intensity Proton Accelerator Project Team. Kek report, accelerator technical design report for high-intensity proton accelerator facility project, j-parc. https://cds.cern.ch/record/747209/files/34072617.pdf, March 2003.

[56] K. Abe et al. (T2K Collaboration). The T2K experiment. *NIM. A*, 659(11):106–135, December 2011.

[57] K. Matsuoka et al. Design and performance of the muon monitor for the t2k neutrino oscillation experiment. *NIM. A*, 624:591–600, September 2010.

[58] C E Doust S J Harris. Energy per ion pair measurements in pure helium and helium mixtures. *Radiat Res.*, 66(1), April 1976.

[59] A. Astbury et al. A 4π Solid Angle Detector for the SPS Used as a Proton-Antiproton Collider at a Centre of Mass Energy of 540 GeV. CERN-SPSC-78-06, January 1978.

[60] S. Aoki et al. The T2K Side Muon Range Detector (SMRD). *NIM. A*, 698:135–146, October 2013.

[61] P.A. Amaudruz et al. The T2K Fine-Grained Detectors. *NIM. A*, 696:1–31, April 2012.

[62] S. Assylbekov et al. The T2K ND280 off-axis pi–zero detector. *NIM. A*, 686:48–63, 2012.

[63] N.Abgrall et al. Time projection chambers for the T2K near detectors. *NIM. A*, 637(1):25–46, May 2011.

[64] D. Allan et al. The electromagnetic calorimeter for the T2K near detector ND280. *Jinst*, 8(P10019), October 2013.

[65] HAMAMATSU. MPPC (Multi-Pixel Photon Counter). https://www.hamamatsu.com/, October 2022.

[66] Y.Itow et al. The JHF-Kamioka neutrino project. arXiv:hep-ex/0106019v1, June 2001.

[67] K. Abe et al. (T2K Collaboration). Measurements of neutrino oscillation parameters from the T2K experiment using 3.6×10^{21} protons on target. *Eur. Phys. J. C*, 83(782), 2023.

[68] Christophe Bronner for the T2K collaboration. Accelerator Neutrino 1 Recent results from T2K. https://zenodo.org/record/6683821, June 2022.

[69] K. Abe et al. (T2K collaboration). Scintillator ageing of the T2K near detectors from 2010 to 2021. *JINST*, 17(P10028), September 2022.

[70] M.Sajjad Ather S.K. Singh. *The Physics of Neutrino Interactions*. Cambridge University Press, 2020.

[71] J. A. Formaggio and G. P. Zeller. From eV to EeV: Neutrino cross sections across energy scales. *Rev. Mod. Phys.*, 84(1307), September 2012.

[72] D. Casper. The nuance neutrino physics simulation, and the future. *Nuclear Physics B - Proceedings Supplements*, 112(1-3):161–170, November 2002.

[73] N. J. Baker et al. Total cross sections for $\nu_\mu n$ and $\nu_\mu p$ charged-current interactions in the 7-foot bubble chamber. *Phys. Rev. D*, 25(617), February 1982.

[74] D.S. Baranov et al. Measurement of the $\nu_\mu n$ total cross section at 2–30 gev in a skat neutrino experiment. *Phys. Lett. B*, 81(2):255–257, February 1979.

[75] Ciampolillo. S. et al. (Gargamelle Neutrino Propane Collaboration and Aachen-Brussels-CERN-Ecole Poly-Orsay-Padua Collaboration). Total cross section for neutrino charged current interactions at 3 GeV and 9 GeV. *Phys. Lett. B*, 84(2):281–284, June 1979.

[76] Y. Nakajima et al. (SciBooNE Collaboration). Measurement of inclusive charged current interactions on carbon in a few-gev neutrino beam. *Phys. Rev. D*, 83(012005), January 2011.

[77] C.H. Llewellyn Smith. Neutirno reactions at accelerator energies. *Physics Reports*, 3(5), 1971.

[78] F. Bumiller M. Croissiaux E. Dally and R. Hofstadter. Dirac and Pauli Form Factors of the Proton. *Phys. Rev.*, 124(1623), Decemeber 1961.

[79] R. Hofstadter C. de Vries and Robert Herman. Dirac and Pauli Form Factors of the Neutron. *Phys. Rev. L*, 6(290), 1961.

[80] T. Kitagaki et al. High-energy quasielastic $\nu_\mu n \rightarrow \mu^- p$ scattering in deuterium. *Phys. Rev. D*, 28(436), 1983.

[81] V. Lyubushkin et al. A study of quasi-elastic muon neutrino and antineutrino scattering in the NOMAD experiment. *Eur. Phys. J. C*, 63(355), 2009.

[82] L. Fields et al. (MINERVA Collaboration). Measurement of Muon Antineutrino Quasielastic Scattering on a Hydrocarbon Target at $E_\nu \sim 3.5$GeV. *Phys. Rev. L*, 111(022501), 2013.

[83] K. Abe et al. (T2K Collaboration). Measurement of the ν_μ charged-current quasielastic cross section on carbon with the ND280 detector at T2K. *Phys. Rev. D*, 92(112003), 2015.

[84] L. Tiator D. Drechsel S. Kamalov M.M. Giannini E. Santopinto and A. Vassallo. Electroproduction of nucleon resonances. *Eur. Phys. J. A*, 19(Suppl 1):55–60, 2004.

[85] Olga Lalakulich Emmanuel A. Paschos and Giorgi Piranishvili. Resonance production by neutrinos: The second resonance region. *Phys. Rev. D*, 74(014009), 2006.

[86] Krzysztof M. Graczyk and Jan T. Sobczyk. Form factors in the quark resonance model. *Phys. Rev. D*, 77(053001), July 2008.

[87] T. Kitagaki et al. Charged-current exclusive pion production in neutrino-deuterium interactions. *Phys. Rev. D*, 34(2554), 1986.

[88] T. Kitagaki et al. Study of $\nu d \rightarrow \mu^- p p_s$ and $\nu d \rightarrow \mu^- \Delta^{++}(1232)$ ns using the BNL 7-foot deuterium-filled bubble chamber. *Phys. Rev. D*, 42(1331), 1990.

[89] G. M. Radecky et al. Study of single-pion production by weak charged currents in low-energy νd interactions. *Phys. Rev. D*, 25(1161), 1982.

[90] C. M. Marshall et al. (MINERvA Collaboration). Measurement of K^+ production in charged-current ν_μ interactions. *Phys. Rev. D*, 94(012002), 2016.

[91] CHARM Collaboration J. V. Allaby et al. Total cross sections of charged-current neutrino and antineutrino interactions on isoscalar nuclei. *Zeitschrift für Physik C Particles and Fields*, 38:403–410, 1988.

[92] S. M. Berman. Lectures on weak interactions. CERN seminars, 1961.

[93] R. A. Smith E.J. Moniz. Neutrino reactions on nuclear targets. *Nucl. Phys. B*, 43(605), 1972.

[94] T. K. Gaisser and J. S. O'Connell. Interactions of atmospheric neutrinos in nuclei at low energy. *Phys. Rev. D*, 34(822), August 1986.

[95] C. W. De Jager H. De Vries and C. De Vries. Nuclear charge- and magnetization-density-distribution parameters from elastic electron scattering. *Atomic Data and Nuclear Data Tables*, 14(5-6):479–508, November-December 1974.

[96] H. De Vries C. W. De Jager C. De Vries. Nuclear charge-density-distribution parameters from elastic electron scattering. *Atomic Data and Nuclear Data Tables*, 36(3):495–536, May 1987.

[97] M. Martini and M. Ericson. Quasielastic and multinucleon excitations in antineutrino-nucleus interactions. *Phys. Rev. C*, 87(065501), June 2013.

[98] J. Nieves I. Ruiz Simo M.J. Vicente Vacas. Two particle–hole excitations in charged current quasielastic antineutrino-nucleus scattering. *Phys. Lett. B*, 721(1-3), April 2013.

[99] A. A. Aguilar-Arevalo et al. (MiniBooNE Collaboration). First measurement of the muon neutrino charged current quasielastic double differential cross section. *Phys. Rev. D*, 81(092005), 2010.

[100] L.Alvarez-Ruso Y.Hayato and J.Nieves. Progress and open questions in the physics of neutrino cross sections at intermediate energies. *New Journal of Physics*, 16(075015), July 2014.

[101] Dieter. Rein Lalit. MSehgal. Neutrino-Excitation of Baryon Resonances and Single Pion Production. *Annals of Physics*, 133(1):79–153, April 1981.

[102] Stephen L. Adler. Tests of the Conserved Vector Current and Partially Conserved Axial-Vector Current Hypotheses in High-Energy Neutrino Reactions. *Phys. Rev.*, 137(B4), March 1965.

[103] L. Alvarez-Ruso L. S. Geng S. Hirenzaki S. Hirenzaki and M. J. Vicente Vacas. Charged current neutrino-induced coherent pion production. *Phys. Rev. C*, 75, May 2009.

[104] N. G. Kelkar E. Oset and P. Fernández de Córdoba. Coherent pion production in neutrino nucleus collision in the 1 GeV region. *Phys. Rev. C*, 55(1), April 1997.

[105] S. K. Singh M. Sajjad Athar and Shakeb Ahmad. Nuclear Effects in Neutrino Induced Coherent Pion Production at K2K and MiniBooNE. *Phys. Rev. L*, 96(241801), June 2006.

[106] R. J. Glauber. Lectures on Theoretical Physics. *Interscience*, 1, 1959.

[107] M.J. Vicente-Vacas M.Kh. Khankhasayev S.G. Mashnik. Inclusive Pion Double Charge Exchange above 0.5 GeV. *arXiv*, Decemeber 1994.

[108] M. SAJJAD ATHAR S. CHAUHAN S. K. SINGH and M. J. VICENTE VACAS. NEUTRINO NUCLEUS CROSS-SECTIONS. *International Journal of Merdern Physics E*, 18(7):1469–1481, 2009.

[109] O. Buss et al. Transport-theoretical Description of Nuclear Reactions. *Phys. Rept*, 512:1–124, 2012.

[110] Tomasz Golan Cezary Juszczak and Jan T. Sobczyk. Effects of final-state interactions in neutrino-nucleus interactions. *Phys. Rev. C*, 86(015505), July 2012.

[111] C.Andreopoulos et al. The GENIE neutrino Monte Carlo generator. *NIM. A*, 614(1):87–104, February 2010.

[112] Y. Hayato. NEUT. *Nucl. Phys. B*, 112(171), November 2002.

[113] P. A. Rodrigues. Comparing pion production models to MiniBooNE data. *AIP Conference Proceedings*, 1189(189), May 2015.

[114] A. A. Aguilar-Arevalo et al. (MiniBooNE Collaboration). Measurement of neutrino-induced charged-current charged pion production cross sections on mineral oil at $e_\nu \simeq 1\text{GeV}$. *Phys. Rev. D*, 83(052007), March 2011.

[115] M Sajjad Athar S Chauhan and S K Singh. The CC1π^+ to CCQE cross section ratio at accelerator energies. *J. Phys. G: Nucl. Part. Phys.*, 37(015005), 2010.

[116] J. Nieves I. Ruiz Simo and M. J. Vicente Vacas. The nucleon axial mass and the miniboone quasielastic neutrino-nucleus scattering problem. *Phys. Lett. B*, 707:72–75, 2012.

[117] T.T. Bohlen et al. The FLUKA Code: Developments and Challenges for High Energy and Medical Applications. *Nuclear Data Sheets*, 120:211–214, 2014.

[118] K. Abe et al. (T2K Collaboration). T2k neutrino flux prediction. *Phys. Rev. D*, 87(012001), 2013.

[119] N. Abgrall et al. (NA61/SHINE Collaboration). Measurements of $\pi^\pm, K^\pm, K_S^0, \Lambda$ and proton production in proton-carbon interactions at 31 GeV/c with the NA61/SHINE spectrometer at the CERN SPS. *Eur. Phys. J. C*, 76(84), 2016.

[120] N. Abgrall et al. (NA61/SHINE Collaboration). Measurement of $\pi^\pm$ differential yields from the surface of the T2K replica target for incoming 31 GeV/c protons with the NA61/SHINE spectrometer at the CERN SPS. *Eur. Phys. J. C*, 76(617), 2016.

[121] N. Abgrall et al. (NA61/SHINE Collaboration). Measurement of $\pi^\pm, K^\pm$ and proton double differential yields from the surface of the T2K replica target for incoming 31 GeV/c protons with the NA61/SHINE spectrometer at the CERN SPS. *Eur. Phys. J. C*, 79(100), 2019.

[122] L. Pickering Y. Hayato. The NEUT neutrino interaction simulation program library. *Eur. Phys. J. Spec. Top.*, 230:4469–4481, October 2021.

[123] K. Abe et al. (T2K Collaboration). Characterization of nuclear effects in muon-neutrino scattering on hydrocarbon with a measurement of final-state kinematics and correlations in charged-current pionless interactions at T2K. *Phys. Rev. D*, 98(032003), 2018.

[124] R.Bradford A.Bodeka H.Budda J.Arrington. A New Parameterization of the Nucleon Elastic Form Factors. *Nucl. Phys. B (Proc. Suppl.)*, 159:127–132, 2006.

[125] M. Martini M. Ericson G. Chanfray and J. Marteau. Unified approach for nucleon knockout and coherent and incoherent pion production in neutrino interactions with nuclei. *Phys. Rev. C*, 80(065501), 2009.

[126] I. Ruiz Simo J. E. Amaro M. B. Barbaro A. De Pace J. A. Caballero and T. W. Donnelly. Extensions of superscaling from relativistic mean field theory: The SuSAv2 model. *Phys. Rev. C*, 90(035501), September 2014.

[127] Ch. Berger L. M. Sehgal. Lepton mass effects in single pion production by neutrinos. *Phys. Rev. D*, 76(113004), December 2007.

[128] Krzysztof M. Graczyk and Jan T. Sobczyk. Form factors in the quark resonance model. *Phys. Rev. D*, 77(053001), 2008.

[129] M.Hasegawa et al. Search for Coherent Charged Pion Production in Neturino-Carbon interactions. *Phys. Rev. L*, 95(252301), December 2005.

[130] D.Rein L.M.Sehgal. PCAC and the deficit of forward muons in π^+ production by neutrinos. *Phys. Lett. B*, 657:207–209, October 2007.

[131] Ch. Berger and L. M. Sehgal. Partially conserved axial vector current and coherent pion production by low energy neutrinos. *Phys. Rev. D*, 79:053003, Mar 2009.

[132] A. Bodek and U. K. Yang. Modeling Neutrino and Electron Scattering Cross Sections in the Few GeV Region with Effective LO PDFs. *AIP Conference Proceedings*, 670(110), July 2003.

[133] P. Gueye et al. Coulomb distortion measurements by comparing electron and positron quasielastic scattering off ^{12}C and ^{208}Pb. *Phys. Rev. C*, 60(044308), September 1999.

[134] D. Ruterbories et al. (MINERvA Collaboration). Measurement of quasielatic-like neutrino scattering at $\langle E_\nu \rangle \sim 3.5$ GeV on a hydrocarbon target. *Phys. Rev. D*, 99(012004), January 2019.

[135] P.A. Rodrigues et al. (MINERvA Collaboration). Identification of Nuclear Effects in Neutrino-Carbon Interactions at Low Three-Momentum Transfer. *Phys. Rev. L*, 116(071802), February 2016.

[136] K. Abe et al. (T2K Collaboration). First combined measurement of the muon neutrino and antineutrino charged-current cross section without pions in the final state at T2K. *Phys. Rev. D*, 101(112001), 2020.

[137] K. Abe et al. (T2K Collaboration). Simultanuous measurement of the muon neutrino charged-current cross section on oxygen and carbon without pions in the final state at T2K. *Phys. Rev. D*, 101(112004), 2020.

[138] C. Maieron T. W. Donnelly and Ingo Sick. Extended superscaling of electron scattering from nuclei. *Phys. Rev. C*, 65(025502), January 2002.

[139] P. Stowell et al. (NUISANCE collaboration). NUISANCE: a neutrino cross-section generator tuning and comparison framework. *Jinst*, 12(01), January 2017.

[140] N. J. Baker et al. Quasielastic neutrino scattering: A measurement of the weak nucleon axial-vector form factor. *Phys. Rev. D*, 23(2499), 1981.

[141] Callum Wilkinson Philip Rodrigues Susan Cartwright Lee Thompson and Kevin McFarland. Reanalysis of bubble chamber measurements of muon-neutrino induced single pion production. *Phys. Rev. D*, 90(112017), December 2014.

[142] A. Higuera et al. (MINERνA Collaboration). Measurement of Coherent Production of $\pi^{\pm}$ in Neutrino and Antineutrino Beams on Carbon from E_ν of 1.5 to 20 GeV. *Phys. Rev. L*, 113(261802), December 2014.

[143] Rene Brun and Fons Rademakers. ROOT - An Object Oriented Data Analysis Framework. *Nucl. Inst. and Meth. in Phys. Res. A*, 389:81–86, September 1996.

[144] Roger Barlow and Christine Beeston. Fitting using finite monte carlo samples. *Computer Phyiscs Communications*, 77:219–228, March 1993.

[145] J. S. Conway. Incorporating Nuisance Parameters in Likelihoods for Multisource Spectra. Proceedings of the PHYSTAT 2011 Workshop on Statistical Issues Related to Discovery Claims in Search Experiments and Unfolding, January 2011.

[146] S. S. Wilks. The large-sample distribution of the likelihood ratio for testing composite hypotheses. *Ann. Math. Statist.*, 9(1):60–62, March 1938.

[147] G.J. Feldman and R.D. Cousins. A unified approach to the classical statistical analysis of small signals. *Phys. Rev. D*, 57:3873–3889, 1998.

[148] The T2K collaboration. Oscillation results from Neutrino 2020. https://t2k-experiment.org/results/, October 2020.

[149] Linyan Wan. Atmospheric neutrino: Super-K. Zenodo. https://doi.org/10.5281/ zenodo.6694761, June 2022.

[150] Roger Wendell. SK atmospheric oscillation analysis 2022 (preliminary) results. https://indico-sk.icrr.u-tokyo.ac.jp/event/7543/, June 2022.

[151] P. Adamson et al. (MINOS+ collaboration). Precision Constraints for Three-Flavor Neutrino Oscillations from the Full MINOS+ and MINOS Dataset. *Phys. Rev. L*, 125(13)(131802), 2020.

[152] M. A. Acero et al. (The NOvA collaboration). Improved measurement of neutrino oscillation parameters by the NOvA experiment. *Phys. Rev. D*, 106(032004), 2022.

[153] Melissa Clegg and NOvA collaboration. Nova 2020 official data release (13.6e20 neutrino + 12.5e20 antineutrino) (public document 17-v1). https://publicdocs.fnal.gov/cgi-bin/ShowDocument?docid=17, August 2021.

[154] Tom Stuttard. Atmospheric neutrino: Particle physics with atmospheric neutrinos at IceCube. Zenodo. https://doi.org/10.5281/zenodo.6694972, June 2022.

[155] Alex Himmel for the NOvA collaboration. New Oscillation Results from the NOvA Experiment. 10.5281/zenodo.3959581, 2020.

[156] K. Abe et al. (T2K Collaboration). First measurement of the ν_μ charged-current cross section on the water target without pions in the final state. *Phys. Rev. D*, 97(012001), January 2018.

[157] Kenji Yasutome for the T2K collaboration. First physics run of the wagasci-babymind detector with full setup. Proceedings, 21st International Workshop on Neutrinos from Accelerators (Nufact19) : Daegu, Korea, August 26-31, 2019, March 2020.

[158] K. Abe et al. (T2K Collaboration). First measurement of the ν_μ charged-current cross section on a water target without pions in the final state. *Phys. Rev. D*, 97(012001), January 2018.

[159] KURARAY CO. Wavelength shifting fibers. http://kuraraypsf.jp/psf/ws.html.

[160] K. Abe et al. (T2K Collaboration). Measurements of $\bar{\nu}u_\mu$ and $\bar{\nu}u_\mu + \nu_\mu$ charged-current cross-sections without detected pions or protons on water and hydrocarbon at a mean anti-neutrino energy of 0.86 GeV. *PTEP*, 2021(043C01), March 2021.

[161] Omega. Spiroc 2 user guide. https://www.omegawatches.com/customer-service/user-manuals, 2009.

[162] S. Agmad et al. OMEGA SiPM readout ASICs. *NIM. A*, 986(11), 2021.

[163] T. Kikawa et al. (the T2K collaboration). Development of the new t2k on-axis neutrino detector, ingrid proton module. *Nucl. Phys. B*, 229-232:451, 2012.

[164] J.Estrada C.Garcia B.Hoenison and P.Rubinov. MCM II and the Trip chip. D0 note 4009, 2003.

[165] Gabriella Rolando et al. (BabyMIND collaboration). New and Optimized Magnetization Scheme for the Baby Magnetized Iron Neutrino Detector at J-PARC. *IEEE Trans Magnetics*, 53-5(8000706), Februaly 2017.

[166] Martin Gardner. The fantastic combinations of john conway's new solitaire game 'life'. *Scentific American,*, 223, 1970.

[167] Particle Data Group. Muons in iron (fe), 2015.

[168] Procédé du Commandant Cholesky. Note sur une méthode de résolution des équations normales provenant de l'application de la méthode des moindres carrés à un système d'équations linéaires en nombre inférieur à celui des inconnues. *Bulletin Géodésique*, 2:66–67, 1924.

[169] J. Beringer et al. (Particle Data Group). Review of particle physics. *Phys. Rev. D*, 86(010001), July 2012.

[170] M. Tanabashi *et al.* Review of Particle Physics, Phys. Rev. D 98, 030001 (2018) and 2019 update. `http://pdg.lbl.gov/2019/tables/contents_tables.html`, 2019.

[171] M. Martini, G. Chanfray, M. Ericson, and J. Marteau. Neutrino interactions with nuclei. *AIP Conf. Proc.*, 1189(1):323–326, 2009.

[172] Jachowicz N., Heyde K., Ryckebusch J., and S. Rombouts. Continuum random phase approximation approach to charged current neutrino nucleus scattering. *Phys. Rev. C*, 65:025501, 2002.

[173] Pandey V., Jachowicz N., Van Cuyck T., Ryckebusch J., and M. Martini. Low-energy excitations and quasielastic contribution to electron-nucleus and neutrino-nucleus scattering in the continuum random-phase approximation. *Phys. Rev. C*, 92(2):024606, 2015.

[174] Martin Gardner. The fantastic combinations of john conway's new solitaire game 'life'. *Scentific American*, 223, October 1970.

[175] PDG. Muons in iron (fe).

[176] Gabriella Rolando et al. New and optimized magnetization scheme for the baby magnetized iron neutrino detector at j-parc. *IEEE TRANSACTIONS ON MAGNETICS*, 53, February 2017.

[177] J. Nieves I. Ruiz Simo and M. J. Vicente Vacas. Inclusive charged-current neutrino-nucleus reactions. *Phys. Rev. C*, 83(045501), April 2011.

[178] C. L. McGivern et al. (MINERvA collaboration). Cross section for ν_μ and $\bar{\nu}_\mu$ induced pion production on hydrocarbon in the few-GeV region using MINERvA. *Phys. Rev. D*, 94(052005), 2016.

[179] P. Adamson et al. (MINOS collaboration). Study of quasielastic scattering using charged-current ν_μ-iron interactions in the minos near detector. *Phys. Rev. D*, 91(012005), 2015.

[180] Teppei Katori. Meson Exchange Current (MEC) Models in Neutrino Interaction Generators. arXiv:1304.6014v3, April 2011.

[181] S. A. Dytman and A. S. Meyer. Final State Interactions in GENIE. *AIP Conference Proceedings*, 1405(213), Novemenber 2011.